

TABLE OF CONTENTS

Abstract	i
Acknowledgements	iii
Co-authorship forms	v
Table of contents	xi
List of figures	xix
List of tables	xxiii
Notation	xxv
Chapter 1 Introduction	1
1.1 Overview	1
1.2 Rocking Walls	2
1.2.1 PreWEC system	4
1.3 Current code provisions	5
1.4 Research motivation	5
1.5 Objectives.....	7
1.6 Scope	8
1.7 Thesis outline	9
1.8 References.....	11
Chapter 2 Literature review	15
2.1 Overview	15
2.2 Rocking behaviour.....	15
2.3 Concrete walls.....	18
2.4 Unbonded PT concrete wall systems	18
2.4.1 PRESSS program	20
2.4.2 Single rocking walls	21
2.4.3 Jointed wall system	22
2.4.4 Hybrid wall system	22
2.4.5 Other sources of energy dissipation in hybrid walls	24
2.4.6 PreWEC system	25
2.5 Section analysis	27
2.6 Unbonded PT systems Dynamic behaviour.....	28
2.6.1 Wall system testing	28

2.6.2	Column testing.....	29
2.6.3	Entire building testing.....	30
2.6.4	Modelling approaches	31
2.6.4.1	Fibre models	31
2.6.4.2	Lumped plasticity models.....	33
2.6.4.3	Multi-spring model	34
2.6.4.4	Finite element models.....	35
2.6.4.5	Other techniques.....	36
2.6.4.6	Conclusions on modelling techniques	37
2.7	Evaluation of damping.....	38
2.7.1	General	38
2.7.2	Contact damping	39
2.8	Codification.....	41
2.9	Design procedures.....	42
2.9.1	DDBD overview	43
2.9.2	EVD in DDBD	45
2.9.2.1	Elastic damping.....	46
2.9.2.2	Hysteretic damping.....	46
2.9.2.3	EVD Design recommendations	48
2.9.2.4	EVD recommendations from NZS3101 and PRESSS Design Handbook.....	49
2.9.3	EVD for jointed type wall systems	50
2.9.3.1	PRESSS programme jointed wall.....	50
2.9.3.2	Priestley et al. [20].....	50
2.9.3.3	NZS3101/PRESSS Design Handbook.....	51
2.10	Residual drift.....	53
2.11	Conclusions.....	53
2.12	References	55
Chapter 3 O-connector testing and design		61
3.1	Introduction.....	61
3.2	Strength and stiffness equations.....	63
3.3	Experimental programme.....	65
3.3.1	Connector specifications	66
3.3.2	Material properties.....	68

3.3.3	Test setup	70
3.3.4	Loading protocol.....	70
3.4	Test Observations and results	71
3.4.1	Test: M1-C1-R-L.....	74
3.4.2	Tests: M2-C2-R-L and M2-S-R-L.....	75
3.4.3	Tests: M3-C2-W-L and M3-C2-R-L	75
3.4.4	Tests: M4-C2-R-WA, M4-C2-W-WA, M4-C2-R-L and M4-C2-W-L	76
3.5	Discussion of results	77
3.5.1	Strength and stiffness calculation	78
3.5.2	Out-of-plane buckling.....	80
3.5.3	Influence of cutting process	80
3.5.4	Influence of steel material	81
3.5.5	Influence of wings	82
3.5.6	Influence of welding process.....	82
3.6	Conclusions.....	83
3.7	References.....	85
Chapter 4 Prototype and model design		87
4.1	Introduction.....	87
4.2	Prototype Building.....	87
4.3	Seismic hazard.....	88
4.4	Displacement based design.....	89
4.5	Prototype wall design.....	93
4.6	Model scaling	95
4.7	Detailed model wall design and construction.....	97
4.7.1	SRW models.....	97
4.7.2	PreWEC models	99
4.7.3	Summary	101
4.7.4	Reinforcement material properties.....	102
4.7.5	O-Connector properties	103
4.8	Chapter summary.....	104
4.9	References.....	106
Chapter 5 Cyclic testing		107
5.1	Experimental programme	107

5.1.1	Wall specifications	108
5.1.2	Material properties.....	109
5.1.3	O-Connector properties.....	109
5.1.4	Test setup	109
5.1.5	Load protocol.....	111
5.1.6	Instrumentation.....	112
5.2	Test observations	113
5.3	Results and discussion	116
5.3.1	Force displacement response.....	116
5.3.2	Initial stiffness.....	117
5.3.3	Equivalent viscous damping	118
5.3.4	Residual drifts	119
5.3.5	Connector behaviour	120
5.3.6	PT force.....	121
5.3.7	Neutral axis depth	123
5.3.8	Concrete strains.....	125
5.4	Influence of O-connectors	127
5.5	Conclusions.....	128
5.6	References	130
Chapter 6 Snap back testing		131
6.1	Introduction.....	131
6.2	Experimental programme.....	132
6.2.1	Wall specifications	132
6.2.2	Material properties.....	133
6.2.3	O-connector properties	133
6.3	Test setup	134
6.4	Test Procedure.....	136
6.5	Observations, results, and discussion	137
6.5.1	Frequency characterisation and stiffness.....	137
6.5.2	Observations and time history response.....	139
6.5.2.1	Displacement decay envelope observations	143
6.5.3	Residual drifts	144
6.5.4	Period dependency with displacement	144

6.5.5	Lateral force displacement behaviour	145
6.5.6	Local parameter response: pseudo-static versus dynamic	148
6.5.7	Equivalent viscous damping (EVD) ratio.....	150
6.5.7.1	Logarithmic decrement theory	150
6.5.7.2	EVD test results	153
6.6	Conclusions.....	156
6.7	References.....	159
Chapter 7	Shake table testing.....	161
7.1	Design and construction of shake table test programme.....	161
7.1.1	Material properties	163
7.1.2	O-connector properties.....	164
7.2	Test setup and instrumentation.....	164
7.3	Testing procedure	166
7.3.1	Ground motion scaling	166
7.3.1.1	NZS1170 scaling and ground motion selection	167
7.3.1.2	Scaling for similitude and shake table limitations.....	172
7.3.2	Test sequence.....	174
7.4	Test observations and white-noise tests.....	177
7.4.1	SRW-ST-A.....	177
7.4.2	PreWEC-ST-A	180
7.4.3	PreWEC-ST-B	181
7.5	Ground motion results and discussion.....	184
7.5.1	Characteristic results.....	184
7.5.2	Summary of key results	187
7.5.3	Sensitivity of results	193
7.5.4	Residual drifts.....	195
7.5.5	DDBD evaluation and ground motion quantification.....	197
7.5.5.1	Ground motion quantification	197
7.5.5.2	Updated design drift determination	200
7.5.5.3	SRW-ST-A.....	201
7.5.5.4	PreWEC walls.....	203
7.5.5.5	Summary	205
7.5.6	Incremental dynamic analyses using shake table results	205

7.6	Harmonic motion results and discussion	209
7.7	Conclusions.....	210
7.8	References.....	213
Chapter 8 Evaluation of damping schemes.....		215
8.1	Introduction.....	215
8.2	Damping scheme theory in current practice.....	216
8.3	SRW numerical analyses.....	217
8.3.1	Model development	217
8.3.2	Damping scheme trials	220
8.3.3	Dynamic backbone best fit model.....	224
8.3.4	Simplified analytical method model (A&S).....	227
8.3.5	Ground motion replication	230
8.3.5.1	Free vibration calibrated damping scheme.....	230
8.3.5.2	Cyclic calibrated damping scheme for ground motions.....	231
8.3.5.3	Summary.....	235
8.4	PreWEC numerical analyses	235
8.4.1	Model development	235
8.4.2	Snap back test replication	240
8.4.3	Ground motion replication.....	242
8.4.3.1	PreWEC-ST-A.....	243
8.4.3.2	PreWEC-ST-B.....	244
8.5	Conclusions and recommendations	246
8.6	References.....	248
Chapter 9 Direct displacement based design evaluation.....		249
9.1	Introduction.....	250
9.2	EVD in DDBD summary	250
9.3	Yield displacement and ductility.....	252
9.3.1	Yield displacement assessment.....	254
9.4	EVD recommendations.....	257
9.4.1.1	Method #1A: Priestley et al. (2007) - Ideal flag-shape hysteresis.....	257
9.4.1.2	Method #1B: Method #1A with effective stiffness for ductility index	258
9.4.1.3	Method #2: PRESSS Design Handbook/Appendix B NZS3101 (Frames +PT)	258
9.4.1.4	Method #3A: PRESSS Design Handbook/Appendix B NZS3101 (Walls +PT).....	259

9.4.1.5	Method #3B: Method #3A with effective stiffness for ductility index.....	260
9.4.1.6	Method #4A: PRESSS Design Handbook (Steel yielding devices + PT).....	260
9.4.1.7	Method #4B: Method #4A with effective stiffness for ductility index.....	261
9.4.1.8	Method #5: Measured area-based EVD from cyclic hysteresis.....	261
9.4.2	EVD summary	261
9.5	DDBD evaluation of EVD methods	265
9.6	Conclusions and recommendations	269
9.7	References.....	271
Chapter 10	Conclusions	273
10.1	Motivation and objectives.....	273
10.2	Summary of conclusions	275
10.2.1	Experimental programme	275
10.2.1.1	O-connector component testing.....	275
10.2.1.2	General wall response and design.....	275
10.2.1.3	O-connector influence.....	276
10.2.1.4	Initial stiffness	276
10.2.1.5	Equivalent viscous damping.....	277
10.2.1.6	Residual drifts.....	278
10.2.1.7	Simplified analytical procedure.....	278
10.2.2	Numerical modelling	278
10.2.3	DDBD	280
10.3	Recommended research	280
10.4	References.....	282
Appendix A:	Test setup and construction details.....	283
Appendix B:	Confined concrete design.....	293
Appendix C:	Measured initial stiffness	299
Appendix D:	Additional snap back test results	303
Appendix E:	Complete shake table test results.....	317
References	379

LIST OF FIGURES

Figure 1.1 – Single rocking wall concept	3
Figure 1.2 – PreWEC system.....	4
Figure 2.1 – Housner rocking block model [37]	16
Figure 2.2 – Unbonded PT concrete wall subjected to lateral load [41].....	19
Figure 2.3 – Idealised hysteretic types for concrete elements (Adapted from [46]).....	20
Figure 2.4 – PRESSS 60% scale test building [3].	21
Figure 2.5 – Force-displacement behaviour of SRW [49].....	22
Figure 2.6 – Elevation of jointed wall system from PRESSS test [54].....	23
Figure 2.7 – Force-drift ratio response [9]	24
Figure 2.8 – PreWEC system concept [59]	26
Figure 2.9 – Fibre analytical wall model [4]	32
Figure 2.10 – Lumped plasticity model [41].....	33
Figure 2.11 – Macro model with contact damping included [31].....	34
Figure 2.12 – DDBD key steps [20]	45
Figure 2.13 – Correction factors to be applied to area-based EVD ([20]).....	48
Figure 3.1 – Deformed shapes of the UFP and O-connector and PreWEC system schematic.....	63
Figure 3.2 – Schematic of O-connector dimensions in relation to a UFP	64
Figure 3.3 – O-connector dimensions	67
Figure 3.4 – Test setup	68
Figure 3.5 – Measured stress-strain properties for tensile coupons	69
Figure 3.6 – Applied connector displacement histories.....	71
Figure 3.7 – Typical O-connector deformed shape during tests	72
Figure 3.8 – Measured force-displacement response for each test	73
Figure 3.9 – Failure and fracture observations	74
Figure 3.10 – Observations of fracture mechanism for each test.....	77
Figure 3.11 – Bilinear approximation based on design equations.....	79
Figure 3.12 – Stress-strain and hysteresis response of tests reported in Henry et al. [15]	79
Figure 3.13 – Direct comparison of material and connector type	82
Figure 4.1 – Prototype structure in elevation and plan	88
Figure 4.2 – Design displacement response spectra (5% damping).....	92
Figure 4.3 – SRW Prototype wall design	95
Figure 4.4 – Elevation of SRW model walls	98
Figure 4.5 – Base of wall reinforcement and construction details	98
Figure 4.6 – Cross-sections of model walls	99
Figure 4.7 – Wall panel reinforcement detail	99
Figure 4.8 – Elevation of PreWEC model walls.....	100
Figure 4.9 – Measured steel material properties for all tests.....	103
Figure 4.10 – O-connector dimensions and steel properties.....	104
Figure 4.11 – O-connector test setup and measured response.....	104
Figure 5.1 – Test setup and instrumentation schematic for PreWEC tests	111
Figure 5.2 – Wall set up details	111
Figure 5.3 – Load protocol.....	112

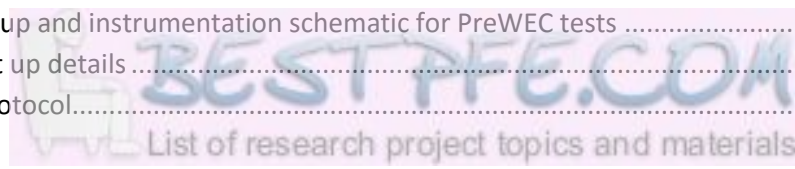


Figure 5.4 – Observed wall behaviour	114
Figure 5.5 – Observations of wall toe damage for all tests	115
Figure 5.6 – Measured lateral force-displacement responses for each test.....	117
Figure 5.7 – Calculated EVD and residual drift for each test.....	120
Figure 5.8 – Measured relative vertical and horizontal deformation of the O-connectors.....	121
Figure 5.9 – Measured wall PT force	122
Figure 5.10 – Change in NA depth and rotation with top lateral drift for SRW	123
Figure 5.11 – Change in NA depth and rotation with top lateral drift for PreWEC.....	124
Figure 5.12 – Measured strain versus lateral drift	126
Figure 5.13 – Average measured strain versus lateral drift	127
Figure 6.1 – Force-displacement response of O-connector component test	134
Figure 6.2 – Setup for snap-back tests	135
Figure 6.3 – Instrumentation plan.....	136
Figure 6.4 – Snap back test load application rig.....	137
Figure 6.5 – Frequency domain response of hammer hit acceleration data	138
Figure 6.6 – SRW-FV-A displacement and acceleration decay.....	139
Figure 6.7 – Wall and connector condition following snap back tests.....	140
Figure 6.8 – PreWEC-FV-A displacement and acceleration decay	141
Figure 6.9 – PreWEC-FV-B displacement and acceleration decay.....	141
Figure 6.10 – PreWEC-FV-C displacement and acceleration decay.....	142
Figure 6.11 – Natural log of displacement peaks over time.....	143
Figure 6.12 – Quarter periods of SRW-FV-A versus peak CoM displacement.....	145
Figure 6.13 – Monotonic pushover moment drift results (black – test, red – A&S)	146
Figure 6.14 – Force-displacement response for all tests.....	147
Figure 6.15 – Local wall parameter response versus drift	149
Figure 6.16 – Example SDOF free vibration with residual drift	152
Figure 6.17 – SRW-FV-A EVD	154
Figure 6.18 – Wall damage photo at end of test.....	154
Figure 6.19 – PreWEC walls EVD	156
Figure 7.1 – Test setup details schematic and photo	164
Figure 7.2 – Test instrumentation schematic.....	166
Figure 7.3 – Unscaled principal component of spectrum compatible ground motions.....	169
Figure 7.4 – Scaled and unscaled pseudo acceleration spectra for all ground motion components (Target design spectrum in solid black).....	170
Figure 7.5 – Unscaled acceleration time history of each recent ground motion.....	171
Figure 7.6 – Example comparison of pseudo-acceleration response for velocity scaled record at model scale after spectrum scaling	173
Figure 7.7 – Model scale design acceleration spectrum for first four intensity levels.....	174
Figure 7.8 – Example transfer function with fitted curve	178
Figure 7.9 – SRW-ST-A seismic excitation white noise tests	179
Figure 7.10 – SRW-ST-A harmonic excitation white noise tests.....	179
Figure 7.11 – PreWEC-ST-A seismic excitation white noise tests.....	181
Figure 7.12 – PreWEC-ST-B1 O-connector #2 photos before and after testing	182
Figure 7.13 – PreWEC-ST-B1 seismic excitation white noise tests.....	183

Figure 7.14 – PreWEC-ST-B2 seismic excitation white noise tests.....	183
Figure 7.15 – Acceleration and drift time history for SRW-ST-A EQ-IV: GM3.....	185
Figure 7.16 – Inertia force and PT force versus drift for SRW-ST-A EQ-IV: GM3	185
Figure 7.17 – Acceleration and drift time history for PreWEC-ST-A EQ-VI: GM2	186
Figure 7.18 – Inertia force and PT force versus drift for PreWEC -ST-A EQ-VI: GM2.....	186
Figure 7.19 – Acceleration and drift time history for PreWEC-ST-B2 EQ-VI: GM5	187
Figure 7.20 – Inertia force and PT force versus drift for PreWEC-ST-B2 EQ-VI: GM5.....	187
Figure 7.21 – Acceleration and drift time history for RGM-I: GM9.....	192
Figure 7.22 – Inertia force versus drift RGM-I: GM9.....	193
Figure 7.23 – Acceleration and drift time history for EQ-III: GM3 and repeats.....	194
Figure 7.24 – PGA versus peak drift for PreWEC-ST-B1 and B2	195
Figure 7.25 – Residual drift for all walls during spectrum compatible ground motions.....	196
Figure 7.26 – Selected pseudo-acceleration spectrum of recorded ground motions	198
Figure 7.27 – Comparison between DDBD method and SRW-ST-A shake table data.....	202
Figure 7.28 – Critical design parameters for PreWEC DDBD.....	203
Figure 7.29 – Comparison between DDBD method and PreWEC shake table data.....	205
Figure 7.30 – $S_A(T_1,5\%)$ versus peak centre of mass acceleration for spectrum compatible ground motions for all walls	207
Figure 7.31 – PGA and $S_A(T_1,5\%)$ versus drift for spectrum compatible ground motions on all walls .	208
Figure 7.32 – Harmonic test results by way of dynamic amplification versus frequency.....	209
Figure 8.1 – SDOF model representation.....	218
Figure 8.2 – SRW-FV-A force displacement behaviour and amplitude dependency of period for different restoring force assumptions	219
Figure 8.3 – Hysteresis rules	220
Figure 8.4 – Effect of pure viscous damping on free vibration response	221
Figure 8.5 – Effect of tangent stiffness proportional viscous damping	222
Figure 8.6 – Effect of friction damping on decay response for $F_f = 1$ kN	223
Figure 8.7 – Effect of cyclic test hysteresis on decay response	224
Figure 8.8 – SDOF best fit free vibration model.....	225
Figure 8.9 – Best fit damping scheme peak envelope and forces.....	226
Figure 8.10 – Best fit damping scheme free vibration disp. and acceleration time history	226
Figure 8.11 – Best fit damping time histories with A&S restoring force for SRW-FV-A.....	227
Figure 8.12 – Best fit damping scheme peak envelope and restoring force-displacement with A&S restoring force for SRW-FV-A.....	228
Figure 8.13 – Best fit damping scheme free vibration displacement and acceleration time history with reduced A&S restoring force for SRW-FV-A.....	229
Figure 8.14 – Best fit damping scheme peak envelope and forces with reduced A&S restoring force for SRW-FV-A	229
Figure 8.15 – Time histories of EQ-III: GM2 for model using reduced simplified analytical restoring force and best fit damping scheme from free vibration calibration.....	231
Figure 8.16 – Force-displacement response (EQ-III: GM2) and model/test best fit free vibration damping scheme for SRW-ST-A shake table tests EQ-III and EQ-IV.....	231
Figure 8.17 – SDOF SRW shake table cyclic calibrated model	232
Figure 8.18 – Cyclic calibrated damping scheme for SRW-ST-A EQ-III: GM2.....	233

Figure 8.19 – Force displacement response and model/test shake table results for cyclic calibrated damping scheme	234
Figure 8.20 – Cyclic calibrated damping scheme for SRW-ST-A EQ-III: GM5	234
Figure 8.21 – O-connector Bouc-wen definition and vertical-lateral disp. relationship	236
Figure 8.22 – PreWEC-A model and cyclic test comparison including spring definitions	238
Figure 8.23 – SDOF PreWEC shake table model.....	239
Figure 8.24 – PreWEC-B model and cyclic test comparison	240
Figure 8.25 – Snap 2% PreWEC-FV-A.....	241
Figure 8.26 – Snap 2% PreWEC-FV-B.....	241
Figure 8.27 – Snap 2% PreWEC-FV-C.....	242
Figure 8.28 – Force-displacement comparison for all PreWEC snap back walls	242
Figure 8.29 – EQ-VI: GM2 PreWEC-FV-A	243
Figure 8.30 – PreWEC-ST-A force displacement response and model/test shake table results	244
Figure 8.31 – EQ-VI: GM2 PreWEC-FV-B	245
Figure 8.32 – PreWEC-ST-B force displacement response and model/test shake table results	245
Figure 9.1 – Correction factors to be applied to area-based EVD ([20])	251
Figure 9.2 – Full force-displacement idealised response using A&S approach.....	254
Figure 9.3 – Bilinear idealisations of force-displacement at design level	255
Figure 9.4 – Bilinear idealisation for SRW-A.....	256
Figure 9.5 – Bilinear idealisation of pushover force-displacement response	257
Figure 9.6 – Key design parameters	262
Figure 9.7 – A&S force-displacement behaviour	262
Figure 9.8 – Calibration factor for area-based damping	263
Figure 9.9 – EVD comparison close up for PreWEC-A (different scales)	264
Figure 9.10 – EVD comparison for each wall tested.....	264
Figure 9.11 – DDBD evaluation algorithm	266
Figure 9.12 – Comparison between DDBD method and SRW-ST-A shake table data for 5% and 6.65% EVD	267
Figure 9.13 – Comparison between EVD methods in DDBD and PreWEC shake table data.....	268

LIST OF TABLES

Table 3.1 – Test variables	66
Table 3.2 – Summary of measured material properties	69
Table 3.3 – Summary of failure mechanism and measured/predicted strength	74
Table 4.1 – Summary of DDBD parameters	90
Table 4.2 - Prototype and model dimensions	95
Table 4.3 - Scale factors.....	96
Table 4.4 – Test wall summary.....	102
Table 5.1 – Wall specifications	109
Table 5.2 – Initial stiffness of each test specimen	118
Table 6.1 – Wall specifications	133
Table 6.2 – Initial stiffness of each test specimen	139
Table 7.1 – Wall specifications	162
Table 7.2 - Design values for SRW and corresponding values for PreWEC.....	163
Table 7.3 – Summary of raw earthquake ground motions	168
Table 7.4 - Fixed base and effective periods of walls.....	170
Table 7.5 – Scaling factors for each wall	171
Table 7.6 – Harmonic loading tests.....	175
Table 7.7 – General ground motion loading sequence	176
Table 7.8 – SRW-ST-A photos of wall condition before and after testing.....	177
Table 7.9 – PreWEC-ST-A photos of wall condition before and after testing	180
Table 7.10 – PreWEC-ST-B photos of wall condition before and after testing	182
Table 7.11 – Peak drift for spectrum compatible ground motion on all walls.....	189
Table 7.12 – Peak centre of mass acceleration for spectrum compatible ground motion on all walls	190
Table 7.13 – Peak parameters for RGM for all walls.....	191
Table 7.14 – Summary of residual drift analysis	197
Table 7.15 – Scaling factors (k_1, k_2) required for recorded ground motion to be ideal match with relevant design spectrum.....	199
Table 8.1 – Bouc-wen parameters for O-connector.....	236
Table 8.2 – Spring properties of PreWEC model.....	239
Table 9.1 – Snap back test specimen bilinear approximations	256
Table 9.2 – Summary of EVD methods.....	262
Table 9.3 – Yield displacements of shake table test specimens	263
Table 9.4 – Mean test/design displacement PreWEC systems for all EVD methods	268

NOTATION

Acronyms:

ACI	=	American Concrete Institute
A&S	=	Aaleti and Sritharan
AFR	=	Axial force ratio
CoM	=	Centre of mass
DDBD	=	Direct displacement based design
ELS	=	Equivalent linear system
ESM	=	Effective stiffness modifier
EVD	=	Equivalent viscous damping
FBD	=	Force based design
FEM	=	Finite element model
GM	=	Ground motion
HM	=	Harmonic motion
IDA	=	Incremental dynamic analysis
ITG	=	Innovation Task Group
LVDT	=	Linear variable displacement transducer
MBA	=	Monolithic beam analogy
MHSG	=	Modified housner substitute gravity approach
NA	=	Neutral axis
NLTHA	=	Nonlinear time history analysis
NZS	=	New Zealand Standards
O-connector	=	Oval shaped flexural plate
PDH	=	PRESSS design handbook
PGA	=	Peak ground acceleration
PRESSS	=	Precast Seismic Structural Systems
PreWEC	=	Precast Wall with End Columns
PT	=	Post-tensioned
RC	=	Reinforced concrete
RGM	=	Recent ground motions
SDOF	=	Single degree of freedom
SRM	=	Simple rocking model
SRW	=	Single rocking wall

UCSD	=	University of California at San Diego
UFP	=	U-shaped flexural plate

Roman characters:

A_g	=	Gross cross-sectional area
A_h	=	Area within one complete cycle of force-displacement response
a_{max}	=	Maximum acceleration
B	=	Width of half wall panel
b	=	UFP width
C	=	Elastic site hazard spectrum
C_h	=	Spectral shape factor
c	=	Damping co-efficient
D	=	Distance to nearest fault
D_{DESIGN}	=	DDBD iterated design drift for ground motion
D_{TEST}	=	Peak test drift from ground motion
d_r	=	Residual displacement at end of excitation
$d_{r,max}$	=	Maximum possible residual displacement
d_{rr}	=	Residual drift ratio
d_y	=	Yield displacement for hysteresis definitions of Chapter 8
E_c	=	Modulus of elasticity
E_D	=	Energy dissipated by structure in force-displacement loop
E_k	=	Kinetic energy in the system
E_n	=	Total strain energy
E_o	=	Initial energy in the system
E_{So}	=	Strain energy
F	=	Force
$F_{c,T}$	=	Total O-connector force from Bouc-wen model
F_{con}	=	Lateral force contribution of O-connector to PreWEC
F_d	=	Design force
F_f	=	Coulomb friction force
F_m	=	Maximum force of force-displacement loop
F_p	=	Plastic strength of O-connector
F_u	=	Ultimate strength of O-connector

F_y	=	Yield strength of O-connector
f	=	Fundamental frequency in Hz
f'_c	=	Characteristic concrete compressive strength
$f'_{c,test}$	=	Average concrete compressive strength from test cylinders
f'_g	=	Characteristic grout compressive strength
$f'_{g,test}$	=	Average grout compressive strength from test cylinders
f_{pi}	=	Initial prestress force
f_y	=	Yield stress
G	=	Permanent actions
g	=	Gravity
H	=	Height of CoM
H_i	=	Height of mass i
H_n	=	Height of building at roof level
h_e	=	Effective height
I_g	=	Gross section moment of inertia
I_0	=	Moment of inertia about point O
i	=	Number of storeys
j	=	Number of cycles
K or k	=	Lateral stiffness
K_b	=	Post-yield stiffness for bilinear assumption for DDBD
K_e	=	Effective stiffness
K_g	=	Gross section stiffness
K_i or k_i	=	Initial stiffness
K_o	=	Initial stiffness for hysteresis definitions in Chapter 8
k_t	=	Tangent stiffness
k_1	=	Record scale factor (Chapter 7 only)
k_2	=	Family scale factor (Chapter 7 only)
l_c	=	Column length in PreWEC system
l_w	=	Wall length in PreWEC system
M or m	=	System mass
M_N	=	Flexural strength contribution from axial load
M_{pt}	=	Flexural strength contribution from PT tendons
M_S	=	Flexural strength contribution from energy dissipating devices
M_{wall}	=	Design moment per wall

m_e	=	Effective mass
m_i	=	Mass of level i
N	=	Near-fault factor
N_{wall}	=	Axial load per wall
n	=	Number of storeys
n	=	Bouc-wen parameter definition (Chapter 8 only)
n_{con}	=	Number of O-connectors in PreWEC system
n_i	=	Number of impacts
$P_{O-connector}$	=	O-connector strength
P_{UFP}	=	UFP strength
Q	=	Imposed actions
R	=	Average radius of O-connector or UFP (For Chapter 3 only)
R	=	Return period factor
R_{ad}	=	Adjusted return period factor
R_H	=	Distance from the rocking edge to centre of mass
R_ξ	=	Damping factor for different structural systems in DDBD
r	=	Post-yield stiffness factor
r_r	=	Coefficient of restitution
$S_{A(T)}$	=	Acceleration design spectra
$S_{A(T_1(5\%))}$	=	5% damped spectral acceleration at the first mode period
$S_{d(T)}$	=	Displacement design spectra
S_p	=	Base shear reduction factor
T	=	Structural period
T_e	=	Effective period
T_1	=	Largest translational period in direction considered
t	=	Thickness of O-connector
t_t	=	time
$\ddot{u}, \dot{u}, \text{ and } u$	=	Lateral acceleration, velocity, and displacement
\ddot{u}_g	=	Ground acceleration
V_{base}	=	Base shear force
V_{wall}	=	Base shear force per wall
W	=	Weight force
w	=	Width of O-connector
Z	=	Hazard factor

Greek characters:

α	=	Equivalent rectangular block constant
α	=	Degrading stiffness coefficient (Chapter 8 only)
$\alpha_{constant}$	=	Constant of proportionality for damping
α_H	=	Angle between the vertical line through the rocking pivot and mass centroid.
α_{SF}	=	Adjustment factor for damping modifier
$\alpha_{updated}$	=	Constant of proportionality updated for damping
β	=	Height of flag in idealised flag-shape hysteresis
β	=	Equivalent rectangular block constant (Chapter 4 only)
β	=	Bouc-wen parameter definition (Chapter 8 only)
γ	=	Bouc-wen parameter definition (Chapter 8 only)
Δ	=	Lateral displacement
Δ_{by}	=	Bilinear yield displacement for O-connector idealisation
Δ_d	=	Design lateral displacement
Δ_i	=	Design displacement at storey i
Δ_m	=	Maximum displacement of force-displacement loop
Δ_{Res}	=	Residual displacement
Δ_y	=	Yield displacement
Δ_{yi}	=	System yield displacement in DDBD
Δ_1	=	Initial displacement guess for DDBD algorithm
Δ_2	=	Final displacement calculated using DDBD algorithm
δ	=	Logarithmic decrement
ε_y	=	Yield strain of vertical reinforcing steel
η	=	Damping modifier
θ	=	Angular displacement
$\dot{\theta}$	=	Angular velocity
$\ddot{\theta}$	=	Angular acceleration
θ_d	=	Design drift
κ	=	Elastic equivalent viscous damping adjustment factor for DDBD
λ	=	Moment contribution ratio
λ'	=	Secant stiffness correction factor for DDBD
μ	=	Structural ductility factor

ξ_{Ad}	=	Equivalent viscous damping evaluated from adjusted logarithmic decrement method
$\xi_{Ad-Energy}$	=	Equivalent viscous damping evaluated from adjusted logarithmic decrement energy method
ξ_{area}	=	Hysteretic damping evaluation using the area of force-displacement loops
ξ_{el}	=	Elastic equivalent viscous damping
ξ_{eq}	=	System equivalent viscous damping
ξ_{hyst}	=	Hysteretic portion of equivalent viscous damping for use in DDBD
ξ_o	=	Equivalent viscous damping evaluated from logarithmic decrement method
ξ_{pt}	=	Equivalent viscous damping for post-tensioned only system
ξ_{upper}	=	Hysteretic equivalent viscous damping for purely dissipative system
σ_e	=	Effective cyclic stress
σ_u	=	Ultimate stress
σ_y	=	Yield stress
ω	=	Forcing frequency of system
ω_i	=	Initial vibration frequency
ω_n	=	Circular natural frequency of the system

Chapter 1

INTRODUCTION

1.1 OVERVIEW

Structural concrete walls provide strong, stiff, primary lateral-load resisting elements that can reduce lateral drifts during earthquakes. Current seismic design standards are focused on the preservation of life safety during large earthquakes through the implementation of ductile design concepts and capacity design principles. Little consideration is given to post-earthquake repairable damage levels. A ductile design philosophy usually requires a Reinforced Concrete (RC) wall to respond to large lateral forces imposed during an earthquake through the formation of a flexural plastic hinge at the base of the wall. A well designed plastic hinge provides sufficient ductility and energy dissipation while maintaining the strength and integrity of the wall. Ductility and energy dissipation arises from the inelastic action of the cracking and crushing of the concrete and yielding of longitudinal reinforcing steel. This inelastic behaviour results in significant structural damage to the plastic hinge region of the wall that would require extensive repair or demolition following a large earthquake. Recent earthquakes have highlighted the impact of damage caused to ductile RC structures, which can result in large economic costs due to business down time, repairs, demolition and rebuilding [1, 2]. The expectations of today's society are placing further demand on seismic engineers to design structures that have a superior

level of performance following a moderate to severe earthquake. This increased level of performance requires engineers to design structures that not only remain standing following an earthquake and preserve life safety principles, but also limit the costs associated with repairs and economic losses associated with business downtime.

In an effort to control the damage in a structure to a certain performance level and isolate irreparable damage to easily replaceable components, engineers and researchers have developed low-damage seismic resisting systems, where inelastic behaviour is concentrated at easily replaceable energy dissipating elements. Low-damage seismic resisting systems can be designed using unbonded Post-Tensioned (PT) precast concrete elements. The concept of connecting precast concrete elements together with unbonded PT was introduced during the PREcast Seismic Structural Systems (PRESSSS) research programme conducted in the 1990's [3]. In contrast to traditional RC construction, distributed flexural cracking is not observed in unbonded PT elements and the inelastic demand is accommodated through the opening and closing of an existing joint at the wall base or beam-column interface, introducing a rocking mechanism. The PT elements are unbonded to reduce the strain demand at high drifts, and in addition to providing lateral strength to the wall, column, or beam, the unbonded PT tendons are designed to remain elastic during a design-level earthquake to provide a restoring force to minimise residual drifts. The required deformations are concentrated at existing joints and damage is limited to the extreme ends of the interface where high compression forces are expected to occur during rocking. Minor spalling and inelastic concrete strains may occur at these isolated locations, but the majority of the structure remains undamaged. The PRESSSS programme developed several PT frame connections and began analytically investigating the behaviour of unbonded PT concrete walls [4].

1.2 ROCKING WALLS

The simplest form of unbonded PT wall system is depicted in Figure 1.1 and referred to herein as a Single Rocking Wall (SRW). The SRW consists of a single precast concrete panel that is connected to the foundation using unbonded post-tensioning. The unbonded PT is designed to extend as uplift occurs at the wall base during rocking. Due to the concentration of inelastic action at the wall base, no flexural cracking or yielding of reinforcement occurs in the SRW

resulting in low energy dissipation capacity during cyclic loading. Following introduction of the PT element concept in the PRESSS programme, several researchers have investigated SRW systems [5-7].

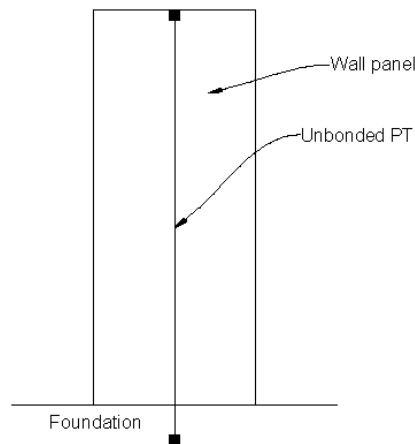


Figure 1.1 – Single rocking wall concept

To improve the energy dissipation ability and seismic performance of the unbonded PT concrete walls, additional energy dissipating elements are often used. During the PRESSS programme the jointed wall system was developed and tested. The jointed wall system consists of two or more unbonded PT precast concrete panels connected by energy dissipating connectors. When subjected to a lateral force the wall panels in the jointed wall system accommodate the inelastic demand through the existing joint at the wall-foundation interface. As the joint opens, uplift occurs causing a relative vertical displacement along the vertical joint between the precast panels, forcing the energy dissipating connectors to undergo large inelastic deformations. The yielding action of the connectors significantly increases the hysteretic energy dissipation of the wall system in comparison to an SRW. The jointed wall system was included in a five storey prototype building that was tested by Priestley et al. [3] and was the first unbonded PT wall system tested.

Following the introduction of the SRW and jointed wall system, researchers have investigated several configurations of unbonded PT concrete wall systems with energy dissipating elements. A hybrid system was developed that consists of a single precast concrete wall with a combination of unbonded PT and mild steel reinforcement at the wall-to-foundation interface. A number of

researchers have experimentally investigated the hybrid system using mild steel dissipaters [8-12] or viscous dampers [13].

1.2.1 PreWEC system

A new unbonded PT wall system with additional energy dissipating elements has been developed that consists of a Precast Wall with End Columns (PreWEC) [14]. The PreWEC system is shown in Figure 1.2 and consists of a single PT precast concrete panel joined horizontally to two PT end columns using special energy dissipating connectors called O-connectors, that were originally developed by Henry et al. [15]. Similarly to the jointed wall system, energy dissipating connectors are attached along the vertical joints between the wall and end columns and undergo a relative vertical displacement as both the wall and end columns rock causing flexural yielding of the O-connector. The PreWEC system has a significant advantage over similar jointed type systems due to the column-wall-column arrangement. The arrangement maximises the lever arm between the PT tendons and compression block allowing the PreWEC system to be designed to have comparable moment resistance to monolithic RC walls of the same geometric dimensions [14]. The PreWEC system also has the advantages of a low damage system, with the damage isolated to the replaceable O-connector dissipaters and only minor damage was observed in the wall toes during the large scale testing performed. It is due to these advantages that the PreWEC system is the focus of the study presented in this thesis.

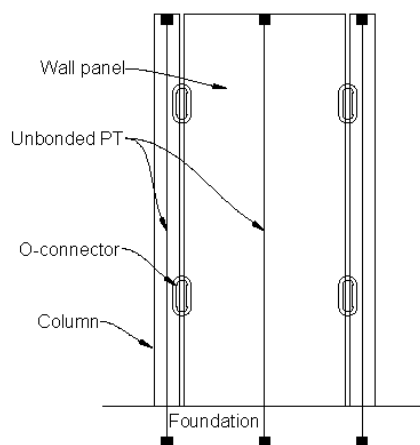


Figure 1.2 – PreWEC system

1.3 CURRENT CODE PROVISIONS

The findings and results from the PRESSS programme and subsequent research on unbonded PT precast concrete elements has led to the technology being included in a number of design provisions. The American Concrete Institute (ACI) set up Innovation Task Group 5 (ITG-5) to develop design provisions for PRESSS type structures in regions of high seismicity. Two documents were produced; ITG-5.1 [16] and ITG-5.2 [17]. ITG-5.1 defines the minimum experimental evidence that can be deemed to satisfy the use of unbonded PT precast concrete walls for building applications. ITG-5.2 defines procedures that may be used to design both jointed and hybrid unbonded PT precast concrete shear walls that have been experimentally validated in accordance ITG-5.1. In 2006 design provisions for the use of unbonded PT precast concrete elements were introduced into the New Zealand concrete design standard as an appendix (NZS 3101-06) [18]. Following this, the New Zealand Concrete Society published the PRESSS Design Handbook [19] that detailed more specific guidelines and design examples.

PT systems are inherently suited to displacement based design methods due to the direct correlation of damage to displacement. Also, previous research has shown that more economical designs of unbonded PT walls can be achieved when using a displacement based design method such as Direct Displacement Based Design (DDBD) [20] over traditional Force Based Design (FBD). This is because the unbonded PT walls are not penalised for the high initial stiffness in DDBD but rather use a secant or effective stiffness to design drift. For these reasons Priestley et al. [20] proposed that DDBD is used for seismic lateral force design of unbonded PT systems.

1.4 RESEARCH MOTIVATION

Unbonded PT precast concrete wall systems have been subject to numerous pseudo-static lateral load tests [7-10, 13, 14, 21, 22] and extensive numerical modelling to simulate the response of the systems to earthquake excitation [23-28]. However, only a limited number of experiments have been conducted to investigate the dynamic response of unbonded PT wall systems. Wight et al. [29, 30] performed shake table testing on unbonded PT masonry wall systems, the first to perform shake table testing on any type of unbonded PT wall system. Marriott et al. [31] performed shake table testing on hybrid walls with various combinations of viscous dampers and mild steel yielding fuses at the base of the unbonded PT wall. Shake table testing has also been

conducted on large scale complete building assemblies as reported by Belleri et al. [32] at University of California San Diego (UCSD) and at the E-Defense laboratory in Japan [33, 34]. Both of these large scale tests incorporated hybrid walls similar to those investigated by Marriott et al. [31]. To the author's knowledge no dynamic testing has been published on unbonded PT precast concrete wall systems that incorporate two or more rocking unbonded PT elements that utilise relative displacement along a vertical joint to mobilise energy dissipaters. This includes jointed, coupled, and PreWEC wall systems.

As a result of this lack of dynamic testing, there is currently a knowledge gap concerning the dynamic characteristics of the vertically jointed unbonded PT systems such as PreWEC. Also, there has been no systematic testing of even a pseudo-static cyclic nature on vertically jointed wall systems investigating different amounts of energy dissipating devices. Furthermore, it is common for a series of experimental tests to include only one loading type, usually concentrating on either pseudo-static cyclic testing or shake table testing alone. Pseudo-static cyclic testing provides the lateral load hysteretic response that is a common method of determining equivalent viscous damping, while shake table testing provides the structures dynamic response to a set input motion. In order to gain excellent understanding of all aspects of a wall systems seismic response, it is valuable to perform a systematic series of testing incorporating different loading types on the same structural system, in this case unbonded PT systems.

Due to the limited dynamic testing on any type of unbonded PT concrete system in literature, there are unknowns concerning the amount of energy dissipation present in these systems and there is subsequently little guidance on appropriate numerical modelling techniques for the damping present in the system. Consequently, the implementation of vertically jointed wall systems into real structures is hampered by the lack of guidelines and procedures to account for the magnitude of Equivalent Viscous Damping (EVD) appropriate when applying DDBD principles to vertically jointed wall systems. As a result of the limited dynamic test data there has been no verification of DDBD procedures for vertically jointed concrete walls using shake table results.

1.5 OBJECTIVES

The main aim of this study was to develop a deeper understanding of the seismic performance of unbonded PT precast concrete walls. This was achieved by systematically investigating the static and dynamic experimental response of unbonded PT precast concrete walls and improving the robustness of design and modelling techniques. Three phases of study were conducted to address this aim, with the following objectives:

- Phase 1: Static and dynamic experimental testing:
 - Experimentally verify the seismic performance of SRW and PreWEC systems subjected to pseudo-static cyclic and dynamic loads including real earthquake ground motions at different intensity levels.
 - Investigate and quantify the dynamic characteristics of SRW and PreWEC systems incorporating different quantities of additional energy dissipating element with particular emphasis on EVD and residual drift.
 - Generate cyclic and dynamic test data for SRW and PreWEC systems to enable calibration and validation of numerical models and the DDBD method.
- Phase 2: Numerical modelling:
 - Investigate and assess simple numerical modelling techniques appropriate for SRW and PreWEC systems that can be easily incorporated into building models for design engineers when conducting Nonlinear Time History Analysis (NLTHA).
- Phase 3: Displacement based design:
 - Verify the DDBD process for unbonded PT precast concrete wall systems.
 - Assess current recommendations for EVD for PreWEC and SRW systems in the current DDBD framework.

1.6 SCOPE

To address the experimental testing objectives, four testing phases were conducted to attain a refined understanding of the experimental response of SRW and PreWEC systems. The four testing phases were:

- O-connector dissipater component testing
- Pseudo-static cyclic testing of SRW and PreWEC systems
- Snap back testing of SRW and PreWEC systems
- Shake table testing of SRW and PreWEC systems

The wall system testing focused on a scaled substructure to enable full understanding of isolated wall systems that could be tested on the University of Auckland shake table facility. It is important to understand the behaviour of all components before considering the response of an entire building. In order to understand all aspects of the wall systems response, the wall system test programme consisted of the three different loading types described above. The loading types were of varying complexity and are all considered to simulate seismic action to some degree. The wall testing initiated with pseudo-static cyclic loading which is the simplest and most commonly used loading type, then progressed to snap back testing, and culminated with shake table testing. Following the extensive experimental programme, the data was used to address issues relating to the numerical modelling and DDBD of SRW and PreWEC unbonded PT wall systems.

The experimental programme reported in this thesis was designed to complement a series of concurrent shake table tests that were undertaken by Nazari et al. [35] from Iowa State University that also incorporated SRW and PreWEC systems. The focus of the research undertaken by Nazari et al. was large scale shake table tests, this differs significantly from the research presented in this thesis which focuses on a systematic investigation into SRW and PreWEC systems with different loading types.

It should be noted that higher mode effects were outside the scope of the thesis and the results of the thesis are limited to buildings where higher mode effects are not significant.

1.7 THESIS OUTLINE

Firstly, a thorough literature review is presented, followed by a discussion of the modified design and testing of the O-connector energy dissipater. The model and prototype wall system design is then presented before the three phases of scaled wall tests are presented. An evaluation of damping schemes for use in a Single Degree Of Freedom (SDOF) numerical model for both PreWEC and SRW systems is then presented. Lastly, a thorough assessment of DDBD for SRW and PreWEC systems is presented using the data from the selection of test chapters.

Overall, the thesis is organised into the following chapters:

Literature review: Chapter 2 provides a review of previous research related to the development of unbonded PT wall systems. Alternative wall systems developed elsewhere are discussed and a summary of experimental and analytical studies is presented along with a thorough description of the DDBD process for unbonded PT wall systems.

O-connector testing and design: Reported in Chapter 3 are the experimental results from a series of nine cyclic tests on various forms of modified O-connector dissipaters. The main focus of the component testing was to develop and assess a modified version of the O-connector tested by Henry et al. [15] for use in the PreWEC system experiments by overcoming previous design flaws. Additionally, this chapter provides further validation of the O-connector for implementation and proposes simple equations to calculate the yield, plastic and ultimate strength and provides insight into the displacement capacity of the O-connector.

Prototype and model design: Chapter 4 provides the details of the prototype building and the subsequent DDBD of the building. The determination of the prototype wall is described in detail followed by the determination of the model wall designs.

Cyclic testing: Chapter 5 provides the experimental results from the pseudo-static cyclic testing performed on four model wall designs. The main parameters investigated included area-based EVD, residual drifts, local wall parameters, and global response. The main focus of this chapter was to systematically investigate the cyclic response of SRW and PreWEC systems with varying amounts of energy dissipation provided by O-connectors and to further validate the

current wall panel design recommendations and to verify an existing simplified analysis and design method for PT wall systems.

Snap back testing: Chapter 6 reports on the experimental results from snap back testing of four model wall designs. The main focus of the testing was to investigate and quantify the dynamic characteristics of identical walls to those described in Chapter 5 that were tested under cyclic loading. Of specific interest were the damping and dynamic residual drift parameters that can only be determined experimentally and are vital to fully understanding the seismic behaviour of unbonded PT walls. Additionally, static pushover data obtained during the loading phase of each snap back test was compared to dynamic data obtained from the free vibration decay snap back phase of each test, to examine the difference in local wall parameter response.

Shake table testing: Chapter 7 describes the test procedure, observations and results from shake table tests on three model wall systems. The main objectives of this chapter were to experimentally verify the seismic performance of SRW and PreWEC systems when subjected to real earthquake ground motions at different intensity levels, and to provide ground motion test data for SRW and PreWEC systems to enable calibration and validation of numerical models and the DDBD method.

Evaluation of damping schemes: Chapter 8 describes the development and assessment of damping schemes for use in the SDOF numerical modelling of SRW and PreWEC systems, and provides validation of the recommended damping scheme using the shake table test data presented in Chapter 7.

Direct displacement based design evaluation: Chapter 9 provides a review of current DDBD methods for the determination of EVD ratios for PreWEC systems. The different methods of determining EVD are evaluated against the shake table test data, and appropriate methods for determination of EVD ratios for PreWEC systems are recommended.

Conclusions: Chapter 10 summarises the main conclusions arrived at in the preceding chapters of the thesis and provides recommendations for future research.

1.8 REFERENCES

1. Kam, W.Y., S. Pampanin, and K. Elwood, *Seismic performance of reinforced concrete buildings in the 22 February Christchurch (Lyttelton) earthquake*. Bulletin of the New Zealand Society for Earthquake Engineering, 2011. **44**(4): p. 239-278.
2. Sritharan, S., K. Beyer, R.S. Henry, Y.H. Chai, M. Kowalsky, and D. Bull, *Understanding Poor Seismic Performance of Concrete Walls and Design Implications*. Earthquake Spectra, 2014. **30**(1): p. 307-334.
3. Priestley, M.J.N., S.S. Sritharan, J.R. Conley, and S. Pampanin, *Preliminary results and conclusions from the PRESSS five-story precast concrete test building*. PCI Journal, 1999. **44**(6): p. 42-67.
4. Kurama, Y., R. Sause, S. Pessiki, and L.W. Lu, *Lateral load behavior and seismic design of unbonded post-tensioned precast concrete walls*. ACI Structural Journal, 1999. **96**(4): p. 622-632.
5. Erkmen, B. and A.E. Schultz, *Self-centering behavior of unbonded, post-tensioned precast concrete shear walls*. Journal of Earthquake Engineering, 2009. **13**(7): p. 1047-1064.
6. Stavridis, A., I. Koutromanos, and P.B. Shing, *Shake-table tests of a three-story reinforced concrete frame with masonry infill walls*. Earthquake Engineering and Structural Dynamics, 2012. **41**(6): p. 1089-1108.
7. Henry, R.S., N.J. Brooke, S. Sritharan, and J.M. Ingham, *Defining concrete compressive strain in unbonded post-tensioned walls*. ACI Structural Journal, 2012. **109**(1): p. 101-112.
8. Holden, T., J. Restrepo, and J.B. Mander, *Seismic performance of precast reinforced and prestressed concrete walls*. Journal of Structural Engineering, 2003. **129**(3): p. 286-296.
9. Restrepo, J.I. and A. Rahman, *Seismic performance of self-centering structural walls incorporating energy dissipators*. Journal of Structural Engineering, 2007. **133**(11): p. 1560-1570.
10. Smith, B.J., Y.C. Kurama, and M.J. McGinnis, *Design and measured behavior of a hybrid precast concrete wall specimen for seismic regions*. Journal of Structural Engineering, 2011. **137**(10): p. 1052-1062.
11. Smith, B.J. and Y.C. Kurama, *Seismic design guidelines for solid and perforated hybrid precast concrete shear walls*. PCI Journal, 2014. **59**(3): p. 43-59.
12. Smith, B.J. and Y.C. Kurama. *Seismic displacement demands for hybrid precast concrete shear walls*. in *Structures Congress 2013: Bridging Your Passion with Your Profession - Proceedings of the 2013 Structures Congress*. 2013.
13. Marriott, D., *The Development of High-Performance Post-Tensioned Rocking Systems for the Seismic Design of Structures*. 2009, University of Canterbury: Christchurch.
14. Sritharan, S., S. Aaleti, R.S. Henry, K.-Y. Liu, and K.-C. Tsai, *Precast concrete wall with end columns (PreWEC) for earthquake resistant design*. Earthquake Engineering & Structural Dynamics, 2015: p. n/a-n/a.
15. Henry, R.S., S. Aaleti, S. Sritharan, and J.M. Ingham, *Concept and finite-element modeling of new steel shear connectors for self-centering wall Systems*. Journal of Engineering Mechanics, 2010. **136**(2): p. 220-229.

16. ACI Innovation Task Group 5., *Acceptance criteria for special unbonded post-tensioned precast structural walls based on validation testing (ITG 5.1-07)*. 2007, American Concrete Institute: Farmington Hills, Mich.
17. ACI Innovation Task Group 5., *Requirements for design of a special unbonded post-tensioned precast shear wall satisfying ACI ITG-5.1 (ACI ITG-5.2-09) and commentary: an ACI standard*. 2009, Farmington Hills, Mich.: American Concrete Institute. 21 p.
18. New Zealand Standard, *Concrete Structures Standard NZS 3101*. 2006: Wellington, New Zealand.
19. Pampanin, S., D. Marriott, A. Palermo, and New Zealand Concrete Society., *PRESSS design handbook*. 2010, Auckland, N.Z.: NZCS. 1 v. (various pagings).
20. Priestley, M.J.N., G.M. Calvi, and M.J. Kowalsky, *Displacement-based seismic design of structures*. 2007, Pavia: IUSS Press : Fondazione Eucentre. xvii, 721 p.
21. Perez, F.J., S. Pessiki, R. Sause, and L.M. Lu, *Lateral load tests of unbonded post-tensioned precast concrete walls*, in *Large-Scale Structural Testing*, M.A. Issa and Y.L. Mo, Editors. 2003, American Concrete Institute: Farmington Hills. p. 161-182.
22. Perez, F.J., S. Pessiki, and R. Sause, *Experimental lateral load response of unbonded post-tensioned precast concrete walls*. ACI Structural Journal, 2013. **110**(6): p. 1045-1055.
23. Pampanin, S. and M. Nishiyama. *Critical aspects in modelling the seismic behaviour of precast/prestressed concrete building connections and systems*. in *1st fib Congress*. 2002. Osaka, Japan.
24. Shen, Q., Y.C. Kurama, and B.D. Weldon, *Seismic design and analytical modeling of posttensioned hybrid coupled wall subassemblages*. Journal of Structural Engineering, 2006. **132**(7): p. 1030-1040.
25. Kurama, Y.C. and Q. Shen, *Seismic design and response evaluation of unbonded post-tensioned hybrid coupled wall structures*. Earthquake Engineering and Structural Dynamics, 2008. **37**(14): p. 1677-1702.
26. Kurama, Y.C., *Seismic design of unbonded post-tensioned precast concrete walls with supplemental viscous damping*. ACI Structural Journal, 2000. **97**(4): p. 648-658.
27. Kurama, Y., S. Pessiki, R. Sause, L.W. Lu, and M. El-Sheikh, *Analytical modelling and lateral load behavior of unbonded post-tensioned precast concrete walls*. 1996, Department of Civil and Environmental Engineering, Lehigh University: Bethlehem, Pennsylvania.
28. Henry, R.S., S. Sritharan, and J.M. Ingham. *Recentering requirements for the seismic design of self-centering systems*. in *Proceedings of the Ninth Pacific Conference on Earthquake Engineering*. 2011. Auckland, New Zealand.
29. Wight, G.D., M.J. Kowalsky, and J.M. Ingham, *Shake table testing of posttensioned concrete masonry walls with openings*. Journal of Structural Engineering, 2007. **133**(11): p. 1551-1559.
30. Wight, G.D., J.M. Ingham, and M.J. Kowalsky, *Shaketable testing of rectangular post-tensioned concrete masonry walls*. ACI Structural Journal, 2006. **103**(4): p. 587-595.
31. Marriott, D., S. Pampanin, D. Bull, and A. Palermo, *Dynamic testing of precast, post-tensioned rocking wall systems with alternative dissipating solutions*. Bulletin of the New Zealand Society for Earthquake Engineering, 2008. **41**(2): p. 90-103.
32. Belleri, A., M.J. Schoettler, J.I. Restrepo, and R.B. Fleischman, *Dynamic behavior of rocking and hybrid cantilever walls in a precast concrete building*. ACI Structural Journal, 2014. **111**(3): p. 661-671.

33. Gavridou, S., M. Melek, and J.W. Wallace. *Conventional and unbonded post-tensioned lateral force resisting systems: A comparative assessment of expected performance and losses*. in *NCEE 2014 - 10th U.S. National Conference on Earthquake Engineering: Frontiers of Earthquake Engineering*. 2014.
34. Nagae, T., T. Matsumori, H. Shiohara, T. Kabeyasawa, S. Kono, M. Nishiyama, J. Moehle, J. Wallace, R. Sause, and W. Ghannoum. *The 2010 E-defense shaking table test on four-story reinforced concrete and post-tensioned concrete buildings*. in *NCEE 2014 - 10th U.S. National Conference on Earthquake Engineering: Frontiers of Earthquake Engineering*. 2014.
35. Nazari, M., S. Aaleti, and S. Sritharan. *Shake table testing of unbonded post-tensioned precast concrete walls*. in *NCEE 2014 - 10th U.S. National Conference on Earthquake Engineering: Frontiers of Earthquake Engineering*. 2014.

Chapter 2

LITERATURE REVIEW

2.1 OVERVIEW

Within this chapter an extensive literature review is presented related to Post-Tensioned (PT) precast concrete wall systems. A description of rocking behaviour is summarised followed by background relating to the use of concrete walls in seismic design. The founding research on self-centering precast concrete wall systems is discussed and a summary of the different systems that have been developed is provided. This is followed by a detailed review of the experimental testing and modelling on the dynamic behaviour of unbonded PT concrete wall systems. Lastly, the current codification and design procedures for unbonded PT precast concrete wall systems are discussed in detail.

2.2 ROCKING BEHAVIOUR

The rocking mechanism has been of interest to the earthquake engineering community for some time. It can be shown that by allowing rocking motion to take place in a structure during a seismic event, the resulting accelerations, and hence forces can be reduced, due to the change in stiffness of the structure once rocking is initiated. It has been suggested that a rocking mechanism may

have been deliberately used for seismic applications for Greek and Roman monuments [36]. The interest of modern earthquake engineers in the rocking mechanism stems from Housner [37] who reported that during the 1960 Chilean earthquake a number of tall, slender structures survived while more stable appearing structures were severely damaged. Housner's observations drew attention to the potential for a rocking mechanism to provide a form of seismic isolation to a structure. Two early New Zealand examples where the rocking mechanism was purposely used to provide seismic isolation to a structure were the South Rangitikei River Rail Bridge and a chimney at Christchurch Airport [38].

In Housner's [37] 1963 paper a Simple Rocking Model (SRM) was developed by analysing the dynamics of a rigid block resting on a rigid base excited into a rocking motion. Housner's SRM makes two important assumptions, firstly, there is conservation of angular momentum about the point of impact, and secondly, impacts are considered to be point impacts with no bouncing or sliding. Housner initially developed an equation of motion as presented in Equation (2-1) for a rigid rocking block with the parameters defined in Figure 2.1. Equation (2-1) was then approximated as Equation (2-2) for tall slender blocks having an angle α_H less than 20° .

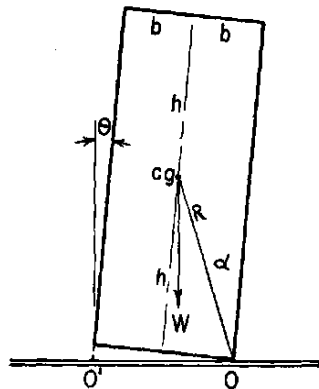


Figure 2.1 – Housner rocking block model [37]

$$I_0 \ddot{\theta} - WR_H \sin(\alpha_H - \theta) = 0 \text{ for } \theta > 0 \quad (2-1)$$

$$I_0 \ddot{\theta} - WR_H \dot{\theta} = -WR_H \alpha_H \quad (2-2)$$

Housner then provided a solution for the equation of motion shown in Equation (2-3) using the initial conditions of $\theta = \theta_0$ and $\dot{\theta} = 0$ at $t = 0$ that represent the block released from an initial rotation.

$$\theta = \alpha_H - (\alpha_H - \theta_0) \cosh pt \quad (2-3)$$

$$\text{Where } p^2 = WR_H/I_0$$

Equation (2-3) describes the rotation of the block about the corner as it returns to the vertical position after being released from an initial rotation. Housner formulated a closed form expression (Equation (2-4)) for the quarter period of a rocking cycle using the solution to the equation of motion (Equation (2-3)) and the conditions of $\theta = \theta_0$ and $\dot{\theta} = 0$ when $t = T/4$.

$$T = \frac{4}{p} \cosh^{-1} \left(\frac{1}{1 - \frac{\theta_0}{\alpha_H}} \right) \quad (2-4)$$

During rocking energy is dissipated when the block impacts the base. To incorporate this loss of energy Housner took advantage of the conservation of angular momentum and formulated an expression described by Equation (2-5) for the reduction in kinetic energy that occurs during impact, also referred to as the apparent coefficient of restitution (r_r).

$$r_r = \frac{\left(\frac{1}{2} I_0 \dot{\theta}_2^2 \right)}{\left(\frac{1}{2} I_0 \dot{\theta}_1^2 \right)} = \left(\frac{\dot{\theta}_2}{\dot{\theta}_1} \right)^2 = \left[1 - \frac{MR_H^2}{I_0} (1 - \cos 2\alpha_H) \right]^2 \quad (2-5)$$

Housner also investigated the overturning potential of a rigid block subjected to constant acceleration, sinusoidal acceleration, and earthquake motion based on energy principles. The acceleration pulses in earthquake motion are random and once a block starts rocking in an earthquake there is an energy build-up in the system. The block is then able to overturn at much smaller peak accelerations than those predicted by the sinusoidal acceleration pulse. Housner showed the existence of a scale effect in the stability of two geometrically similar blocks. In other words, the larger of two blocks with the same aspect ratio, but of varying size, will be more stable against overturning.

Many studies have validated Housner's rocking theory through experimental testing. Aslam et al. [39] confirmed the use of Housner's SRM by conducting free vibration and forced vibration testing of concrete blocks using a shake table. A computer program was written to numerically solve the equation of motion of the block with the loss of energy due to impact represented by a coefficient of restitution. The coefficient of restitution was calculated by fitting an analytical solution to the experimental data for the free vibration tests. Aslam et al. demonstrated the

rocking problems high sensitivity to the chosen coefficient of restitution, and highlighted the lack of understanding surrounding the energy dissipation mechanism associated with the impacts. The energy dissipation mechanism associated with the velocity reduction at impact is known as contact or radiation damping. Aslam et al. also introduced the concept of adding vertical prestressing to the blocks to increase the stability of the system. The addition of a vertical prestress force to a rocking system is often referred to as controlled rocking.

2.3 CONCRETE WALLS

Concrete structural walls are often used as the primary lateral force resisting system in a building as they provide an efficient lateral load resisting system for both wind and seismic loading. Structural walls can be constructed from either cast-in-place or precast concrete. Precast concrete has advantages over cast-in-place construction, including high quality control, reduction in site formwork and site labour plus the bonus of rapid construction and optimised use of materials [40]. However, the use of precast concrete in seismic regions was initially limited due to lack of research and the subsequent limits put in design codes [41].

Concrete structural walls have previously been found to perform well during earthquakes; including precast concrete walls designed to emulate cast-in-place Reinforced Concrete (RC) walls [42, 43]. Fintel [44] reported that concrete shear wall structures demonstrated the ability to fulfil the life safety requirements of seismic design and also suffered little damage. Typically precast concrete walls are constructed to emulate cast-in-place RC walls. Designing precast concrete walls to emulate cast-in-place RC walls requires in situ concrete joints during construction that limit the advantages provided by the use of precast concrete [45]. A significant research effort has been undertaken to overcome the limitations of using precast concrete in seismic regions, this is discussed in section 2.4.

2.4 UNBONDED PT CONCRETE WALL SYSTEMS

Self-centering concrete systems such as that shown in Figure 2.2 incorporate precast concrete elements with post-tensioning tendons. The use of precast concrete introduces dry connections that accommodate inelastic demand through opening and closing of an existing crack,

introducing a rocking mechanism. The unbonded post-tensioning is designed to remain elastic during a design-level earthquake, and therefore provides a self-centering restoring force and the moment resistance for the system. The restoring force provided by the post-tensioning increases the stability of the rocking system against overturning. The combination of precast elements and unbonded post-tensioning generates a response that undergoes inelastic deformations with minimal damage. Unbonded PT precast concrete members have limited energy dissipation compared to a traditional RC structure due to the minimal damage sustained from a seismic event.

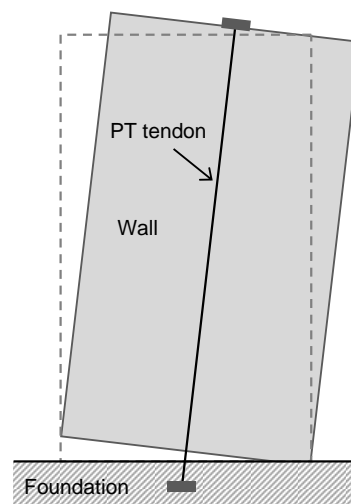


Figure 2.2 – Unbonded PT concrete wall subjected to lateral load [41]

Figure 2.3 shows the idealised behaviour of concrete elements. The combination of precast concrete wall and post-tensioning produces the idealistic bilinear hysteresis shown in Figure 2.3. The decreased amount of hysteretic energy dissipation due to decreased damage is evident when you compare the bilinear hysteresis to a traditional full hysteretic (i.e. purely yielding) system. The low energy dissipation of the purely unbonded PT system typically leads to higher displacements during an earthquake and has led researchers to add further damping to the system, producing an idealised flag-shape hysteresis behaviour shown in Figure 2.3. The development of these systems is discussed in detail below.

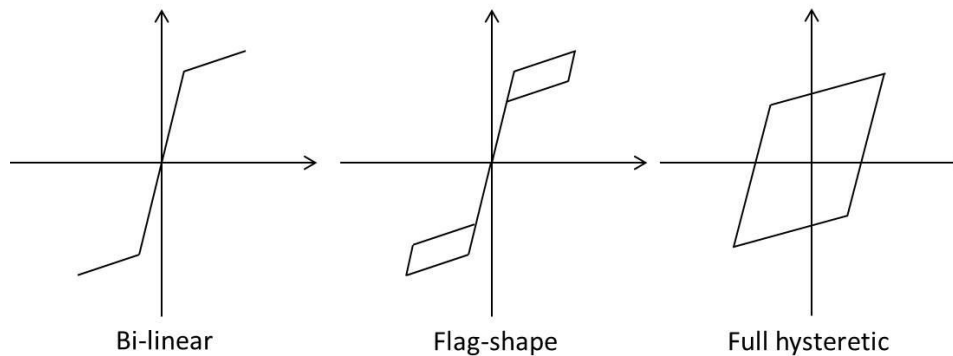


Figure 2.3 – Idealised hysteretic types for concrete elements (Adapted from [46])

2.4.1 PRESSS program

The PREcast Seismic Structural Systems (PRESSSS) research programme was initiated in 1991 in a joint effort by the United States and Japan to develop new technology that overcame the limitations associated with using precast concrete in seismic regions [47]. The main focus of the PRESSSS research programme was the use of unbonded post-tensioning to connect precast concrete structural elements. The concept was initially investigated analytically for use in concrete frames [48] and then extended to precast concrete walls [27]. During the PRESSSS programme four types of connections for PT frame were conceptualised and investigated. Concurrently, unbonded PT precast concrete walls were being investigated analytically at Lehigh University [4, 45].

The final phase of the PRESSSS programme included the pseudo-dynamic testing of a 60% scale five-story precast concrete building that is shown in Figure 2.4. The test building used unbonded PT frames to resist lateral loads in the longitudinal direction while a jointed wall system was used to resist lateral loads in the transverse direction. The building was tested in both the frame and wall directions independently by subjecting the building to simulated seismic loads. The principal method of testing was pseudo-dynamic testing; this involves applying displacements in small increments to represent a seismic event based on an assumed stiffness matrix, and then updating the stiffness matrix at set intervals depending on the displacements and forces achieved in the previous step. The jointed wall system sustained minimal damage even when subjected to an earthquake 50% above the design level earthquake intensity. Minor crushing developed in each toe at the base of the wall, but this damage was essentially cosmetic and could easily be repaired without disrupting the normal operations of the building [3].

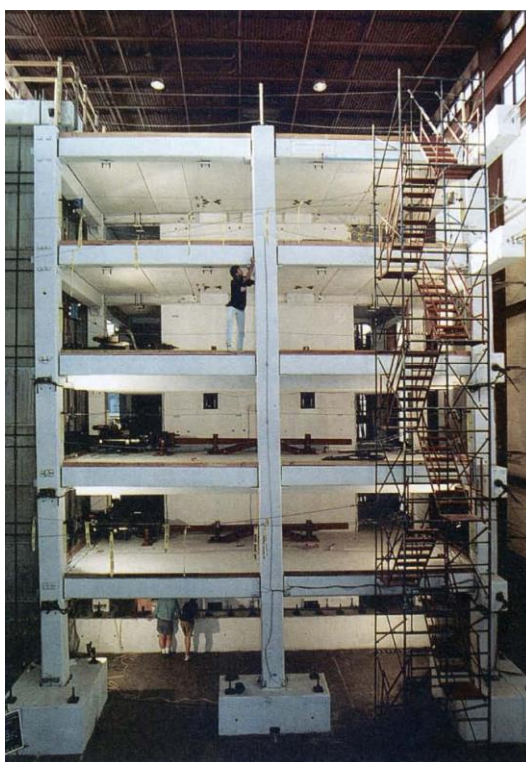


Figure 2.4 – PRESSS 60% scale test building [3].

2.4.2 Single rocking walls

A Single Rocking Wall (SRW) is the simplest form of self-centering concrete system and consists of an individual PT precast concrete wall with no additional damping. Numerous analytical and experimental investigations have been undertaken to study the lateral load behaviour of SRWs [5-7, 13, 21, 49-53]. The majority of the experimental investigations were either pseudo-static monotonic or cyclic tests. The results of the pseudo-static cyclic testing performed by Perez et al. [49] showed that the unbonded PT precast concrete wall exhibited a nearly nonlinear elastic load-deformation response with only limited energy dissipation per cycle of loading, as seen in Figure 2.5. Henry et al. [53] experimentally and analytically investigated the calculation of concrete compressive strains generated in PT concrete walls at nominal flexural strength. The lateral load resistance was found to be maintained well beyond the code-defined maximum allowable strain of 0.003, and minimal concrete damage was observed at that limit state. A higher strain limit of 0.005 was suggested to be more suitable for describing the nominal flexural strength of PT concrete walls. Due to localised behaviour strongly affecting the strain measurements during experimental testing, it was recommended that an average from several gauges be used for the most reliable strain measurement.

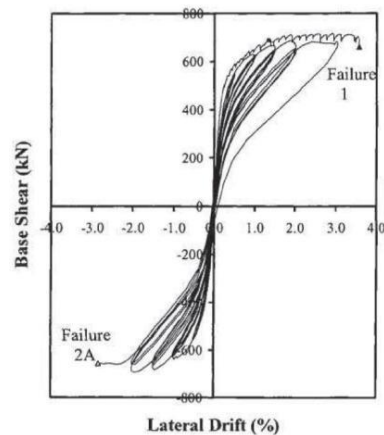


Figure 2.5 – Force-displacement behaviour of SRW [49]

2.4.3 Jointed wall system

As discussed in section 2.4.1 the jointed wall system was developed and tested during the PRESSS research program. Jointed wall systems consist of two or more precast concrete walls, and are designed with PT tendons and special energy dissipating connectors placed along the vertical joints between the wall panels. The jointed wall system that was included in the PRESSS test building used U-shaped flexure plates (UFP) as the energy dissipating connectors between the precast concrete wall panels. The UFPs are designed to yield when subjected to the vertical displacement that occurs across the joint as the wall panels uplift and rock, increasing the hysteretic energy dissipation of the jointed wall system while limiting the damage to the wall itself [54]. UFPs require heat treatment during the manufacturing process to ensure no residual stresses occur from the bending process. The connectors are designed to be replaced following a seismic event, resulting in an undamaged structure following connector replacement. The elevation of the jointed wall system used in the PRESSS programme is presented in Figure 2.6.

2.4.4 Hybrid wall system

The alternative hybrid wall concept extended on the hybrid beam-column connections that were investigated during the PRESSS program. A hybrid wall consists of a single precast wall panel (SRW) with a combination of unbonded PT and additional energy dissipation in the form of mild steel bars that are placed across the interface between the wall and the foundation. As with a SRW, when a hybrid wall is subjected to a lateral force, rocking is initiated and a gap opens at the wall base. When wall uplift occurs, the mild steel bars crossing the interface between the

wall and foundation yield, increasing the hysteretic energy dissipation of the system. Typically the mild steel bars are debonded over a short length to reduce the strain in the steel to prevent the bars fracturing prematurely. As well as increasing the energy dissipation of the system, the mild steel bars contribute to the moment capacity of the system.

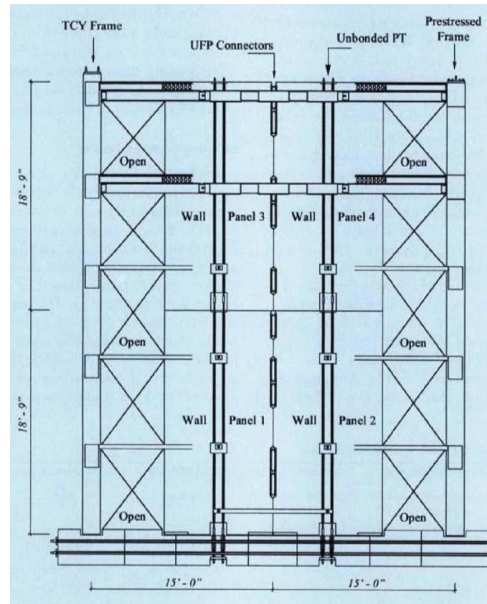


Figure 2.6 – Elevation of jointed wall system from PRESS test [54]

Rahman and Restrepo [55] performed a series of experimental tests on such hybrid wall systems. The series of experimental testing consisted of three half-scale precast concrete wall units subjected to pseudo-static cyclic loading. Standard reinforcing bar with a reduced diameter over a specific length was placed across the wall-to-foundation interface to provide energy dissipation. There was a strong bond between the energy dissipater and the surrounding concrete, which caused high strains and hence damage when uplift occurred. Despite the damage to the concrete panel, the energy dissipaters proved to be effective in providing energy dissipation to the system with Equivalent Viscous Damping (EVD) ratios of up to 14%. Figure 2.6 shows a comparison of the measured lateral force-drift ratio response between a wall with and without additional energy dissipating bars [9].

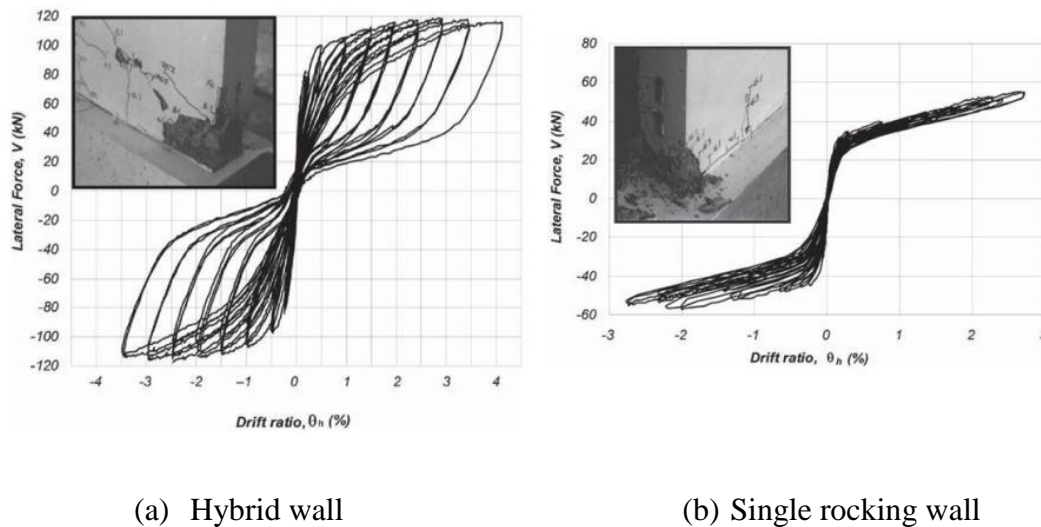


Figure 2.7 – Force-drift ratio response [9]

Testing of hybrid walls was also conducted by Holden et al. [8] where two identical half-scale precast concrete wall units, were constructed and tested by subjecting the walls to pseudo-static reverse cyclic loading. One wall was a code-compliant conventionally reinforced specimen designed to emulate a cast-in-place wall, while the other was a PT precast wall with additional energy dissipation devices. The devices used by Holden et al. were low yield strength tapered longitudinal reinforcement that crossed the interface of the wall and foundation. Both walls performed as expected with the hybrid wall sustaining no visible damage, while the conventional specimen performed in the expected ductile manner with extensive damage in the form of flexural cracking in the lower portion of the wall. A number of other researchers have experimentally investigated the hybrid system using mild steel dissipaters [10-12].

2.4.5 Other sources of energy dissipation in hybrid walls

Researchers have gone on to investigate other sources of additional energy dissipation for unbonded PT wall systems. Kurama [26] used nonlinear dynamic time history analysis to investigate the feasibility and effectiveness of supplemental viscous damping for unbonded PT precast walls. Additionally, Kurama [56] analytically investigated the use of supplemental friction dampers for rocking wall systems. Both of the aforementioned methods of increasing energy dissipation of unbonded PT rocking walls were found to reduce drift levels in comparison to a wall with no additional energy dissipating devices. Marriott et al. [31] continued research in the area of viscous damping and performed experimental testing to confirm the response of an

unbonded PT wall with supplemental viscous damping. Marriott et al. also investigated the use of tension-compression yielding steel dampers externally mounted on a precast wall. This approach resulted in no additional damage from mild steel crossing the interface, in contrast to the traditional hybrid system, as the dissipaters were externally mounted. However, it should be noted that the externally mounted dissipaters require careful design to avoid buckling due to the tension compression yielding.

2.4.6 PreWEC system

Although self-centering structural components exhibit superior seismic performance in comparison to conventional reinforced structures, they must also be economically and architecturally viable to be considered an alternative. It has been speculated that hybrid and jointed wall systems have lacked implementation into real structures due to a failure to meet the aforementioned criteria. In a hybrid wall system the placement of energy dissipation devices is the main difficulty for the system to be economically and architecturally viable in comparison to a conventional structure [41]. Mild steel energy dissipaters can be placed across the wall to foundation interface enabling the wall to be designed to match the moment capacity of a traditional wall. The disadvantage of this is the difficulty in inspecting and/or replacing the dissipaters following an earthquake. In a jointed wall system the wall is divided up into two or more panels to allow energy dissipating connectors to be placed along the vertical joints. There is a reduced lever arm between the PT tendons and the wall compression toe resulting in a reduced moment capacity when compared to a monolithic RC wall with similar dimensions [41]. To provide a solution to these problems in the design of a fully resilient building the PreWEC system was developed consisting of a PREcast Wall with End Columns [57].

The PreWEC system was developed from analytical research that investigated the effects of different parameters on the lateral load resistance of jointed wall systems. The aim of this investigation was to study variations of the jointed wall system which led to the discovery of a system that had a comparable moment resistance to a cast-in-place structural wall with similar dimensions; the PreWEC system [58]. The PreWEC system consists of a single precast wall connected to two end columns using specially designed energy dissipating O-connectors [15], as shown in Figure 2.8. As with previous jointed wall systems the wall and columns are anchored to the foundation using unbonded PT and are designed to rock and uplift during an earthquake.

The uplift at the wall base results in a relative vertical displacement along the joint between the wall and end columns where the O-connectors are attached. As a result of this vertical displacement, the O-connectors undergo flexural yielding and dissipate seismic energy. Another advantage of the system is that the columns undergo relatively small uplift and can therefore be used to support the floor diaphragms and transfer gravity loads. Also, as is the case with other self-centering wall systems, the post-tensioning is designed to remain elastic and provide the restoring force for the system eliminating residual displacements.

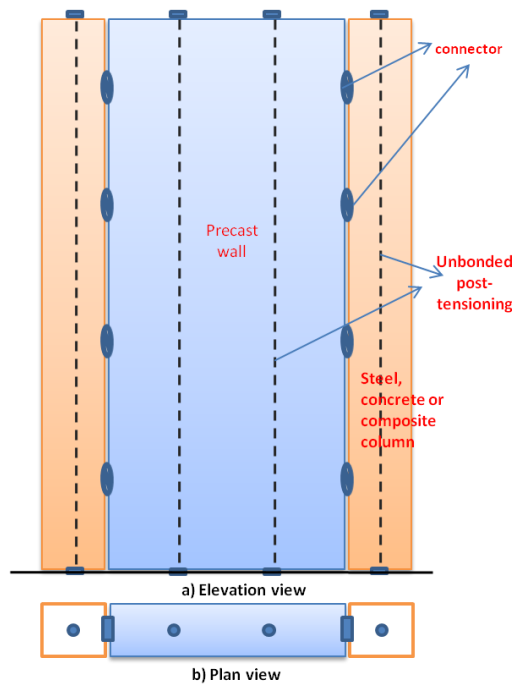


Figure 2.8 – PreWEC system concept [59]

The PreWEC system has been validated experimentally with large scale pseudo-static cyclic testing [14]. A new energy dissipating connector was designed for the PreWEC system test by Henry et al. [15]. The energy dissipating connectors for unbonded PT precast concrete systems, also referred to as shear connectors, have two functions; the first is to transfer forces between the wall and column elements therefore contributing to the system moment capacity. Second, the energy dissipating connectors undergo large inelastic deformations and thus act as the primary source of energy dissipation in the system. Henry et al. conducted a series of finite element analyses on different connector designs and found the most suitable connector for the PreWEC system was the O-connector. The O-connector is easy to manufacture being laser cut from mild steel plate and requires no heat treatment process. The PreWEC specimen tested by Sritharan et

al. [14] incorporated the O-connector and was designed to match or exceed the response of a cast-in-place RC wall. During the large scale PreWEC test the O-connectors required restraint to prevent out-of-plane buckling that was observed during component tests [15]. PreWEC test specimen performed exceptionally well compared to other RC walls. The wall system experienced only minor damage which was limited to spalling of cover concrete in the toe regions of the wall panel. The PreWEC system had stable hysteretic loops and good energy dissipation until failure occurred in the connectors [59].

2.5 SECTION ANALYSIS

The aforementioned unbonded PT concrete systems have one fundamental difference to traditional RC structural systems that significantly changes the design and analysis procedures. Due to the unbonded nature of the PT the strain compatibility between the concrete and steel is violated. Also, plastic curvature is not over a plastic hinge length but at a specific location, therefore a moment-curvature analysis is not applicable but rather a moment-rotation analysis. Initially as part of the section analysis procedure for these systems the Monolithic Beam Analogy (MBA) was proposed by Pampanin et al. [60]. The MBA was validated with the experimental tests on hybrid beam-column sub assemblages conducted at the National Institute of Standard and Technology. This procedure considers a global member-compatibility condition and assumes that the lateral displacement of a PT ductile connection is equal to that of an equivalently reinforced monolithic connection for the same lateral load. In other words, for the precast rocking connection the inelastic action is concentrated at the single crack while for the monolithic connection the inelastic action is distributed along the plastic hinge length with both cases resulting in the same global displacement. As described by Pampanin et al. [60] one of the main limitations of MBA is that the neutral axis position cannot be estimated by a closed form equation meaning a trial and error approach able to satisfy both equilibrium and strain compatibility conditions must be utilised.

The MBA was later revised by Palermo [61]. The revised MBA recognises that the PT system is significantly more flexible than the equivalent monolithic element. The principle behind the revised version of the MBA is that prior to the decompression point (when the strain in the outermost fibre reaches zero due to uplift) the concrete strain distribution is identical within the

two sections and therefore the displacement is equal. For lateral loads greater than the decompression point the additional monolithic displacement is equal to the rigid rotation displacement of the PT element.

More recently a simplified analysis procedure has been developed by Aaleti and Sritharan [62]. The variation of neutral axis depth with wall base rotation is simplified to a tri-linear approximation that does not require iteration, greatly reducing the complexity in comparison to the MBA. The procedure has been validated against monotonic test data and shown to accurately predict the response of SRWs and jointed wall systems.

2.6 UNBONDED PT SYSTEMS DYNAMIC BEHAVIOUR

Understanding the dynamic behaviour of unbonded PT wall systems is essential to fully understand their seismic performance. However, only a limited number of experiments have been conducted to investigate the dynamic response of unbonded PT wall systems. The limited dynamic testing which has been carried out is presented in this section accompanied by a summary of previous analytical modelling and the advantages and disadvantages of the various approaches. In the experimental testing summary unbonded PT masonry walls and PT precast piers are also reported on as the fundamental rocking response applies to all of these systems.

2.6.1 Wall system testing

Marriott [13] reported on experimental dynamic testing of unbonded PT precast concrete rocking walls including shake table testing and free vibration testing. In Marriott's study five configurations of precast concrete rocking wall were investigated, including a SRW and hybrid walls with either fluid viscous dampers, tension-compression yielding dampers, or a combination of the two. Marriott conducted free vibration testing of these walls for release drift amplitudes of 1.5% and 2.5%. The tests were performed with the walls secured to a shake table which lead to undesirable energy fluctuations as the table would move in response to the impacts. Based on analysis of the results of the free vibration tests the contact damping was found to be proportional to the vertical acceleration during impact and hence the horizontal velocity. For the lightly damped SRW high vertical accelerations up to 0.35 g were recorded. Since velocity is also proportional to displacement a contact damping model with damping forces proportional to both

velocity and displacement was proposed. Marriott also estimated the EVD associated with contact damping based on the free vibration displacement decay using an energy balance approach. For a SRW the EVD ratio was evaluated to be 2.4%. To evaluate the contact damping the magnitude of the damping coefficient was estimated to be proportional to the secant stiffness at the maximum displacement. The same walls were also subjected to four earthquake ground motions using the University of Canterbury shake table. Both the walls that incorporated tension-compression yielding dissipaters were the most effective PT wall systems. The peak displacement response was consistently low and the high level of structural damping ensured peak accelerations were low. The SRW returned the largest peak displacement and acceleration; however still satisfied the target drift ratio of 1.5% when subjected to ground motions that were scaled to the maximum credible event seismic intensity.

Wight et al. [29, 30] performed shake table testing on unbonded PT masonry walls to investigate the dynamic response and this was the first experimental dynamic test on any type of PT rocking wall system. The voids within the concrete masonry walls were partially grouted and the tendons were unbonded over their entire length. The seismic performance of the system was found to be desirable due to the nonlinear elastic response and the low damage sustained. The level of prestress was shown to have a large influence on the peak wall displacement. Traditionally masonry walls have a vastly different response to concrete walls under earthquake excitation but when PT a very similar rocking behaviour is exhibited.

2.6.2 Column testing

Similar PT concepts have been applied to precast concrete bridge piers. Cheng [63] conducted free vibration testing on four rocking bridge piers, three PT and one free of prestressing. The aim was to validate the theoretical contact damping proposed by previous researchers, including theoretical models proposed by Mander and Cheng [64], Makris and Konstantinidis [65], and recommendations from the Federal Emergency Management Agency 356 document [66]. These theoretical models are discussed further in section 2.7. A number of different parameters were investigated that included steel and plastic materials used as rocking interfaces, area of anchor bars, aspect ratio and size effect of columns. Before evaluating the theoretical contact damping, the experimental EVD of the system was evaluated using the same assumptions made by

Priestley [67], these assumptions will also be discussed further in section 2.7. The results found the EVD to range from 1-3% for PT columns and 2-5% for free rocking columns.

Cheng [68] also performed shake table tests on a self-centering bridge substructure varying the material used for the rocking interface and the input ground motions. Both PT and free rocking substructures were studied. The theoretical contact damping was evaluated using the same three different methods discussed in the previous paragraph, including theoretical models proposed by Mander and Cheng [64], Makris and Konstantinidis [65], and recommendations by FEMA [66]. A fourth method investigated used a modified response spectra to measure experimentally the contact damping of the system. The bridge structure was analysed using a fast Fourier transform (FFT) which showed the variable vibrating frequencies. This exhibits a unique advantage in preventing resonance of structural response to ground shaking.

2.6.3 Entire building testing

Recently, as part of a large collaborative project to establish diaphragm seismic design methodology (DSDM), shake table testing was conducted on a prototype precast concrete parking structure at the University of California at San Diego (UCSD) [69]. Although the focus of the test was diaphragms, the three storey, half scale test structure's lateral force resisting system consisted of two hybrid walls. The energy dissipation of these walls was increased using reinforcing bars placed across the joint between the wall and foundation. To transfer shear forces from the floors into the walls, vertical, slotted shear connectors were used. This detail excluded the walls from carrying gravity load but allowed transfer of horizontal inertia forces between the floor and wall. Preliminary results confirmed that these connectors performed well under small intensity earthquake loads, but failed when the building was subjected to maximum considered input motions due to uplift of the wall exceeding the slot capacity. Recently, Belleri et al. [32] reported on the performance of the hybrid walls from the testing performed at UCSD which highlighted the excellent performance of the hybrid wall systems. There has also been full scale testing on a four storey building that utilised PT hybrid walls at the E-Defense laboratory in Japan [34]. The building was subjected to several high intensity base motions with the hybrid walls sustaining limited damage and performing well.

2.6.4 Modelling approaches

Many approaches have been investigated in an attempt to accurately model unbonded PT rocking wall systems. The following paragraphs provide an overview on these approaches and summarise the advantages and disadvantages of each.

2.6.4.1 *Fibre models*

An approach used to model unbonded PT precast concrete walls consists of an analytical fibre element model as depicted in Figure 2.9 proposed by Kurama et al. [4]. A fibre model divides an element into a number of segments along its length, with each segment consisting of a number of discrete fibre layers. Each fibre represents either concrete or steel and is associated with an appropriate uniaxial stress-strain relationship. The model developed by Kurama et al. [4] used the DRAIN-2DX program and represented a six-story unbonded PT precast concrete wall. The model was used to conduct both nonlinear static pushover analysis and nonlinear dynamic time-history analysis. The concrete wall panels were modelled using fibre elements and the unbonded PT steel tendons were modelled using truss members. The wall model was found to account for axial-flexural interaction, hysteretic behaviour of the PT steel, and concrete including crushing of concrete and gap opening along the horizontal joints. To account for the displacement compatibility of the system the tendons were constrained only at the top and bottom of the concrete panels to represent the anchorages. The damping incorporated in the model for dynamic analysis was 3% viscous damping. The response calculated by the fibre model closely matched the response measured during the experimental test; however the model did not capture the behaviour during unloading with great accuracy. The nonlinear time history analysis showed that an unbonded PT precast wall experienced larger peak lateral displacements than a comparable monolithic cast-in-place RC when subjected to earthquake loading, but has significantly less residual displacement following the earthquake.

A limitation of the fibre model is that the wall panel fibre elements are based on the assumption that plane sections remain plane which is not true for regions of the wall panel immediately adjacent to the horizontal joints. Therefore the model does not accurately capture the local stresses and strains of these regions. However, the main advantage of using fibre elements is that a reasonably accurate model can be developed using only uniaxial stress-strain models compared to cyclic test data.

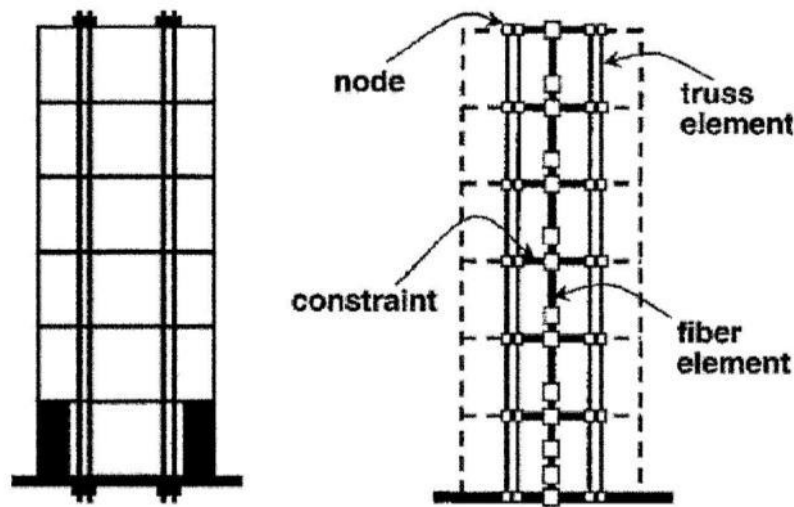


Figure 2.9 – Fibre analytical wall model [4]

Kurama [26] extended the fibre model to investigate the inclusion of supplemental energy dissipation to unbonded PT precast concrete walls. The proposed supplemental energy dissipation system used linear viscous fluid dampers placed diagonally in-plane with the wall. The wall system was modelled in a similar manner to the fibre model discussed previously, with truss elements used to represent the viscous dampers. The system without supplemental energy dissipation was assumed to have 3% equivalent viscous damping and the additional dampers used stiffness proportional damping. The nonlinear dynamic time-history analyses of walls with and without supplemental energy dissipation show that the inclusion of damping is, on average, very effective in reducing the maximum lateral drift at the roof level. Further studies have used similar fibre models to represent unbonded PT walls with various forms of additional energy dissipation devices [56, 70, 71].

Erkman and Schultz [5] also used an extension of the fibre model originally described by Kurama [4] to investigate the seismic response of unbonded PT walls where the prestressing tendons were allowed to yield. Five different walls with various prestressing tendon configurations were investigated. It was found that the tendon location had a significant effect on wall stiffness and maximum lateral displacements, but negligible impact on self-centering behaviour. Self-centering was achieved for all walls even when significant yielding of the tendons and subsequent loss of the initial prestressing force occurred.

2.6.4.2 Lumped plasticity models

Another approach used to model self-centering walls is a lumped plasticity model or concentrated plasticity model (a simple macro-model). A lumped plasticity model relies on the assumption that the main inelastic demand occurs at discrete critical sections. This is appropriate for an unbonded PT wall where the inelastic demand is concentrated at a single crack at the wall-foundation interface. Due to the opening and closing of a single crack during rocking, an infinite curvature is developed at the critical section resulting in the moment-rotation relationship being preferred over traditional moment-curvature when characterising the section behaviour. Rotational inelastic springs with appropriate nonlinear hysteresis behaviour can be assigned to represent the inelastic action at the wall-foundation interface, while elastic elements are used to represent the structural members. The rotational springs which are usually in parallel have been extensively developed to model the moment rotation response of PT rocking systems [23, 41, 60, 72, 73].

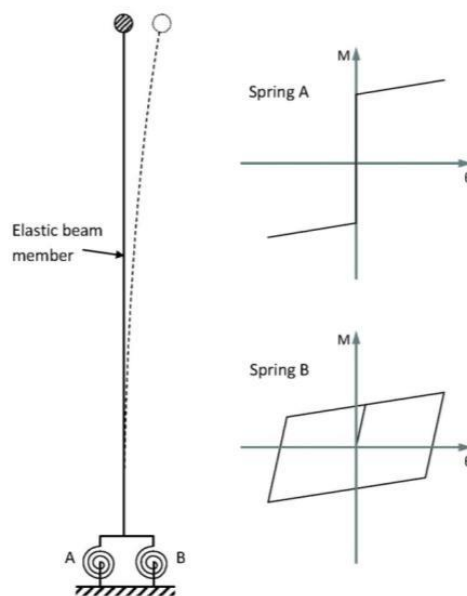


Figure 2.10 – Lumped plasticity model [41]

A typical example of a lumped plasticity model is shown in Figure 2.10 from Henry [41]. In the example two springs are used at the wall base with one spring representing the bilinear elastic response of a rocking wall (Spring A) and the second spring representing the elasto-plastic hysteresis response of the supplementary energy dissipating elements (Spring B). It is important to note that the spring elements are situated at the rocking interface and are therefore of zero

length. The limitation of lumped plasticity models is that proper understanding of the physical problem is required to attain accurate results, because the assigned properties of each spring are usually based on a section analysis or experimental results.

2.6.4.3 Multi-spring model

A multi-spring model adopts a series of axial springs to represent the interface between the wall and the foundation, with additional springs to represent dampers and PT tendons. The springs across the interface are compression only springs that allow gap opening during rocking. This method is an approximation of the actual rocking response of each wall by characterising the critical section.

Pennucci [74] developed a multi-spring model where the PT tendons were represented by pre-stressed elasto-plastic springs. The hysteretic dampers in the form of mild steel reinforcing bars were represented by elasto-plastic springs, with degrading stiffness in order to account for the Bauschinger effect which decreases the unloading and reloading stiffness in the case of repeated cyclic loads. The damping was modelled using the Wilson-Penzien model that allows different values of damping to be defined for every mode. The multi-spring model technique was shown to efficiently reproduce the stiffness degradation of the PT wall system.

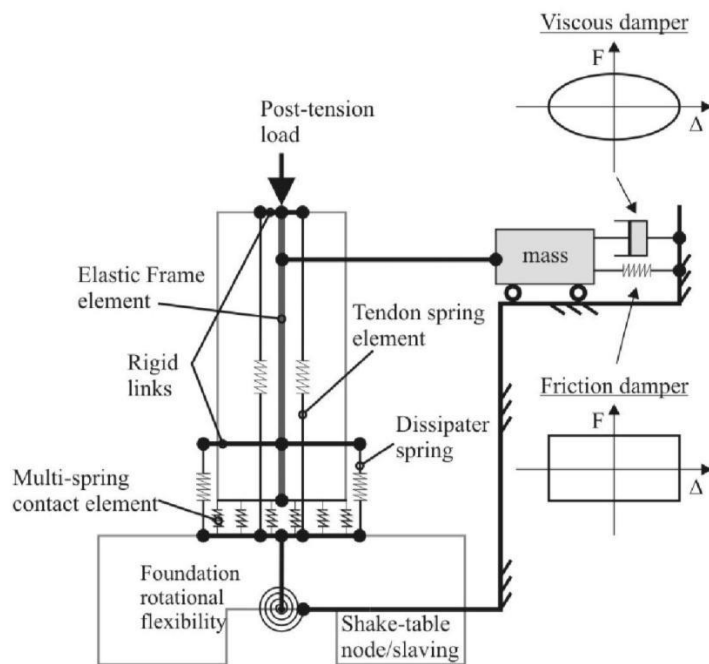


Figure 2.11 – Macro model with contact damping included [31]

Marriott et al [31] used the macro model shown in Figure 2.11 to represent both a SRW and hybrid wall. Based on Marriott's experimental test of SRW and hybrid walls described in section 2.6.1 the contact damping was evaluated to be 2.4%. Also, based on other analysis described in Marriott [13] the damping model was assumed to be proportional to both velocity and displacement. However, the actual portion of contact energy dissipation attributed to both velocity and displacement was not quantified. A 50/50 split was assumed to represent the response well based on analytical comparisons with free vibration decay. Therefore a damping model utilising a velocity proportional damper (viscous damper) element and a displacement proportional damper (friction damper) element was implemented in the model shown in Figure 2.11. From previous research, Marriott concluded that the response of a PT rocking wall can be insensitive to the amount of energy dissipation included and the model should be as simple as possible. It is for this reason that the contact energy is accounted for by means of an additional damper element at the effective height of the system as shown in Figure 2.11. The secant stiffness, which is defined by the maximum displacement of the system, was used to determine the damping coefficient and friction damper force. The model did not compare well with the dynamic snap back tests of the SRW, but proved more accurate for systems with additional damping. It is important to realise that despite this model not accurately predicting the time history response of the unbonded PT wall, it is still representing the contact damping more effectively than previous researchers who neglected it completely.

2.6.4.4 Finite element models

Finite Element Models (FEM) have been used to model PT precast walls with and without supplementary damping. Kurama [26] used the finite element method to model an unbonded PT precast concrete wall with supplemental viscous damping in an attempt to validate the fibre model discussed in section 2.6.4.1. The model was developed using ABAQUS with nonlinear rectangular plane stress elements to represent the wall panels, and gap/contact elements to model the gap opening behaviour along the horizontal joints. The fibre model and FEM were found to produce very similar results. Henry [41] developed a FEM using ABAQUS for both a single rocking wall and the PreWEC system. A 3D FEM was developed to calculate the full cyclic response of the PreWEC test specimen which captured the cyclic response with excellent accuracy. A FEM is the most complex of modelling techniques and therefore computationally intensive, however it does produce detailed results of both the local and global behaviour of a

wall system. Ma et al. [75] found that modelling of the dynamic behaviour is not well handled by ABAQUS.

2.6.4.5 Other techniques

Ma et al. [75] undertook an assessment of the current procedures for predicting the in-plane behaviour of “controlled rocking walls”, otherwise known as unbonded PT walls. One method investigated was idealising the wall as a single degree of freedom (SDOF) structure and implementing a nonlinearly elastic rotational base connection then solving its governing differential equation using numerical integration techniques. This is similar to the lumped plasticity model in theory, except instead of using EVD, the damping was incorporated using an apparent coefficient of restitution approach. Using this approach, the rotation speed of the wall was reduced by an apparent coefficient of restitution whenever the wall rotated through zero displacement position. This was the simplest approach investigated by Ma et al. and proved to be no less accurate than the other more complicated approaches. Ma et al. showed that the selection of damping mechanism greatly varies the response of the PT rocking wall and selecting a damping scheme compatible with a mechanism of intermittent, instantaneous dissipation of energy gave the best result.

Ma [76] investigated two possible techniques for predicting the time-history response of a controlled rocking wall using shake table and free vibration data from Wight [29] who tested PT masonry walls. The techniques investigated were 1) a nonlinearly elastic equivalent SDOF approximation, and 2) solving the modified Housner type free rocking governing differential equations adopting the principle of equating the prestress as additional gravity load. The first technique used a Dirac- δ function for the damping force, as described by Prieto et al. [77], that emulates the energy dissipation of the wall as it passes through the upright position. The Dirac- δ function allows a user to use a continuous equation for damping rather than a piecewise formulation as required for the coefficient of restitution approach and still uses a coefficient of restitution in the damping force equation. Several simulations were performed with different values of coefficient of restitution and this highlighted that there was no single coefficient of restitution that could simulate the energy dissipation correctly. The second approach called the Modified Housner Substitute Gravity (MHSG) method considered the PT wall system as a free standing wall with the influence of post-tensioning simulated by an additional gravity load. When using a single coefficient of restitution within this approach more accurate results were

obtained in comparison to the equivalent SDOF approach. However, the MHS approach was found to be unable to emulate the distinctive velocity and acceleration behaviours of the free vibration response of a PT masonry rocking wall. The MHS approach was then improved by adopting a Dirac- δ function to represent the assumption that the centre of rotation migrates smoothly from the centre of the wall to the wall edge with increasing displacement. This greatly improved the simulated response in comparison to the original MHS investigated. The MHS procedure is still poor at estimating the response of the controlled rocking wall at small displacements. Additionally, for both these approaches the best results were developed by implementing a stepwise reduction in wall velocity when the wall crossed zero displacement position. A stepwise reduction in velocity was implemented by using a different value of the coefficient of restitution depending on the current velocity and the best results were obtained via a trial and error method.

2.6.4.6 Conclusions on modelling techniques

All methods can predict the static cyclic response with reasonable accuracy, from simplified models with calibrated springs to detailed FEM that represent the actual mechanics and material properties. The fibre model does not accurately capture the local stresses and strains of the regions located adjacent to the horizontal joints due to violation of the assumption that plane sections remain plane. The significant advantage of using fibre elements is that a reasonably accurate model can be developed using only uniaxial stress-strain models. A multi-spring model is advantageous as it is an approximation of the actual rocking response of each wall allowing the user to attain local deformation such as uplift of the wall. A multi-spring model is also more complicated than a lumped plasticity model and requires accurate calibration of springs and dampers to correctly model the response. The limitation of a lumped plasticity model is that proper understanding of the physical problem is required to attain sensible results but if this can be done accurately good results can be produced.

The majority of these modelling techniques have been used based on either no validation at all or validating against a static moment-rotation or force-displacement response. Ma [75] demonstrated that a model which can predict the correct static response of a PT rocking wall does not necessarily predict the correct dynamic response. Also it is apparent if the model is validated against a real dynamic test a technique which has instantaneous energy dissipation gives the best result. Despite this, the majority of modelling research assumes an equivalent

viscous damping for the system. The ways which damping can be incorporated into a model are limited depending of the model type. In a lumped plasticity model explicit modelling of contact damping is impossible, equivalent viscous damping is the only option. While for a multi-spring or FEM model contact damping options are available but equivalent viscous damping is usually assumed.

2.7 EVALUATION OF DAMPING

This section describes structural damping in general and specifically discusses the evaluation of contact damping which is the energy dissipation due to impact when rocking. The intent of this section is to provide background for the current state-of-art of structural damping evaluation.

2.7.1 General

All structural systems consist of a number of different sources of energy dissipation or damping. The inherent damping mechanisms can consist of air resistance, external friction, internal friction, and imperfect elasticity (even when stresses do not exceed the elastic limit) [78]. All of these mechanisms can contribute to the ‘elastic damping’ in the structure, often characterised as the damping when the structure remains in the elastic range. Other common energy dissipation sources in RC structures include the energy loss due to repeated movements along internal cracks, friction etc. Of course, damping forces are complex in nature and difficult to determine and no real structural system will have perfect viscous damping forces, and hysteretic damping may also occur due to repeated cyclic loading of structural elements in the inelastic range. Estimates of EVD associated with hysteresis are often calculated using the force-displacement behaviour of a structural system measured during pseudo-static cyclic testing. Another type of damping relevant to unbonded PT walls is contact damping. Contact damping is the energy dissipation that occurs at impact during rocking motion and can only be determined experimentally. As discussed in the following section there has been several pieces of research related to evaluation of contact damping for rocking structures. Despite the often low magnitude of contact damping, often estimated to be between 2-3%, an examination of any earthquake response spectrum will show that even small amounts of damping, such as 2-5%, will significantly reduce the response of the structure.

Overall, a suitable damping model is required in structural analysis to represent all the energy dissipation occurring in the structure. The state-of-the-art structural damping does not provide a method to determine the damping capacity based on material properties and geometrical characteristics of a structure. Usually it is appropriate to attain a damping model that is capable of modelling realistic damping forces that provide an accurate estimation of the seismic response of a structure. Development and validation of these types of damping model can often only be achieved by conducting dynamic testing. As described in the previous section few researchers have performed dynamic testing, and as a result there has been limited validation of numerical models from dynamic test data. There has been no validation of numerical models for a jointed type wall system.

2.7.2 Contact damping

A number of theoretical equations have been developed to evaluate contact damping. Investigations into rocking behaviour were initially on structures free to rock on their foundations [67]. Priestley et al. [67] compared the theory developed by Housner for free rocking of a rigid block, to a series of experimental shake table tests that were conducted using a number of different foundation conditions. Priestley [67] used the EVD exponential decay relationship for a linear system (Equation (2-6)) to derive an equation for EVD of a rocking system. Taking advantage of the fact that lateral displacement was proportional to angular displacement and that two impacts occurred per cycle Equation (2-6) was adjusted to Equation (2-7). Using Housner theory for the predicted angular displacement of the system after n impacts the theoretical equivalent viscous damping could be calculated for a rocking system. The coefficient of restitution was incorporated within the angular displacement relationships developed by Housner. Priestley et al. adopted the best fit approach for the selection of the numerical r value using the experimental results. Many other researchers have also adopted this approach due to the inaccuracy associated with violation of the assumption of purely inelastic impacts.

$$\xi_{eq} = \frac{1}{2\pi j} \ln\left(\frac{u_i}{u_{i+j}}\right) \quad (2-6)$$

$$\xi_{eq} = \frac{1}{\pi n_i} \ln\left(\frac{\theta_i}{\theta_n}\right) \quad (2-7)$$

Makris and Konstantinidis [65] approximated the relationship to Equation (2-8) due to the observation that the relation presented in Equation (2-7) was relatively insensitive to initial rotation and number of impacts (n_i).

$$\xi_{eq} = -0.34 \ln(r_r) \quad (2-8)$$

In the same study Makris and Konstantinidis investigated the fundamental differences between the oscillatory response of a SDOF oscillator (regular pendulum) and the rocking response of a slender rigid block (inverted pendulum). The study identified the differences in the restoring mechanisms, stiffness and damping values of the SDOF oscillator and the rocking block. It was concluded that the two systems are fundamentally different and the response of one should not be used to draw conclusions on the response of the other. Importantly the paper also addressed the existing rocking design methodology included in FEMA 356 document [79]. The FEMA 356 rocking design methodology was based on the earlier experimental study by Priestley et al. [67] and proposed Equation (2-9) as a simplified expression for the evaluation of the equivalent viscous damping ratio. Makris and Konstantinidis found that the FEMA 356 procedure grossly overestimated the rotations of rocking structures to the extent that the method is fundamentally flawed and proposed the more accurate Equation (2-8) for the equivalent viscous damping of a rocking structure. It is important to note that both Equation (2-8) and Equation (2-7) were developed for free rocking structures as opposed to a controlled rocking structure, as they were based on Housner predictions of angular displacement after impact for a simple rocking block.

$$\xi_{eq} = 0.4(1 - \sqrt{r_r}) \quad (2-9)$$

Mander and Cheng [64] developed a theoretical relationship for the contact damping of rocking bridge piers that utilised post-tensioning. An energy approach was adopted to assess the EVD of the PT rocking piers by assessing the energy absorbed and dissipated in each half cycle. For each half cycle a single impact occurs, thus the EVD effectively represented the contact damping from an impact. Quincy et al. [75] used the relationship proposed by Mander and Cheng to produce

Equation (2-10) which estimates the equivalent viscous damping for a PT only rocking wall using the coefficient of restitution.

$$\xi_{eq} = (1 - r_r) / [\pi \left(1 - \frac{\Delta}{B}\right)] \quad (2-10)$$

A number of researchers have calculated the contact damping of SRWs from experimental test results in terms of the EVD. Ma [76] reported on the free vibration test results of PT masonry walls conducted by Wight et al. [80]. The EVD due to contact damping was evaluated and found to range from 2.61% to 3.28%. For the same tests the equivalent viscous damping calculated using Equation 2.8 was found to be 1.96% and 3.06%.

Marriott [31] investigated the contact damping of a SRW. By studying the energy content of a free vibration test and using the principle of conservation of energy the total EVD of the wall system was evaluated. By modifying the EVD exponential decay relationship for a linear system described by Equation (2-6), Equation (2-11) was proposed by Marriott to calculate EVD.

$$\xi_{eq} = \frac{1}{2t\omega_n} \ln \left(\frac{E_o}{E_k(t)} \right) \quad (2-11)$$

Where ξ_{eq} is the EVD ratio, t is the time since release, E_o is this initial energy in the system, $E_k(t)$ is the kinetic energy of the system at time t , and ω_n is the circular natural frequency of the system.

As the wall was a SRW, the EVD evaluated was likely to be a combination of contact damping, material nonlinearity of the concrete at the rocking interface and intrinsic material damping of the precast element. From the energy analysis a damping ratio of 2.4% was evaluated and estimated to be proportional to the secant stiffness at release. By applying an error of $\pm 25\%$ to 2.4%, the experimental data fell within the limits.

2.8 CODIFICATION

In 2006 design provisions for the use of unbonded PT precast concrete members were introduced into the New Zealand concrete design standard (NZS 3101-06) [18]. Appendix B of NZS 3101 is termed ‘Special provisions for the seismic design of ductile jointed precast concrete structural

systems' and it details provisions that must be accounted for when detailing jointed precast concrete components. Jointed systems are defined as structural systems in which the connections between the precast concrete elements are weaker than the elements themselves. Following the inclusion of the aforementioned appendix in NZS 3101 the New Zealand Concrete Society published a design handbook titled the PRESSS Design Handbook [19] that detailed more specific guidelines and design examples.

Following the development of self-centering concrete walls in the US, the American Concrete Institute (ACI) set up Innovation Task Group 5 (ITG-5) to develop design provisions for such structures in regions of high seismicity. Two documents were produced; ITG-5.1 [16] and ITG-5.2 [17]. ITG-5.1 defines the minimum experimental evidence that can be deemed to satisfy the use of unbonded PT precast concrete walls for building applications. The test methodology to be used and the performance targets are also described in ITG-5.1. Two separate experimental tests are required to satisfactorily meet the performance targets to successfully validate a new wall system. ITG-5.2 defines procedures that may be used to design both jointed and hybrid unbonded PT precast concrete shear walls which have been experimentally validated in accordance ITG-5.1.

2.9 DESIGN PROCEDURES

The traditional structural design approach is to use force-based design (FBD). In this approach design base shear is obtained from the estimated fundamental period and total mass of the structure, incorporating the influence of seismic intensity in terms of a design spectral acceleration. Using FBD the target level lateral displacement of the building is not directly used to quantify the design base shear [81]. In contrast, direct displacement-based design (DDBD) is a performance based methodology for seismic design that considers material strain limits at the start of the design process which are able to be related to damage states and target drifts.

Numerous studies have investigated the appropriateness of FBD for unbonded PT systems in comparison to DDBD. Rahman and Sritharan [81] conducted extensive nonlinear dynamic analysis of the wall system used in the PRESSS test building with the aim of investigating the performance of the wall system when both FBD and DDBD were used. The results showed that when designed with DDBD, the wall system attained higher inter-storey drifts than the building

designed used FBD, but the maximum floor accelerations were higher for the FBD wall system. The use of DDBD results in a significantly lower design base shear, thus the actual strength of the system is lower; therefore higher ductility demands are expected, resulting in increased accuracy of the design.

Specifically, force-based design characterises a structure in terms of elastic, pre-yield, properties (initial stiffness (k_i) and elastic equivalent viscous damping (ξ_{el})) while DDBD characterises the structure by a secant stiffness at maximum displacement and a level of EVD, representative of the combined elastic damping and hysteretic energy absorbed during inelastic response. For unbonded PT wall systems it is recognised that the strength and hysteretic damping of jointed PT systems is dependent on lateral drifts [3, 82]. Also, FBD penalises unbonded PT wall systems due to the high initial stiffness. For these reasons Priestley et al. [20] proposes that DDBD is used for seismic lateral force design of unbonded PT systems.

2.9.1 DDBD overview

As just described DDBD is the recommended design procedure for unbonded PT wall systems. DDBD utilises the concept of an Equivalent Linear System (ELS) defined by an equivalent damping and equivalent stiffness to represent the response of a nonlinear system. This concept is based on the substitute structure approach pioneered by Gulkan and Sozen [83]. The substitute structure approach adopted by DDBD involves estimating the maximum response of a nonlinear MDOF system with a linear viscoelastic SDOF system with appropriately defined damping and stiffness properties [84]. A schematic is presented in Figure 2.12 where the key steps of DDBD are highlighted as described by Priestley et al. [20]. The steps are as follows:

1. As shown by Figure 2.12(a) and (b) the first step is to convert the structure of interest from a multi-degree of freedom system into an equivalent single degree of freedom system (SDOF) or “substitute structure”. A target drift is selected and a displaced shape is assumed. The design lateral displacement (Δ_d) is calculated using Equation (2-12) and the effective mass (m_e) and height (h_e) of the equivalent SDOF are calculated using Equation (2-13) and Equation (2-14).

$$\Delta_d = \frac{\sum_{i=1}^n (m_i \Delta_i^2)}{\sum_{i=1}^n m_i \Delta_i} \quad (2-12)$$

Where n is the number of storeys, Δ_i is the design displacement at storey i and m_i is the mass of level i

$$m_e = \frac{\sum_{i=1}^n m_i \Delta_i}{\Delta_d} \quad (2-13)$$

$$h_e = \frac{\sum_{i=1}^n (m_i \Delta_i H_i)}{\sum_{i=1}^n (m_i \Delta_i)} \quad (2-14)$$

2. Once the design displacement at maximum response is determined the corresponding EVD is estimated from the expected ductility demand as shown in Figure 2.12(c). The system EVD should be checked and revised following member design.
3. The effective period (T_e) at maximum displacement response measured at the effective height can be read from a set of displacement spectra for different levels of damping as shown in Figure 2.12(d).
4. The effective stiffness of the equivalent SDOF at maximum displacement is then calculated using Equation (2-15).

$$K_e = \frac{4\pi^2 m_e}{T_e^2} \quad (2-15)$$

5. The base shear force which is also the design lateral force can then be calculated using Equation (2-16)

$$F = V_{base} = K_e \Delta_d \quad (2-16)$$

6. Lastly, the design base shear is distributed to the entire structure and the member actions are calculated.

Overall, DDBD requires a number of assumptions, for instance the displacement profile must be assumed in order to estimate the design displacement. For precast walls with unbonded PT, the deformation at the maximum lateral displacement is dominated by the base rotation due to rocking which results in a linear displacement profile. For this reason Priestley et al. [20]

recommends that for PT precast concrete rocking wall buildings up to 10 storeys high the displacement at each storey can be calculated using Equation (2-17).

$$\Delta_i = \theta_d H_i \tag{2-17}$$

Where Δ_i is the design displacement at storey i and H_i is the height of level i .

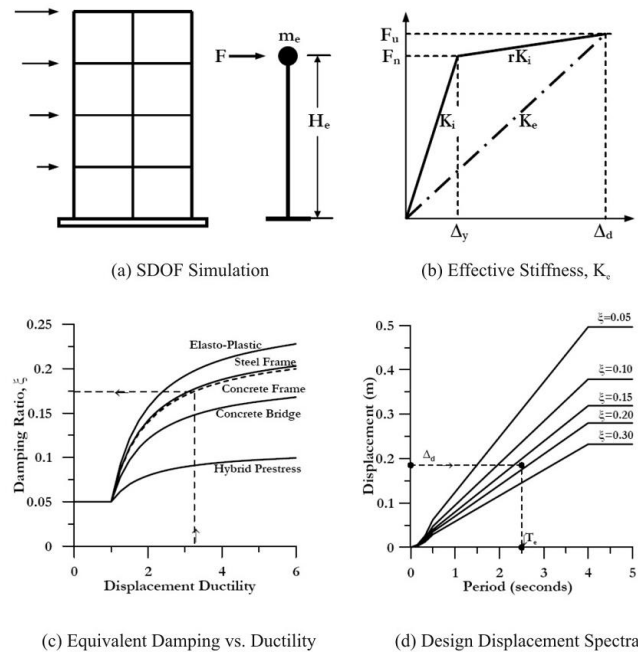


Figure 2.12 – DDBD key steps [20]

2.9.2 EVD in DDBD

One of the other key elements of the DDBD design procedure is the determination of EVD. DDBD requires relationships between displacement ductility and EVD as previously shown in Figure 2.12(c). Priestley et al. [20] defines the total EVD (ξ_{eq}) as equal to the sum of the elastic (ξ_{el}) and hysteretic (ξ_{hyst}) damping as described by Equation (2-18). The hysteretic damping (ξ_{hyst}) depends on the hysteresis rule appropriate for the structure being designed. Normally for concrete structures the elastic damping ratio is taken as 5% critical damping.

$$\xi_{eq} = \xi_{el} + \xi_{hyst} \tag{2-18}$$

2.9.2.1 *Elastic damping*

The elastic damping component of EVD is usually included in time history analysis to account for damping that is not captured by the hysteretic model. An issue addressed in recent literature is what stiffness the elastic portion of the EVD ratio should be proportional to during nonlinear time history analyses, with findings pointing to use of tangent stiffness instead of initial stiffness to avoid unrealistically large damping values at high natural frequencies.

However, as discussed by Priestley et al. in DDBD the initial elastic damping adopted is related to the secant stiffness to maximum displacement. Since the response velocities of the “real” and “substitute” structures are expected to be similar under earthquake loading, the damping force will be much lower in the “substitute” structure due to the lower stiffness in comparison to the real structure. Grant et al. [85] has determined a method to adjust the DDBD elastic damping required to ensure compatibility between the “real” and “substitute” structure. The adjustment required depends on whether initial stiffness damping or tangent stiffness damping is adopted for time history analyses, only tangent stiffness damping is discussed here as it is believed to be the correct procedure. When tangent stiffness damping is adopted for time-history analysis the elastic damping coefficient used in DDBD must be less than the specified tangent stiffness coefficient. Grant et al. compared results of elastic substitute structure analyses with inelastic time history results to determine the correction factor to be applied to the elastic damping coefficient which alters Equation (2-18) to Equation (2-19) with the introduction of the adjustment factor (κ) where κ is defined by Equation (2-20) and λ' is the secant stiffness correction factor defined in Priestley et al.

$$\xi_{eq} = \kappa \xi_{el} + \xi_{hyst} \quad (2-19)$$

$$\kappa = \mu^{\lambda'} \quad (2-20)$$

2.9.2.2 *Hysteretic damping*

How to approximate the hysteretic damping best has been a topic of discussion among researchers for many years. Jacobsen [86] first proposed using the energy dissipated in one cycle of harmonic response for the equivalent linear representation of a nonlinear viscous damping term assuming an arbitrary corresponding stiffness value to determine the damping. Rosenblueth and Herrera [87] modified the approach of Jacobsen, by equating the energy dissipated in a cycle of harmonic hysteresis with the same quantity for a linear viscous system at resonance. The linear

system was assigned an effective stiffness equal to the secant stiffness to the point of maximum displacement. This resulted in an expression for EVD described by Equation (2-21), where A_h is the area within one complete cycle of force-displacement response and F_m and Δ_m are the maximum force and displacement achieved in the loops. This damping is related to the secant stiffness to maximum response and is thus compatible with the assumption of structural characterisation by stiffness and damping at peak response.

$$\xi_{hyst} = \frac{A_h}{2\pi F_m \Delta_m} \quad (2-21)$$

Grant et al. [85] discusses how Rosenblueth and Herrera's EVD method generally predicts lower displacements than calculated for the nonlinear system, i.e. the method over damps. In general they found that a linear system with an effective stiffness significantly greater than secant achieves more accurate predictions.

The approach used in and recommended by Priestley et al. [20] uses values of EVD that have been calibrated for different hysteresis rules to give the same peak displacements as the hysteretic response, using inelastic time history analysis. Grant et al. [85] undertook a detailed study using a wide range of hysteresis rules based on a small number of spectrum-compatible artificial accelerograms where the results of the elastic and inelastic analyses were separately averaged and compared. In each the EVD was varied until the elastic results of the equivalent substitute structure matched that of the real hysteretic model. The study was carried out without additional elastic damping and the hysteretic damping was found to be in the form of Equation (2-22), where a, b, c, and d, are coefficients that represent period-dependency and the specific hysteretic rule.

$$\xi_{hyst} = a \left(1 - \frac{1}{\mu^b}\right) \left(1 + \frac{1}{(T_e + c)^d}\right) \quad (2-22)$$

Dwairi and Kowalsky [88] also conducted a similar study that involved the use of a large number of real earthquake accelerograms and the EVD was calculated for each record, ductility level, effective period, and hysteresis rule separately, and then averaged over the records to provide a relationship for a given rule, ductility, and period. The study was also carried out without additional elastic damping and the hysteretic damping was found to be in the form of Equation (2-23), where the coefficient C depends on the hysteresis rule.

$$\xi_{hyst} = C \left(\frac{\mu - 1}{\mu\pi} \right) \tag{2-23}$$

2.9.2.3 EVD Design recommendations

Priestley et al. [20] formulated Equation (2-24) by adopting the simpler damping-ductility equation developed by Dwairi and Kowalsky [88] incorporating the elastic damping, where R_ξ is described as the damping factor for different structural systems and μ is the system displacement ductility. This equation is only valid for elastic damping equal to 5% and the specific hysteretic rules investigated in Priestley et al. [20].

$$\xi_{eq} = 0.05 + R_\xi \left(\frac{\mu - 1}{\mu\pi} \right) \tag{2-24}$$

When hysteretic rules whose characteristics differ from those investigated in Priestley et al. are used an appropriate ductility-damping relationship can be developed based on inelastic time history analysis using a similar method to Grant et al. Although, it is recognised that this will not be done in design practice as such some reasonable estimates of the relationship can be obtained by comparing the relationships between the area-based viscous damping given by Equation (2-21) with the hysteretic component of the calculated viscous damping as plotted in Figure 2.13 taken from Priestley et al.

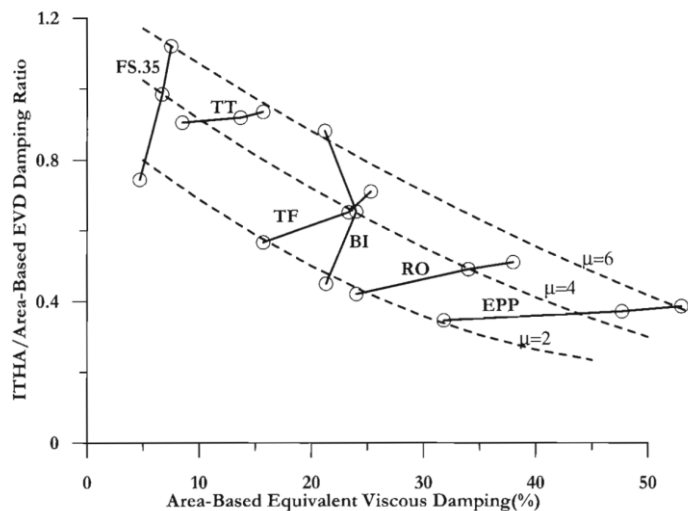


Figure 2.13 – Correction factors to be applied to area-based EVD ([20])

2.9.2.4 EVD recommendations from NZS3101 and PRESSS Design Handbook

The following describes EVD recommendations from the PRESSS Design Handbook and Appendix B of NZS3101 for “hybrid connections/systems”. It should be noted that a hybrid connection/system in Appendix B of NZS3101 refers to a jointed structure in which the self-centering capability is provided by PT and/or axial compressive load, and the energy dissipation is provided by yielding non-prestressed reinforcement or other special devices, this incorporates walls of both a “jointed” and “hybrid” nature. The recommendation for calculation of EVD of a jointed connection/system in Appendix B of NZS3101 is to use the moment contribution ratio (λ), which is the ratio of the PT and axial load moment contribution to that of the dissipating devices and interpolate between a lower and upper bound. The lower value is defined as the unbonded only connection with an EVD value equal to 5% and the upper bound is defined as a monolithic frame system described by Equation (2-25), where μ is the structural ductility factor. The monolithic frame system EVD equation is for a degrading-stiffness Takeda rule and was given by Priestley [89]. The weighted approach to calculate total EVD using a sum of the contributions from the post-tensioned only to the purely dissipative system is a conservative yet conceptually viable approach originally proposed by Priestley [89].

$$\xi_{upper} = \xi_{hyst} = 5 + 30 \left(1 - \frac{1}{\sqrt{\mu}}\right) \quad (2-25)$$

The PRESSS Design Handbook simplifies the interpolation procedure by arranging it into a single equation as specified by Equation (2-26), where λ is the moment contribution ratio, as defined by Equation (2-27).

$$\begin{aligned} \xi_{eq} &= \xi_{pt} + \xi_{hyst} \\ &= \frac{M_{pt} + M_N}{M_{total}} \cdot \xi_{pt} + \frac{M_s}{M_{total}} \cdot \xi_{upper} \\ &= \frac{\lambda}{\lambda + 1} \cdot \xi_{pt} + \frac{1}{1 + \lambda} \cdot \xi_{upper} \\ &= 5\% + 30 \frac{\left(1 - \frac{1}{\sqrt{\mu}}\right)}{(\lambda + 1)} \end{aligned} \quad (2-26)$$

$$\lambda = \frac{M_{pt} + M_N}{M_s} \geq \alpha_o \quad (2-27)$$

Where M_{pt} , M_N , and M_S are the flexural strength contributions of the PT tendons, axial load, and energy dissipating devices, and α_o is the overstrength factor for the energy dissipating devices.

Contact damping can be added to the hysteretic damping provided experimental evidence of the dynamic rocking behaviour of the connection/system is available.

2.9.3 EVD for jointed type wall systems

This section provides a specific interpretation of the EVD determination methods proposed by Priestley et al. [20] and those proposed by Appendix B/PRESSS Design Handbook for jointed type wall systems. The method used to determine the EVD for the design of the original jointed wall used in the PRESSS programme test building is also identified.

2.9.3.1 *PRESSS programme jointed wall*

For the DDBD of the jointed wall system used in the PRESSS test building Nakaki et al. [54] estimated the EVD from the model hysteretic loop behaviour and checked the value at the end of design. If they differed significantly, the process was repeated with a new value of assumed EVD. This process directly uses the EVD at set drifts, disregarding any damping-ductility relationship. However, as discussed by Priestley et al. [20] the EVD evaluated from hysteretic behaviour needs adjustment to represent the EVD appropriate for inelastic time history analysis.

2.9.3.2 *Priestley et al. [20]*

Priestley et al. [20] recommends that design of precast PT walls closely follows the methodology outlined for PT frames in the same text. Yield displacements can be based on the stiffness of the un-cracked wall sections up the full height, and effective damping levels for walls without supplemental damping can be assumed to be 5%, related to the effective stiffness. For systems with a portion of the flexural strength provided by added mild-steel reinforcement or by shear links, the effective damping can be determined from the bilinear flag-shape hysteresis. The overall recommendations by Priestley et al. are the same for both hybrid and jointed type wall systems.

The EVD area formulation for a standard bilinear flag-shape hysteresis is shown in Equation (2-28) where β is the height of the flag as expressed by Equation (2-29), and r is the post-yield

stiffness. β is a similar parameter to the moment contribution ratio specified in Appendix B of NZS3101 described by Equation (2-27). The area based EVD calculated using Equation (2-28) must be multiplied by the correction factor from Figure 2.13 and subsequently added to the elastic damping component to calculate the total EVD for jointed type wall systems.

$$\xi_{hyst_area} = \frac{A_h}{2\pi F_m \Delta_m} = \frac{\beta(\mu - 1)}{\mu\pi(1 + r(\mu - 1))} \quad (2-28)$$

$$\beta = \frac{2M_S}{M_S + (M_{Pt} + M_N)} \quad (2-29)$$

Where M_{Pt} , M_N , and M_S are the flexural strength contributions of the PT tendons, axial load, and energy dissipating devices.

2.9.3.3 NZS3101/PRESSS Design Handbook

To determine an EVD using Equation (2-26), a structural ductility must be assumed that is based on the yield displacement of the system. For any rocking system of either a hybrid or jointed wall nature, yielding does not occur in a traditional sense leading to uncertainty around the determination of an appropriate yield displacement. This is reiterated in the PRESSS Design Handbook for a coupled wall system incorporating UFP devices as the yield displacement of a UFP is very small leading to large theoretical ductility if the yield of the UFP is taken as first yield. Instead the design damping is computed independently of the design displacement using Equation (2-30). Equation (2-30) was developed based on the maximum value of Equation (2-25) which approaches 35% when ductility is large, the maximum of the PT only system which is 5% and the weighted moment contribution method as described by Equation (2-26). Additionally, the factor of 0.67 is used as the hysteretic damping component is assumed equal to 67% of the theoretical maximum of 35%. How the 0.67 factor was chosen is not stated, however it is likely to be some reasonable reduction in total possible hysteretic damping which was deemed most appropriate for the system.

$$\xi_{eq} = \frac{\lambda}{\lambda + 1} 5\% + \frac{1}{\lambda + 1} 35\% \cdot 0.67 \quad (2-30)$$

The PRESSS Design Handbook also recommends an alternative method that incorporates the refined ductility-EVD relationships developed by Priestley et al. [20]. This involves modification of Equation (2-24) to include the moment contribution ratio that accounts for the system re-

entering as presented in Equation (2-31). Where R_ξ would change depending on the type of additional damping incorporated. As an example R_ξ would be equal to 0.577 for externally mounted mild steel yielding devices, which was interpreted from Priestley et al. who found R_ξ equal to 0.577 for the Ramberg-Osgood hysteretic rule intended for steel frames. In the PRESSSS Design Handbook the same logic that resulted in Equation (2-30) with respect to the yield displacement is suggested to be applied where ductility is bypassed and the EVD can be calculated using Equation (2-32) with 23.4% being the maximum value of hysteretic EVD calculated from Equation (2-24) when R_ξ is equal to 0.577.

$$\xi_{eq} = 0.05 + \frac{R_\xi}{(\lambda + 1)} \left(\frac{\mu - 1}{\mu\pi} \right) \quad (2-31)$$

$$\xi_{eq} = \frac{\lambda}{\lambda + 1} 5\% + \frac{1}{\lambda + 1} 23.4\% \cdot 0.67 \quad (2-32)$$

In summary, the PRESSSS Design Handbook recommends two methods to calculate the EVD for a UFP coupled wall that result in vastly different EVD recommendations. The first method is based on Appendix B of NZS3101 and uses Equation (2-30) which is based on the expected hysteresis of a concrete frame using a modified Takeda hysteresis rule. The second method incorporates Appendix B recommendations with a different purely dissipative system hysteretic rule as described by Equation (2-32), which is based on the expected hysteresis from mild steel dissipaters using the Ramberg-Osgood hysteretic rule. It would seem that the second method is more appropriate as it is actually based on the expected hysteresis from the yielding members i.e. the UFP dissipaters. It is relevant to note that since the first method uses the recommended EVD-ductility equation for a concrete frame originally derived in Priestley [89] it would make more sense for Equation (2-25) to be adjusted to Equation (2-33) by replacing 30 with 23 as recommended for RC wall structures. The selection of the 0.67 factor is also arbitrary and should require a robust method of calculation.

$$\xi_{wall} = \xi_{hyst} = 5 + 23 \left(1 - \frac{1}{\sqrt{\mu}} \right) \quad (2-33)$$

2.10 RESIDUAL DRIFT

Performance based design objectives are becoming increasingly common and as a result the potential residual drift of a structure is ever more important. The residual drift is a seismic performance factor that is often overlooked, and one of the key advantages to self-centering systems. The residual drift of a structure has been shown to be a function of hysteresis definition, and the intensity of the seismic input by previous researchers [90]. In the past the residual drift was assessed from hysteretic behaviour as the drift at zero force after unloading. The drift on the unloading curve at zero force in a hysteretic definition is actually the maximum possible residual drift.

Recent work has shown that an important phenomenon known as the “shake-down” effect is responsible for lower than maximum residual drifts resulting at the end of ground shaking [117]. MacRae and Kawashima recognised that the residual drift of a structure was a function of the hysteresis behaviour and ground motion and subsequently conducted a series of NLTHA to investigate the behaviour of SDOF systems. MacRae and Kawashima found that even for elasto-plastic hysteresis definitions significant reduction in residual drift was observed due to the shake-down effect. The residual drift at the end of ground shaking was normalised by the maximum possible residual drift to define the ‘residual displacement ratio,’ or d_{rr} . This is the ratio that Henry {Henry, 2011 #273} also used as a tool to develop a simple design check that included a residual drift limit. The check involved 1) Establishing suitable residual drift performance limits, 2) Complete preliminary design of the structure, 3) Estimate of cyclic hysteresis behaviour, 4) From cyclic behaviour estimate maximum possible residual drift corresponding to the design target, 5) Estimate upper bound residual drift ratio, 6) Calculate upper limit of the design residual drift, and 7) Check if the design residual drift ratio is below the residual drift performance limit for each hazard level, if not revise.

2.11 CONCLUSIONS

An extensive literature review was presented outlining the development, testing, modelling techniques, and design of unbonded PT precast concrete wall systems. Wall systems that have been investigated include SRWs, jointed or coupled wall systems and hybrid wall systems. Although there has been extensive numerical modelling and experimental testing on a number

of different unbonded PT wall systems, there has however, been only a limited number of experiments conducted to investigate the dynamic response of unbonded PT wall systems. To the author's knowledge no dynamic testing has been published on unbonded PT precast concrete wall systems that incorporate two or more rocking unbonded PT elements that utilise relative displacement along a vertical joint to mobilise energy dissipaters. This includes jointed, coupled, and PreWEC wall systems.

As a result of this lack of dynamic testing there is currently a knowledge gap concerning the dynamic characteristics of the vertically jointed unbonded PT systems such as the PreWEC system. Dynamic testing is necessary to investigate critical dynamic parameters such as damping and residual drifts. Also, there has been no set of systematic testing even of a static nature on vertically jointed wall systems investigating the wall systems response with varying amounts of energy dissipating devices.

A significant amount of numerical or analytical research has been carried out on unbonded PT wall systems that have ranged from complex FEM or fibre models to simple macro element type models. While complex modelling techniques such as FEM can provide accurate representations of pseudo-static cyclic response previous researchers have shown FEM models provide inaccurate results for dynamic behaviour. Simple macro element models are attractive due to the low computational cost, easy implementation, and the ability of rocking mechanisms to be modelled as simple systems. As a consequence of the lack of dynamic test data many researchers have used numerical models to analyse unbonded PT wall systems, but almost always without dynamic experimental validation. Subsequently, there is a lack of systematic dynamic test validated recommendations for appropriate damping schemes that can be easily incorporated into numerical models for jointed or PreWEC wall systems.

As a consequence of the lack of dynamic testing there is little experimental evidence of the damping present in vertically jointed unbonded PT wall systems. This has resulted in a lack of robust guidelines and procedures to account for the magnitude of EVD appropriate for use within the current DDBD framework. Also, as a result of the limited dynamic test data there has been no verification of DDBD procedures for vertically jointed concrete walls using shake table results.

2.12 REFERENCES

3. Priestley, M.J.N., S.S. Sritharan, J.R. Conley, and S. Pampanin, *Preliminary results and conclusions from the PRESSS five-story precast concrete test building*. PCI Journal, 1999. **44**(6): p. 42-67.
4. Kurama, Y., R. Sause, S. Pessiki, and L.W. Lu, *Lateral load behavior and seismic design of unbonded post-tensioned precast concrete walls*. ACI Structural Journal, 1999. **96**(4): p. 622-632.
5. Erkmen, B. and A.E. Schultz, *Self-centering behavior of unbonded, post-tensioned precast concrete shear walls*. Journal of Earthquake Engineering, 2009. **13**(7): p. 1047-1064.
6. Stavridis, A., I. Koutromanos, and P.B. Shing, *Shake-table tests of a three-story reinforced concrete frame with masonry infill walls*. Earthquake Engineering and Structural Dynamics, 2012. **41**(6): p. 1089-1108.
7. Henry, R.S., N.J. Brooke, S. Sritharan, and J.M. Ingham, *Defining concrete compressive strain in unbonded post-tensioned walls*. ACI Structural Journal, 2012. **109**(1): p. 101-112.
8. Holden, T., J. Restrepo, and J.B. Mander, *Seismic performance of precast reinforced and prestressed concrete walls*. Journal of Structural Engineering, 2003. **129**(3): p. 286-296.
9. Restrepo, J.I. and A. Rahman, *Seismic performance of self-centering structural walls incorporating energy dissipators*. Journal of Structural Engineering, 2007. **133**(11): p. 1560-1570.
10. Smith, B.J., Y.C. Kurama, and M.J. McGinnis, *Design and measured behavior of a hybrid precast concrete wall specimen for seismic regions*. Journal of Structural Engineering, 2011. **137**(10): p. 1052-1062.
11. Smith, B.J. and Y.C. Kurama, *Seismic design guidelines for solid and perforated hybrid precast concrete shear walls*. PCI Journal, 2014. **59**(3): p. 43-59.
12. Smith, B.J. and Y.C. Kurama. *Seismic displacement demands for hybrid precast concrete shear walls*. in *Structures Congress 2013: Bridging Your Passion with Your Profession - Proceedings of the 2013 Structures Congress*. 2013.
13. Marriott, D., *The Development of High-Performance Post-Tensioned Rocking Systems for the Seismic Design of Structures*. 2009, University of Canterbury: Christchurch.
14. Sritharan, S., S. Aaleti, R.S. Henry, K.-Y. Liu, and K.-C. Tsai, *Precast concrete wall with end columns (PreWEC) for earthquake resistant design*. Earthquake Engineering & Structural Dynamics, 2015: p. n/a-n/a.
15. Henry, R.S., S. Aaleti, S. Sritharan, and J.M. Ingham, *Concept and finite-element modeling of new steel shear connectors for self-centering wall Systems*. Journal of Engineering Mechanics, 2010. **136**(2): p. 220-229.
16. ACI Innovation Task Group 5., *Acceptance criteria for special unbonded post-tensioned precast structural walls based on validation testing (ITG 5.1-07)*. 2007, American Concrete Institute: Farmington Hills, Mich.
17. ACI Innovation Task Group 5., *Requirements for design of a special unbonded post-tensioned precast shear wall satisfying ACI ITG-5.1 (ACI ITG-5.2-09) and commentary: an ACI standard*. 2009, Farmington Hills, Mich.: American Concrete Institute. 21 p.

18. New Zealand Standard, *Concrete Structures Standard NZS 3101*. 2006: Wellington, New Zealand.
19. Pampanin, S., D. Marriott, A. Palermo, and New Zealand Concrete Society., *PRESSS design handbook*. 2010, Auckland, N.Z.: NZCS. 1 v. (various pagings).
20. Priestley, M.J.N., G.M. Calvi, and M.J. Kowalsky, *Displacement-based seismic design of structures*. 2007, Pavia: IUSS Press : Fondazione Eucentre. xvii, 721 p.
21. Perez, F.J., S. Pessiki, R. Sause, and L.M. Lu, *Lateral load tests of unbonded post-tensioned precast concrete walls*, in *Large-Scale Structural Testing*, M.A. Issa and Y.L. Mo, Editors. 2003, American Concrete Institute: Farmington Hills. p. 161-182.
23. Pampanin, S. and M. Nishiyama. *Critical aspects in modelling the seismic behaviour of precast/prestressed concrete building connections and systems*. in *1st fib Congress*. 2002. Osaka, Japan.
26. Kurama, Y.C., *Seismic design of unbonded post-tensioned precast concrete walls with supplemental viscous damping*. ACI Structural Journal, 2000. **97**(4): p. 648-658.
27. Kurama, Y., S. Pessiki, R. Sause, L.W. Lu, and M. El-Sheikh, *Analytical modelling and lateral load behavior of unbonded post-tensioned precast concrete walls*. 1996, Department of Civil and Environmental Engineering, Lehigh University: Bethlehem, Pennsylvania.
29. Wight, G.D., M.J. Kowalsky, and J.M. Ingham, *Shake table testing of posttensioned concrete masonry walls with openings*. Journal of Structural Engineering, 2007. **133**(11): p. 1551-1559.
30. Wight, G.D., J.M. Ingham, and M.J. Kowalsky, *Shaketable testing of rectangular post-tensioned concrete masonry walls*. ACI Structural Journal, 2006. **103**(4): p. 587-595.
31. Marriott, D., S. Pampanin, D. Bull, and A. Palermo, *Dynamic testing of precast, post-tensioned rocking wall systems with alternative dissipating solutions*. Bulletin of the New Zealand Society for Earthquake Engineering, 2008. **41**(2): p. 90-103.
32. Belleri, A., M.J. Schoettler, J.I. Restrepo, and R.B. Fleischman, *Dynamic behavior of rocking and hybrid cantilever walls in a precast concrete building*. ACI Structural Journal, 2014. **111**(3): p. 661-671.
34. Nagae, T., T. Matsumori, H. Shiohara, T. Kabeyasawa, S. Kono, M. Nishiyama, J. Moehle, J. Wallace, R. Sause, and W. Ghannoum. *The 2010 E-defense shaking table test on four-story reinforced concrete and post-tensioned concrete buildings*. in *NCEE 2014 - 10th U.S. National Conference on Earthquake Engineering: Frontiers of Earthquake Engineering*. 2014.
36. Pampanin, S., *Controversial aspects in seismic assessment and retrofit of structures in modern times: Understanding and implementing lessons from ancient heritage*. Bulletin of the New Zealand Society for Earthquake Engineering, 2006. **39**(2): p. 120-134.
37. Housner, G.W., *The behavior of inverted pendulum structures during earthquakes*. Bulletin of the Seismological Society of America, 1963. **53**(2): p. 403-417.
38. Skinner, R.I., W.H. Robinson, and G.H. McVerry, *An introduction to seismic isolation*, ed. Wiley. 1993, Chichester, England.
39. Aslam, M., W.G. Godden, and D.T. Scalise, *EARTHQUAKE ROCKING RESPONSE OF RIGID BODIES*. Journal of the Structural Division-Asce, 1980. **106**(2): p. 377-392.
40. Park, R., *A perspective on the seismic design of precast concrete structures in New Zealand*. PCI Journal, 1995. **40**(3): p. 40-60.
41. Henry, R.S., *Self-centering precast concrete walls for buildings in regions with low to high seismicity*. 2011, University of Auckland. p. 441.

42. Weldon, B.D. and Y.C. Kurama, *Nonlinear behavior of precast concrete coupling beams under lateral loads*. Journal of Structural Engineering, 2007. **133**(11): p. 1571-1581.
43. Soudki, K.A., J.S. West, S.H. Rizkalla, and B. Blackett, *Horizontal connections for precast concrete shear wall panels under cyclic shear loading*. PCI Journal, 1996. **41**(3): p. 64-80.
44. Fintel, M., *Performance of buildings with shear walls in earthquakes of the last thirty years*. PCI Journal, 1995. **40**(3): p. 62-80.
45. Kurama, Y., S. Pessiki, R. Sause, and L.W. Lu, *Seismic behavior and design of unbonded post-tensioned precast concrete walls*. PCI Journal, 1999. **44**(3): p. 72-89.
46. Stanton, J., W.C. Stone, and G.S. Cheok, *A hybrid reinforced precast frame for seismic regions*. PCI Journal, 1997. **42**(2): p. 20-32.
47. Priestley, M.J.N., *Overview of PRESSSS research program*. PCI Journal, 1991. **36**(4): p. 50-57.
48. Priestley, M.J.N. and J.R. Tao, *Seismic Response of Precast Prestressed Concrete Frames with Partially Debonded Tendons*. PCI Journal, 1993. **38**(1): p. 58-69.
49. Perez, F.J., R. Sause, S. Pessiki, and L.W. Lu, *Lateral load behavior of unbonded post-tensioned precast concrete walls*. Advances in Building Technology, Vols I and II, Proceedings, ed. M. Anson, J.M. Ko, and E.S.S. Lam. 2002, Amsterdam: Elsevier Science Bv. 423-430.
50. Perez, F.J., S. Pessiki, and R. Sause, *Lateral load-behavior of unbonded post-tensioned precast concrete walls with vertical joints*. PCI Journal, 2004. **49**(2): p. 48-+.
51. Perez, F.J., S. Pessiki, and R. Sause, *Seismic design of unbonded post-tensioned precast concrete walls with vertical joint connectors*. PCI Journal, 2004. **49**(1): p. 58-+.
52. Perez, F.J., R. Sause, and S. Pessiki, *Analytical and experimental lateral load Behavior of unbonded posttensioned precast concrete walls*. Journal of Structural Engineering-Asce, 2007. **133**(11): p. 1531-1540.
53. Alexander, N.A., O. Oddbjornsson, C.A. Taylor, H.M. Osinga, and D.E. Kelly, *Exploring the dynamics of a class of post-tensioned, moment resisting frames*. Journal of Sound and Vibration, 2011. **330**(15): p. 3710-3728.
54. Nakaki, S.D., J.F. Stanton, and S. Sritharan, *Overview of the PRESSSS five-story precast test building*. PCI Journal, 1999. **44**(2): p. 26-39.
55. Rahman, A.M. and J.I. Restrepo, *Earthquake resistant precast concrete buildings : seismic performance of cantilever walls prestressed using unbonded tendons*. Research report., 2000, Christchurch, NZ: Dept. of Civil Engineering, University of Canterbury. xvii, 110 p.
56. Kurama, Y.C., *Simplified seismic design approach for friction-damped unbonded post-tensioned precast concrete walls*. ACI Structural Journal, 2001. **98**(5): p. 705-716.
57. Sritharan, S., S. Aaleti, R.S. Henry, K.Y. Liu, and K.C. Tsai, *Introduction to PreWEC and key results of a proof of concept test*. M.J. Nigel Priestley Symposium, North Lake Tahoe, California, August 4-5, 2008, ed. M.J.N. Priestley, M.J. Kowalsky, and S. Sritharan. 2008, Pavia, Italy: IUSS Press. 267.
58. Aaleti, S. and S. Sritharan. *A precast wall with End Columns (PreWEC) for Seismic Applications*. in *8th Pacific Conference on Earthquake Engineering*. 2007. Singapore.
59. Aaleti, S., R.S. Henry, K.Y. Liu, S. Sritharan, and K.C. Tsai. *Experimental investigation of a precast wall with end columns (PreWEC) system*. in *Eleventh East Asia-Pacific Conference on Structural Engineering & Construction (EASEC-11) "Building a Sustainable Environment"*. 2008. Taipei, Taiwan.

60. Pampanin, S., M.J.N. Priestley, and S. Sritharan, *Analytical modelling of the seismic behaviour of precast concrete frames designed with ductile connections*. Journal of Earthquake Engineering, 2001. **5**(3): p. 329-367.
61. Palermo, A., *The use of controlled rocking in the seismic design of bridges*, in *Civil Engineering*. 2004, Technial University of Milan: Milan.
62. Aaleti, S. and S. Sritharan, *A simplified analysis method for characterizing unbonded post-tensioned precast wall systems*. Engineering Structures, 2009. **31**(12): p. 2966-2975.
63. Cheng, C.T., *Energy dissipation in rocking bridge piers under free vibration tests*. Earthquake Engineering and Structural Dynamics, 2007. **36**(4): p. 503-518.
64. Mander, J.B., C.-T. Cheng, and National Center for Earthquake Engineering Research (U.S.), *Seismic resistance of bridge piers based on damage avoidance design*. Technical report / National Center for Earthquake Engineering Research. 1997, Buffalo, N.Y.: National Center for Earthquake Engineering Research. 1 v. (various pagings).
65. Makris, N. and D. Konstantinidis, *The rocking spectrum and the limitations of practical design methodologies*. Earthquake Engineering and Structural Dynamics, 2003. **32**(2): p. 265-289.
66. FEMA 356, *Prestandard and commentary for the seismic rehabilitation of buildings*. 2000, Prepared by the American Society of Civil Engineering for the Federal Emergency Management Agency: Washington (DC).
67. Priestley, M.J.N., R.J. Evison, and A.J. Carr, *Seismic response of structures free to rock on their foundations*. Bulletin of the New Zealand National Society for Earthquake Engineering, 1978. **11**(3): p. 141-150.
68. Cheng, C.T., *Shaking table tests of a self-centering designed bridge substructure*. Engineering Structures, 2008. **30**(12): p. 3426-3433.
69. Schoettler, M.J., A. Belleri, Z. Dichuan, J.I. Restrepo, and R.B. Fleischman, *Preliminary results of the shake-table testing for the development of a diaphragm seismic design methodology*. PCI Journal, 2009. **54**(1): p. 100-124.
70. Kurama, Y.C., *Hybrid post-tensioned precast concrete walls for use in seismic regions*. PCI Journal, 2002. **47**(5): p. 36-59.
71. Kurama, Y.C., R. Sause, S. Pessiki, and L.W. Lu, *Seismic response evaluation of unbonded post-tensioned precast walls*. ACI Structural Journal, 2002. **99**(5): p. 641-651.
72. Palermo, A., S. Pampanin, and D. Marriott, *Design, modeling, and experimental response of seismic resistant bridge piers with posttensioned dissipating connections*. Journal of Structural Engineering, 2007. **133**(11): p. 1648-1661.
73. Palermo, A., S. Pampanin, and G.M. Calvi, *Concept and development of hybrid solutions for seismic resistant bridge systems*. Journal of Earthquake Engineering, 2005. **9**(6): p. 899-921.
74. Pennucci, D., G.M. Calvi, and T.J. Sullivan, *Displacement - Based Design of Precast Walls with Additional Dampers*. Journal of Earthquake Engineering, 2009. **13**(sup1): p. 40-65.
75. Ma, Q., G.D. Wight, J. Butterworth, and J.M. Ingham, *Assessment of current procedures for predicting the in-plane behaviour of controlled rocking walls*. Proceedings of the 8th U.S. National Conference on Earthquake Engineering, 2006.

76. Ma, Q.T.M., *The mechanics of rocking structures subjected to ground motion*. 2010, University of Auckland. p. xxxii, 280 p.
77. Prieto, F., P.B. Lourenço, and C.S. Oliveira, *Impulsive Dirac-delta forces in the rocking motion*. *Earthquake Engineering and Structural Dynamics*, 2004. **33**(7): p. 839-857.
78. Humar, J.L., *Dynamics of structures*. 3rd ed.. ed. 2012, Boca Raton, Fla.: Boca Raton, Fla. : CRC Press - Taylor & Francis Group c2012.
79. American Society of Civil Engineers. and United States. Federal Emergency Management Agency., *Prestandard and commentary for the seismic rehabilitation of buildings*. 2000, Washington, D.C.: Federal Emergency Management Agency. 1 v. (various pagings).
80. Wight, G.D., *Seismic performance of a post-tensioned concrete masonry wall system*. 2006, University of Auckland. p. xx, 200 p.
81. Rahman, M. and S. Sritharan, *An evaluation of force-based design vs. direct displacement-based design of jointed precast post-tensioned wall systems*. *Earthquake Engineering and Engineering Vibration*, 2006. **5**(2): p. 285-296.
82. Priestley, M.J.N. and G.A. MacRae, *Seismic tests of precast beam-to-column joint subassemblages with unbonded tendons*. *PCI Journal*, 1996. **41**(1): p. 64-80.
83. Gulkan, P. and M. Sozen, *Inelastic response of reinforced concrete structures to earthquake motions*. *ACI Journal*, 1974. **71**(12): p. 604-610.
84. Shibata, A. and M.A. Sozen, *Substitute-structure method for seismic design in R/C*. *Journal of the Structural Division-Asce*, 1976. **102**(1): p. 1-8.
85. Priestley, M.J.N. and D.N. Grant, *Viscous damping in seismic design and analysis*. *Journal of Earthquake Engineering*, 2005. **9**(SPEC. ISS. 2): p. 229-255.
86. Jacobsen, L.S. *Damping in composite structures*. in *Proceedings of the 2nd World Conference on Earthquake Engineering*. 1960. Tokyo and Kyoto, Japan.
87. Rosenblueth, E. and I. Herrera, *On a kind of hysteretic damping*. *Journal of the Engineering Mechanics Division, ASCE*, 1964. **90**(No. EM4): p. 37-48.
88. Dwairi, H.M., M.J. Kowalsky, and J.M. Nau, *Equivalent damping in support of direct displacement-based design*. *Journal of Earthquake Engineering*, 2007. **11**(4): p. 512-530.
89. Priestley, M.J.N., *Direct displacement-based design of precast/prestressed concrete buildings*. *PCI Journal*, 2002. **47**(6): p. 66-79.
90. Christopoulos, C., S. Pampanin, and M.J. Nigel Priestley, *Performance-Based Seismic Response of Frame Structures Including Residual Deformations. Part I: Single-Degree of Freedom Systems*. *Journal of Earthquake Engineering*, 2003. **7**(1): p. 97-118.

Chapter 3

O-CONNECTOR TESTING AND DESIGN

The motivation for the O-connector study reported here was briefly provided in the literature review that outlined the previous research on O-connector performance and the need to develop an O-connector that did not experience out-of-plane buckling. Also, a suitably sized O-connector was required for the PreWEC wall system tests performed and described later in Chapters 5, 6, and 7, that required experimental validation to ensure adequate performance. Subsequently, a unique series of nine cyclic tests were performed on energy dissipating O-connectors where the effect of the O-connector profile, steel material, and welding process for attaching the O-connectors was investigated and two different failure mechanisms were identified. Finally design equations to estimate the ultimate strength of the O-connector are proposed and used to develop a bilinear force-displacement approximation.

3.1 INTRODUCTION

The following is an in depth introduction into energy dissipating elements for rocking wall systems, specifically background related to the development of the O-connector. In theory any structural element with sufficient strength, ductility and energy dissipating capability can be used as a replaceable energy dissipating device in low-damage structures. For rocking wall systems,

simple, cheap, and replaceable energy dissipating devices are required to develop cost-effective low-damage structural solutions. As a result of these requirements, steel plate type energy dissipating connectors have become common, including slit and butterfly shaped fuses [91], and the U-shaped Flexural Plate connectors (UFP) [92] and the O-connectors [15] previously mentioned in Chapter 2. As part of the PRESSS programme a study on the behaviour of different energy dissipating connectors was undertaken and the UFP was found to be a suitable energy dissipater for the unbonded PT wall system [93]. More recently, an alternative cost-effective steel plate O-connector was developed by Henry et al. [15] for use as an energy dissipating device in unbonded PT wall systems as described in Chapter 2.

The O-connector is an oval-shaped profile dissipater cut from mild steel plate that undergoes a flexural yielding mechanism similar to the UFP dissipater as demonstrated by the deformed shapes presented in Figure 3.1. Unlike the UFP which is restrained to roll between two vertical surfaces, the O-connector is attached to the exterior face of the wall or column and is unrestrained, resulting in flexural yielding of the straight leg portion of the oval profile. The O-connector fulfils two purposes when used in unbonded PT wall systems, firstly it is the primary source of energy dissipation for the system, and secondly it contributes to the systems moment capacity by transferring shear between adjacent elements. The O-connector has been used successfully in unbonded PT wall systems, including the large scale PreWEC system test [57]. Despite its many advantages, a tendency for out-of-plane buckling of the O-connectors was observed during initial tests by Henry et al. [15]. To prevent out-of-plane buckling the O-connectors were restrained during further component testing and during the large scale test of the PreWEC system [57]. Overall the O-connectors were able to produce stable hysteretic behaviour when out-of-plane buckling was restrained, and are inexpensive to fabricate and easy to install and replace. Despite being initially designed for the PreWEC system, O-connectors could potentially be used as cost-effective energy dissipating elements in a wide range of low-damage structural systems.

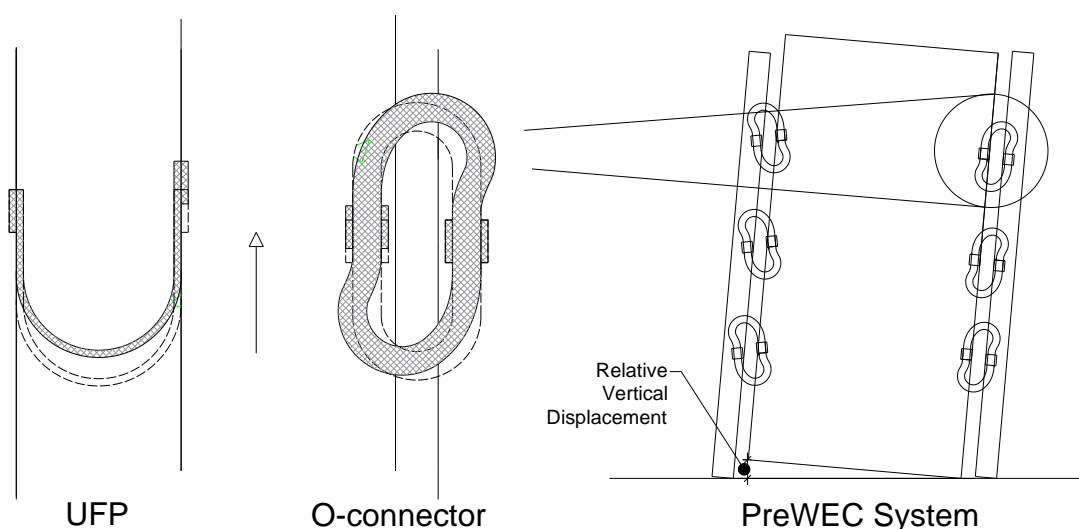


Figure 3.1 – Deformed shapes of the UFP and O-connector and PreWEC system schematic

The objective of this chapter was to develop and quantify the performance of a modified version of the O-connector tested by Henry et al [15] for use in the series of PreWEC system experiments reported in Chapter 5, 6, and 7. The tested O-connector was first modified by decreasing the length to thickness ratio in an attempt to avoid out-of-plane buckling without requiring additional restraint and then further modified to mitigate an identified undesirable failure mechanism. The secondary objectives were to propose simple equations to calculate the yield, plastic and ultimate strength of the O-connector and provide insight into the displacement capacity of the O-connector before failure by proposing a bilinear force-displacement approximation. A series of nine pseudo-static cyclic tests were performed on two variations of the reduced size O-connector, using four different mild steel materials, two different profile cutting techniques and three different welding processes.

3.2 STRENGTH AND STIFFNESS EQUATIONS

Both the UFP and O-connector energy dissipaters are designed to yield in flexure and provide stable hysteretic energy dissipation. The UFP and O-connector consist of a U or oval shape profile with straight legs connected by a radius bend, and the key dimensions of each are shown in Figure 3.2. The UFP was initially developed by Kelly et al. [92] who derived Equation (3-1) to predict the strength of a UFP by relating the coupling shear of the UFP to the plastic moment

of the rectangular cross-section depending on the effective cyclic stress (σ_e), width (b), thickness (t), and average radius (R). The bending stress distribution for the plastic section capacity was assumed to be a rectangular stress block as shown in Figure 3.2. As presented in Equation (3-2), the UFP strength equation can be adapted to O-connectors by taking the thickness (t) and width (b) of the UFP as the width (w) and thickness (t) of the O-connector. The O-connector thickness is multiplied by two to account for the top and bottom U-shape sections that make up the O-connector.

$$P_{UFP} = \frac{\sigma_e b t^2}{4R} \tag{3-1}$$

$$P_{O-connector} = \frac{\sigma_e 2t w^2}{4R} \tag{3-2}$$

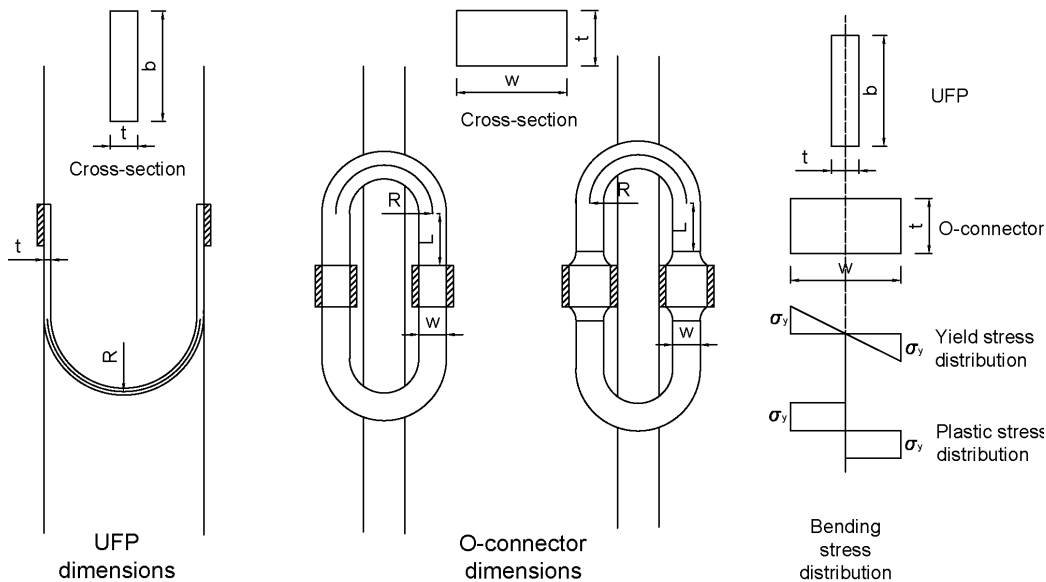


Figure 3.2 – Schematic of O-connector dimensions in relation to a UFP

The plastic strength of an O-connector (F_p) can be calculated by substituting the yield stress (σ_y) for the effective cyclic stress, as shown by Equation (3-3). Also, the strength at first yield of an O-connector (F_y) can be calculated by recognising that the yield strength is 2/3 times the plastic strength, due to the assumed triangular stress block which results in Equation (3-4). The strength at first yield is important for calculating the theoretical initial stiffness of the connector. The yield displacement and hence initial stiffness of UFPs can be determined analytically using energy methods, as described by Baird et al. [94]. Due to the similar flexural yielding manner

and geometry of UFPs to O-connectors, the equations developed by Baird et al. can be directly applied to O-connectors. The resulting two expressions for the yield displacement and the initial stiffness for O-connectors are presented in Equation (3-5) and (3-6) respectively, where E is the steel modulus of elasticity.

$$F_p = \frac{\sigma_y 2tw^2}{4R} \quad (3-3)$$

$$F_y = \frac{\sigma_y 2tw^2}{6R} \quad (3-4)$$

$$\Delta_y = \frac{27\pi F_y (2R)^3}{16Et w^3} \quad (3-5)$$

$$k_i = \frac{16Et w^3}{27\pi (2R)^3} = \frac{F_y}{\Delta_y} \quad (3-6)$$

As described by Kelly et al. [92], the plastic or yield strengths are not relevant when assessing the expected maximum strength of the connector since after a few loading cycles no defined yield point exists and strain hardening results in higher steel stresses than yield. An estimate of the ultimate strength of an O-connector can be derived from the plastic force equation by multiplying it by an overstrength factor which is equal to the ultimate stress (σ_u) divided by the yield stress, as shown in Equation (3-7).

$$F_u = F_p \frac{\sigma_u}{\sigma_y} = \frac{\sigma_y 2tw^2}{4R} \frac{\sigma_u}{\sigma_y} \quad (3-7)$$

3.3 EXPERIMENTAL PROGRAMME

The experimental programme was designed to investigate the behaviour of two types of O-connector profile when subjected to relative vertical displacements that would be applied to the O-connectors during a PreWEC wall test. Combined loading in both the vertical and horizontal directions was not considered as the columns and wall in a PreWEC system would be forced to displace laterally together by the floor diaphragm and no significant horizontal actions would be applied to the O-connectors. Two different O-connector profiles were tested, consisting of regular oval shaped connectors and a new type of O-connector with a widened leg section at the weld, referred to as wings. The nine different O-connectors tested were constructed using four

different grades of mild steel, manufactured using two cutting techniques, and subjected to three different loading protocols. Additionally, the influence of MIG (Metal Inert Gas) and Arc (Metal arc welding with coated electrode) welding methods was also investigated during the tests. The different test parameters of the O-connectors are summarised in Table 3.1. Each test was given a test code that described the key parameters of each test (material - displacement history - connector profile - cutting process).

Table 3.1 – Test variables

Test No.	Test Code	Material	Test loading history	Connector profile	Cutting process	Connector type	Welding Type
1	M1-C1-R-L	M1-250S0	Expected cyclic history (C1)	Regular (R)	Laser (L)	O1	ARC*
2	M2-C2-R-L	M2-250HA	Recorded cyclic history (C2)	Regular (R)	Laser (L)	O1	MIG
3	M2-S-R-L	M2-250HA	Recorded snap back history (S)	Regular (R)	Laser (L)	O1	MIG
4	M3-C2-R-L	M3-300HA	Recorded cyclic history (C2)	Regular (R)	Laser (L)	O2	MIG
5	M3-C2-W-L	M3-300HA	Recorded cyclic history (C2)	Wings (W)	Laser (L)	OW1	MIG
6	M4-C2-R-WA	M4-300S0	Recorded cyclic history (C2)	Regular (R)	Water (WA)	O2	Arc*
7	M4-C2-W-WA	M4-300S0	Recorded cyclic history (C2)	Wings (W)	Water (WA)	OW1	Arc*
8	M4-C2-W-L	M4-300S0	Recorded cyclic history (C2)	Wings (W)	Laser (L)	OW1	Arc+
9	M4-C2-R-L	M4-300S0	Recorded cyclic history (C2)	Regular (R)	Laser (L)	O2	Arc+

Arc+ welding used a high penetration ability electrode with a smaller diameter than ARC*

3.3.1 Connector specifications

The O-connectors were cut out of 10 mm thick mild steel plate with the geometry shown in Figure 3.3. To suit the scale of the PreWEC walls they were designed for, the O-connectors geometry was approximately a ½ scale version of the O-connector used by Sritharan et al. [57]. To prevent out of plane buckling the plate thickness was kept the same while decreasing the profile geometry of the O-connector, and so the effective thickness to length was doubled. Two

different O-connector profiles were tested, they consisted of regular oval shaped connectors, namely O1 and O2, and a new type of O-connector referred to as an O-connector with wings, namely OW1. The O-connector with wings was developed to minimise the effect of welding while maintaining all the advantages of the O-connector. The critical section of the O-connector is forced away from the weld zone by increasing the leg width by the addition of the wings, as shown in Figure 3.3. The only difference between O1 and O2 was the leg length and height of the curved portion of the O-connector, O2 has 2.5 mm longer legs and 2.5 mm shorter curved sections. However, this small difference in leg length was not expected to have any significant influence on the strength of the O-connector as reported in Henry [41]. The influence of fabrication process was also investigated with the O-connectors cut from mild steel plates using either laser or water cutting techniques. Both techniques were chosen to limit the residual stresses induced during the fabrication process. Water cutting introduces the least amount of heat and hence residual stresses into the connector, although, it is three to four times more expensive than laser cutting.

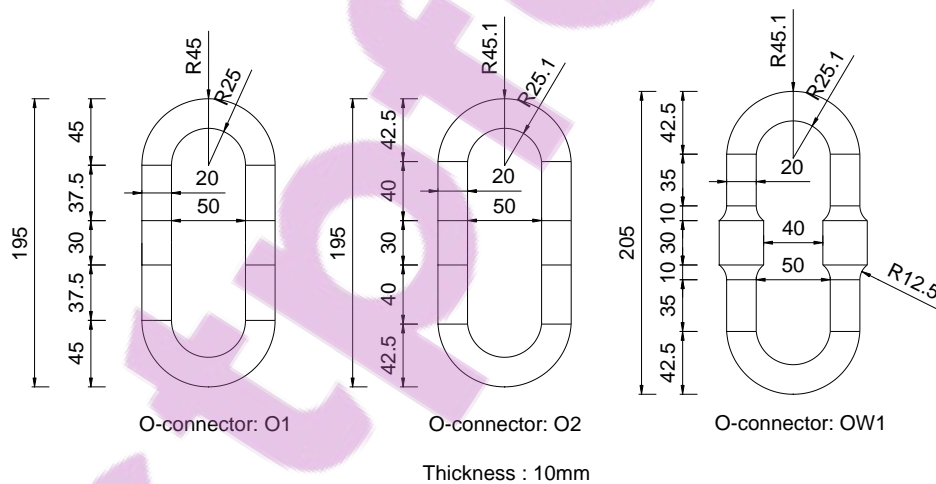


Figure 3.3 – O-connector dimensions

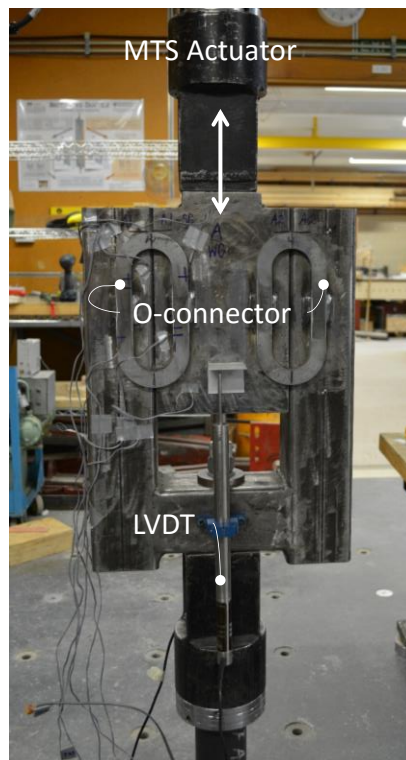


Figure 3.4 – Test setup

3.3.2 Material properties

The O-connectors used for this experimental programme were fabricated using four different grades of mild steel. In New Zealand there are two material standards that specify grades of steel plate, AS/NZS 3678 [95] covers grade 250S0 and grade 300S0, and AS/NZS 1594 [96] covers grade 250HA and grade 300HA. HA steel is produced from the hot strip mill in coil form while S0 steel is produced by plate mill in flat plate form. These different processes result in physical variations such as grain structure, flatness, and strength. The significant difference in the steel materials with respect to the O-connector was the minimum guaranteed elongation which is 22% for grade 250S0 and 17% for grade 250HA [97, 98]. All four of these listed grades of steel were used during this testing programme and four tensile coupons were machined from samples of each steel plate to determine the true properties of each batch of steel plate used to manufacture the different O-connectors. The tensile coupons were tested in accordance with Australian standard for tension testing of metallic materials [99], and the measured stress-strain behaviour of each mild steel plate is shown in Figure 3.5. A summary of the typical measured material

properties for each of the four mild steels (M1 to M4) is presented in Table 3.2. As expected the two HA steels were found to have higher strengths and lower elongation than the two S0 steels.

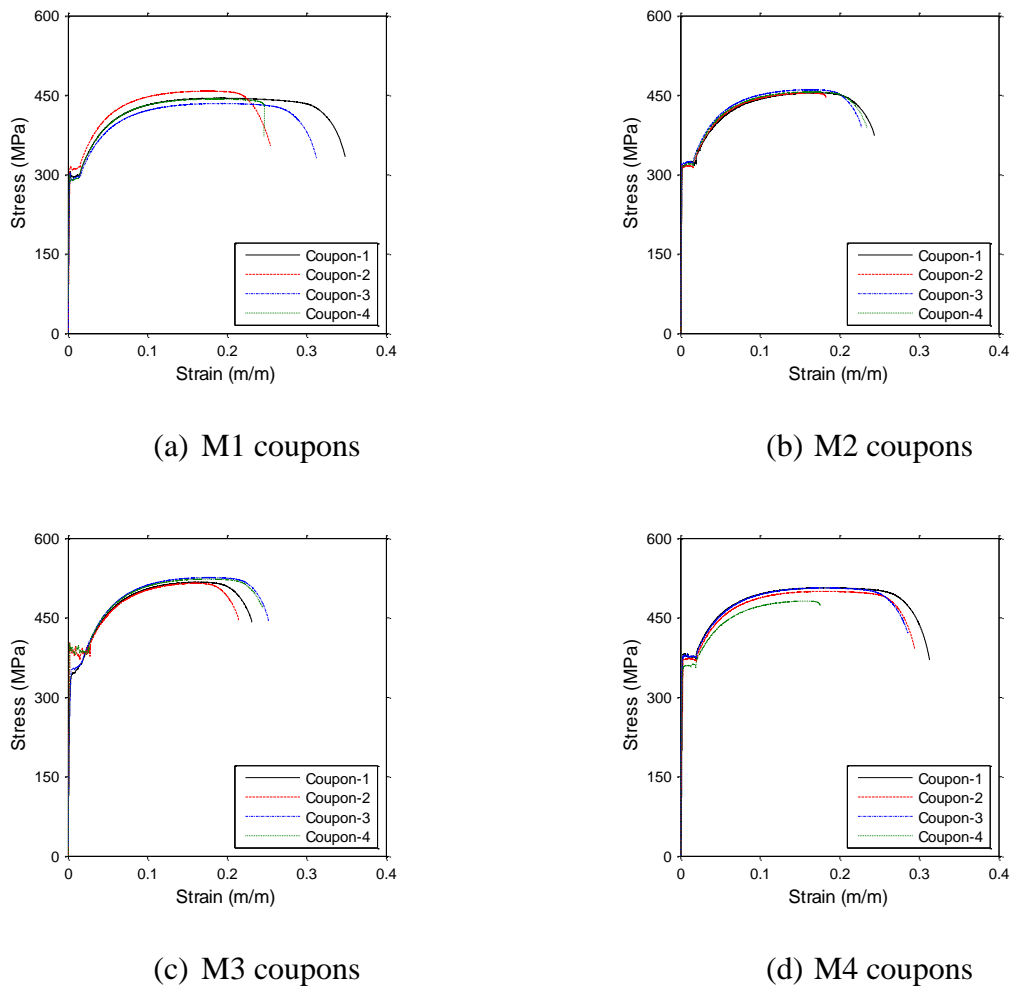


Figure 3.5 – Measured stress-strain properties for tensile coupons

Table 3.2 – Summary of measured material properties

Material	Yield stress (MPa)	Ultimate stress (MPa)	Uniform strain	Ultimate elongation	Modulus of elasticity (MPa)
M1 (250S0)	306	443	19.1%	34.9%	205,660
M2 (250HA)	317	453	17.0%	24.3%	205,940
M3 (300HA)	393	522	17.6%	24.9%	201,538
M4 (300S0)	380	503	18.3%	31.2%	200,000

3.3.3 Test setup

The test setup simulated the relative vertical displacement applied to the O-connectors when mounted between the wall and end column in the PreWEC system. The test rig shown in Figure 3.4 was designed to carry out the vertical displacement protocols and modelled off the previous testing carried out by Henry et al. [15]. The test rig was designed to minimise any eccentric loading on the actuator and was fabricated from a 100 x 100 mm square hollow section and 20 mm thick steel plates. The bottom U-shaped portion of the test rig was restrained to the strong floor while the centre section was attached to the MTS machine above. The vertical joints between these two sections were greased to minimise any influence due to friction between the sections. For each test, two O-connectors were welded centred around the vertical joints on each side of the test rig so that four connectors were tested simultaneously to provide an average connector response. The load was measured by the internal load cell on the actuator and the displacement loading was controlled by an externally mounted LVDT, as indicated in Figure 3.4.

3.3.4 Loading protocol

In the PreWEC system, the O-connectors are subjected to vertical displacements that are larger in one direction than the other due to the difference in magnitude of uplift between the column and wall base. Three different asymmetric cyclic loading protocols were used during the connector test programme and are each shown in Figure 3.6. The first cyclic displacement history (C1) was developed to simulate the expected displacement history that the O-connectors would be subjected to during the PreWEC-A cyclic test reported in Chapter 5. The C1 displacement history consisted of 32 cycles up to 29.3 mm peak positive displacement and -3.2 mm peak negative displacement with three cycles carried out at each displacement level. The second cyclic displacement history (C2) consisted of the O-connector vertical displacement response that was measured during the true cyclic test on the PreWEC-A2 wall documented in Chapter 5. The C2 displacement history consisted of 35 cycles up to 29.88 mm peak positive displacement and -9.1 mm peak negative displacement again with three cycles at each displacement level. The C1 and C2 displacement histories consisted of three cycles at each displacement amplitude to observe the stability of the O-connector response. The third cyclic displacement history (S) consisted of the O-connector vertical displacement response that was measured during two PreWEC snap back tests reported in Chapter 6. A snap back test consisted

of the wall being pulled to a set lateral displacement and then a quick release mechanism was activated, releasing the wall and allowing it to rock and vibrate freely until rest. The first half of the S displacement history was the relative vertical displacement between the column and wall of the PreWEC specimen for a 1% lateral drift snap back test and the second half was the relative vertical displacement measured from a 2% lateral drift snap back test. The S displacement history consisted of 25 cycles with a maximum of 13.7 mm peak positive displacement and -1.7 mm peak negative displacement. In contrast to the C1 and C2 displacement histories the S displacement cycles started at the largest displacement cycles and decayed to zero.

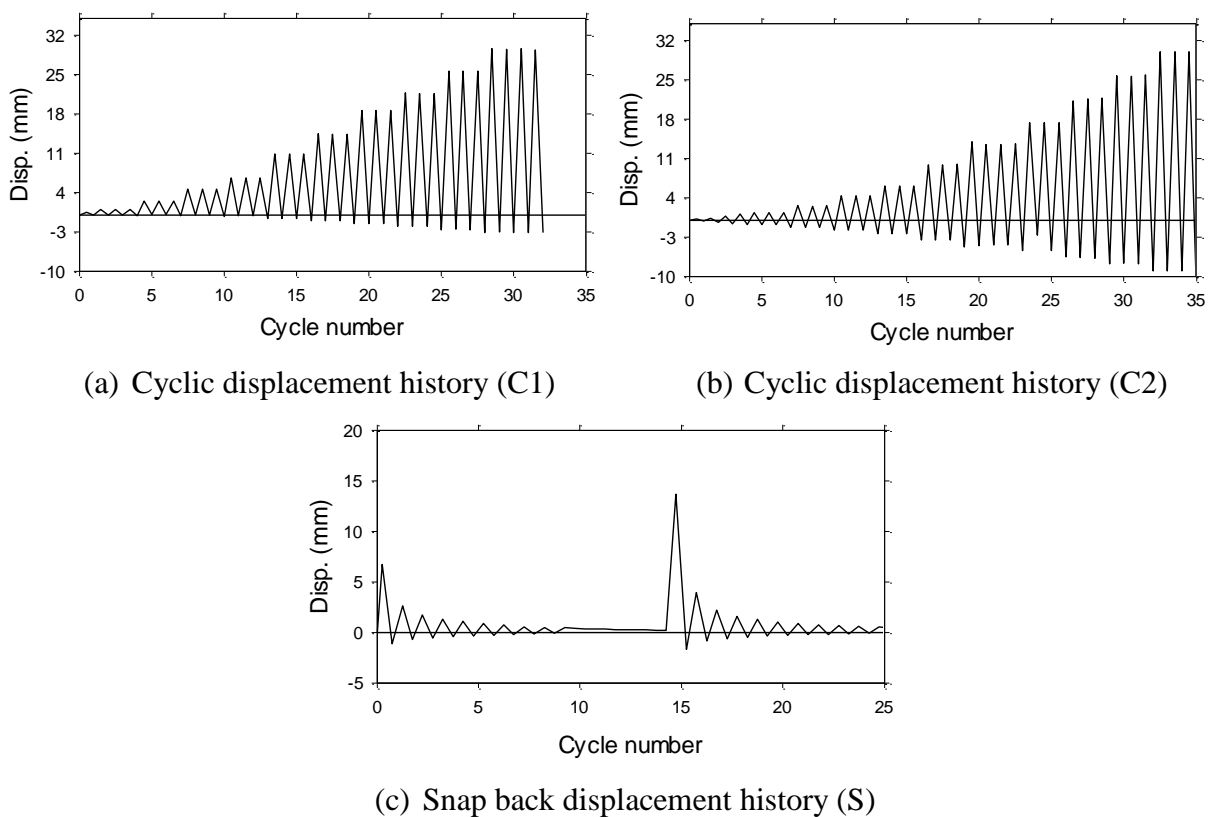


Figure 3.6 – Applied connector displacement histories

3.4 TEST OBSERVATIONS AND RESULTS

When subjected to vertical displacement, each O-connector exhibited the expected deformed shape during all of the nine cyclic tests. A typical example of the deformed shape of an O-connector with and without wings is depicted in Figure 3.7, with flexural yielding of the straight portion of the legs clearly visible.



Figure 3.7 – Typical O-connector deformed shape during tests

The measured force displacement behaviour of a single O-connector for each cyclic test is presented in Figure 3.8 overlaid with the predicted yield, plastic and ultimate strength of the O-connectors that were calculated using Equations (3-3), (3-4) and (3-7). It can be seen from the force displacement responses that the connectors provide stable hysteresis loops with good energy dissipation capability. Throughout the nine cyclic tests two types of failure were observed based on the location of fracture. Failure mechanism type one occurred when fracture initiated in the connector leg directly adjacent to the weld edge, as shown in Figure 3.9(a). Failure mechanism type two occurred when the O-connector experienced distributed cracks along the leg, as shown in Figure 3.9(b), followed by fracture at the curved radius to straight leg transition, as shown in Figure 3.9(c). Fracture of the connector legs for both failure mechanisms started with a tear which then propagated through the full width of the O-connector. The failure mechanism observed, measured positive and negative peak forces, displacement corresponding to the peak positive force, and strength prediction for each test are summarised for each test in Table 3.3.

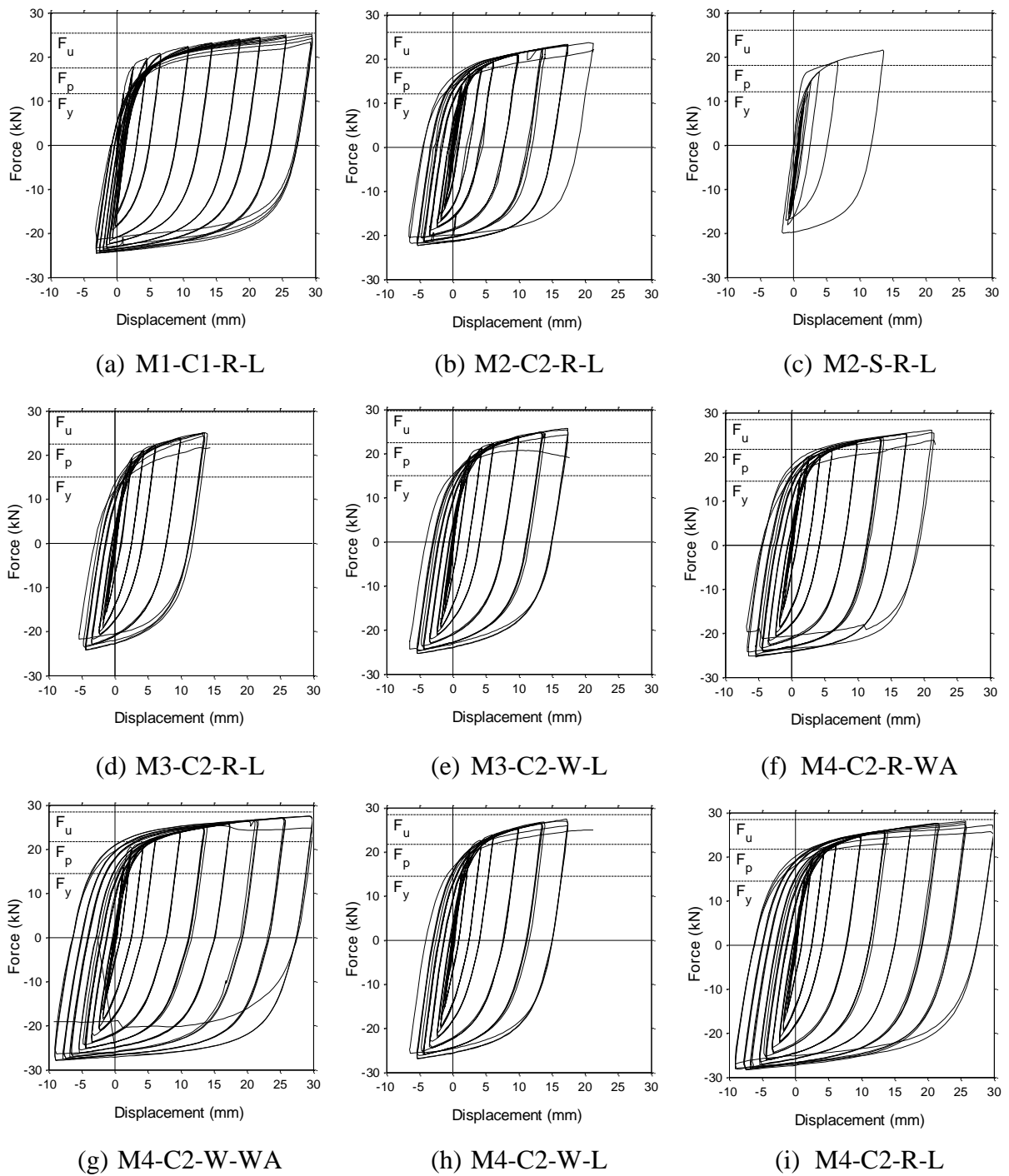


Figure 3.8 – Measured force-displacement response for each test

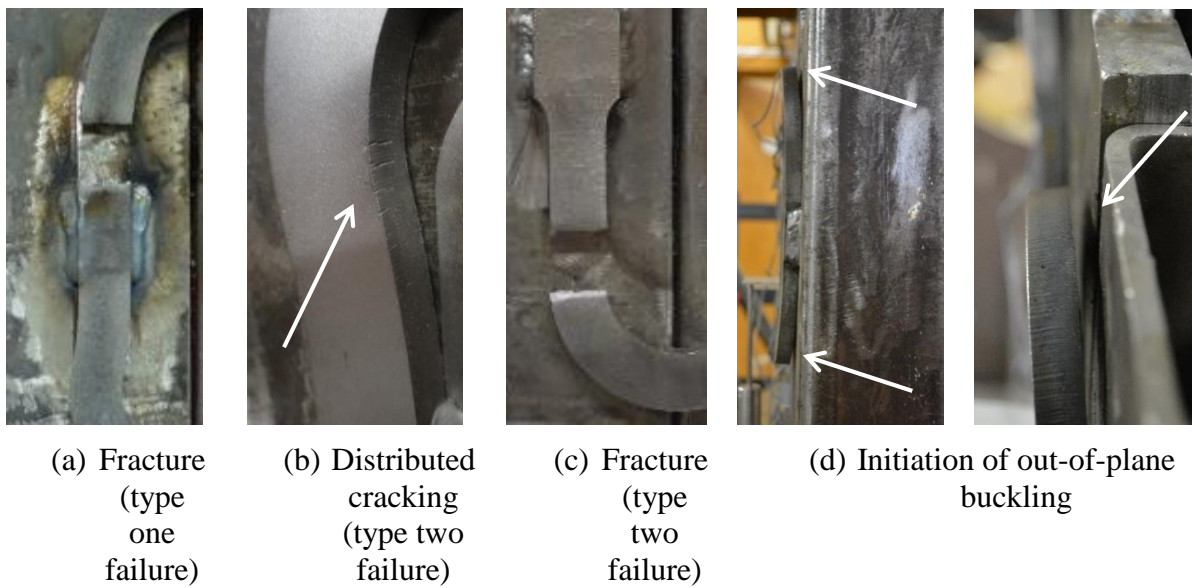


Figure 3.9 – Failure and fracture observations

Table 3.3 – Summary of failure mechanism and measured/predicted strength

Test	Failure mechanism	Predicted ultimate load (FU) (kN)	Peak positive load (kN)	Displacement at peak positive load (mm)	Cycles at peak positive load
M1-C1-R-L	Type two	25.4	25.16 (0.99FU)	29.43	32
M2-C2-R-L	Type one	26.0	23.59 (0.91FU)	21.21	27
M2-S-R-L	No Failure	26.0	21.21 (0.82FU)	13.63	N/A
M3-C2-R-L	Type one	29.7	25.05 (0.84FU)	13.65	23
M3-C2-W-L	Type one/two	29.7	25.76 (0.87FU)	17.34	26
M4-C2-R-WA	Type one	28.5	26.04 (0.91FU)	21.18	28
M4-C2-W-WA	Type two	28.5	27.5 (0.96FU)	29.66	34
M4-C2-W-L	Type two	28.5	27.44 (0.96FU)	17.35	26
M4-C2-R-L	Type two	28.5	28.15 (0.99FU)	25.71	32

3.4.1 Test: M1-C1-R-L

The first test undertaken was M1-C1-R-L which used laser cut, grade 250S0, O1 shaped O-connectors subjected to the C1 displacement history. The O-connectors failed by failure

mechanism type two as multiple areas of each O-connector sustained distributed cracks. The onset of fracture occurred at the radius to leg transition for the initial connector, however, secondary fractures occurred in the leg directly adjacent to the weld edge (type one failure mechanism), as depicted in Figure 3.10. As presented in Figure 3.8(a) M1-C1-R-L completed all 32 cycles with no significant strength degradation and achieved a maximum positive strength of 25.16 kN at a corresponding vertical displacement of 29.43 mm. The largest vertical displacement that the connector was subjected to in the negative direction was 3.2 mm.

3.4.2 Tests: M2-C2-R-L and M2-S-R-L

Tests M2-C2-R-L and M2-S-R-L each of which used laser cut, grade 250HA, O1 shaped O-connectors subjected to C2 and S displacement histories respectively. As depicted in Figure 3.10 (b), failure mechanism type one was observed for M2-C2-R-L with no distributed cracks and fracture occurred in the legs directly adjacent to the weld edge. As presented in Figure 3.8(b) M2-C2-R-L completed 27 cycles with no significant strength degradation and achieved a maximum positive strength of 23.59 kN at a corresponding vertical displacement of 21.21 mm. The M2-S-R-L test behaved in a similar manner, but the snap back loading history did not result in failure of any of the O-connectors, as shown in Figure 3.10 (c). M2-S-R-L was subjected to a maximum vertical displacement of 13.63 mm with a positive strength of 21.21 kN measured at this peak displacement.

3.4.3 Tests: M3-C2-W-L and M3-C2-R-L

After observing failure type one in tests M2-C2-R-L and M2-S-R-L the new O-connector with wings was developed and tested in an attempt to initiate a more ductile type two failure mode. The O-connector with wings utilised an enlarged section at the weld that was intended to shift the heat affected zone away from the yielding leg of the connector. The first O-connector with wings that was tested was M3-C2-W-L which used laser cut, grade 300HA, OW1 shaped, O-connectors and was subjected to the C2 displacement history. The M3-C2-R-L test was identical to M3-C2-W-L except that it used the regular O-connector profile to provide a baseline to gauge the effectiveness of the wings. Test M3-C2-R-L with regular oval shaped O-connectors failed with a type one mechanism in the exact same manner to the M2-C2-R-L with fracture at the weld edge, as depicted in Figure 3.10 (d). Test M3-C2-W-L failed in a similar manner to the first test M1-C1-R-L with fracture occurring at the radius to leg transition and secondary fracture at the

weld edge, as shown in Figure 3.10 (e). As shown in Figure 3.8(d) and (e) M3-C2-W-L and M3-C2-R-L completed 26 and 23 cycles, respectively, with no significant strength degradation and achieved maximum positive strengths of 25.76 kN and 25.05 kN, respectively, which corresponded to vertical displacements of 17.34 mm and 13.65 mm respectively.

3.4.4 Tests: M4-C2-R-WA, M4-C2-W-WA, M4-C2-R-L and M4-C2-W-L

The final four tests each used a different combination of O-connector profile (O2 or OW1) and cutting process (laser or water) while keeping the material (grade 300S0 steel) and displacement history (C2) the same. M4-C2-R-WA failed with a type one mechanism with tearing and fracture at the weld of multiple connector simultaneously and no distributed cracks were observed, as shown in Figure 3.10 (f). Test M4-C2-R-WA reached a maximum positive strength of 26.04 kN at a peak vertical displacement of 21.18 mm after completing 28 cycles.

As depicted in Figure 3.10 (g), test M4-C2-W-WA failed with a type two mechanism with failure initially occurring at the radius to leg transition zone with some distributed cracking and secondary failure occurring at the weld edge. Test M4-C2-W-WA reached a maximum positive strength of 27.5 kN at a peak vertical displacement of 29.66 mm after completing 34 as presented in Figure 3.8(g).

Test M4-C2-R-L initially underwent a type two failure mechanism with distributed cracking and failure at the radius to leg transition zone, but only in one connector, as shown in Figure 3.10 (h). During the test a gap started to open between the U-shaped and centre portion of the test rig which may have caused asymmetric loading on the test rig causing a particular connector to undergo larger displacements causing premature fracture of the test as a whole. This gap opening had not been observed in the previous test and it is thought that the lateral stiffness of the test rig had reduced from the large number of tests performed using it. It was only after complete failure of one connector that another started to show significant signs of failure. Test M4-C2-R-L reached a maximum positive strength of 28.15 kN at a peak vertical displacement of 25.61 mm after completing 32 cycles as presented in Figure 3.8(i).

Test M4-C2-W-L resulted in an ideal ductile failure mechanism (type two) as depicted in Figure 3.10 (i). All O-connectors demonstrated distributed cracking in multiple locations and fracture occurred at the radius to leg transition zone for all O-connectors. Test M4-C2-W-L had a

maximum positive strength of 27.44 kN at a peak vertical displacement of 17.35 mm, and completed 26 cycles.

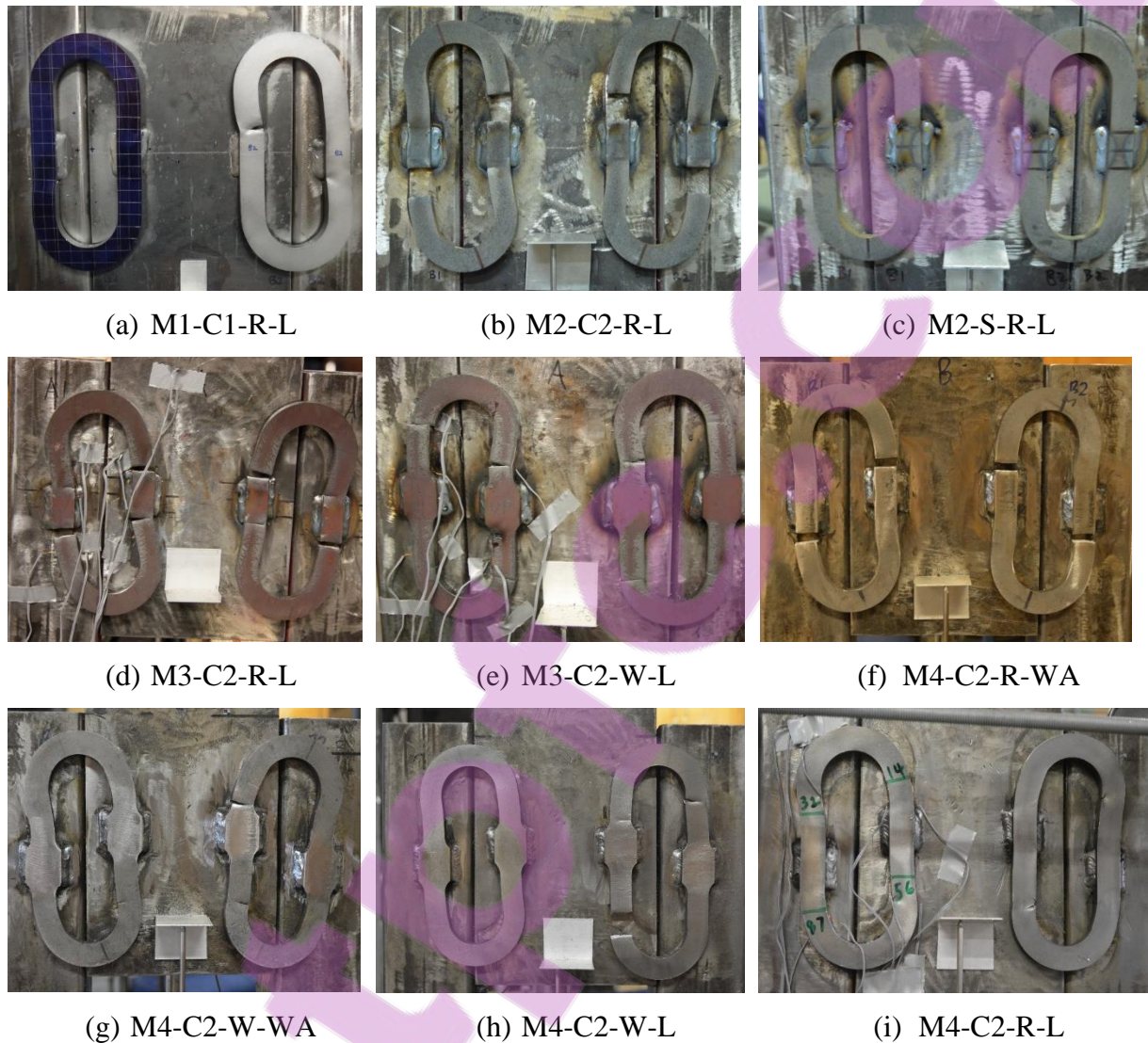


Figure 3.10 – Observations of fracture mechanism for each test

3.5 DISCUSSION OF RESULTS

The following discussion highlights potential reasons for the different failure mechanisms observed and provides recommendations for future O-connector design and construction. The topics discussed include accuracy of strength and stiffness predictions, out-of-plane buckling, and the influence of cutting process, material properties, welding process and O-connector profile.

3.5.1 Strength and stiffness calculation

The yield, plastic, and ultimate strengths calculated with the measured material properties for each connector test using Equations (3-3), (3-4) and (3-7) are shown alongside the force-displacement response of each connector in Figure 3.8. For tests M1-C1-R-L, M4-C2-W-WA, M4-C2-W-L, and M4-C2-R-L the predicted ultimate strength was within 96% of the measured strength at fracture. All of these tests portrayed the preferred type two failure mechanism with a ductile response. Thus, when a type two failure mechanism was achieved the O-connector reached the expected ultimate strength and the corresponding ultimate displacement. Additionally, two of the tests with accurate ultimate strength prediction were with O-connectors with wings, validating the use of the strength equations for both profiles of O-connector. On the contrary, the tests that experienced a type one failure mechanism only reached 80-90% of the predicted ultimate strength which further confirmed that premature fracture occurred for these connectors.

A bilinear approximation was developed for the O-connector based on the force-displacement results of tests M1-C1-R-L, M4-C2-W-WA, and M4-C2-R-L, that displayed the preferred type two failure mechanism. The bilinear yield strength was defined equal to the plastic strength (F_p) calculated using Equation (3-3), and the bilinear yield displacement (Δ_{by}) was calculated using the initial stiffness presented in Equation (3-6). The bilinear ultimate strength is equal to the ultimate strength (F_u) calculated using Equation (3-7), and the corresponding bilinear ultimate displacement was assumed to be equal to $20\Delta_y$. The resulting bilinear approximation is overlaid on the force-displacement response of the M1-C1-R-L, M4-C2-W-WA, and M4-C2-R-L tests in Figure 3.11. Overall a good estimate of the O-connector envelop response was achieved using the bilinear approximation and the initial stiffness was well captured for small displacement cycles. The assumed bilinear ultimate displacement equal to $20\Delta_y$ provided an accurate estimate of the ultimate displacement for the tests presented in Figure 3.11. However, the materials used in these tests were M1 and M4 which are both high ductility materials able to elongate up to 34.9%, hence the ultimate displacement for tests which use a lower ductility steel would be reduced.

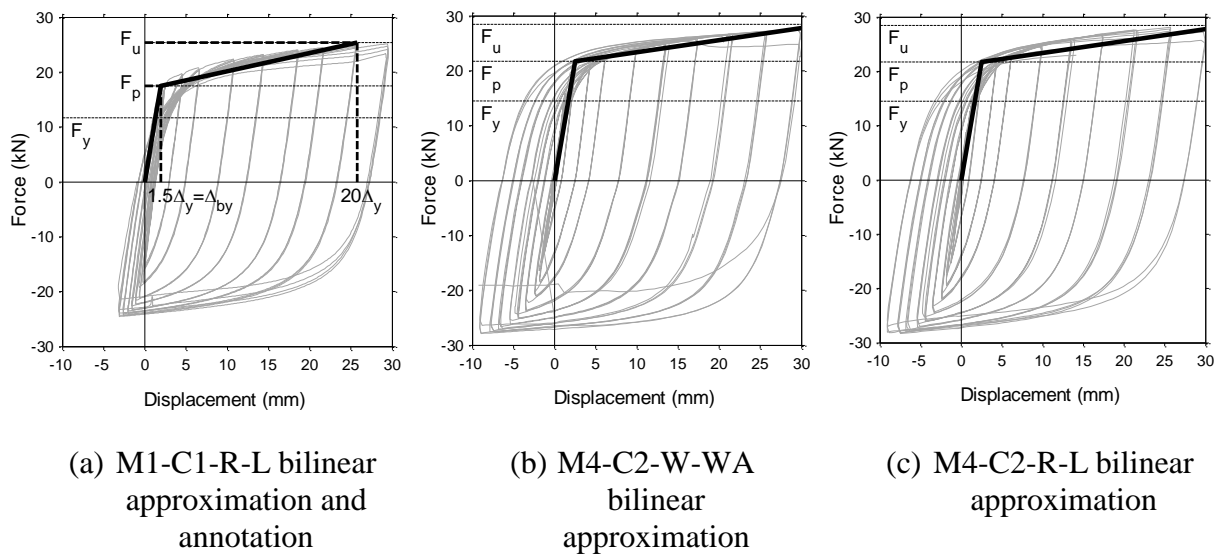


Figure 3.11 – Bilinear approximation based on design equations

To further validate use of Equations (3-3), (3-4) and (3-7) for predicting the O-connector strength and the bilinear approximation for O-connectors with different geometry, the test reported by Henry et al. [15] was also studied. The stress-strain steel properties and hysteresis response of the test reported by Henry et al. are presented in Figure 3.12. From the tensile test the yield stress was 340 MPa and the ultimate stress was 476 MPa. The measured ultimate strength of the O-connector was within 96% of the predicted ultimate strength, providing further validation the strength equations presented earlier. The bilinear approximation is overlaid on the hysteresis response in Figure 3.12(b), and again showed a good estimate of the response considering the different geometry of the connector.

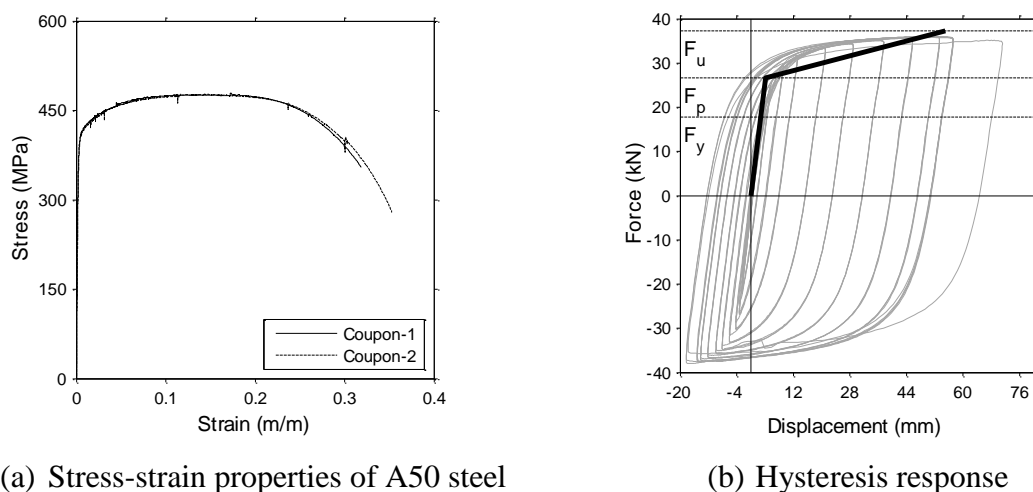


Figure 3.12 – Stress-strain and hysteresis response of tests reported in Henry et al. [15]

3.5.2 Out-of-plane buckling

As stated in the introduction, the O-connectors tested by Henry et al. [15] experienced out-of-plane buckling. In an effort to reduce the likelihood of buckling, the O-connectors tested herein were designed with a reduced leg length to thickness ratio. The leg length (381 mm) to plate thickness (9.35 mm) ratio of the O-connector tested by Henry et al. was 40.7, while the length to thickness ratios of the O-connectors tested herein were 19.5 and 20.5. Out-of-plane buckling of the O-connector was not observed during any of the tests that followed a type one failure mechanism with premature fracture adjacent to the weld. However, slight onset of buckling, as shown in Figure 3.9(d), was observed for the tests that followed the more ductile type two failure mechanism with fracture at the radius to leg transition zone. In all cases the out-of-plane displacement of the O-connectors was minor and occurred during the final cycles of the test as the O-connectors were fracturing. It appeared that decreasing the leg length to thickness ratio delayed out-of-plane buckling until the displacement capacity of the connector was reached. It is also important to note that the increase in thickness increases the strength of the O-connector but has no significant influence on the displacement capacity, as shown by a parametric finite element model study reported by Henry [41].

3.5.3 Influence of cutting process

Laser cutting and water cutting techniques were investigated to investigate the influence of the magnitude of heat induced when cutting, possible residual stresses induced at the cut edge, and the possible influence of the cut surface roughness on the fracture initiation and crack propagation. Generally, laser cutting induces greater heat and residual stress in the specimen which leads to an increased degree of embrittlement [100]. To investigate the influence of the cutting process test M4-C2-R-L can be compared to test M4-C2-R-WA, where the only differences between the tests were the cutting method and welding process. Test M4-C2-R-L used laser cut connectors and lasted for four more cycles than the same connectors water cut (M4-C2-R-WA). Since laser cutting induces more heat and residual stress the laser cut connectors should have a reduced displacement capacity compared to the water cut connectors, however, the opposite trend was observed. Therefore it was concluded that the difference in the displacement capacity of tests M4-C2-R-L and M4-C2-R-WA was due to the welding process and that there was no significant influence due to the different cutting techniques used. The

additional expense of water cutting does not appear to be justified and laser cutting is recommended to fabricate the O-connectors.

3.5.4 Influence of steel material

A comparison of material three and material four is presented in Figure 3.13(a) by plotting M3-C2-W-L and M4-C2-W-WA on the same graph. Both tests were subjected to the C2 displacement history and tested the OW1 connector profile. Although M3-C2-W-L used laser cut connectors and M4-C2-W-WA used water cut connectors the influence from the cutting process has already been determined to be negligible. The connectors in both tests initially failed with a type two failure mechanism, although the connectors in test M3-C2-W-L then quickly progressed to a type one fracture adjacent to the weld due to the low strain capacity of the HA grade material three. As shown in Figure 3.13(a) there is overlap of the dotted and continuous lines until failure of M3-C2-W-L. This observation indicates that the strengths of the O-connectors were similar as they were both grade 300 steels. However, the two tests resulted in significantly different displacement capacities due to the lower strain capacity of the 300HA material three in comparison to the 300S0 material four. In general, when the steel had a higher tensile strain capacity the O-connector was able to sustain distributed cracking before fracture and achieve a higher displacement capacity.

The 300S0 material four can also be compared to the 250S0 material one by plotting the results of test M1-C1-R-L and M4-C2-R-L on the same graph, as in Figure 3.13(b). The connectors in tests M4-C2-R-L had a higher strength and similar displacement capacity when compared to test M1-C1-R-L. This behaviour was expected since the 300S0 material four is a high strain capacity grade 300 steel while the 250S0 material one is a high strain capacity grade 250 steel. As the displacement capacity of the O-connector is correlated to the uniaxial tensile strain capacity, and the overstrength is dependent on the yield and ultimate stress from a uniaxial tensile test, it is important to be certain about the parameters of the steel used in the design and construction of O-connectors.

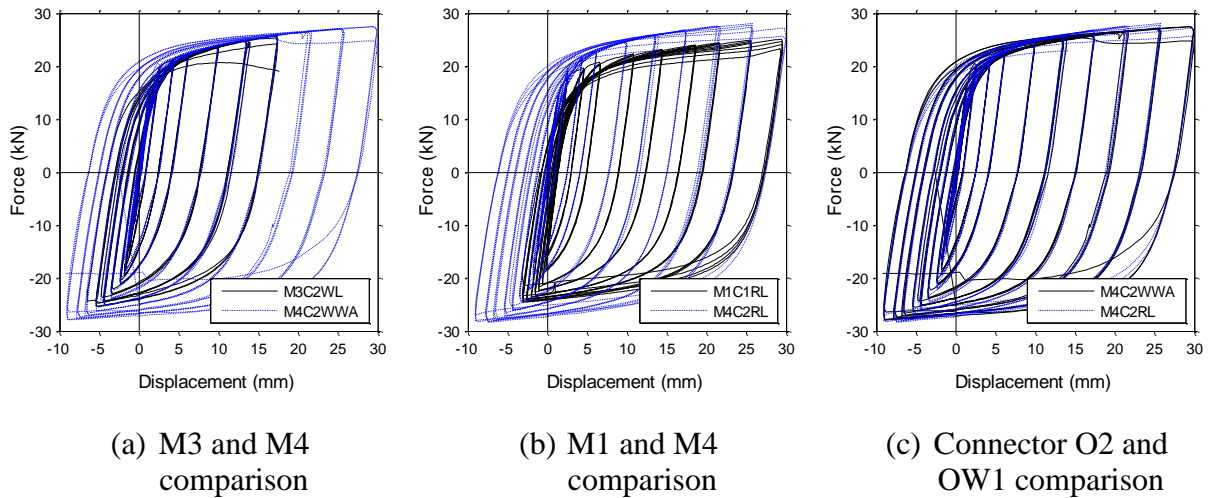


Figure 3.13 – Direct comparison of material and connector type

3.5.5 Influence of wings

The influence of the addition of wings to the O-connector was investigated by overlaying the hysteretic responses of tests M4-C2-W-WA and M4-C2-R-L in Figure 3.13(c). It is clear that the force-displacement behaviour of the two tests was almost identical with the response difficult to differentiate. It was therefore concluded that the wing profile had no significant influence on the strength of the O-connector. However, the wing profile has several other advantages such as providing a template to clearly identify the weld location and length, and removing the sensitivity to welding process by shifting the heat affected region away from the yielding leg, as is discussed below in more detail.

3.5.6 Influence of welding process

Initially the welding process was thought to be insignificant due to the use of mild low carbon steel [100]. However, due to different technicians and equipment two different welding techniques were used during the series of connector tests. The type of welding process used for each test was presented in Table 3.1. During the welding process a heat affected zone is formed in the area of the base metal that is not melted during the welding operation, but whose physical properties are altered by the heat induced [100]. Within the heat affected zone the metal will tend to have residual stresses, be weaker and more brittle. A combination of MIG and two ARC welding processes were used during the connector tests. Welding referred to as ARC+ used a

higher penetration, all angle, smaller diameter electrode in comparison to the ARC* welding. The three different welding processes would have induced different quantities of heat in the O-connectors. For instance, ARC welding utilises different electrodes for different applications and these will require different currents and therefore induce different levels of heat. The O-connectors without wings that were MIG or ARC* welded all failed with premature fracture in the leg adjacent to the weld (failure mechanism 1). In contrast, the O-connectors without wings that were ARC+ welded, all displayed the more desirable ductile failure mode with fracture at the radius to leg transition (failure mechanism type two). Although variables other than the welding process were also changed, it has already been determined that they had negligible influence on the O-connector failure mechanism. It follows that the heat induced from welding in the heat affected zone must have had a significant effect on the failure mode of the O-connector. When a regular profile O-connector is used, care needs to be taken such that welding process is appropriate to ensure that a ductile type two failure mechanism is achieved. It is recommended that ARC welding with a high penetration, all angle electrode is used when installing O-connectors. Since the O-connectors tested were of a relatively small scale it is expected that the heat affected zone would be more influential than for larger O-connectors. However, regardless of the O-connector scale or size as an alternative solution to minimise the effect of the weld type, the O-connector with wings can be used as the heat affected zone is shifted away from the critical yielding section of the connector, removing the sensitivity to welding.

3.6 CONCLUSIONS

A unique experimental investigation into the cyclic response of energy dissipating O-connectors for use in unbonded PT concrete rocking wall systems has been presented. Nine cyclic tests were performed on two different O-connector profiles with four different materials and two cutting processes. The tests confirmed the suitability of the O-connector as a cost effective energy dissipating connector that is easy to install and demonstrates stable hysteresis behaviour. The large parameter set enabled the O-connector failure mechanisms to be identified and the cause of each mechanism to be understood. As discussed below a number of conclusions have been drawn based on the test observations and measured response.

Failure in the connector leg adjacent to the weld demonstrates the importance of the welding process and the corresponding heat affected zone on the O-connector. MIG welding was found to cause failure adjacent to the weld while ARC welding with the appropriate electrode (small diameter, high penetration ability, low current) had a smaller heat affected zone and shifted the failure to the preferred ductile failure mechanism at the radius to leg transition.

The O-connector with wings is a novel design and provides an alternative method that is recommended to ensure that the preferred ductile failure mechanism is achieved at the radius to leg transition, by locating the heat affected zone in an area with a larger cross-section than the leg. A further advantage is that the wing provides a template for the location and length of weld and since the O-connector is laser cut the slight increase in complexity adds little cost.

The strain capacity of the steel is directly related to the displacement capacity of the O-connector. Therefore it is important to ensure that the steel specified in design has a high specified ductility. It is recommended that independent tensile coupons are tested for O-connectors used in practise when particularly high displacement capacities are required.

Out-of-plane buckling of the O-connector was avoided with an improved O-connector design that consisted of a reduction in the length to thickness ratio. A length to thickness ratio less than 20 is recommended to delay onset of buckling of unrestrained O-connectors until after fracture has initiated.

Negligible difference was observed between laser and water cut O-connectors and so it is recommended that laser cutting is used for economic considerations.

Simple analytical equations were validated to predict the yield, plastic and ultimate strength of the O-connector. For connectors that failed at the radius to leg transition the calculated ultimate strength was within 96% of the measured ultimate strength. A bilinear approximation was also proposed that showed good estimation of the O-connector response for design purposes.

It is also recommended that given that variability of mild steel available and the fabrication process, the design of O-connectors for structural systems should always be validated with full-scale tests prior to implementation.

3.7 REFERENCES

15. Henry, R.S., S. Aaleti, S. Sritharan, and J.M. Ingham, *Concept and finite-element modeling of new steel shear connectors for self-centering wall Systems*. Journal of Engineering Mechanics, 2010. **136**(2): p. 220-229.
41. Henry, R.S., *Self-centering precast concrete walls for buildings in regions with low to high seismicity*. 2011, University of Auckland. p. 441.
57. Sritharan, S., S. Aaleti, R.S. Henry, K.Y. Liu, and K.C. Tsai, *Introduction to PreWEC and key results of a proof of concept test*. M.J. Nigel Priestley Symposium, North Lake Tahoe, California, August 4-5, 2008, ed. M.J.N. Priestley, M.J. Kowalsky, and S. Sritharan. 2008, Pavia, Italy: IUSS Press. 267.
91. Ma, X., E. Borchers, A. Pena, H. Krawinkler, S. Billington, and G. Deierlein, *Report No. 173: Design and behavior of steel shear plates with openings as energy dissipating fuses*. 2011, Department of Civil and Environmental Engineering, Stanford University: Stanford, CA.
92. Kelly, J.M., R.I. Skinner, and A.J. Heine, *Mechanisms of energy absorption in special devices for use in earthquake resistant structures*. Bulletin of New Zealand Society for Earthquake Engineering, 1972. **5**(3).
93. Shultz, A.E. and R.A. Magana, *Seismic behavior of connections in precast concrete walls*, in *Mete A. Sozen Symposium*. 1996, American Concrete Institute: Farmington Hills, MI.
94. Baird, A., T. Smith, A. Palermo, and S. Pampanin, *Experimental and numerical study of U-shape flexural plate (UFP) dissipators*, in *New Zealand Society for Earthquake Engineering 2014 Technical Conference and AGM*. 2014, New Zealand Society for Earthquake Engineering: Auckland, New Zealand.
95. Standards New Zealand, *AS/NZS 3678: Structural steel - Hot-rolled plates, floorplates and slabs*. 2011: Wellington.
96. Standards New Zealand, *AS/NZS 1594: Hot-rolled steel flat products*. 2002: Wellington.
97. Bluescope *AS/NZS 3676 - 250 XLERPLATE steel: Revision 1*. 2014.
98. Bluescope *AS/NZS 1584 - HA250: TRU-SPEC Coil Plate Steel*. 2014.
99. Standards Association of Australia, *Metallic materials : tensile testing at ambient temperature*. 4th ed. ed. AS 1391-2007. 2007, Sydney, NSW: Sydney, NSW : Standards Australia 2007.
100. Weman, K., *Welding processes handbook*. 2003, Cambridge, England: CRC Press.

Chapter 4

PROTOTYPE AND MODEL DESIGN

4.1 INTRODUCTION

This chapter describes the design and construction of the test walls studied within this thesis. The layout and seismic hazard of the prototype structure is first described, followed by an outline of the Direct Displacement Based Design (DDBD) process adopted. The prototype building and wall design was based on existing design guidance and incorporated recommendations from Appendix B of the New Zealand Concrete Structures Standard [18] and the PRESSS Design Handbook [19]. Similitude scaling of the prototype is described in detail followed by a description of the detailed model wall design and construction. Finally a summary of the wall system testing reported in the following chapters is given.

4.2 PROTOTYPE BUILDING

The prototype building was designed such that scale models of SRW and PreWEC systems from the building could be tested using the University of Auckland shake table. The prototype structure was based on a four storey building and designed according to New Zealand earthquakes loadings standard, NZS 1170.5:2004 [101], and Appendix B of the New Zealand

Concrete Standard, NZS 3101:2006 [18], that outlines special provisions for the seismic design of ductile jointed precast concrete structural systems. The prototype building is shown in plan and elevation in Figure 4.1 with overall dimensions of 16×24 m. The lateral resistance was provided by two unbonded Post-Tensioned (PT) precast concrete walls or Single Rocking Walls (SRWs) in the north-south direction and a Reinforced Concrete (RC) moment resisting frame in the east-west direction. The walls, frames, and internal columns were designed to carry the appropriate tributary area of gravity load using either a rigid or semi rigid floor connection. A rigid connection would be a result of a cast-in-place floor while a semi rigid floor connection would come from precast flooring spanning perpendicular to the unbonded PT walls. The building was divided into bays of 16 m by 8 m with an effective floor weight from permanent (G) and imposed (Q) actions of 7.8 kPa and an effective roof weight from permanent (G) and imposed (Q) actions of 6.7 kPa. The exact arrangement of the prototype was chosen such that the seismic mass associated with each wall could be simulated in the laboratory.

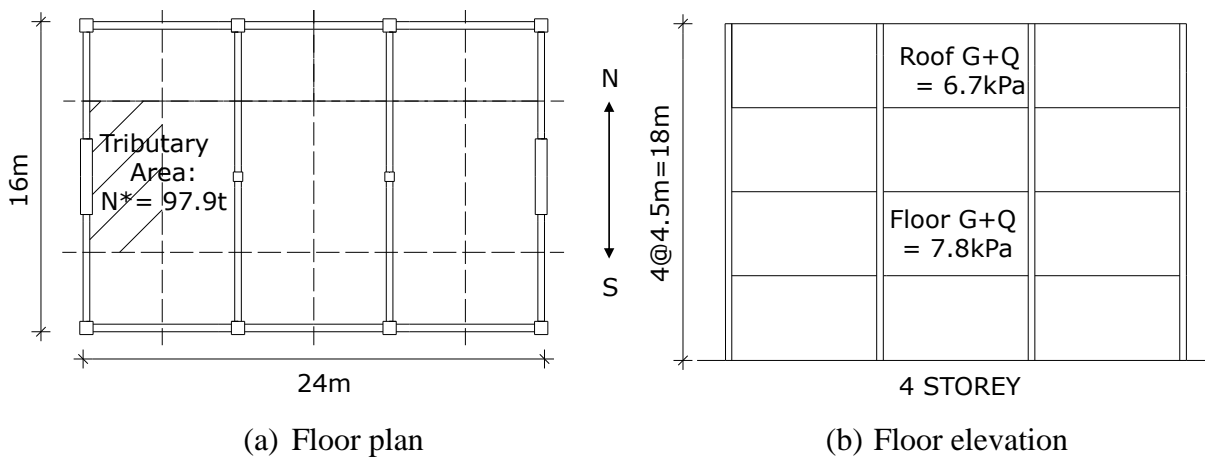


Figure 4.1 – Prototype structure in elevation and plan

4.3 SEISMIC HAZARD

The prototype building was intended to be located in Wellington, New Zealand, and classed with an Importance Level 2, as per NZS 1170.0 [101]. The effect of a near fault rupture was represented by assuming a distance to nearest fault (D) equal to zero to adjust the seismic demand by altering the near fault factor, $N(T,D)$. The building was assumed to be founded on Site Soil Class C (shallow soil) according to NZS1170.5 [101], with a Z hazard factor of 0.4 and a return period factor (R) of 1.0 corresponded to the design level earthquake. The design level seismic

hazard corresponding to this importance level is representative of ground motions having a 500 year return period. The structural performance factor (S_p) was 0.7 as defined in the appropriate concrete materials standard [18] for structures with ductility greater than three. Despite questions over how S_p should be applied, as discussed by Pampanin et al. [19] who states that S_p is a base shear reduction factor and should be directly applied to the base shear calculation, the design of the walls discussed here retain S_p as the acceleration spectrum factor to be compatible with the current New Zealand loadings code [101].

4.4 DISPLACEMENT BASED DESIGN

Direct Displacement Based Design (DDBD) methodology was used to design the prototype building incorporating two SRW systems in the north-south direction to resist seismic loads. DDBD utilises the secant stiffness to maximum displacement based on the substitute structure approach and an equivalent elastic representation of the hysteretic damping at maximum response. The DDBD methodology is outlined in detail by Priestley et al. [20] and reiterated in the steps conducted below for the prototype SRW design. Guidance was also taken from the PRESSS Design Handbook [19] and Appendix B of the New Zealand Concrete Structures Standard (NZS3101:2006) [18] where appropriate to ensure relevance to New Zealand design standards.

Step 1 – A target drift (θ_d) is selected based on material strain damage criteria or directly by code defined drift limits. The material strain damage criteria could include limits on concrete compression strain or PT steel tension strain for unbonded PT walls. For the SRW design the target drift was selected to be 1.20%. For an unbonded PT wall the displaced shape is assumed to be a linear profile up the building height, as described by Equation (2-17).

$$\Delta_i = \theta_d H_i \quad (4-1)$$

Where Δ_i is the design displacement at storey i and H_i is the height of level i .

A summary of the DDBD parameters is provided in Table 4.1, which is a convenient method of calculating the required quantities for the DDBD process as laid out in the PRESSS Design Handbook [19]. The table is developed using the inter-storey height of 4.5 m, the design drift of 1.2%, the mass of each storey (m_i) and the other building parameters defined in section 4.2.

Using the design drift the design lateral displacement (Δ_d) of an equivalent Single Degree Of Freedom system (SDOF) is calculated using Equation (2-12) and the assumed displaced shape of the structure.

Table 4.1 – Summary of DDBD parameters

Floor	m_i (tonne)	H_i (mm)	Δ_i (mm)	$m_i\Delta_i$	$m_i\Delta_i^2$	$m_i\Delta_iH_i$
4	264	18000	216	5.71E+04	1.23E+07	1.03E+09
3	306	13500	162	4.95E+04	8.03E+06	6.69E+08
2	306	9000	108	3.30E+04	3.57E+06	2.97E+08
1	306	4500	54	1.65E+04	8.92E+05	7.43E+07
Total	1182			1.56E+05	2.48E+07	2.07E+09

$$\Delta_d = \frac{\sum_{i=1}^n (m_i\Delta_i^2)}{\sum_{i=1}^n m_i\Delta_i} = 158.9 \text{ mm} \quad (4-2)$$

Where n is the number of storeys.

Step 2 - The effective mass, m_e , and the effective height, h_e , of the equivalent SDOF system is calculated, as shown in Equation (4-3) and Equation (4-4).

$$m_e = \sum_{i=1}^n \frac{m_i\Delta_i}{\Delta_d} = 982.7 \text{ tonnes} \quad (4-3)$$

$$h_e = \frac{\sum_{i=1}^n (m_i\Delta_iH_i)}{\sum_{i=1}^n (m_i\Delta_i)} = 13240.5 \text{ mm} \quad (4-4)$$

Step 3 - The system yield displacement ($\Delta_{y,i}$) [19], ductility (μ) and system damping (ξ_{eq}) is estimated based on the system type. The yield displacement is required to obtain the ductility and the corresponding Equivalent Viscous Damping (EVD) from existing relationships described in Priestley et al. [20], or in Appendix B of the New Zealand Concrete Standard [18]. However, for an unbonded PT only system, such as the SRW, the EVD is assumed to be 5% according to Appendix B of the New Zealand Concrete Standard [18]. Therefore determination of the ductility was not required for the SRW. The EVD used for the prototype design is stated in Equation (4-5).

$$\xi_{eq} = \xi_{pt} = 5\% \quad (4-5)$$

Step 4 - The displacement design spectra is used to calculate the effective period of the structure, T_e , based on the design displacement and damping calculated. This series of testing was designed according to the target spectrum for numerical time history analysis in NZS 1170.5 [101] defined by Equation (4-6). The structural performance factor S_p was assumed to be equal to 0.7 as previously stated, and the ordinate of the elastic site hazard spectrum, $C(T_1)$, was determined by Equation (4-7).

$$SA_{target} = \left(\frac{1 + S_p}{2} \right) C(T) \quad (4-6)$$

$$C(T) = C_h(T)ZRN(T, D) \quad (4-7)$$

$C_h(T)$ is the spectral shape factor determined from Clause 3.1.2 of the New Zealand loadings standard for site subsoil class C. For this design the spectral shape factor for modal analysis and numerical integration time history analysis was used. Z is the hazard factor equal to 0.4 for Wellington and R is the return period factor equal to 1.0 for the 1/500 annual probability of exceedance, $N(T, D)$ is the near-fault factor and is equal to $N_{max}(T)$ due to the distance to a major fault listed as 0-8 for Wellington.

An approximate relationship between peak acceleration and displacement response based on steady-state sinusoidal response is presented by Priestley et al. [20] and was used to derive the elastic displacement spectra from the target spectral acceleration as described by Equation (4-8). An effective period of T_e equal to 1.44 s was found as shown in Figure 4.2 for EVD of 5%.

$$S_{d(T)} = \frac{T^2}{4\pi^2} S_{A(T)} g \quad (4-8)$$

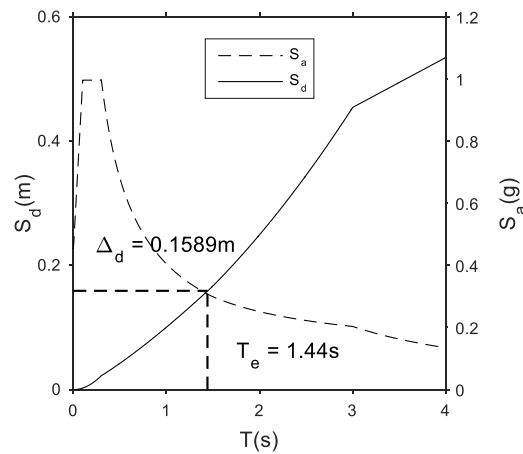


Figure 4.2 – Design displacement response spectra (5% damping)

The design displacement spectrum was derived from the design acceleration spectrum specified in NZS1170.5 [101] using the appropriate factors defined previously and Equation (4-8). If the EVD varies from 5% the elastic design spectrum is altered by a spectral reduction factor or damping modifier (η) which is supported by Priestley et al. [20] and described by Equation (4-9). Where α_{SF} is equal to 0.5 for sites located away from a major fault and the ground motions do not comprise of near-fault, forward directivity. By reducing the design displacement spectra, the ductile response of the structural system is taken into account. This method is advantageous over inelastic displacement spectra as a single design spectrum can be used for all structural systems but damping-ductility relationships must be developed for the specific system. This adjustment was not required for the current design due to damping being assumed as 5% for the SRW, irrespective of the design displacement or displacement ductility.

$$\eta = \left(\frac{7}{2 + \xi_{eq}} \right)^{\alpha_{SF}} = \frac{\Delta(T, \xi)}{\Delta(T, 5\%)} \quad (4-9)$$

Step 5 - The effective (secant) stiffness (K_e) of the equivalent SDOF structure at maximum displacement was calculated using the Equation (2-15).

$$K_e = \frac{4\pi^2 m_e}{T_e^2} = 18,709.7 \text{ kN/m} \quad (4-10)$$

Step 6 - The design base shear (V_{base}) of the structure was calculated using Equation (2-16).

$$V_{base} = K_e \Delta_d = 2,972.7 \text{ kN} \quad (4-11)$$

Step 7 - The design base shear was distributed to the structure and the actions on each wall were calculated, recalling that two walls support the lateral load in the north-south direction. Requirements for accidental eccentricity i.e. torsion, were ignored as only the 2D design and analysis of the building were of interest.

$$V_{wall} = 1,486.3 \text{ kN} \quad (4-12)$$

$$M_{wall} = 19,680.0 \text{ kNm} \quad (4-13)$$

Step 8 - Based on the tributary area shown in Figure 4.1, the axial load per wall due to gravity was calculated, as shown in Equation (4-14) and Equation (4-15). Where W is the total building weight and 1/12 is the ratio of tributary area of gravity load for each wall to the total gravity load. The gravity load on each wall is approximately 1/5th of the seismic mass assumed to be carried by each wall.

$$N_{wall} = \frac{1}{12} \sum W = \frac{1}{12} 11,591.6 = 965.9 \text{ kN} = 98.5 \text{ tonnes} \quad (4-14)$$

$$N_{wall} = \frac{1}{12} \sum W \approx \frac{1}{5} \text{ equivalent seismic mass per wall} \quad (4-15)$$

4.5 PROTOTYPE WALL DESIGN

The prototype SRW system was designed according to the moment, shear, and axial load actions determined from the DDBD at 1.2% drift. For the prototype wall design the prototype building loads were not factored and a strength reduction factor was not applied to the moment capacity of the prototype wall, such that the moment capacity and shear capacity of the prototype wall were equal to the required design moment and base shear force. This allowed for a direct comparison of the wall response with design estimates. Through a trial and error approach the dimensions of the prototype SRW system were selected considering appropriate initial PT stresses, and dimension constraints from the shake table capacity.

According to NZS 3101 Appendix B, the unbonded PT tendons must be designed to remain elastic during a design earthquake. However, due to the nature of the test programme planned there was a need to be able to repeat the loadings without tendon yielding to drifts greater than the design level drift of 1.2%. As a result the tendon arrangement and initial prestress were

designed to ensure that the tendon force would not exceed the yield strength of the strand until lateral drifts over 3% were reached. Concurrently, the targeted initial prestress force, number of tendons, and size of tendons were also designed to maximise the wall moment capacity while keeping the axial force ratio (AFR) below 10% to ensure no significant crushing occurred in the wall compression toe [41]. The AFR is defined as the ratio of post-tensioning tendon force plus the wall self-weight and additional weight divided by the axial crushing capacity of the concrete section ($f'_c A_g$). The concrete strength was designed to be 40 MPa. Knowing the likely scale of the model wall, the tendon arrangement was chosen to consist of three multi-strand tendon bundles to be spaced evenly along the prototype wall length at 1 m centre to centre. The multi-strand bundles consisted of 25 15.2 mm strand. The unbonded length of the tendons was designed to be equal to 18 m.

Accounting for these PT requirements the prototype SRW dimensions were determined such that the strength of the wall was equal to the design actions at 1.2% drift using the simplified analytical force-displacement prediction procedure for unbonded PT walls proposed and validated by Aaleti and Sritharan [62]. The key prototype wall dimensions were a wall length of 4 m, a wall thickness of 0.625 m, a wall height of 18 m, an effective mass of 491 tonnes, and an effective mass height of 13.24 m, as presented in Table 4.2. Considering all the PT requirements and the dimensions of the prototype wall the targeted initial prestress (f_{pi}) in the prototype wall PT for each strand was 696 MPa ($0.45f_y$). The force displacement backbone for the prototype wall is presented in Figure 4.3 with the design displacement and corresponding base shear force identified. The design actions such as design shear, moment and drift are also summarised in Table 4.2.

The exact panel reinforcement detail of the prototype wall was not significant as only minimum horizontal and vertical reinforcement was required as no flexural yielding was expected within the SRW panel itself. However, the confinement detail in the toe regions did require special attention to ensure confined concrete crushing did not occur until well beyond tendon yielding. The detailed design of the confined regions is described for the SRW panel model design in section 4.7.1.

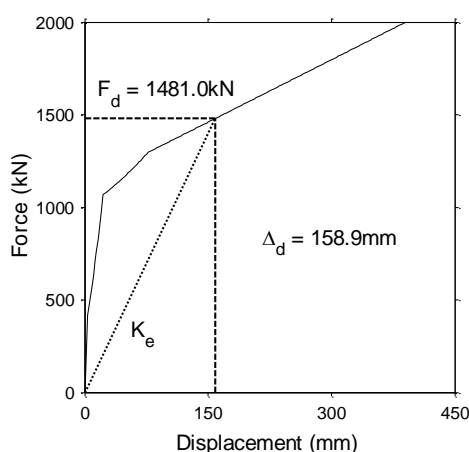


Figure 4.3 – SRW Prototype wall design

Table 4.2 - Prototype and model dimensions

Parameter	Prototype	Model
Wall length (mm)	4000	800
Wall thickness (mm)	625	125
Wall height (mm)	18000	3600
Effective mass (tonne)	491	3.93
Height of effective mass (mm)	13240	2648
no. of PT strands	75	3
Unbonded length (mm)	18000	3600
Concrete strength, f'_c , (MPa)	40	40
Confined concrete strength, f'_{cc} , (MPa)	54	54
Initial stress, f_{pi} , (MPa)	696	696
α	0.908	0.908
β	0.910	0.910
Design Moment	19680	157.4
Design Shear	1486	59.4
Design Drift	1.20%	1.20%
Moment Capacity @ Design Drift (kNm)	19608	156.8

4.6 MODEL SCALING

A length scale factor of 1/5th was required for the prototype SRW system to be tested at model scale in the laboratory on the shake table. The prototype SRW wall was scaled according to similitude scaling laws that maintain constant stress and density between the model and prototype, as explained by Harris and Sabnis [102]. It is common for a lateral load resisting wall

to be expected to carry a large portion of lateral inertia load during an earthquake while carrying only a portion of that as gravity load. The prototype seismic and gravity mass were 491 tonnes and 98.5 tonnes, respectively. It is clear that the seismic mass was five times larger than the gravity mass carried by the wall since the gravity mass was based on the tributary area while the seismic mass was half the total mass of the prototype building. For the shake table testing it was not possible to install a system that would carry additional gravity load to simulate the difference between the gravity and seismic mass. Instead guidance was taken from Stavridis et al. [6] who used a gravitational acceleration scale factor of one and hence the appropriately scaled gravity mass and then scaled the seismic acceleration and seismic mass such that the force scale factor was preserved in the vertical and horizontal direction. The result of this scaling method is that the mass carried by the specimen accurately represents the gravity mass carried by the prototype, which induces the same static axial stresses in the specimen.

The scaling law and resulting scale factors for the basic quantities are summarised in Table 4.3. The scale factor for the seismic mass to the gravity mass was five for the prototype (referred to as λ_m in Table 4.3) but one for the specimen. Therefore the scale factor for the seismic mass was 1/125 as shown in Table 4.3. The scale factors for the stress and gravitational acceleration are 1 and the length scale is 1/5, because of this the scale factors for the force and gravity mass had to be 1/25 to satisfy similitude law. Hence, the input ground acceleration time histories for the shake table testing had to be scaled in time and amplitude to result in consistently scaled seismic forces. The resulting key model dimensions and parameters are summarised alongside the prototype values in Table 4.2.

Table 4.3 - Scale factors

Quantity	Scaling Law	Scale Factor
Length	S_L	1/5
Stress	S_σ	1
Gravitational Acceleration	S_a^g	1
Strain	$S_\epsilon = S_\sigma$	1
Force	$S_F = S_L^2 S_\sigma$	1/25
Gravitational Mass	$S_m^g = S_F (S_a^g)^{-1}$	1/25
Seismic acceleration	$S_a^s = S_F (S_m^s)^{-1}$	5
Seismic mass	$S_m^s = S_m^g \lambda_m^{-1}$	1/125
Time	$S_t = (S_L)^{0.5} (S_a^s)^{-0.5}$	1/5
Frequency	$S_f = (S_t)^{-1}$	5

4.7 DETAILED MODEL WALL DESIGN AND CONSTRUCTION

4.7.1 SRW models

The dimensions of the SRW model scaled from the prototype were presented in Table 4.2. The key dimensions of the SRW model were a wall length of 800 mm, a wall width of 125 mm, an effective height of 2648 mm, and an effective mass of 3.93 tonnes. This SRW model is referred to as SRW-A for the rest of this thesis. A second SRW was also investigated, to study the behaviour of two different SRW systems with different geometry and initial PT force, referred to as SRW-B.

The corresponding cross-sections of each of the SRW model designs are provided in Figure 4.6. SRW-A and SRW-B consisted of a precast concrete wall panel cast with ducts along the length for placement of the unbonded PT tendons. The wall panel used for SRW-A had a length, thickness and height of 800 mm, 125 mm and 2860 mm, respectively, while the wall panel used for SRW-B had a length, thickness and height of 1000 mm, 120 mm and 3000 mm, respectively. The PT tendons used for SRW-A were 15.2 mm prestressing strand, and the PT tendons used for SRW-B were 15 mm diameter high strength bars. The elevation detail of SRW-A and SRW-B is depicted in Figure 4.4. The targeted initial prestress (f_{pi}) in the wall PT was 239 MPa ($0.24f_y$) for SRW-B and 696 MPa ($0.45f_y$) for SRW-A. Test wall SRW-A used three tendons and SRW-B used only two tendons. As described in the prototype wall design section the targeted initial prestress force was selected to maximise the wall moment capacity while keeping the axial force ratio (AFR) below 10% to ensure no significant crushing occurred in the wall compression toe. The wall PT tendons used in SRW-A had a typical unbonded length of 3600 mm, while the typical unbonded tendon length for SRW-B was 3900 mm.

The panels were reinforced with minimum horizontal reinforcement at 100 mm centres, minimum vertical reinforcement with the layout shown in Figure 4.6 and Figure 4.7, and with specially designed confinement reinforcement at the wall base spaced at 40 mm centres over a height of 200 mm up the wall, as shown in Figure 4.5(a) and (b). The confinement reinforcement was designed for the wall toe using the confined concrete model described by Mander et al. [103] with the maximum expected compressive strain in the wall toe calculated using the simplified analysis method proposed by Aaleti and Sritharan [62]. Detailed confinement calculations are

provided in Appendix B for the two wall panels of SRW-A and SRW-B. A steel angle base frame constructed from 25×25×5 mm equal angle was cast into each precast wall end for additional confinement and protection of the panel edge, as shown in Figure 4.5(c). Detailed construction drawings of the two SRW panels are provided in Appendix A.

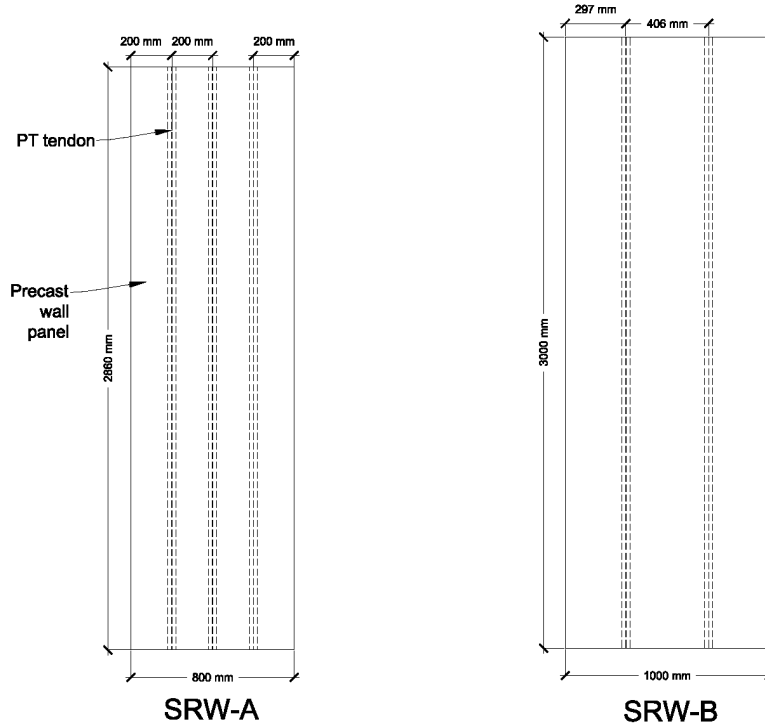


Figure 4.4 – Elevation of SRW model walls



(a) SRW-B

(b) SRW-A and PreWEC-A/B

(c) Armouring angle frame

Figure 4.5 – Base of wall reinforcement and construction details

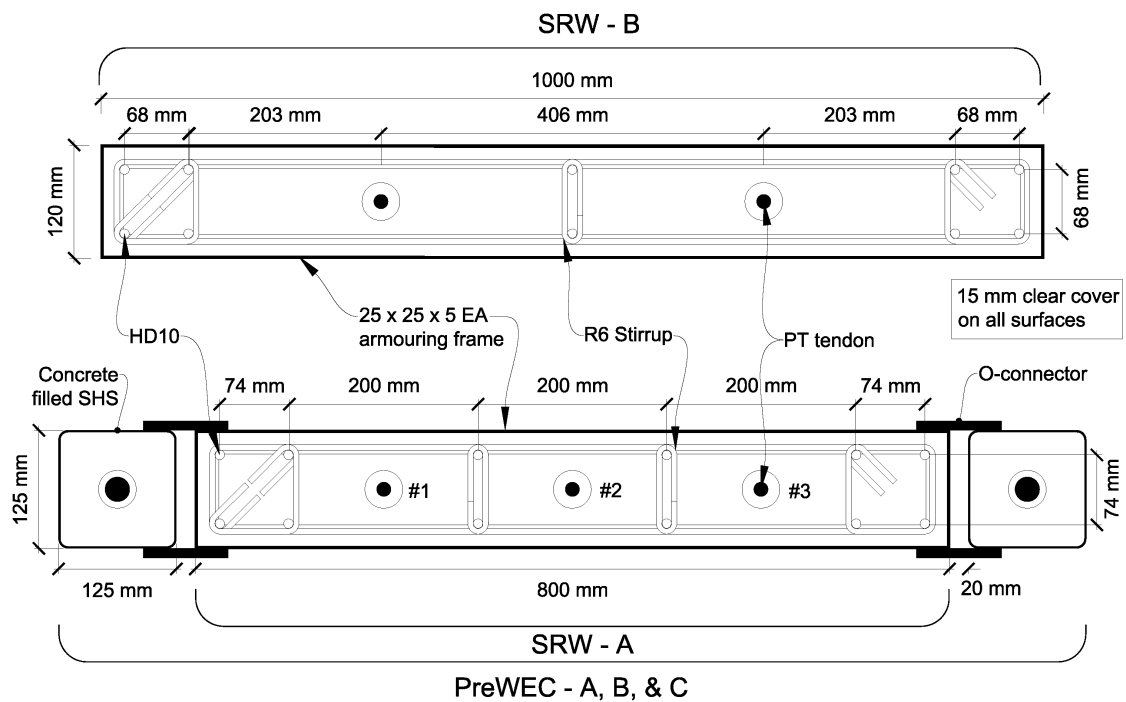


Figure 4.6 – Cross-sections of model walls

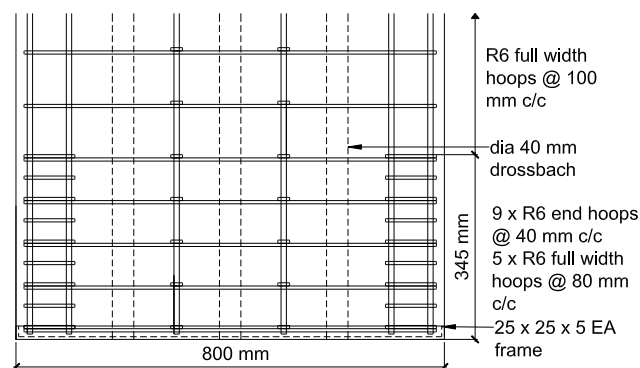


Figure 4.7 – Wall panel reinforcement detail

4.7.2 PreWEC models

Three PreWEC system models were investigated which are referred to as PreWEC-A, PreWEC-B and PreWEC-C. The PreWEC system designs were based on the SRW-A model with the addition of end columns and varying amounts of additional energy dissipating devices that provided higher energy dissipation capacity and strength. To isolate the influence of the number of O-connectors, all parameters between SRW-A, PreWEC-A and PreWEC-B systems were kept constant except for the number of O-connectors. The parameters of PreWEC-C were chosen to

attain a moment capacity comparable to PreWEC-A with a different combination of dissipation devices and initial PT force. As a result of the addition of O-connectors and columns the PreWEC models are theoretically over-designed for the given prototype scenario.

The PT tendons used for PreWEC-A, B, and C were 15.2 mm prestressing strand, the same as that used for SRW-A. The targeted initial prestress (f_{pi}) in the wall PT was 696 MPa ($0.45f_y$) for PreWEC-A, B, and C. PreWEC-A, B, and C. PreWEC-A, and B, each used three tendons and PreWEC-FV-C used only two tendons (#1 and #3 for PreWEC-C as labelled in Figure 4.6). PreWEC-A, B, and C consisted of identical precast concrete wall panels to SRW-A with the addition of two PT end columns constructed from concrete filled square steel hollow sections (SHS) with a width, length and thickness of 125×125×5 mm and a height of 2350 mm. The corresponding cross-sections of each of the PreWEC model designs are provided in Figure 4.6.

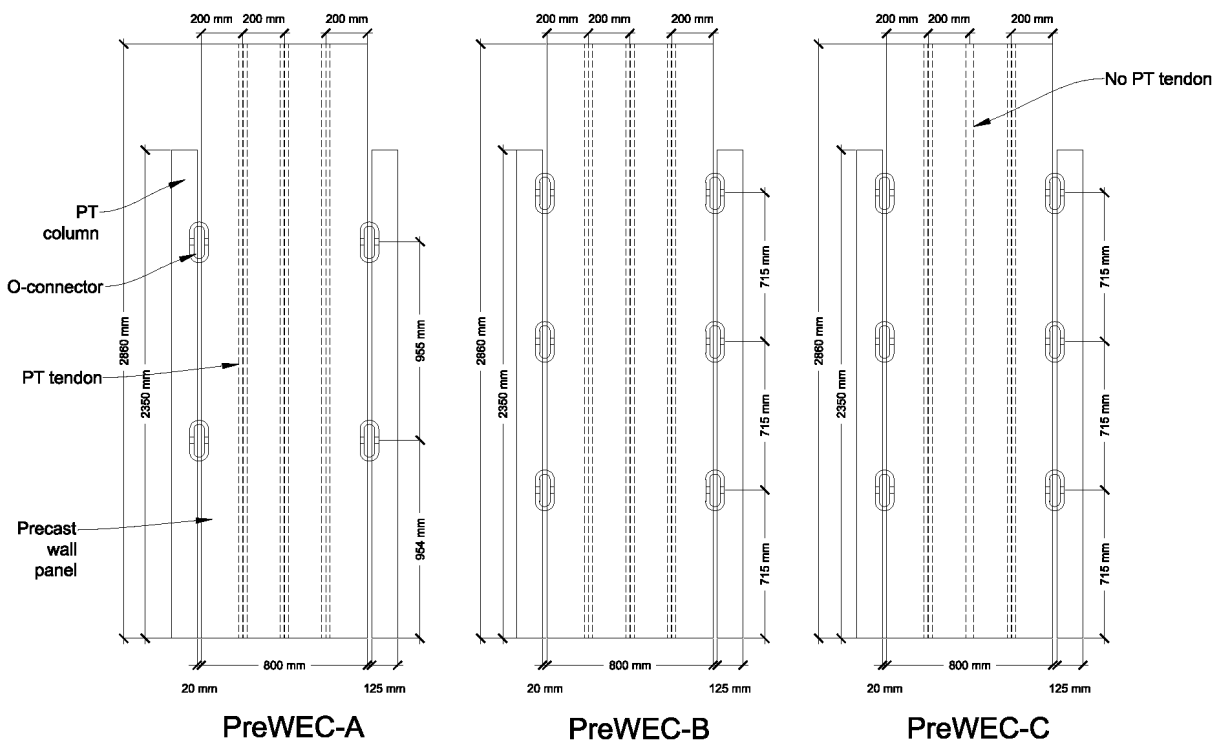


Figure 4.8 – Elevation of PreWEC model walls

The design initial PT force of the columns was 220 kN per column using a 26.5 mm diameter stress-bar with an unbonded length of 3000 mm for all PreWEC tests. The targeted initial PT force in the columns was selected to ensure that the columns did not lift off the foundation using the design procedure published by Aaleti and Sritharan [104]. The O-connectors were placed

across the wall-to-column joint, welded between the SHS and steel plates embedded into the precast concrete wall panel. As presented in Figure 4.8, PreWEC-A, B, and C were designed to have four, six and six O-connectors per joint, respectively, creating three systems with different quantities of hysteretic energy dissipation and varying flexural capacities. The measured initial prestress, concrete compressive strength and other measured properties are provided in the relevant chapters. The elevation detail of the three PreWEC systems are depicted in Figure 4.8 and detailed construction drawings of the three PreWEC panels are provided in Appendix A.

4.7.3 Summary

The wall system testing presented in this thesis used the SRW and PreWEC system designs described in the previous parts of this chapter. To address the static and dynamic experimental testing objectives, three wall testing phases were conducted to attain a refined understanding of the experimental response of SRW and PreWEC systems using loading types of varying complexity that are considered to simulate seismic action. The wall testing begins with pseudo-static cyclic testing which is the simplest and most commonly used loading type and is reported in Chapter 5. The wall testing then progresses to snap back tests as reported in Chapter 6. Snap back testing is able to provide both a monotonic pushover force-displacement response and also the dynamic displacement and acceleration decay of the wall systems. The wall tests culminated with shake table testing which allows measurement of the dynamic response of the wall systems to ground motions.

A summary of the design parameters and types of test performed in this thesis on each design of SRW and PreWEC systems investigated is presented in Table 4.4. The design AFR was 7.5% for SRW-A, PreWEC-A, and B, 2.0% for SRW-B, and 5.0% for PreWEC-C. Pseudo-static cyclic testing was performed on SRW-A, and B, PreWEC-A, and B. Snap back testing was performed on SRW-A, PreWEC-A, B, and C. Lastly, shake table testing was performed on SRW-A, PreWEC-A, and PreWEC-B. A new wall panel was used for each new loading type and test.

Table 4.4 – Test wall summary

Wall Label	Tendon Type	O-connectors per joint	AFR (f_c/f'_c) (%)	Test type
SRW-A	Strand	-	7.5	Cyclic, FV, ST
SRW-B	Bar	-	2.0	Cyclic
PreWEC-A	Strand	4	7.5	Cyclic, FV, ST
PreWEC-B	Strand	6	7.5	Cyclic, FV, ST
PreWEC-C	Strand	6	5.0	FV

4.7.4 Reinforcement material properties

As stated earlier, both 15 mm diameter high strength bars and 15.2 mm diameter strands were used for the wall PT tendons. Three tensile tests per PT tendon were conducted and the measured stress-strain behaviours of the two types of tendon are given in Figure 4.9(a). All steel tensile testing was conducted in accordance with the metallic materials tensile testing standard [99]. The 15 mm stress bar had an average measured yield stress of 997 MPa, ultimate stress of 1156 MPa, modulus of elasticity of 201 GPa, and cross-sectional area of 177 mm². The 15.2 mm strand had an average measured yield stress of 1540 MPa, modulus of elasticity of 199.5 GPa, cross-sectional area of 143 mm² and a measured ultimate stress of 1735 MPa. The ultimate strength was lower than the 1825 MPa stated on the mill test certificate due to premature fracture of strand at the anchorage at strains of approximately 1%, which has been found to be a common problem with existing monostrand anchors [105], and new anchorage systems have been developed to overcome this issue [106]. In this case the strand failure strain was not considered critical as the initial prestress was selected to prevent the strand reaching yield during testing. The concrete filled steel tube had an average concrete compressive strength of 38.2 MPa determined on the day of testing of the pseudo-static cyclic test PreWEC-A wall, this value is therefore a minimum for all subsequent tests as the same undamaged columns were reused for all tests. The wall vertical and horizontal reinforcement consisted of HD10 (10 mm diameter grade 500 MPa deformed bar) and R6 (6 mm diameter grade 300 MPa round bar) bars respectively. The measured stress-strain response for the reinforcing steel samples are presented in Figure 4.9(b), including HD10#1 the vertical reinforcement for SRW-B, HD10#2 the vertical reinforcement for SRW-A, PreWEC-A, B, and C and R6, the horizontal reinforcement for all

test walls. The stress-strain response of the HD10 bars showed no significant yield plateau due to the small diameter bars being manufactured from straightened coil stock.

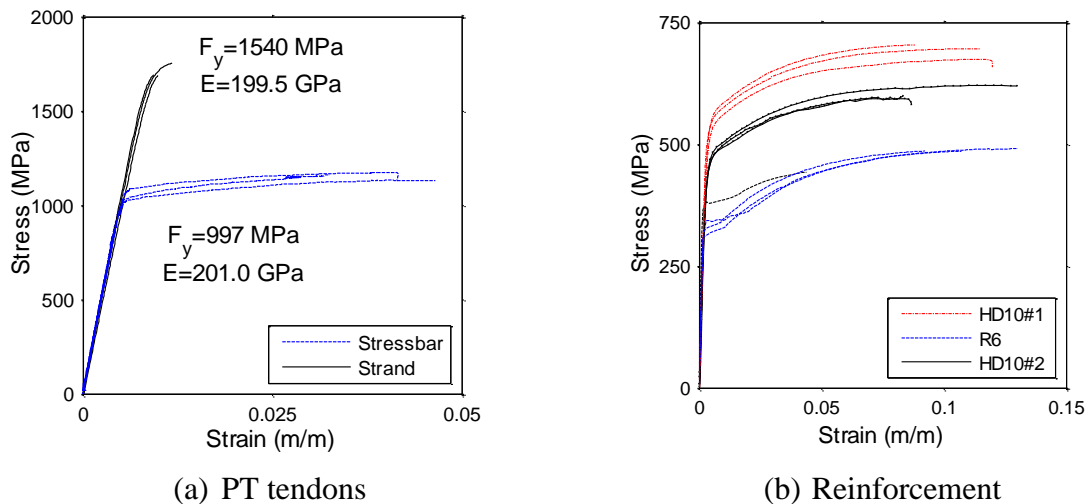


Figure 4.9 – Measured steel material properties for all tests

4.7.5 O-Connector properties

Each wall and corresponding two end columns in each PreWEC system were connected horizontally by 10 mm thick mild steel O-connectors. The O-connectors used in the testing of all PreWEC systems are referred to as O-connector geometry type “O1” as described in Chapter 3. The expected structural responses and construction details of relevant O-connector to the wall systems tested are reiterated here for clarity. The O-connectors were laser cut out of 10 mm thick mild steel plate with the geometry shown in Figure 4.10(a). The stress-strain behaviour of the mild steel plate established from uniaxial tension tests is shown in Figure 4.10(b). A component test was performed on the O-connector using the setup shown in Figure 4.11(a). The test setup consisted of four O-connectors which provided an average connector response. The displacement protocol applied to the O-connectors was identical to the relative vertical displacement of the column to wall measured during the PreWEC-A2 cyclic test reported in Chapter 5. The measured force-displacement response of a single O-connector for the applied relative vertical displacement is shown in Figure 4.11(b). A stable force-displacement response was observed until fracture of the O-connectors initiated during the second cycle to 22 mm vertical displacement, which corresponded to 3% lateral wall drift during the PreWEC-A test.

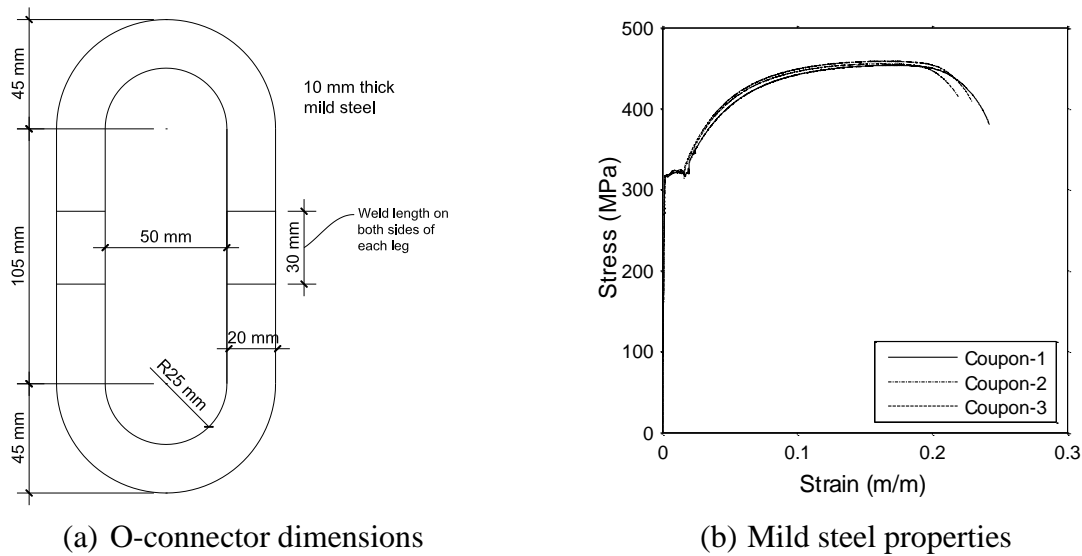


Figure 4.10 – O-connector dimensions and steel properties

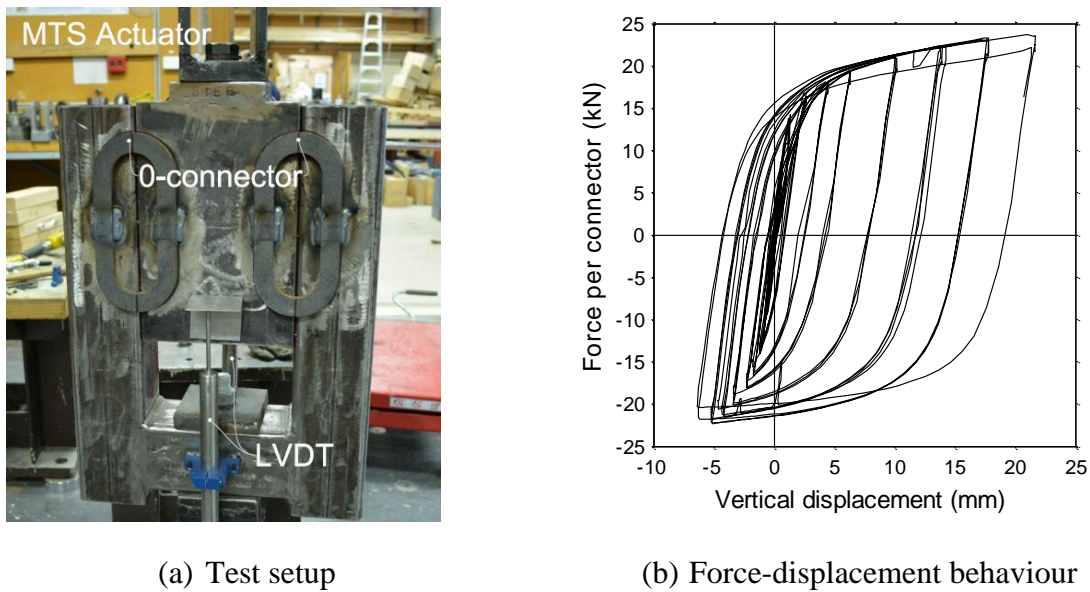


Figure 4.11 – O-connector test setup and measured response

4.8 CHAPTER SUMMARY

This chapter presented the DDBD steps conducted for the prototype wall design used to develop the design the prototype wall. The similitude scaling procedures used to define the model SRW were then described. The design of all test walls reported in this thesis was then discussed. The test walls consisted of two SRW designs referred to as SRW-A and SRW-B, and three PreWEC system designs referred to as PreWEC-A, B, and C. The different designs and parameters for

each wall were described in detail in this chapter. The measured reinforcement material properties are presented to reduce repetition throughout the following test chapters. Lastly, the measured O-connector properties and geometry incorporated in the wall designs was presented.

4.9 REFERENCES

6. Stavridis, A., I. Koutromanos, and P.B. Shing, *Shake-table tests of a three-story reinforced concrete frame with masonry infill walls*. Earthquake Engineering and Structural Dynamics, 2012. **41**(6): p. 1089-1108.
18. New Zealand Standard, *Concrete Structures Standard NZS 3101*. 2006: Wellington, New Zealand.
19. Pampanin, S., D. Marriott, A. Palermo, and New Zealand Concrete Society., *PRESSS design handbook*. 2010, Auckland, N.Z.: NZCS. 1 v. (various pagings).
20. Priestley, M.J.N., G.M. Calvi, and M.J. Kowalsky, *Displacement-based seismic design of structures*. 2007, Pavia: IUSS Press : Fondazione Eucentre. xvii, 721 p.
41. Henry, R.S., *Self-centering precast concrete walls for buildings in regions with low to high seismicity*. 2011, University of Auckland. p. 441.
62. Aaleti, S. and S. Sritharan, *A simplified analysis method for characterizing unbonded post-tensioned precast wall systems*. Engineering Structures, 2009. **31**(12): p. 2966-2975.
99. Standards Association of Australia, *Metallic materials : tensile testing at ambient temperature*. 4th ed. ed. AS 1391-2007. 2007, Sydney, NSW: Sydney, NSW : Standards Australia 2007.
101. Standards New, Z., *Structural design actions : AS/NZS 1170*. 2005, Wellington, N.Z. : Standards New Zealand.
102. Harris, H.G., *Structural modeling and experimental techniques [electronic resource] / Harry G. Harris and Gajanan M. Sabnis*, ed. G.M. Sabnis. 1999: Boca Raton : CRC Press c1999.
103. Mander, J.B., M.J.N. Priestley, and R. Park, *Theoretical stress-strain model for confined concrete*. Journal of structural engineering New York, N.Y., 1988. **114**(8): p. 1804-1826.
104. Sritharan, S., S. Aaleti, and D.J. Thomas, *Seismic analysis and design of precast concrete jointed wall systems*, in *ISU-ERI-Ames Report ERI-07404*. 2007, Department of Civil, Construction and Environmental Engineering, Iowa State University: Ames, IA.
105. Walsh, K.Q. and Y.C. Kurama, *Behavior of unbonded post-tensioning monostrand anchorage systems under monotonic tensile loading*. PCI Journal, 2010. **55**(1): p. 97-117.
106. Abramson, D., *Comprehensive Evaluation of Multistrand Post-Tensioning Anchorage Systems for Seismic Resilient Rocking Wall Structures*. 2013, The University of Minnesota.

Chapter 5

CYCLIC TESTING

To better understand the seismic behaviour of unbonded Post-Tensioned (PT) concrete wall systems a cyclic testing experimental study was conducted and subsequently reported in this chapter. A total of four wall systems were considered, including two single unbonded PT only walls, referred to as Single Rocking Walls (SRW), and two PreWEC systems as described in Chapter 4. The objective of these four wall tests was to systematically investigate the cyclic response of walls with varying amounts of supplemental damping in the form of energy dissipating O-connectors while keeping the initial post-tensioning, wall dimensions and confinement details constant. The wall tests also provided an opportunity to further validate the wall panel design, including the choice of Axial Force Ratio (AFR) and confinement details, and to compare the experimental results of the walls against an existing simplified analysis method used for the design of PT wall systems.

5.1 EXPERIMENTAL PROGRAMME

The experimental programme consisted of pseudo-static cyclic testing of four walls, two SRWs (SRW-A, and SRW-B) and two PreWEC systems (PreWEC-A, and PreWEC-B). The variation of parameters between the test walls was outlined in Chapter 4. SRW-A and SRW-B were varied

to investigate the behaviour of two different SRW systems with different geometry and initial post-tensioning force. PreWEC-A and PreWEC-B specimens were designed based on the addition of end columns and energy dissipating O-connectors to SRW-A. To isolate the influence of the number of O-connectors, all other parameters between SRW-A, PreWEC-A and PreWEC-B systems were kept constant. Two cyclic tests were performed on PreWEC-A which are referred to as PreWEC-A1 and PreWEC-A2 as explained in further detail in section 5.2.

5.1.1 Wall specifications

The design parameters of the four walls tested are provided in Table 5.1. The measured AFR of each test wall, SRW-A, SRW-B, PreWEC-A1, PreWEC-A2, and PreWEC-B were 9.53%, 2.49%, 7.84%, 7.96%, and 8.4% respectively. Where the AFR is defined as the ratio of post-tensioning tendon force plus the wall self-weight and additional weight divided by the axial crushing capacity of the concrete section. Appendix B of the New Zealand Concrete Structures Standard (NZS 3101:2006) [18] outlines special provisions for the design of ductile jointed precast concrete structural systems as described in Chapter 4. The moment contribution ratio (λ) was described in Chapter 4 for its use in determining the EVD of unbonded PT systems with additional energy dissipating devices, however λ is also used as an index that is intended to ensure self-centring. NZS 3101 states that the moment contribution from the restoring forces (PT and axial load) to the energy dissipating elements must be greater than or equal to the overstrength factor for the energy dissipating devices. However, previous research has found that this procedure is inadequate to ensure that self-centring is achieved when realistic PT concrete systems are subjected to earthquake loads [28, 107]. Despite these limitations, λ is still a useful property that represents the relative amount of energy dissipation in PT systems. As presented in Chapter 4, and reiterated in Table 5.1, PreWEC-A and PreWEC-B had four and six O-connectors per joint, respectively. For design lateral drifts between 1-2%, the λ ratio for PreWEC-A and PreWEC-B remained approximately constant at 3.25 and 2.30, respectively, which are greater than the minimum value of 1.15 prescribed in Appendix B of NZS 3101:2006 to ensure re-centering.

Table 5.1 – Wall specifications

Wall Label	Tendon type	f_{pi} (MPa)		$f'_{c,test}$ (MPa)	$f'_{g,test}$ (MPa)	AFR (f_c/f'_c) (%)		O – Con. per joint
		Target	Achieved			Target	Achieved	
SRW-A	Strand	696	686	35.0	36.3	7.5	9.53	-
SRW-B	Bar	239	233	32.0	60.0*	2.0	2.49	-
PreWEC -A (1/2)	Strand	696	694/705	42.7	60.2	7.5	7.84/7.96	4
PreWEC -B	Strand	696	710	40.7	48.4	7.5	8.4	6

*grout strength measured one week prior to wall test

5.1.2 Material properties

In accordance with New Zealand Standards [108] test cylinders and cubes were used to determine the compressive strength of each wall and the grout pad. The measured concrete ($f'_{c,test}$) and grout ($f'_{g,test}$) strengths on the day of testing for each wall are provided in Table 5.1. As stated in Chapter 4, 15.2 mm strand was used for the wall PT tendons in SRW-A, PreWEC-A, and B, and 15 mm high strength bar was used for SRW-B. Three tensile tests were conducted on each type of PT tendon to determine the material properties. The properties of the PT tendons and vertical and horizontal reinforcement have already been reported in Chapter 4 and are consequently not reiterated here.

5.1.3 O-Connector properties

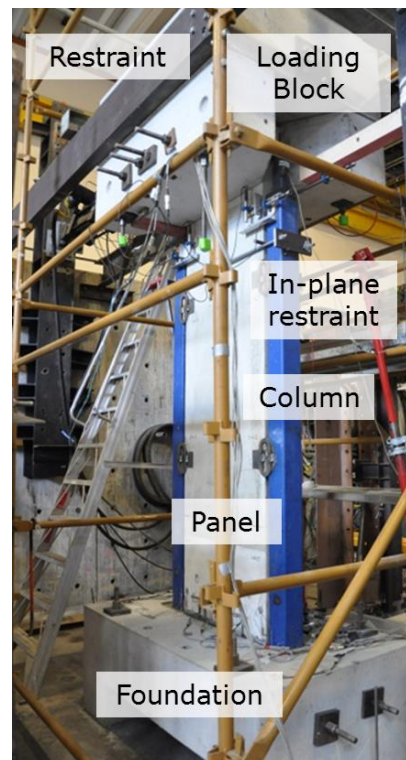
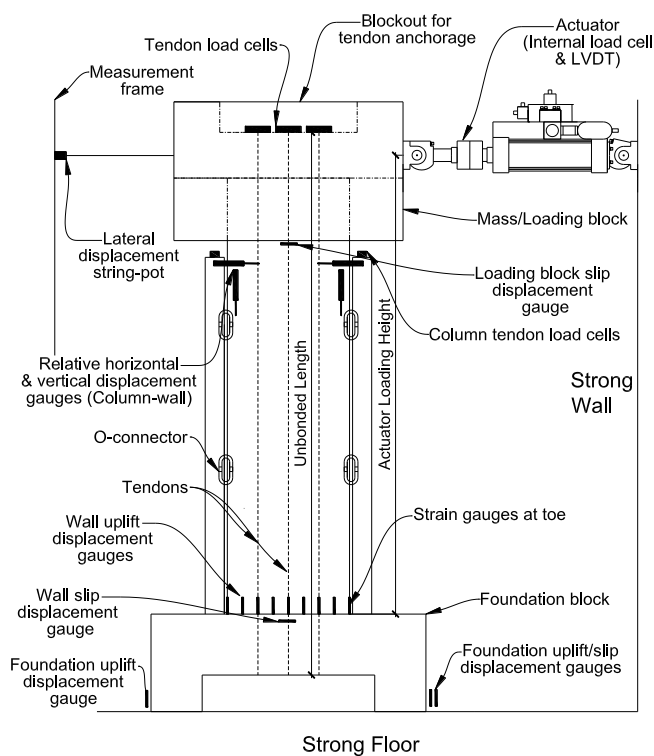
Each wall and corresponding two end columns in each PreWEC system were connected horizontally by 10 mm thick mild steel O-connectors. Expected structural responses and construction details are specified in Chapter 4 and are referred to as connector type “O1” in Chapter 3.

5.1.4 Test setup

A schematic and photo of the typical test setup and instrumentation of a PreWEC test is presented in Figure 5.1. The wall panels were erected onto a foundation block that was post-tensioned to the strong floor. A 40 mm deep by 160 mm wide shallow pocket which ran the length of the wall system was provided in the top of the foundation. The wall was initially supported on small 30 mm high shims and high strength grout was flowed under the wall to fill the pocket and provide an even bearing surface at the wall-to-foundation interface. The wall was embedded

approximately 10 mm into the grout pocket to increase the sliding shear resistance. To limit the concrete compressive strains and spalling of cover concrete in the toe region, SRW-A, PreWEC-A and PreWEC-B had a foam strip across the width of the cover region (15 mm) glued at each wall end, as depicted in Figure 5.2(a). It is important to note that use of the foam effectively shortens the length of the wall by 30 mm to 770 mm.

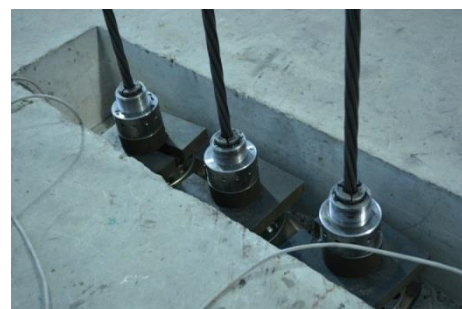
A concrete block was attached and grouted on top of the wall and steel beams were placed adjacent to the block to prevent out-of-plane deformations of the wall. To perform the pseudo-static cyclic testing, a hydraulic actuator was attached through the loading block at a height of 3.11 m for SRW-B and 3 m for SRW-A, PreWEC-A, and PreWEC-B from the wall base. The PT tendons of the walls and columns were anchored between the foundation and top block and remained unbonded over the entire height. The typical unbonded length of wall tendons for SRW-A, PreWEC-A and PreWEC-B was 3600 mm and 3900 mm for SRW-B. The typical strand anchorage is shown in Figure 5.2(b). A specially designed and manufactured threaded barrel with round nut was used to finely adjust the initial tendon stress and de-stress without having to release the wedges from the barrel. For SRW-A, PreWEC-A and PreWEC-B the top concrete block weighed 31.35 kN and for SRW-B the top concrete block weighed 20.11 kN. The top block provided additional mass for dynamic tests that were performed using the same test setup, that are discussed in Chapter 6 and Chapter 7. Due to the slightly different setup between SRW-B and the other test walls SRW-B had a centre of mass, including wall mass, of 2841 mm from the base of the wall while SRW-A, PreWEC-A and PreWEC-B had a centre of mass of 2657 mm from the base of the wall. Further details of the test relevant to the dynamic tests are described in the relevant chapters. Specific detail of the two test setups is provided in Appendix A.



(a) Test setup and instrumentation schematic

(b) Photo of test setup - PreWEC-A

Figure 5.1 – Test setup and instrumentation schematic for PreWEC tests



a) Wall placement (SRW-A)

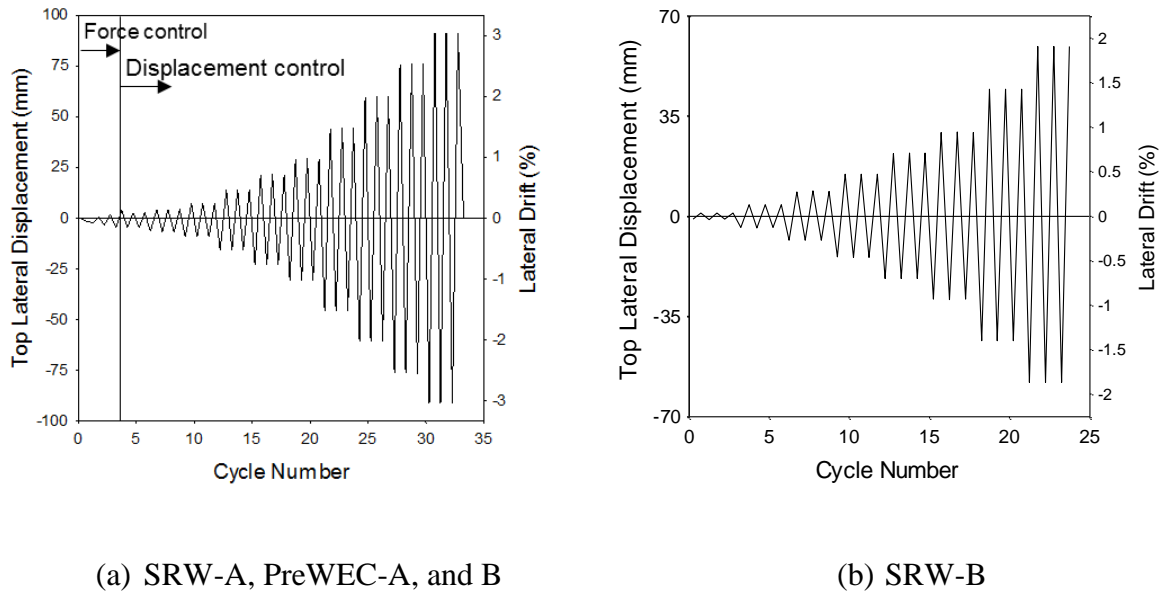
b) PT anchorage setup

Figure 5.2 – Wall set up details

5.1.5 Load protocol

The loading protocol for the test was developed in accordance with ACI guidelines for the acceptance criteria for unbonded PT concrete walls, ACI ITG-5.1 [109]. For SRW-A, PreWEC-A and PreWEC-B, three force based cycles to a maximum of 0.6 times the decompression

moment were applied first followed by displacement controlled cycles up to a maximum of 3% lateral drift, as shown in Figure 5.3(a). For SRW-B, a maximum lateral drift of 2% was applied to prevent yielding of the tendons, as shown in Figure 5.3(b).



(a) SRW-A, PreWEC-A, and B

(b) SRW-B

Figure 5.3 – Load protocol

5.1.6 Instrumentation

The walls were extensively instrumented as depicted in Figure 5.1(a). Displacement gauges were placed at the base of the wall to measure uplift. Additional displacement gauges were placed at the foundation-floor and wall-loading block interface to monitor slip and unintended uplift of the foundation. A string-pot was used to measure the top lateral displacement at the actuator height. Load cells were used to measure the lateral load in the actuator as well as the wall and column PT tendon forces. For the PreWEC tests, LVDTs (Linear Variable Differential Transformer) were used to measure the relative vertical and horizontal displacements between the wall and each end column.

Strain gauges were placed both inside and on the surface of the concrete at the wall toe to measure the strain demand. Embedded concrete strain gauges were cast in the confined concrete region of each wall toe for each test. The two embedded gauges for SRW-B had a gauge length of 30 mm and were placed 10 mm in from the wall compression edge, 65 mm up from the wall base and 40 mm from each side. For SRW-A, PreWEC-A1, PreWEC-A2 and PreWEC-B, embedded

strain gauges with a 60 mm gauge length were used. For SRW-A the two embedded gauges were placed 10 mm in from the wall compression edge, 25 mm up from the wall base and 42 mm in from each side at each toe. For PreWEC-A and PreWEC-B, the two embedded gauges in each wall toe were placed 30 mm in from the wall compression edge, 35 mm up from the wall base and 45 mm in from each side at each toe. Surface mounted strain gauges were also placed on the end of each wall panel for each test. The SRW-B surface strain gauges were 30 mm long and placed 60 mm up from the wall base and 43 mm in from each side. The surface strain gauges were 60 mm long for SRW-A, PreWEC-A, and PreWEC-B and were placed 60 mm up from the wall base and 35 mm in from each side. All measurements reported are to the centre of the strain gauge.

5.2 TEST OBSERVATIONS

The four test walls all performed well with uplift occurring at the wall base when compared to the distributed cracking expected from traditional reinforced concrete walls. The typical behaviour of the test walls is shown in Figure 5.4(a) for PreWEC-B at 3% lateral drift. No flexural cracks were observed in the wall panels and no significant crushing occurred in the compression toe for any of the tests. Only a minor amount of spalling was observed in the wall toes at drifts greater than 2% and no bending of the steel angle armouring frame used for confinement was observed. Additionally, no slip was observed or measured between the wall and foundation during any of the tests.

Although the damage to the wall toes was isolated to a small area and had an insignificant effect on the overall behaviour of the walls, a close up of the toe damage at the end of each test is shown in Figure 5.5. There is only a small increase in spalling between SRW-B and SRW-A despite SRW-A having almost four times the AFR. The foam strip used in the corner of walls SRW-A, PreWEC-A and PreWEC-B was successful in limiting the spalling of the wall toe, with similar damage observed for all four test walls despite SRW-A, PreWEC-A and PreWEC-B walls having much higher AFR's than SRW-B.

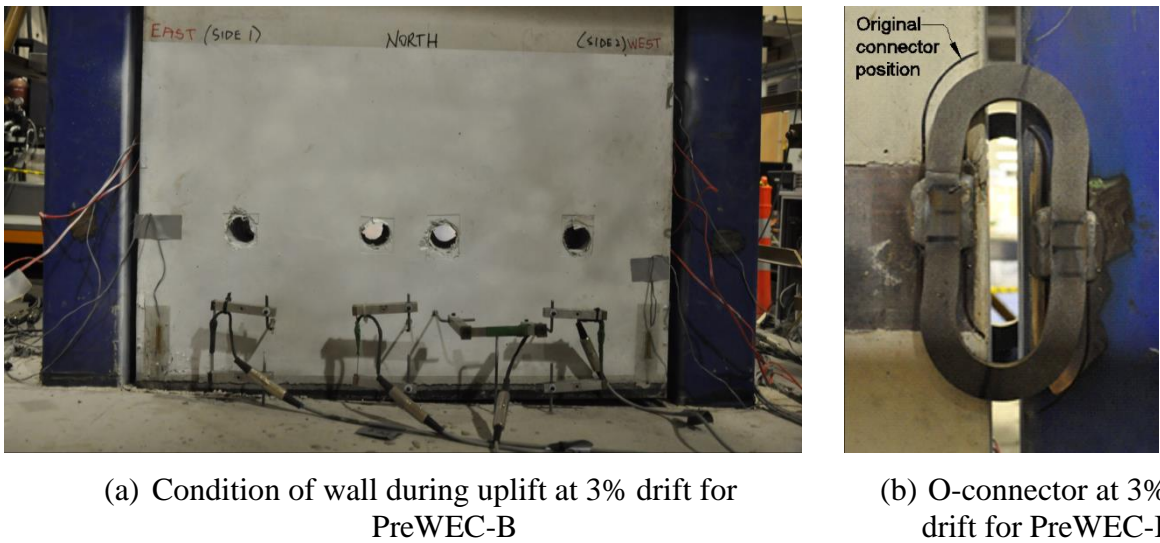


Figure 5.4 – Observed wall behaviour

The wall and end columns rocked independently during the PreWEC tests and imposed a vertical deformation on the O-connectors at the wall-to-column joint. The deformed shape of one of the O-connectors in PreWEC-B at 3% lateral drift is shown in Figure 5.4(b). As expected, the O-connector behaviour was dominated by flexural yielding of legs up until failure which occurred during cycles to 3% lateral drift. The displacement capacity and failure mode of the O-connectors was similar to that observed during the component tests discussed earlier in Chapter 3. Despite failure of the connectors occurring at 3% lateral drift for most PreWEC tests, it should be noted that the O-connectors can be designed to achieve greater displacement capacity depending on their geometry and steel grade as demonstrated in Chapter 3 and previous research [15, 57].

Two cyclic tests were performed on the PreWEC-A wall. The first test (PreWEC-A1) relied solely on the O-connectors to connect the wall to the end columns. During this test it was observed that the columns were pushed and pulled with the wall by the O-connectors causing horizontal compression and tension to be imposed on the O-connectors. As a result larger than expected horizontal displacements were imposed on the O-connectors resulting in premature failure during the 2.5% lateral drift cycles. Following the first test, the fractured O-connectors were removed and new connectors were welded onto the PreWEC-A wall. An in-plane lateral restraint as shown in Figure 5.1(b) was added during the second test (PreWEC-A2) to enable the end columns to laterally displace with the wall without relying on the O-connectors. Use of the restraint for PreWEC-A2 resulted in the O-connectors achieving their design displacement, with

failure occurring during the 3% lateral drift cycles as expected from the component test. The end column restraints were also used successfully during the PreWEC-B test, with the columns displacing laterally with the wall and O-connector failure again occurring during cycles to 3% lateral drift.

Struts or restraints were also attached between the wall and end columns during the PreWEC test reported by Aaleti and Sritharan (A&S) [59], but were later found to not be required during the test. In contrast the restraint was required during the tests reported herein due to the relative strengths of the wall, end columns, and O-connectors. A horizontal force of 0.86 kN per O-connector was required to pull the end column to 2% drift during the PreWEC-A test compared to a horizontal force of 0.24 kN per O-connector for the A&S PreWEC test. Due to the different connector size, these horizontal forces equated to 3.6% and 0.5% of the O-connector vertical force capacity for the PreWEC-A and A&S PreWEC tests respectively. These calculations demonstrate that a seven time's greater demand was placed on each O-connector during the PreWEC-A test compared to the A&S PreWEC test. Therefore the requirement of the restraints is a function of the relative strengths of the end column and connectors, and should be considered during the design of the O-connectors. It should be noted that in practice the floor diaphragm would serve the function of the struts.

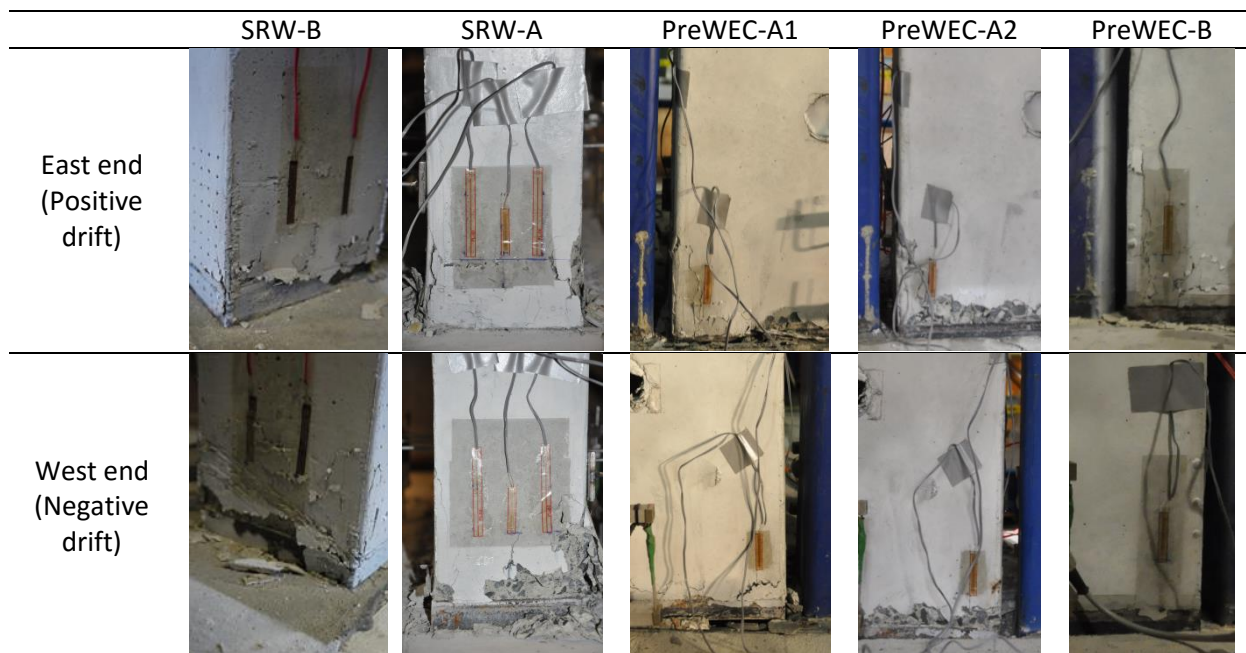


Figure 5.5 – Observations of wall toe damage for all tests

5.3 RESULTS AND DISCUSSION

5.3.1 Force displacement response

The measured lateral force-displacement response for each of the four test walls are shown in Figure 5.6. The overall behaviour was good with no significant strength degradation until the O-connectors started fracturing during the PreWEC tests, and only minor stiffness degradation. A simplified analysis approach developed by Aaleti and Sritharan (A&S) [62] was used to predict the behaviour of the four test walls, and is compared against the measured experimental results in Figure 5.6. The simplified analysis method accurately captured the envelope of the global behaviour of both the SRW and PreWEC systems.

SRW-B exhibited an imperfect bilinear elastic response with a small amount of hysteresis up until the test finished at 2% lateral drift. SRW-A also exhibited an imperfect bilinear response up until 2% lateral drift at which stage the unloading path altered with increased hysteresis introduced into the system. The change in unloading path could be due to PT loss within the system, debris becoming trapped underneath the wall, or minor inelastic concrete strains in the wall toe.

Both PreWEC-A1 and A2 tests resulted in a similar global force-displacement response with increased hysteresis area when compared to the two SRW tests. Less stiffness softening was observed for PreWEC-A2 when compared to PreWEC-A1 due to the small amount of inelastic concrete strains that occurred in the wall toe during PreWEC-A1. PreWEC-A2 achieved a more desirable force-displacement response in comparison to PreWEC-A1 as the O-connectors fractured during the 3% lateral drift cycles instead of 2.5% lateral drift cycles due to the addition of the end column restraints. As shown in Figure 5.6(d), PreWEC-B exhibited increased hysteresis area when compared to the SRW tests and the PreWEC-A system due to a 50% increase in the number of connectors. Fracture of the connectors initiated at 3% lateral drift, similar to that observed during the PreWEC-A2 test. The increase in lateral strength and hysteresis from SRW-A to PreWEC-A to PreWEC-B was due to the strength provided by the increasing number of O-connectors, and was accurately predicted by the Aaleti and Sritharan simplified analysis method.

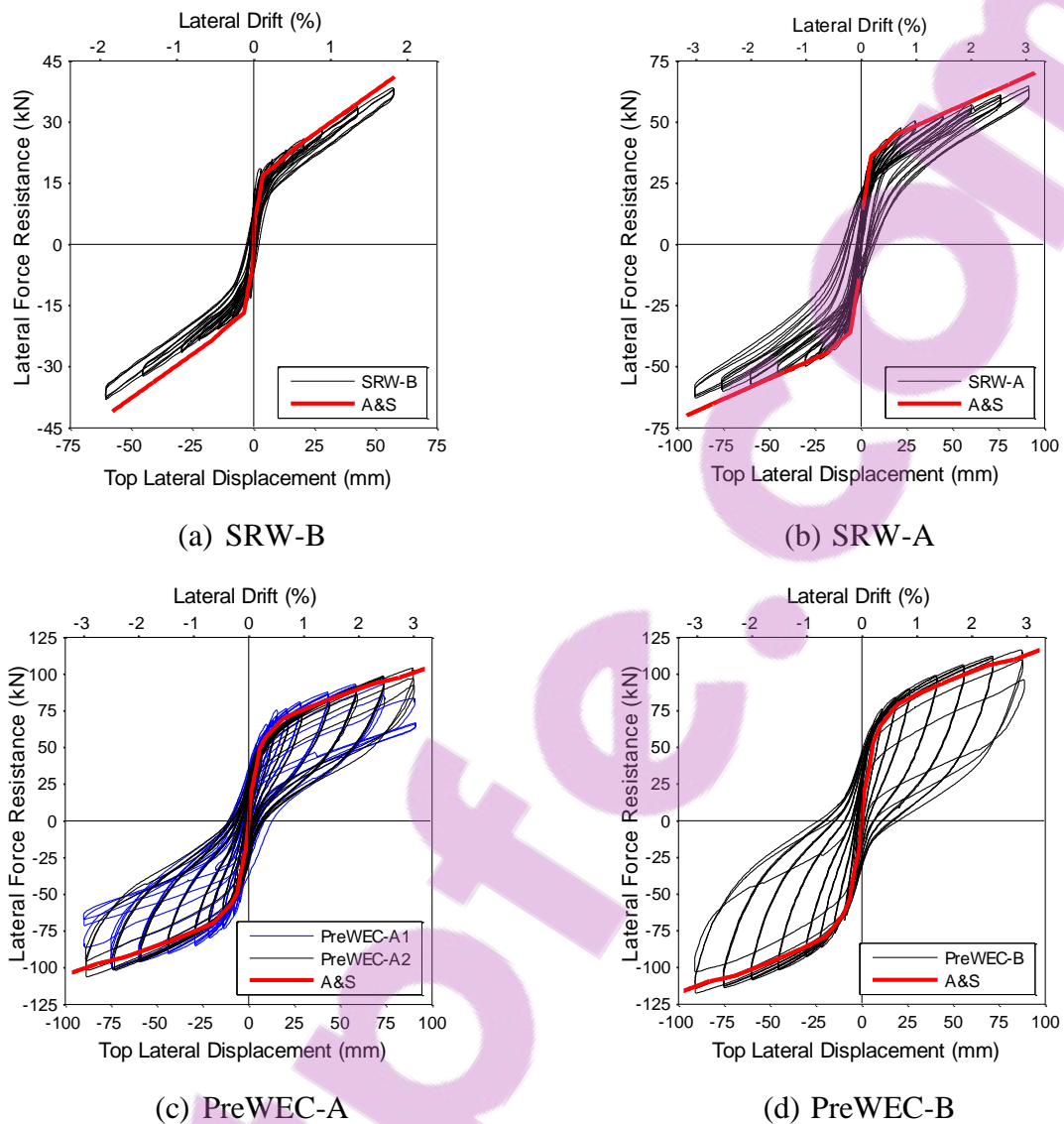


Figure 5.6 – Measured lateral force-displacement responses for each test

5.3.2 Initial stiffness

The stiffness of structural walls is important when calculating the fundamental period of a structure. The initial stiffness of the four test walls was determined from the force based cycles applied at the start of the loading protocol. A best fit linear trend was used to find the slope (initial stiffness) of the force displacement loading curve for the largest cycle below decompression of each wall system. As presented in Table 5.2, the measured initial stiffness' of SRW-B, SRW-A, PreWEC-A1, PreWEC-A2 and PreWEC-B were 16.36 kN/mm, 8.89 kN/mm, 12.90 kN/mm, 6.34 kN/mm, and 12.19 kN/mm, respectively. During the force based cycles no uplift occurred at the wall base which implies that the expected lateral stiffness should

theoretically be calculated based on the gross section moment of inertia (I_g). A prediction of the initial stiffness of each wall is also presented in Table 5.2, and was calculated assuming a lateral stiffness (K) equal to the sum of $3EI_g/h^3$ for each component (walls and end columns), where E is the modulus of elasticity, I_g the moment of inertia and h the height of the applied load [110]. The calculation assumed a concrete modulus of elasticity (E_c) equal to $4700\sqrt{f'_c}$, where f'_c is the characteristic compressive strength of concrete in MPa. For the calculations $f'_{c,test}$ was used as f'_c to attain realistic results. The height used for the column stiffness calculation was the height of load application. The final row in Table 5.2 is the Effective Stiffness Modifier (ESM) which is the measured initial stiffness divided by the predicted initial stiffness. For all walls use of the gross section properties significantly overestimates the initial stiffness. Despite the two SRW specimens having different section properties they had similar effective stiffness modifier ratios of 0.62 and 0.61 and the two undamaged PreWEC specimens PreWEC-A1 and PreWEC-B had similar effective stiffness modifier ratios of 0.79 and 0.77. The ESM ratio of PreWEC-A2 is not comparable as the wall had already been subjected to the PreWEC-A1 test. A close up of the force based cycles used to determine the measured initial stiffness is given in Appendix C.

Table 5.2 – Initial stiffness of each test specimen

	SRW- B	SRW- A	PreWEC- A1	PreWEC- A2	PreWEC- B
Measured initial stiffness ($K_{i(m)}$) kN/mm	15.69	8.89	12.90	6.34	12.19
Predicted initial stiffness ($K_{i(p)}$) kN/mm	25.52	14.69	16.42	16.42	15.84
Effective stiffness modifier ($K_{i(m)}/K_{i(p)}$)	0.62	0.61	0.79	0.39	0.77

5.3.3 Equivalent viscous damping

Equivalent viscous damping (EVD) is used as a measure of performance as it is essential to displacement based design procedures commonly used for unbonded PT structures. The EVD calculated from the force-displacement hysteresis response for each cycle of the five wall tests is shown in Figure 5.7(a). The EVD (ξ_{area}) was calculated using Equation (5-1) as presented in Chopra [110]. Both the SRW specimens had relatively low EVD in comparison to the PreWEC systems due to the lack of energy dissipating O-connectors. The two SRW specimens had a similar amount of EVD up until 1% lateral drift, after which point SRW-A had a slight increase

in EVD due to higher compressive strains. SRW-A is expected to have higher compressive strains due to the higher AFR of 9.53% compared to 2.49% for SRW-B. The EVD for the two SRW remained between 3-5% throughout the tests. The difference in EVD between PreWEC-A1 and A2 was attributed to the energy dissipation from irrecoverable inelastic strains that had already been imposed on the wall specimen during the A1 test. The EVD at 2% lateral drift was 4.7%, 15.8%, 14.9% and 17.9% for SRW-A, PreWEC-A1, PreWEC-A2 and PreWEC-B, respectively. The EVD of SRW-A represents the inherent energy dissipation of the PT wall without connectors. Therefore it is reasonable to assume that the EVD difference between SRW-A and the PreWEC systems is equal to the EVD contribution from the O-connectors. For the three PreWEC tests, the EVD per O-connector ranged from 1.1-1.4% at 2% drift.

$$\xi_{area} = \frac{A_h}{2\pi F_m \Delta_m} = \frac{1}{4\pi} \frac{E_D}{E_{S0}} \quad (5-1)$$

5.3.4 Residual drifts

The residual drift is a critical aspect of seismic resilient design and it is important to determine if the self-centring objective has been achieved. For the pseudo-static cyclic tests the residual drift was defined as the displacement at zero lateral force after unloading from the first peak displacement of each cycle. These calculated residual drifts are plotted for each of the wall tests in Figure 5.7(b). As expected from the hysteresis response, the residual drifts increased as the lateral drift or supplementary damping increased. From the results for the two SRW systems, it is clear that a higher AFR introduced higher residual drifts due to increased compression strains in the wall toes. For the PreWEC walls the residual drift increased with an increasing number of O-connectors as the hysteresis loops became fatter. However, it was interesting that the residual drift for the PreWEC walls decreased or recovered from 2.5% to 3% drift as the connectors started to fracture. It is important to note that the calculated residual drifts from the pseudo-static cyclic test results do not account for dynamic response and therefore do not necessarily represent the residual drifts expected following an earthquake due to the “shake-down” effect, such as that reported by Henry et al. [28].

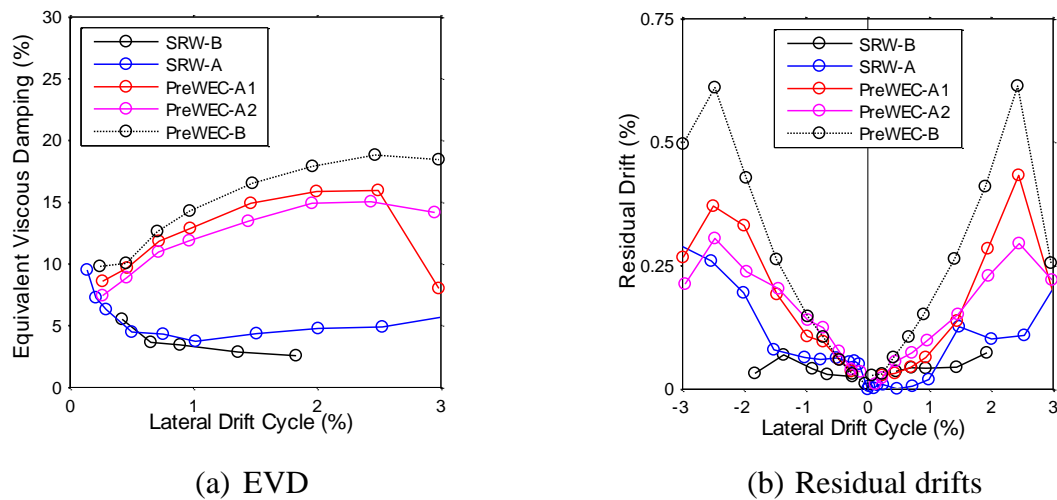


Figure 5.7 – Calculated EVD and residual drift for each test

5.3.5 Connector behaviour

The relative vertical displacement measured between each end column and the wall at the location of the top O-connectors for the three PreWEC cyclic tests is presented in Figure 5.8(a). The relative vertical displacement between the wall and end columns reached up to 23 mm at the wall-column joint with wall uplift and up to 7 mm at the wall-column joint with wall toe compression. By comparing the measured connector displacements from the PreWEC tests to that of the component test shown previously in Figure 4.11(b), it is proven that the O-connectors yield in both loading directions in the PreWEC system. The relative vertical displacement measured between each end column and the wall was almost identical for all of the PreWEC tests, which implies similar panel behaviour regardless of O-connector number.

Figure 5.8(b) presents the change in relative horizontal displacement between the wall and east column with lateral drift. Only the east column is presented due to the symmetrical behaviour observed. PreWEC-A1 achieved the highest relative horizontal displacement, up to 6 mm, due to the lack of a restraint between the wall and columns. PreWEC-A2 and PreWEC-B indicate significantly lower relative horizontal displacements due to the addition of the restraint between the wall and columns that limited the horizontal force resisted by the O-connectors. The higher relative horizontal displacement caused the early failure of the O-connectors during the PreWEC-A1 test due to the increased strain demand. The effect of the increased strain demand was successfully eliminated for the PreWEC-A2 and PreWEC-B tests through the addition of the restraints. Evidence of this is shown by the increased performance of the O-connectors failing

during the 3% lateral drift cycle for both PreWEC-A2 and PreWEC-B, and also the purely vertical displacement component test presented earlier in Figure 4.11(b) in Chapter 4, that showed failure during the same lateral drift cycle as the PreWEC-A2 wall test.

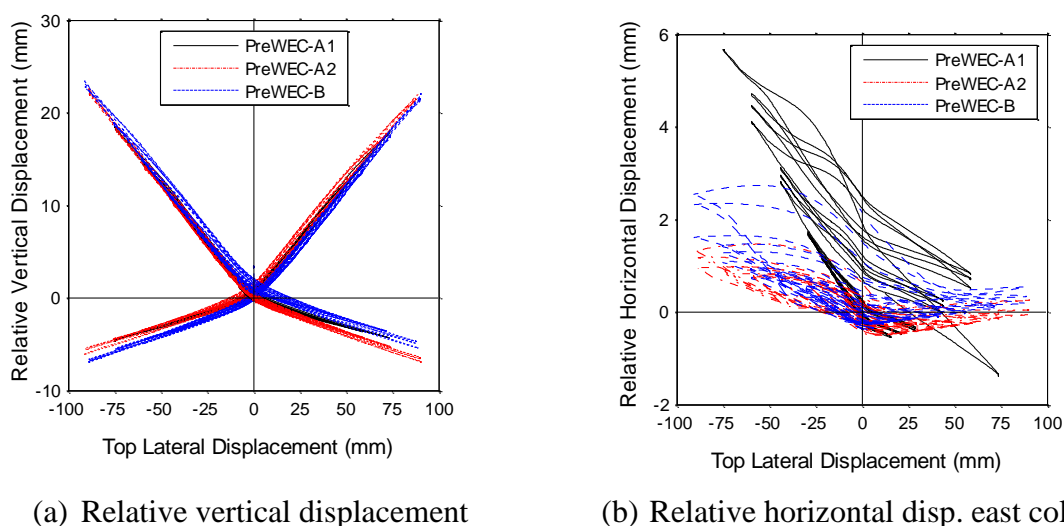


Figure 5.8 – Measured relative vertical and horizontal deformation of the O-connectors

5.3.6 PT force

The measured change in total wall PT force with lateral drift for the five tests are shown in Figure 5.9, alongside the predicted PT force from the Aaleti and Sritharan (A&S) simplified analysis method. As expected, gap opening at the wall base caused the PT force to increase with increasing lateral drift. The overall behaviour of the tendons for all tests was essentially elastic as the PT tendon type and initial prestress were specifically designed to avoid any tendon yielding up to 3% lateral drift for SRW-A, PreWEC-A and PreWEC-B and up to 2% lateral drift for SRW-B. The prestress losses were minimised by pre-seating the tendon anchorage up to a force equivalent of $0.68f_y$. Despite pre-seating the tendons and avoiding tendon yielding, prestress losses occurred consistently throughout the tests at the peak of each first drift cycle. The total prestress loss measured for SRW-B, SRW-A, PreWEC-A1, PreWEC-A2, and PreWEC-B was 16.6%, 7.3%, 16.2%, 6.6%, and 14.4%, respectively. As a result of these losses, the predicted tendon force was overestimated by the simplified analytical method at high lateral drifts. The losses were attributed to further wedge draw in at the anchor as the tendon force increased and wall shortening as the compression toes were subjected to inelastic strains. As depicted in Figure 5.9(c), PreWEC-A2 underwent less prestress loss compared to PreWEC-A1

as the tendon anchorages had technically been pre-seated further due to the PreWEC-A1 test. PreWEC-A1 and PreWEC-B experienced similar prestress loss throughout each test, this shows a degree of predictability with the amount of prestress loss.

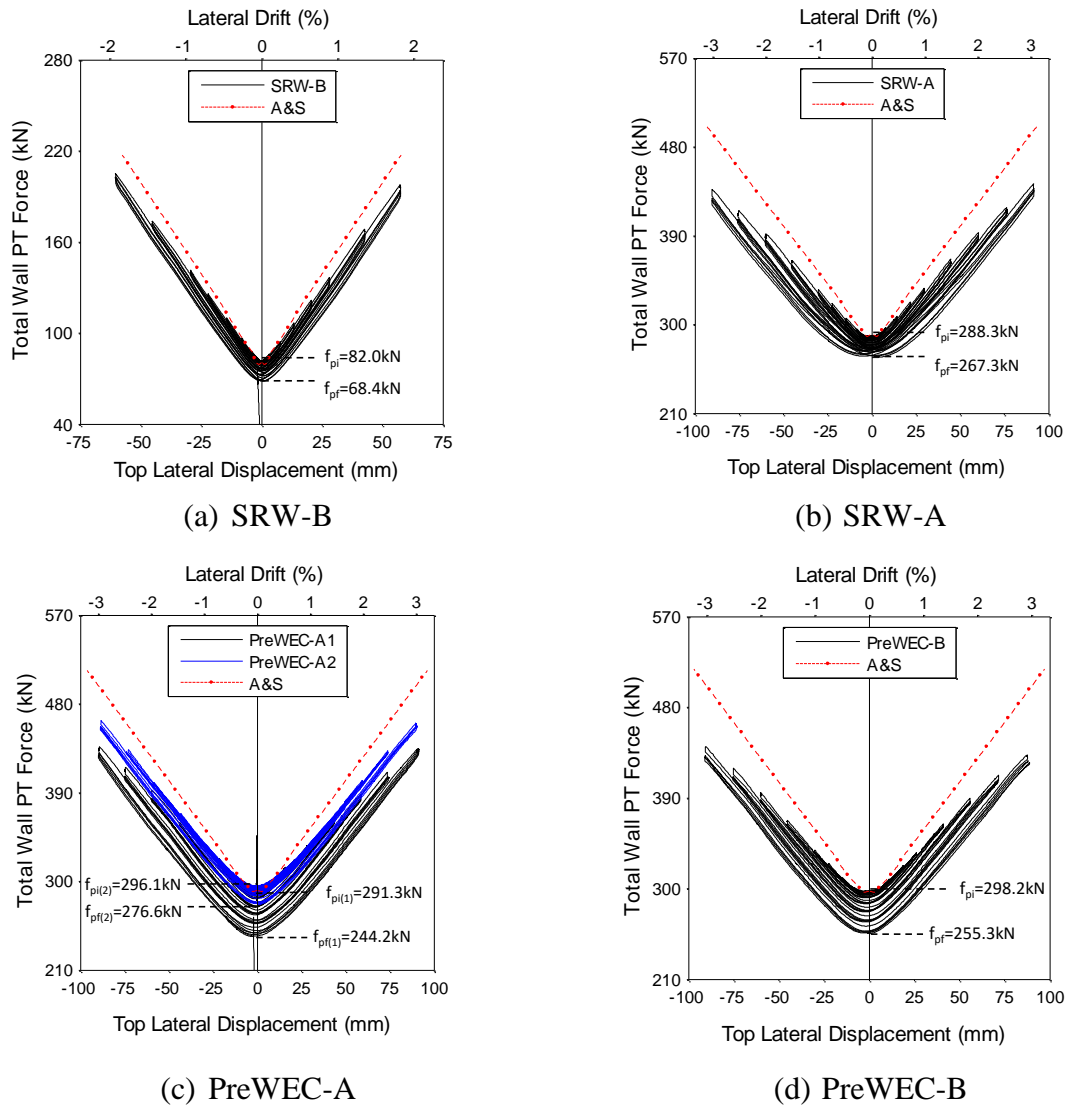


Figure 5.9 – Measured wall PT force

If the entire loss was assumed to be due to wedge draw in at the anchor the quantity of draw in based on the total prestress loss and unbonded tendon length would be equal to 2.0 mm for PreWEC-A1 and 1.8 mm for PreWEC-B. However, it is important to note that the wedge draw occurs as a fixed displacement irrespective of tendon length. Therefore, the PT losses observed in the four reported tests are likely to have been amplified due to the reduced wall scale and short tendon length. Significantly less PT loss would be expected in a full-scale PT wall.

5.3.7 Neutral axis depth

As previously described in section 5.2, all of the test walls exhibited uplift at the wall base due to rocking. An important parameter to understanding the behaviour of the systems is the length of wall in contact with the foundation known as the neutral axis (NA) depth. The NA depth of each wall was calculated by fitting a linear function through the measured uplift of the displacement gauges at the wall base. The rotation at the wall base was first calculated and then the NA depth determined from rotation, uplift and the known wall length. The width of foam strip at each wall end was 15 mm i.e. 30 mm total was taken into account when determining the NA depth for SRW-A, PreWEC-A and PreWEC-B by using an effective wall length of 770 mm.

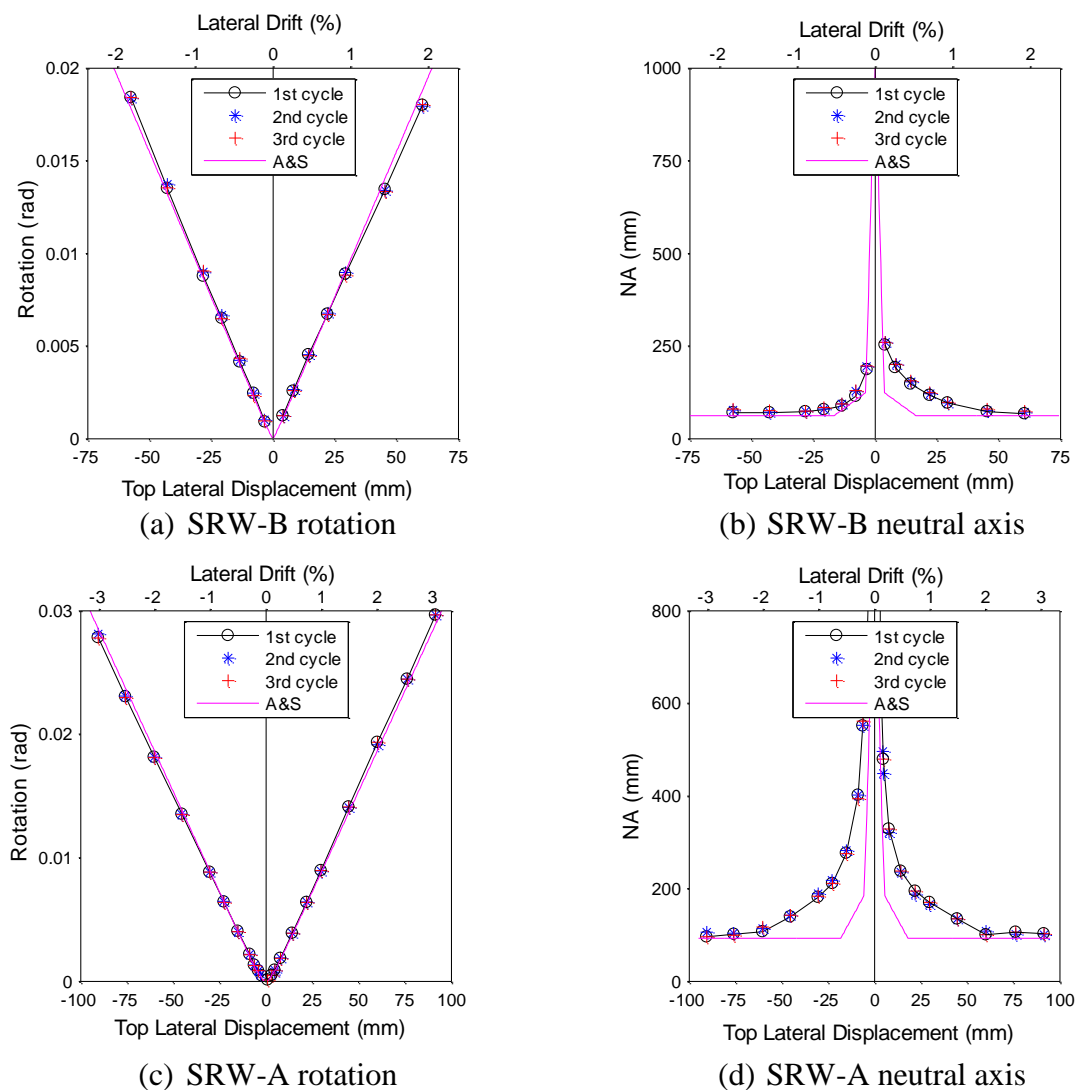


Figure 5.10 – Change in NA depth and rotation with top lateral drift for SRW

Both the measured rotation and NA depth at the peak of each lateral drift cycle are presented for the SRW tests in Figure 5.10 and for the PreWEC systems in Figure 5.11. The measured NA was stable between the three cycles with no NA migration for all tests. The stable NA between cycles demonstrates that no significant crushing occurred and that the walls were well designed.

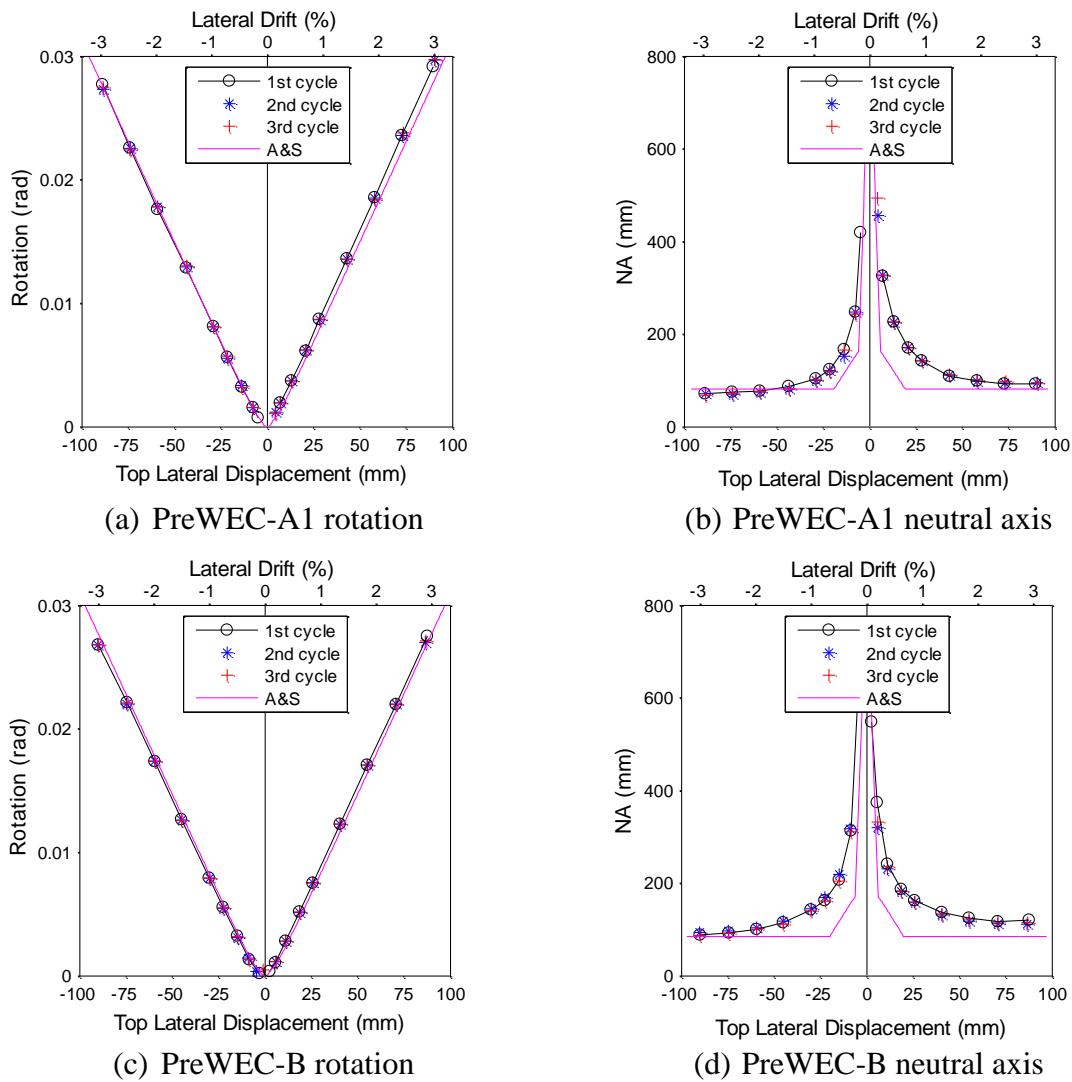


Figure 5.11 – Change in NA depth and rotation with top lateral drift for PreWEC

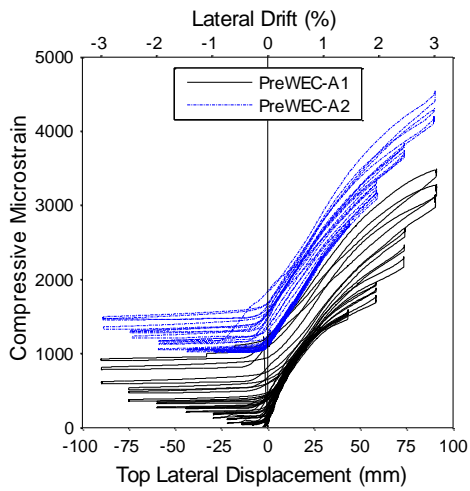
As shown by Figure 5.10(a) and (c) and Figure 5.11(a), and (c) the rotation was well predicted by the simplified analytical method proposed by Aaleti and Sritharan (A&S) [62] for all tests. The experimental NA at larger lateral drifts correlated well with analytical predictions, but was typically under-predicted for lateral drifts less than 2%, as demonstrated by Figure 5.10(b) and (d) and Figure 5.11(b), and (d). The average measured NA depths at 3% lateral drift for SRW-A, PreWEC-A and PreWEC-B were 99.3, 82.78, and 103.6 mm, respectively. The relatively

similar NA depths demonstrate that the wall behaviour appeared to be independent of the number of O-connectors when considering the differences expected due to the concrete strengths, grout strengths and PT force.

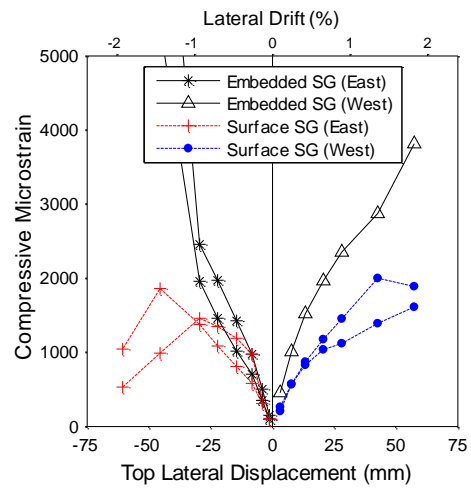
5.3.8 Concrete strains

The compressive strains measured using both the surface and embedded strain gauges for all wall tests are plotted in Figure 5.12. An example of the full cyclic response of the compressive strain versus lateral drift of an embedded strain gauge in the east toe for PreWEC-A is presented in Figure 5.12(a). Since the strain gauge is located at the east toe there is an increase in compressive strain with increasing positive lateral displacement. The observed constant strain in the negative displacement direction represents the irrecoverable residual strain. The PreWEC-A2 test wall had already undergone the A1 test and therefore initially measured the total residual strain at the completion of the PreWEC-A1 test.

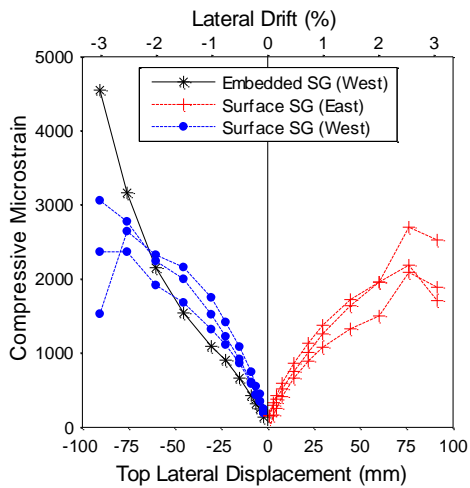
To assess the maximum strain demand clearly, the envelope peak strains in the compressive toe for the first cycle to each drift level are plotted in Figure 5.12(b-f) for all of the working strain gauges. For SRW-B, strains in excess of 0.004 were measured by the embedded strain gauges at 2% lateral drift in both directions. This measured compressive strain was reasonably consistent with the maximum compressive strain of 0.0064 at 2% lateral drift calculated by the simplified analysis method and used for the wall design. For SRW-A, PreWEC-A1, PreWEC-A2 and PreWEC-B which used the foam strips at the toes, the maximum concrete compressive strain at 3% lateral drift calculated using the simplified analysis method were 0.0147, 0.0128, 0.0129, and 0.0133, respectively. The measured compressive strains for these walls were significantly lower than this analytical prediction ranging from 0.0025 to 0.005. The measured strains were generally below concrete crushing strain of 0.003 which correlated well the minimal damage observed in the wall toe and proved that the walls were well designed and that the foam strip was successful in minimising compressive strains and spalling of the cover concrete in the wall toe.



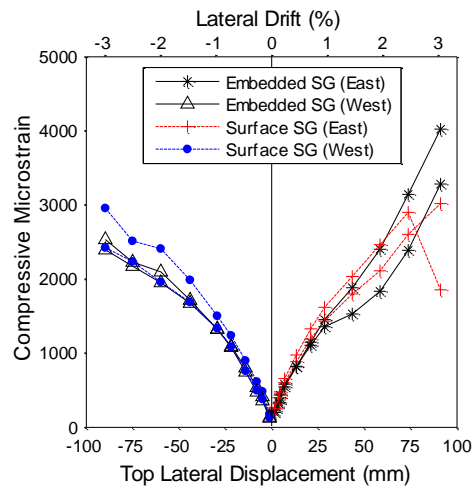
(a) PreWEC-A Embedded strain gauge



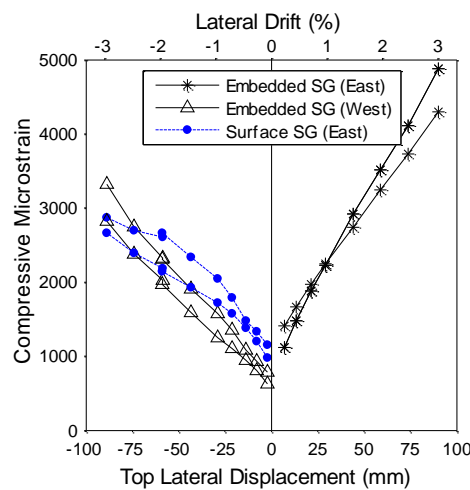
(b) SRW-B



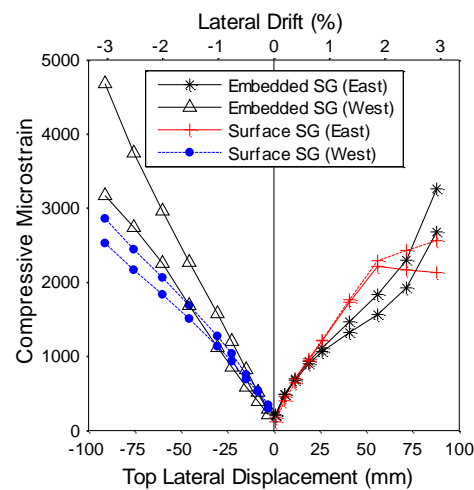
(c) SRW-A



(d) PreWEC-A1



(e) PreWEC-A2



(f) PreWEC-B

Figure 5.12 – Measured strain versus lateral drift

A comparison of the average measured surface strain at each wall end for the SRW-A, PreWEC-A1, PreWEC-A2 and PreWEC-B tests is shown in Figure 5.13. These walls provided a valid comparison of strains as the same dimensions were used and foam strips were used for all four walls. The average measured surface strain for walls SRW-A, PreWEC-A1 and PreWEC-B were similar in amplitude and followed a consistent trend with increasing lateral drift. Thus the compressive strain in the wall toe strains were independent of whether the system was SRW-A or PreWEC-A or B, further confirming that the wall axial force was independent of the number of O-connectors.

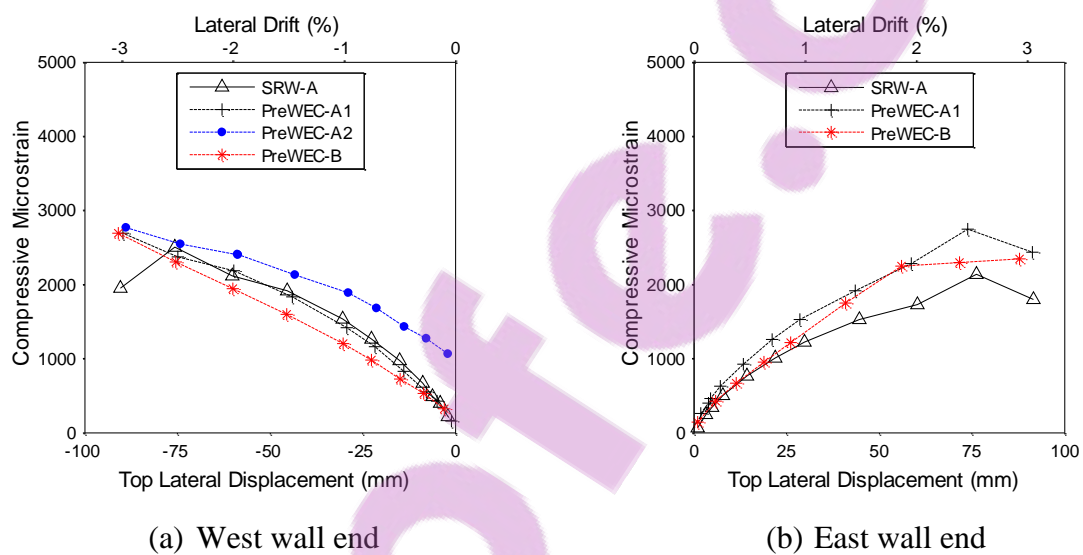


Figure 5.13 – Average measured strain versus lateral drift

5.4 INFLUENCE OF O-CONNECTORS

The PreWEC system was designed so that the O-connectors would yield in both directions of loading as both uplift and compression occurred at the ends of the wall. By undergoing a full cyclic hysteresis the O-connectors can dissipate significant energy and improve the seismic performance of the PreWEC system. The relative vertical displacement imposed on the O-connector measured during the PreWEC tests confirmed that the O-connectors yield at both ends of the wall. Because the inelastic strength of the O-connector in both the positive and negative loading directions is similar, the connectors impose equal and opposite forces on the wall panel and the axial load on the wall is not significantly affected by the number of connectors. This mechanism was confirmed by the similarities in the observed wall behaviour, damage, and

measured neutral axis depth and compressive strains for SRW-A, PreWEC-A and PreWEC-B which had consistent dimensions and PT arrangement. The fact that the wall behaviour is independent of the number of O-connectors in the PreWEC system offers a significant advantage over other wall systems as supplemental damping can be added without compromising the wall design or performance.

As O-connectors were added in the PreWEC system, a significant increase in the hysteretic energy dissipation was observed from SRW-A to PreWEC-A and PreWEC-B. This increase in energy dissipation would have substantial benefits when considering the seismic performance, but did lead to an increase in residual drifts of the overall wall system. Because the concrete compressive strains and neutral axis depth were the same for SRW-A, PreWEC-A1 and PreWEC-B, the increase in measured residual drift between the SRW and PreWEC systems was primarily attributed to the increased hysteresis area provided by the O-connectors. However, it should be noted that the residual drifts observed during the PreWEC tests are not an issue if the requirements for self-centring are considered appropriately during the design process using procedures previously developed [41] and briefly highlighted in section 2.10.

5.5 CONCLUSIONS

An experimental programme consisting of five cyclic tests on four unbonded PT precast concrete wall systems was conducted including two SRW (SRW-A and SRW-B) and two PreWEC systems (PreWEC-A and PreWEC-B). This experimental study systematically investigated the cyclic response of specimens with varying amounts of energy dissipation while keeping constant the initial post-tensioning, wall dimensions and confinement details for three walls and altering them significantly for the fourth wall. This allowed comparison of a variety of wall behaviours against a previously developed simplified analysis method. For all tests the walls generally behaved as expected with only minor damage occurring at large lateral drifts. As discussed below a number of conclusions have been drawn based on the test observations and measured response.

All of the four test walls were well designed with sufficient confinement and armouring details. Selection of an axial force ratio less than 10% led to an efficient design with a reduced risk of crushing in the wall toe. The use of the foam strip below the wall toe in SRW-A, PreWEC-A and

PreWEC-B helped to further reduce the compressive strains and prevent the cover concrete spalling.

Both SRW-A and SRW-B exhibited an approximate bilinear response with a small amount of hysteresis equal to 3-5% EVD. The increase in EVD of SRW-A compared to SRW-B from 5% to 3% at 2% lateral drift demonstrated the influence of axial force ratio and inelastic strain in the wall toe on the hysteretic damping in the system.

PreWEC-A and PreWEC-B showed increased strength and hysteresis due to the addition of the O-connectors. The EVD increased in proportion to the number of O-connectors with between 1.1-1.4% EVD provided by each O-connector in the PreWEC walls tested.

The PreWEC arrangement results in connector forces imposed on the wall panel that are equal and opposite. As a result of these balanced connector forces, the wall panel behaviour is independent of the number of O-connectors and so supplemental damping can be added without compromising the wall design or performance.

The increase in hysteresis area from an increase in O-connector number introduced higher residual drifts during the tests that need to be considered when designing the wall system to self-centre.

The simplified analytical method published by Aaleti and Sritharan [62] was able to capture both the global and local response parameters of all tests with sufficient accuracy. There were some small discrepancies in the prediction of the neutral axis depth at low lateral drifts and the deviation between the measured and predicted PT tendon force was due to minor prestress losses observed during each test.

The initial stiffness of the walls was lower than the expected stiffness calculated using the gross section moment of inertia. An effective stiffness modifier was calculated based on the measured initial stiffness and the predicted initial stiffness. The proportion of the gross section moment of inertia required for the effective initial stiffness to be equal to the measured initial stiffness was between 0.61-0.62 I_g for SRW specimens and 0.77-0.79 I_g for PreWEC specimens.

5.6 REFERENCES

15. Henry, R.S., S. Aaleti, S. Sritharan, and J.M. Ingham, *Concept and finite-element modeling of new steel shear connectors for self-centering wall Systems*. Journal of Engineering Mechanics, 2010. **136**(2): p. 220-229.
18. New Zealand Standard, *Concrete Structures Standard NZS 3101*. 2006: Wellington, New Zealand.
28. Henry, R.S., S. Sritharan, and J.M. Ingham. *Recentering requirements for the seismic design of self-centering systems*. in *Proceedings of the Ninth Pacific Conference on Earthquake Engineering*. 2011. Auckland, New Zealand.
41. Henry, R.S., *Self-centering precast concrete walls for buildings in regions with low to high seismicity*. 2011, University of Auckland. p. 441.
57. Sritharan, S., S. Aaleti, R.S. Henry, K.Y. Liu, and K.C. Tsai, *Introduction to PreWEC and key results of a proof of concept test*. M.J. Nigel Priestley Symposium, North Lake Tahoe, California, August 4-5, 2008, ed. M.J.N. Priestley, M.J. Kowalsky, and S. Sritharan. 2008, Pavia, Italy: IUSS Press. 267.
59. Aaleti, S., R.S. Henry, K.Y. Liu, S. Sritharan, and K.C. Tsai. *Experimental investigation of a precast wall with end columns (PreWEC) system*. in *Eleventh East Asia-Pacific Conference on Structural Engineering & Construction (EASEC-11) "Building a Sustainable Environment"*. 2008. Taipei, Taiwan.
62. Aaleti, S. and S. Sritharan, *A simplified analysis method for characterizing unbonded post-tensioned precast wall systems*. Engineering Structures, 2009. **31**(12): p. 2966-2975.
107. Henry, R.S., S. Aaleti, S. Sritharan, and J.M. Ingham, *Seismic analysis of a low-damage PREcast Wall with End Columns (PreWEC) including interaction with floor diaphragms*. SESOC Journal, 2012. **25**(1).
108. New Zealand Standard, *Methods of test for concrete NZS 3112.2:1986 in Tests relating to the determination of strength of concrete*. 1986: Wellington.
109. ACI Innovation Task Group 5., *Acceptance criteria for special unbonded post-tensioned precast structural walls based on validation testing and commentary : an ACI standard*. 2008, Farmington Hills, Mich.: American Concrete Institute. 19 p.
110. Chopra, A.K., *Dynamics of structures : Theory and applications to earthquake engineering*. 3rd ed. 2007, Upper Saddle River, NJ: Prentice Hall. xxxiv, 876 p.

Chapter 6

SNAP BACK TESTING

6.1 INTRODUCTION

The dynamic response of a system that is not subjected to any external force but is excited by initial disturbances alone is referred to as a free-vibration response [110]. To investigate the dynamic characteristics of SRW and PreWEC systems, a unique series of snap back testing was performed. Of particular interest was the magnitude of damping as it is not possible to analytically determine the damping ratio of structures. The objective of the four wall experiments was to systematically investigate the dynamic characteristics of wall systems with varied amounts of additional damping and initial post-tensioning tendon force. Additionally, a snap back test consists of two phases of response, the pseudo-static pushover or pull-back, when the wall is initially displaced, and the subsequent dynamic free vibration decay. These two distinct phases of the response provide valuable data for comparison of dynamic versus static measured parameters. The pseudo-static cyclic tests on identical walls reported in Chapter 5 provided the opportunity to make a valuable comparison between the pseudo-static cyclic and dynamic force-displacement measurements and Equivalent Viscous Damping (EVD) estimates.

6.2 EXPERIMENTAL PROGRAMME

The experimental programme consisted of snap back tests on four walls, including one SRW (SRW-FV-A) and three PreWEC systems (PreWEC-FV-A, B, and C). The three PreWEC walls were identical in dimensions and material properties, but varied the initial PT force and number of O-connectors as described in Chapter 4. Test walls SRW-FV-A, PreWEC-FV-A, and B had the same dimensions and parameters as three walls previously subjected to pseudo-static cyclic testing reported in Chapter 5.

6.2.1 Wall specifications

The design parameters of each test wall are provided in Table 6.1. The AFRs calculated from the measured material properties and tension forces for walls SRW-FV-A, PreWEC-FV-A, B, and C were 9.9%, 9.4%, 8.0%, and 6.8% respectively. The wall PT tendons had a typical unbonded length of 3600 mm as described in Chapter 4. The anchorage detail is the same as that described in Chapter 5. As presented in Table 6.1, PreWEC-FV-A, B, and C were designed to have four, six and six O-connectors per joint, respectively, creating three systems with different quantities of hysteretic energy dissipation and varying flexural capacities as described in Chapter 4. For design lateral drifts between 1-2%, the moment contribution ratios for PreWEC-FV-A, and B varied between 3.4-3.2, and 2.4-2.2, respectively, indicating that self-centering should easily be achieved as the restoring force was significantly greater than the hysteretic component of the response. As described in Chapter 4 the parameters of PreWEC-FV-C were chosen to attain a moment capacity comparable to PreWEC-FV-A with a different combination of O-connectors and initial PT force. The moment contribution ratio for PreWEC-FV-C was 2.1-1.85 between design drifts of 1-2% which is closer to the recommended minimum of 1.15 in NZS 3101:2006 Appendix B [18] to ensure self-centering. Details of the calculation of the λ ratios are described in Appendix D of this thesis.

Table 6.1 – Wall specifications

Wall Label	Tendon #	f_{pi} (MPa)		$f'_{c,test}$ (MPa)	$f'_{g,test}$ (MPa)	AFR (f_c/f'_c) (%)		O - Connectors per joint
		Target	Achieved			Target	Achieved	
SRW-FV-A	3	696	714	34.8	57.5	7.5	9.9	-
PreWEC-FV-A	3	696	696	35.8	61.4	7.5	9.4	4
PreWEC-FV-B	3	696	699	42.4	39.6	7.5	8.0	6
PreWEC-FV-C	2	696	762	37.4	59.5	5	6.8	6

6.2.2 Material properties

In accordance with New Zealand Standards [108] test cylinders and cubes were used to determine the compressive strength of each wall and the grout pad. The measured concrete ($f'_{c,test}$) and grout ($f'_{g,test}$) strengths on the day of testing for each wall are provided in Table 6.1. As stated in Chapter 4, 15.2 mm strand was used for the wall PT tendons for all four of the tested wall systems. The material properties of the PT strand and vertical and horizontal reinforcement have already been reported in Chapter 4 and are consequently not repeated here.

6.2.3 O-connector properties

Each wall and corresponding two end columns in each PreWEC system were connected horizontally by 10 mm thick mild steel O-connectors. Expected structural responses and construction details are specified in Chapter 4 and are referred to as connector type “O1” in Chapter 3. One of the component tests reported in Chapter 3 used a displacement protocol identical to the relative vertical displacement between the column and wall measured during the two PreWEC-FV-A snap back tests reported in this chapter. The measured force-displacement response of a single O-connector from that component test is repeated in Figure 6.1 for reference within this chapter.

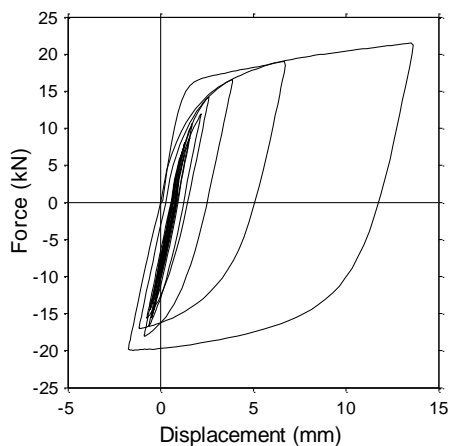


Figure 6.1 – Force-displacement response of O-connector component test

6.3 TEST SETUP

A schematic of the SRW-FV-A geometry and test setup is presented in Figure 6.2(a). The typical PreWEC system test setup was identical except for the inclusion of PT end columns and O-connectors. The wall panel in each test was seated in a shallow pocket on top of the foundation that was filled with grout to provide an even bearing surface at the wall-to-foundation interface. The wall panel was embedded approximately 10 mm into the grout pocket to increase the sliding shear resistance. To limit the concrete compressive strains and spalling of cover concrete in the toe region, each wall panel had a foam strip glued across the wall thickness for the width of the cover region (15 mm) as described and depicted in Chapter 5. It is important to note that use of the foam strip effectively shortened the length of the wall by 30 mm to 770 mm. Concrete mass blocks were attached to the top of the wall providing anchorage for the tendons, seismic mass for the dynamic testing, and a loading beam for the load application snap back test rig. A photo of the load application rig used for the snap back testing is shown in Figure 6.4. The rig consisted of a hydraulic jack and load cell connected by heavy duty chain to a quick release mechanism. The quick release mechanism was a shackle that could be remotely triggered to open when under load. A steel lateral support frame provided out-of-plane restraint to the wall during testing. The total mass of the wall and additional weight was 3813 kg with a centre of mass of 2.657 m above the wall base. A photo of the overall test setup for a typical PreWEC test is shown in Figure 6.2(b). Note that this test set up is identical to that reported for SRW-A, PreWEC-A, and B in Chapter 5.

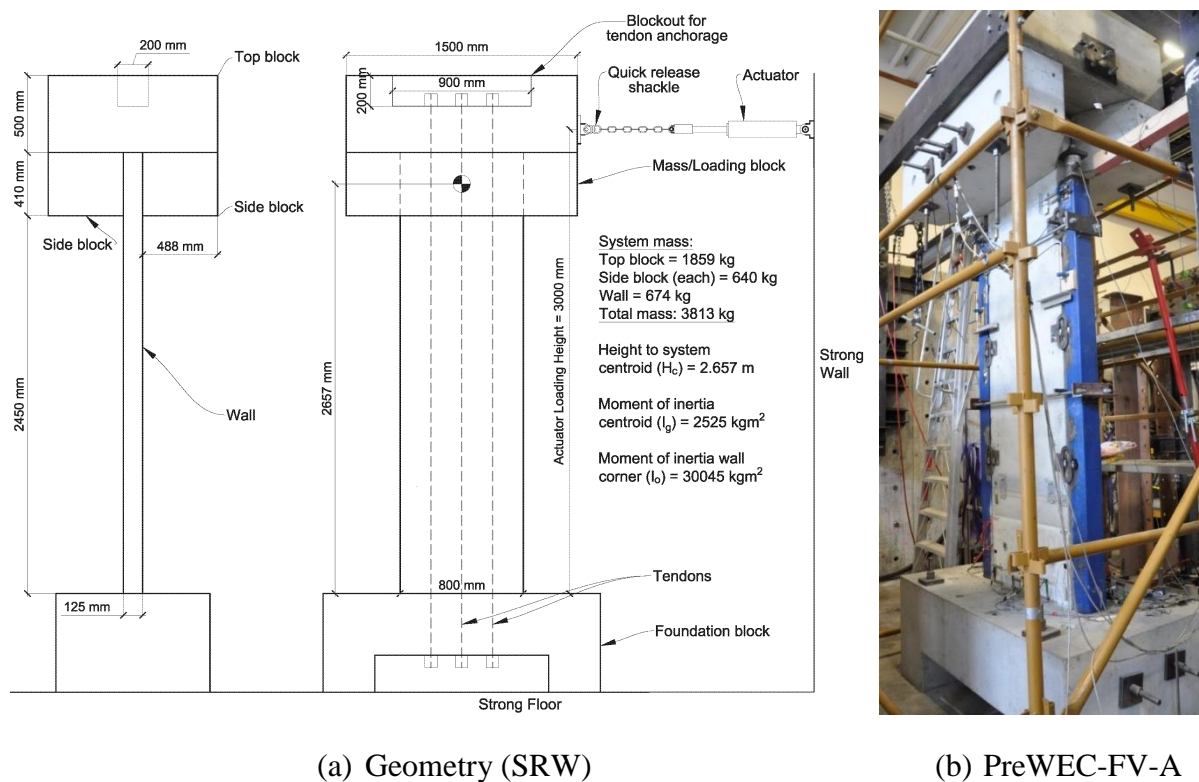


Figure 6.2 – Setup for snap-back tests

Extensive instrumentation was installed on all walls to capture both the pseudo-static pushover and free-vibration response, with the typical sensor layout shown in Figure 6.3. Displacement gauges were used to measure wall lateral displacement, wall uplift, and potential slip at the wall-foundation interface, wall-anchorage block interface, and the foundation to strong floor interface. Strain gauges were also placed at the wall toes to capture the peak compressive strains. Load cells were used to measure and apply the tendon forces in the wall and columns, as well as to measure the lateral load applied during the pushover phase of the snap back test. For each PreWEC test, displacement gauges were also used to measure the relative vertical and horizontal displacement along each column-wall joint to capture the displacements applied to the O-connectors. An array of accelerometers was used to measure in-plane, out-of-plane, and vertical accelerations at several locations on the test setup as presented in Figure 6.3. The data acquisition system recorded at a sampling rate of 2000 Hz. All of the dynamic test data reported has been filtered with a 30 Hz low pass filter to remove any high frequency noise from the data acquisition system unless otherwise stated, and all lateral motion results are reported at the height of the centre of mass.

6.4 TEST PROCEDURE

In addition to the main snap back tests, small vibration impact tests were performed on each wall by striking the top of the wall with an impact hammer to identify the fundamental natural frequency of each wall system. The impact tests were performed before snap back testing for the PreWEC systems but after for the SRW. Since negligible damage was observed during the snap-back testing, the timing of hammer excitation was expected to have no significant influence on the frequency response of SRW-FV-A. The snap back tests were conducted by pulling the wall back to a specified lateral drift and activating the quick release mechanism, allowing the wall to vibrate freely until rest. Each wall was subjected to snap back tests from lateral drifts of 1% and 2%. These drifts correspond to appropriate design level drifts for concrete wall systems, and were sufficient to induce rocking and nonlinear response that would be expected to occur during a design level earthquake.

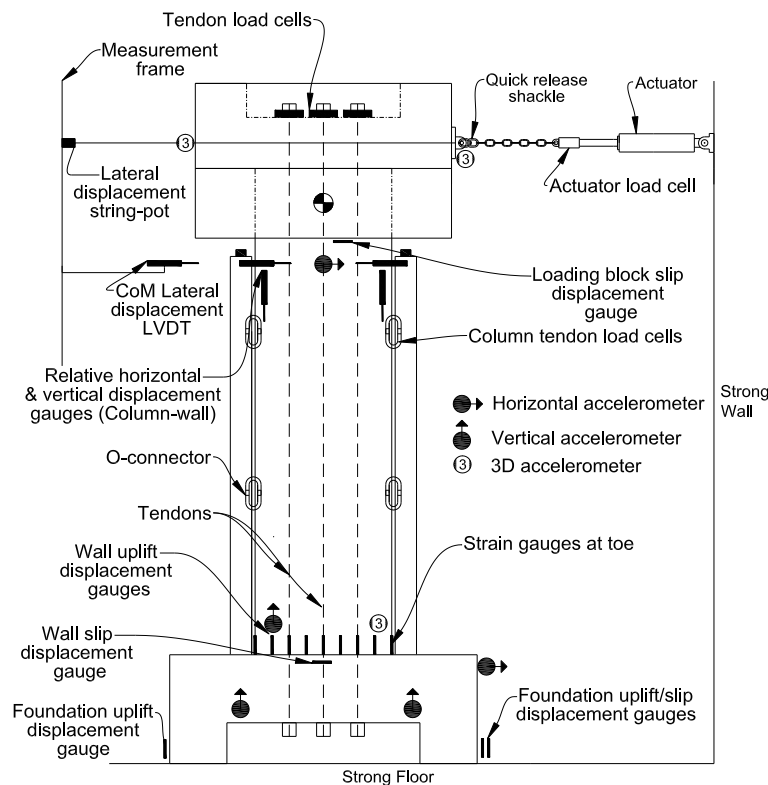


Figure 6.3 – Instrumentation plan

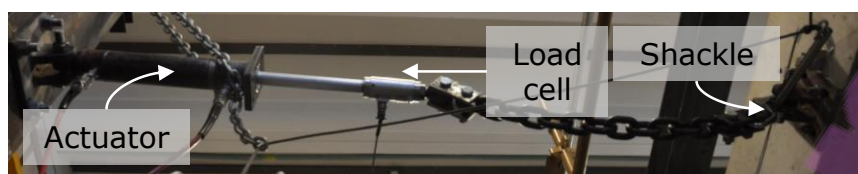


Figure 6.4 – Snap back test load application rig

6.5 OBSERVATIONS, RESULTS, AND DISCUSSION

This section presents test results that describe the frequency characterisation of the walls, followed by a discussion of the observations from the snap back tests combined with the general free vibration time history response. A description of the wall behaviour and a discussion of the critical results including residual drifts, period-displacement behaviour, lateral force-displacement behaviour, and local parameter response is also presented. Lastly, a description of methods to determine the EVD is provided and the most appropriate technique is used to assess the damping in each of the wall systems compared to the EVD found from the cyclic tests reported in Chapter 5. Complete results of the snap back tests are described in Appendix C of this thesis. Also, videos of the snap back tests performed can be viewed at: <https://www.youtube.com/user/UoAConcrete>.

6.5.1 Frequency characterisation and stiffness

The natural frequencies of the four test walls were calculated from the recorded acceleration data at the top of the wall during hammer hit excitation. To eliminate the high frequency noise the acceleration records were filtered with a low pass 40 Hz filter. A fast Fourier transform was applied to the recorded acceleration data for each wall and the results are presented in Figure 6.5, where the y-axis is the Fourier amplitude normalized by the maximum Fourier amplitude for each wall. It can be seen that SRW-FV-A had a fundamental frequency of 8.2 Hz and the three PreWEC walls had similar fundamental frequencies of approximately 10.6 Hz. As expected from the design, the PreWEC systems had a higher stiffness than SRW-FV-A due to the contribution of the O-connectors and end columns. However, the number of O-connectors connecting the columns did not significantly affect the initial stiffness of the PreWEC systems, indicating that the coupling between the wall and columns was not significantly different between the PreWEC walls.

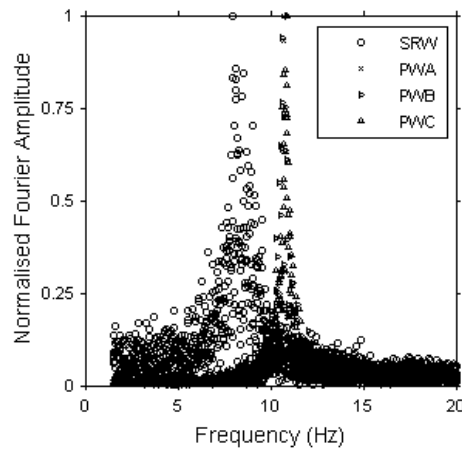


Figure 6.5 – Frequency domain response of hammer hit acceleration data

During the hammer hits no uplift occurred at the wall base and the panel remained uncracked which implies that the theoretical lateral stiffness should be calculated based on the gross section moment of inertia (I_g). A prediction of the stiffness of each wall is presented in Table 5.2, and was calculated assuming a lateral stiffness (K) equal to the sum of $3EI_g/h^3$ for each component (walls and end columns), where E is the modulus of elasticity, I_g the moment of inertia and h the height of the applied load which is the centre of mass for dynamic loading [110]. The calculation assumed a concrete modulus of elasticity (E_c) equal to $4700\sqrt{f'_c}$, where f'_c is the compressive strength of concrete in MPa.

A measured initial stiffness was derived from the measured fundamental frequency using the relationships described by Equation (6-1), where f is the frequency in Hz, ω is the circular frequency in rad/s, K is the lateral stiffness in N/mm and M is the system mass in tonnes.

$$f = \frac{\omega_n}{2\pi} = \frac{\sqrt{K/M}}{2\pi} \quad (6-1)$$

Using Equation (6-1) and a mass of 3813 kg, the measured experimental stiffness was derived for each wall and is also presented in Table 5.2. The measured stiffness of SRW-FV-A was 10.4 kN/m, and 17.3 kN/mm for all PreWEC walls. The final row in Table 5.2 is the Effective Stiffness Modifier (ESM) which is the measured stiffness divided by the predicted stiffness. For the SRW the ESM was 0.49 and ranged between 0.74-0.8 for the PreWEC systems, demonstrating that use of the gross section properties significantly overestimates the stiffness. The ESM values aligned well with previously calculated values presented in Chapter 5 for the

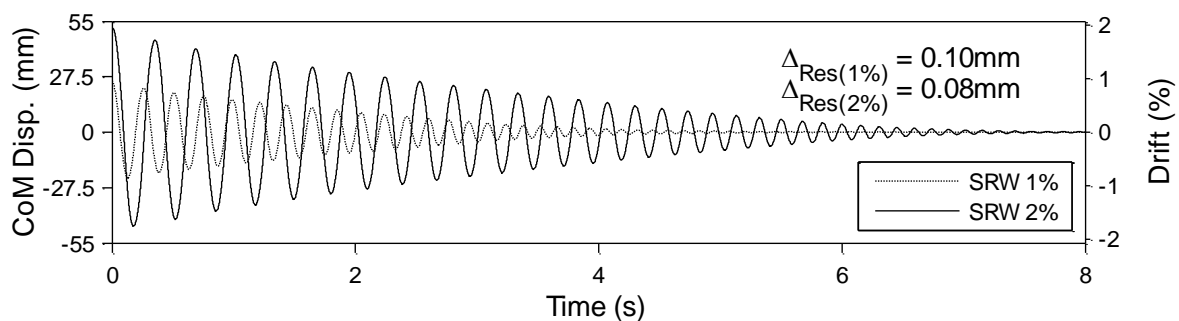
PreWEC systems and were reasonably close for the SRW system. In Chapter 5 the ESM values were estimated using the initial cycles of pseudo-static cyclic testing.

Table 6.2 – Initial stiffness of each test specimen

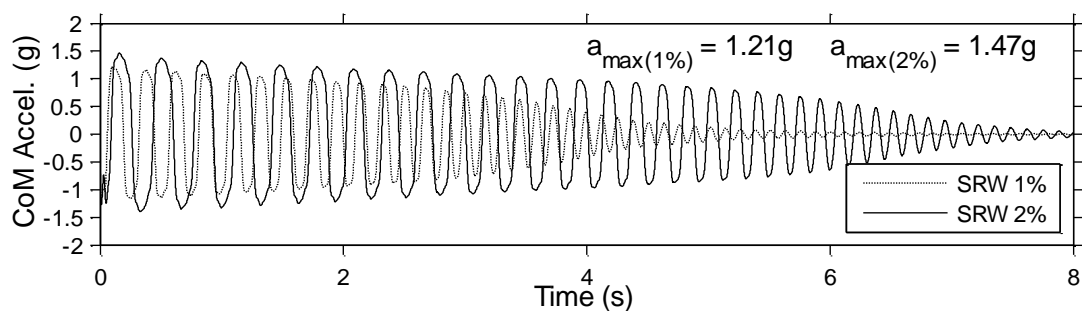
	SRW-FV-A	PreWEC-FV-A	PreWEC-FV-B	PreWEC-FV-C
Measured initial stiffness ($K_{i(m)}$) kN/mm	10.4	17.3	17.3	17.3
Predicted initial stiffness ($K_{i(p)}$) kN/mm	21.1	21.6	23.5	22.1
Effective stiffness modifier ($K_{i(m)}/K_{i(p)}$)	0.49	0.80	0.74	0.78

6.5.2 Observations and time history response

The two snap back tests performed on SRW-FV-A resulted in large amplitude rocking that lasted up to 8s for the 2% drift test. The SRW-FV-A displacement and acceleration free vibration decays during snap back tests to both 1% and 2% lateral drift are presented in Figure 6.6. During each of the tests, no significant damage was observed in the wall panel toes, as demonstrated by the photo of the wall base after the snap back tests in Figure 6.7(a).

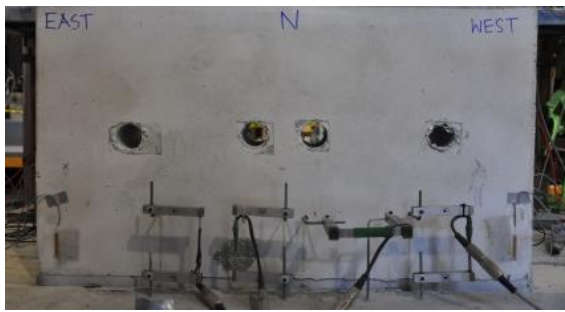


(a) SRW-FV-A displacement decay



(b) SRW-FV-A acceleration decay

Figure 6.6 – SRW-FV-A displacement and acceleration decay



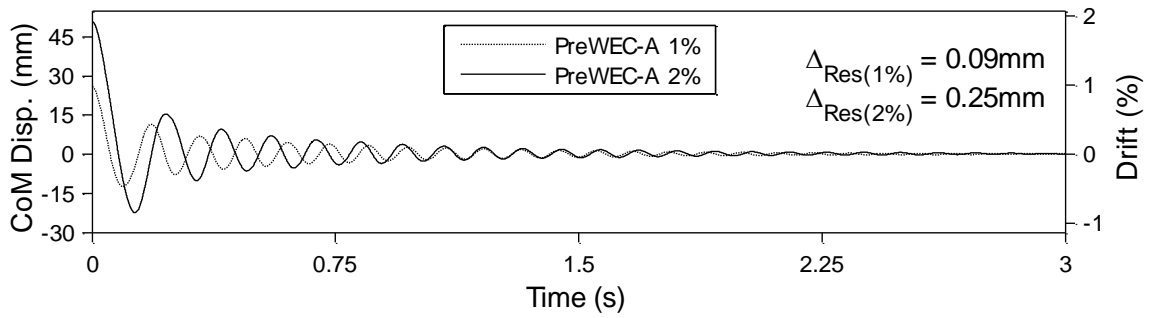
(a) Typical condition of wall base post-test



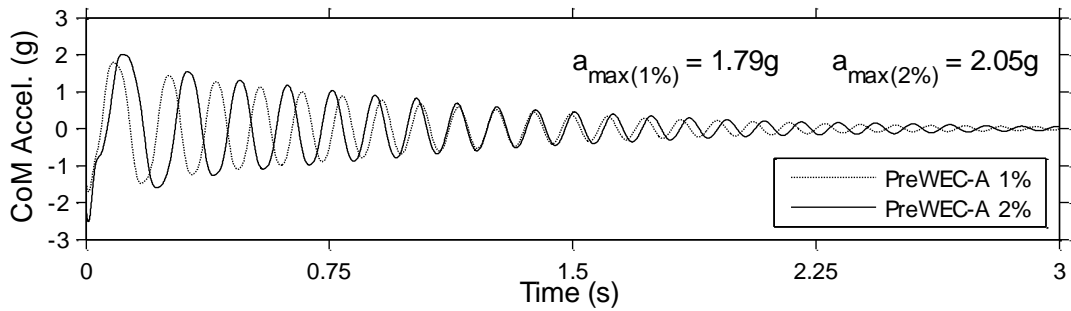
(b) Typical O-connector condition post-test (PreWEC-FV-A)

Figure 6.7 – Wall and connector condition following snap back tests

The displacement and acceleration decays for snap back tests from 1% and 2% lateral drift for PreWEC-FV-A, B and C are presented in Figure 6.8, Figure 6.9, and Figure 6.10, respectively. Each of the PreWEC systems exhibited noticeable rocking at the wall base for only two to three cycles and the system vibration lasted approximately 3s, less than half the vibration time of SRW-FV-A. The snap back tests performed on the three PreWEC walls also resulted in negligible damage to the wall panels and the O-connector displacements were within their design range, with no connector failure during any of the tests. An example of the O-connector condition after the PreWEC-FV-A snap back tests is shown in Figure 6.7(b). The release amplitudes specified for the two snap back tests on each wall were 1% (26.6 mm) and 2% (53.1 mm) drift which were approximately achieved except for the PreWEC-FV-C 2% drift test which was released from 2.4% drift due to a displacement gauge error that was later corrected. Hence, conclusions can be directly drawn between the first three walls and assessed for PreWEC-FV-C considering that higher displacements were expected from PreWEC-FV-C.

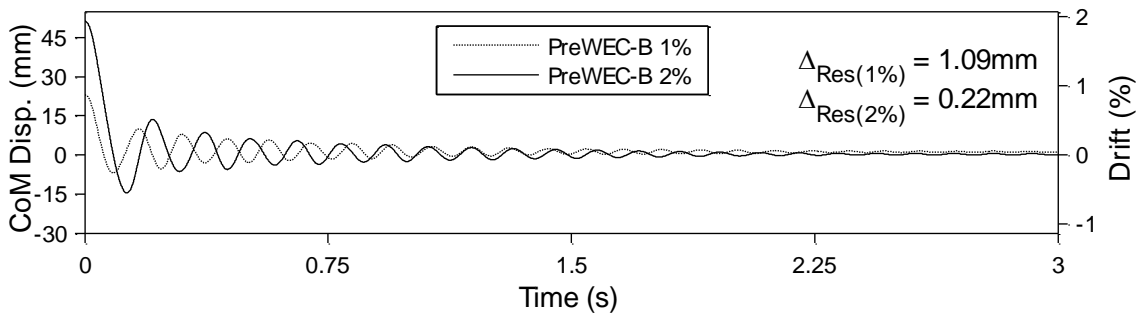


(a) PreWEC-FV-A displacement decay

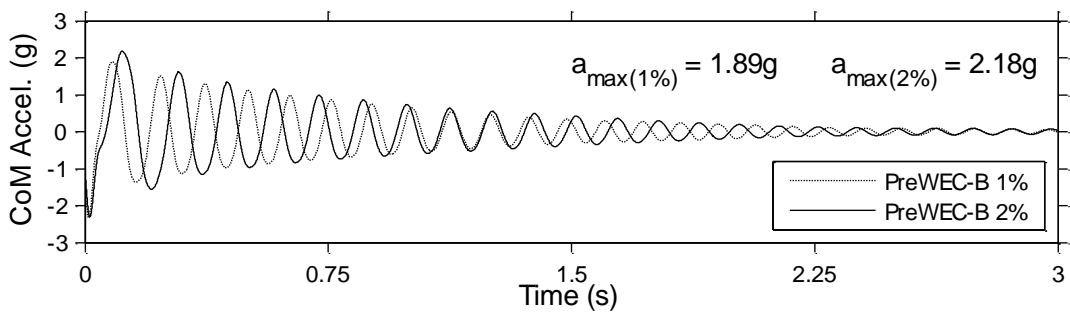


(b) PreWEC-FV-A acceleration decay

Figure 6.8 – PreWEC-FV-A displacement and acceleration decay

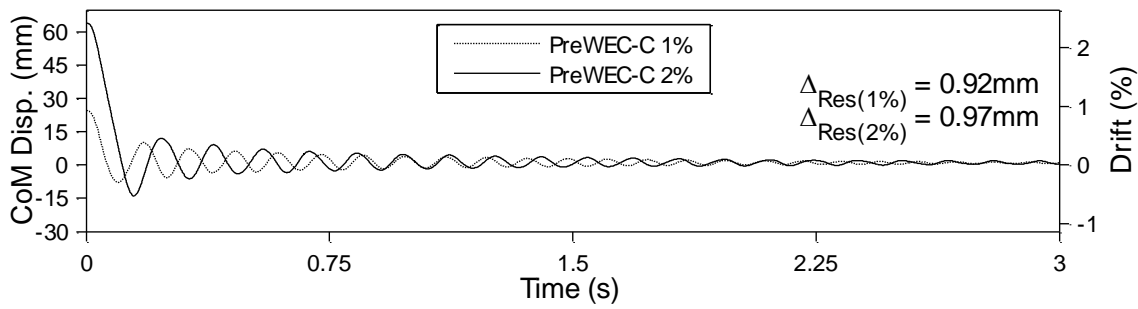


(a) PreWEC-FV-B displacement decay

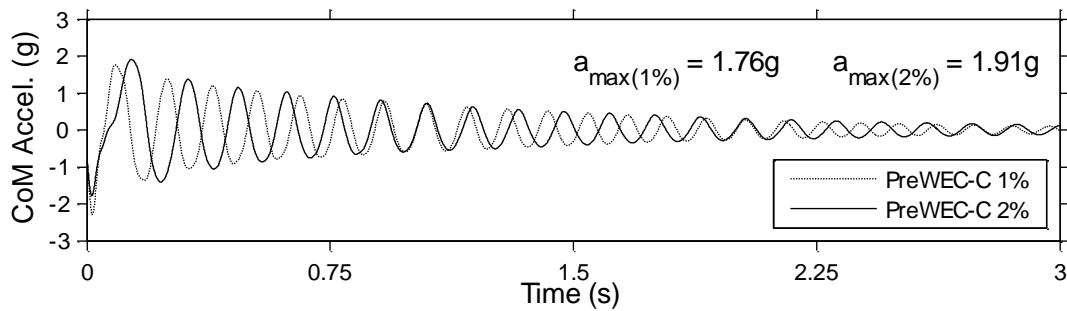


(b) PreWEC-FV-B acceleration decay

Figure 6.9 – PreWEC-FV-B displacement and acceleration decay



(a) PreWEC-FV-C displacement decay



(b) PreWEC-FV-C acceleration decay

Figure 6.10 – PreWEC-FV-C displacement and acceleration decay

The recorded peak accelerations (a_{max} in the acceleration plots) following release (ignoring the impulse at the start of the decay) for the 1% drift tests were 1.21 g, 1.79 g, 1.89 g, and 1.76 g for SRW-FV-A, PreWEC-FV-A, B, and C, respectively, and 1.47 g, 2.05 g, 2.18 g, and 1.91 g for 2% drift tests, respectively. Once rocking occurred in both the SRW and PreWEC systems the stiffness was reduced and the acceleration increased less significantly when compared to the increase in displacement, as the acceleration is proportional to the force capacity of the system. All of the PreWEC walls had measured peak accelerations higher than that of SRW-FV-A due to the higher moment capacity of the systems. However, the lower stiffness and force capacity of SRW-FV-A results in higher drifts and a longer time to come to rest. Recalling that PreWEC-FV-C was designed to have comparable moment capacity to PreWEC-FV-A, snap back results indicated that a lower acceleration of 1.91 g was attained by PreWEC-FV-C in comparison to the 2.05 g attained by PreWEC-FV-A for the 2% drift test. These findings confirmed that the increased hysteretic energy dissipation from the additional O-connectors in PreWEC-FV-C reduced the peak accelerations.

6.5.2.1 Displacement decay envelope observations

To examine the displacement decay envelope for each snap back test the natural log of the displacement peaks over time was calculated and is plotted in Figure 6.11 for SRW-FV-A, and PreWEC-FV-A, B, and C. For a perfectly viscous system with an exponential free vibration decay, the natural log of the displacement peaks during the decay results in a linear trend [110]. For SRW-FV-A the envelope of the natural log of the displacement peaks was clearly not linear, and instead consisted of two distinct phases of response that align with full rocking and non-rocking displacement amplitudes. There was a steeper gradient during the second phase of response where rocking was not occurring that suggests increased damping during that phase of the response.

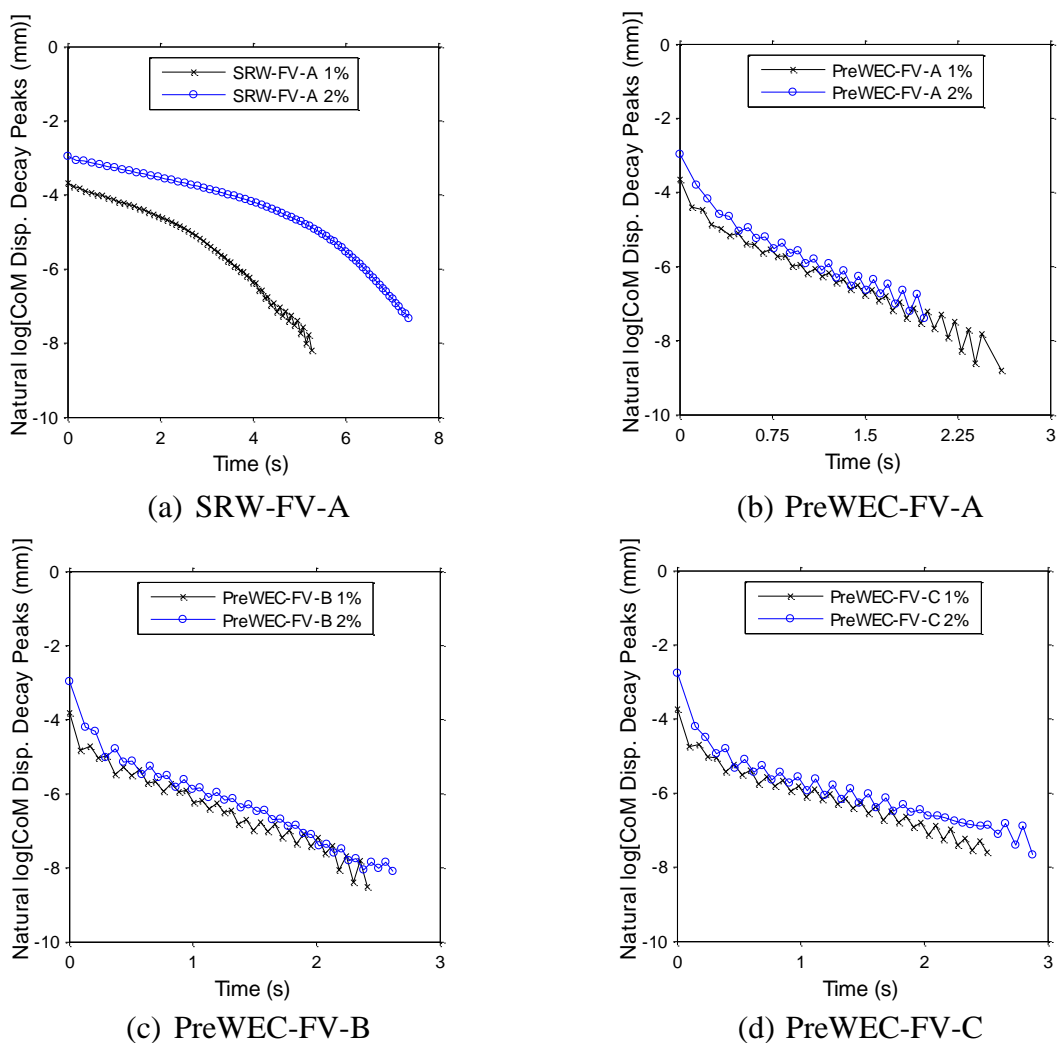


Figure 6.11 – Natural log of displacement peaks over time

All of the PreWEC walls showed high nonlinearity for only the first 1-3 cycles of vibration with a steep gradient demonstrating high damping. After the first few cycles the gradient of the natural log of the displacement peaks was approximately linear, demonstrating the viscous nature of the low amplitude vibrations when full rocking was no longer occurring. Overall these results confirm that pure viscous damping is not appropriate for rocking systems.

6.5.3 Residual drifts

All of the walls returned to their original vertical alignment with insignificant residual drift at the conclusion of the free vibration decay. The measured residual displacements (Δ_{Res}) were reported previously within each displacement decay plot as shown in Figure 6.6, Figure 6.8, Figure 6.9, and Figure 6.10, and the residual drifts can be calculated by dividing the residual displacement by the height to the centre of mass (2657 mm). SRW-FV-A sustained residual drifts of 0.0038% and 0.0030% following the 1% and 2% drift tests and PreWEC-FV-A, B, and C sustained residual drifts of 0.0034% and 0.0094%, 0.041% and 0.0083%, 0.035% and 0.037% following the 1% and 2% drift tests respectively. In general the PreWEC walls had higher residual displacements than SRW-FV-A but never of a magnitude higher than 0.04%. It is significant to note that extremely low residual drifts were measured despite much higher peak residual drifts being reported for the pseudo-static cyclic testing reported in Chapter 5 that were in the order of 0.1-0.6%. This finding highlights the importance of dynamic response on residual drift. Although the snap back tests do not simulate earthquake excitation, the snap back tests still provide evidence for the tendency of the system to self-centre during the free vibration phase at the end of a ground motion. The significant difference between the residual drift observed in the hysteresis response of the cyclic test walls and the residual drift observed during dynamic free vibration decay is in agreement with previous analytical research [28].

6.5.4 Period dependency with displacement

The free vibration decay of SRW-FV-A was further examined by extracting the time period between the displacement peaks and zero positions for the entire decay, referred to as the quarter period in previous literature describing the mechanics of rocking blocks [76]. The calculated quarter periods from the test free vibration response are plotted against the magnitude of the peak displacement at which the cycle began in Figure 6.12. The highest measured quarter period was

0.09s at a displacement corresponding to 2% drift decreasing to 0.0325s at zero drift with a clear nonlinear response. The nonlinear relationship depicted in Figure 6.12 supports the finding by Ma [76] that the rocking period of a PT wall is strongly amplitude dependent. The period dependence on amplitude has also been shown analytically by Housner [37] for a rigid rocking block and by Barthes et al. [111] for a PT rigid rocking block. The dotted line in in Figure 6.12 indicates the fixed base quarter period, which is the period at zero displacement or the y intercept. The calculated fixed base quarter period of 0.0325s aligned well with the identified natural frequency of 8.15 Hz or quarter period of 0.0306s from the hammer hits presented in section 6.5.1.

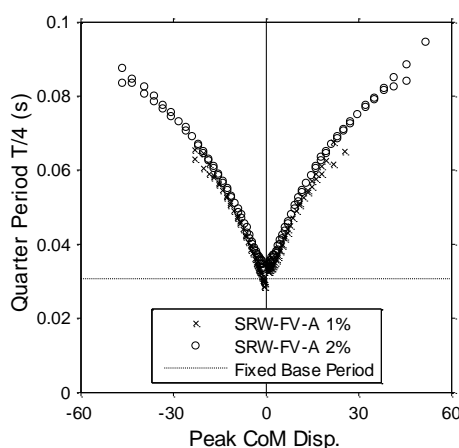


Figure 6.12 – Quarter periods of SRW-FV-A versus peak CoM displacement

6.5.5 Lateral force displacement behaviour

In addition to providing the free vibration decay of the system, the snap back tests provided the static pushover moment-drift response, measured when the wall was initially displaced. For all wall configurations, the measured monotonic pushover moment drift responses for 1% and 2% drift are presented in Figure 6.13 (a) and (b), respectively. As expected the PreWEC systems had a much higher moment capacity than the SRW due to the addition of O-connectors and end columns. Although PreWEC-FV-A and C were designed to have a similar moment drift response by decreasing the wall PT force and increasing the number of O-connectors, a slightly higher moment capacity was measured for PreWEC-FV-C. Also included in Figure 6.13 is an analytical pushover force-displacement prediction proposed by Aaleti and Sritharan (A&S) [62]. The analytical method is plotted in red with the corresponding pattern for each wall specified in the legend. The analytical predictions in red for PreWEC-FV-A and PreWEC-FV-C are almost

identical and therefore overlaid on each other. The results of the analytical method correlated well with the measured response for all four walls and is recommended for use in design of unbonded PT concrete wall systems.

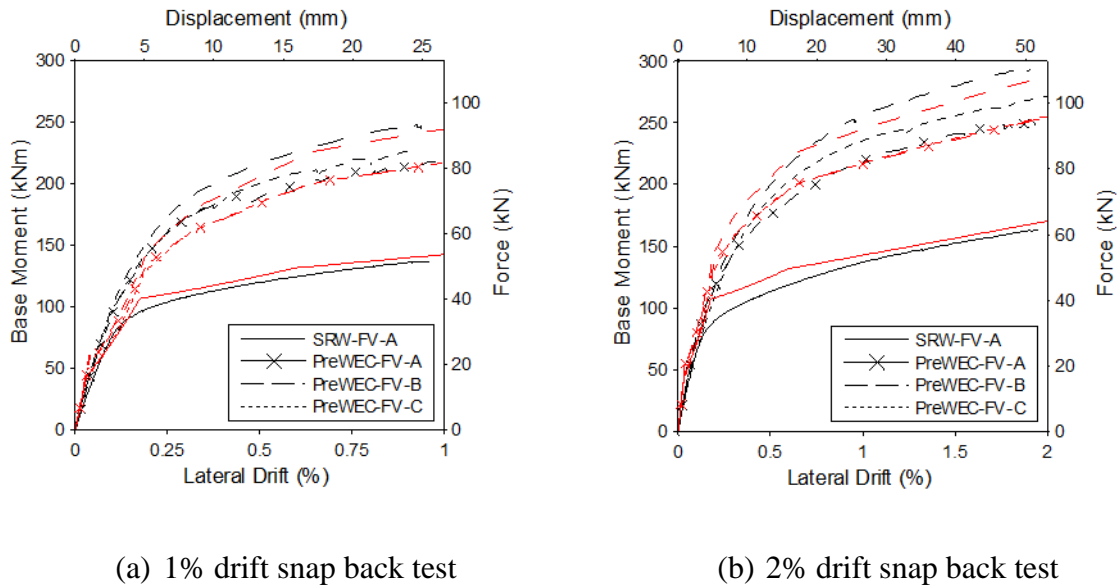


Figure 6.13 – Monotonic pushover moment drift results (black – test, red – A&S)

The pseudo-static pushover and free vibration decay force-displacement response of each wall for both the 1% and 2% drift snap back tests is shown in Figure 6.14. The free vibration decay force is the inertia force acting on the wall and was calculated by multiplying the total mass by the acceleration at the centre of mass that was found by linear interpolation from the recorded accelerations. The inertia force displacement response of SRW-FV-A shown in Figure 6.14(a) exhibited an imperfect bilinear elastic response with a small amount of hysteresis. As expected the PreWEC walls exhibited fatter loops with increased hysteresis area due to the addition of the O-connector dissipaters. PreWEC-FV-A shown in Figure 6.14(b) has the smallest ratio of hysteresis area to the maximum achieved force when comparing the three PreWEC walls followed by PreWEC-FV-B and PreWEC-FV-C. This was expected due to the strength and energy dissipation provided by each O-connector. For each wall the pushover monotonic force-displacement response indicated some stiffness degradation in the system between the 1% and 2% drift tests due a small amount of PT loss and a small amount of inelastic concrete strains in the wall toes. In addition, Figure 6.14(a), (b), and (c) also include the pseudo-static cyclic force-displacement cycles for 2% lateral drift that were recorded during previous cyclic tests reported

in Chapter 5 where three tests with identical wall designs to SRW-FV-A, PreWEC-FV-A and B were reported. When considering the different measurement techniques, the close correlation between the pseudo-static cyclic results and the dynamic inertia force displacement response measured during the snap back tests is remarkable. The cyclic data indicated slightly higher strengths at large drifts, most likely due to the strain hardening effect on the O-connectors during cumulative reverse cyclic loading. The good alignment of the cyclic test, monotonic pushover, and inertia force during free vibration decay demonstrates the consistency in behaviour of unbonded PT walls regardless of loading rate.

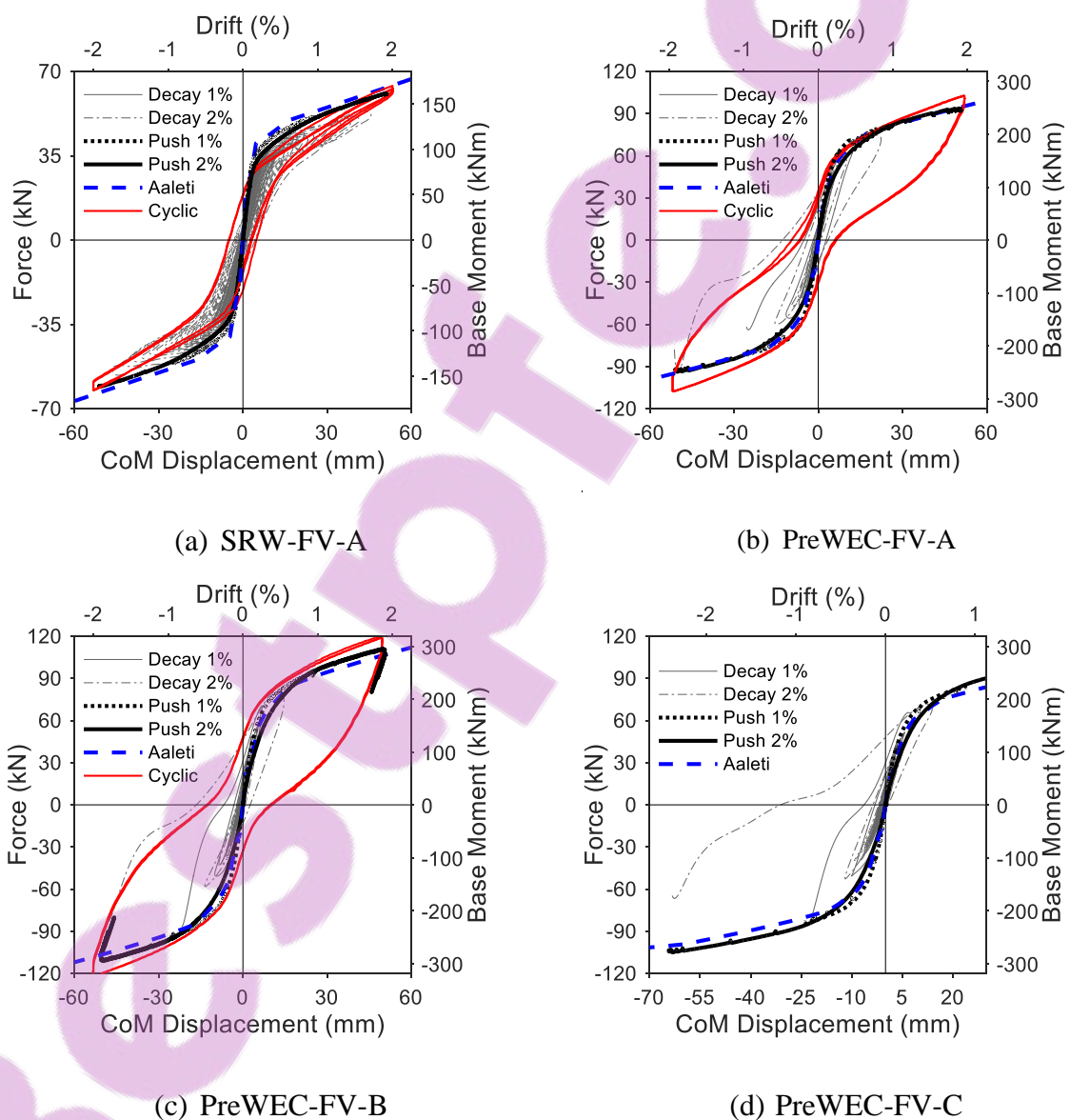


Figure 6.14 – Force-displacement response for all tests

6.5.6 Local parameter response: pseudo-static versus dynamic

To investigate the change in local response parameters between pseudo-static and dynamic loading rates the neutral axis (NA), post-tensioning force, and compressive concrete toe strains for each wall are plotted separately for the monotonic pushover and free vibration decay in Figure 6.15. The average initial stress per tendon and axial force ratio for the 1% snap back test were presented in Table 6.1. For the 2% snap back test prestress loss occurred during the pushover resulting in an average initial stress per tendon of 702 (1.7% loss), 690 (0.9% loss), 691 (1.1% loss), and 757 MPa (0.7% loss) and an AFR of 9.8%, 9.3%, 7.9% and 6.8% at the culmination of each test for specimens SRW-FV-A, PreWEC-FV-A, B, and C, respectively as depicted in Figure 6.15. As shown in Figure 6.15(a), the total post-tensioning force for SRW-FV-A increased during the 1% drift pushover (labelled 1% PO) due to gap opening at the wall base. It is clear when comparing the green pushover PT response with the blue 1% decay PT response that a small amount of prestress loss resulted from the pushover phase, evidenced by the 1% decay path being lower than the initial prestress at zero drift. The prestress loss results from wedge-draw in as the force on the anchorage is increased. Since the PT force only decreases during the decay phase, no further loss developed during free vibration response. For SRW the 2% drift test pushover (2% PO) followed the same path as the 1% decay and prestress loss resulted again from the wedge draw-in that occurred during the pushover resulting in the 2% decay following a lower path. Similar behaviour to SRW-FV-A was observed for each the PreWEC systems as shown in Figure 6.15 (d), (g), and (j).

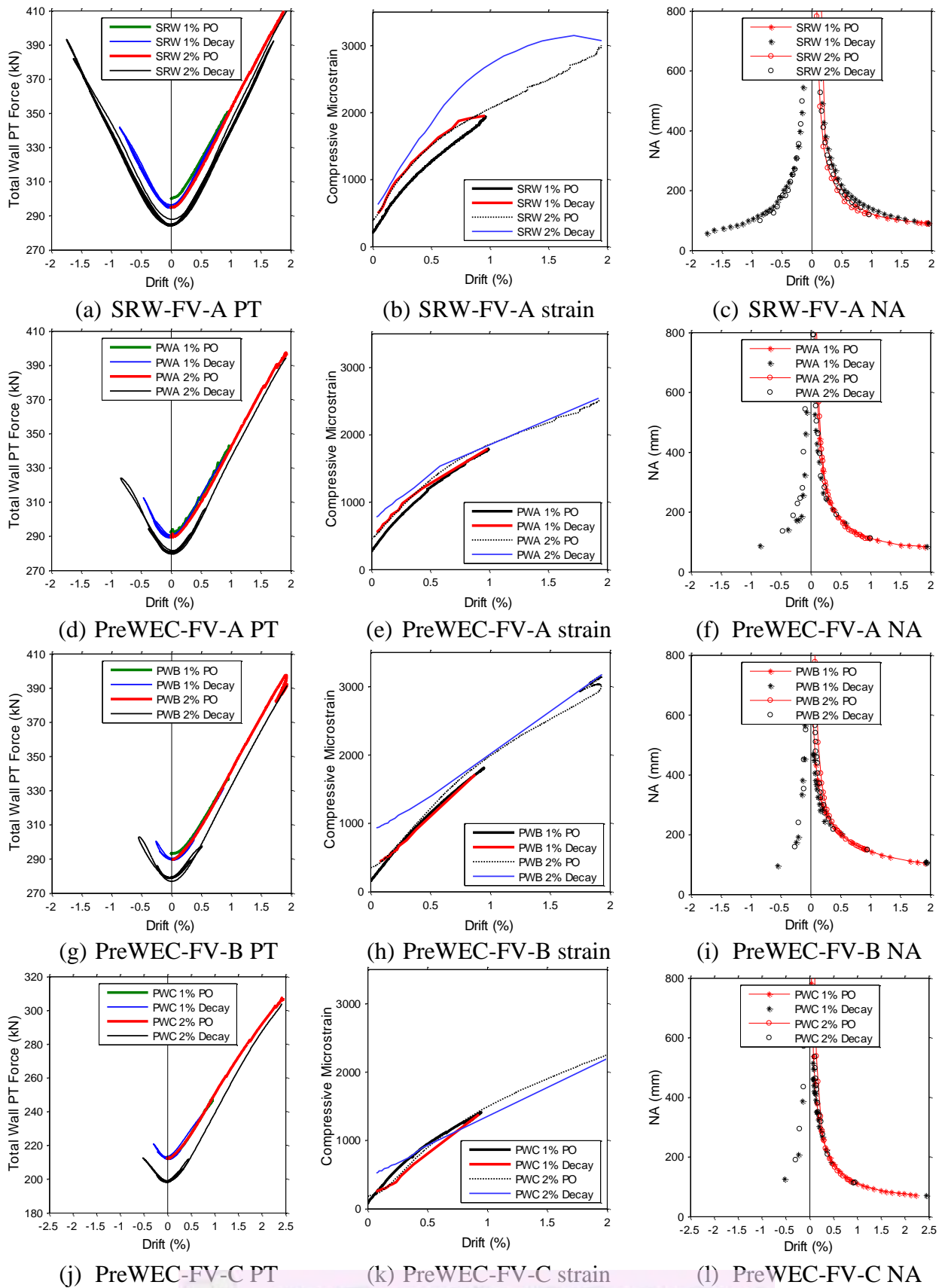


Figure 6.15 – Local wall parameter response versus drift

An example of the measured compressive microstrain in one of the wall toes when loaded in compression is plotted for SRW-FV-A, PreWEC-FV-A, B, and C in Figure 6.15 (c), (f), (i), and (l), respectively. The exact location of the strain gauge is not significant, instead it is important to compare the strains measured in the same location during the different loading types and rates. To assess the strain demand during the two different test phases, the pushover response and free vibration are identified separately and only the peak strains in the compression toe at each displacement peak during the free vibration decay phase are plotted. For SRW-FV-A the decay strains were higher than the pseudo-static pushover showing that the dynamic impact forces cause higher wall strains. However, for the three PreWEC systems this pattern was not observed, likely due to the rapid decay of the walls resulting in no strain data points existing at drifts greater than 0.5% for the free vibration phase. It is expected that higher strains during the dynamic response would have occurred in the PreWEC walls if higher drifts during rocking were achieved. As demonstrated by Figure 6.15 (b), (e), (h), and (k) the neutral axis for all four walls during static and dynamic testing is in excellent agreement. The local parameters demonstrate that the dynamic behaviour of unbonded PT wall systems can be well represented by pseudo-static tests for parameters such as neutral axis and PT force, however higher strains can be expected due to toe impact during rocking.

6.5.7 Equivalent viscous damping (EVD) ratio

6.5.7.1 *Logarithmic decrement theory*

A common method used to experimentally evaluate the EVD of linear structures is the logarithmic decrement method described by Equation (6-2) [110], where u_n and u_{n+2} are a pair of positive or negative successive displacement peaks in the decay, shown graphically in Figure 6.16(a). Due to the amplitude dependence of the PT rocking system the classical equations for free vibration of a linear SDOF system are not strictly appropriate, however, the logarithmic decrement method is still often used for nonlinear structures as it is an easy technique to get an indication of the proportion of damping appropriate to the system.

$$\delta = \ln \left(\frac{u_n}{u_{n+2}} \right) = \frac{2\pi\xi_{eq}}{\sqrt{1 - \xi_{eq}^2}} \quad (6-2)$$

During an experimental free vibration decay residual drift may occur. Any residual drift that occurs will influence the EVD evaluated using logarithmic decrement method, especially as the amplitude of displacement approaches the magnitude of residual drift. An adjusted logarithmic decrement method that accounts for residual drift has been proposed by O'Hagan [112] and is described by Equation (6-3). The adjusted logarithmic decrement method adjusts the pair of successive peaks used in Equation (6-2) by replacing u_n with the absolute total of $u_n + u_{n+1}$, and u_{n+2} with the absolute total of $u_{n+1} + u_{n+2}$. The use of the total of consecutive pairs of peaks effectively cancels out any residual drift that would affect the regular logarithmic decrement method.

$$\delta = \ln \left(\frac{\text{abs}(u_n - u_{n+1})}{\text{abs}(u_{n+1} - u_{n+2})} \right) = \frac{2\pi\xi_{eq}}{\sqrt{1 - \xi_{eq}^2}} \quad (6-3)$$

An example free vibration decay analysis is presented to provide evidence for the validity of the adjusted logarithmic decrement method proposed by O'Hagan [112]. The free vibration displacement decay of a linear Single-Degree-Of-Freedom (SDOF) with a specified damping ratio of 5% and a fundamental frequency of 0.75 Hz is calculated and presented in Figure 6.16 (a), with an applied residual displacement of 1 mm. The damping in the SDOF is linear viscous and should be constant over all cycles. The EVD is evaluated using the adjusted and original logarithmic decrement method for each cycle of vibration for the SDOF and is shown in Figure 6.16 (b) plotted against the corresponding average displacement of the peaks used (u_a). Despite the low magnitude of residual drift of 1 mm, the original logarithmic decrement method results in a large variation of evaluated damping ratio which should be equal to the specified 5%. However, the adjusted logarithmic decrement method produces the correct damping ratio of 5% at all displacement amplitudes for all cycles of motion. These results show the significant effect small magnitudes of residual drift have on the EVD evaluated using the logarithmic decrement and validate the adjusted logarithmic decrement procedure proposed by O'Hagan [112].

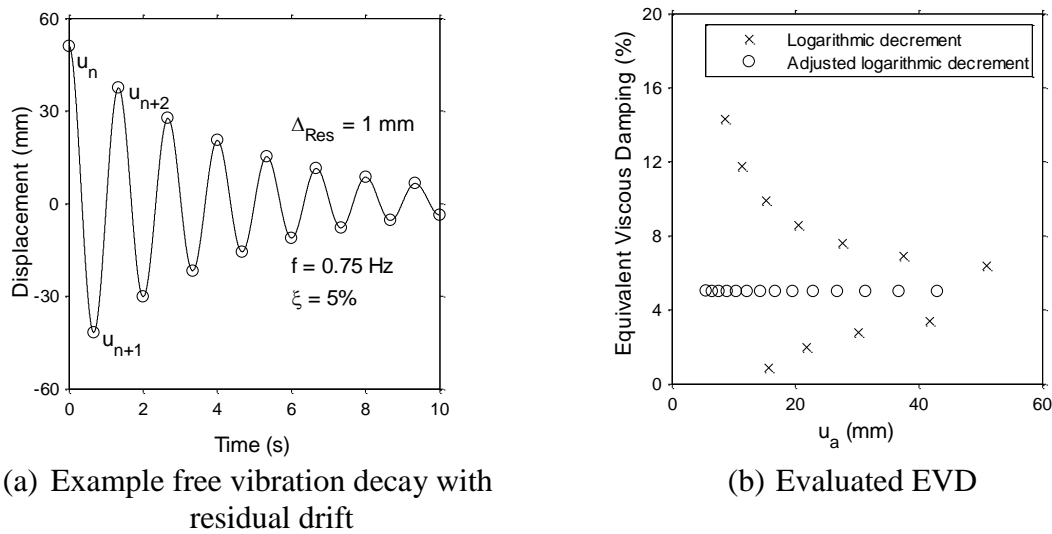


Figure 6.16 – Example SDOF free vibration with residual drift

As discussed previously the logarithmic decrement method uses the ratio of successive displacement peaks to determine an EVD ratio for linear systems assuming constant stiffness. For nonlinear systems the stiffness changes (usually the system softens) and the ratio of successive displacement peaks would tend to estimate EVD values that are too high. To better represent a nonlinear system Marriott [13] showed that the square root of the initial input energy over the kinetic energy can be used in place of successive displacement peaks, as it can be proved for a linear system that the ratio of successive displacement peaks is equal to the square root of the ratio of the total energy at the displacement peaks as described by Equation (6-4). For a nonlinear structure it is more appropriate to use the energy peaks as this takes the nonlinearity into account. Equation (6-5) describes the logarithmic decrement method adjusted for residual drift and using total energy peaks in place of the successive displacement, referred to in the next section as the adjusted logarithmic decrement energy method. When using the adjusted logarithmic decrement energy method in the following section the total energy in a PT wall system at displacement peaks was assumed to be equal to the gravitational potential plus the total stored strain energy. The total strain energy was calculated using the peak displacement and the correlated amount of energy stored under the force-displacement loop. The gravitational potential energy was calculated as the total mass multiplied by the acceleration due to gravity and the vertical displacement at the wall centre which was measured directly during the tests.

$$\frac{u_n}{u_{n+2}} = \sqrt{\frac{E_n}{E_{n+2}}} \quad (6-4)$$

$$\delta = \ln \left(\sqrt{\frac{\text{abs}(E_n - E_{n+1})}{\text{abs}(E_{n+1} - E_{n+2})}} \right) = \frac{2\pi\xi_{eq}}{\sqrt{1 - \xi_{eq}^2}} \quad (6-5)$$

6.5.7.2 EVD test results

The EVD was evaluated for the 2% drift test for SRW-FV-A using the three methods described by Equations (6-2), (6-3), and (6-5), that correspond to the logarithmic decrement method (ξ_o), the adjusted logarithmic decrement method (ξ_{Ad}), and the adjusted logarithmic decrement energy method ($\xi_{Ad-Energy}$). The calculated EVD for the three methods is plotted against the average of the drift peaks (u_a) in Figure 6.17(a). It is particularly important to use the average of the drift peaks when damping is high as the average can be significantly less than the initial peak drift of the cycle if the decay is rapid. Firstly, comparing the EVD calculated from the logarithmic decrement method (ξ_o) and the adjusted logarithmic decrement method (ξ_{Ad}), it is clear that there is increased reliability and stability of the EVD response by eliminating the effect of even slight residual drifts. By comparing the EVD calculated from the adjusted logarithmic decrement method (ξ_{Ad}) and the adjusted logarithmic decrement energy method ($\xi_{Ad-Energy}$), a decrease in EVD is shown at higher drifts but the same EVD is calculated at low drifts as the system is elastic and displacement peaks and energy peaks would give the same result. The energy method provides more realistic insight into the EVD of nonlinear systems as it accounts for the energy dissipated directly. Therefore ξ_o and ξ_{Ad} were not calculated or compared for the PreWEC wall systems.

The EVD was calculated using the adjusted logarithmic decrement energy method for each cycle and plotted against the corresponding average of the peak drifts of the respective cycle for SRW-FV-A in Figure 6.17(b) for both 1% and 2% drift tests. For SRW-FV-A both the 1% and 2% drift tests showed a similar EVD trend with drift, the damping is lower for higher displacements (early in the decay) and then damping increases as the wall exits full rocking and moves into vibrating within the stiffer portion of the force-displacement behaviour. The EVD was found to be 0.9% for displacements between 1.8-0.75% drift and increased up to 3.8% with decreasing drift. Also included in Figure 6.17(a) is the EVD evaluated from the cyclic test on an identical

wall (labelled SRW-B-CYCLIC in the plot) described in Chapter 5 using Equation (5-1) based on the hysteretic area of the force-displacement response. Interestingly much higher EVD was found for the cyclic test in comparison to the free vibration test, although a similar trend is observed with higher EVD at small amplitude cycles. The variability was considered to be partially due to the increased damage in the wall toe that accumulated during the cyclic test described in Chapter 5 that led to increased hysteretic energy dissipation. Although the damage was only minor and limited to the wall toe during the cyclic test, the different degree of damage is obvious when comparing the damage photos at the culmination of the two tests in Figure 6.18. However, the variability is also likely due to the method of EVD evaluation. Both the logarithmic decrement method and the hysteretic area based EVD method are valid in their own right for the respective test methods, however they are based on different theory and will result in different results.

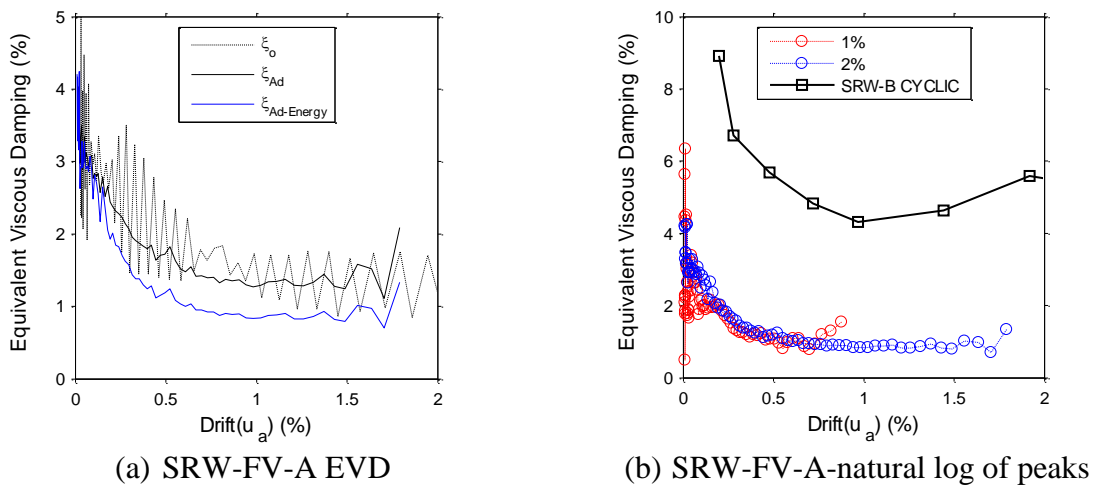
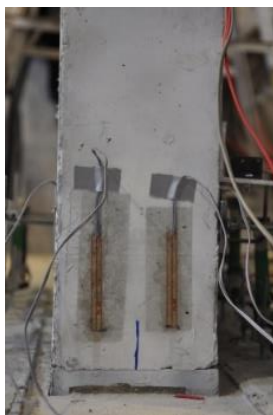
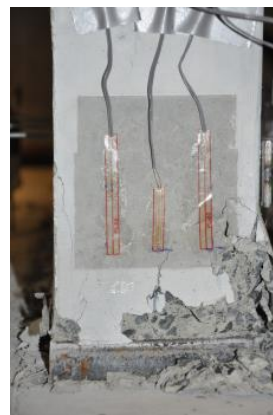


Figure 6.17 – SRW-FV-A EVD



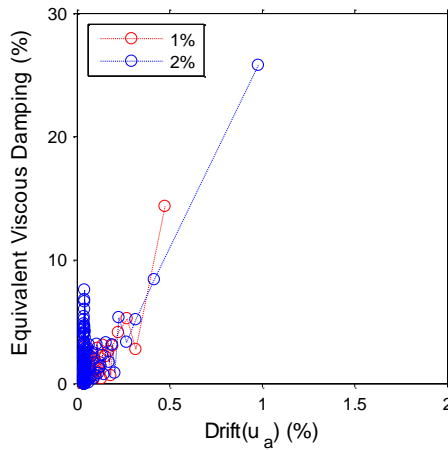
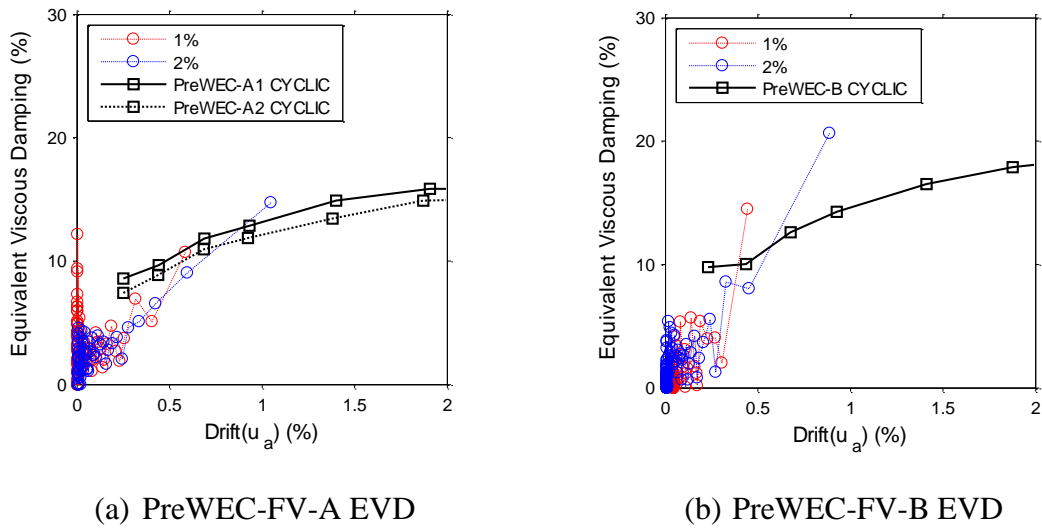
(a) SRW-FV-A



(b) SRW-A (Refer Chapter 5)

Figure 6.18 – Wall damage photo at end of test

The EVD was calculated using the adjusted logarithmic decrement energy method and plotted against the corresponding average of the peak drifts of the respective cycle for all PreWEC walls and is presented in Figure 6.19(a), (b), and (c). The highest EVD ratios calculated for PreWEC-A, B, and C at average drifts of 1.05%, 0.89%, and 0.98% were 14.7%, 20.7%, and 25.8%, respectively. All three PreWEC walls showed increasing EVD with increasing lateral drift. PreWEC-FV-A was expected to and had the lowest damping of the PreWEC walls as it had the lowest number of O-connectors per joint. PreWEC-FV-C attained the highest amount of EVD due to the higher number of O-connectors per joint and the lower PT force resulting in the highest hysteretic energy dissipation as described in section 6.5.5. Also included in Figure 6.19(a), and (b) is the EVD evaluated from cyclic tests presented in Chapter 5 on identical walls labelled PreWEC-A1/2-CYCLIC and PreWEC-B-CYCLIC. For the two cyclic test comparisons the free vibration EVD was consistently higher at high drifts and lower at drifts below 0.75%. Although there was a significant difference between the magnitudes of EVD ratio between the two test methods a similar trend was observed. The higher EVD ratio at higher drifts calculated for the free vibration response of the PreWEC walls is likely due in part to the inclusion of contact damping, but also due to the different test and evaluation methods as previously stated. The PreWEC walls suffered minimal damage when undergoing the snap back testing, and the cyclic test PreWEC walls suffered slightly increased damage in comparison to the snap back test walls but still minimal as reported in Chapter 5. Higher damping is found from the cyclic tests at low drifts due to the concrete crushing and O-connector yielding that occurred as the drift levels were slowly increased, while for the snap back testing less cycles were made at the lower drifts and the concrete crushing and O-connector yielding would have been incorporated into the higher drift response and then occurred to a lesser degree at the lower drifts.



PreWEC-FV-C EVD

Figure 6.19 – PreWEC walls EVD

6.6 CONCLUSIONS

An experimental investigation of the dynamic properties of unbonded PT precast concrete rocking walls was presented. One SRW and three PreWEC systems were subjected to snap back testing that included a monotonic pushover response and dynamic free vibration decay. During testing the walls behaved as expected, with rocking initiated at the wall base and negligible damage was observed for all specimens. In addition to examining the snap back test results, valuable comparisons were also made between the snap back tests and the cyclic testing that was reported in Chapter 5 on identical walls. As discussed subsequently a number of conclusions have been drawn based on the test observations and response comparisons.

Despite previous cyclic testing of identical wall specimens reported in Chapter 5 indicating significant residual drifts in the order of 0.1-0.4%, negligible residual drifts occurred during all snap back tests on all walls regardless of the PT force and number of O-connectors.

The fundamental frequency of all four wall systems was found to be significantly lower than the expected fundamental frequency calculated using a stiffness based on the gross section moment of inertia. This further confirmed the stiffness results found from pseudo-static cyclic testing performed on identical walls systems in Chapter 5. The proportion of the gross section moment of inertia required to attain the measured fundamental frequency was $0.48I_g$ for SRW-FV-A and between $0.74-0.8I_g$ for the PreWEC walls.

The advantage of a stiffness reduction with onset of rocking was highlighted by the acceleration that was controlled by the force capacity of the system, although this resulted in higher drifts and a longer decay time as demonstrated by SRW-FV-A. Also, the inclusion of more dissipaters decreased the accelerations seen by the wall when comparing systems of the same strength.

As expected SRW-FV-A exhibited an approximate bilinear response and the PreWEC walls showed increased strength and energy dissipation due to the addition of O-connectors under dynamic loading. The good alignment of the previously reported cyclic test with the pushover data and inertia force demonstrated the consistency in behaviour of unbonded PT walls regardless of loading rate.

The local parameters demonstrated that the dynamic behaviour of unbonded PT wall systems is well represented by pseudo-static tests for parameters such as neutral axis and PT force, however higher strains can be expected due to toe impact during dynamic rocking.

An adjusted logarithmic decrement energy method was used to evaluate the EVD of the four wall systems. SRW-FV-A was found to have EVD between 0.9-3.8% corresponding to drifts between 2-0%. PreWEC-FV-A, B, and C were found to have maximum EVD ratios of 14.7%, 20.7%, and 25.8% respectively. The EVD evaluated using the adjusted logarithmic decrement energy method and the snap back test data and EVD found from cyclic testing presented in Chapter 5 was compared. The snap back test EVD results showed increased EVD at high drifts for all PreWEC walls and lower EVD at low drifts when compared to the cyclic test EVD. This is due to the nature of the loading and the influence of dynamic effects. However, for SRW-FV-

A higher EVD was calculated for the cyclic tests in comparison to the snap back tests. This was due to the increased cycles and corresponding inelastic toe strains and damage observed in the cyclic test in comparison to the snap back test.

6.7 REFERENCES

13. Marriott, D., *The Development of High-Performance Post-Tensioned Rocking Systems for the Seismic Design of Structures*. 2009, University of Canterbury: Christchurch.
18. New Zealand Standard, *Concrete Structures Standard NZS 3101*. 2006: Wellington, New Zealand.
28. Henry, R.S., S. Sritharan, and J.M. Ingham. *Recentring requirements for the seismic deisgn of self-centering systems*. in *Proceedings of the Ninth Pacific Conference on Earthquake Engineering*. 2011. Auckland, New Zealand.
37. Housner, G.W., *The behavior of inverted pendulum structures during earthquakes*. Bulletin of the Seismological Society of America, 1963. **53**(2): p. 403-417.
62. Aaleti, S. and S. Sritharan, *A simplified analysis method for characterizing unbonded post-tensioned precast wall systems*. *Engineering Structures*, 2009. **31**(12): p. 2966-2975.
76. Ma, Q.T.M., *The mechanics of rocking structures subjected to ground motion*. 2010, University of Auckland. p. xxxii, 280 p.
108. New Zealand Standard, *Methods of test for concrete NZS 3112.2:1986 in Tests relating to the determination of strength of concrete*. 1986: Wellington.
110. Chopra, A.K., *Dynamics of structures : Theory and applications to earthquake engineering*. 3rd ed. 2007, Upper Saddle River, NJ: Prentice Hall. xxxiv, 876 p.
111. Barthes, C., M. Hube, and B. Stojadinovic. *Dynamics of a Post-Tensioned Rocking Block*. in *Proceedings of the 9th US National and 10th Canadian Conference on Earthquake Engineering*. 2010.
112. O'Hagan, J., *Damping*, in *Civil and Environmental Engineering*. Unpublished, The University of Auckland: Auckland.

Chapter 7

SHAKE TABLE TESTING

Presented in this chapter are shake table tests of one single rocking wall (SRW) and two Precast Wall with End Column (PreWEC) systems performed on a unidirectional shake table. The shake table tests extended on the previously reported pseudo-static cyclic and snap back tests reported in Chapter 5 and 6. Shake table testing provides the most realistic loading conditions to a real earthquake as it includes not only the restoring force but inertia and damping forces. The primary objective of the shake table testing was to verify the seismic performance of SRW and PreWEC systems using real earthquake ground motions, including validation of the wall system concepts, DDBD design procedure, and construction details. Secondly, the investigation compared the response of three systems with varied energy dissipation and provided a systematic investigation into the dynamic behaviour of unbonded PT walls subjected to different ground motion intensity levels.

7.1 DESIGN AND CONSTRUCTION OF SHAKE TABLE TEST PROGRAMME

The shake table testing programme consisted of three walls that had the same specifications and design parameters as three of the walls tested in the cyclic and snap back testing reported in

Chapter 5 and Chapter 6. The three model walls tested are referred to as SRW-ST-A, PreWEC-ST-A and PreWEC-ST-B. As explained in detail in later sections two testing sequences were performed on PreWEC-ST-B that are referred to as PreWEC-ST-B1 and PreWEC-ST-B2. The design parameters of each test wall are provided in Table 7.1, and more extensive details of the wall design and construction were reported in Chapter 4. The achieved initial prestress for each test is given alongside the target in Table 7.1, which were 699 MPa, 700 MPa, and 697 MP for SRW-ST-A, PreWEC-ST-A and B2, respectively. The Axial Force Ratios (AFR) calculated from the measured material properties and PT forces for walls SRW-FV-A, PreWEC-FV-A, and B2 were 10.5%, 9.6%, and 9.5% respectively. The wall PT tendons had a typical unbonded length of 3600 mm as described in Chapter 4. The PT tendon anchorage detail was the same as that described in Chapter 5. The detailed design of the reinforcement and confinement was described in Chapter 4.

Table 7.1 – Wall specifications

Wall Label	f_{pi} (MPa)		$f'_{c,test}$ (MPa)	$f'_{g,test}$ (MPa)	AFR (f_c/f'_c) (%)		O - Connectors per joint
	Target	Achieved			Target	Achieved	
SRW-ST-A	696	699	32.1	56.2	7.5	10.5	-
PreWEC-ST-A	696	700	35.3	54.7	7.5	9.6	4
PreWEC-ST-B(2)	696	697	35.3	70.2	7.5	9.5	6

As presented in Table 7.1, PreWEC-ST-A, and B were designed to have four and six O-connectors per joint, respectively, creating two systems with different quantities of hysteretic energy dissipation and varying flexural capacities. The PreWEC models were theoretically over-designed for the given prototype scenario, which was based on the design of SRW-A. However, for ground motion scaling purposes the SRW design spectrum and the DDBD procedure previously discussed in Chapter 4 were used to back calculate a design drift target and effective period for each of the PreWEC systems given their additional strength and damping. The back calculation procedure involved repeating the DDBD procedure outlined in Chapter 4 for the specified design displacement spectra and the measured wall parameters given in Table 7.1. The as built parameters such as concrete strength were used in the simplified analytical method proposed by Aaleti and Sritharan [62] to determine the force displacement behaviour of the PreWEC walls and the EVD was evaluated using Equation (7-2), previously described in Chapter

2, an option for EVD determination recommended by the PRESSS Design Handbook that ignores ductility and assumes externally mounted mild steel yielding devices. The back calculation method involved an iterative process where a design drift was guessed, an EVD estimated using Equation (7-2), an effective period calculated, the displacement spectra reduced according to the damping modifier (η), as described by Equation (4-9), and finally the final drift estimated. The initial drift was then updated based on the calculated final drift until the initial drift and final drift matched for the given wall properties. A final design drift and effective period were determined on this basis for the PreWEC systems. The SRW design drift and effective period were also updated for the as built properties. Table 7.2 describes the moment capacity, EVD, effective period at design drift, and design drift for each of the model walls.

$$\eta = \left(\frac{7}{2 + \xi_{eq}} \right)^{\alpha_{SF}} \quad (7-1)$$

Where α_{SF} is equal to 0.5 for sites located away from a major fault and the ground motions do not comprise of near-fault, forward directivity. Note: due to the limited velocity of the shake table, ground motions comprising of near-fault, forward directivity could not be accurately replicated and were therefore not selected as discussed in section 7.3.1, this is why 0.5 was chosen for α_{SF} instead of 0.25 for sites located near a major fault.

$$\xi_{eq} = \frac{\lambda}{\lambda + 1} 5\% + \frac{1}{\lambda + 1} 23.4\% \cdot 0.67 \quad (7-2)$$

Table 7.2 - Design values for SRW and corresponding values for PreWEC

Wall	Drift	M _{capacity} (kNm)	EVD	T _e (s) (model)	T _e (s) (Prototype)
SRW-ST-A	1.27%	148.7	5%	0.298	1.49
PreWEC-ST-A	0.57%	194.6	7.01%	0.179	0.897
PreWEC-ST-B	0.49%	205.3	7.50%	0.162	0.809

7.1.1 Material properties

In accordance with New Zealand Standards [108] test cylinders and cubes were used to determine the compressive strength of each wall and the grout pad. The measured concrete ($f'_{c,test}$) and grout ($f'_{g,test}$) strengths on the day of testing for each wall are provided in Table 7.1. As stated in Chapter 4, 15.2 mm strand was used for the wall PT tendons for all three wall

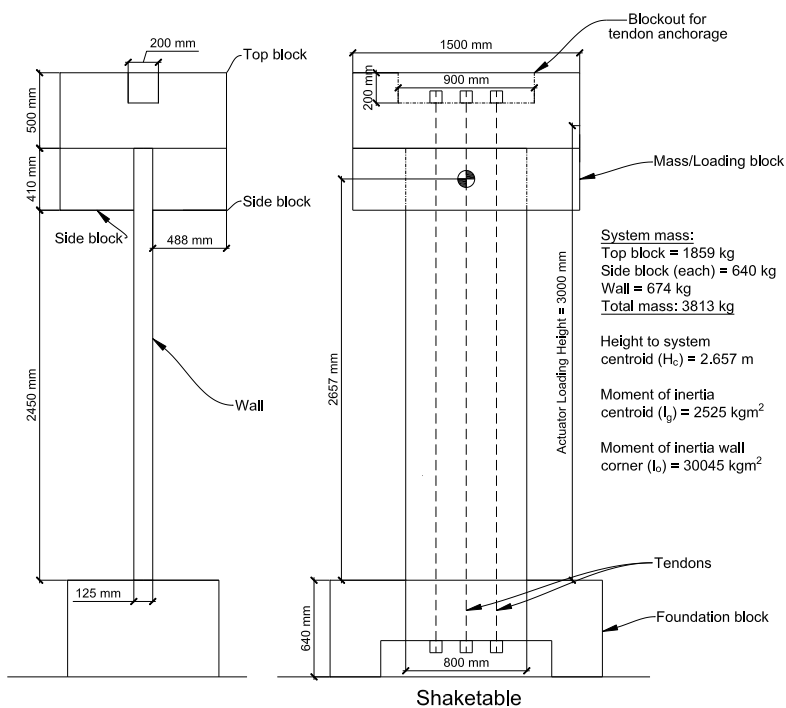
systems. The material properties of the PT strand and vertical and horizontal reinforcement have already been reported in Chapter 4 and are consequently not reiterated here.

7.1.2 O-connector properties

Each wall and corresponding two end columns in each PreWEC system were connected horizontally by 10 mm thick mild steel O-connectors. Expected structural responses and construction details of the O-connectors incorporated in the test units are specified in Chapter 4 and are referred to as connector type “O1” in Chapter 3.

7.2 TEST SETUP AND INSTRUMENTATION

A schematic of the typical test setup with key geometric parameters is presented in Figure 7.1(a) for SRW-ST-A. The set-up was identical for the PreWEC walls except with the addition of two end columns and the previously indicated number of connectors. A photo of the PreWEC-ST-A test before onset of shake table testing is presented in Figure 7.1 (b).



(a) Test setup



(b) Photo

Figure 7.1 – Test setup details schematic and photo

The assembly and construction process was identical to that already presented in Chapter 5 and 6 except that the foundation was post-tensioned to the shake table in place of the strong floor. The wall panel was erected on the foundation block and shimmed 30 mm above the surface of a 40 mm recess inside the foundation. High strength grout was flowed under the wall to fill the pocket and provide an even bearing surface at the wall-to-foundation interface. The walls were embedded approximately 10 mm into the grout pocket to increase the sliding shear resistance. To limit the concrete compressive strains in the toe region the walls had a foam strip glued across the width of the cover region at each wall end as described in Chapter 5. It is important to note that use of the foam strip effectively shortened the length of the wall by 30 mm to 770 mm, despite the panel length being 800 mm. Concrete mass blocks were attached and grouted at the top of the wall for seismic mass and steel beams were assembled on both sides of the setup at the mass height to prevent significant out-of-plane deformations.

Extensive instrumentation was employed to measure the behaviour of the test walls with the typical sensor layout shown in Figure 7.2. Displacement gauges were used to measure wall lateral displacement, wall uplift, and potential slip at the wall-foundation interface, wall-anchorage block interface and the foundation and shake table interface. Strain gauges were placed at the wall toes to capture the peak compressive strains. Load cells were used to measure and apply the tendon forces in the wall and columns. For each PreWEC test, displacement gauges were also used to measure the relative vertical and horizontal displacement along each column-wall joint to capture the displacements applied to the O-connectors. An array of accelerometers were used to measure in-plane, out-of-plane, and vertical accelerations at several locations on the test setup as presented in Figure 7.2. The data acquisition system recorded at a sampling rate of 2000 Hz. All of the dynamic test data reported has been filtered with a 25 Hz low pass filter to remove any high frequency noise from the data acquisition system unless otherwise stated, and all lateral motion results are reported at the height of the centre of mass.

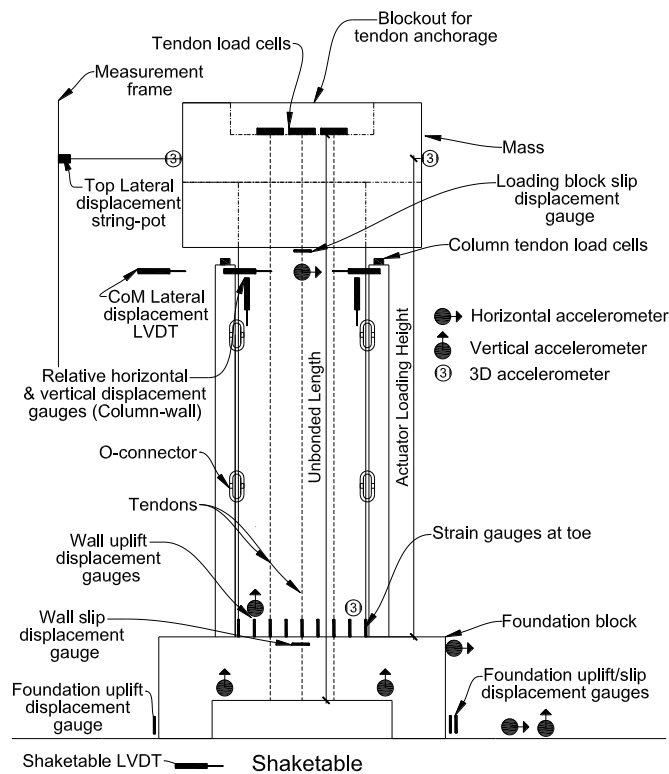


Figure 7.2 – Test instrumentation schematic

7.3 TESTING PROCEDURE

Testing consisted of subjecting each wall to a series of scaled and unscaled ground motions at a variety of intensity levels in an attempt to get a broad spectrum of motions that would allow good understanding of the behaviour of unbonded PT walls subjected to ground motions. SRW-ST-A was also subjected to an additional series of harmonic excitations as the low damage nature of the system meant almost unlimited testing could be conducted and it was of interest to investigate any resonant behaviour that may occur with SRW-ST-A. The ground motions were chosen and scaled based on a number of criteria that are outlined and explained below.

7.3.1 Ground motion scaling

The method for selecting and scaling ground motions followed that used for Nonlinear Time History Analysis (NLTHA) usually undertaken in practice, closely following the method recommended in the New Zealand loadings standard [101] for the spectrum compatible test sequences. All the ground motions applied to the test walls including those that were not

spectrum compatible were scaled to ensure the velocity limit of the shake table was safely not exceeded and for similitude requirements where specified.

7.3.1.1 NZS1170 scaling and ground motion selection

The New Zealand loadings standard [101] requires that a family of not less than three ground motion records be used for numerical time history analyses with the maximum response used for design. It is common in other codes around the world to use a minimum of seven spectrum compatible records with the average being adopted for the response parameter. As such a suite of seven ground motions were selected as the average response parameters were most useful to assess the performance of the wall designs.

Although NZS1170.5 provides sections that define the criteria for the selection and scaling of records to be used in time-history analysis, there is little guidance on which records to use for different locations. Oyarzo-Vera et al. [113] addresses this issue and provides recommendations on suites of seven records to use for different site soil classes (C and D) and different zones that are considered to have relatively uniform seismological characteristics in the North Island of New Zealand. The suite of records recommended by Oyarzo-Vera et al. [113] for Wellington site soil class C were initially chosen to be considered as the ground motions to be used during the shake table tests. The uni-directional shake table at the University of Auckland has a displacement capacity of ± 200 mm and a velocity limit of 276 mm/s. Since three of the seven records recommended by Oyarzo-Vera et al [113] contained forward directivity pulses they were difficult for the shake table to replicate considering this velocity limit. As a result, two of the records were unable to be accurately replicated with sufficient accuracy on the shake table due to the records containing velocities of up to 1 m/s. The five records that were able to be accurately replicated on the shake table were Tabas (Iran), Duzce (Duzce, Turkey), HKD085 (Hokkaido, Japan), El Centro (Imperial Valley, USA), and La Union (Mexico). Two further records that could be better replicated on the shake table were selected, these were San Fernando and Loma Prieta. These two records were chosen due to the familiarity that the earthquake engineering community has with these records because they were used in the PRESSS Programme pseudo-dynamic testing and were near what would be considered site soil class C for New Zealand. All seven records were downloaded from either the PEER database (<http://peer.berkeley.edu/smcat/>) or Cosmos (<http://strongmotioncenter.org/>) and the details are given in Table 7.3 and the unscaled records used are presented in Figure 7.3.

Table 7.3 – Summary of raw earthquake ground motions

Ground motion	Earthquake	Year	Station	M_w
GM1	Tabas (Iran)	1978	Tabas	7.4
GM2	San Fernando (USA)	1989	LA Hollywood	6.6
GM3	Loma Prieta (USA)	1971	Saratoga Aloha Ave	6.9
GM4	Duzce (Turkey)	1999	Duzce	7.1
GM5	Hokkaido (Japan)	2003	HKD085	8.3
GM6	La Union (Mexico)	1985	La Union	8.1
GM7	Imperial Valley (USA)	1940	EI Centro	7.0

M_w is the moment magnitude, PGA is the Peak Ground Acceleration, and PGV is the peak ground velocity, PGA and PGV are both the geometric mean of the two directions.

As previously stated, the suite of selected earthquakes were scaled using the procedure outlined by the New Zealand loadings standard (NZS1170.5) [101]. Each selected record has two record components and they must both be scaled by two factors: the record scale factor (k_1) and the family scale factor (k_2). The principal component is determined as the component that has the smaller k_1 value. The aim of the NZS 1170.5 procedure is to minimise the difference between the response spectra of the chosen records and the target spectrum in the period range of interest. NZS 1170.5 defines this range of period to be between $0.4 T_1$ and $1.3 T_1$, where T_1 is the largest translational period in the direction being considered. Priestley et al. [20] emphasises the importance of the appropriate selection of the period range of interest when spectrum matching, and states that it is best practice to use longer periods that include the period shift expected as the structure responds nonlinearly. As a result for ground motion scaling the minimum period was defined as the fixed base period and the maximum period was defined as the effective period from DDBD for the design level for each wall individually. By using the effective period from DDBD as the maximum period the period lengthening associated with rocking was accounted for. The fixed base period can be a difficult parameter to estimate accurately for reinforced concrete walls due to the effective stiffness changing depending on a number of parameters. Fortunately, the fixed base period has been calculated for similar walls to those tested herein in previous Chapter 5 and 6. As a result an effective stiffness modifier (ESM) of 0.625 was used for SRW-ST-A and 0.78 for the PreWEC systems when calculating the stiffness and corresponding period. The fixed base and design periods for both the model and prototype scale are given in Table 7.4.

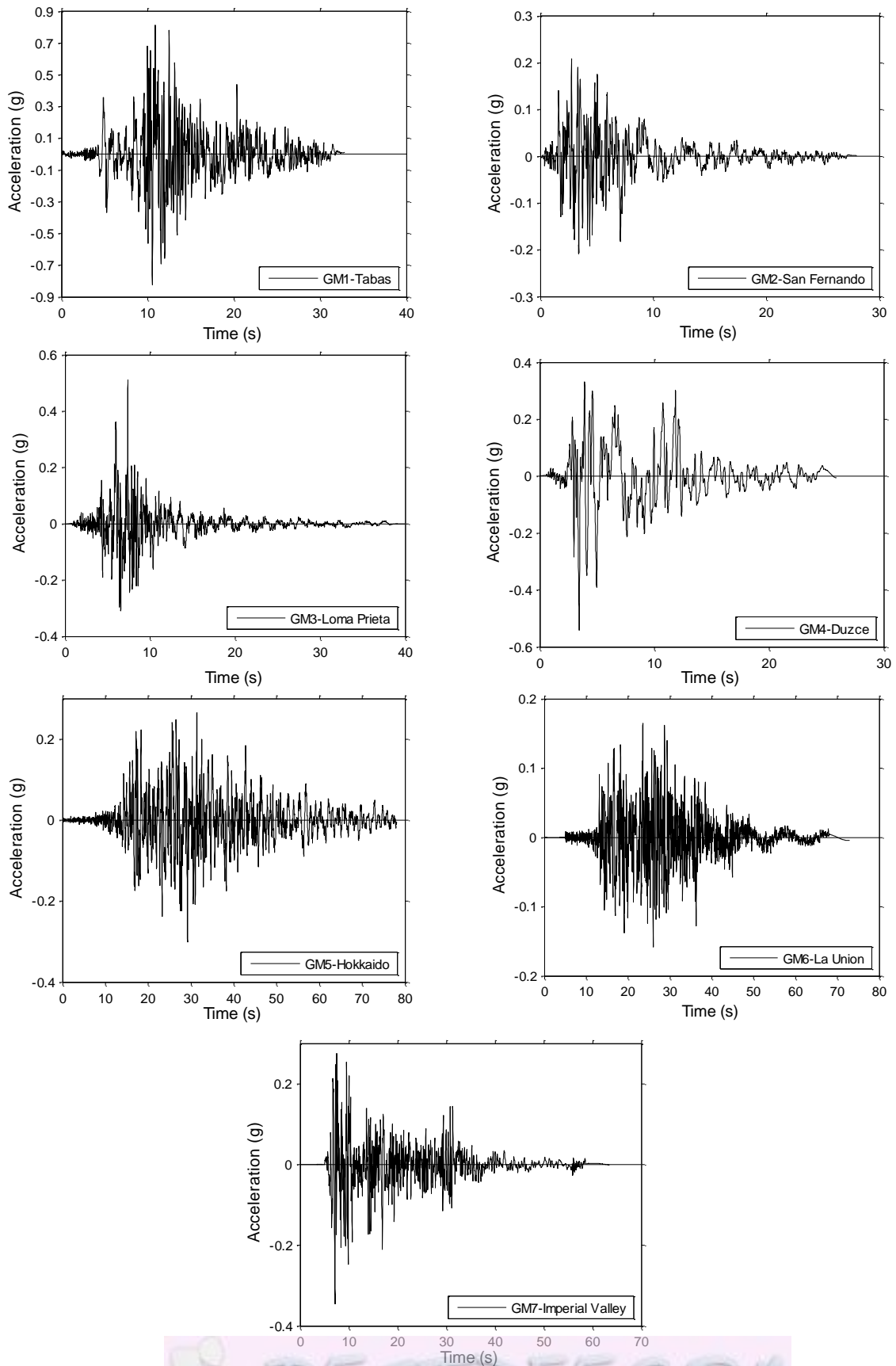


Figure 7.3 – Unscaled principal component of spectrum compatible ground motions

Each principal component of each ground motion was scaled by the corresponding k_1 and k_2 values for the design spectrum specified in the DDBD between the period values given in Table 7.4. The k_1 and k_2 scale factors used for each wall and each ground motion component are presented in Table 7.5. The unscaled and scaled principal component spectrums of the seven ground motions for the design level event are presented in Figure 7.4 for all three walls.

Table 7.4 - Fixed base and effective periods of walls

Wall label	Period	
	Fixed Base (T_{min})	Design effective (T_{max})
SRW-ST-A	0.11	0.298
<i>Prototype SRW</i>	0.55	1.49
PreWEC-ST-A	0.096	0.179
<i>Prototype PreWEC-A</i>	0.48	0.897
PreWEC-ST-B	0.096	0.162
<i>Prototype PreWEC-B</i>	0.48	0.809

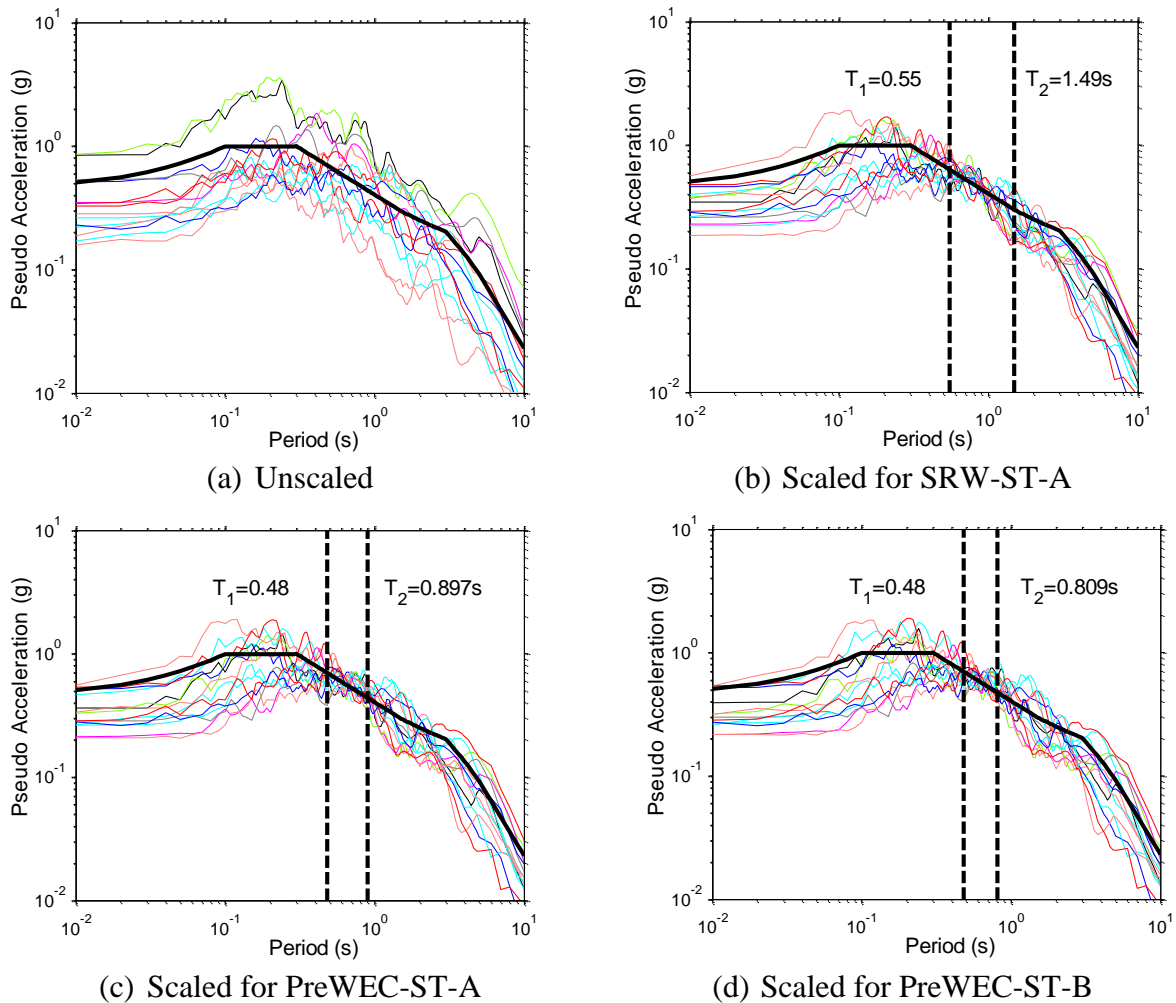


Figure 7.4 – Scaled and unscaled pseudo acceleration spectra for all ground motion components (Target design spectrum in solid black)

Table 7.5 – Scaling factors for each wall

Ground motion	SRW-ST-A		PreWEC-ST-A		PreWEC-ST-B	
	k_1	k_2	k_1	k_2	k_1	k_2
GM1	0.410		0.409		0.443	
GM2	1.808		2.007		2.214	
GM3	0.894		0.963		0.961	
GM4	0.486	1.0	0.506	1.05	0.533	1.048
GM5	0.657		0.699		0.726	
GM6	1.532		1.478		1.460	
GM7	0.854		0.792		0.788	

In addition to the suite of seven scaled spectrum compatible ground motions already discussed a further suite of three natural scale ground motions was used during the test sequence on each wall. Each of the three ground motions were from recent earthquakes that included Chile (2010 station: Santiago, 100% amplitude referred to as GM8), Christchurch (2011 station: Christchurch REHS, 100% amplitude referred to as GM9), and Kobe (1995 station: Takatori, 60% amplitude referred to as GM10). The unscaled acceleration time history of each of the recent earthquake ground motions is presented in Figure 7.5.

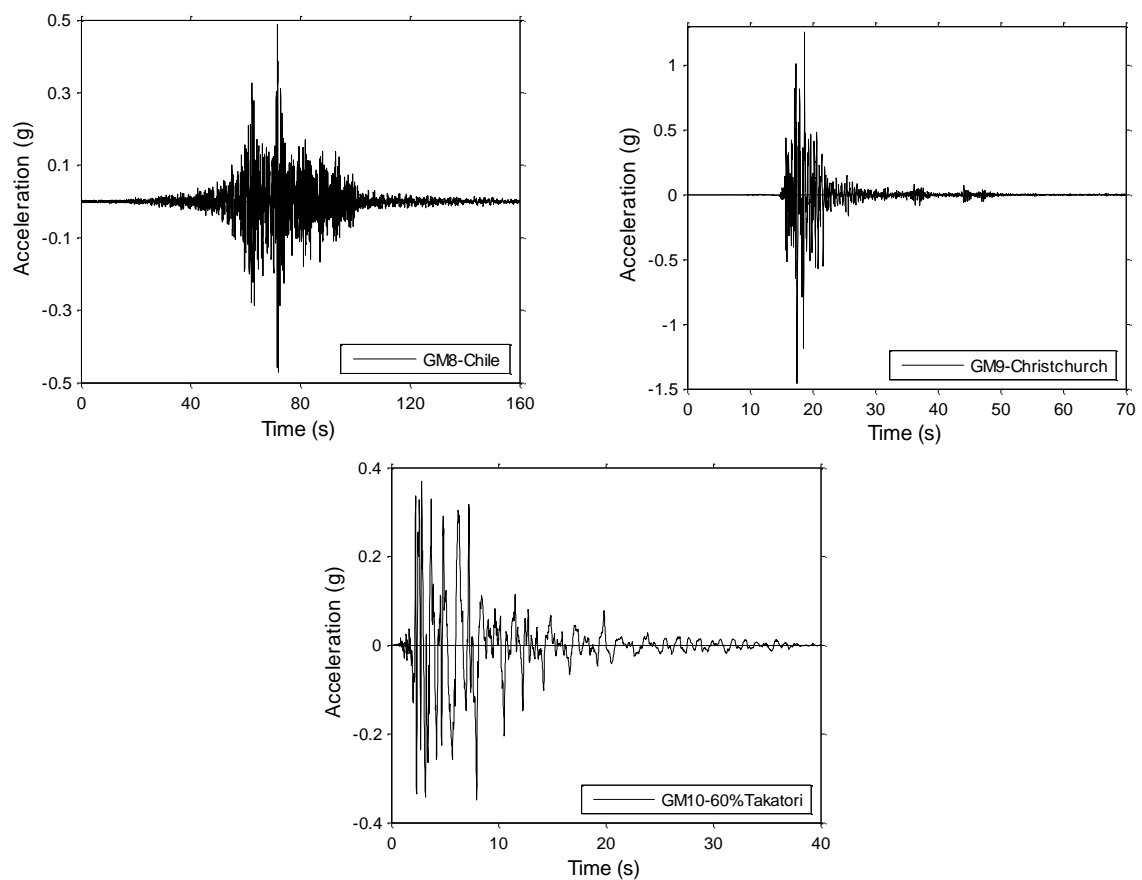


Figure 7.5 – Unscaled acceleration time history of each recent ground motion

This suite of three records (GM8, GM9 & GM10) was not scaled for a spectrum but kept at natural scale to observe the behaviour of the walls under natural scale earthquakes and allow direct comparison between the three test walls as identical ground motions were applied.

7.3.1.2 *Scaling for similitude and shake table limitations*

To comply with similitude requirements presented in Chapter 4 the acceleration of the records was scaled up by a factor of 5 and time was compressed by a factor of 5 for all spectrum compatible motions. The three recent ground motions were run twice, once with the similitude scaling and once without.

No two earthquakes are identical and attempting to replicate a ground motion on a shake table is inevitably subject to some error. As previously discussed the shake table used had a velocity limit of 276 mm/s which inhibited the ability of the shake table to perfectly replicate the desired ground motions. If the desired ground motions are run and the shake table attempts to go above the velocity limit, high acceleration spikes may occur. To avoid acceleration spikes and velocity saturation the records were scaled for the velocity limit of the shake table. The spectrum compatible ground motions were velocity scaled at the design intensity level as this was of most interest. Velocity scaling entails following a method described by Chase et al [114] and used by Marriott [13] that adjusts the velocity when the table limit is exceeded while still attempting to maintain the same pseudo-acceleration response. An example of this method is presented in Figure 7.6(a), (b), and (c) which shows the original acceleration, velocity and displacement overlaid on the modified acceleration, velocity and displacement. No significant deviation from the original records is observed, only the velocity has a noticeable difference with the velocity spike truncated. The pseudo-acceleration response spectra for both the modified and original acceleration time history is presented in Figure 7.6 (d). The region of interest is between the two black dashed lines that indicate the period limits applied during the spectrum scaling, hence the region of spectrum likely to affect the test walls. As observed the difference is negligible and so the velocity scaling method was considered acceptable.

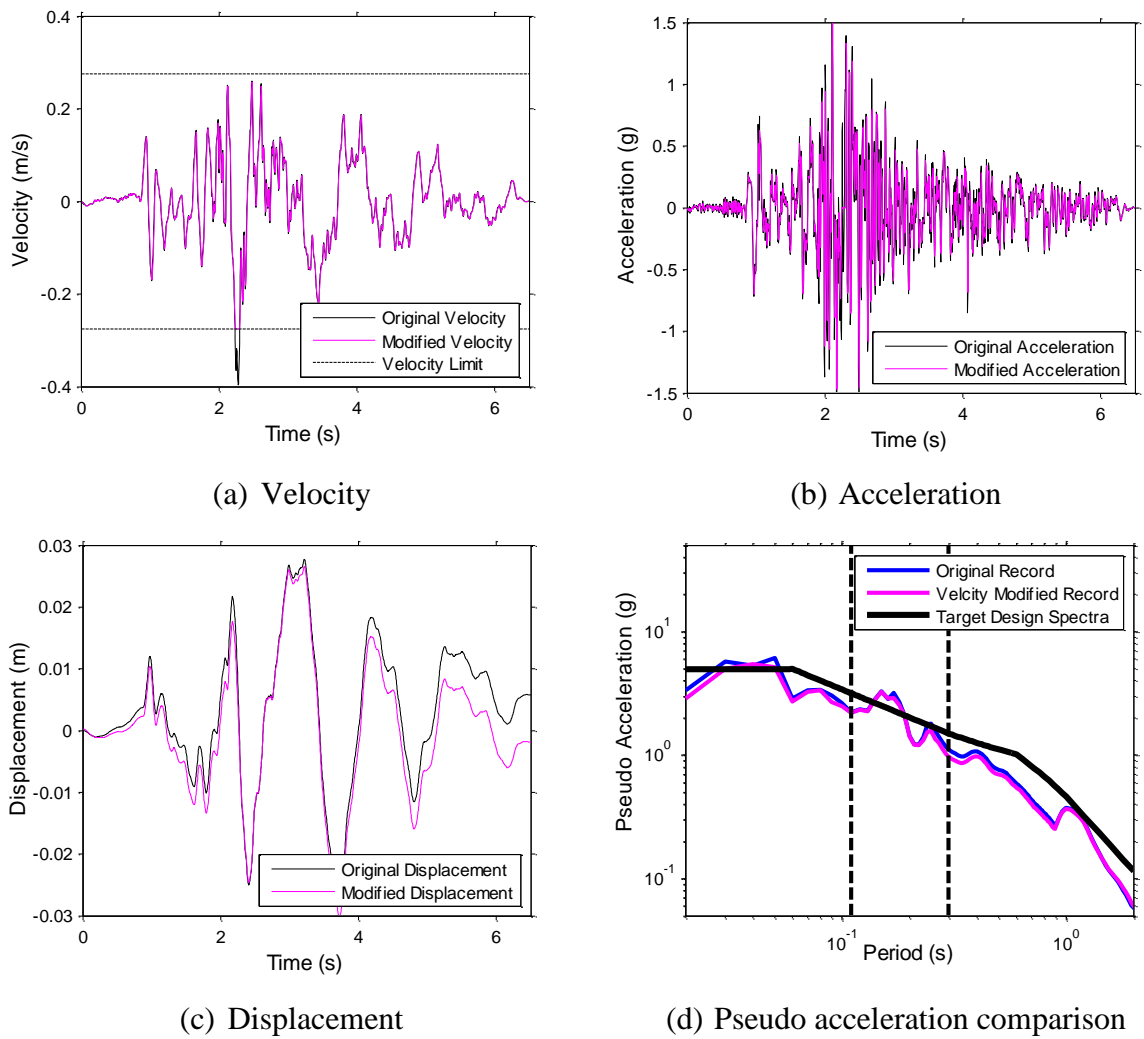


Figure 7.6 – Example comparison of pseudo-acceleration response for velocity scaled record at model scale after spectrum scaling

7.3.2 Test sequence

To evaluate the performance of the systems six intensity levels were determined based on amplifying or reducing the design level previously defined in Chapter 4 for a location in Wellington with site soil class C, S_p of 0.7, D of 0 and a return period of 1/500 years. The six intensity levels based on this design level were:

- **EQ-I:** 1/25 year event ($R=0.25$) – Serviceability I
- **EQ-II:** 1/100 year event ($R=0.5$) – Serviceability II
- **EQ-III:** 1/500 year event ($R=1.0$) – Design Level
- **EQ-IV:** 1/1500 year event ($R=1.5$) – Maximum intensity for SRW
- **EQ-V:** >1/2500 year event ($R=2.25$) – Higher demand applied to PreWEC walls
- **EQ-VI:** >>1/2500 year event ($R=3.0$) – Higher demand applied to PreWEC walls

For each test wall the suite of spectrum compatible ground motions were scaled to the EQ-III level for the appropriate period range. The scaled design level records were then amplified or reduced according to the R value of the other intensity levels. The 5% damped acceleration design spectrum for each of the six intensity levels are shown in Figure 7.7. Intensities EQ-V and VI were applied only to the PreWEC systems in an attempt to attain what can be considered appropriate ‘design’ level drifts in the order of 1-2%. The higher intensity was required for the PreWEC systems due to their increased moment capacity when compared to SRW-ST-A.

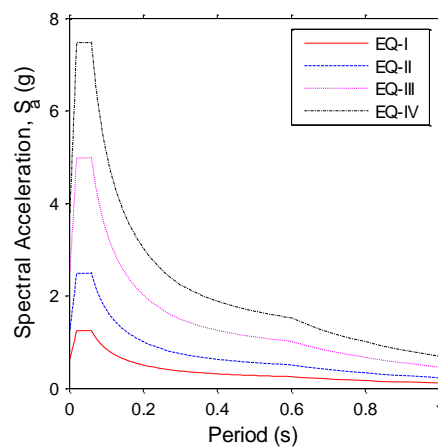


Figure 7.7 – Model scale design acceleration spectrum for first four intensity levels

SRW-ST-A was subjected to EQ-I through IV to represent the intensity levels up to the maximum considered event that is commonly referred to as 1.5 times greater than design. The seven ground motions in the suite were run in numerical order for intensity levels EQ-I to EQ-III and then in numerical order except GM-2 was shifted to the end of the sequence as a particularly large response was observed during the design level intensity (EQ-III). After the four levels of spectrum compatible ground motions EQ-III:GM2 (labelled with ‘R’) was repeated three times as a higher response was observed during EQ-III than EQ-IV. Between repeat two and three SRW-ST-A was restressed to check the sensitivity of the results to the exact PT force. Following the spectrum compatible tests the similitude scaled Recent Ground Motions (RGM) suite (RGM-I) was applied, and subsequently the same recent ground motion suite without similitude scaling (RGM-II). The final phases of testing on SRW-ST-A consisted of various harmonic loading that are described in Table 7.6. White noise tests were performed at the start of testing, after each of the suites of EQ-I and EQ-II and then after every individual motion from the start of intensity level EQ-III until culmination of the test sequence. The general test sequence is given in Table 7.7.

PreWEC-ST-A was subjected to EQ-I through IV followed by RGM-I and II, and finally EQ-V and EQ-VI. White noise tests were performed at the start of testing, after each of the suites of EQ-I and EQ-II and then after every individual motion from the start of intensity level EQ-III until culmination of the test sequence. The general test sequence of PreWEC-ST-A is given in Table 7.7 in comparison to the other walls.

Table 7.6 – Harmonic loading tests

Test Label	Motion Label	Frequency (Hz)	Duration (s)	Amplitude (mm)
HM-1	Sweep-sine 1 (SS1) (linear)	0-12	20	5
	Sweep-sine 2 (SS2)	0-10	10	5
HM-2	Sine 1 (SN1)	2.5	10	2
	Sine 2 (SN2)	7.5	10	5
	Sine 3 (SN3)	5	10	3
	Sine 4 (SN4)	4	15	3
	Sine 5 (SN5)	12	5	3
	Sine 6 (SN6)	3	20	5
	Sine 7 (SN7)	4	12	5

Table 7.7 – General ground motion loading sequence

Test Label	Description	SRW-ST-A	PreWEC-ST-A	PreWEC-ST-B1	PreWEC-ST-B2
EQ-I	Suite of spectrum compatible ground motions of R=0.25	•	•	•	•
EQ-II	Suite of spectrum compatible ground motions of R=0.5	•	•	•	•
EQ-III	Suite of spectrum compatible ground motions of R=1.0	•	•	•	•
EQ-IV	Suite of spectrum compatible ground motions of R=1.5	•	•	•	•
RGM-I	Suite of recent ground motions similitude scaled	•	•	•	•
RGM-II	Suite of recent ground motions without similitude scaling	•	•	•	•
EQ-V	Suite of spectrum compatible ground motions of R=2.0		•	•	•
EQ-VI	Suite of spectrum compatible ground motions of R=2.5		•		•
HM Series	Harmonics described in Table 7.6	•			

PreWEC-ST-B was subjected to EQ-I through IV followed by RGM-I and II, and finally EQ-V. During EQ-V GM2 the weld connecting one of O-connectors to the wall began to fracture. This was due to insufficient weld quality and all the O-connectors were removed and replaced and the entire test series re-run. The first test series is referred to as PreWEC-ST-B1 and the second referred to as PreWEC-ST-B2. The second test series (B2) underwent the same test sequence as PreWEC-ST-A as shown in Table 7.7. The first test sequence still provides useful data up until the onset of weld fracture and provides a good opportunity to investigate the consistency of results. White noise tests were performed at the start of testing, after each of the suites of EQ-I and EQ-II and then after every individual motion from the start of intensity level EQ-III until culmination of the test sequences.

White noise tests were performed before and after significant shaking to measure and detect any changes in the vibration properties of the test walls that may indicate non-visible degradation. All white noise tests were generated by the shake table controller to have an amplitude of 3 mm for a frequency range of 0 to 25 Hz for 5s duration. All walls were intended to be stressed to 696 MPa for each tendon at the start of each test sequence. The achieved initial PT values were given in Table 7.1. During the testing of all walls if the initial PT decreased more than 5% the wall was restressed. This resulted in SRW-ST-A being restressed three times, PreWEC-ST-A not being restressed and PreWEC-ST-B being restressed once between B1 and B2 test sequences.

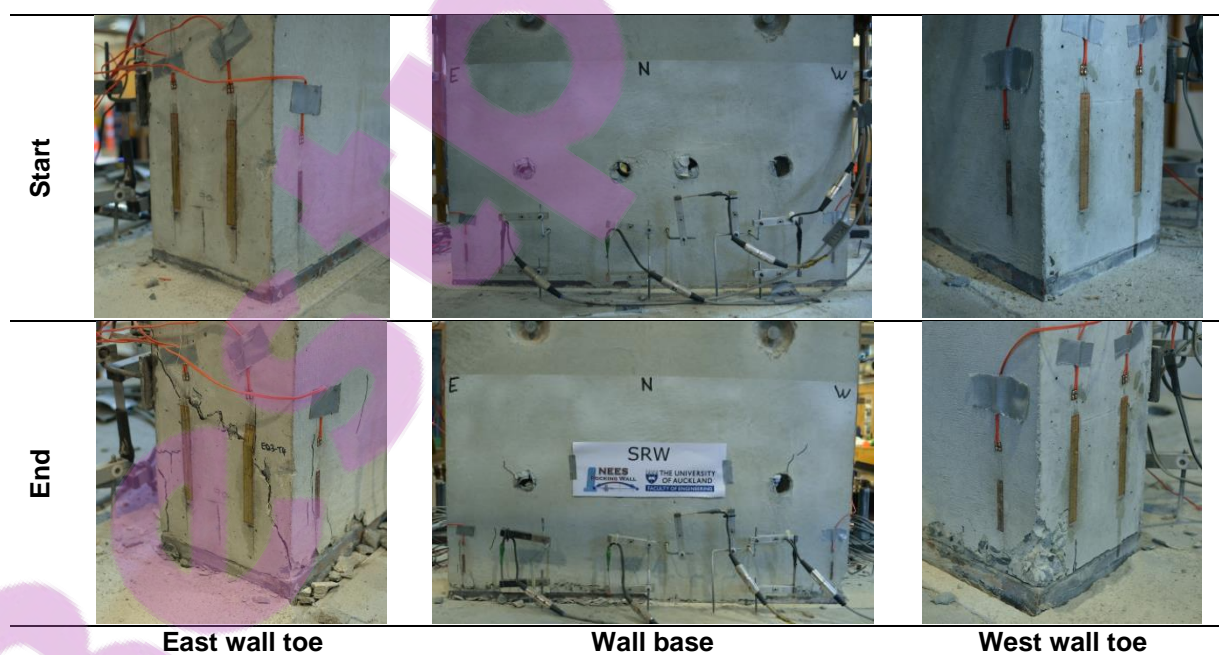
7.4 TEST OBSERVATIONS AND WHITE-NOISE TESTS

The three walls tested performed as expected displaying excellent seismic behaviour under many ground motions. All walls demonstrated rocking behaviour with uplift occurring at the wall-foundation interface and the column-foundation interface. No distributed flexural cracks were observed on any wall and any damage was confined to cracking and crushing in the wall toes and yielding of the O-connector dissipaters, similar behaviour to that observed during the cyclic tests reported in Chapter 5. Also, videos of the shake table tests performed can be viewed at: <https://www.youtube.com/user/UoAConcrete>.

7.4.1 SRW-ST-A

The condition of SRW-ST-A both before and after the completion of testing is shown in Table 7.8. Only minor damage was observed in the wall toes of SRW-ST-A after undergoing more than 40 ground motions which did not affect the wall performance. The largest crack sustained in the east wall toe occurred during EQ-IV: GM3 and did not penetrate further than the cover concrete.

Table 7.8 – SRW-ST-A photos of wall condition before and after testing



To measure and monitor the natural frequency and damping of the test walls, band limited white noise tests were run before and after the suite of EQ-I and EQ-II and before and after each ground motion from the start of EQ-III. Transmissibility theory of single degree of freedom systems was used to determine the frequency and damping from each white noise test. A transmissibility transfer function was obtained for each white noise test by dividing the transform of the acceleration response at the centre of mass (output) by the transform of the driving white noise acceleration (input). Specifically, the transmissibility transfer function was calculated by first calculating the cross spectral density and power spectral density of the two signals in the Fourier domain and subsequently taking the ratio of those at any frequency which provides the transmissibility transfer function. This was done with guidance by Inman who described how transfer functions can be used to measure structural properties from vibration data [115]. After the transmissibility transfer function was obtained an EVD and fundamental frequency were calculated based on the best fit values to the transfer function data when used in the SDOF equation for transmissibility described by Equation (7-3) [116], as shown in Figure 7.8. This method assumes a linear structure which is true for the white noise tests as no uplift occurs, as a result the EVD represents an estimate of the inherent damping of the walls.

$$TR = \left| \frac{F_T}{F_0} \right| = \sqrt{\frac{1 + (2\xi\omega/\omega_n)^2}{[1 - (\omega/\omega_n)^2]^2 + [2\xi\omega/\omega_n]^2}} \quad (7-3)$$

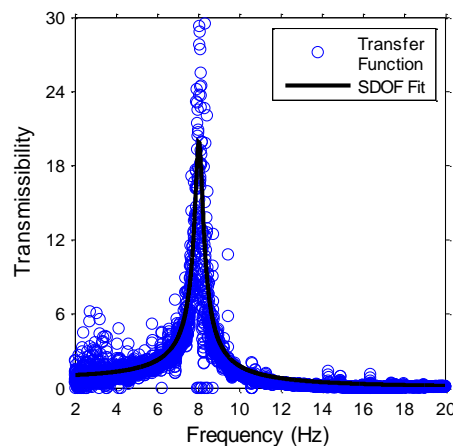


Figure 7.8 – Example transfer function with fitted curve

The change in EVD and fundamental frequency throughout the test sequence of SRW-ST-A is shown in Figure 7.9 for the earthquake ground motions and in Figure 7.10 for the harmonic ground motions. It is clear from Figure 7.9 and Figure 7.10 that the fundamental frequency

dropped steadily until halfway through EQ-IV when it levelled off and remained reasonably constant for the remainder of the test sequence. At the start of the test sequence the frequency was 7.91 Hz which correlated well with the fixed base period of 0.11s or 9.1 Hz used when scaling the spectrum compatible records as stated in Table 7.4. From the start to the end of the test sequence there was a drop in fundamental frequency of 25% which demonstrated significant stiffness degradation, despite minimal observable damage. This is similar to the cyclic test findings of Chapter 5, where it was reported that SRW-A suffered minimal damage but showed stiffness degradation in the hysteretic behaviour. As previously discussed the largest crack in the east wall toe occurred during EQ-IV: GM3, which was between WN-10 and 11. There was a small noticeable drop in frequency corresponding to the damage (recall that GM2 was shifted to end of the EQ-IV intensity level hence GM3 was the second ground motion run). Following EQ-IV: GM3 the wall was restressed and there was a slight increase in fundamental frequency. The EVD or inherent damping during all ground motions remained relatively constant. The average EVD during each of the earthquake and harmonic ground motion series were 3.62% and 3.32% respectively. These give an overall average for SRW-ST-A of 3.47% inherent damping.

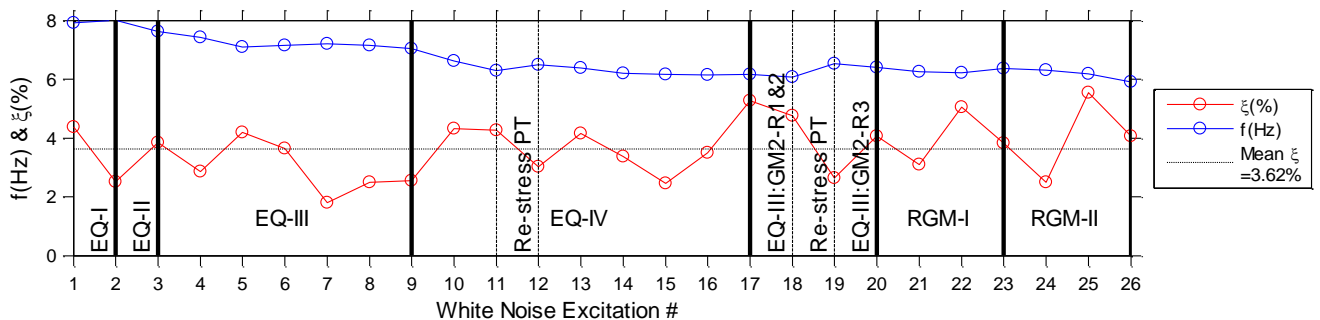


Figure 7.9 – SRW-ST-A seismic excitation white noise tests

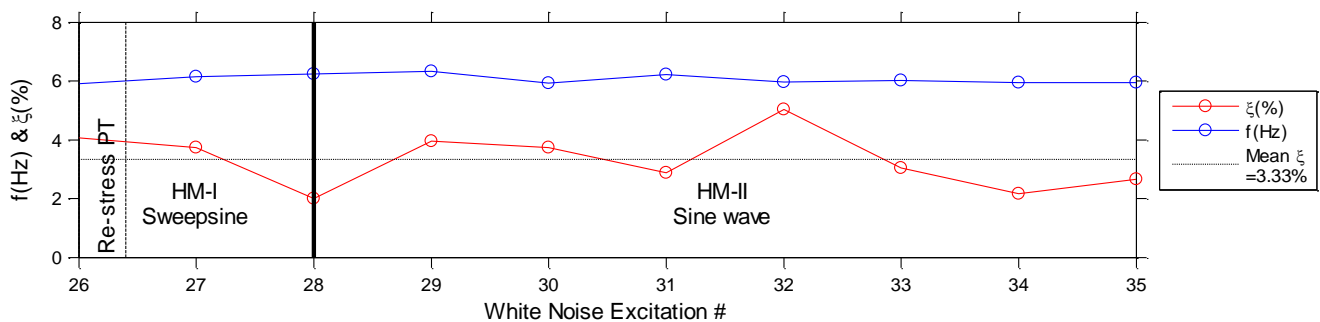
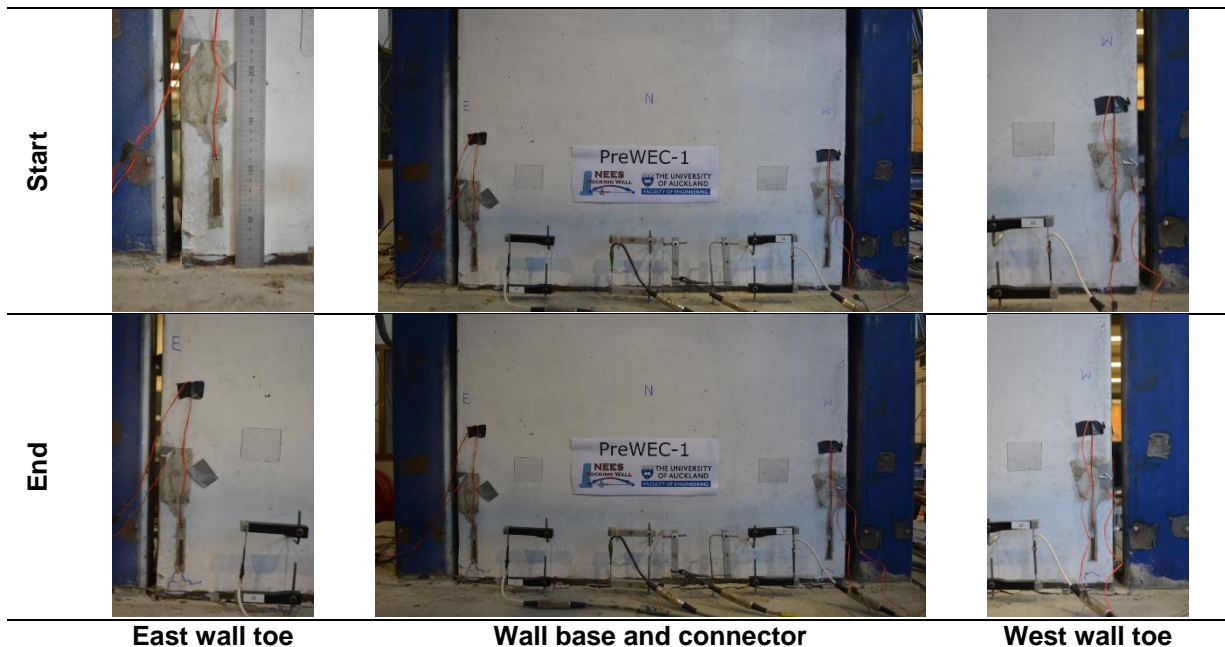


Figure 7.10 – SRW-ST-A harmonic excitation white noise tests

7.4.2 PreWEC-ST-A

The condition of PreWEC-ST-A before and after completion of testing is shown in Table 7.9. PreWEC-ST-A only suffered very fine cracks in the wall toes at the culmination of the test sequence that are barely visible in the observation photos. Similar observations and damage occurred during the cyclic testing reported in Chapter 5 for PreWEC-A. At the end of the test sequence one O-connector had partially fractured and two had full fractures in one leg. The change in EVD and fundamental frequency throughout the test sequence of PreWEC-ST-A is shown in Figure 7.11. It is clear from Figure 7.11 that the fundamental frequency dropped only slightly but steadily throughout the test sequence. At the start of the test the frequency was 9.96 Hz which correlated well with the fixed base period of 0.096s or 10.4 Hz used when scaling the spectrum compatible records, as stated in Table 7.4. From the start to the end of the test sequence there was a drop in fundamental frequency of 13.7% which demonstrates significant stiffness degradation despite almost no observable damage, although, less degradation than what was found for SRW-ST-A. The average EVD or inherent damping during the test sequence was 3.11% which is similar to the EVD found for SRW-FV-A.

Table 7.9 – PreWEC-ST-A photos of wall condition before and after testing



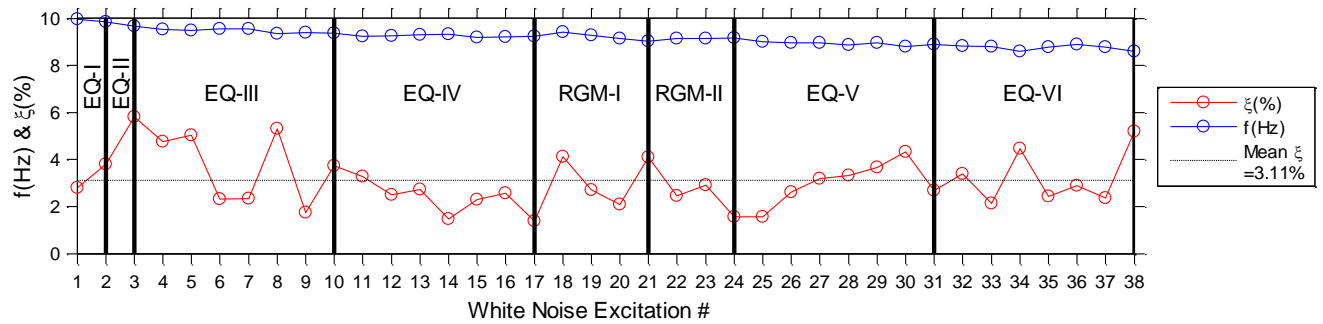


Figure 7.11 – PreWEC-ST-A seismic excitation white noise tests

7.4.3 PreWEC-ST-B

As previously discussed PreWEC-ST-B underwent two test sequences referred to as PreWEC-ST-B1 and PreWEC-ST-B2. The same wall panel was used but new O-connectors were attached between sequences. The condition of PreWEC-ST-B before and after completion of testing sequence B1 and before and after testing sequence B2 is shown in Table 7.10. During all stages of testing PreWEC-ST-B suffered negligible damage on the wall panel itself, similar to that reported in Chapter 5 for PreWEC-B during the cyclic testing. During the B1 test sequence an O-connector weld began to fracture during EQ-V: GM2 due to insufficient weld quality before onset of fracture in any O-connector. The suite of records in EQ-V was finished and the O-connectors removed. Due to the undesirable failure mechanism of weld fracture, new O-connectors were welded in place and the test sequence performed again with excellent quality MIG welds as reported in Chapter 3. This was deemed necessary to ensure data was collected on the performance of the wall with the O-connectors themselves fracturing not the welds. At the culmination of the B2 test sequence five O-connectors had partially fractured and two fully fractured. An example of an O-connector at the start of testing and fully fractured at the end of testing is given in Figure 7.12.

Table 7.10 – PreWEC-ST-B photos of wall condition before and after testing

Start A			
End A/Start B			
End B			
	East wall toe	Wall base and connector	West wall toe



(e) Start of test



(f) End of test

Figure 7.12 – PreWEC-ST-B1 O-connector #2 photos before and after testing

The change in EVD and fundamental frequency throughout the two test sequences of PreWEC-ST-B are shown in Figure 7.13 and Figure 7.14. At the start of test sequence B1 the fundamental frequency was 8.8 Hz which was lower than expected when compared to the fixed base period of 0.096s or 10.4 Hz used for scaling of the spectrum compatible records as stated in Table 7.4. This was due to slight damage that had occurred to the wall during assembly. From the start to the end of the B1 test sequence there was a drop in fundamental frequency of 12.1% that demonstrated a similar proportion of stiffness degradation to PreWEC-ST-A. From the start to the end of the B2 test sequence there was a drop in fundamental frequency of 17.1% from 8.95 Hz to 7.42 Hz, although more than half of this reduction occurred during EQ-I as shown in Figure 7.14. If the initial frequency was taken post EQ-I, the frequency reduction would only be 8.4%, from 8.1 Hz to 7.42 Hz. Throughout the B2 test sequence the frequency remained reasonably constant until EQ-VI where a slight reduction is observed, this was due to the onset of O-connector fracture. Onset of fracture was first observed in one O-connector during EQ-VI: GM1, a further two O-connectors in EQ-VI: GM3, a further three O-connectors in EQ-VI: GM5 and a further O-connector in EQ-VI: GM6, leaving five not fractured. The average EVD or inherent damping during B1 test sequence was 3.43% which aligned well with previous walls and 4.36% for the B2 test sequence. The combined average for PreWEC-ST-B was 3.9% inherent damping.

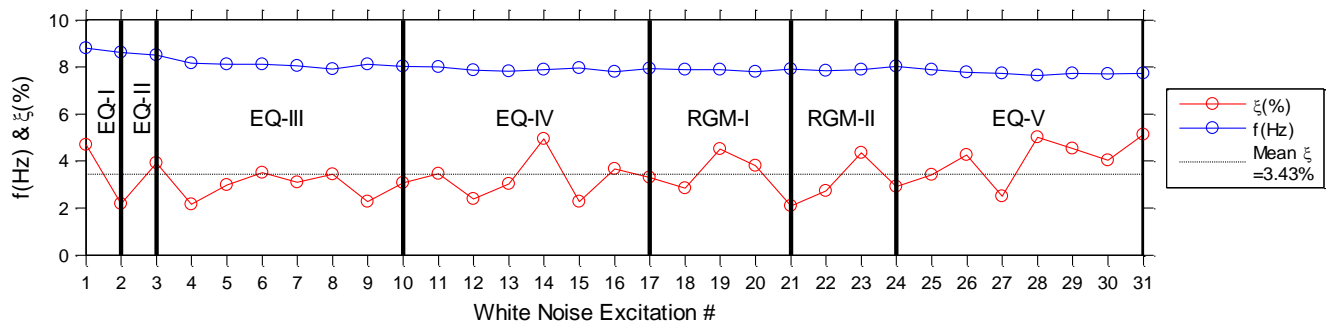


Figure 7.13 – PreWEC-ST-B1 seismic excitation white noise tests

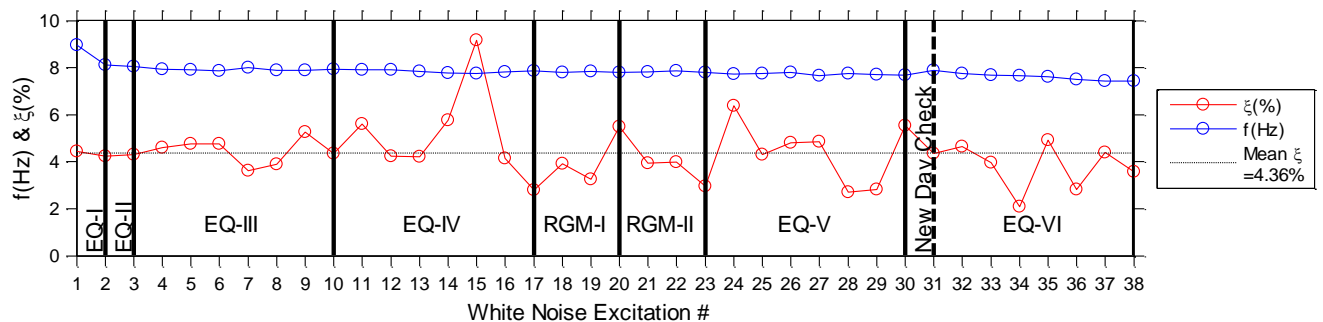


Figure 7.14 – PreWEC-ST-B2 seismic excitation white noise tests

7.5 GROUND MOTION RESULTS AND DISCUSSION

This section summarises the results of the seismic testing presented at test structure scale. All of the data reported has been filtered with a 25 Hz low pass filter to remove high frequency noise. Wall drifts were calculated by subtracting the measured shake table displacement from the displacement recorded at the centre of mass, divided by the height of the centre of mass. For SRW-ST-A and PreWEC-ST-B the displacement sensor used was a Linear Variable Differential Transformer (LVDT) however draw wire or string pot displacements were used during PreWEC-ST-A testing due to LVDT measurement error. Indicative examples of each wall during spectrum compatible loading are presented below for the ground motion that induced the highest drift. Additionally, both the measured table acceleration, centre of mass acceleration and drift time histories recorded for the complete set of ground motions on all walls are included in Appendix E. Unless otherwise stated the wall acceleration and displacement refer to the absolute Centre of Mass (CoM) acceleration and displacement.

7.5.1 Characteristic results

The lateral drift time history and corresponding acceleration time history measured when SRW-ST-A was subjected to ground motion EQ-IV:GM3 which induced the highest lateral drift of 3.48%, are shown in Figure 7.15. The corresponding inertia force versus drift response, and total wall PT force versus drift for SRW-ST-A is presented in Figure 7.16. Rocking behaviour of the wall was clearly observed due to the clean harmonic type response, despite the jagged ground acceleration. The inertia force versus drift response in Figure 7.16 shows a clear example of the nonlinear elastic behaviour typical of a SRW with no significant loss in strength and a small quantity of hysteretic energy dissipation. The total PT force versus drift response shows that some PT loss did occur during EQ-IV:GM3 with the total PT reduced by 12.9% from 287 kN to 250 kN. Following this test the wall was restressed as greater than 5% PT force was lost. This is shown in Figure 7.9 by the “PT re-stress” between WN11 and 12.

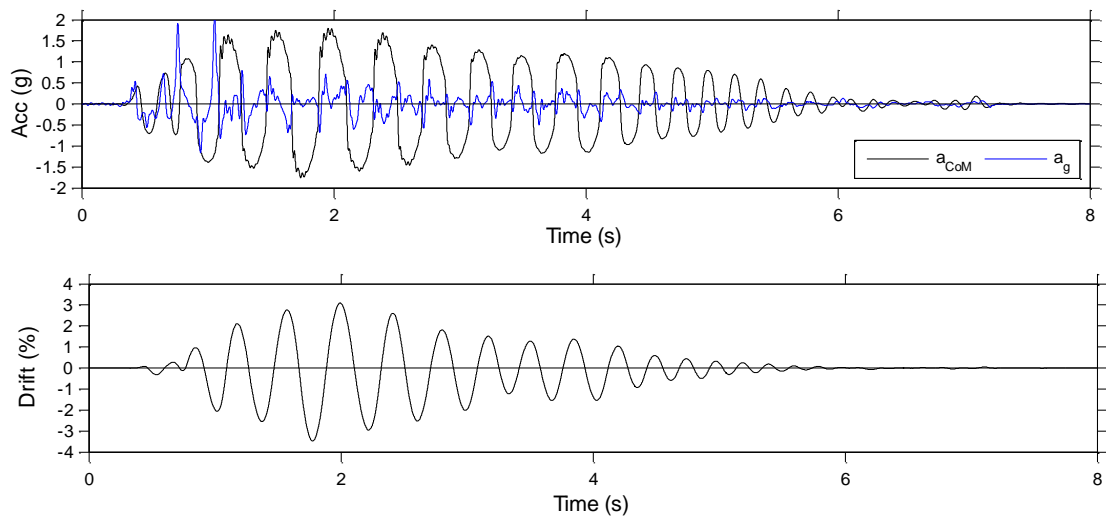


Figure 7.15 – Acceleration and drift time history for SRW-ST-A EQ-IV: GM3

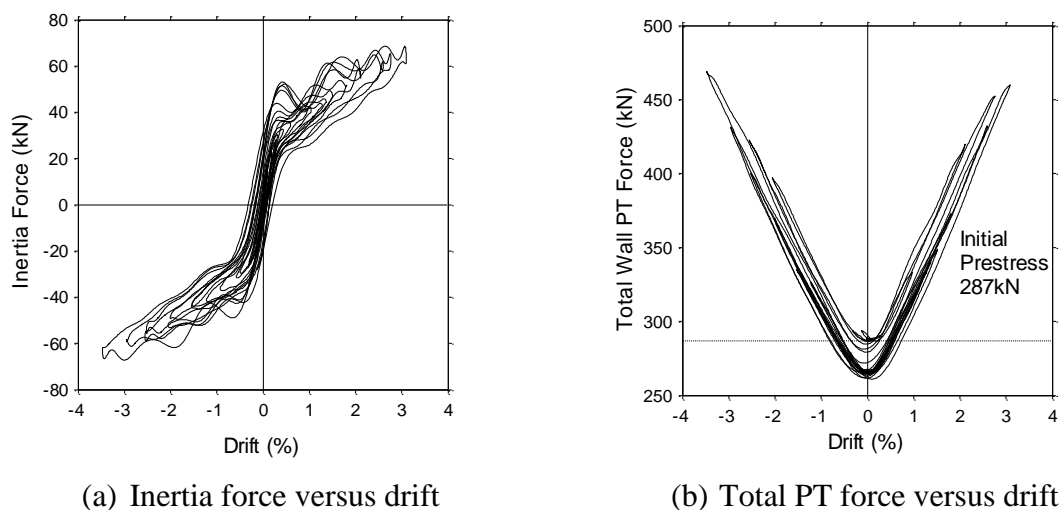


Figure 7.16 – Inertia force and PT force versus drift for SRW-ST-A EQ-IV: GM3

An indicative example of the lateral drift time history, acceleration time history, inertia force drift response, and total wall PT force versus drift for PreWEC-ST-A is presented in Figure 7.17 and Figure 7.18 when subjected to EQ-VI: GM2. This ground motion forced the PreWEC-ST-A wall to reach the highest peak drift of 1.79% and returned the wall to the upright position resulting in negligible residual drift. Rocking was clearly observed during the first two seconds of ground motions evidenced by the clean harmonic type drift response. The inertia force versus drift in Figure 7.18 displays larger force-drift loops than SRW-ST-A due to the increased hysteretic energy dissipation and strength from the O-connectors. It is also apparent that there

was no significant loss in strength during the ground motion. It is clear from the total PT versus drift that no PT loss occurred during the ground motion.

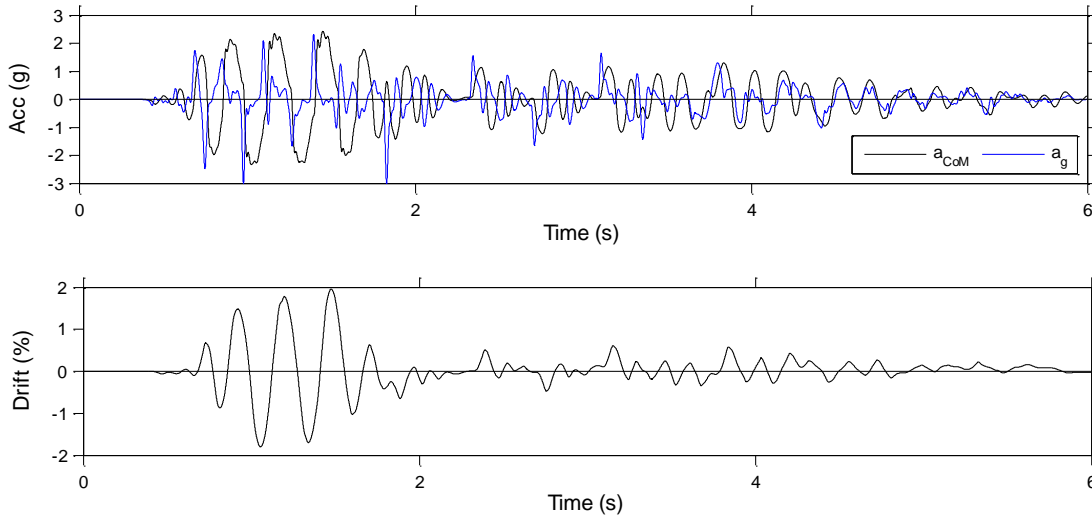


Figure 7.17 – Acceleration and drift time history for PreWEC-ST-A EQ-VI: GM2

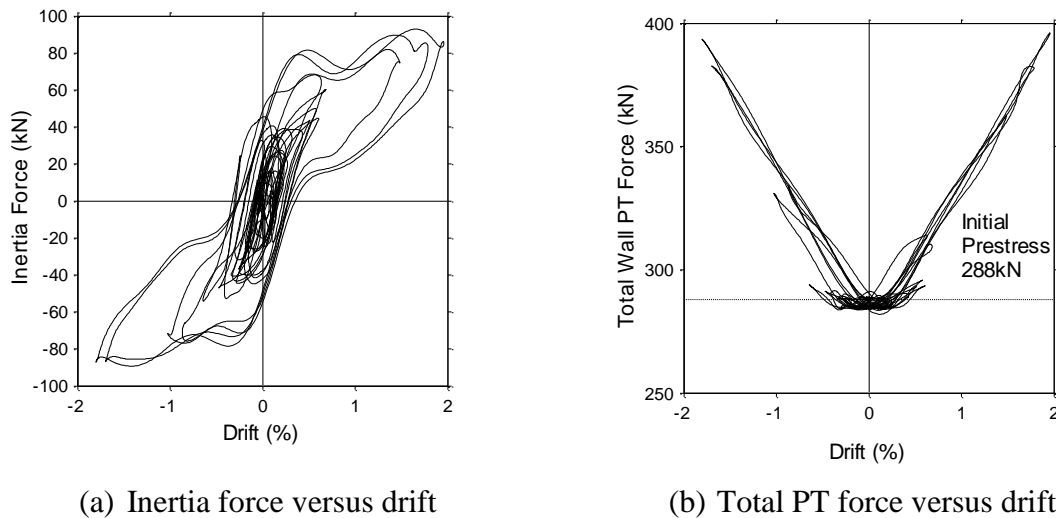


Figure 7.18 – Inertia force and PT force versus drift for PreWEC -ST-A EQ-VI: GM2

The lateral drift time history and corresponding acceleration time history shown in Figure 7.19 were measured when PreWEC-ST-B2 was subjected to ground motion EQ-VI: GM5 which induced the highest lateral drift of 1.68%. The corresponding inertia force versus drift response, and total wall PT force versus drift for PreWEC-ST-B2 is presented in Figure 7.20. The same clear harmonic type rocking behaviour was not observed although uplift did occur consistently throughout the test. The inertia force versus drift in Figure 7.20 displays larger force-drift loops

and slightly higher strength than both SRW-ST-A and PreWEC-ST-A due to the increased number of O-connectors and there was no significant loss in strength during the ground motion. It is clear from the total PT versus drift that no PT loss occurred during the ground motion.

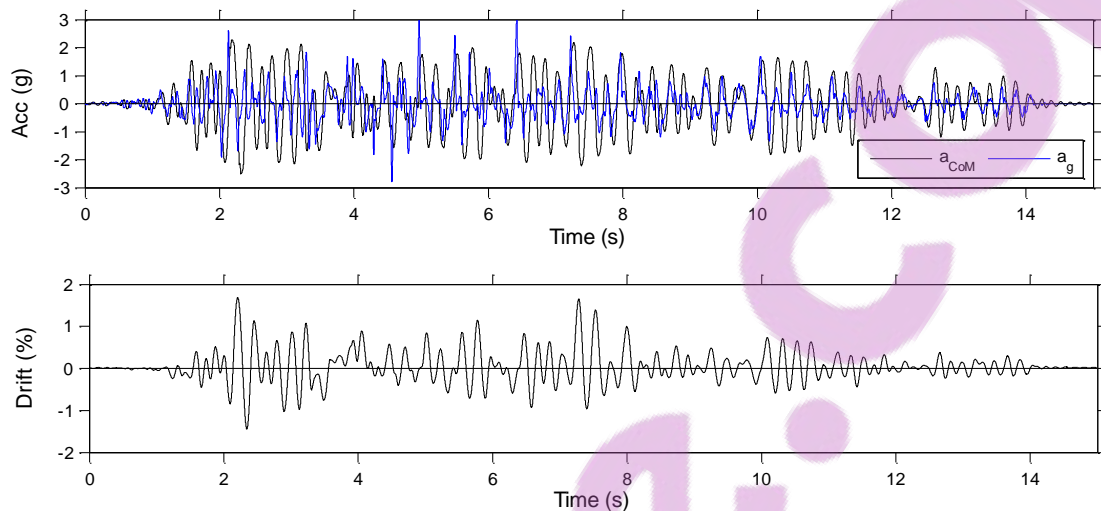


Figure 7.19 – Acceleration and drift time history for PreWEC-ST-B2 EQ-VI: GM5

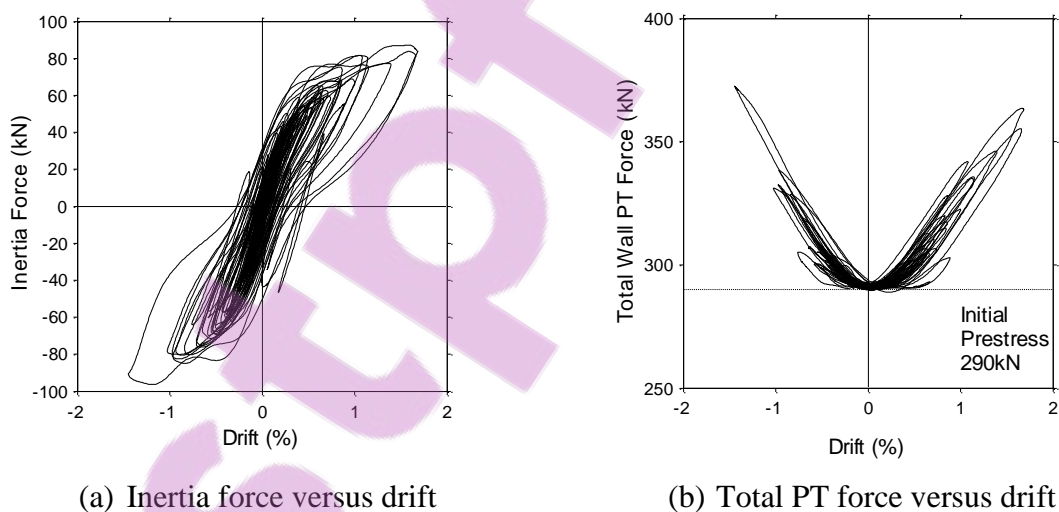


Figure 7.20 – Inertia force and PT force versus drift for PreWEC-ST-B2 EQ-VI: GM5

7.5.2 Summary of key results

Table 7.11 and Table 7.12 list the peak drift and peak acceleration at the centre of mass recorded during each spectrum compatible ground motion for each wall, respectively. The peak ground acceleration (PGA) for each ground motion is given in Appendix E and was calculated as the average of two accelerometers attached to the shake table and the centre of mass acceleration

was calculated by assuming rigid body motion with an average of the accelerometers at the top of the wall.

Peak drifts for SRW-ST-A ranged from less than 0.06% during the EQ-I intensity levels to 3.48% during the largest drift response which was EQ-IV: GM3. The average peak lateral drift reached by SRW-ST-A for each intensity level were 0.08%, 0.2%, 1.12%, and 2.01% from EQ-I through to EQ-IV, respectively. The peak drifts for the PreWEC systems were 1.79% and 1.68%, for PreWEC-ST-A and B2, respectively. The average peak lateral drift reached by PreWEC-ST-A for each intensity level were 0.07%, 0.14%, 0.37%, 0.68%, 1.07%, and 1.26% from EQ-I through to EQ-VI, respectively. The average lateral drift reached by PreWEC-ST-B2 for each intensity level were 0.10%, 0.23%, 0.55%, 0.87%, 1.17%, and 1.36% from EQ-I through to EQ-VI, respectively.

Peak accelerations for SRW-ST-A ranged from less than 0.37 g during the EQ-I intensity levels to 1.72 g during the largest acceleration and drift response which was EQ-IV: GM3. The average peak accelerations for SRW-ST-A at each intensity level were 0.41 g, 0.81 g, 1.2 g, and 1.36 g from EQ-I through to EQ-IV, respectively. The peak accelerations for the PreWEC systems were 2.38 g and 2.53 g for PreWEC-ST-A and B2, respectively. The average peak accelerations reached by PreWEC-ST-A for each intensity level were 0.42 g, 0.86 g, 1.51 g, 1.83 g, 2.02 g, and 2.01 g from EQ-I through to EQ-VI, respectively. The average peak accelerations reached by PreWEC-ST-B2 for each intensity level were 0.48 g, 1.03 g, 1.72 g, 2.01 g, 2.21 g, and 2.23 g from EQ-I through to EQ-VI, respectively.

Typically the lateral drifts increased significantly with increased intensity level while the peak accelerations increased proportionally less with intensity level. This is due the pushover response of the walls which requires considerably higher drifts for a small increase in acceleration once the drift extends beyond uplift. It is unusual that PreWEC-B on average had both higher accelerations and drifts than PreWEC-A, although reached a lower peak drift overall.

Table 7.11 – Peak drift for spectrum compatible ground motion on all walls

Intensity Level		EQ-I	EQ-II	EQ-III	EQ-IV	EQ-V	EQ-VI
SRW-ST-A	GM1	0.07	0.18	0.55	1.99	-	-
	GM2	0.10	0.26	2.49	1.85	-	-
	GM3	0.08	0.19	1.71	3.48	-	-
	GM4	0.06	0.19	0.73	0.90	-	-
	GM5	0.08	0.18	0.70	2.93	-	-
	GM6	0.06	0.19	0.87	1.90	-	-
	GM7	0.07	0.19	0.80	1.01	-	-
	<i>GM2-R1</i>	-	-	1.54	-	-	-
	<i>GM2-R2</i>	-	-	1.55	-	-	-
	<i>GM2-R3</i>	-	-	1.53	-	-	-
PreWEC-ST-A	GM1	0.06	0.13	0.40	0.63	0.88	1.17
	GM2	0.08	0.15	0.39	0.67	1.57	1.79
	GM3	0.08	0.18	0.38	0.64	0.96	1.00
	GM4	0.06	0.13	0.38	0.71	0.81	0.86
	GM5	0.08	0.18	0.41	0.76	1.15	1.54
	GM6	0.07	0.12	0.29	0.69	1.02	1.09
	GM7	0.04	0.10	0.31	0.68	1.11	1.35
PreWEC-ST-B (sequence B1 in italics)	GM1	0.11	0.28	0.50	0.85	1.26	1.32
		<i>0.10</i>	<i>0.24</i>	<i>0.54</i>	<i>0.71</i>	<i>1.00</i>	-
	GM2	0.08	0.20	0.51	1.08	1.48	1.61
		<i>0.07</i>	<i>0.17</i>	<i>0.43</i>	<i>0.94</i>	<i>1.31</i>	-
	GM3	0.11	0.25	0.56	0.90	1.18	1.28
		<i>0.10</i>	<i>0.22</i>	<i>0.52</i>	<i>0.81</i>	<i>1.03</i>	-
	GM4	0.09	0.23	0.57	0.72	0.81	1.00
		<i>0.09</i>	<i>0.19</i>	<i>0.48</i>	<i>0.62</i>	<i>0.71</i>	-
	GM5	0.12	0.29	0.71	0.92	1.35	1.68
		<i>0.11</i>	<i>0.25</i>	<i>0.65</i>	<i>0.85</i>	<i>1.25</i>	-
	GM6	0.08	0.20	0.53	0.84	1.03	1.18
		<i>0.07</i>	<i>0.16</i>	<i>0.47</i>	<i>0.77</i>	<i>0.92</i>	-
	GM7	0.07	0.18	0.47	0.76	1.11	1.41
		<i>0.06</i>	<i>0.15</i>	<i>0.42</i>	<i>0.71</i>	<i>1.07</i>	-

Table 7.12 – Peak centre of mass acceleration for spectrum compatible ground motion on all walls

Intensity Level		EQ-I	EQ-II	EQ-III	EQ-IV	EQ-V	EQ-VI
SRW-ST-A	GM1	0.44	0.85	1.19	1.42	-	-
	GM2	0.39	0.77	1.50	1.35	-	-
	GM3	0.43	0.80	1.35	1.72	-	-
	GM4	0.37	0.80	1.04	1.05	-	-
	GM5	0.37	0.80	1.10	1.61	-	-
	GM6	0.47	0.83	1.12	1.28	-	-
	GM7	0.41	0.85	1.07	1.10	-	-
	<i>GM2-R1</i>	-	-	1.29	-	-	-
	<i>GM2-R2</i>	-	-	1.32	-	-	-
	<i>GM2-R3</i>	-	-	1.28	-	-	-
PreWEC-ST-A	GM1	0.47	0.93	1.61	1.87	2.03	2.11
	GM2	0.43	0.92	1.48	1.86	2.28	2.31
	GM3	0.43	0.86	1.40	1.61	1.89	1.68
	GM4	0.41	0.84	1.69	1.96	1.91	1.81
	GM5	0.39	0.74	1.40	1.81	2.09	2.24
	GM6	0.41	0.86	1.48	1.86	2.00	1.97
	GM7	0.37	0.84	1.48	1.79	1.95	1.99
PreWEC-ST-B (sequence B1 in italics)	GM1	0.56	1.16	1.85	2.16	2.34	2.38
		<i>0.55</i>	<i>1.11</i>	<i>1.75</i>	<i>2.11</i>	<i>2.28</i>	-
	GM2	0.48	1.04	1.69	2.18	2.41	2.53
		<i>0.46</i>	<i>0.98</i>	<i>1.61</i>	<i>2.10</i>	<i>2.32</i>	-
	GM3	0.46	0.93	1.56	1.80	1.96	1.87
		<i>0.47</i>	<i>0.92</i>	<i>1.50</i>	<i>1.70</i>	<i>1.89</i>	-
	GM4	0.52	1.21	1.99	2.07	2.12	2.06
		<i>0.47</i>	<i>1.15</i>	<i>1.95</i>	<i>2.05</i>	<i>2.03</i>	-
	GM5	0.49	1.08	1.82	2.06	2.35	2.50
		<i>0.44</i>	<i>0.98</i>	<i>1.75</i>	<i>1.98</i>	<i>2.30</i>	-
	GM6	0.50	1.00	1.68	2.01	2.20	2.23
		<i>0.50</i>	<i>1.02</i>	<i>1.68</i>	<i>1.99</i>	<i>2.09</i>	-
	GM7	0.37	0.81	1.48	1.82	2.09	2.04
	<i>0.38</i>	<i>0.84</i>	<i>1.48</i>	<i>1.76</i>	<i>1.94</i>	-	

Table 7.13 lists the PGA, peak acceleration at the centre of mass, and the peak drift for the two recent ground motion suites for each wall. The recent ground motion suites allow for direct comparison of the wall response as the ground motions were identical for each wall, despite the

increase in energy dissipation and strength between the walls. On average SRW-ST-A reached considerably lower peak accelerations and higher peak lateral drifts than both the PreWEC walls.

Table 7.13 – Peak parameters for RGM for all walls

		RGM-I			RGM-II		
		PGA (g)	Peak CoM Acc (g)	Peak Drift (%)	PGA (g)	Peak CoM Acc (g)	Peak Drift (%)
SRW-ST-A	GM8	2.08	1.12	1.19	0.68	0.67	0.43
	GM9	3.23	1.10	0.82	2.14	1.76	3.60
	GM10	2.06	1.31	1.75	1.52	0.99	1.35
PreWEC-ST-A	GM8	1.74	1.77	0.47	0.66	0.77	0.38
	GM9	2.50	2.15	1.00	2.02	1.27	0.71
	GM10	2.35	1.86	0.75	1.40	1.21	0.72
PreWEC-ST-B1	GM8	2.10	1.69	0.40	0.57	0.85	0.44
	GM9	2.82	2.23	1.13	1.69	1.65	1.25
	GM10	3.35	2.10	0.94	1.26	1.18	1.03
PreWEC-ST-B2	GM8	1.98	1.56	0.39	0.65	0.84	0.44
	GM9	2.67	2.18	0.99	1.96	1.45	0.93
	GM10	2.61	2.00	0.83	1.51	1.26	1.07

The lateral drift time history, ground acceleration time history and peak centre of mass acceleration time history is presented in Figure 7.21 for RGM-I:GM9 for each of the walls tested. Almost identical ground acceleration traces were applied to each wall. Interestingly, for this particular ground motion both a higher peak drift and acceleration were found for the PreWEC walls in comparison to the SRW. Although, the SRW has a lower peak drift than the PreWEC walls the SRW does have significantly higher drifts than the PreWEC walls at other times during the time history. Throughout almost the entire time history the centre of mass acceleration is lower for the SRW than both PreWEC systems. For all other RGM-I tests SRW reached higher drifts and lower accelerations than the two PreWEC walls. For RGM-II SRW had lower peak accelerations and higher drifts than the PreWEC walls, except for GM9 which forced SRW-ST-A to reach 3.6% drift and a correspondingly high acceleration.

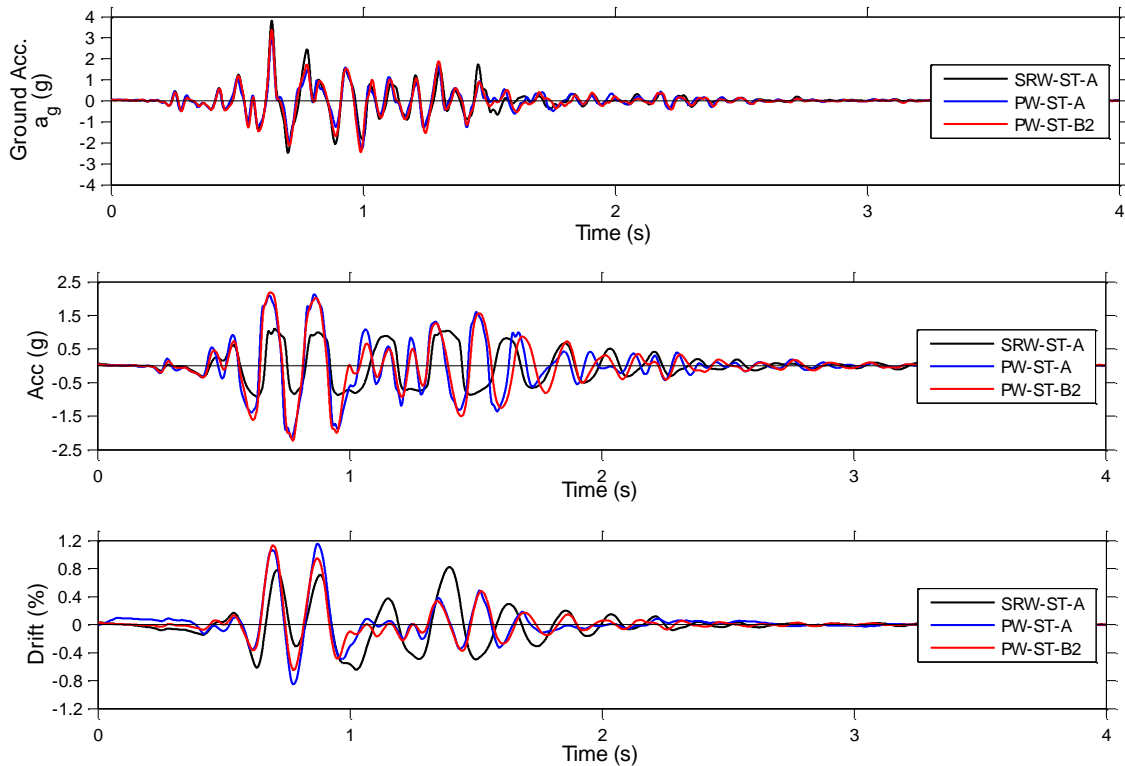


Figure 7.21 – Acceleration and drift time history for RGM-I: GM9

The inertia force drift response is presented in Figure 7.22 for each of the walls for RGM-I: GM9. Similar hysteretic response was observed as for the spectrum compatible ground motion inertia force drift responses. In Figure 7.22 the significantly lower strength and bilinear elastic behaviour of SRW-ST-A is apparent in comparison to the two PreWEC walls which are considerably stronger and have larger hysteretic energy dissipation due to the yielding O-connectors. A greater strength difference was expected between PreWEC-ST-A and B, although the amount of yielding in the O-connectors that had previously occurred to the wall will have influenced the over-strength of the mild steel O-connectors and hence the overall strength of the wall.

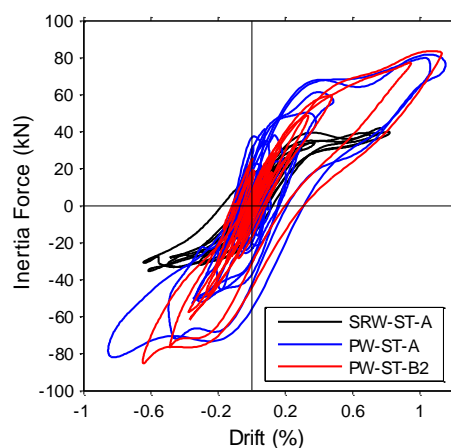


Figure 7.22 – Inertia force versus drift RGM-I: GM9

7.5.3 Sensitivity of results

As previously stated, during testing of SRW-ST-A a particularly large drift response was measured for EQ-III: GM2 of 2.49%, double the design drift of 1.25%. Given the high drift during the design level ground motion, an exceptionally large drift was expected for GM2 during the MCE level EQ-IV. However, a lower drift of only 1.85% was reached. To investigate the lower response to the higher intensity level of this particular ground motion EQ-III: GM2 was repeated three times at the culmination of the EQ-IV suite of ground motions. The wall was restressed between repeat two and three to check the effect of the exact PT force. The ground acceleration and drift time history of all four EQ-III: GM2 tests is presented in Figure 7.23. The three peak drifts for the three repeats were 1.54%, 1.55%, and 1.53% for R1, R2, and R3, respectively. As evidenced by the peaks drifts and shown in the drift time history, the three repeats showed almost exactly the same response even when restressed. The average drift of the repeated tests aligned well with the 1.85% drift measured for the EQ-IV intensity.

The only possible reasons for the large difference in lateral drift responses are either unintended differences in ground motion input or the natural frequency of the wall during the specific ground motion, which reduced slightly during the test sequence, as shown previously in Figure 7.9. Although the input ground motion was identical for all tests there are noticeable spikes in the EQ-III: GM2 measured ground acceleration which was most likely due to the walls large response inducing forces in the table that were unexpected, causing acceleration spikes. Importantly, the noticeable ground acceleration spikes did not occur before the highest response.

This provides evidence that the likely reason for the large response is due to the extreme sensitivity of the fundamental frequency of the SRW to the ground motion content. It appears that GM2 had the perfect frequency content to excite the wall near resonance while GM2 did not have the appropriate frequency content to excite the slightly less stiff wall later in the test sequence. During the PreWEC wall tests, higher intensity levels resulted in higher measured drifts for all ground motions. This confirms that the PreWEC walls are less sensitive to resonant excitation when compared to the unpredictably shown in SRW-ST-A.

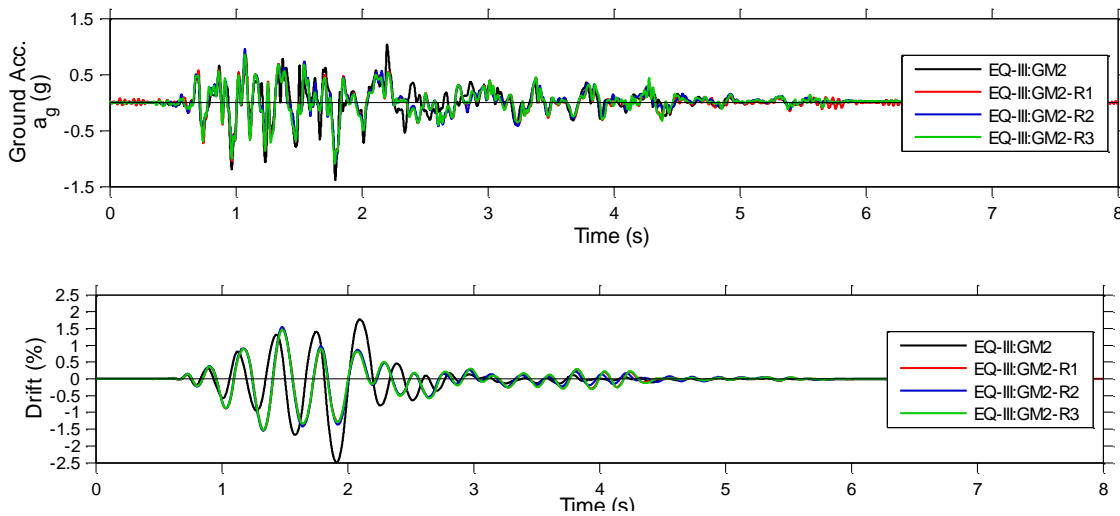


Figure 7.23 – Acceleration and drift time history for EQ-III: GM3 and repeats

As previously stated PreWEC-ST-B was subjected to two test sequences with new O-connectors. A comparison of the PGA versus peak drift for the two sequences of testing are shown in Figure 7.24. PreWEC-ST-B2 also includes the additional test suite EQ-VI which are shown in Figure 7.24 as the highest PGA red dots. Overall a similar trend is observed, although it is clear identical PGA and peak drift were not achieved. The overall behaviour is considered similar enough to only focus on the B2 sequence of testing.

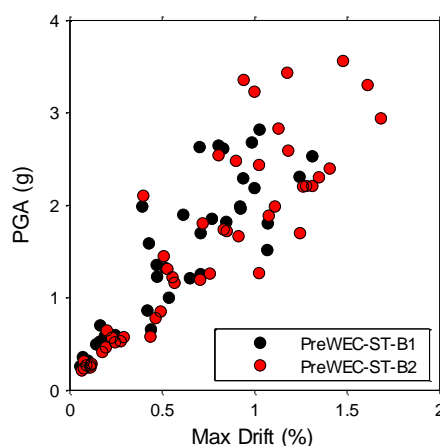


Figure 7.24 – PGA versus peak drift for PreWEC-ST-B1 and B2

7.5.4 Residual drifts

The residual drift is an important parameter in the seismic performance assessment of a building that is able to characterise the status of a structure after the earthquake. The measured residual drift at the culmination of every test for each wall versus the peak drift reached during that test is plotted in Figure 7.25. The average residual drifts for SRW-ST-A at each intensity level were 0.003%, 0.002%, 0.005%, and 0.009% from EQ-I through to EQ-IV, respectively. The average residual drifts reached by PreWEC-ST-A for each intensity level were 0.010%, 0.011%, 0.012%, 0.014%, 0.009%, and 0.016% from EQ-I through to EQ-VI, respectively. The average residual drifts reached by PreWEC-ST-B2 for each intensity level were 0.002%, 0.003%, 0.006%, 0.011%, 0.009%, and 0.024% from EQ-I through to EQ-VI, respectively. PreWEC-ST-A measured slightly higher residual drifts than PreWEC-ST-B during the low intensity levels due to the displacement transducer used; the measured residual drifts at the high intensities are expected to be accurate. The maximum residual drift for any wall was approximately 0.05% proving that the design of the walls was sufficient to practically eliminate residual drift from ground motions and was significantly below residual drifts limits defined by Henry [41] of 0.2% and 0.3% for design and maximum credible earthquake levels.

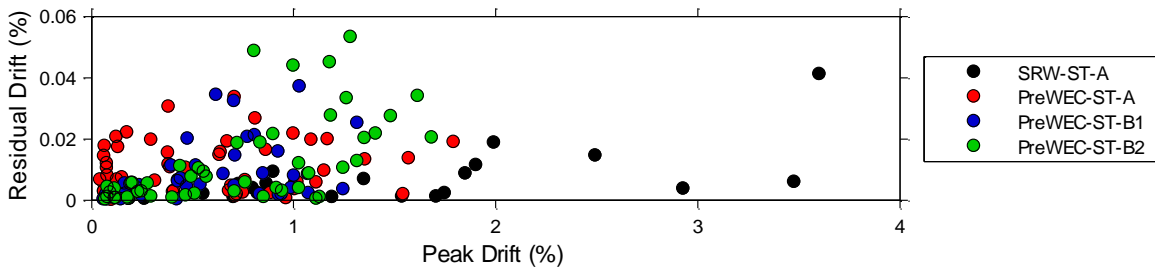


Figure 7.25 – Residual drift for all walls during spectrum compatible ground motions

From Figure 7.25 it is clear that negligible residual drifts occurred for all walls and all tests regardless of peak drift attained. The low residual drifts at the end of the shake table tests are significantly lower than the residual drifts calculated using the hysteresis response from cyclic tests reported in Chapter 5. This is because the dynamic response reduces the residual drift via a shake-down phase at the end of the motion as described by MacRae and Kawashima [117]. In depth residual drift modelling of a PreWEC system reported by Henry [41] showed similar results with much lower residual drifts at the conclusion of dynamic analyses than the maximum possible residual drift observed from the cyclic hysteresis loop. Henry established a residual drift ratio (d_{rr}) that defines the shake-down behaviour to be used in design. The residual drift ratio is presented in Equation (7-4) and is calculated by dividing the residual drift at the end of the ground motion (d_r), by the maximum possible residual drift ($d_{r,max}$), which is the residual drift calculated from pseudo-static cyclic testing or analyses after unloading from a certain peak drift.

$$d_{rr} = \frac{d_r}{d_{r,max}} \quad (7-4)$$

The series of testing in this thesis, with both pseudo-static cyclic testing and shake table testing, provides a unique opportunity to determine the residual drift ratio from experiments. For each of the walls tested a critical ground motion was chosen to provide an indication of critical residual drift ratio by calculating a maximum residual drift from the cyclic testing depending on the peak drift reached during the ground motion. A summary of the residual drift analysis is given in Table 7.14. For SRW-ST-A the ground motion chosen was EQ-IV: GM1 which reached a peak drift of 1.99% and concluded with a residual drift of 0.019. For PreWEC-ST-A the ground motion chosen was EQ-VI: GM6 which reached a peak drift of 1.17% and concluded with a residual drift of 0.020%. For PreWEC-ST-B1 the ground motion chosen was EQ-V: GM6 which reached a peak drift of 1.03% and concluded with a residual drift of 0.037%. For PreWEC-ST-B2 the

ground motion chosen was EQ-VI: GM3 which reached a peak drift of 1.28% and concluded with a residual drift of 0.053%. The maximum residual drifts were linearly interpolated from Figure 5.7 using the peak drift for the respective ground motions, and were calculated to be 0.190%, 0.153%, 0.151%, and 0.218% for SRW-ST-A, PreWEC-ST-A, B1, and B2 respectively. The calculated residual drift ratios are therefore 0.10, 0.13, 0.25, and 0.24 for SRW-ST-A, PreWEC-ST-A, B1, and B2 respectively. These experimental residual drift ratios provide experimental evidence and reinforce previous findings from numerical work by Henry that large reductions in residual drift occur during dynamic loading in comparison to residual drift defined by cyclic hysteresis loops. The upper limit residual drift ratio of 0.3 proposed by Henry [41] appears to be a slightly conservative but a reasonable estimate given the observed scatter in results.

Table 7.14 – Summary of residual drift analysis

Wall Label	Ground motion	Peak drift (%)	Residual drift (d_r) (%)	Maximum residual drift ($d_{r,max}$) (%)	Residual drift ratio (d_{rr})
SRW-ST-A	EQ-IV:GM1	1.99	0.019	0.190	0.10
PreWEC-ST-A	EQ-VI:GM6	1.17	0.020	0.153	0.13
PreWEC-ST-B1	EQ-V:GM6	1.03	0.037	0.151	0.25
PreWEC-ST-B2	EQ-VI:GM3	1.28	0.053	0.218	0.24

7.5.5 DDBD evaluation and ground motion quantification

7.5.5.1 *Ground motion quantification*

The recorded table ground motion excitations were close to the intended records, however acceleration amplitudes were sometimes higher or lower than expected. The University of Auckland shake table does not have a sophisticated feedback control system, as such some differences between intended motion and applied motion occurred. Deviations from the intended motion occur because of many reasons, including the mass on the table and shake table velocity limits. The deviation of the measured ground acceleration from the intended acceleration is only critical when evaluating the DDBD procedure if there is a significant difference in the period range of interest. To quantify the deviation of the measured ground accelerations from the intended intensity level the required k_1 and k_2 scale factors for the measured ground motions to be the appropriate magnitude were determined. The combination of the k_1 and k_2 scale factors

represents the reduction of the ground acceleration required for the magnitude to be appropriate for the specified return period factor (R). These k factors are presented in Table 7.15 for each wall and spectrum compatible ground motion run. A graphical representation of the pseudo-acceleration response spectra of each of the spectrum compatible recorded input motions, at each intensity, for each wall are presented in Appendix E, and two examples are shown in Figure 7.26. Figure 7.26(a) shows the pseudo-acceleration spectra of each of the ground motions run during EQ-II for SRW-ST-A, and Figure 7.26(b) shows the same for EQ-III for PreWEC-ST-A. All of the pseudo-acceleration spectra in both plots show a drop in amplitude at periods just higher than T_1 . When all ground motions in a series show a consistent drop such as this, the k_2 scale factor is determined as the factor required for at least one ground motion to have a pseudo-acceleration amplitude above the target spectra at every period in the period range of interest. Therefore examples such as the two shown would result in k_2 factors greater than 1.0.

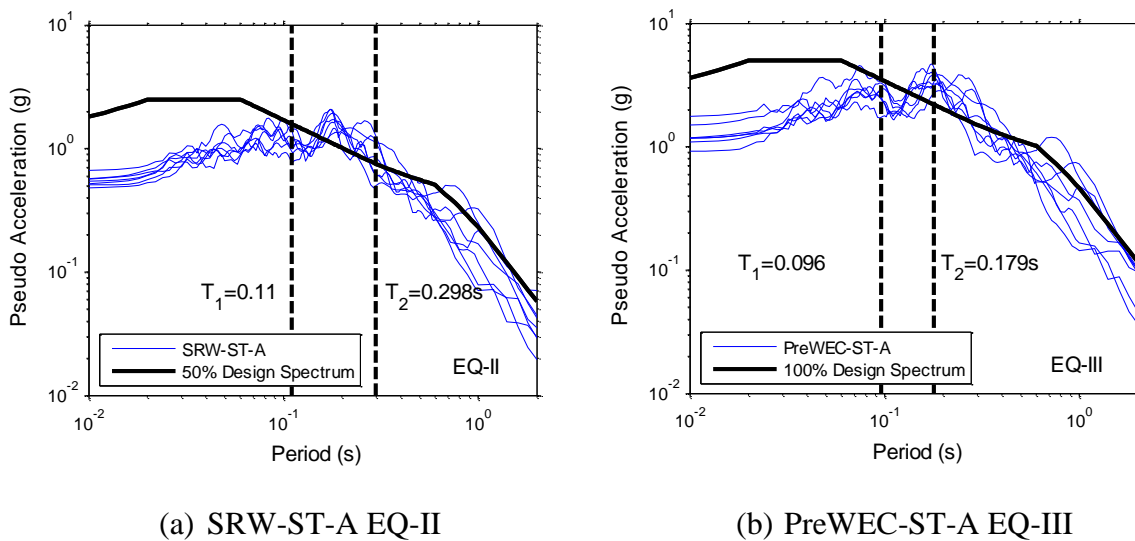


Figure 7.26 – Selected pseudo-acceleration spectrum of recorded ground motions

Overall, the combination of the k_1 and k_2 factors for the different intensity tests applied to SRW-ST-A were near 1.0 for EQ-III and EQ-IV, which demonstrates the achieved ground motions were close to the intended motion. However, for SRW-ST-A the two lower intensities of EQ-I and EQ-II required up to 50% higher pseudo-accelerations in the period range of interest, due to the consistent drop in pseudo-acceleration amplitude shown in Figure 7.26(a). For the PreWEC walls intensity levels EQ-V and EQ-VI had a combination of k_1 and k_2 factors above 1.0

demonstrating lower intensity than intended. This is due to the velocity limit of the shake table which was being exceeded during these high intensity ground motions.

Table 7.15 – Scaling factors (k_1, k_2) required for recorded ground motion to be ideal match with relevant design spectrum

		EQ-I		EQ-II		EQ-III		EQ-IV		EQ-V		EQ-VI	
		k_1	k_2	k_1	k_2	k_1	k_2	k_1	k_2	k_1	k_2	k_1	k_2
SRW-ST-A	GM1	1.00	1.52	0.93	1.34	0.93	1.00	0.95	1.00	-	-	-	-
	GM2	0.86		0.79		0.88		0.99		-	-	-	-
	GM3	1.02		1.00		1.09		1.21		-	-	-	-
	GM4	0.98		0.96		1.14		1.07		-	-	-	-
	GM5	1.10		1.02		0.89		0.95		-	-	-	-
	GM6	0.99		0.98		1.05		0.88		-	-	-	-
	GM7	1.06		0.97		1.03		1.04		-	-	-	-
	GM2-R1	-	-	-	-	0.97	-	-	-	-	-	-	-
	GM2-R2	-	-	-	-	0.97	-	-	-	-	-	-	-
	GM2-R3	-	-	-	-	0.96	-	-	-	-	-	-	-
PreWEC-ST-A	GM1	0.88	1.62	0.81	1.49	0.83	1.21	1.24	1.00	1.34	1.00	1.60	1.04
	GM2	0.99		0.95		0.99		1.12		1.28		1.64	
	GM3	1.02		1.03		1.26		1.32		1.45		2.29	
	GM4	0.92		0.83		1.03		1.17		1.51		2.12	
	GM5	0.95		0.93		1.05		1.08		1.39		1.50	
	GM6	1.12		1.02		1.08		1.13		1.43		1.64	
	GM7	1.13		1.09		1.19		1.50		1.54		1.56	
PreWEC-ST-B (sequence B1 in italics)	GM1	1.06	1.08	1.15	1.01	1.26	1.00	1.00	1.00	1.14	1.00	1.66	1.13
		0.92		0.91		1.27		1.10		1.28			
	GM2	1.04		0.97		1.17		1.08		1.21		1.58	
		1.09		0.99		1.13		1.08		1.42			
	GM3	1.41		1.31		1.20		1.09		1.18		1.64	
		1.21		1.26		1.17		1.03		1.25			
	GM4	1.26		1.26		1.20		1.20		1.38		1.90	
		1.12	1.15	1.14	1.13	1.62							
	GM5	1.13	1.12	1.10	1.12	1.25	1.38						
		1.01	1.02	1.12	1.05	1.31							
	GM6	1.22	1.24	1.20	1.11	1.11	1.29	-					
		1.08	1.09	1.22	1.12	1.26							
	GM7	1.61	1.47	1.44	1.37	1.32	1.33						
	1.44	1.41	1.37	1.38	1.40								

7.5.5.2 Updated design drift determination

To enable a design versus test comparison of the maximum drifts attained for each spectrum compatible ground motion for each wall, an adjusted design drift was determined for each record based on an adjusted return period factor (R), to account for the deviation of the measured ground motion from the intended. The adjusted R was determined by dividing the intended R of each intensity level by the combination of the k_1 and k_2 scale factors, amplifying or reducing the R for each individual ground motion accordingly. The adjusted R value and original R value for each ground motion is given in Appendix E. An iterative DDBD method was then performed with the adjusted R value for each individual ground motion using the corresponding force-displacement behaviour for each wall based on the simplified analytical method proposed by Aaleti and Sritharan (A&S) [62]. Individually adjusted design drifts were determined for each recorded ground motion assuming 5% damping for SRW-ST-A, and assuming EVD can be calculated using Equation (7-2) for the PreWEC systems which is based on the variation of λ . By using an adjusted design spectrum each spectrum compatible ground motion can be used to evaluate the DDBD procedure using current code requirements. For clarity the steps involved in determining the adjusted design drift were as follows:

1. Calculate the pseudo-acceleration spectra for the suite of recorded shake table ground motions being studied (i.e. each intensity level for each wall).
2. Calculate the k_1 and k_2 factors required for the suite of recorded ground motions to have the correct intensity for the intended design level, which is defined by the return period factor (old R or design R).
3. Calculate the adjusted return period factor (R_{ad}) by dividing design R by (k_1+k_2) for each ground motion.
4. Repeating the DDBD procedure outlined in Chapter 4 with each of the adjusted return period factors and the measured wall parameters described in section 7.1. This step involved an iterative process where a design drift was guessed and then updated until the initial drift and final drift match for the given wall properties. A final “adjusted” design drift was determined on this basis. For clarity, the DDBD evaluation algorithm is outlined here:

Algorithm steps:

1. Guess initial “design” displacement (Δ_1).
2. Calculate EVD (ξ_{eq}).
3. Find force (F_d) for initial displacement (Δ_1) from assumed A&S force-displacement behaviour.
4. Calculate effective stiffness (k_e) using Equation (7-5) and subsequently the effective period (T_e) using Equation (7-6).

$$K_e = \frac{F_d}{\Delta_1} \quad (7-5)$$

$$T_e = \sqrt{\frac{4\pi^2 m_e}{K_e}} \quad (7-6)$$

5. Calculate the EVD reduced displacement design spectra (based on the adjusted return period factor) for the specific ground motion using the spectral reduction factor or damping modifier (η) described by Equation (4-9).
6. Using the EVD reduced displacement spectra and the effective period, find the final “design” displacement (Δ_2).
7. Check if the initial displacement is equal to the final displacement i.e. $\Delta_1 = \Delta_2$. If so the design displacement has been calculated i.e. $\Delta_{design} = \Delta_1$. However, if they are not equal update the initial design displacement guess accordingly and redo steps 1-7 until a solution is found.

7.5.5.3 SRW-ST-A

The ratio of the peak test drift to the adjusted design drift versus the adjusted return period factor (R_{ad}) for each of the spectrum compatible motions applied to SRW-ST-A are presented in Figure 7.27. Each intensity level is colour coded with each individual ground motion shown by the dot and the average of the intensity level shown by the same coloured bar. The average of all spectrum compatible ground motions was 1.04 and is shown by the thick black dotted line. On average the correlation between the design and test data for SRW-ST-A is shown to be in

excellent agreement, however there is considerable scatter in the data due to the sensitive nature of SRW, likely from the low damping. The EQ-I intensity level drifts are consistently under predicted with values greater than one indicating that the damping value of 5% was too large for these low ground accelerations where rocking did not occur. This aligns well with the measured inherent damping of SRW-ST-A which had an average EVD of 3.47%. Intensity level EQ-II had little scatter and an average close to one. The two higher intensity levels had the most scatter but on average were found to have conservative over predicted drifts which indicates damping greater than 5%. Recalling that this test regime was intended to represent a physical form of the numerical integration time history method described in NZS 1170.5, the design inter-storey drift for ultimate limit state is specified to be the maximum inter-storey drift obtained for all ground motion records that do not include forward directivity and 0.67 of that maximum for records that do include forward directivity. Judging specifically the intensity level EQ-III (design level) the critical response would be the ratio of 1.6 i.e. 60% larger drift than that predicted by design, this would be significantly reduced when including appropriate reduction factors. However, NZS 1170.5 only requires that three spectrum compatible records be used and consequently, if only three of the five earthquakes with lower response were selected the design would have been conservative. Other codes specify the use of seven spectrum compatible records and adopt the average value of response. Adopting an average of the design intensity level of EQ-III would give 0.87, an over prediction of displacements by 13% which is on the conservative side and close to the target design drifts.

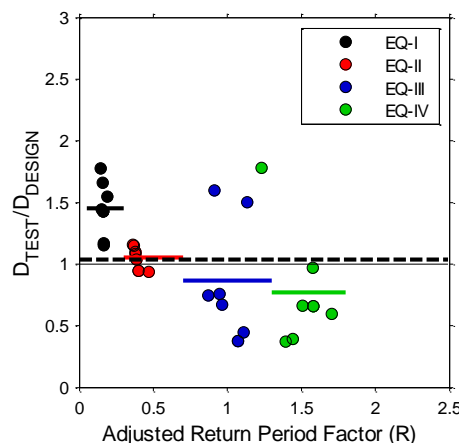


Figure 7.27 – Comparison between DDBD method and SRW-ST-A shake table data

A general limit for the ultimate or design limit state from NZS 1170.5 states that the inter-storey deflection limit shall not exceed 2.5% of the corresponding storey height or such lesser limit as may be prescribed in the appropriate material standard. For SRW-ST-A all seven peak drifts were below this limit with GM2 just reaching this limit. The return period factor (R) was intended to be 1 for the design intensity EQ-III and 1.5 for maximum credible event intensity EQ-IV. The average adjusted R values for two intensity levels were close to intended with 1.08 for EQ-III and 1.5 for EQ-IV. It is interesting to note that the average drift of the design ground motions was 1.12%, and the average drift for the maximum credible event intensity was 2%. On average the maximum credible intensity drift was 1.7 times greater than the average design intensity drifts which is significantly larger than the margin of 1.5 times the displacement capacity assumed in the US code where structures are expected to have 50% excess displacement capacity above the corresponding design [20].

7.5.5.4 PreWEC walls

When conducting the iterative DDBD for the PreWEC walls the EVD was based on the provisions outlined in Appendix B of the New Zealand Concrete Standard [18] and the PRESSS design handbook [19] as described by Equation (7-2). The moment contribution ratio (λ) and corresponding damping (ξ_{eq}) values for the spectrum compatible ground motions for each PreWEC wall are shown in Figure 7.28 versus drift assuming A&S force-displacement behaviour.

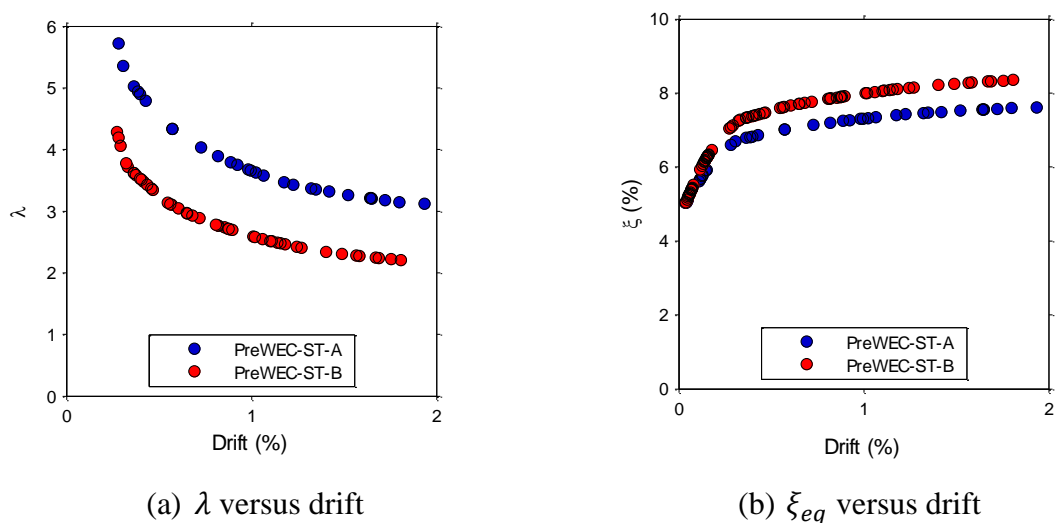


Figure 7.28 – Critical design parameters for PreWEC DDBD

Using the assumed EVD relationship the DDBD iterative procedure was performed with the adjusted R values to determine adjusted design drifts. The ratio of the peak test drift to the adjusted design drift versus the adjusted return period factor (R_{ad}) for each of the spectrum compatible motions applied to PreWEC-ST-A and B2 are presented in Figure 7.29. As with SRW-ST-A each intensity level is colour coded with each individual ground motion shown by the dot and the average of the intensity level shown by the same coloured bar. The average of all spectrum compatible ground motions is shown by the thick black dotted line.

On average the correlation between the design and test data for PreWEC-ST-A is shown to be in excellent agreement for the EVD evaluated using Equation (7-2) with an overall average of 1.01. There is noticeable scatter in the data, but significantly less so than SRW-ST-A implying a more stable and predictable response. For PreWEC-ST-B2 the correlation between design drift and achieved drifts was not as good, with the peak test drift exceeding the design drift estimations by approximately 29% for EVD calculated with Equation (7-2). These under estimated drifts implying less damping was present in PreWEC-ST-B than expected by the EVD design assumption. A similar trend was observed for the PreWEC walls to SRW-ST-A with the lower level intensity suites of ground motions having drifts significantly greater than predicted which indicates lower damping than 5% when no rocking occurred and aligns well with the measured inherent damping of 3.11% and 3.9% during the white noise tests for the two PreWEC walls.

Despite EVD evaluated using Equation (7-2) giving good estimates of average test drifts, over all intensities for PreWEC-ST-A, the four highest intensity levels reached drifts that were consistently slightly over predicted, with an average of 85%. For PreWEC-ST-B2 the three highest intensity levels reached drifts that were near the target drift with an average of 3% under the DDBD predicted drift for EVD evaluated using Equation (7-2).

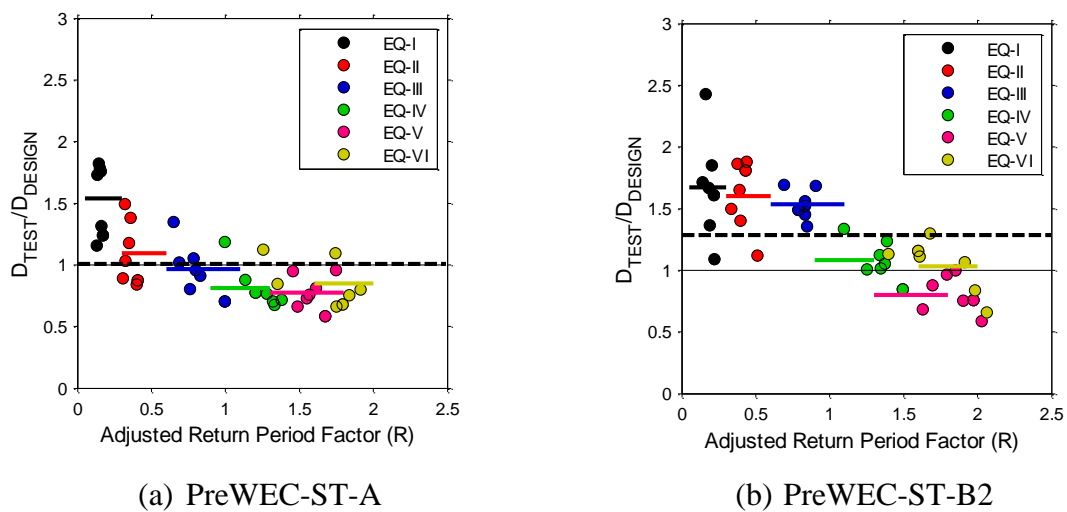


Figure 7.29 – Comparison between DDBD method and PreWEC shake table data

7.5.5.5 Summary

Overall it is clear that the current damping assumptions give reasonable results when considering all ground motions run, but could be greatly improved to achieve more consistent results across all levels of intensity which induce different levels of ductility and drift targets. It is clear especially that at low drifts or demands 5% damping is too great and this should be refined for single wall systems, however it is acknowledged that 5% damping is recommended by codes as it would usually include damping from non-structural elements and represent the building as a whole. Overall the tests give reasonable results but further refinement of design assumptions including, damping, yield displacement and force-displacement response would enable for increased accuracy.

7.5.6 Incremental dynamic analyses using shake table results

Incremental dynamic analysis (IDA) is a parametric analysis method which can be used to understand structural performance under seismic loads. It usually involves subjecting a structural model to one or more ground motions, each scaled to multiple levels of intensity, which produces a curve of response or damage parameter versus intensity level [118]. In this case three walls have been subjected to a suite of seven ground motions scaled to either four or six intensity levels. A method similar to IDA is used here with the shake table data to provide insight into the performance of the three wall systems despite the slight changes in structural properties that do occur during the test sequences. Normally, IDA would analyse models that have not suffered

any strength or stiffness degradation or hardening. The parameters used here to give a measure of intensity are PGA and 5% damped spectral acceleration ($S_A(T_1, 5\%)$) at the first mode period (fixed base mode assumed from Table 7.4). The parameters used here as response or damage measures are the peak drift and peak centre of mass acceleration. The peak acceleration is important for objects in a building and non-structural component performance while the peak drift can provide an indication of global dynamic stability.

Firstly, the PGA versus peak drift for each ground motion at each intensity level is plotted in Figure 7.31 (a), (c), and (e) for each of the three wall systems SRW-ST-A, PreWEC-ST-A, and B2, respectively. The 5% damped spectral acceleration at the first mode period versus peak drift for each ground motion at each intensity level is plotted in Figure 7.31 (b), (d), and (f) for SRW-ST-A, PreWEC-ST-A, and B, respectively. All curves exhibit a distinct elastic linear region at low drifts which diverges as rocking starts to occur. Although it was expected it is very clear that there is large record to record variability after this elastic region.

For SRW-ST-A, GM2 reverses from intensity level EQ-III to EQ-IV where a higher PGA does not result in a higher lateral drift response. This is not unusual and demonstrates that it is not just the intensity but the pattern and timing that make a difference for nonlinear systems, in this case rocking systems. For instance, as the intensity increases the weaker sections at the start of the earthquake become large enough for a rocking response to occur resulting in period elongation which alters how the wall behaves for the remaining part of the earthquake, perhaps leading to a lower response. For GM1 and GM5 a sudden increase in drift is observed without a large increase in either intensity measure demonstrating that SRW-ST-A was nearing dynamic instability for that particular ground motion.

For the two PreWEC walls the behaviour of PGA and S_A versus peak drift is more regular than SRW-ST-A, increasing relatively linearly and consistently for each ground motion with less variability between the ground motions showing less sensitivity to the particular frequency content. The linear behaviour also shows an approximate equal displacement approximation especially for PreWEC-ST-B. Also plotted in each S_A versus peak drift figure is the static pushover curve (PO) in dashed black lines calculated using the simplified analytical method proposed by Aaleti and Sritharan [62]. The PO curve is included in the figures by dividing the force by the structure mass, which is all that is required for SDOF systems [118]. The dynamic response of the walls is consistently larger than the PO for all walls as found in previous IDA

numerical research. For SRW-ST-A the overall shape of the shake table data aligns well with the PO curve. For the two PreWEC walls the shape is similar but not as apparent.

The 5% damped spectral acceleration at the first mode period versus peak centre of mass acceleration for each ground motion at each intensity level is plotted in Figure 7.30(a), (b), and (c) for each of the three wall systems SRW-ST-A, PreWEC-ST-A, and B2, respectively. The peak acceleration is important for damage to non-structural components. It is clear that in each wall the centre of mass acceleration is limited and the “stiffness” in each plot increases resulting in only small increases in centre of mass acceleration despite large increases in spectral acceleration. At what magnitude this acceleration is limited depends on the strength of the wall.

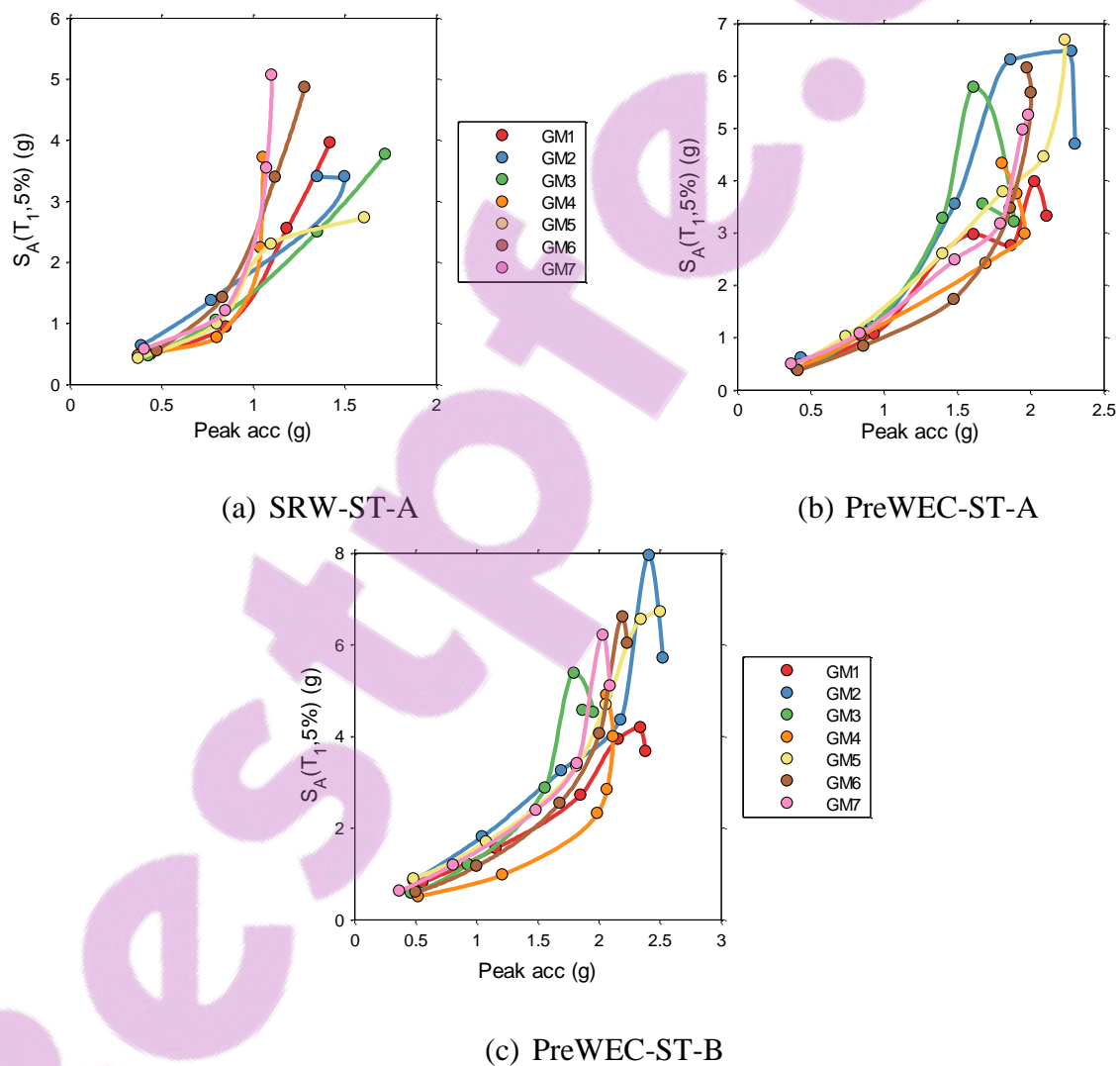
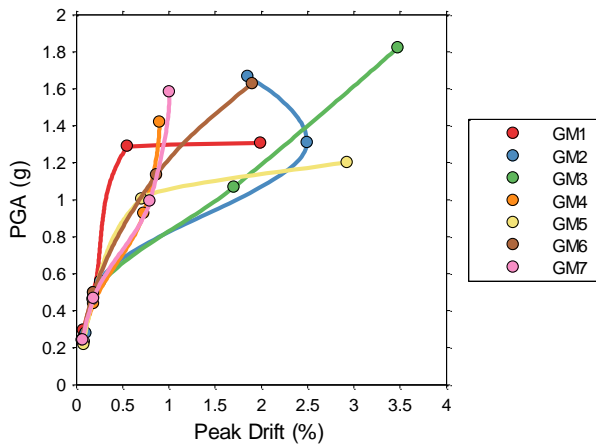
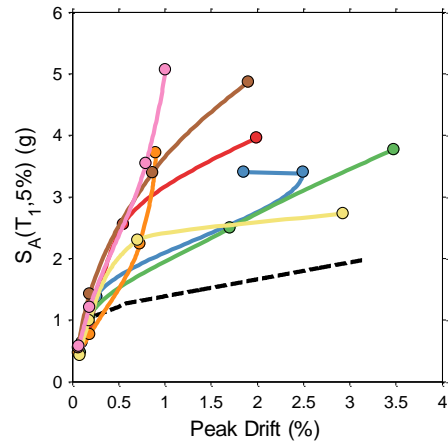


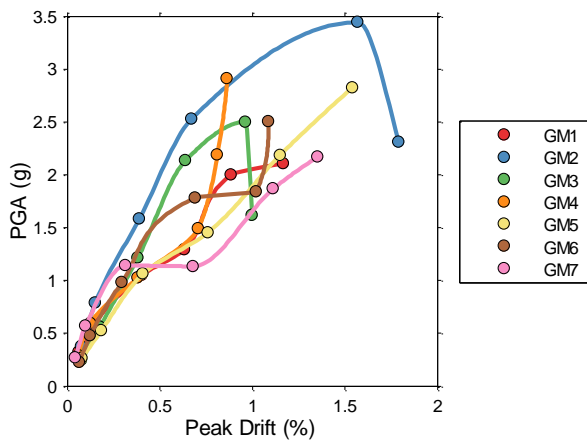
Figure 7.30 – $S_A(T_1, 5\%)$ versus peak centre of mass acceleration for spectrum compatible ground motions for all walls



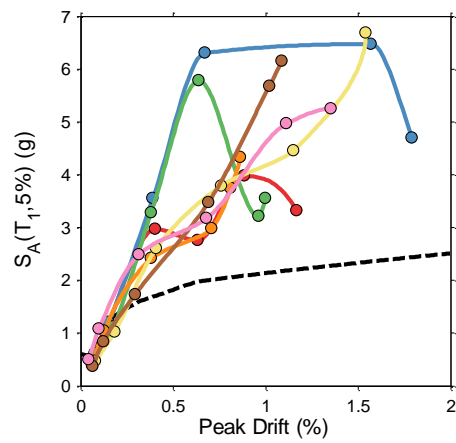
(a) SRW-ST-A PGA



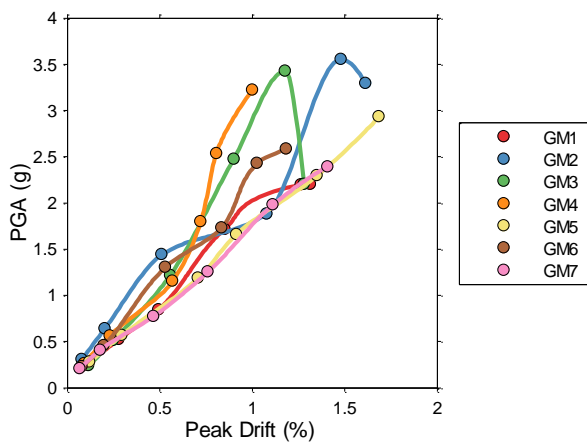
(b) SRW-ST-A S_A



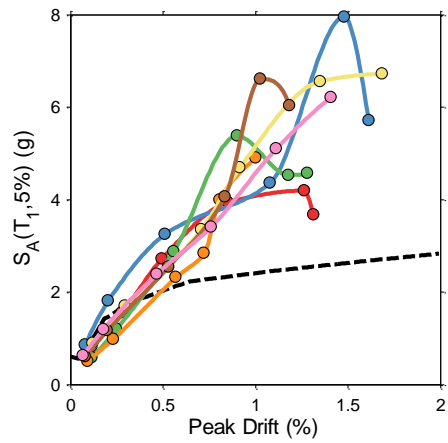
(c) PreWEC-ST-A PGA



(d) PreWEC-ST-A S_A



(e) PreWEC-ST-B2 PGA



(f) PreWEC-ST-B2 S_A

Figure 7.31 – PGA and $S_A(T_{1,5\%})$ versus drift for spectrum compatible ground motions on all walls

7.6 HARMONIC MOTION RESULTS AND DISCUSSION

Harmonic tests were performed to investigate the steady state response of SRW-ST-A with controlled sine waves in comparison to what is expected of a linear single degree of freedom system. The harmonic loads applied were defined in Table 7.6. A summary of the harmonic test results is presented in Figure 7.32 where the dynamic amplification factor is plotted versus the input displacement forcing frequency. The dynamic amplification factor, also known as the deformation response factor, is the ratio of the absolute output displacement at the centre of mass to the static deformation or measured input displacement. The dynamic amplification factor was calculated for each HM-2 sine wave by taking the ratio of the average of the displacement peaks of the input and output displacement. Also plotted in Figure 7.32 are the displacement transmissibility functions of the two sweep sine tests from HM-1, which show a similar overall behaviour to the dynamic amplification of the HM-1 tests. The peak response is clearly at a lower frequency than the fixed base frequency measured at the end of testing of 5.87 Hz. Usually the dynamic amplification would be plotted versus the frequency ratio (ω/ω_n) where ω is the forcing frequency and ω_n is the natural frequency of the structure. However for rocking walls the frequency is shortened (period elongation) once rocking occurs due to the decrease in stiffness which means that the natural frequency changes with input. This leads to a “pseudo” resonance at a lower frequency which in this case is between 3.7-4.1 Hz, a 50% reduction in fundamental frequency.

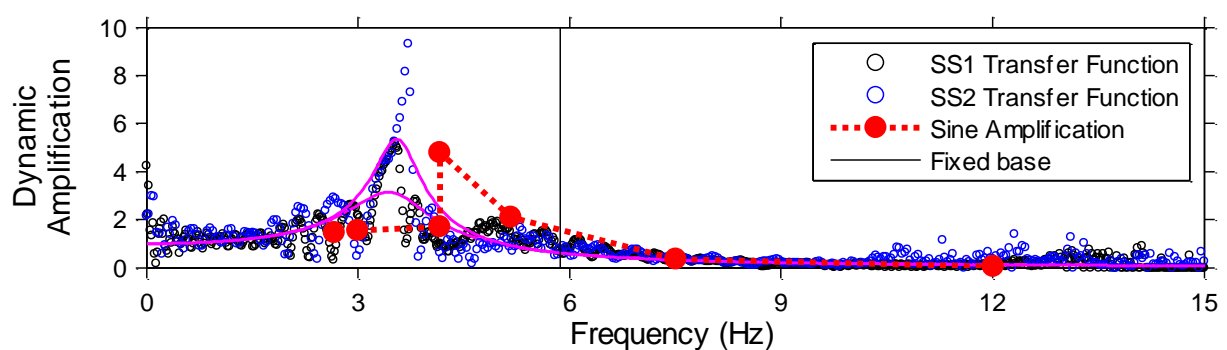


Figure 7.32 – Harmonic test results by way of dynamic amplification versus frequency

7.7 CONCLUSIONS

Presented in this chapter were shake table tests of three unbonded PT precast concrete walls, including one single rocking wall and two PreWEC systems that incorporate O-connector dissipaters. The wall systems tested were the same as three of the walls tested in Chapter 5 and 6. A suite of seven spectrum compatible ground motions were applied to each of the wall systems at up to six different intensity levels. Two suites of three recent ground motions at natural scale were also applied. White noise tests were performed between each ground motion to determine the change in fundamental frequency or stiffness and the overall inherent damping in each wall system.

Negligible damage was observed for all three wall systems throughout the entire sequence of testing. Any damage was limited to minor cracking and spalling of concrete in the compressive toe region of the precast concrete wall panel and the intended yielding of the O-connector dissipaters. The damage observed was similar to that found for the cyclic testing performed in Chapter 5. This result demonstrated the excellent design and performance of the wall systems that each underwent up to 50 ground motions.

Despite the small amount of observable damage, stiffness degradation did occur, evidenced by the decrease in the measured fundamental frequency from white noise tests throughout the test sequences. SRW-ST-A had a 25% decrease in fundamental frequency from 7.91 Hz at the culmination of the test sequence. PreWEC-ST-A showed a decrease of 13.7% from 9.96 Hz and PreWEC-ST-B2 showed a decrease of 17.1% from 8.95 Hz.

The inherent damping when no rocking occurred was also calculated from the white noise tests. The measured inherent damping was found to be 3.47%, 3.11%, and 3.90% for SRW-ST-A, PreWEC-ST-A, and PreWEC-ST-B, respectively.

During the ground motions clear rocking behaviour was observed during various events for all walls. SRW-ST-A reached drifts of up to 3.48% while the highest drifts reached for the two PreWEC systems were 1.79% and 1.68% for PreWEC-ST-A, and B, respectively. This was expected due to the increased hysteretic energy dissipation and strength of the PreWEC systems in comparison to the SRW. The walls exhibited the expected force displacement behaviours with the SRW showing a generally nonlinear elastic response and the PreWEC walls having increased

strength and hysteretic loop area in comparison. The corresponding peak accelerations at the maximum achieved drifts were 1.72 g, 2.31 g, and 2.53 g for SRW-ST-A, PreWEC-ST-A, and B, respectively. Although lower drifts were reached by the PreWEC systems, higher accelerations were reached due to the increased strength.

The residual drifts at the end of all shake table tests were minimal, rarely exceeding 0.05%, which was significantly lower than those observed in the pseudo-static cyclic tests, and less than previously stated drift limits. A residual drift ratio was calculated to give an indication of the shake-down effect with SRW-A, PreWEC-A, PreWEC-B1 and B2 having residual drift ratios of 0.1, 0.25, 0.24, and 0.25 which demonstrates that the dynamic residual drift was only 25% of that expected for the same peak drift from cyclic testing at a maximum.

A comparison of design drifts and achieved experimental drifts was made to evaluate the DDBD procedure employed. On average the correlation between the design and test data for SRW-ST-A and PreWEC-ST-A was shown to be in good agreement, however there was considerable scatter in the data due to the sensitive nature of SRW. The average correlation between design drift and achieved drifts was not as good for PreWEC-ST-B2 with design drifts under predicting the response overall by approximately 29%, indicating less damping was present than expected in design. However, for PreWEC-ST-B2 the three highest intensity levels reached drifts that were on average near the target drift with an average of 3% under the DDBD predicted drift. For all walls the low intensity ground motions were consistently under predicted with values greater than 1 indicating damping of 5% was too large when no rocking was occurring which aligns well with the calculated inherent damping values of less than 4%.

Overall the current damping assumptions from the PRESSS Design Handbook and NZS3101 Appendix B gave reasonable results when considering all ground motions run. However, the results could be greatly improved to achieve more consistent results across all levels of intensity that relate to different drift targets. Currently, the design drifts at low intensities are overestimated and the design drifts tend to be underestimated at high drifts, the consequence being a good average overall. Further refinement of design assumptions including, damping, yield displacement and force-displacement response to attain increased accuracy and robustness is recommended.

Analysis of the intensity and damage measures for all walls demonstrated that it is not just the intensity but the pattern and timing that are significant for rocking systems due to the effect of period elongation. The reduced variability and sensitivity of the PreWEC walls response in comparison to SRW-ST-A was also shown by the relatively linear and consistent increase in drift with spectral acceleration of the PreWEC walls. A comparison of spectral acceleration to peak acceleration demonstrated the peak acceleration being limited by the wall strength as spectral accelerations significantly increased.

The harmonic tests performed on SRW-ST-A demonstrated that the peak response during harmonic tests occurs at a lower frequency than the fixed base frequency measured at the end of testing to be 5.87 Hz due to period elongation. A pseudo-resonance frequency is estimated to be between 3.7-4.1 Hz which is a 50% reduction in frequency from the fixed base.

7.8 REFERENCES

13. Marriott, D., *The Development of High-Performance Post-Tensioned Rocking Systems for the Seismic Design of Structures*. 2009, University of Canterbury: Christchurch.
18. New Zealand Standard, *Concrete Structures Standard NZS 3101*. 2006: Wellington, New Zealand.
19. Pampanin, S., D. Marriott, A. Palermo, and New Zealand Concrete Society., *PRESSS design handbook*. 2010, Auckland, N.Z.: NZCS. 1 v. (various pagings).
20. Priestley, M.J.N., G.M. Calvi, and M.J. Kowalsky, *Displacement-based seismic design of structures*. 2007, Pavia: IUSS Press : Fondazione Eucentre. xvii, 721 p.
41. Henry, R.S., *Self-centering precast concrete walls for buildings in regions with low to high seismicity*. 2011, University of Auckland. p. 441.
62. Aaleti, S. and S. Sritharan, *A simplified analysis method for characterizing unbonded post-tensioned precast wall systems*. *Engineering Structures*, 2009. **31**(12): p. 2966-2975.
101. Standards New, Z., *Structural design actions : AS/NZS 1170*. 2005, Wellington, N.Z. : Standards New Zealand.
108. New Zealand Standard, *Methods of test for concrete NZS 3112.2:1986 in Tests relating to the determination of strength of concrete*. 1986: Wellington.
113. Oyarzo-Vera, C.A., G.H. McVerry, and J.M. Ingham, *Seismic zonation and default suite of ground-motion records for time-history analysis in the North Island of New Zealand*. *Earthquake Spectra*, 2012. **28**(2): p. 667-688.
114. Chase, J.G., N.H. Hudson, J. Lin, R. Elliot, and A. Sim, *Nonlinear shake table identification and control for near-field earthquake testing*. *Journal of Earthquake Engineering*, 2005. **9**(4): p. 461-482.
115. Inman, D.J., *Engineering vibration*. Fourth edition.. ed. 2014: Boston : Pearson. 2014.
116. Thomson, W.T., *Theory of vibration with applications*. 4th ed.. ed. 1993, Englewood Cliffs, N.J.: Englewood Cliffs, N.J. : Prentice Hall ©1993.
117. Macrae, G.A. and K. Kawashima, *Post-earthquake residual displacements of bilinear oscillators*. *Earthquake Engineering and Structural Dynamics*, 1997. **26**(7): p. 701-716.
118. Vamvatsikos, D. and C. Allin Cornell, *Incremental dynamic analysis*. *Earthquake Engineering and Structural Dynamics*, 2002. **31**(3): p. 491-514.

Chapter 8

EVALUATION OF DAMPING SCHEMES

8.1 INTRODUCTION

Following experimental testing of the SRW and PreWEC systems as reported in Chapters 5, 6, and 7, numerical analysis of the test walls was undertaken to assist in understanding the observed behaviour and to assess the suitability of different numerical damping schemes. The current state-of-the-art of structural damping determination does not provide a method to determine the damping in a system based on material properties and geometrical characteristics of a structure. Usually it is appropriate to attain a damping model that is capable of modelling realistic damping forces that provide an accurate estimation of the seismic response of a structure. Development and validation of these types of damping model can often only be achieved by conducting dynamic testing. Due to the lack of dynamic test data there has been limited numerical models that have been validated against such data, hence this is a unique opportunity to demonstrate a models ability to capture the typical nonlinear response associated with unbonded PT rocking wall systems.

The ability of commonly used damping schemes available in many software packages to simulate the global response of unbonded PT walls was investigated using a simple Single Degree Of

Freedom (SDOF) model. A simple SDOF modelling procedure was chosen due to its simplicity and ease of application into models of entire buildings. The numerical modelling presented in this chapter investigated the ability of various damping schemes to accurately model realistic damping forces in the SRW and PreWEC systems tested. The overall objective of the chapter is to determine damping schemes appropriate for use in SDOF models of SRW and PreWEC systems that are able to accurately emulate the seismic response.

8.2 DAMPING SCHEME THEORY IN CURRENT PRACTICE

Current guidance on how to accurately model energy dissipation in rocking walls is limited due to the scarce dynamic test data. The damping in a SRW consists mainly of inherent, contact and a small amount of hysteretic damping. The inherent damping is associated with the material and in concrete structures usually consists of friction or micro-cracking. The hysteretic damping is minor and is as a result of imperfect elasticity and any degradation that occurs in the concrete wall corners and any slip at the PT anchorage. Damping in a PreWEC system consists of all the components of the SRW damping as well as additional hysteretic damping from the specially designed O-connectors. It is essential that these damping mechanisms are known so that appropriate equivalent viscous damping (EVD) values or definitions can be used in the design process.

Current state-of-the-art for modelling damping in any structure uses the best representation hysteretic model with some linear viscous damping model to represent the inherent ‘elastic’ damping. This method assumes the inherent damping is proportional to the velocity of the system, and does not depend on the level of nonlinear behaviour of the structural system. An issue addressed in recent literature is what stiffness the damping ratio should be proportional to during analyses, with findings pointing to use of tangent stiffness instead of initial stiffness to avoid unrealistically large damping values at high natural frequencies. For SDOF systems the constant value of damping co-efficient (c) if determined with respect to the initial vibration frequency (ω_i) and initial loading stiffness (k_i) is described by Equation (8-1). The vast majority of analysts use initial-stiffness proportional elastic damping for SDOF analysis without considering whether or not it is appropriate. When the damping co-efficient is proportional to the instantaneous value of stiffness or the tangent stiffness, it is updated whenever the stiffness

changes, as described by Equation (8-2). The constant of proportionality ($\alpha_{constant}$) is determined based on the initial, elastic vibrational properties as shown by Equation (8-3). Therefore, at any instant c may be determined from the ratio of tangent stiffness to initial stiffness. It is also possible to update the constant of proportionality as described by Equation (8-4) ($\alpha_{updated}$) to the current stiffness properties and determine an updated vibration frequency at every time step of a Nonlinear Time History Analyses (NLTHA).

$$c = 2m\omega_i\xi_{eq} = 2\xi\sqrt{mk_i} \quad (8-1)$$

$$c = 2m\omega_i\xi_{eq} \frac{k_t}{k_i} = \alpha k_t \quad (8-2)$$

$$\alpha_{constant} = \frac{2\xi_{eq}}{\omega_i} \quad (8-3)$$

$$\alpha_{updated} = \frac{2\xi_{eq}}{\omega_t} \quad (8-4)$$

Despite limited dynamic testing on unbonded PT walls there have been numerous NLTHA performed on various forms of unbonded PT walls. In general the inherent damping in these analyses was modelled as viscous damping between 3%-5% with any supplemental damping modelled separately. The viscous damping is usually modelled as mass and stiffness proportional Rayleigh damping, stiffness proportional damping (proportional to which stiffness is not specified) or proportional to elastic modes of vibration i.e. initial stiffness [70]. More recently damping has been modelled as proportional to tangent stiffness of critical damping [119] following recommendations by Priestley et al. [20].

8.3 SRW NUMERICAL ANALYSES

8.3.1 Model development

In order to assess appropriate methods of modelling damping of SRW and PreWEC systems in a numerical simulation, an investigative model was first run where all other parameters in the model were based on test measurements so as not to distort the damping force term. The critical aspect of modelling precast post-tensioned concrete structures is modelling the rocking

mechanism and contact interface at joints. A common method of modelling unbonded PT walls is to use a lumped plasticity model based on a section analysis representing the wall to foundation connection with a hysteretic model. In the nonlinear analysis of structures, hysteresis models, defined at the section level are often used to represent the material nonlinearity of structures. A hysteresis model is usually defined to represent the behaviour of a particular material and member type and is developed based on experimental pseudo-static cyclic testing. A simple SDOF model was used here to represent the test walls in the form of a combination of springs in parallel that represent the geometric nonlinearity and material nonlinearity of the observed hysteretic behaviours of the SRW and PreWEC walls.

The numerical model was developed in Matlab [120] to enable different damping schemes to be easily implemented. The experiments were approximated as SDOF systems and the analysis used the generic second order governing differential equation of motion described by Equation (8-5), which is based on horizontal force equilibrium of an idealised single degree of freedom structure as depicted in Figure 8.1. Where \ddot{u} , \dot{u} , and u are the relative acceleration, velocity and displacement and m , c and k are the total mass, damping co-efficient and stiffness. The governing equation of motion describes the motion at the centre of mass and assumes the entire system mass acts at that point. The system mass was equal to 3.9 tonnes as described in Chapters 6 and 7. To solve this equation a restoring force relationship and damping relationship must be assumed.

$$m\ddot{u} + c\dot{u} + ku = -m\ddot{u}_g \tag{8-5}$$

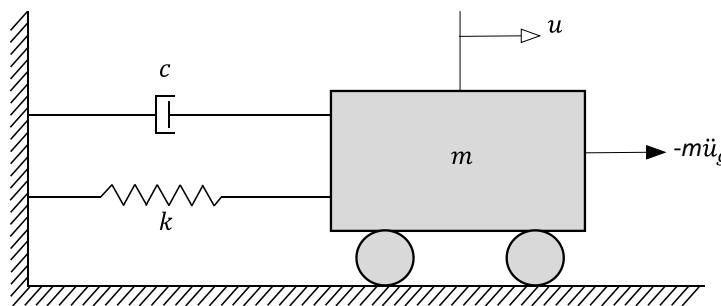
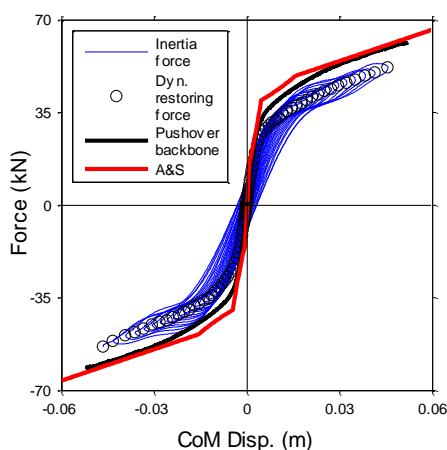


Figure 8.1 – SDOF model representation

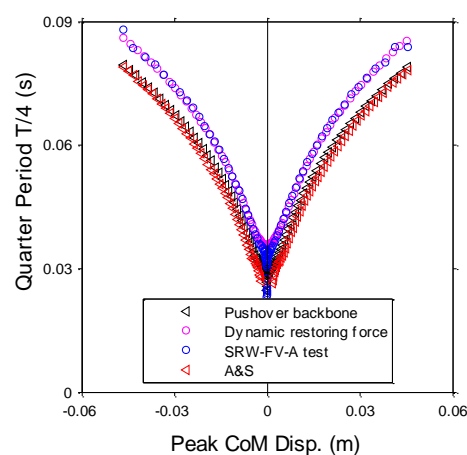
Initially, the restoring force-displacement relationship was defined by the measured pushover backbone from the snap back test, as presented in Figure 8.2(a), using a nonlinear elastic spring,

however, the measured pushover backbone proved to have an incorrect period-displacement relationship, as shown in Figure 8.2(b). As the aim was to accurately evaluate the damping in the test wall systems, it was considered essential to accurately replicate the restoring force-displacement behaviour to remove all significant assumptions other than damping. To achieve this goal, the restoring force-displacement relationship was estimated using the inertia force-displacement recorded during the snap back test. The restoring force was calculated from the inertia force by multiplying the test acceleration at the centre of mass by total mass of the system. When velocity is zero and assuming damping forces are proportional to velocity the restoring force from dynamic test results can be calculated using Equation (8-6). The calculated dynamic restoring force is shown in Figure 8.2(a) and was lower than the measured pushover backbone. The dynamic restoring force was used to calculate the period-displacement relationship and there was an excellent match as shown by Figure 8.2(b), thus eliminating any errors from assuming the restoring force-displacement behaviour. It is also of interest to show the restoring force-displacement behaviour calculated using the simplified analytical method proposed by Aaleti and Sritharan [62] (indicated as A&S in Figure 8.2(a)) as this will be used in further model development in the chapter. The restoring force-displacement relationship and corresponding period-displacement relationship for the A&S simplified analytical method are also shown in Figure 8.2(a) and Figure 8.2(b).

$$ku = -m\ddot{u} \text{ if } \dot{u} = 0 \text{ and } \ddot{u}_g = 0 \quad (8-6)$$



(a) Restoring force-displacement definition



(b) Period dependency with displacement

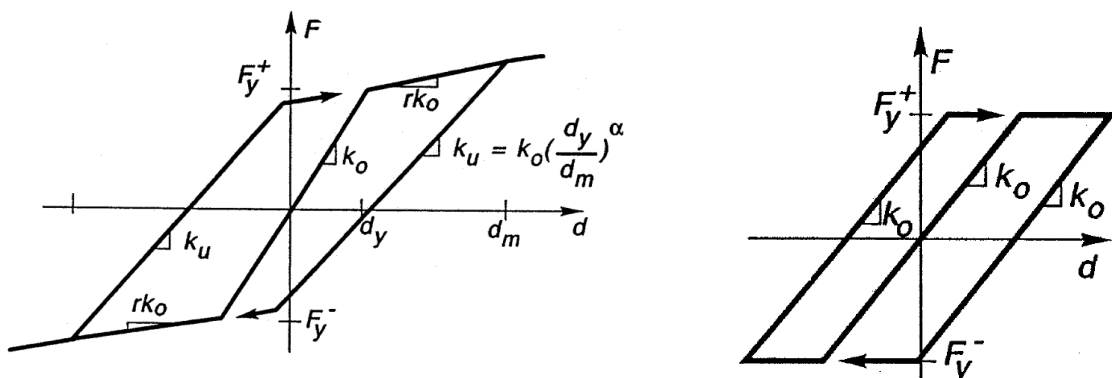
Figure 8.2 – SRW-FV-A force displacement behaviour and amplitude dependency of period for different restoring force assumptions

Using the dynamic restoring force definition and a mass of 3.9 tonnes, a selection of hysteretic definition and damping model combinations were investigated using NLTHA as presented in the following section. The different models were compared to the SRW-FV-A snap back test. An integration time step of 0.0005 was used for all free vibration analysis. The Newmark Explicit analysis method was used due to its computational efficiency.

8.3.2 Damping scheme trials

Many damping formulations were trialled separately and in combinations to assess their ability to capture the decay observed during the snap back tests for SRW-FV-A. The aim was to attain a damping model that was capable of modelling realistic damping forces that provide a realistic dynamic response of SRW-FV-A. The damping schemes trialled included:

- Pure viscous damping. (Refer to Equation (8-1))
- EVD proportional to tangent stiffness with constant and updated α . (Refer to Equations (8-2), (8-3), and (8-4))
- Hysteretic damping in the form of friction/coulomb damping.
- Hysteretic damping in the form of a bilinear degrading stiffness as shown in Figure 8.3(a). When r is equal to 0 and α is equal to 0 the bilinear degrading stiffness simplifies to an elasto-plastic rule as described by Figure 8.4.



(a) Degrading Bilinear rule [121]

(b) Elasto-plastic rule [121]

Figure 8.3 – Hysteresis rules

Firstly the effect of pure viscous damping was investigated due to the easy implementation and familiarity in the engineering community. To demonstrate the response of the pure viscous damping model the natural log of the displacement peaks over time has been plotted in Figure 8.4(a) for damping ratios ranging from 0.4% to 0.8% along with the measured the SRW-FV-A 2% drift free vibration response. It is clear that a low level of viscous damping ratio fits well for the initial section of the free vibration response during the full rocking phase, but as the wall enters the second phase and rocking ceases far higher damping is required. The damping force versus displacement for a damping ratio of 0.5% is presented in Figure 8.4(b). The damping force displacement behaviour is elliptical due to the nonlinear restoring force-displacement relationship. For the appropriate decay shape to be attained more energy needs to be dissipated near zero displacement than that demonstrated by the pure viscous damping force.

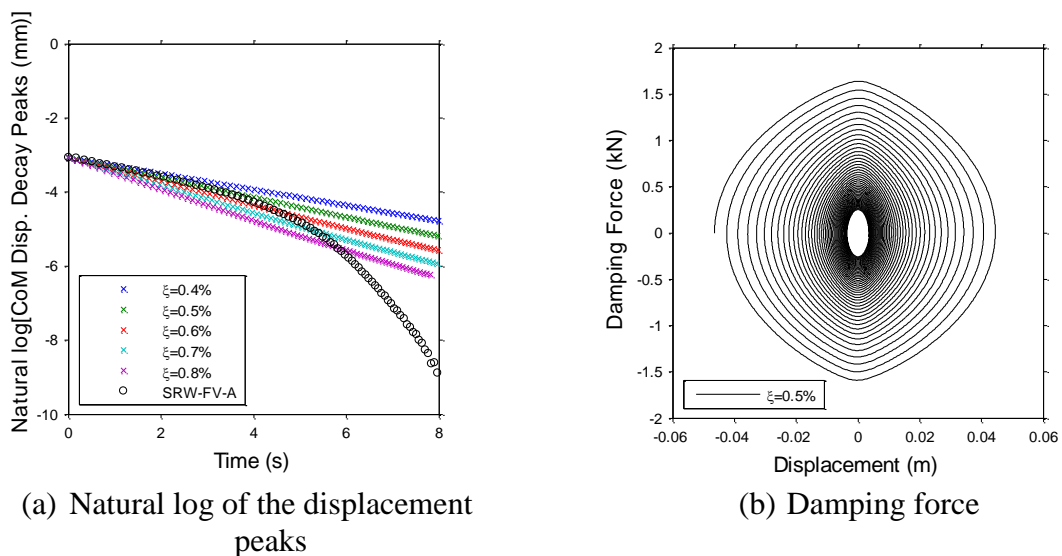
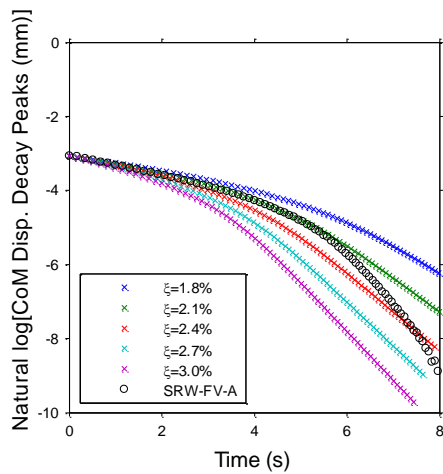


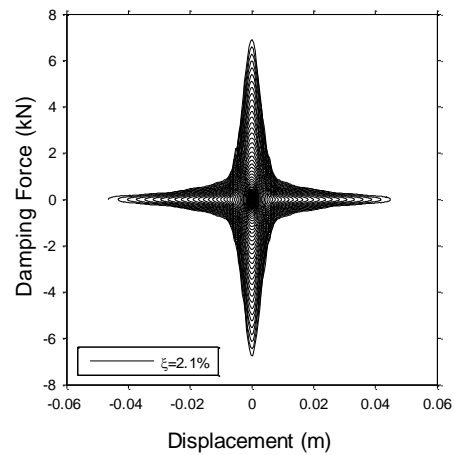
Figure 8.4 – Effect of pure viscous damping on free vibration response

The next damping scheme investigated was viscous damping proportional to tangent stiffness with constant and updated α using Equations (8-2), (8-3) and (8-4). The natural log of the displacement peaks and the damping force versus displacement for tangent stiffness damping with constant α and updated α are presented separately in Figure 8.5 with the SRW-FV-A 2% drift free vibration response. For the constant α tangent stiffness scheme, damping ratios ranging from 1.8% to 3.0% were chosen to show the general trend of how the decay shape changes, while for the updated α tangent stiffness damping scheme, damping ratios from 1.0% to 1.4% are shown. It is clear that the constant α tangent stiffness damping scheme is more appropriate for

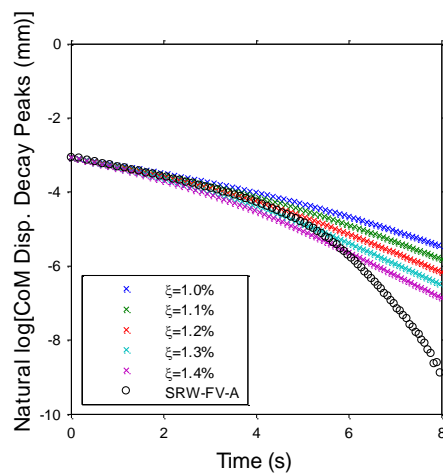
the behaviour observed in SRW-FV-A due to the large damping forces occurring near zero displacement which emulates the rocking behaviour of higher damping as rocking ceases. The need for higher damping near zero displacement aligns with the required damping from impacts at zero displacement crossings.



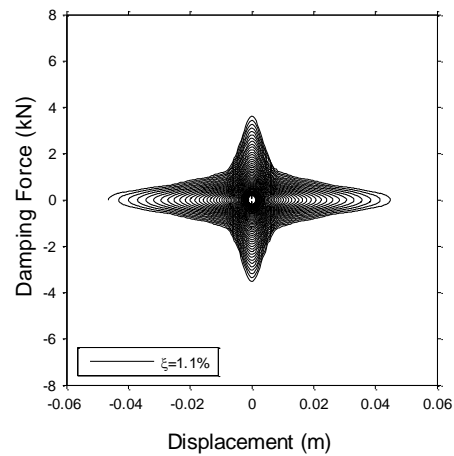
(a) Natural log of the disp. peaks (constant α)



(b) Damping force (constant α)



(c) Natural log of the disp. peaks (updated α)

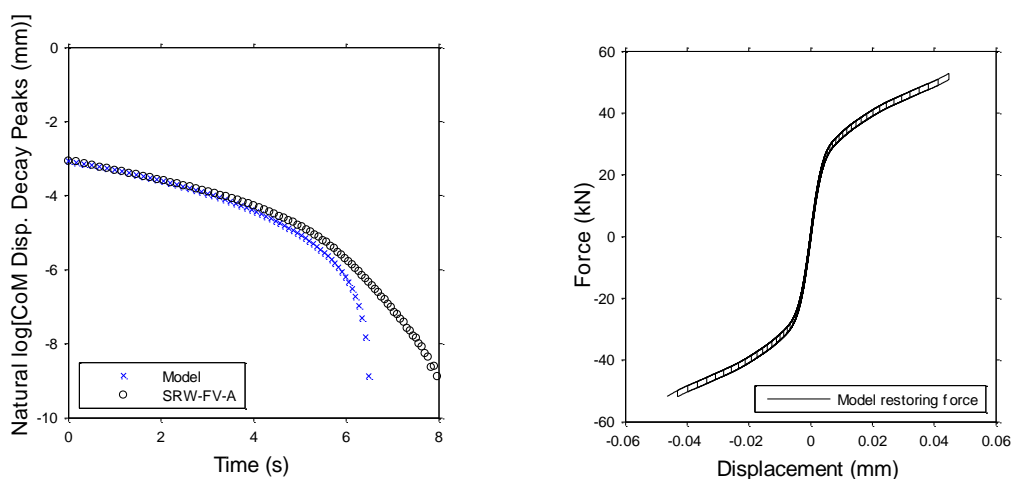


(d) Damping force (updated α)

Figure 8.5 – Effect of tangent stiffness proportional viscous damping

The previous damping schemes investigated have used the dynamic restoring force as a nonlinear elastic spring. The next scheme investigated uses coulomb damping otherwise known as friction damping without any viscous damping force in combination with the nonlinear elastic spring. The natural log of the displacement peaks is plotted in Figure 8.6(a) for a coulomb force (F_f) equal to 1.0 kN. The energy dissipation from coulomb damping is incorporated in the hysteretic response which is plotted in Figure 8.6(b) using an additional spring. The hysteretic response

shows the combination of nonlinear restoring force backbone with the 1 kN coulomb damping. Overall the displacement peak envelope response fits the test data reasonably well until 6s into the response when the numerical damping become exponentially too high as displacements approached zero.



(a) Natural log of the displacement peaks (b) Restoring force-displacement

Figure 8.6 – Effect of friction damping on decay response for $F_f = 1$ kN

The final scheme investigated used the bilinear degrading hysteresis model presented in Figure 8.3(a). The properties of the example bilinear degrading hysteresis spring investigated were chosen based on fitting the spring to the cyclic hysteresis of SRW-A presented in Chapter 5. The spring properties that fit the SRW-A cyclic hysteresis well are as follows, initial stiffness (k_0) of 4000 kN, stiffness reduction factor (r) of 0, yield displacement (d_y) of 1 mm, and degrading factor (α) of 0 as defined in Figure 8.3(a) and shown in Figure 8.7(b). These spring properties make the bilinear degrading stiffness hysteresis an elasto-plastic definition as defined in Figure 8.3(b). The resulting restoring force of the nonlinear elastic spring and elasto-plastic spring combination is presented in Figure 8.7(c), overlaid on the cyclic hysteresis of SRW-A from Chapter 5 and the dynamic restoring force. The SRW-A pseudo-static cyclic force required a 0.8 factor to reduce the force to a similar strength of the dynamic restoring force from the snap back testing. This is a similar magnitude of force reduction to that shown in Figure 8.2(a) for the snap back test pushover response and dynamic restoring force. The displacement decay envelope is shown in Figure 8.7(a) for the elasto-plastic rule that best fit the cyclic test. It is clear that the

rate of decay is far too high for the free vibration decay of SRW-FV-A when a realistic cyclic restoring force behaviour is used.

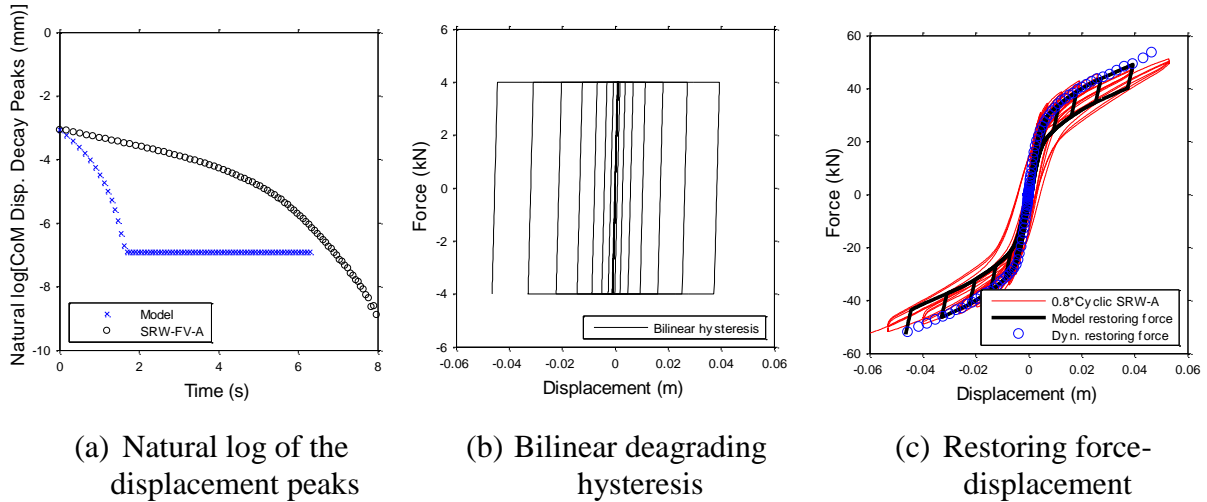


Figure 8.7 – Effect of cyclic test hysteresis on decay response

8.3.3 Dynamic backbone best fit model

Previous researchers have struggled to capture the different phases of rocking that include full base uplift rocking and partial base uplift rocking. These two phases of response are clearly exhibited from the two gradients of the displacement decay envelope for SRW-FV-A, as shown in Figure 8.7(a) and several other figures. Several analyses were undertaken combining the damping schemes discussed to develop the most appropriate scheme to best fit the displacement decay SRW-FV-A test data using a brute force trial and error approach. The damping scheme that was able to emulate the free vibration response of SRW-FV-A with the greatest accuracy was a combination of bilinear degrading hysteresis spring, friction damping spring, and tangent stiffness proportional damping with constant α . During development of the model when springs were required to increase the hysteresis area the combination of backbone response was calculated to ensure the Aaleti and Sritharan prediction was closely matched. The properties of the bilinear degrading hysteresis used are an initial stiffness (k_0) of 50 kN, a stiffness reduction factor (r) of 0, a yield displacement (d_y) of 1 mm, and degrading factor (α) of 0 i.e. elasto-plastic as before. The friction damper had a friction force (F_f) equal to 0.16 kN which was only activated below ± 4 mm (x_{lim}) displacement amplitude as described by Equation (8-5). Although the limited displacement friction damper is unusual it is effectively emulating the damping due to

impact as the wall rocks through zero position. The tangent stiffness proportional damping used was equal to 2%. A schematic of the best fit SDOF model is shown in Figure 8.8, where $k_1(u)$ is the nonlinear dynamic restoring force-displacement behaviour, $k_2(u)$ is the elasto-plastic spring and $F_f(u)$ is the friction damper previously described.

$$F_f(u) = \begin{cases} F_f, & -x_{lim} < u < x_{lim} \\ 0, & \text{Otherwise} \end{cases} \quad (8-7)$$

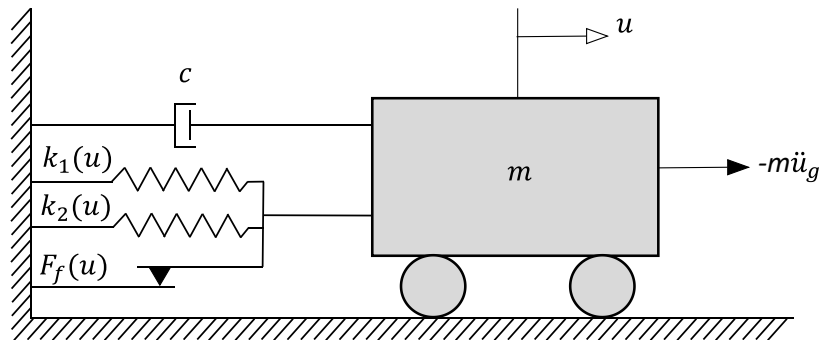


Figure 8.8 – SDOF best fit free vibration model

The natural log of the displacement peaks envelope, viscous damping force, and model restoring force are presented in Figure 8.9(a), (b) and (c) for both the best fit model and the SRW-FV-A test data. The displacement and acceleration time histories of the test and best fit combination damping scheme are plotted in Figure 8.10. The correlation between the calibrated model and test data is excellent, this demonstrates the ability of the numerical modelling technique to capture the overall damping behaviour of SRW-FV-A emulating the correct damping forces through each phase of the response. In general, it seems that some representation of the hysteretic response with 2% tangent stiffness proportional damping provides adequate numerical damping force representative of the real system. The end result of this numerical damping calibration procedure is a simple approach to modelling SRW damping that provides accurate simulation results for unbonded PT walls with no additional energy dissipation devices and shows adequate matching of response for both phase and amplitude when vibration is both small and large. Of course this damping scheme has only been calibrated from one wall test with one set of parameters, but it provides an indication of a simple way to model damping for SRW systems.

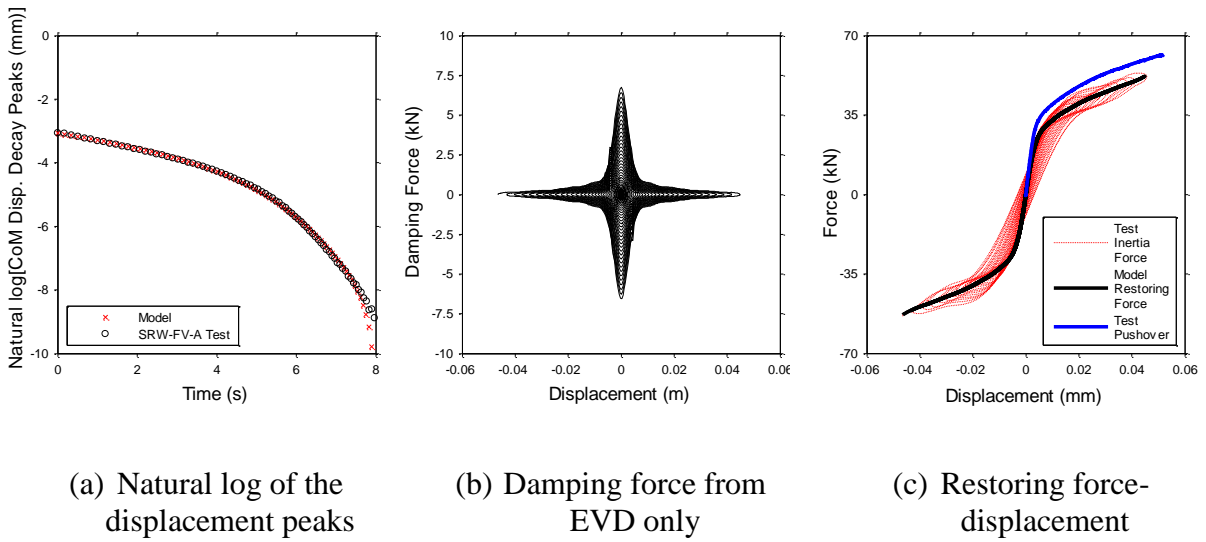


Figure 8.9 – Best fit damping scheme peak envelope and forces

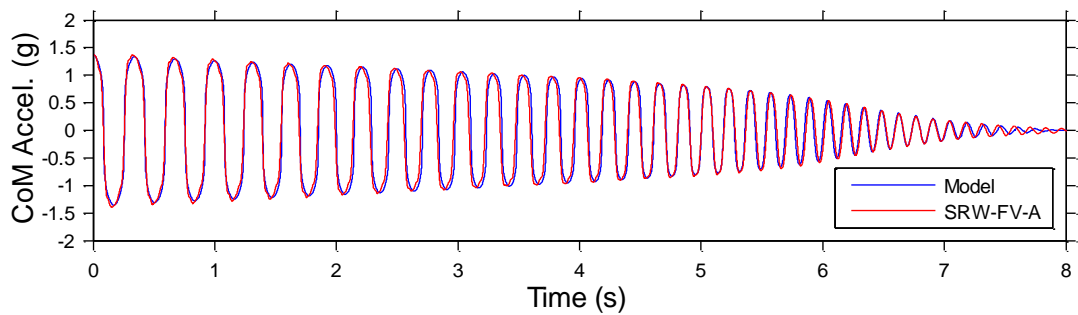
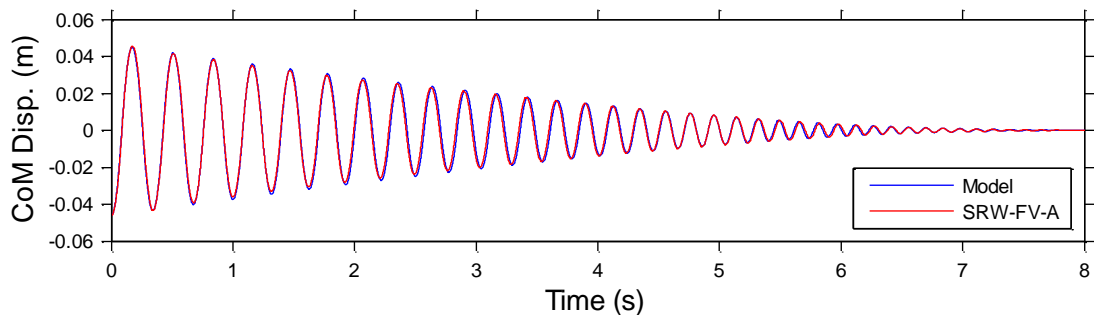
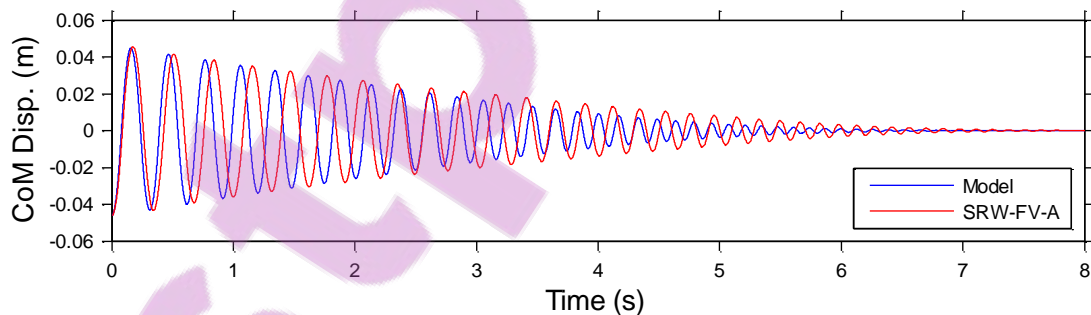


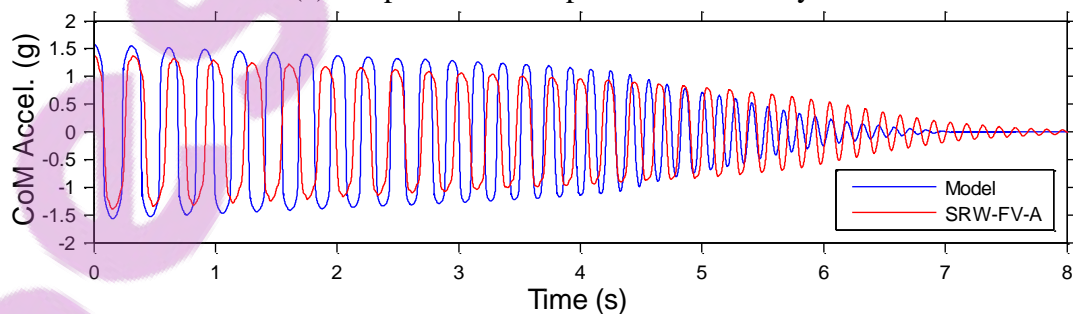
Figure 8.10 – Best fit damping scheme free vibration disp. and acceleration time history

8.3.4 Simplified analytical method model (A&S)

Now that an accurate simple representative damping scheme has been determined for SRW-FV-A, the best fit damping scheme can be used with a predictive force-displacement behaviour calculated using the A&S method [62] for SRW-FV-A. The free vibration acceleration and displacement response from 2% drift using the restoring force behaviour defined by the simplified analytical model and best fit damping scheme is plotted alongside the measured test response in Figure 8.11. The corresponding peak decay envelope and restoring force-displacement behaviour is shown in Figure 8.12. It is clear from the displacement and acceleration time histories presented in Figure 8.11 and the displacement peak envelope shown in Figure 8.12(a) that the match is significantly out of phase compared to when the dynamic restoring force backbone is used. The A&S restoring force-displacement used in the model is given in Figure 8.12(b), along with the snap back test pushover of SRW-FV-A and the SRW-FV-A test inertia force-displacement shown. Both the test pushover and S&A model behaviour are of a significantly higher strength compared to the SRW-FV-A test inertia force. This over prediction of strength from the A&S method is what causes the test and model responses to be out of phase and the increased rate of decay observed in Figure 8.12(a). It should be noted that the A&S backbone was adjusted to a smoothed spline with the ‘spaps’ function in Matlab.

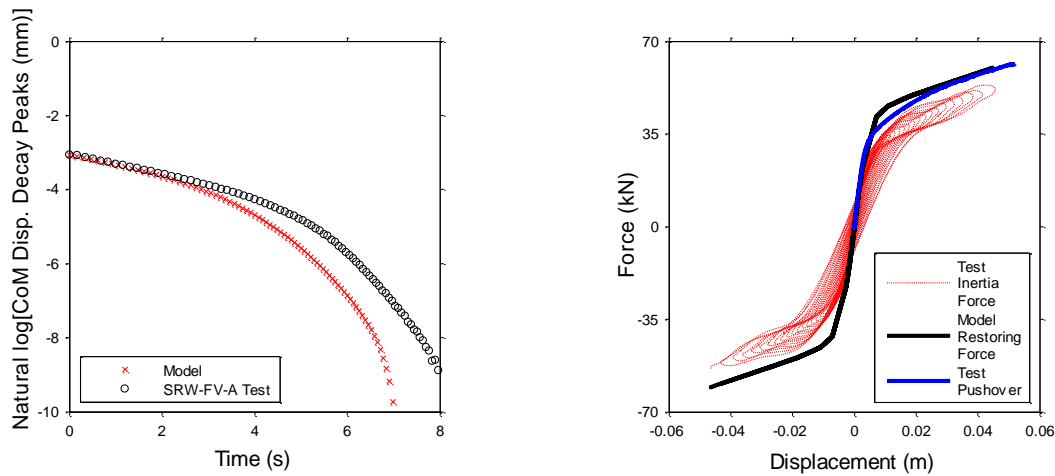


(a) Displacement snap back time history



(b) Acceleration snap back time history

Figure 8.11 – Best fit damping time histories with A&S restoring force for SRW-FV-A

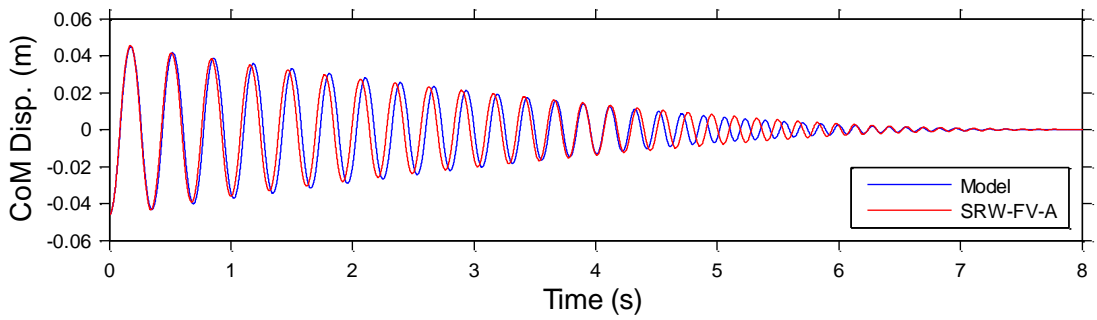


(a) Natural log of the displacement peaks

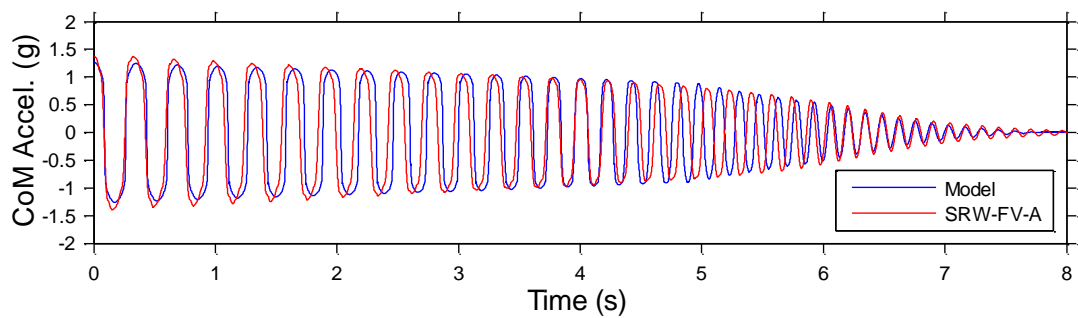
(b) Restoring force-displacement

Figure 8.12 – Best fit damping scheme peak envelope and restoring force-displacement with A&S restoring force for SRW-FV-A

To be able to achieve reasonable results the A&S force-displacement behaviour needed to be reduced by a reduction factor to better match the test inertia force response. The over prediction of the SRW force capacity by the A&S method proposed by Aaleti and Sritharan is partially due to the small error in predicting even the static pushover and cyclic response as shown in Chapter 5 and Chapter 6, but also due to the lower force capacity observed during dynamic loading for SRW-FV-A as demonstrated by the lower dynamic restoring force compared to the experimental pushover response, as highlighted in Figure 8.2(a). The A&S force was reduced by 20% using a 0.8 force reduction factor and the snap back analysis was performed again using the new restoring force behaviour and the best fit damping scheme. The free vibration acceleration and displacement response from 2% drift snap back test using the reduced restoring force behaviour defined by the A&S method and best fit damping scheme is plotted alongside the measured test response in Figure 8.13. The corresponding peak decay envelope and restoring force-displacement behaviour is shown in Figure 8.14. The A&S label in the plot is the non-reduced A&S prediction. The reduced A&S restoring force behaviour resulted in adequate phase and amplitude emulation when compared to SRW-FV-A 2% with relatively good representation at high and low displacement amplitudes.

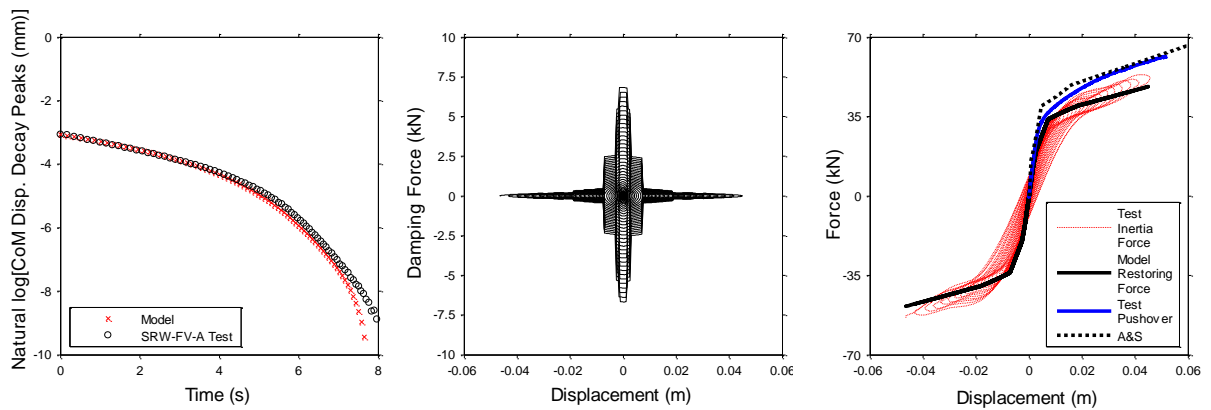


(a) Displacement snap back time history



(b) Acceleration snap back time history

Figure 8.13 – Best fit damping scheme free vibration displacement and acceleration time history with reduced A&S restoring force for SRW-FV-A



(a) Natural log of the displacement peaks

(b) Damping force from EVD only

(c) Restoring force

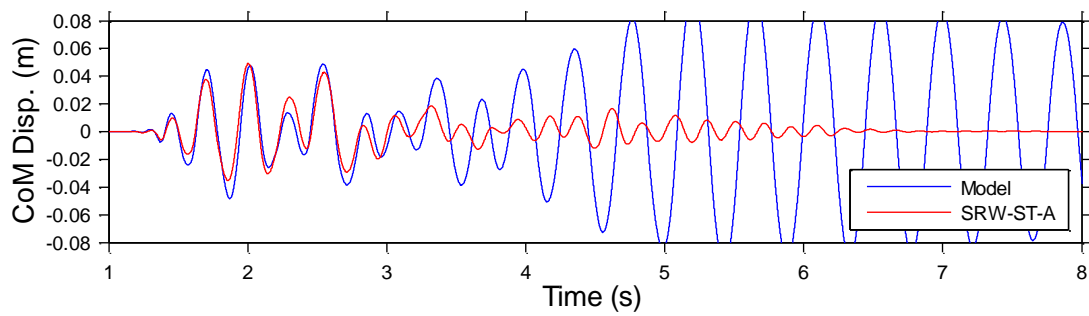
Figure 8.14 – Best fit damping scheme peak envelope and forces with reduced A&S restoring force for SRW-FV-A

8.3.5 Ground motion replication

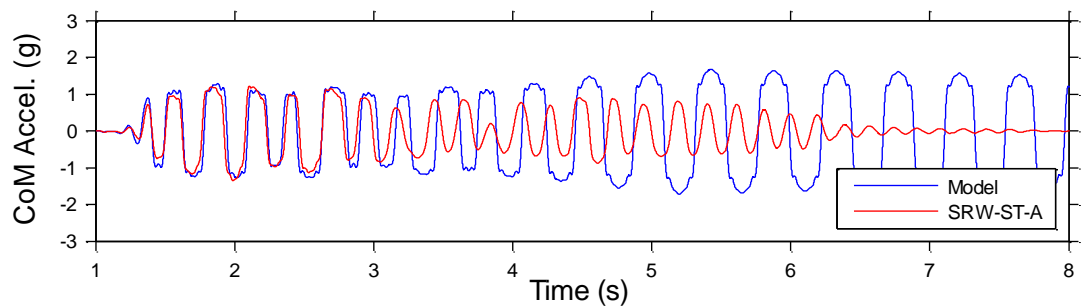
8.3.5.1 *Free vibration calibrated damping scheme*

The calibrated damping scheme from the free vibration response was used with the reduced A&S restoring force for SRW-ST-A in an attempt to emulate the shake table test result using the SDOF model previously discussed. The restoring force for SRW-ST-A was again calculated using the A&S method with the force reduction factor of 0.8 that was found to accurately represent the SRW-FV-A snap-back test. The fourteen intensity level EQ-III and EQ-IV ground motions applied during the shake table tests described in Chapter 7 were used here to evaluate the accuracy of the numerical model to emulate the SRW-ST-A test specimen with NLTHA. Only the two series of ground motions at high intensity were used as these are the most representative of an intensity level that would typically be modelled during design, and the accuracy at low intensity shaking is not as critical. An integration time step of 0.0005 was used for all ground motion analysis.

An example displacement and acceleration time history simulation is presented in Figure 8.15 for EQ-III:GM2 compared to the measured response for SRW-ST-A. The model shows excellent matching of both acceleration and displacement during the first 3s. However, after 3s the model result becomes seemingly chaotic and large amplitude oscillations are observed. The model restoring force, test inertia force and unreduced A&S force-displacement prediction (A&S) is shown in Figure 8.16(a) for EQ-III: GM2, and the overall shape of the test inertia and model restoring force aligned well. However, it is clear from the test inertia force-displacement relationship that significant hysteresis occurred for SRW-ST-A during the shake table test not accounted for in the best fit free vibration damping scheme. The ratio of the model to test peak displacement and acceleration for each of the 14 ground motions are shown in Figure 8.16(b). Similar behaviour to EQ-III: GM2 was observed for a large number of the ground motions, with an average ratio of model/test peak displacement of 1.95 (ranging from 0.87-3.88 for individual records) while the average ratio of model/test peak acceleration was 1.17 (ranging between 0.91 and 1.81 for individual records). The acceleration has an average ratio of 1.17 as the peak accelerations have lower sensitivity to the amount of damping due to the non-linear restoring force-displacement behaviour. Although the average peak model to test ratio was seemingly close to 1, the model acceleration exceeded the acceleration recorded in the test over many cycles.

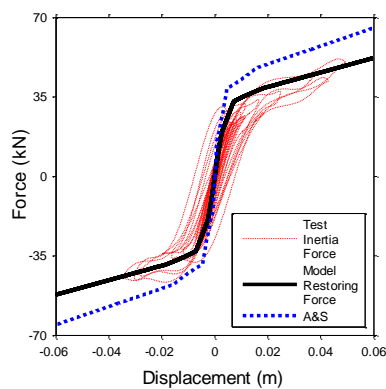


(a) Displacement time history

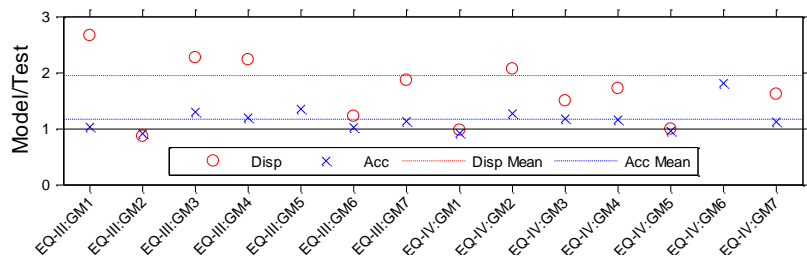


(b) Acceleration time history

Figure 8.15 – Time histories of EQ-III: GM2 for model using reduced simplified analytical restoring force and best fit damping scheme from free vibration calibration



(a) Restoring force-disp.



(b) Model/test for peak disp and acc

Figure 8.16 – Force-displacement response (EQ-III: GM2) and model/test best fit free vibration damping scheme for SRW-ST-A shake table tests EQ-III and EQ-IV

8.3.5.2 Cyclic calibrated damping scheme for ground motions

The combination of the significantly over predicted displacements and the additional hysteresis area shown in the inertia force-displacement shake table data in Figure 8.16 led to the decision to include further hysteretic damping for modelling of SRW-ST-A. The additional hysteretic damping was intended to represent the influence of the inelastic strains in the wall toe as expected

from the cyclic testing reported in Chapter 5. Recall that the hysteresis behaviour of the SRW-A cyclic test was trialled for the free vibration response in section 8.3.2 but was found to simulate too much damping for the free vibration loading type. The difference in wall behaviour between the cyclic and free vibration loading was highlighted in Chapter 6.

To increase the hysteretic energy dissipation of the model the elasto-plastic spring previously calibrated for the cyclic hysteresis of SRW-A was implemented in the model in place of the smaller elasto-plastic spring that best fit the free vibration response. The friction damper previously used was eliminated as the effect of this was small for the shake table analysis once the elasto-plastic definition was altered, and removal of the friction damper reduced the complexity of the model. Recall from section 8.3.2 that the cyclic calibrated elasto-plastic spring had an initial stiffness of 4000 kN/m and a yield displacement of 1 mm. The 2% tangent stiffness proportional damping was retained. A schematic of the updated shake table SDOF model is shown in Figure 8.17, where $k_1(u)$ is the reduced A&S restoring force-displacement behaviour, and $k_2(u)$ is the cyclic test calibrated elasto-plastic spring.

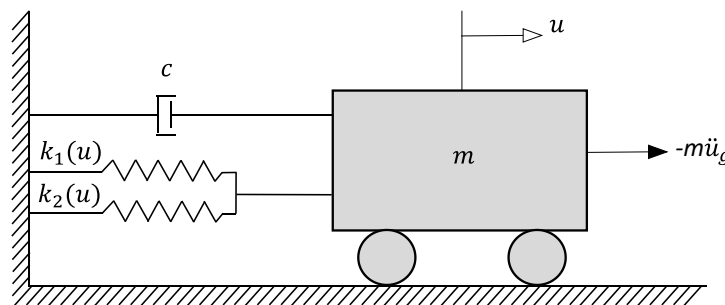
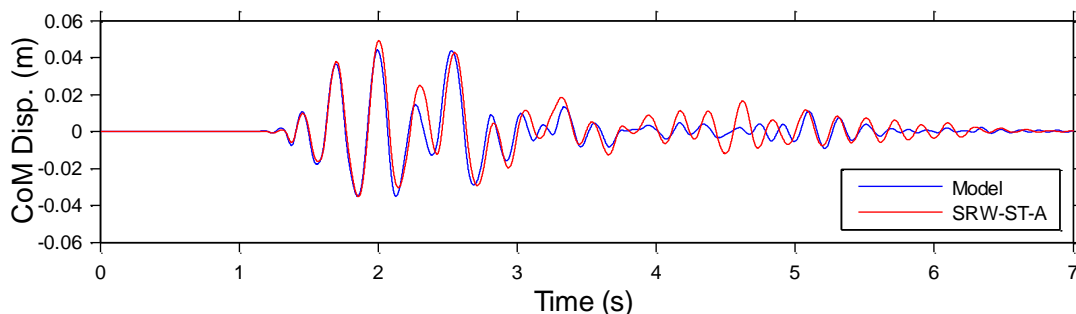


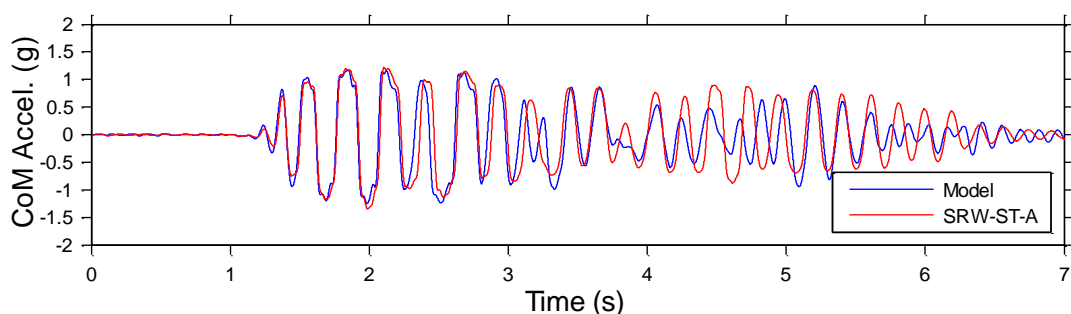
Figure 8.17 – SDOF SRW shake table cyclic calibrated model

By altering the simple SDOF model to use the elasto-plastic definition in combination with the nonlinear restoring force behaviour and tangent stiffness proportional damping, excellent results were found. For example, the same ground motion that demonstrated unstable behaviour for the free vibration best fit model was run and the time histories are shown for the new adjusted model in Figure 8.18 compared against the test result. It is clear that there is excellent emulation of the test for both acceleration and displacement. Good accuracy was achieved in terms of peak displacements and accelerations, and phase for both small and large amplitude cycles. For the small shake-down cycles at the end of the ground motion better accuracy could be achieved in terms of phase and amplitude. The corresponding restoring force-displacement behaviour is

presented in Figure 8.19(a). The new restoring force-displacement behaviour that included the elasto-plastic definition aligned well with the recorded inertia force-displacement behaviour.



(a) Displacement time history



(b) Acceleration time history

Figure 8.18 – Cyclic calibrated damping scheme for SRW-ST-A EQ-III: GM2

The same fourteen ground motions were run using the cyclic calibrated model and the ratio of the model to test peak displacement and acceleration are shown in Figure 8.19(b). The average ratio of model prediction to test measurement for the displacement peaks was 1.05 with a range of 0.53 to 3.13 for individual records. The average ratio of model/test for the acceleration peaks was 0.96 with a range of 0.79-1.24 for individual records. On average the ability of the model to replicate the test peaks of both acceleration and displacement was excellent.

The large range in displacement peak model/test ratio in the NLTHA demonstrates the high sensitivity of SRWs to specific input motion and current wall state, as was also noted during the shake table test analysis in Chapter 7. The maximum ratio of model/test for peak displacement prediction was 3.13 for EQ-III: GM5, which is a large over prediction of peak displacement, however this event was almost an exception with the next largest model/test ratio being only 1.55 which is reasonable considering the high sensitivity of the system. The displacement and acceleration time histories of EQ-III: GM5 are presented in Figure 8.20. It is interesting to note

the model displacement and acceleration time history follows the test data well until some disturbance that causes almost no motion in the test structure causes high amplitude vibrations in the model results which again highlights the sensitivity of the SRW and the history dependence.

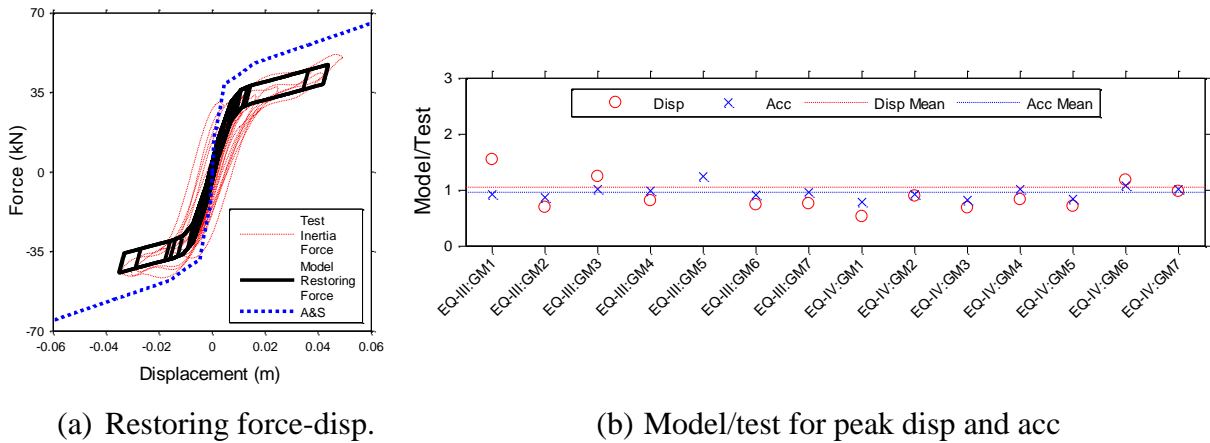


Figure 8.19 – Force displacement response and model/test shake table results for cyclic calibrated damping scheme

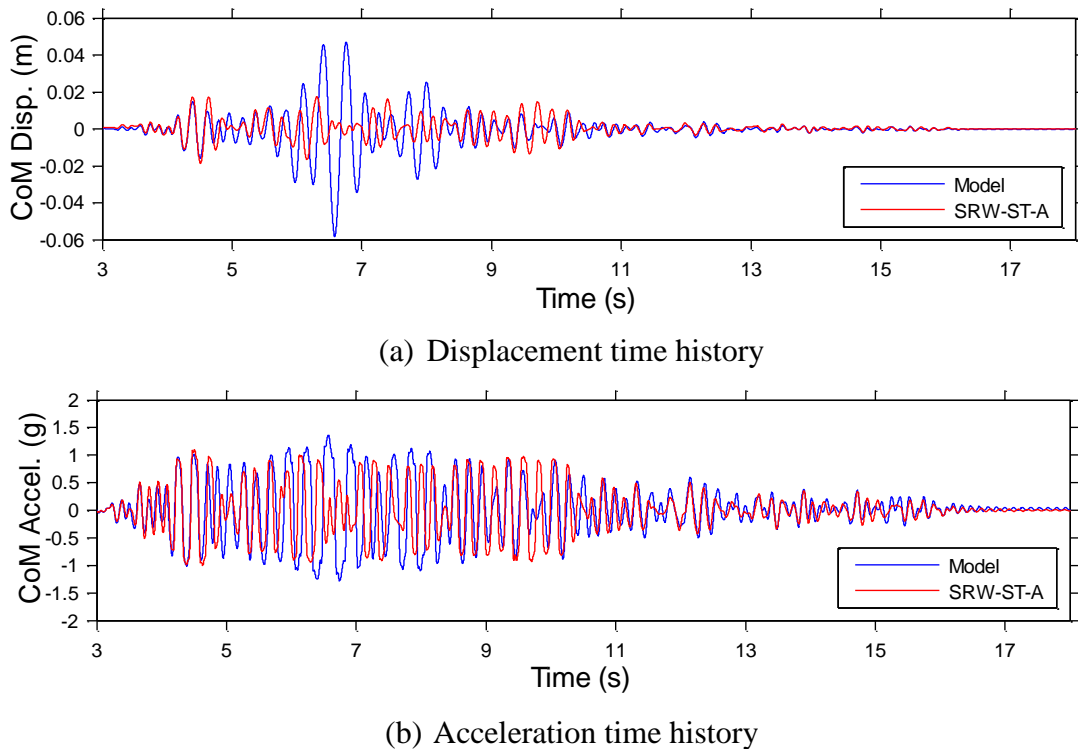


Figure 8.20 – Cyclic calibrated damping scheme for SRW-ST-A EQ-III: GM5

8.3.5.3 *Summary*

Overall, the average peak displacements and accelerations of SRW-ST-A during shake table testing can be predicted within 5% using the simple cyclic calibrated model presented herein, which is excellent considering the simplicity of the model. The recommended model for ground motions uses 2% tangent stiffness proportional damping and a nonlinear restoring force-displacement definition defined using the reduced A&S method. An elasto-plastic spring is included within the model to represent the wall hysteresis calibrated from the cyclic test data of Chapter 5. This elasto-plastic spring definition was found to produce too much damping for the free vibration response due to the difference in inelastic damage in the wall toes. A consistent 20% reduction on the A&S force-displacement behaviour was required for both the shake table and snap back testing. Since drastically different damping schemes were required between the two loading types to achieve good predictions, it is apparent that for a SRW, numerical models calibrated to free vibration decay do not result in accurate emulation of displacement and acceleration response when subjected to ground motion.

8.4 PREWEC NUMERICAL ANALYSES

Following analysis of the SRW, a PreWEC model was also developed. The PreWEC model was based on the final SRW model calibrated for ground motions plus additional energy dissipation to represent the O-connectors. The PreWEC model was first calibrated using the pseudo-static cyclic test results reported in Chapter 5 and the resulting model was used to simulate both the free vibration and ground motion NLTHA.

8.4.1 Model development

The critical part of the PreWEC model development was to accurately capture the hysteretic behaviour so as to have adequate damping during dynamic analyses. The different hysteretic components of the PreWEC system consisted of the strength contribution of the wall and column PT, the wall hysteresis, and O-connector hysteresis. As with the SRW model a nonlinear elastic spring was used to represent the wall PT strength, and for the PreWEC system also the column PT strength based on predictions using the simplified analytical method proposed by Aaleti and Sritharan. During development of the model when additional springs were required to increase the hysteresis area the combination of further spring strength contribution and the PT nonlinear

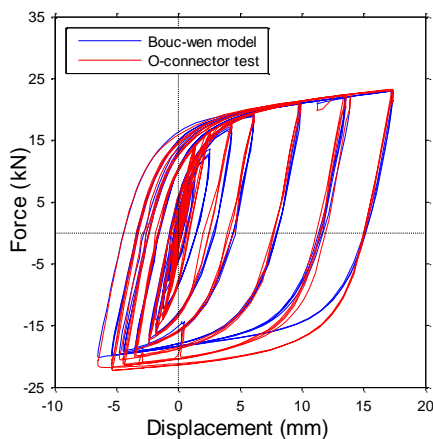
elastic spring was made to closely match the A&S prediction. The wall hysteresis component was assumed to be an elasto-plastic spring with initial stiffness of 4000 kN/m and a yield displacement of 1 mm, as determined during the SRW cyclic calibrated shake table analyses. The O-connector spring definition used the Bouc-wen hysteretic model [122] which is defined by Equation (8-8) and Equation (8-9), where F_r is the restoring force and definition of the other parameters can be found in Ikhouane et al. [122]. The Bouc-wen model parameters used are shown in Table 8.1 and were determined by calibrating the model to one of the O-connector component tests reported in Chapter 3 with a comparison of the test and best fit model parameters for one O-connector shown in Figure 8.21(a).

$$F_r = \alpha_b k_b u_b(t) + (1 - \alpha_b) D_y k_b z(t) \tag{8-8}$$

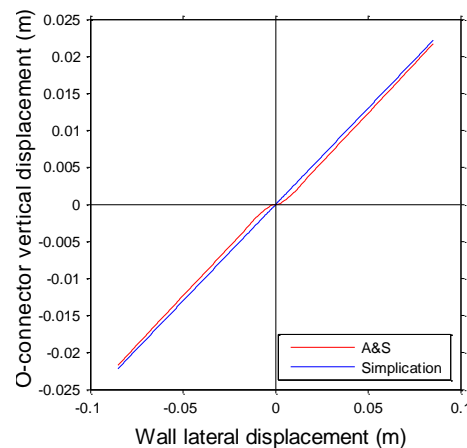
$$\dot{z}(t) = \frac{\dot{u}(t)}{D_y} (1 - (\beta \text{sgn}(\dot{u}(t)z(t)) + \gamma) |z(t)|^n) \tag{8-9}$$

Table 8.1 – Bouc-wen parameters for O-connector

Parameter	Value
F	19 kN
d_y	2.2 mm
K_2	266
β	0.55
γ	0.45
n	1



(a) Bouc-wen component test emulation



(b) Vertical O-connector displacement

Figure 8.21 – O-connector Bouc-wen definition and vertical-lateral disp. relationship

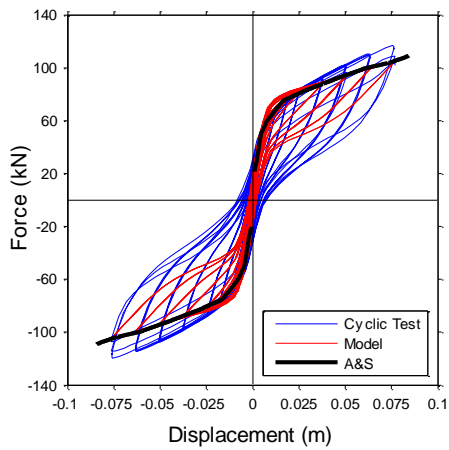
In order to use the best fit Bouc-wen model parameters calibrated using the O-connector component test, a relationship was defined between the O-connector displacement and wall lateral displacement, and the O-connector force and corresponding contribution to the PreWEC system lateral force. The lateral force contribution of the O-connectors is defined by Equation (8-10) derived from Aaleti and Sritharan and the basic mechanics of the rocking wall assuming the O-connector forces on each end of the wall are equal and opposite. Where l_c is the column length, n_{con} is the number of O-connectors per joint, l_w is the wall length, and $F_{c,T}$ is the total O-connector force.

$$F_{con} = (l_c n_{con} F_{c,T} + 0.5 l_w n_{con} F_{c,T}) / H \quad (8-10)$$

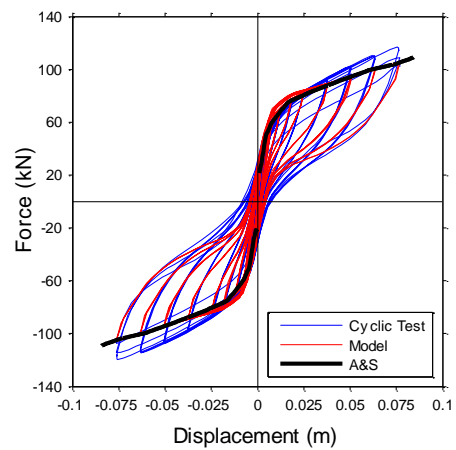
The relationship between the wall lateral displacement and the O-connector vertical displacement was simplified to be a linear fit of the relationship defined by the simplified analytical method proposed by Aaleti and Sritharan (A&S), as shown in Figure 8.21(b), where the O-connector vertical displacement is the sum of the vertical displacement of both sides of the wall.

The global force-displacement behaviour of the PreWEC-A model, consisting of the nonlinear elastic spring shown in Figure 8.22(c), wall hysteresis spring shown in Figure 8.22(d) and O-connector spring shown in Figure 8.22(e), is compared against the pseudo-static cyclic test reported in Chapter 5 as shown in Figure 8.22(a). It can be seen that the model underestimated the hysteresis behaviour of PreWEC-A. Henry [41] found a similar result when using a simplified lumped plasticity model of a large scale PreWEC wall test.

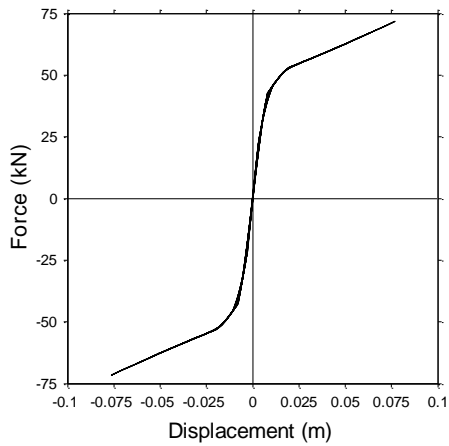
Subsequently a further spring was included that provided additional hysteresis to better emulate the cyclic test behaviour. The spring definition used was a bilinear degrading hysteresis previously defined in Figure 8.3(a), with an initial stiffness equal to 4000kN/m, a yield displacement equal to 1 mm, an r factor equal to 0 (i.e. 0 second stiffness), and α equal to 0.5 as shown in Figure 8.22(f). The results of the cyclic analysis of the final model with additional hysteresis is shown in Figure 8.22(b) for PreWEC-A and a summary of the four spring parameters that make up the model is provided in Table 8.2. It can be seen that the combination of four springs captured the experimental cyclic response with good accuracy.



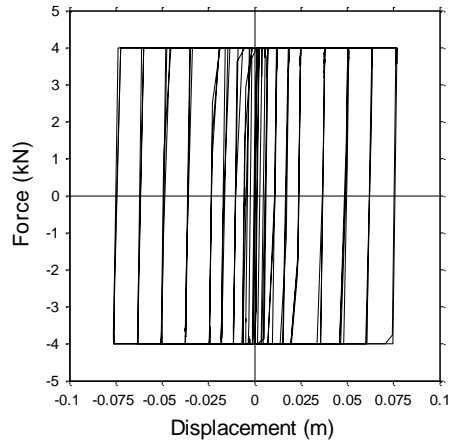
(a) PreWEC-A model with O-connector and SRW hysteresis



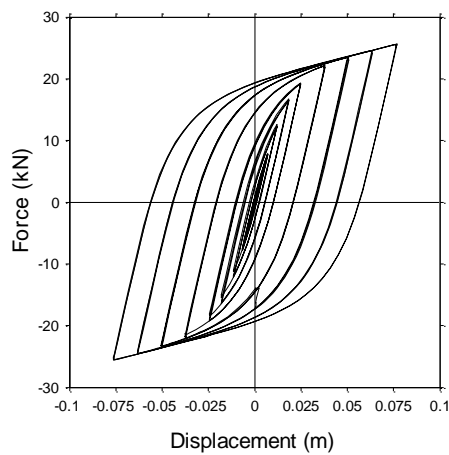
(b) PreWEC-A model with O-connector, SRW hysteresis, and additional hysteresis



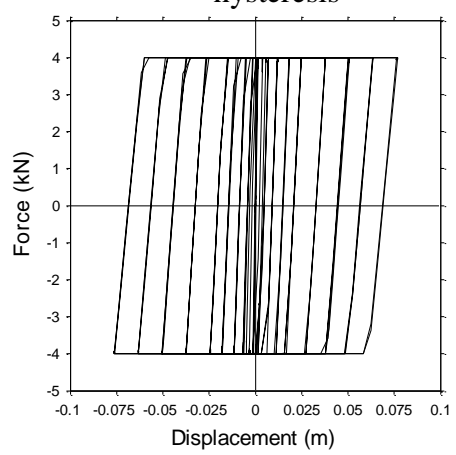
(c) Nonlinear elastic spring



(d) Elasto-plastic definition for wall hysteresis



(e) Bouc-wen definition for O-connector hysteresis



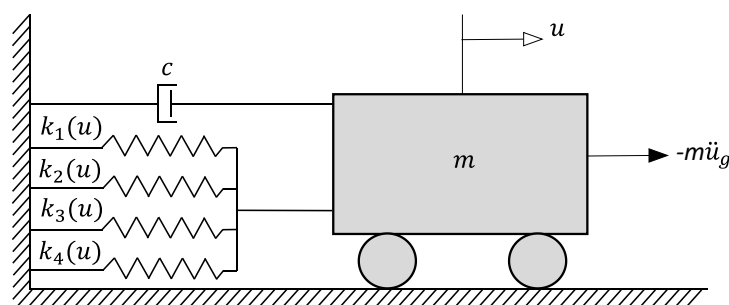
(f) Degrading Elasto-plastic definition additional hysteresis

Figure 8.22 – PreWEC-A model and cyclic test comparison including spring definitions

Table 8.2 – Spring properties of PreWEC model

Spring	Hysteresis	Properties
Wall backbone	Nonlinear elastic	Defined by A&S and reduced according to the increase in strength from the wall and additional hysteresis
Wall hysteresis	Elasto-plastic	$r=0$ $d_y=1$ mm $K_o=4000$ kN/m
O-connector hysteresis	Bouc-wen	$F=19$ kN $d_y=2.2$ mm $K_2=266$ $\beta=0.55$ $\gamma=0.45$ $n=1$
Additional hysteresis	Bilinear degrading	$\alpha=0.5$ $r=0$ $d_y=1$ mm $K_o=4000$ kN/m

A schematic of the final SDOF model used for the PreWEC walls is depicted in Figure 8.23. As just defined the model consists of four springs, where $k_1(u)$ is the nonlinear elastic spring, $k_2(u)$ is the wall hysteresis spring, $k_3(u)$ is the O-connector spring, and $k_4(u)$ is the additional hysteresis spring.

**Figure 8.23 – SDOF PreWEC shake table model**

The model was adjusted for PreWEC-B by changing only the O-connector spring from four O-connectors per joint to six per joint, and then cyclic analysis was also performed. A comparison of the pseudo-static cyclic test data from Chapter 5 and the model result for PreWEC-B is shown in Figure 8.24. Reasonable emulation of the cyclic test is shown, as with PreWEC-A. The unloading path and hysteresis near zero did not match as well as PreWEC-A, suggesting that increased hysteresis may be appropriate for PreWEC-B, however analysis proceeded with the simple model to retain the low complexity.

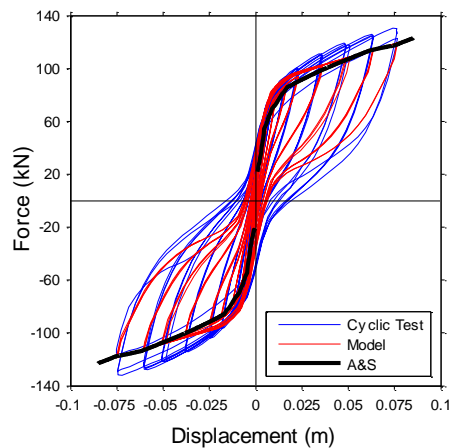


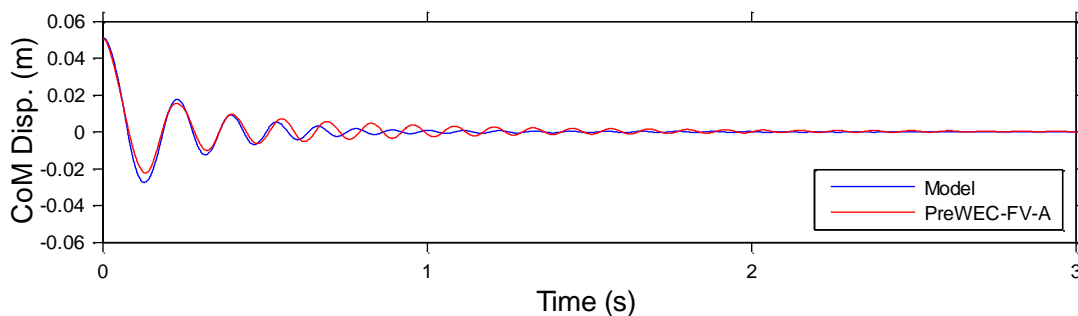
Figure 8.24 – PreWEC-B model and cyclic test comparison

8.4.2 Snap back test replication

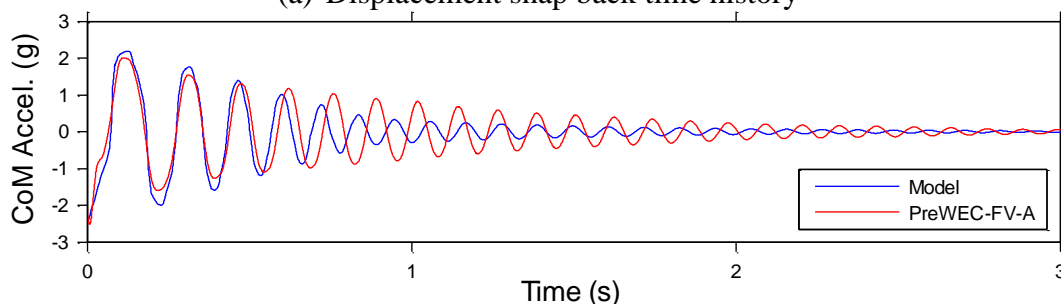
Following reasonable replication of the PreWEC pseudo-static cyclic testing, the SDOF model defined in Figure 8.23 was used with the spring definitions shown in Figure 8.22(c)-(f), a mass of 3.9 tonnes and tangent stiffness damping of 2%, the same as that used during the final analyses of the SRW, for dynamic analyses. Firstly, a model was developed for each of the snap back test PreWEC systems (PreWEC-FV-A, PreWEC-FV-B, and PreWEC-FV-C) described in Chapter 6. Each of the models were run for the 2% drift snap back tests and a comparison of the test acceleration and displacement free vibration time history and the model acceleration and displacement free vibration time history is shown for PreWEC-FV-A, PreWEC-FV-B, and PreWEC-FV-C in Figure 8.25, Figure 8.26, and Figure 8.27, respectively. For all three walls reasonable estimates of the free vibration decay were achieved with the model, with PreWEC-FV-A having the closest match. For all PreWEC systems the model shows good replication of displacement and acceleration phase and amplitude during large cycles but slightly overdamps at small cycles, as shown in the later portion of the free vibration decay. The accuracy of the model was excellent, especially when considering the simplicity of the model that uses a simple predictive backbone and a simple combination of springs that can be easily implemented in common software packages.

A comparison of the test inertia force-displacement, model restoring force-displacement, test pushover and Aaleti and Sritharan backbone (A&S) is shown for each of the snap back tests in Figure 8.28. There is a good match between the Aaleti and Sritharan backbone, the backbone of the model restoring force, and the test pushover, however the backbone of the test inertia force

is slightly reduced. The test inertia also has increased hysteresis area in comparison to the model restoring force. It is significant to note that unlike the SRW, no force reduction was required for the backbone response of the PreWEC systems.

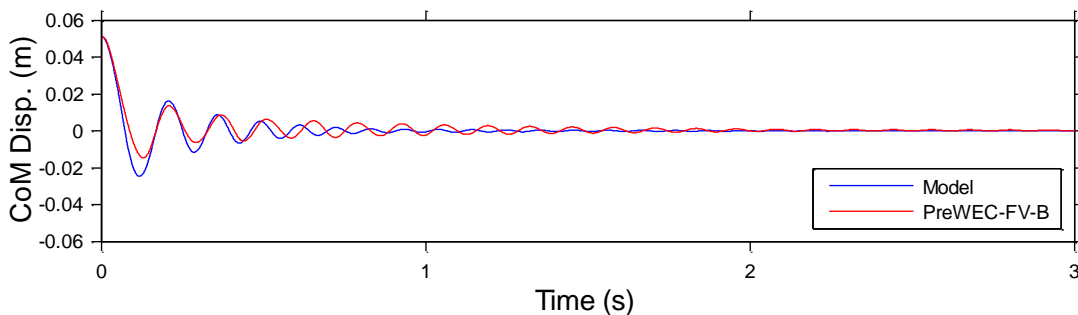


(a) Displacement snap back time history

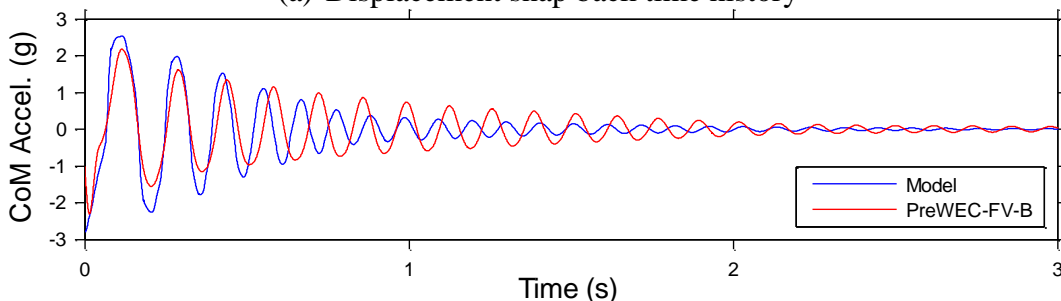


(b) Acceleration snap back time history

Figure 8.25 – Snap 2% PreWEC-FV-A

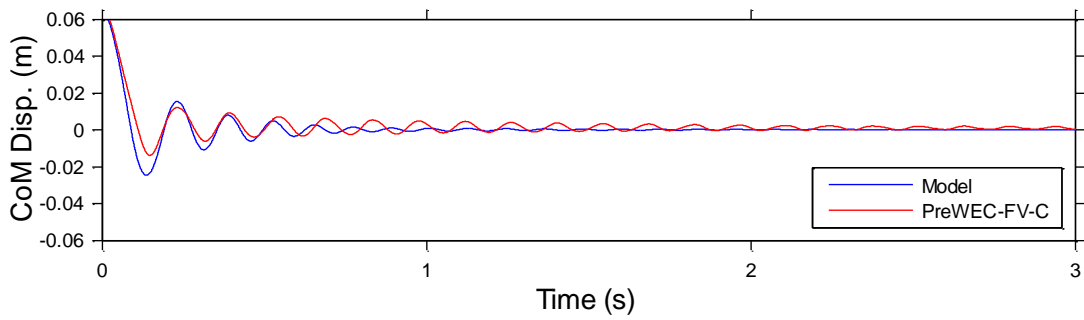


(a) Displacement snap back time history

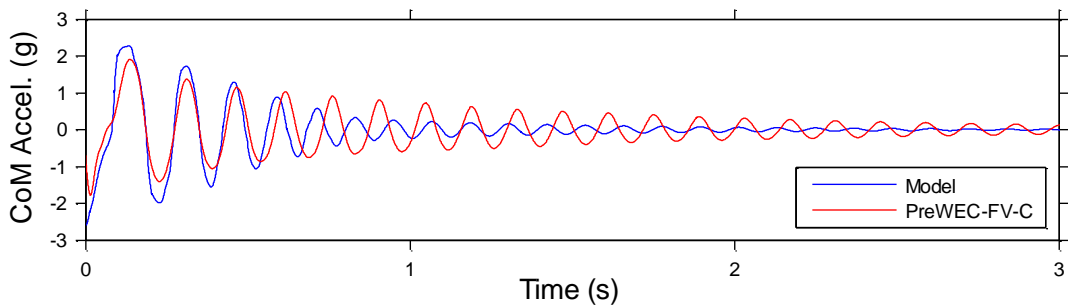


(b) Acceleration snap back time history

Figure 8.26 – Snap 2% PreWEC-FV-B

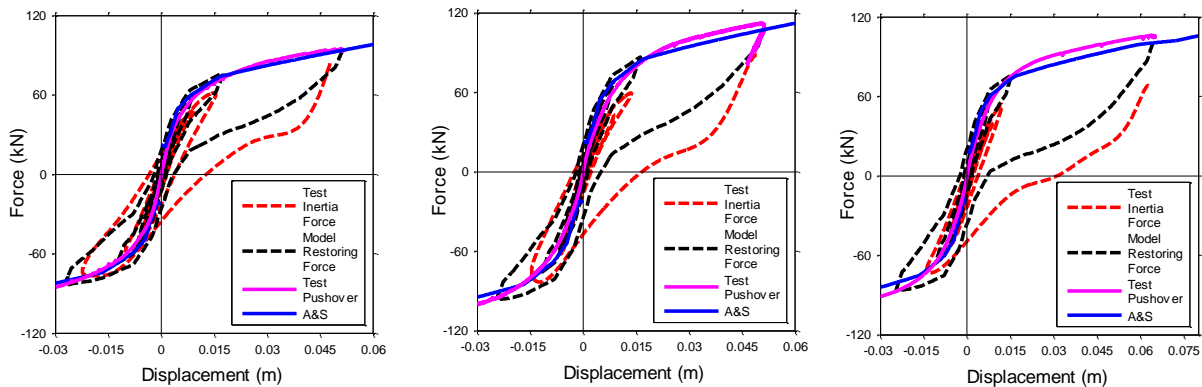


(a) Displacement snap back time history



(b) Acceleration snap back time history

Figure 8.27 – Snap 2% PreWEC-FV-C



(a) PreWEC-FV-A

(b) PreWEC-FV-B

(c) PreWEC-FV-C

Figure 8.28 – Force-displacement comparison for all PreWEC snap back walls

8.4.3 Ground motion replication

The same model type that was used for the PreWEC snap back test analyses was adjusted for the wall parameters of concrete strength and PT force of the two PreWEC shake table specimens previously reported in Chapter 7, and several analyses were run to determine the PreWEC system models ability to replicate the test response to ground motions. The fourteen ground motions

from EQ-V and EQ-VI described in Chapter 7 were used here to evaluate the accuracy of the numerical model of PreWEC-ST-A and PreWEC-ST-B. As with the SRW the two series of ground motions at the highest intensity were used for the model evaluation as the higher intensity ground shaking is most relevant to the wall design, and the accuracy of small intensities is not as critical.

8.4.3.1 *PreWEC-ST-A*

An example displacement and acceleration time history for PreWEC-ST-A comparing the model and test response for EQ-VI: GM2 is presented in Figure 8.29. The corresponding model restoring force-displacement behaviour and test inertia force-displacement behaviour are presented in Figure 8.30(a) along with the force-displacement A&S prediction [62]. Overall, there is good correlation between the model and tests response for both displacement and acceleration at both high and low amplitude shaking. The peak displacements, peak accelerations and phase are emulated exceptionally well for large amplitude shaking, and with reasonably good accuracy during the latter part of the motion when small amplitude shaking occurs. The model restoring force behaviour also emulated the test inertia force-displacement well, with good estimation of the overall strength and unloading behaviour.

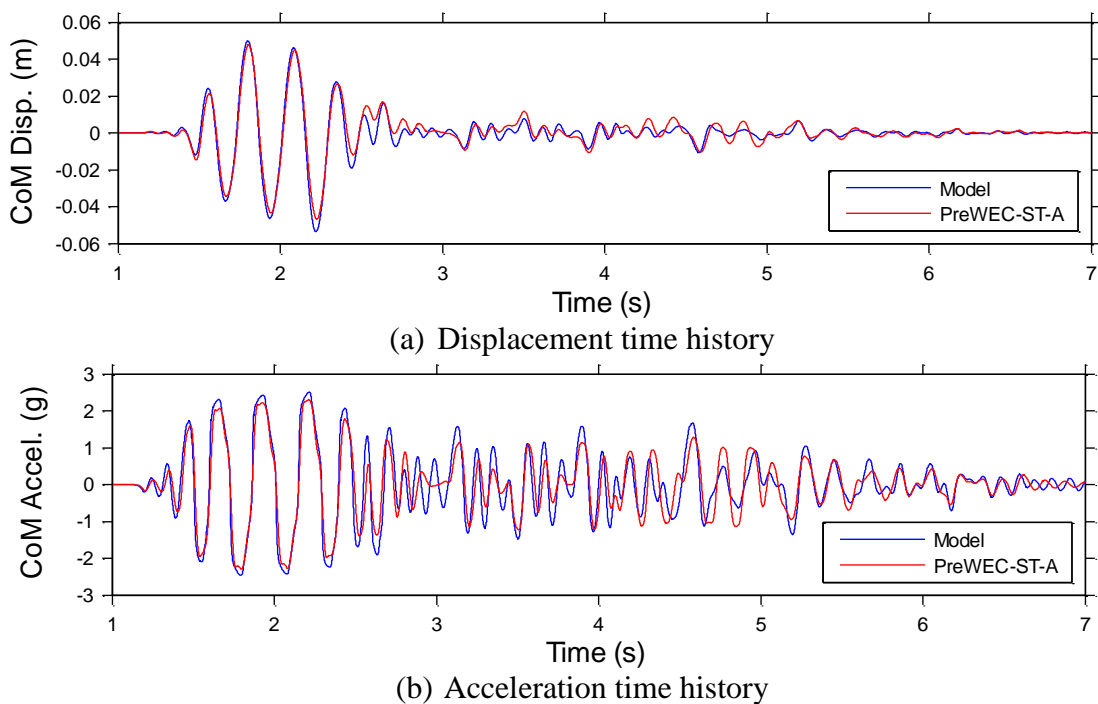
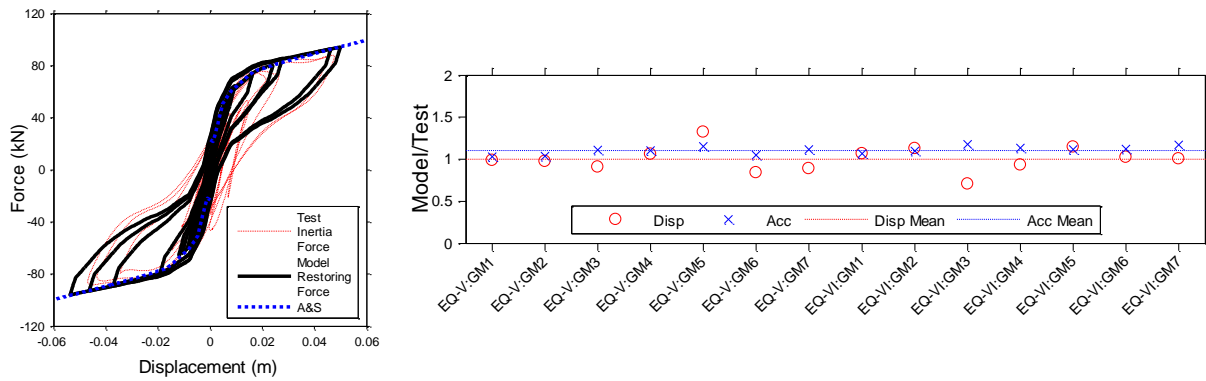


Figure 8.29 – EQ-VI: GM2 PreWEC-FV-A



(a) Restoring force-disp.

(b) Model/test for peak disp and acc

Figure 8.30 – PreWEC-ST-A force displacement response and model/test shake table results

The analysis was run for all fourteen records and the ratio of model to test for both the peak displacement and peak acceleration was calculated and is presented in Figure 8.30(b). For PreWEC-ST-A the average ratio of model/test peak displacements was 1.00 ranging from 0.70 to 1.32 for individual records, while the average ratio of model/test peak accelerations was 1.11 ranging from 1.03 to 1.17 for individual records. The range of the acceleration and displacement peak model/test ratios are far lower than SRW demonstrating the increased predictability, consistency and insensitivity to ground motion frequency content of the PreWEC-ST-A system.

8.4.3.2 PreWEC-ST-B

An example displacement and acceleration time history is presented in Figure 8.31 for PreWEC-ST-B comparing the model and test response for EQ-VI: GM2. The corresponding model restoring force-displacement behaviour and test inertia force-displacement behaviour are presented in Figure 8.32(a) along with the force-displacement from the A&S method [62]. Overall, there is good correlation for both the test displacement and acceleration at both high and low amplitude shaking as with PreWEC-ST-A. There is good replication of peak acceleration and displacements and phase is replicated well except during 1.1-1.5s. The smaller amplitude motion is not replicated as well for PreWEC-ST-B as was shown for PreWEC-ST-A. The model does consistently slightly over predict the acceleration even when perfectly in phase. The model restoring force behaviour also emulated the test inertia force-displacement reasonably well, although there is a significantly lower strength in the negative displacement direction and slightly

lower hysteresis area in the model than test inertia force. The lower strength is due to onset of O-connector fracture having already occurred during EQ-IV: GM1.

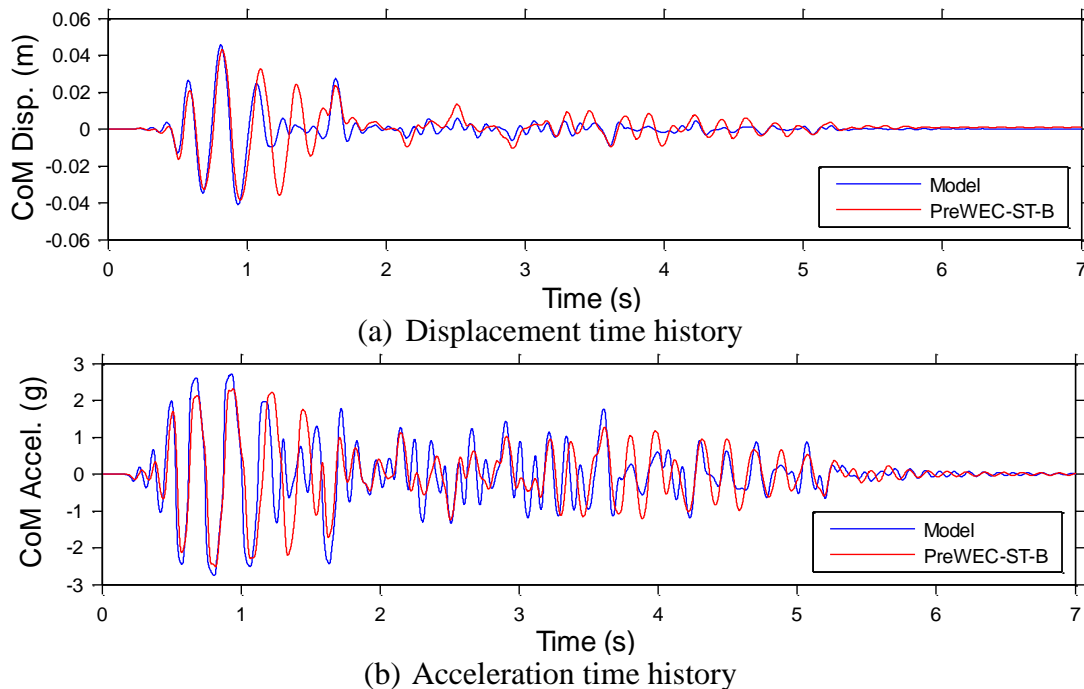


Figure 8.31 – EQ-VI: GM2 PreWEC-FV-B

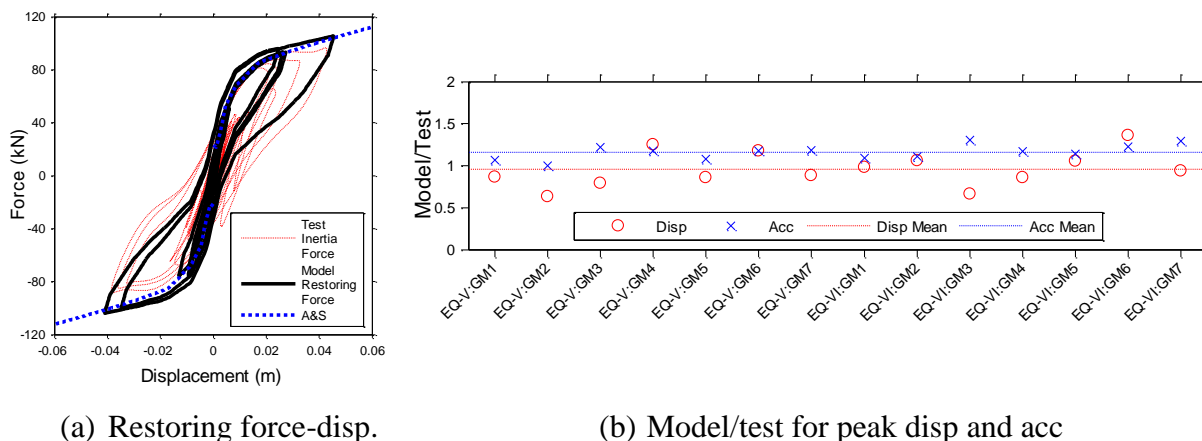


Figure 8.32 – PreWEC-ST-B force displacement response and model/test shake table results

The analyses were run for all fourteen records and the ratio of model to test was calculated for both the peak displacement and acceleration as presented in Figure 8.32(b). The average ratio of model to test peak displacements was 0.96 ranging from 0.63 to 1.36 for individual records. The average ratio of model to test peak accelerations was 1.16 ranging from 1.0 to 1.31. The range of the acceleration and displacement peak model/test ratios are again far lower than SRW, as

was observed for PreWEC-ST-B demonstrating the increased predictability, consistency of the PreWEC-ST-B system also

8.5 CONCLUSIONS AND RECOMMENDATIONS

Nonlinear time history analysis (NLTHA) of SRW and PreWEC systems was performed using a simple single degree of freedom model. The dynamic tests presented in previous chapters provided a unique opportunity to validate a simple modelling technique with high quality dynamic test data for unbonded PT concrete wall systems. Firstly, different damping schemes were trialled to find the best fit damping scheme for the free vibration response of SRW-FV-A reported in Chapter 6. Initially, the restoring force-displacement behaviour adopted for the NLTHA of the free vibration response was a measured “dynamic” restoring force evaluated from the test inertia force-displacement data of SRW-FV-A. The dynamic restoring force was used to eliminate all variable parameters in the SRW SDOF model other than damping scheme. One of the damping schemes trialled used a hysteretic response that approximately matched the pseudo-static cyclic test of SRW-A reported in Chapter 5, but this was found to have too much damping for the free vibration response of SRW-FV-A. A best fit damping scheme was evaluated for SRW-FV-A using a trial and error approach that could emulate the displacement and acceleration decay with excellent accuracy.

The best fit damping scheme was then used with an updated restoring force-displacement behaviour defined by the simplified analytical method proposed by Aaleti and Sritharan [62]. This was done to evaluate the prediction capability of the model when test data is not used to define the numerical model. To achieve accurate results the simplified analytical method force-displacement behaviour required multiplication by a reduction factor of 0.8, called the reduced A&S method within the body of the chapter. When the reduced A&S force-displacement behaviour was used in combination with the best fit damping scheme, reasonable replication of the free vibration displacement and acceleration response of SRW-FV-A was found.

The best fit damping scheme and reduced A&S force-displacement SDOF model were then used to model the shake table results of SRW-ST-A. When this SDOF model was used to model the shake table test results the displacements were greatly over predicted compared to the test response of SRW-ST-A and the quantity of energy dissipation present in the SDOF was deemed

too low to emulate the shake table tests accurately. The damping scheme was altered to use only an elasto-plastic spring calibrated from the cyclic testing of SRW-A and 2% tangent stiffness damping, in a SDOF model with the reduced A&S force-displacement behaviour. When using the cyclic calibrated damping scheme for shake table analyses, the average peak displacements and accelerations of SRW-ST-A were predicted within 5%, which is an excellent result considering the simplicity of the model.

The elasto-plastic spring definition calibrated from cyclic testing of SRW-A was found to produce too much damping for the free vibration response, however consistent reduced A&S force-displacement behaviours were required for both shake table and snap back testing. Since drastically different damping schemes were required between the two loading types to achieve good predictions, it is apparent that for a SRW, numerical models calibrated to free vibration decay do not result in accurate emulation of displacement and acceleration response when subjected to ground motion.

Overall, the PreWEC systems shake table response could be emulated well using a combination of springs that best represent the cyclic hysteresis behaviour with an additional 2% tangent stiffness damping implemented in a simple SDOF model. On average the peak model displacements and accelerations of PreWEC-ST-A were within 1% and 11%, respectively, when compared to that measured during testing. On average the peak model displacements and accelerations of PreWEC-ST-B were within 4% and 16%, respectively, when compared to that measured during testing. A more predictable and consistent behaviour was found for the PreWEC systems than the SRW, evidenced by the low range of model to test ratios for both displacement and acceleration peaks when compared to SRW-ST-A.

Overall, the results showed that adequate prediction of the seismic response of SRW and PreWEC systems can be achieved using 2% tangent stiffness damping in combination with an appropriate hysteresis model as defined by cyclic testing. The results may not be directly applicable to full-scale structures, which also have floor diaphragms, gravity frame, non-structural components and different foundation conditions. Further research is required for full-scale structures in situ, particularly for higher modes and at large response amplitudes.

8.6 REFERENCES

20. Priestley, M.J.N., G.M. Calvi, and M.J. Kowalsky, *Displacement-based seismic design of structures*. 2007, Pavia: IUSS Press : Fondazione Eucentre. xvii, 721 p.
41. Henry, R.S., *Self-centering precast concrete walls for buildings in regions with low to high seismicity*. 2011, University of Auckland. p. 441.
62. Aaleti, S. and S. Sritharan, *A simplified analysis method for characterizing unbonded post-tensioned precast wall systems*. *Engineering Structures*, 2009. **31**(12): p. 2966-2975.
70. Kurama, Y.C., *Hybrid post-tensioned precast concrete walls for use in seismic regions*. *PCI Journal*, 2002. **47**(5): p. 36-59.
119. Kam, W.Y., S. Pampanin, A. Palermo, and A.J. Carr, *Self-centering structural systems with combination of hysteretic and viscous energy dissipations*. *Earthquake Engineering and Structural Dynamics*, 2010. **39**(10): p. 1083-1108.
120. The MathWorks Inc, *Matlab R2014a*. 2014: Natick, Massachusetts, United States.
121. Carr, A., *Ruaumoko*, in *Inelastic Dynamic Analysis Program Manual*. 2003, University of Canterbury: Christchurch, New Zealand.
122. Ikhouane, F., J. Rodellar, and J.E. Hurtado, *Analytical Characterization of Hysteresis Loops Described by the Bouc-Wen Model*. *Mechanics of Advanced Materials & Structures*, 2006. **13**(6): p. 463-472.

Chapter 9

DIRECT DISPLACEMENT BASED DESIGN EVALUATION

This chapter presents a summary and critical evaluation of current direct displacement based design (DDBD) guidelines for equivalent viscous damping (EVD) of unbonded PT precast concrete wall systems with and without additional energy dissipating elements. An overview of the DDBD process and specific EVD recommendations were presented in Chapter 2, along with the DDBD of the prototype building that was presented in Chapter 4. In Chapter 7 the DDBD process was assessed for the three unbonded PT wall systems tested on the shake table. The DDBD assessment presented in Chapter 7 used the design displacement spectra appropriate for each ground motion and assumed EVD based on one of the methods recommended in the PRESSS Design Handbook [19] and Appendix B of the New Zealand Concrete Code [18]. The recommendations from these documents were used as they present the currently recommended EVD determination procedure for New Zealand. The analyses presented in this chapter focus on assessing the shake table results more critically and in greater detail than that briefly presented in Chapter 7. Firstly, current EVD recommendations for the PreWEC and SRW systems are outlined and subsequently compared with the EVD evaluated from the pseudo-static cyclic tests reported in Chapter 5. The aim of this chapter is to demonstrate the lack of consistent

recommendations for calculating the EVD of jointed type unbonded PT walls that include PreWEC systems, and subsequently attempt to provide more robust and consistent EVD estimates that can be used for DDBD of PreWEC systems.

9.1 INTRODUCTION

DDBD utilises the concept of an equivalent linear system (ELS) defined by an EVD (ξ_{eq}) and equivalent stiffness to represent the response of a nonlinear system. This concept is based on the substitute structure approach pioneered by Gulkan and Sozen [83]. The substitute structure approach adopted by DDBD involves estimating the maximum response of a nonlinear MDOF system with a linear single-degree-of-freedom (SDOF) system with appropriately defined damping and stiffness properties [84]. The approximation of the system nonlinearity with equivalent linear properties involves many assumptions. Summarised in Priestley et al. [20] are previous studies that have estimated equivalent linear properties for nonlinear SDOF oscillators with hysteretic behaviour defined using common models [85]. For DDBD applications it is important to obtain appropriate values of EVD that are representative of real structural response for an accurate design process.

9.2 EVD IN DDBD SUMMARY

As described in Chapter 2 EVD is usually incorporated in the DDBD process using an EVD-ductility relationship where EVD is equal to the sum of elastic and hysteretic damping. Priestley et al. [20] supports the use of the EVD-ductility relationship described by Equation (2-24) that was originally developed by Dwairi and Kowalsky [88]. Equation (2-24) incorporates 5% elastic damping proportional to tangent stiffness, where R_ξ is described as the damping factor for specific structural systems investigated and μ is the system displacement ductility.

$$\xi_{eq} = 0.05 + R_\xi \left(\frac{\mu - 1}{\mu\pi} \right) \quad (9-1)$$

A rigorous approach to determine the EVD associated with hysteretic damping for alternative systems to those investigated by Priestley et al. [20] would involve time consuming Nonlinear Time History Analyses (NLTHA). An alternative method was proposed by Priestley et al. that

does not require extensive time history analyses, but by all accounts ensures adequate estimation of appropriate hysteretic damping for DDBD. The procedure was described in the literature review but is repeated here for convenience. The procedure is based on calculating the area-based damping for a structural system using Equation (9-2) as defined in Chapter 2 and Chapter 5. Priestley et al. describes how the area-based damping is not directly relevant to ground motion NLTHA as it is formulated on the assumption that the system responds in a steady state, which is not the case for ground motions. Therefore Priestley et al. [20] proposed a “correction factor,” (cf), to be applied to Equation (9-2) to achieve appropriate hysteretic EVD ratios. The correction factor is depicted in Figure 2.13 for various idealized hysteretic systems of variable ductility.

$$\xi_{area} = \frac{A_h}{2\pi F_m \Delta_m} = \frac{1}{4\pi} \frac{E_D}{E_{S0}} \tag{9-2}$$

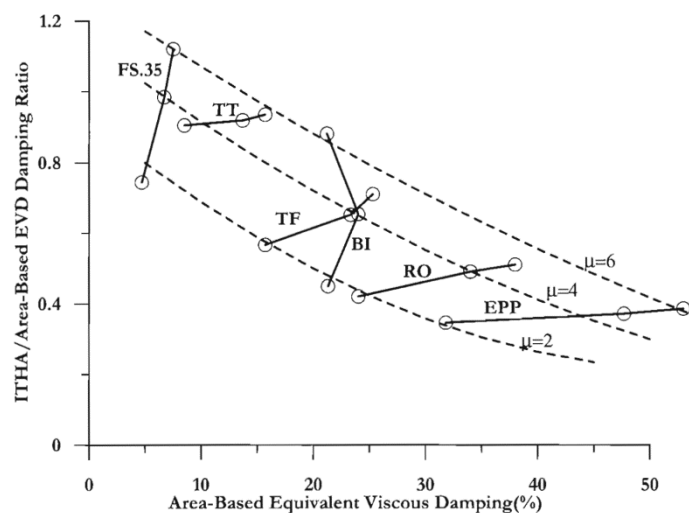


Figure 9.1 – Correction factors to be applied to area-based EVD ([20])

As described in the literature review the elastic damping component of EVD is usually included in time history analysis to account for damping that is not captured by the hysteretic model. An issue addressed in recent literature is what stiffness the elastic portion of the EVD ratio should be proportional to during nonlinear time history analyses, with findings pointing to use of tangent stiffness instead of initial stiffness to avoid unrealistically large damping values at high natural frequencies. To reflect the assumption of tangent stiffness proportional elastic damping, the elastic damping specified is reduced by an adjustment factor (κ) as presented in Equation (9-3)

and Equation (2-20), where μ is the ductility factor and λ' is factor that controls the adjustment factor based on the hysteretic rule.

$$\xi_{eq} = \kappa \xi_{el} + \xi_{hyst} \quad (9-3)$$

$$\kappa = \mu^{\lambda'} \quad (9-4)$$

9.3 YIELD DISPLACEMENT AND DUCTILITY

As previously described within the framework of DDBD proposed by Priestley et al. [20], EVD is calculated using an EVD-ductility relationship. As a result the ductility is an index of EVD when used in DDBD. The important aspect of determining ductility is that it is consistent with the assumed ductility used for the development of the EVD-ductility relationship employed in the design process. EVD-ductility relationships have been developed for idealized bilinear systems such as the ideal flag-shape, which is a commonly assumed idealisation for unbonded PT systems.

In order to calculate ductility, the yield displacement of the system must be known. For a bilinear system the defined yield point is obvious, however for realistic systems there is some ambiguity as to the definition of the yield point, particularly for unbonded PT systems. As described in Priestley et al. [20] there has been difficulty within the engineering community in reaching a consensus on the appropriate definition of yield displacements. Priestley et al. go on to provide a definition of ductility capacity that assumes a bilinear approximation of either the force-displacement or moment-curvature response. The recommended definition of yield displacement is based on secant stiffness through the first yield point up to the nominal strength. The flexural yield displacement (Δ_{yi}) of a RC shear wall is commonly determined using Equation (9-5), which is based on assuming a simple triangular distribution of first-mode curvature with height at yield. Priestley et al. [20] states that yield displacements for unbonded PT walls can be based on the stiffness of the un-cracked wall sections up the full height, without stating what lateral strength should correspond to yield. This is in direct contrast to RC walls that use a secant stiffness to first yield that accounts for the cracked section response. For RC walls the first yield is either when the extreme tension reinforcement first attains yield strain, or when the extreme concrete compression fibre attains a strain of 0.002.

$$\Delta_{yi} = \frac{\varepsilon_y H_i^2}{l_w} \left(1 - \frac{H_i}{3H_n} \right) \quad (9-5)$$

Where ε_y is the yield strain of the vertical reinforcing steel, H_i is the height of mass i in building design, l_w is the wall length, and H_n is the height of building to roof level.

The analyses performed to develop the EVD-ductility equations recommended by Priestley et al. [20] were based on ideal systems often with ideal bilinear backbones. As a result it would make sense to propose a bilinear force-displacement relationship for unbonded PT wall systems to attain consistent and appropriate ductility index values for use in ideal hysteretic definitions. Since no traditional yielding occurs, it would also make sense for the yield point to be based on a form of yielding due to uplift or rocking as this is when the system stiffness reduces. Alternatively, the ductility-EVD relationship could be substituted with a drift-EVD relationship to avoid the need to calculate a yield displacement and ductility at all. After all, when used in DDBD ductility is purely an index of the drift normalized by some definition of yield drift (or displacement). If yield displacements of realistic force-displacement behaviours are not calculated consistently, ductility estimates will not be consistent and the ductility-EVD relationships are not necessarily appropriate, using drift directly would eliminate this ambiguity.

In literature related to the design of unbonded PT wall systems a number of limit states have been defined [26, 45]. Usually these have consisted of 1) Decompression at the tension edge, 2) Concrete crushing in the compression toe, 3) PT tendon yielding, and 4) Confined concrete crushing or PT rupture. Decompression identifies the initiation of gap opening between the wall and foundation. This is when the initial compression stress in the wall due to the PT is overcome at the extreme edge of the wall base. Before decompression the wall is assumed to behave linearly. After decompression the wall starts to behave nonlinearly, although it is generally assumed that the effect of this nonlinear behaviour on the lateral stiffness is small until the gap extends over a “significant” portion of the wall length as described by Kurama et al. [45]. After decompression the wall stiffness softens as further uplift occurs or depending on the magnitude of the initial compression stress in the concrete, the wall may soften due to nonlinear behaviour of the concrete, as specified by limit state 2). Usually the next state reached is PT yielding, which is controlled by selection of initial PT stress, tendon location, and the unbonded length. The failure state is defined as crushing of the confined concrete or rupture of the PT. For a well-

designed wall, failure should occur at a much later stage than the PT yielding state. A schematic of the idealized force-displacement behaviour using the backbone defined by Aaleti and Sritharan (A&S) [62] is presented in Figure 9.2, where the limit states are highlighted.

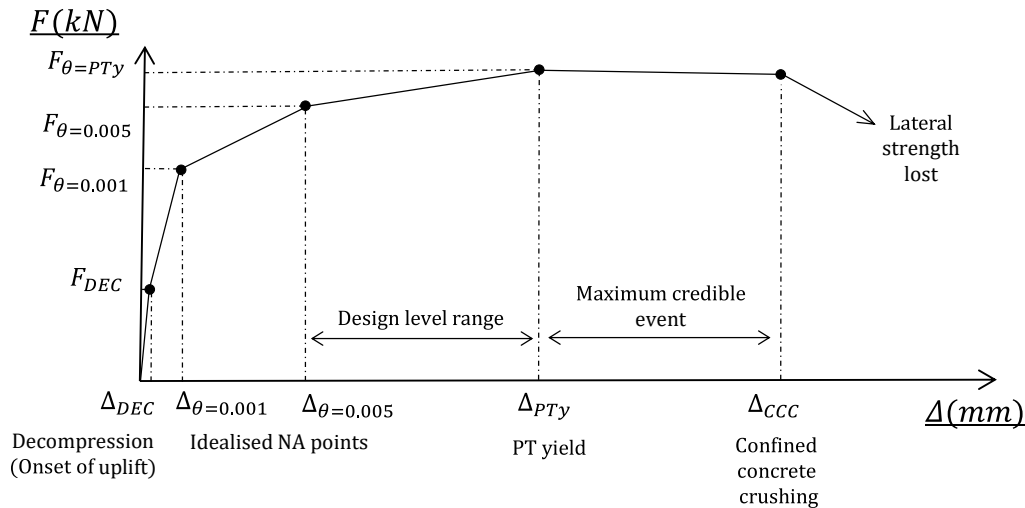


Figure 9.2 – Full force-displacement idealised response using A&S approach

9.3.1 Yield displacement assessment

There is currently no guidance for unbonded PT walls that recommends a method to calculate an idealized bilinear force-displacement for design, which is necessary to calculate consistent yield displacements and ductility estimates. Consequently, a method to calculate the bilinear yield strength and post-yield stiffness is proposed using the simplified analytical method proposed by Aaleti and Sritharan [62]. A key part of the bilinear force-displacement idealisation is the assumed initial stiffness. Two alternative initial stiffness assumptions and the corresponding yield displacements were investigated using the experimentally tested wall systems SRW-A, PreWEC-A, and PreWEC-B. The first assumption for initial stiffness encompassed Priestley et al.’s recommendation that the yield displacement be based on the stiffness of the un-cracked wall sections up the full height, as shown in Figure 9.3 and denoted by $K_{i(1)} = K_g$. The second assumption for initial stiffness was based on an effective stiffness, as shown in Figure 9.3, and denoted as $K_{i(2)} = K_e$. The effective stiffness definition was proposed in an effort to estimate yield displacements of SRW and PreWEC systems that provide more consistent ductility estimates to those of traditional RC walls. The effective stiffness was calculated using the secant stiffness from the origin through the second point in the simplified analytical method proposed

by Aaleti and Sritharan (A&S) [62], identified as the point of the force displacement curve at $F_{\theta=0.001}$ and $\Delta_{\theta=0.001}$ in Figure 9.2. This point represents a midway point of uplift that can be considered as a good estimate of stiffness reduction due to rocking i.e. yielding. A schematic of the two bilinear force-displacement idealisations is presented in Figure 9.3. The proposed procedure to estimate the bilinear response is outlined below:

1. Calculate the initial stiffness (K_i) of the bilinear idealisation assuming either 1) Priestley’s method: assuming a gross section stiffness (K_g), or 2) Proposed method: use secant stiffness (K_e) through the point ($\Delta_{\theta=0.001}, F_{\theta=0.001}$) from A&S.
2. Calculate the post-yield stiffness using Equation (9-6), which is based on the tangent stiffness between the second point ($\Delta_{\theta=0.005}, F_{\theta=0.005}$) of A&S and either the design force/displacement point or the point representing onset of PT yielding. (Recognizing that the design point will be less than PT yielding but greater than a rotation of 0.005)
3. The post-yield stiffness line is then extrapolated back until it intersects with the assumed bilinear initial stiffness. The corresponding displacement at intersection is the yield displacement (Δ_y).

$$K_b = \frac{((F_d \text{ or } F_{PTy}) - F_{\theta=0.005})}{((\Delta_d \text{ or } \Delta_{PTy}) - \Delta_{\theta=0.005})} \quad (9-6)$$

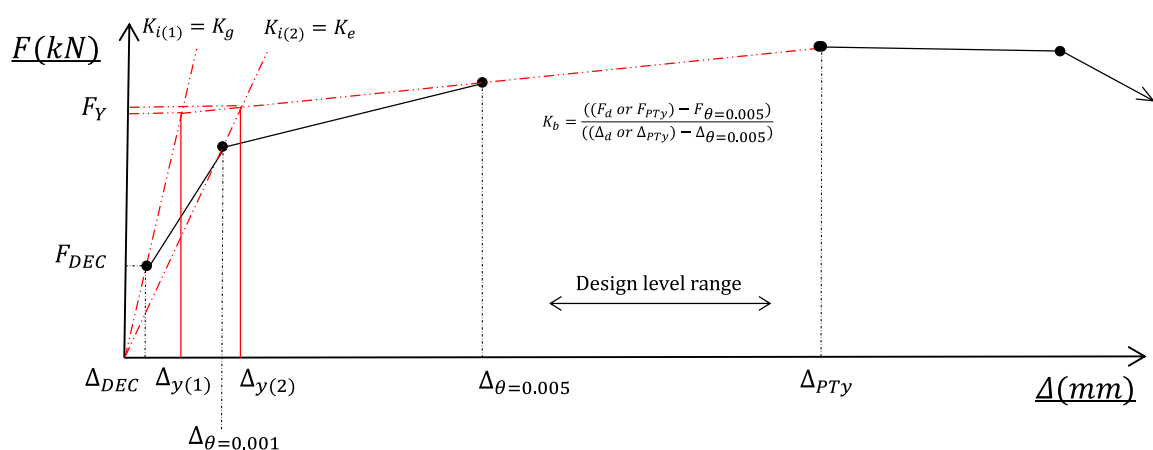


Figure 9.3 – Bilinear idealisations of force-displacement at design level

The two bilinear force-displacement idealisations were calculated for SRW-A, PreWEC-A, and B, using the two different initial stiffness assumptions at the centre of mass of the wall system and are shown in Figure 9.4 for SRW-A and Figure 9.5 for the two PreWEC systems, respectively. The measured pushover force-displacement responses from the snap back testing reported in Chapter 6 are also plotted in the appropriate figure for the respective wall. For all three wall systems the ductility calculated using the effective stiffness provided a better fit for the initial stiffness of the bilinear representation, in comparison to the ductility calculated using the gross section stiffness assumption. A summary of the gross section initial stiffness, the effective stiffness, and the corresponding yield forces and yield displacements are presented in Table 9.1 for each of the wall systems. Overall, the bilinear force-displacement representation that used the effective stiffness resulted in yield displacement estimates that were 2-2.5 times larger than those calculated using the gross section stiffness method.

Table 9.1 – Snap back test specimen bilinear approximations

Wall	$F_{y(1)}$ (kN)	K_g (KN/m)	$\Delta_{y(1)}$ (mm)	$F_{y(2)}$ (kN)	K_e (KN/m)	$\Delta_{y(2)}$ (mm)	$\Delta_{y(2)}/\Delta_{y(1)}$
SRW-FV-A	43.5	2.014e4	2.16	44.7	8.58e3	5.22	2.42
PreWEC-FV-A	66.4	2.035e4	3.26	68.5	9.73e3	7.05	2.16
PreWEC-FV-B	76.6	2.169e4	3.53	79.2	1.05e4	7.54	2.14

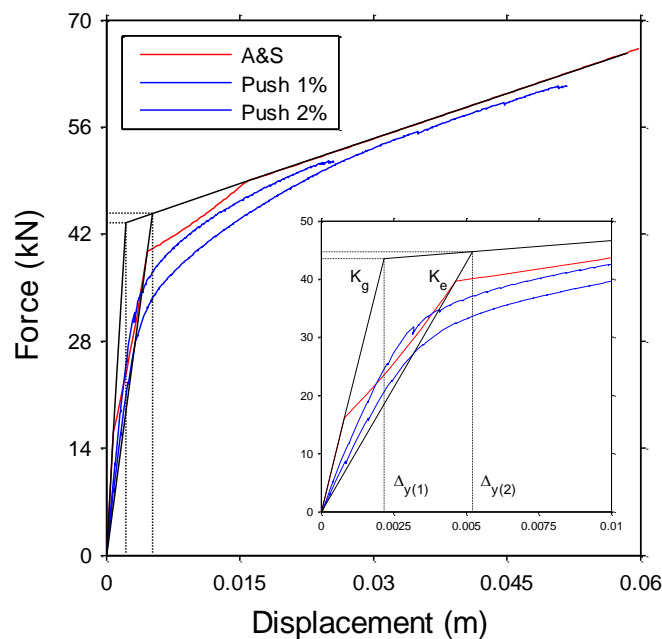


Figure 9.4 – Bilinear idealisation for SRW-A

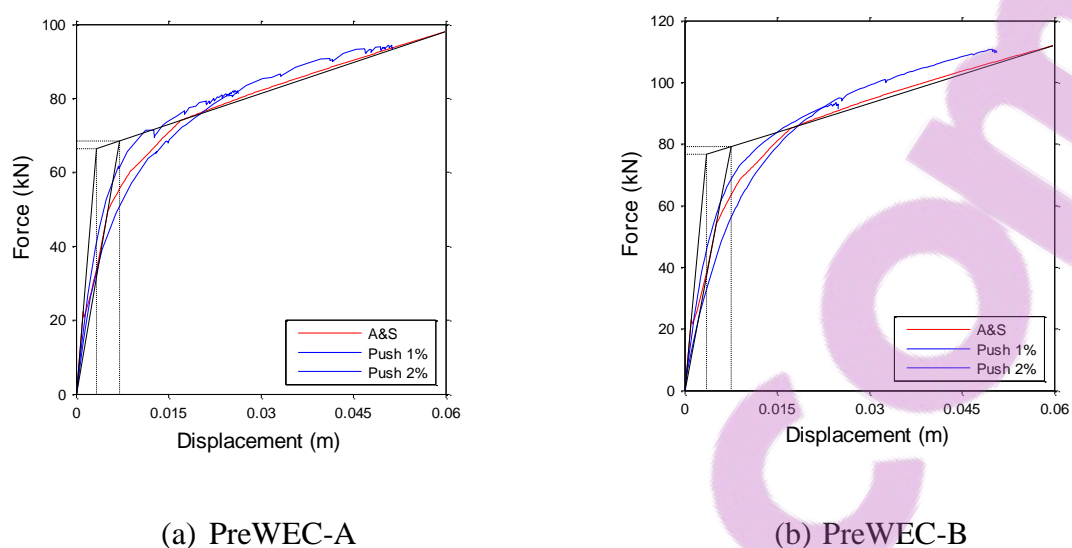


Figure 9.5 – Bilinear idealisation of pushover force-displacement response

9.4 EVD recommendations

This section outlines current methods for determining the EVD appropriate for SRW and PreWEC systems within the DDBD framework. Eight methods are described in detail for PreWEC systems with recommendations from Priestley et al. [20], Appendix B of NZS3101, and the PRESSS Design Handbook [19]. For SRWs Appendix B of the New Zealand Concrete Standard [18] specifies 5% EVD for unbonded PT only systems, which stems from previous recommendations by Priestley [89].

9.4.1.1 Method #1A: Priestley et al. (2007) - Ideal flag-shape hysteresis

Priestley et al. [20] recommends using the EVD area formulation for a standard bilinear flag-shape hysteresis as presented in Equation (2-28) for jointed type wall systems i.e. PreWEC systems. In Equation (2-28) β is the height of the flag as expressed by Equation (2-29), and r is the post-yield stiffness. The area-based EVD calculated using Equation (2-28) must be multiplied by the correction factor shown in Figure 2.13, and subsequently added to the elastic damping component to calculate the total EVD for PreWEC systems.

$$\xi_{\text{area}} = \frac{A_h}{2\pi F_m \Delta_m} = \frac{\beta(\mu - 1)}{\mu\pi(1 + r(\mu - 1))} \quad (9-7)$$

$$\beta = \frac{2M_S}{M_S + (M_{Pt} + M_N)} \quad (9-8)$$

Where M_{Pt} , M_N , and M_S are the flexural strength contributions of the PT tendons, axial load, and energy dissipating devices.

In order to easily implement the relationship that is required for the conversion of area-based EVD to EVD appropriate for NLTHA, as depicted in Figure 2.13, Marriott [13] developed Equation (9-9). Thus, ξ_{hyst} can be determined using Equation (9-10) by calculating the area-based hysteretic EVD and multiplying it by a correction factor (cf) taken from the linearized form of Figure 2.13, as presented by Marriott [13]. To use the area-based hysteretic damping correction factor an estimation of system ductility is required. For assessment of this method the ductility was estimated using the gross section stiffness as recommended by Priestley et al. [20].

$$\frac{\xi_{THA}}{\xi_{area}} = -0.018\xi_{area} + (0.0875\mu + 0.723) \quad (9-9)$$

$$\xi_{hyst} = cf \times \xi_{area} \quad (9-10)$$

9.4.1.2 Method #1B: Method #1A with effective stiffness for ductility index

This method was the same as Method #1A, except that the ductility index was estimated using the proposed effective stiffness bilinear idealisation instead of the gross section stiffness.

9.4.1.3 Method #2: PRESSS Design Handbook/Appendix B NZS3101 (Frames +PT)

The method recommended for determination of EVD for unbonded PT systems in NZS3101:2006 Appendix B, in combination with recommendations from the PRESSS Design Handbook, is a weighted approach between the unbonded PT only system with 5% EVD and the EVD of a purely dissipative system. The purely dissipative system is assumed to be a RC frame as described by Equation (2-25). The weighted approach results in the total formulation for EVD described by Equation (9-12), where the moment contribution ratio (λ) is described by Equation (2-27). In Equation (2-27) M_{Pt} , M_N , and M_S are the flexural strength contributions of the PT tendons, axial load, and energy dissipating devices.

$$\xi_{upper} = \xi_{hyst} = 5 + 30 \left(1 - \frac{1}{\sqrt{\mu}}\right) \quad (9-11)$$

$$\xi_{eq} = 5\% + 30 \frac{\left(1 - \frac{1}{\sqrt{\mu}}\right)}{(\lambda + 1)} \quad (9-12)$$

$$\lambda = \frac{M_{pt} + M_N}{M_S} \quad (9-13)$$

Due to uncertainties related to the yield displacement of jointed type wall systems the PRESSS Design Handbook computes EVD independently of the ductility using Equation (2-30). Equation (2-30) was developed using a weighted moment contribution method between the maximum value of Equation (2-25), which approaches 35% when ductility is large, and the maximum of the PT only system which is 5%. Additionally, a factor of 0.67 is used as the hysteretic damping component is assumed equal to 67% of the theoretical maximum of 35%. Exactly how the 0.67 factor was chosen is not stated, however it is likely to be some reasonable reduction in total possible hysteretic damping that was deemed most appropriate for the system. It should be noted that the hysteretic damping equation for frames is still used despite the design example in the PRESSS handbook concerning coupled walls.

$$\xi_{eq} = \frac{\lambda}{\lambda + 1} 5\% + \frac{1}{\lambda + 1} 35\% \cdot 0.67 \quad (9-14)$$

9.4.1.4 Method #3A: PRESSS Design Handbook/Appendix B NZS3101 (Walls +PT)

An alternative method that is not explicitly recommended in the PRESSS Design Handbook but could provide a valid alternative is to use the EVD equation for RC walls as the purely dissipative system in place of the RC frames EVD. This leads to Equation (9-15) which is identical to Equation (2-30) presented in Method #2B, except with the 35% for RC frames, replaced with 28% for RC walls. The 28% comes from Equation (9-16) which describes the EVD for RC walls initially proposed in Priestley [89], the same article that proposed the EVD equation for RC frames described by Equation (2-25).

$$\xi_{eq} = \frac{\lambda}{\lambda + 1} 5\% + \frac{1}{\lambda + 1} 28\% \cdot 0.67 \quad (9-15)$$

$$\xi_{upper} = \xi_{hyst} = 5 + 23 \left(1 - \frac{1}{\sqrt{\mu}}\right) \quad (9-16)$$

9.4.1.5 Method #3B: Method #3A with effective stiffness for ductility index

This method is similar to both method #2 and #3A as it is based on the weighted moment contributions of the PT only system and the purely dissipative system. The purely dissipative system is assumed to be a RC wall as was described in method #3A by Equation (9-16). However, instead of bypassing ductility and including the arbitrary 0.67 factor, the EVD is evaluated using Equation (9-17) which is based on the development of Equation (9-12) as described in the literature review. The ductility index is based on the effective stiffness bilinear idealisation described in Figure 9.3.

$$\xi_{eq} = 5\% + 23 \frac{\left(1 - \frac{1}{\sqrt{\mu}}\right)}{(\lambda + 1)} \quad (9-17)$$

9.4.1.6 Method #4A: PRESSS Design Handbook (Steel yielding devices + PT)

The PRESSS Design Handbook also recommends an alternative method to Method #2 that incorporates refined ductility-EVD relationships developed by Priestley et al. [20], as described previously by Equation (2-24). In the PRESSS Design Handbook the same logic that resulted in Equation (2-30) with respect to exclusion of ductility was applied and the EVD was calculated using Equation (2-32). The value of 23.4% is the maximum value of hysteretic EVD calculated from Equation (2-24) when R_{ξ} is equal to 0.577 for externally mounted mild steel yielding devices. The mild steel yielding devices could be O-connectors as for the PreWEC system or other devices such as the UFP. The 0.67 factor is still applied to the hysteretic weighted component will no guidance as to its determination. This method was also briefly assessed for the shake table test data in Chapter 7.

$$\xi_{eq} = \frac{\lambda}{\lambda + 1} 5\% + \frac{1}{\lambda + 1} 23.4\% \cdot 0.67 \quad (9-18)$$

Note that if ductility is not bypassed, the formulation for EVD is described by Equation (9-19). The background of which was described in Chapter 2.

$$\xi_{eq} = 0.05 + \frac{R_{\xi}}{(\lambda + 1)} \left(\frac{\mu - 1}{\mu\pi} \right) \quad (9-19)$$

9.4.1.7 *Method #4B: Method #4A with effective stiffness for ductility index*

This method uses the weighted moment contribution method in combination with the EVD-ductility Equations proposed by Priestley et al. [20] based on the purely dissipative system being mild steel yielding devices as described by Method #4A. However, instead of bypassing ductility, the EVD is evaluated using Equation (9-19) where R_{ξ} is equal to 0.577, where the ductility estimate is based on the effective stiffness bilinear idealisation described in Figure 9.3.

9.4.1.8 *Method #5: Measured area-based EVD from cyclic hysteresis*

The EVD can also be determined in a similar manner to Method #1A/B where the area-based EVD can be calculated from pseudo-static cyclic testing using Equation (5-1), as was performed in Chapter 5. The area-based EVD is then adjusted using the correction factor described by Equation (9-9) to “transform” the area-based EVD into an NLTHA appropriate EVD. Despite using test data this method still requires an estimate of yield displacement to calculate ductility for use in Equation (9-9). For this method the proposed effective stiffness assumption was used to estimate the bilinear idealisation based on the A&S prediction.

9.4.2 EVD summary

A summary of the key parameters of each of the EVD methods is provided in Table 9.2, where PDH refers to PRESSS Design Handbook. For the two PreWEC systems tested in Chapter 7 the parameters λ , and β have been calculated and are presented in Figure 9.6 versus drift. Calculation of λ , and β was based on the lateral force-displacement behaviour determined using the simplified analytical procedure proposed by Aaleti and Sritharan (A&S) [62], as presented in Figure 9.7. The yield displacements of the three shake table walls are given in Table 9.3 for both stiffness assumptions. The yield displacement is required to calculate the ductility for EVD methods #1A/B, #3B, #4B, and #5. The ductility index has a large influence on the area-based methods, which are #1A/B, and #5, as they require a calibration factor based on ductility to estimate EVD appropriate for NLTHA. The calculated calibration factor is plotted versus the area-based damping for each area-based EVD method in Figure 9.8 for both PreWEC walls.

Table 9.2 – Summary of EVD methods

Method	Hysteresis model/system	Source	Initial stiffness	Required parameters
#1A	Flag-shape	Priestley et al. [20]	K_g	β, τ, cf, μ
#1B	Flag-shape	Modified from: Priestley et al. [20]	K_e	β, τ, cf, μ
#2	PT + RC frames	App.B [18]/PDH[19]	N/A	λ
#3A	PT + RC walls	Modified from: App.B [18]/PDH[19]	N/A	λ
#3B	PT + RC walls	Modified from: App.B [18]/PDH[19]	K_e	λ, μ
#4A	PT + steel	App.B [18]/PDH[19]	N/A	λ
#4B	PT + steel	Modified from: App.B [18]/PDH[19]	K_e	λ, μ
#5	Measured cyclic EVD	Modified from: Priestley et al. [20]	K_e	μ, cf

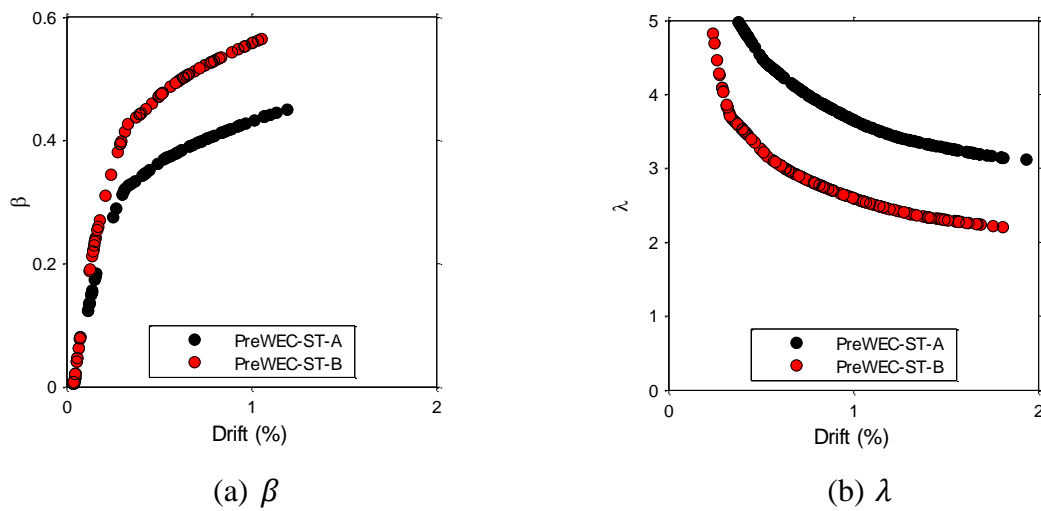


Figure 9.6 – Key design parameters

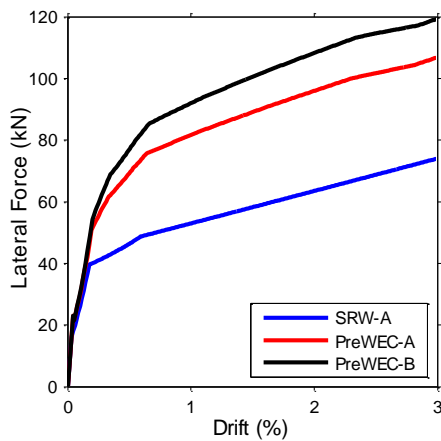
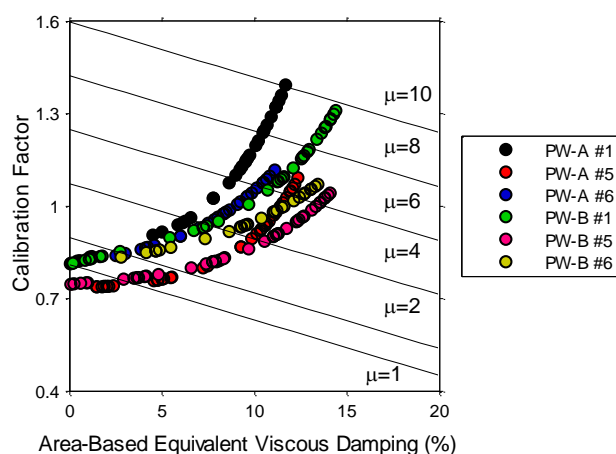


Figure 9.7 – A&S force-displacement behaviour

Table 9.3 – Yield displacements of shake table test specimens

Wall	$\Delta_{y(1)}$ (mm)	$\Delta_{y(2)}$ (mm)	$\Delta_{y(2)}/\Delta_{y(1)}$
SRW-ST-A	2.16	5.22	2.42
PreWEC-ST-A	3.26	7.05	2.16
PreWEC-ST-B	3.53	7.54	2.14

**Figure 9.8 – Calibration factor for area-based damping**

To demonstrate the influence of ductility (i.e. yield displacement) on the magnitude of EVD, the EVD ratios calculated using method #1A and #1B are plotted versus drift in Figure 9.9(a). Method #1A incorporates the gross section stiffness and as a result has a much lower yield displacement, hence larger ductility estimates than method #1B at the same drift levels. Method #1B uses an effective stiffness that results in a larger yield displacement. As a result of the larger ductility estimates there are also larger EVD ratios due to the assumed relationship between ductility and EVD. As an example at 0.75% drift for PreWEC-A method #1A gives an EVD of 15.8% while method #1B gives an EVD of 10%, i.e. 50% greater.

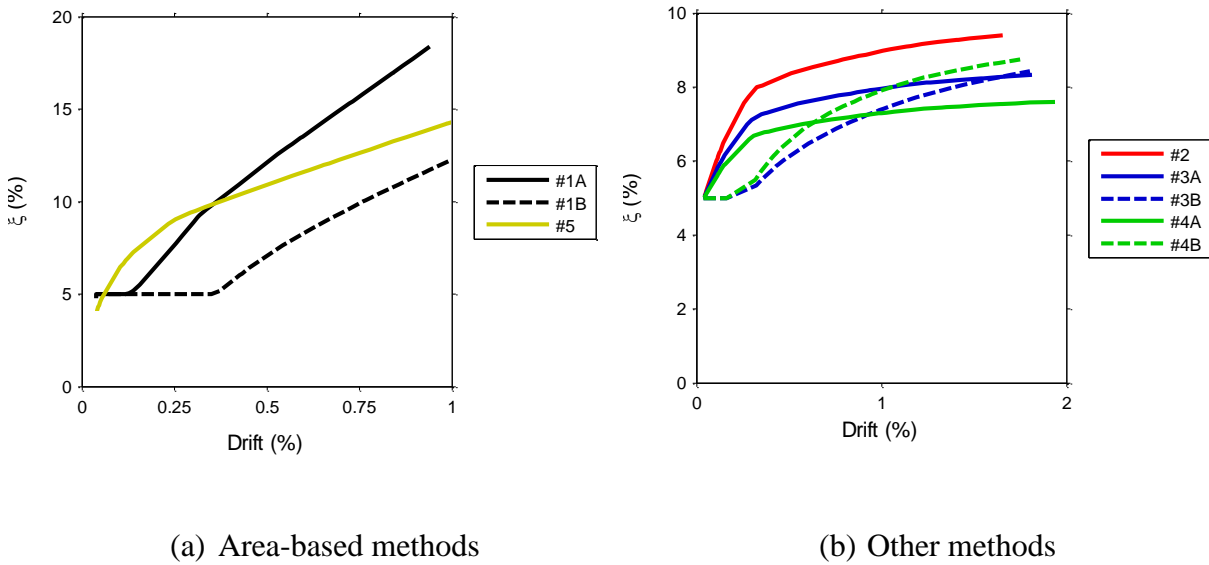


Figure 9.9 – EVD comparison close up for PreWEC-A (different scales)

Also shown in Figure 9.9(a) is the EVD versus drift of method #5, which is the EVD calculated from the measured cyclic area-based damping with the appropriate calibration factor. Due to the relatively large ductility estimates, even when the effective stiffness is used the area-based EVD is amplified by the calibration factor. All three area-based EVD methods result in large EVD ratios, up to 18% at 1% drift, in comparison to the other methods shown in Figure 9.9(b), that have a maximum value of 8.5% at 1% drift. The EVD ratios versus drift for both PreWEC walls and all EVD methods are presented in Figure 9.10. It is apparent that there is significant variation between all of these seemingly valid methods of EVD determination.

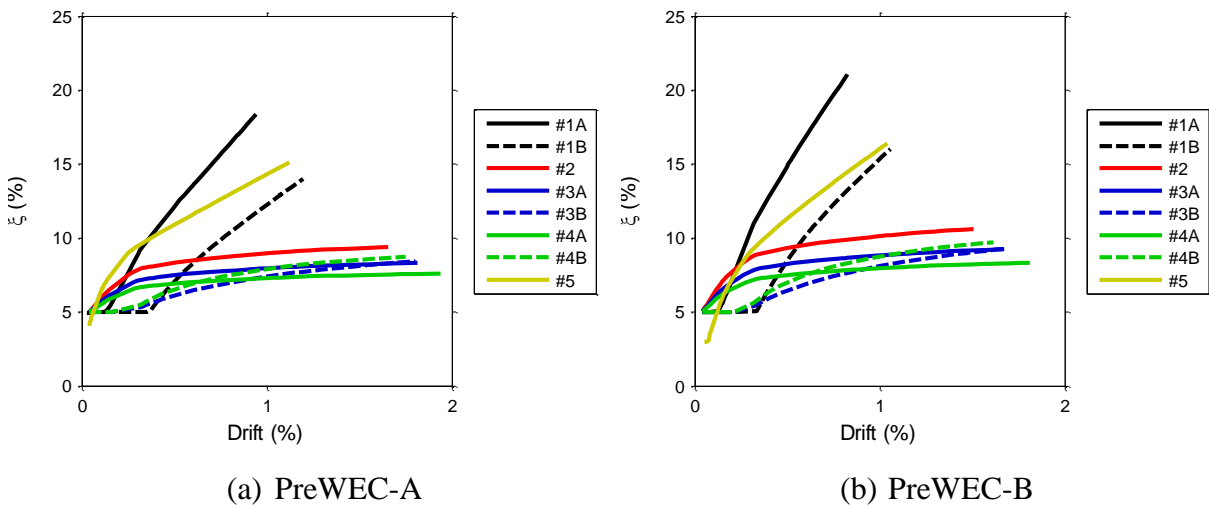


Figure 9.10 – EVD comparison for each wall tested

9.5 DDBD EVALUATION OF EVD METHODS

DDBD was used to evaluate the EVD methods described above using the shake table test results presented in Chapter 7. In Chapter 7 a DDBD algorithm was described that was used to evaluate adjusted design displacements for the SRW system assuming 5% EVD, and for the two PreWEC systems using EVD evaluated using method #4A, to provide a brief assessment of DDBD using current New Zealand recommended design procedures for such systems. For the evaluation carried out here the same adjusted R values (R_{ad}) described in Chapter 7 are adopted to determine the design spectra for each of the ground motions used to assess the EVD methods. As in the Chapter 8, only the two highest intensity level ground motion suites were used to evaluate the EVD methods as these are of the most interest to designers. For SRW these were the seven records run for EQ-III and EQ-IV as reported in Chapter 7. For the two PreWEC walls these were the seven records run for EQ-V and EQ-VI. The DDBD evaluation algorithm is outlined below and illustrated in Figure 9.11. The assumptions required for implementation of the algorithm are:

- System force (F) - displacement (Δ) behaviour (As depicted in Figure 9.7)
- EVD-ductility or EVD-drift relationship (As depicted in Figure 9.10)

Algorithm steps:

1. Guess initial “design” displacement (Δ_1).
2. Calculate EVD (ξ_{eq}) using initial design displacement (Δ_1) based on one of the methods.
3. Find lateral force (F_d) corresponding to the initial displacement (Δ_1) from assumed force-displacement behaviour.
4. Calculate effective stiffness (k_e) using Equation (9-20) and subsequently the effective period (T_e) using Equation (9-21).

$$K_e = \frac{F_d}{\Delta_1} \quad (9-20)$$

$$T_e = \sqrt{\frac{4\pi^2 m_e}{K_e}} \tag{9-21}$$

- Calculate the EVD reduced displacement design spectra (based on the adjusted return period factor described in Chapter 7 and given in Appendix E) for the specific ground motion using the spectral reduction factor or damping modifier (η) described by Equation (7-1).

$$\eta = \left(\frac{7}{2 + \xi_{eq}} \right)^{\alpha_{SF}} \tag{9-22}$$

Where α_{SF} is equal to 0.5 for sites located away from a major fault and the ground motions do not comprise of near-fault, forward directivity.

- Using the reduced displacement spectra and the effective period, find the final “design” displacement (Δ_2) as shown in Figure 9.11.
- Check if the initial displacement is equal to the final displacement i.e. $\Delta_1 = \Delta_2$ or within 1%. If so the design displacement has been calculated i.e. $\Delta_{design} = \Delta_1$. However, if they are not equal, update the initial design displacement guess accordingly, and redo steps 1-7 until a solution is found.

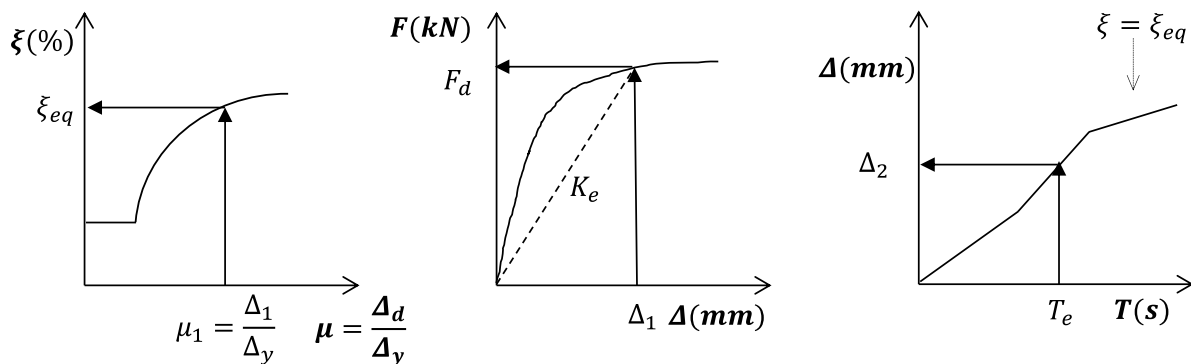


Figure 9.11 – DDBD evaluation algorithm

The measured maximum peak displacement (D_{TEST}) of each ground motion from EQ-III and EQ-IV, divided by the iterated design displacement (D_{DESIGN}) for that record is plotted versus the test peak drift for SRW-ST-A in Figure 9.12(a) assuming 5% EVD. The average of the fourteen records is 0.82, which implies that the design is underdamped. Therefore the EVD was increased until the average was one. An average of one suggests that on average the design process will

accurately predict the test peak drift. The EVD found to satisfy this condition was 6.65% EVD, although it is clear from Figure 9.12(b) that there is considerable scatter in the data with the test approximately two times greater than the design in some cases.

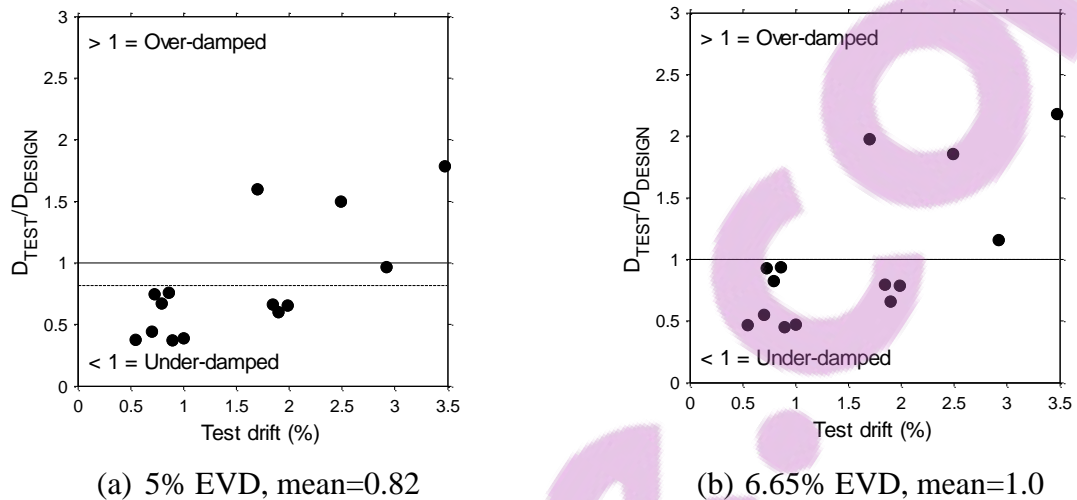
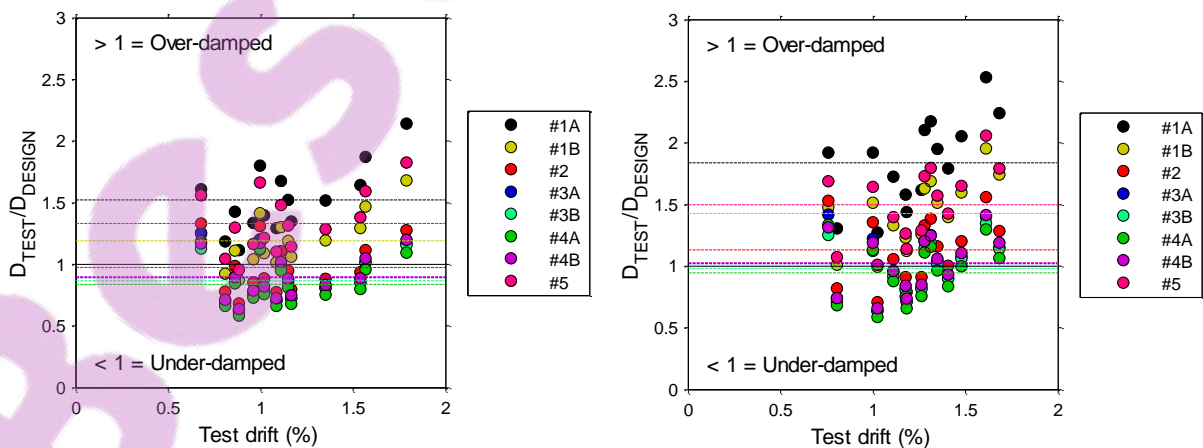


Figure 9.12 – Comparison between DDBD method and SRW-ST-A shake table data for 5% and 6.65% EVD

The measured peak displacement of each ground motion from EQ-V and EQ-VI, divided by the iterated design displacement for that record is plotted versus the test peak drift for PreWEC-ST-A in Figure 9.13(a), for each of the eight EVD methods. The same peak displacement over design displacement index is plotted for PreWEC-ST-B for the fourteen ground motion records of EQ-V and EQ-IV in Figure 9.13(b). The average of the fourteen records for each of the EVD methods is presented in Table 9.4 for both PreWEC-ST-A and B and shown by the corresponding coloured line in Figure 9.13.



(a) PreWEC-A

(b) PreWEC-B

Figure 9.13 – Comparison between EVD methods in DDBD and PreWEC shake table data**Table 9.4 – Mean test/design displacement PreWEC systems for all EVD methods**

Method	PreWEC-A	PreWEC-B	Average of both walls
#1A	1.52	1.84	1.68
#1B	1.19	1.43	1.31
#2	0.97	1.13	1.05
#3A	0.89	1.02	0.96
#3B	0.87	0.98	0.92
#4A	0.84	0.94	0.89
#4B	0.90	1.03	0.96
#5	1.33	1.50	1.42

Both method #1A and #1B significantly overestimate the EVD required to achieve accurate design drifts in comparison to the peak test drifts. On average for both walls, EVD method #1A predicts design drifts 68% lower than the measured peak drift. Method #1B is an improvement on #1A with design drifts on average 31% lower than the measured peak drift. The improvement is purely a result of the yield displacement being calculated using an effective stiffness, that leads to lower ductility estimates, and as a result lower EVD estimates. Ductility has a significant effect on the area-based EVD methods due to the calibration factor required to transform the area-based EVD into an EVD appropriate for NLTHA. EVD method #5 is based on the measured area-based EVD that must also incorporate this NLTHA calibration, and as a result is also affected by the ductility assumption. On average the design drifts estimated using method #5 are 42% underestimated in comparison to the test peak drifts. It would be useful if a calibration factor could be applied to the measured area-based EVD, based purely on drift, rather than ductility, as this would avoid ambiguous assumptions that can clearly lead to unconservative results.

Ideally, the area-based EVD from the measured force-displacement response should be able to be calibrated for NLTHA and directly used in design with confidence. Based on this assessment for the particular tests studied the EVD used in DDBD evaluated from realistic area-based EVD is too high for realistic design displacements. Previous researchers such as Punnucci et al. [74] have suggested that pseudo-static cyclic tests in which repeated and closely spaced cycles

are applied, might be over-demanding for hysteretic damping evaluation. This is an area for future research.

The other five EVD methods, #2, #3A/B, and #4A/B, all, on average between the two walls and all fourteen records, produce reasonable results with average drifts predicted within 11% (between 0.89-1.05 for the test over design displacement index). The three methods (#2, #3A, #4A) that ignore ductility and incorporate a seemingly arbitrary factor of 0.67, on average predict design drifts 5% lower, 4% higher, and 11% higher than the measured peak drift for method #2, #3A, and #4A, respectively. These results are reasonable; however, a more rigorous approach based on method #3B or #4B is more desirable, as use of the arbitrary 0.67 factor is not required. Method #3B and #4B on average over predict the test drifts by 11% and 4%, respectively, between the two walls and all fourteen records. Therefore, method #4B is recommended for the calculation of EVD of PreWEC systems, and is slightly on the conservative side of design estimates. It should be noted that the ductility index must be calculated using the procedure detailed in this chapter that uses the effective stiffness. If the gross section ductility is used, ductility estimates of more than twice those estimated from the effective stiffness method would be calculated, leading to larger EVD ratios.

9.6 CONCLUSIONS AND RECOMMENDATIONS

The DDBD process for the SRW and PreWEC systems that underwent shake table testing as reported in Chapter 7 was evaluated. The focus of this evaluation was on current EVD recommendations for jointed type wall systems as applied within the framework of the DDBD proposed by Priestley et al. [20].

Firstly, a discussion on appropriate yield displacements for SRW and PreWEC systems for estimation of ductility in DDBD was presented. A bilinear idealisation method was proposed based on the multi-linear force-displacement response predicted using the simplified analytical method proposed by Aaleti and Sritharan. Two assumptions for calculating yield displacement for the bilinear idealisation were investigated, one based on the gross section stiffness and the other on an effective stiffness. Traditionally, it has been assumed that the initial stiffness of unbonded PT walls should be based on the gross section, but use of an effective stiffness for the bilinear idealisation was considered to give more appropriate values of ductility. The effective

stiffness assumption produced yield displacements 2.1-2.5 times greater than the gross section stiffness.

Eight methods of evaluating the EVD of jointed type wall systems were outlined and investigated using the shake table results reported in Chapter 7. The methods were based on current EVD recommendations that are described in Appendix B of NZS3101, PRESSS Design Handbook, and Priestley et al. [20] for jointed type wall systems. Additionally, the area-based EVD-drift relationships calculated from the pseudo-static cyclic tests reported in Chapter 5 was also used and assessed in the DDBD process.

A number of the EVD methods investigated purposely avoid estimating ductility due to the ambiguity around its definition. However, if EVD is determined using an EVD-ductility relationship a yield displacement must be assumed. As recommended by Priestley et al. two EVD methods used the idealised flag-shape hysteresis definition in combination with either the yield displacement based on gross section stiffness (Method #1A) or the yield displacement based on the effective stiffness (Method #1B). The comparison between these two methods provided a clear indication of how significant the selection of yield displacement is when used to calculate a ductility index for determination of EVD. The two different stiffness assumptions resulted in EVD ratios that varied by up to 50%.

For SRW an EVD of 6.65% resulted in the average design displacement equalling the average peak test displacement, which indicates that the use of higher EVD is acceptable for SRWs at design levels. For the PreWEC systems the most appropriate method of determining the EVD for DDBD was found to be a weighted moment contribution method as specified in Appendix B of NZS3101 and the PRESSS Design Handbook, except with the dissipative system EVD consisting of the EVD-ductility equation given by Priestley et al. [20] for yielding steel systems, where the ductility index is based on the effective stiffness bilinear idealisation. When using this EVD-damping recommendation on average the design estimates over predict the test drifts by only 4%. This method is recommended as it incorporates appropriate and robust values of ductility by using yield displacement based on the effective stiffness. Overall, this process has provided validation for the use of DDBD for the design of SRW and PreWEC systems.

9.7 REFERENCES

13. Marriott, D., *The Development of High-Performance Post-Tensioned Rocking Systems for the Seismic Design of Structures*. 2009, University of Canterbury: Christchurch.
18. New Zealand Standard, *Concrete Structures Standard NZS 3101*. 2006: Wellington, New Zealand.
19. Pampanin, S., D. Marriott, A. Palermo, and New Zealand Concrete Society., *PRESSS design handbook*. 2010, Auckland, N.Z.: NZCS. 1 v. (various pagings).
20. Priestley, M.J.N., G.M. Calvi, and M.J. Kowalsky, *Displacement-based seismic design of structures*. 2007, Pavia: IUSS Press : Fondazione Eucentre. xvii, 721 p.
26. Kurama, Y.C., *Seismic design of unbonded post-tensioned precast concrete walls with supplemental viscous damping*. ACI Structural Journal, 2000. **97**(4): p. 648-658.
45. Kurama, Y., S. Pessiki, R. Sause, and L.W. Lu, *Seismic behavior and design of unbonded post-tensioned precast concrete walls*. PCI Journal, 1999. **44**(3): p. 72-89.
62. Aaleti, S. and S. Sritharan, *A simplified analysis method for characterizing unbonded post-tensioned precast wall systems*. Engineering Structures, 2009. **31**(12): p. 2966-2975.
74. Pennucci, D., G.M. Calvi, and T.J. Sullivan, *Displacement - Based Design of Precast Walls with Additional Dampers*. Journal of Earthquake Engineering, 2009. **13**(sup1): p. 40-65.
83. Gulkan, P. and M. Sozen, *Inelastic response of reinforced concrete structures to earthquake motions*. ACI Journal, 1974. **71**(12): p. 604-610.
84. Shibata, A. and M.A. Sozen, *Substitute-structure method for seismic design in R/C*. Journal of the Structural Division-Asce, 1976. **102**(1): p. 1-8.
85. Priestley, M.J.N. and D.N. Grant, *Viscous damping in seismic design and analysis*. Journal of Earthquake Engineering, 2005. **9**(SPEC. ISS. 2): p. 229-255.
88. Dwairi, H.M., M.J. Kowalsky, and J.M. Nau, *Equivalent damping in support of direct displacement-based design*. Journal of Earthquake Engineering, 2007. **11**(4): p. 512-530.
89. Priestley, M.J.N., *Direct displacement-based design of precast/prestressed concrete buildings*. PCI Journal, 2002. **47**(6): p. 66-79.

Chapter 10

CONCLUSIONS

This chapter provides an overview of the work that has been presented in the preceding chapters. The motivation and objectives of the work are briefly summarised, and the main outcomes from each chapter are presented to demonstrate how this work has addressed the objectives. Lastly, key areas where further research is recommended are described.

10.1 MOTIVATION AND OBJECTIVES

The primary aim of this study was to develop a deeper understanding of the seismic performance of unbonded PT precast concrete rocking walls by systematically investigating the pseudo-static cyclic and dynamic experimental response, and improving the robustness of design and modelling procedures. The existing literature contained a lack of systematic cyclic and dynamic testing programmes focused on any form of vertically jointed unbonded PT precast concrete wall system. As a result of the lack of rigorous testing, verification of damping schemes used for numerical modelling and DDBD methods against shake table test data was not possible. This research was conducted to fill these knowledge gaps and contribute to the robustness of the design process in order to increase the implementation of SRW and PreWEC systems.

To achieve the overall objective, three phases of research were performed and reported in the previous chapters. The first phase concerned all of the experimental testing reported in Chapters 3, 5, 6, and 7. The testing phase of this thesis aimed to experimentally verify the seismic performance of SRW and PreWEC systems subjected to static and dynamic loads including real earthquake ground motions at varying intensity levels. This involved the development of a modified and scaled version of the previously developed O-connector dissipater that overcame previous design flaws for inclusion in the scaled PreWEC systems tested. In order to fully understand the seismic response of the SRW and PreWEC systems, a test series incorporating different loading types was performed on a series of walls to provide a comprehensive understanding of all aspects of the response of variety of wall systems. The three test types performed were pseudo-static cyclic testing, snap back testing, and shake table testing.

The objective of the pseudo-static cyclic testing was to systematically investigate the cyclic response of SRW and PreWEC systems with different levels of damping achieved by varying the number of energy dissipating O-connectors in each test. This specifically included validation of the current wall panel design recommendations and verification of an existing simplified analysis method used for the design of PT wall systems. The objective of the snap back testing was to investigate and quantify the dynamic characteristics of SRW and PreWEC systems, with particular emphasis on the damping and dynamic residual drifts which are vital parameters required to fully understand the seismic behaviour of unbonded PT walls that can only be determined experimentally. Additionally, the snap back tests provided an opportunity to investigate the difference in the local response parameters obtained from static and dynamic test data, using the pushover and free vibration decay phases of each snap back test. The main aim of the shake table testing was to experimentally verify the seismic performance of SRW and PreWEC systems subjected to different ground motion intensity levels and to provide test data to enable calibration and validation of numerical models and the DDBD method.

The shake table testing programme was designed with two additional objectives in mind to be achieved with the generated data. The first objective was to investigate and assess numerical modelling techniques appropriate for SRW and PreWEC systems that could be easily incorporated into building models for design engineers when conducting nonlinear time history analysis. The second was to enable verification of the current Direct Displacement Based Design

(DDBD) process for SRW and PreWEC unbonded PT precast concrete wall systems and provide recommendations for accurate determination of equivalent viscous damping ratios for design.

10.2 SUMMARY OF CONCLUSIONS

Outlined below are discussions of the results and summaries of the key conclusions from the experimental programmes, numerical analyses, and design process assessments presented in this thesis. It should be noted that the results may not be directly applicable to full-scale structures, the response of which is likely to be complicated by the presence of floor diaphragms, gravity frames, non-structural components and differing foundation conditions.

10.2.1 Experimental programme

10.2.1.1 O-connector component testing

The unique experimental investigation into the cyclic response of the O-connector energy dissipaters confirmed the suitability of the O-connector as a cost effective energy dissipater that demonstrates stable hysteresis behaviour while being easy to install and replace. Two failure mechanisms were identified associated with the method of welding and the heat affected zone. The novel design of the O-connector with wings was proposed and tested that enabled the preferred ductile failure mechanism to occur, by locating the heat affected zone in an area with a larger cross-section compared to the O-connector leg. It is clear that the strain capacity of the steel is directly related to the displacement capacity of the O-connector and it is important to ensure that the strain specified in design is achieved by conducting independent tensile coupon testing, especially when high displacement capacities are required. Out-of-plane buckling of the O-connector was avoided with the improved O-connector design that consisted of a reduction in the length to thickness ratio, a ratio less than 20 is recommended to limit out of plane buckling. Finally, simple analytical equations were validated to predict the yield, plastic and ultimate strength of the O-connector.

10.2.1.2 General wall response and design

The eleven SRW and PreWEC systems tested demonstrated consistent damage and behaviour across all loading types. As expected rocking initiated at the wall base and negligible damage was observed regardless of the wall parameters or loading type. Any damage was limited to

minor cracking and spalling of concrete in the compressive toe region of the precast concrete wall panel and the intended yielding of the O-connector dissipaters.

The SRW systems exhibited an approximate bilinear response and the PreWEC walls showed increased strength and energy dissipation due to the addition of O-connectors under both pseudo-static and dynamic loading rates. There was good alignment of the force-displacement behaviour of the walls when comparing the cyclic test, snap back pushover response, and the inertia force-displacement response from the snap back decay. This demonstrated the consistent behaviour of the SRW and PreWEC systems regardless of loading rate.

Assessment of the static and dynamic phases of response from snap back testing demonstrated that the dynamic behaviour of SRW and PreWEC systems is well represented by static tests for parameters such as neutral axis and PT force, however higher wall toe strains can be expected under dynamic loading due to impact at the wall/foundation interface during rocking. The consistent behaviour for all test walls and different loading types indicate that the methods used to design the confinement and armouring details in the test walls were appropriate and effective.

10.2.1.3 O-connector influence

The hypothesis that the arrangement of the PreWEC wall system ensures that connector forces imposed on the wall panel are equal and opposite was proved by the consistency in compression toe strains and neutral axis depth between the SRW and PreWEC systems during cyclic testing. As a result of these balanced connector forces, the wall panel behaviour and peak compressive forces in the toe are independent of the number of O-connectors and consequently, supplemental damping can be added without compromising the wall design or performance.

10.2.1.4 Initial stiffness

Assessment of the initial stiffness of the SRW and PreWEC systems tested under pseudo-static cyclic loading found that the measured stiffness was lower than expected if calculated assuming a gross section moment of inertia (I_g). An effective stiffness modifier was calculated based on the ratio of measured initial stiffness and the predicted initial stiffness. The effective stiffness modifiers were calculated using the pseudo-static cyclic test data to be between 0.61-0.62 I_g for the SRWs and 0.77-0.79 I_g for the PreWEC systems.

The fundamental frequency of the wall systems was also measured via impact tests performed on the snap back test walls before the snap back testing. For all four wall systems tested, the fundamental frequency based on the impact tests was found to be significantly lower than the expected fundamental frequency calculated using a stiffness based on the gross section moment of inertia. Effective stiffness modifiers were also calculated based on the impact test data with the proportion of the gross section moment of inertia required to attain the measured fundamental frequency being $0.48I_g$ for the SRW and between $0.74-0.8I_g$ for the PreWEC walls. These values aligned well with those from the cyclic testing.

Additionally, white noise tests performed before the shake table testing estimated fundamental frequencies of 7.9 Hz for the SRW and 10.0-9.0 Hz for the PreWEC systems which correlated well with the measured fundamental frequencies from the impact tests on the snap back test walls of 8.2 Hz for SRW and 10.6 Hz for the PreWEC systems. These observations reinforce the conclusion that the initial stiffness of SRW and PreWEC systems is lower than that calculated using a gross section stiffness.

No data was collected that could isolate why the stiffness' of the walls were lower than predicted, however it is thought that the grout joint interface between the wall and foundation would influence the stiffness of the system. It is therefore important to ensure careful grouting when installing PT walls to ensure an even bearing surface.

10.2.1.5 Equivalent viscous damping

The equivalent viscous damping (EVD) was estimated from both the cyclic and snap back decay responses. The SRW systems were found to have EVD equal to 3-5% from the cyclic testing and 0.9-3.8% evaluated from snap back testing depending of the level of drift. The PreWEC systems showed increased hysteresis and energy dissipation due to the addition of the O-connectors for both cyclic and snap back testing. The EVD increased in proportion to the number of O-connectors with between 1.1-1.4% EVD provided by each O-connector in the PreWEC walls tested under cyclic loading. For the snap back testing the PreWEC systems were found to have maximum EVD ratios of 14.7%, 20.7%, and 25.8% respectively depending on the O-connector number and initial PT force. The snap back test EVD results showed increased EVD at high drifts and lower EVD at low drifts for all PreWEC walls when compared to the EVD from the cyclic tests. This is due to the nature of the loading and the influence of dynamic effects.

However, for SRW-FV-A higher EVD was calculated for the cyclic tests in comparison to the snap back tests. This was due to the increased cycles and corresponding inelastic toe strains and damage observed in the cyclic test in comparison to the snap back test. Additionally, the inherent damping of the systems when rocking or uplift was not occurring was estimated from white noise tests performed during shake table testing. Measured EVD ratios from the white noise tests were found to range between 3.1-3.9% for the wall systems tested.

10.2.1.6 Residual drifts

During the pseudo-static cyclic tests an increase in hysteresis area from an increase in O-connector number introduced higher static residual drifts in the cyclic hysteresis response. Up to a 0.6% static residual drift at 2.5% lateral drift was measured for PreWEC-B. Despite the measured static residual drifts, negligible residual drifts occurred during all snap back tests on all walls, regardless of the PT force and number of O-connectors. Additionally, the residual drifts at the end of all shake table tests were minimal, rarely exceeding 0.05%. The residual drifts from shake table tests were significantly lower than those expected from the pseudo-static cyclic tests, and less than the drift limits set at 0.2% and 0.3% for the design earthquake and the maximum credible earthquake. A residual drift ratio was calculated to give an indication of the shake-down effect with SRW-ST-A, PreWEC-ST-A, PreWEC-ST-B1 and B2 having residual drift ratios of 0.1, 0.25, 0.24, and 0.25, which demonstrates that the dynamic residual drift was less than 25% of that expected for the same peak drift from cyclic testing at a maximum.

10.2.1.7 Simplified analytical procedure

The simplified analytical method published by Aaleti and Sritharan [62] was able to capture both the global and local response parameters of the static tests with sufficient accuracy. There were some small discrepancies in the prediction of the neutral axis depth at low lateral drifts and the deviation between the measured and predicted PT tendon force was due to minor prestress losses observed during each test.

10.2.2 Numerical modelling

Nonlinear time history analysis of SRW and PreWEC systems was performed using a simple single degree of freedom model. The dynamic tests reported in this thesis provided a unique opportunity to validate a simple modelling technique with high quality dynamic test data for SRW and PreWEC systems. A selection of damping schemes were investigated to determine the

most appropriate damping scheme for SRW and PreWEC systems to be used by structural design engineers.

In order to provide recommendations for numerical modelling in design, a predictable restoring force-displacement behaviour was necessary. As a result the simplified analytical method proposed by Aaleti and Sritharan [62] was employed to describe the restoring force-displacement behaviour of the SRW and PreWEC systems. To achieve accurate results for the SRW system the force calculated using the simplified analytical method required multiplication by a factor of 0.8, called the reduced A&S method, however this factor was not required for the PreWEC systems.

For SRW systems the damping scheme that was found to best emulate the shake table test results in terms of peak displacements and accelerations used 2% tangent stiffness damping, and an elasto-plastic spring calibrated to the hysteresis measured during the cyclic testing of SRW-A. This damping scheme in combination with the reduced A&S force-displacement behaviour was on average able to predict the peak displacements and accelerations of the shake table tests within 5%, which is an excellent result considering the simplicity of the model. The damping scheme that produced excellent results for the SRW shake table tests provided poor estimation of the snap back decay due to excessive damping. It is therefore apparent that SRW numerical models calibrated for free vibration decay do not result in accurate emulation of displacement and acceleration response to ground motions. An alternative damping scheme was developed for the SRW that was able to produce good emulation of the snap back decay.

Overall, the PreWEC systems shake table response could be emulated well using a combination of springs that best represented the cyclic hysteresis behaviour with an additional 2% tangent stiffness damping implemented in a simple SDOF model. On average the peak model displacements and accelerations of PreWEC-ST-A were within 1% and 11%, respectively, when compared to that measured during testing. On average the peak model displacements and accelerations of PreWEC-ST-B were within 4% and 16%, respectively, when compared to that measured during testing. A more predictable and consistent behaviour was found for the PreWEC systems than the SRW, evidenced by the low range of model to test ratios for both displacement and acceleration peaks when compared to SRW-ST-A.

10.2.3 DDBD

An assessment was performed on the current methods of EVD determination for SRW and PreWEC systems as applied within the framework of the DDBD proposed by Priestley et al. [20]. A bilinear idealisation method was proposed based on the multi-linear force-displacement response predicted using the simplified analytical method proposed by Aaleti and Sritharan, that incorporates an effective stiffness in place of the normally assumed gross section stiffness. Eight methods of evaluating the EVD of jointed type wall systems are outlined and then investigated using the shake table data reported in Chapter 7.

For SRW an EVD of 6.65% resulted in the average design displacement equalling the average peak test displacement, which indicates that the use of higher EVD is acceptable for SRWs at design levels. For the PreWEC systems the most appropriate method of determining the EVD for DDBD was found to be a weighted moment contribution method as specified in Appendix B of NZS3101 and the PRESSS Design Handbook, except with the dissipative system EVD consisting of the EVD-ductility equation given by Priestley et al. [20] for yielding steel systems, where the ductility index is based on the effective stiffness bilinear idealisation. When using this EVD-damping recommendation on average the design estimates over predict the test drifts by only 4%. This method is recommended as it incorporates appropriate and robust values of ductility by using yield displacement based on the effective stiffness. Overall, this process has provided validation for the use of DDBD for the design of SRW and PreWEC systems.

10.3 RECOMMENDED RESEARCH

In Chapter 3 the O-connector tests focused on one size of O-connector, it is suggested that a larger matrix of lengths and thicknesses of O-connector are tested to eliminate any size effect. This could increase implementation of O-connectors into construction, as a design engineer would have access to the experimentally confirmed behaviour of a variety of O-connectors. This would also allow the design equations to be confirmed for larger scale O-connectors. Use of the O-connectors with a bolted connection detail instead of welded detail could also be investigated for even easier replacement following an earthquake.

Further research is required to fully understand and be able to isolate the source of the different components of the hysteretic behaviour of the PreWEC system. An investigation into the cause of the additional hysteresis required during the numerical modelling to complete the full hysteretic behaviour of the PreWEC system, would enable complete understanding of the cyclic static behaviour of the PreWEC system. From the test observations it appears that the additional hysteresis may be a result of the PT columns.

It is recommended that the single degree of freedom numerical modelling be extended into more advanced macro-element modelling to represent the system components directly. Such types of model are commonly used but have typically only been validated from pseudo-static test results. A fibre element model that is based purely on the uniaxial stress strain properties of the materials could be used and compared to the dynamic testing to validate the modelling procedure.

Multi-degree of freedom structures were outside the scope of this study but it is recommended that research focus on this area and the dynamic analysis of 3D buildings with investigation into all component interactions including out-of-plane loading on the wall systems. Further research is required for full-scale structures in situ, particularly for higher modes and at large response amplitudes. Additionally, forward directivity effects were not explicitly incorporated which is an area for future research.

In regards to DDBD, robust and rigorous equivalent viscous damping-ductility equations could be developed using extensive time history analysis for a realistic hysteretic behaviour of the PreWEC system using the updated method for ductility determination. There should also be further research focused on converting the area-based EVD into the NLTHA EVD as the current assessment of this procedure for PreWEC systems produced inaccurate results.

10.4 REFERENCES

20. Priestley, M.J.N., G.M. Calvi, and M.J. Kowalsky, *Displacement-based seismic design of structures*. 2007, Pavia: IUSS Press : Fondazione Eucentre. xvii, 721 p.
62. Aaleti, S. and S. Sritharan, *A simplified analysis method for characterizing unbonded post-tensioned precast wall systems*. *Engineering Structures*, 2009. **31**(12): p. 2966-2975.

Appendix A.

TEST SETUP AND CONSTRUCTION DETAILS

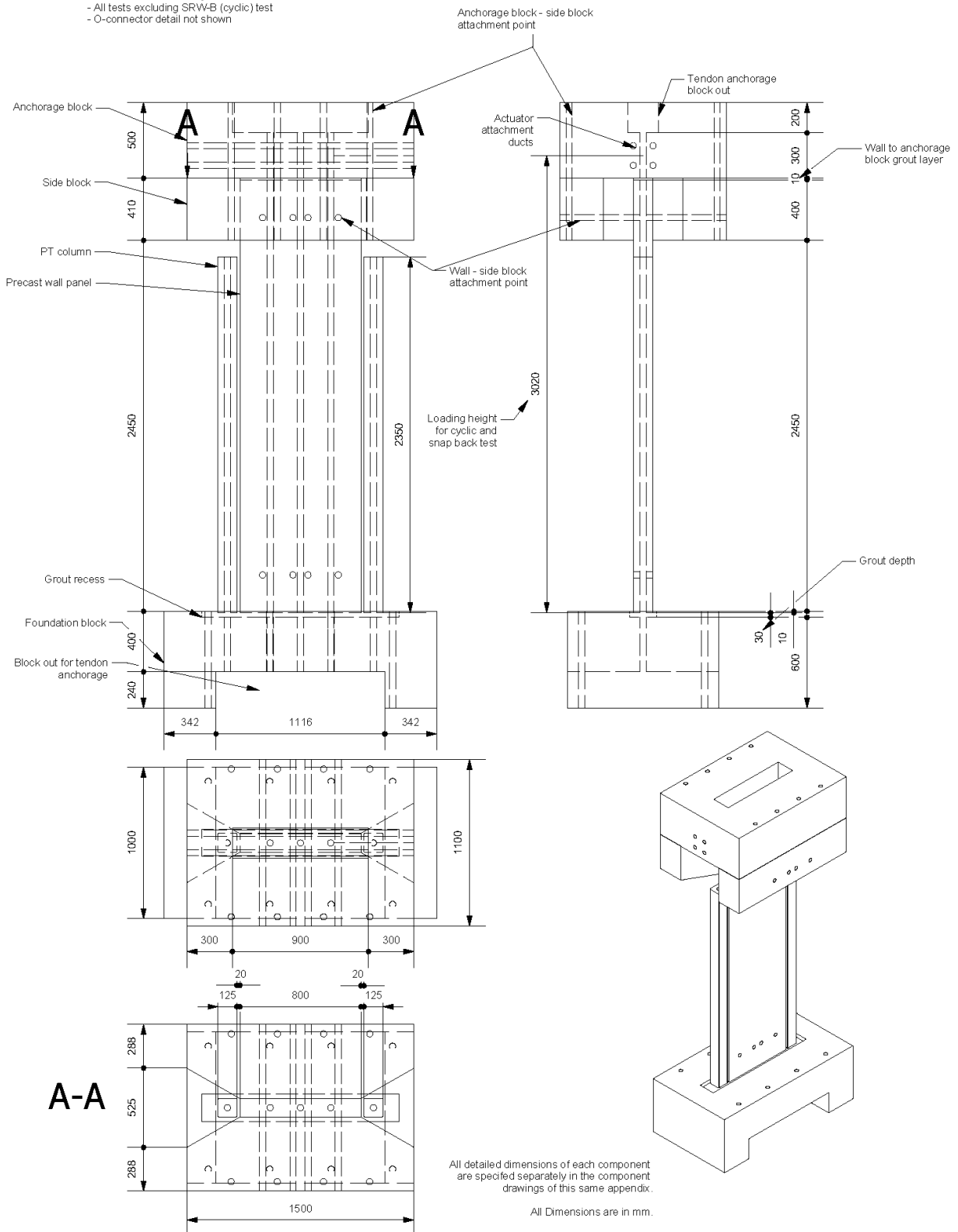
A.1 DETAILED DRAWINGS OF TEST UPS

Two test setups were employed during the pseudo-static cyclic tests reported in Chapter 5. The setups were similar overall but had slightly varied dimensions. The two test setups are referred to as Test Setup #1 and Test Setup #2. Test Setup #1 applied for testing of SRW-A, PreWEC-A, and B during the cyclic tests and all of the wall tests reported in Chapters 6 and 7. Test Setup #2 was only used for pseudo-static cyclic testing of SRW-B reported in Chapter 5. Detailed drawings are outlined for Test Setup #1, followed by Test Setup #2.

Appendix A Test setup and construction details

Overall setup for wall tests.

- All tests excluding SRV-B (cyclic) test
- O-connector detail not shown



All detailed dimensions of each component are specified separately in the component drawings of this same appendix.
All Dimensions are in mm.

Figure A.1 – Overall Test Setup #1 details

Overall setup SRW-B Cyclic Test only

- SRW-B (cyclic) test
- Additional mass of 794kg on top of anchorage block.

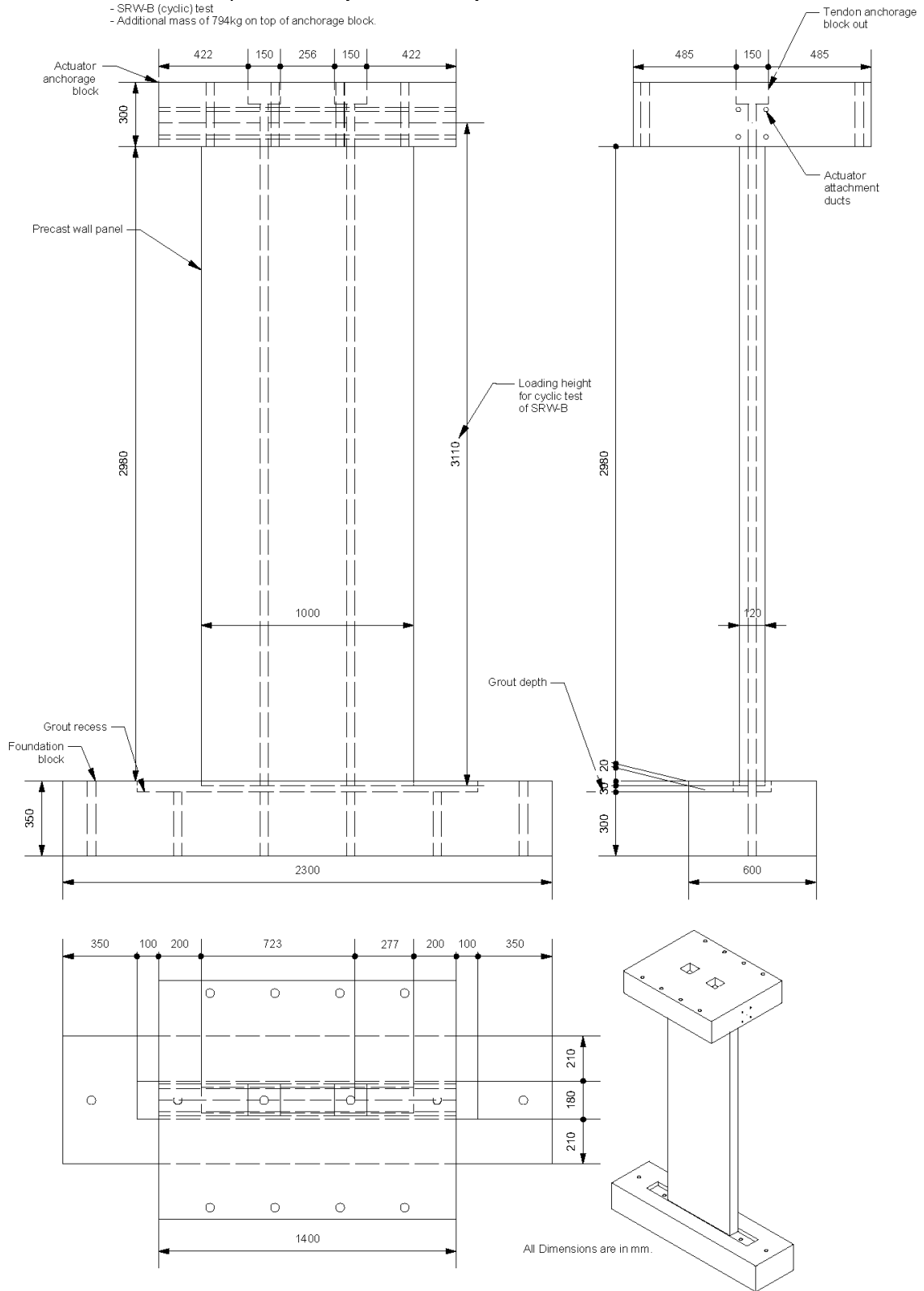


Figure A.2 – Overall Test Setup #2 details (SRW-B Cyclic only)

A.2 DETAILED CONSTRUCTION DRAWINGS OF WALL PANELS

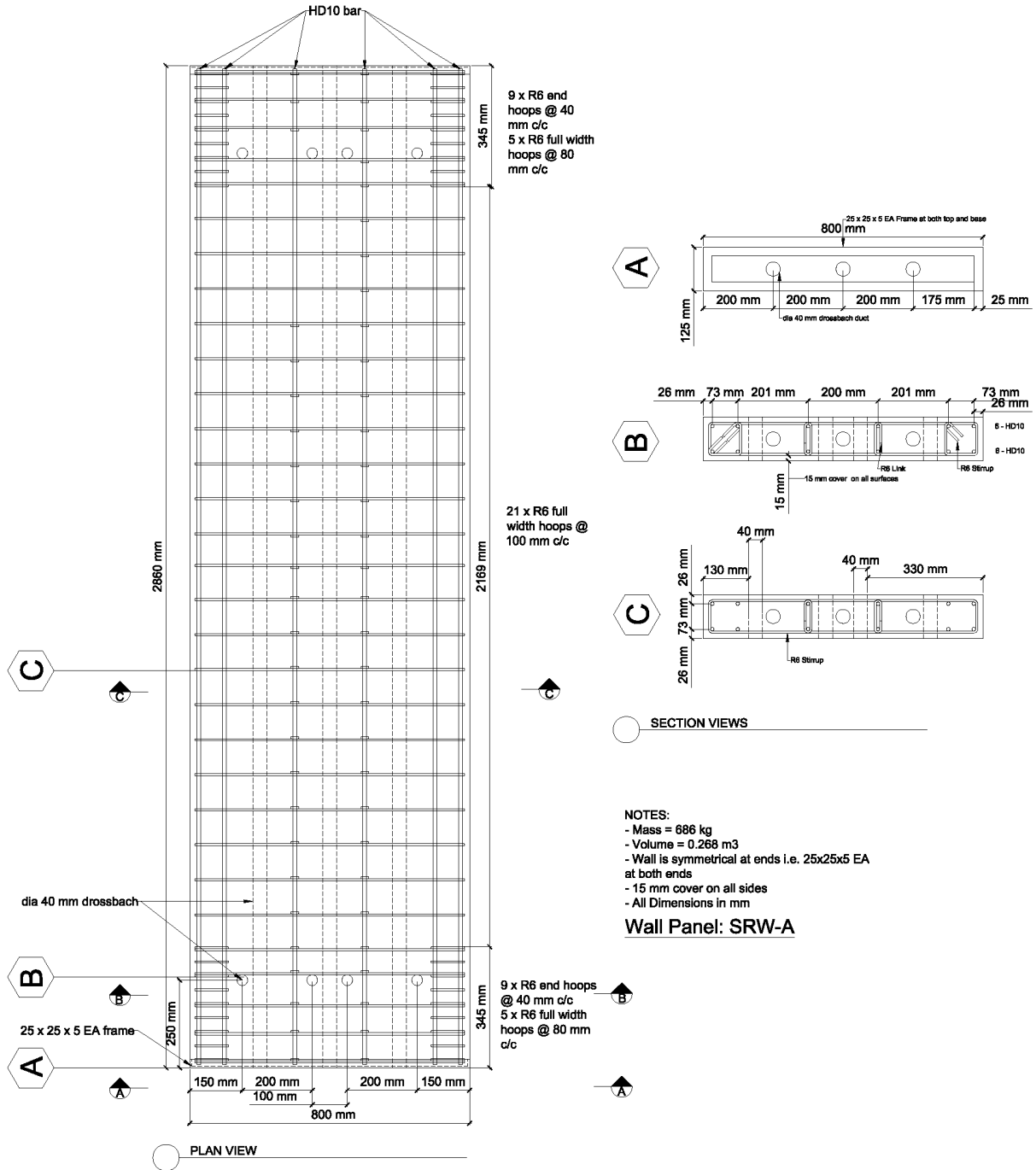


Figure A.3 –SRW-A Construction Details

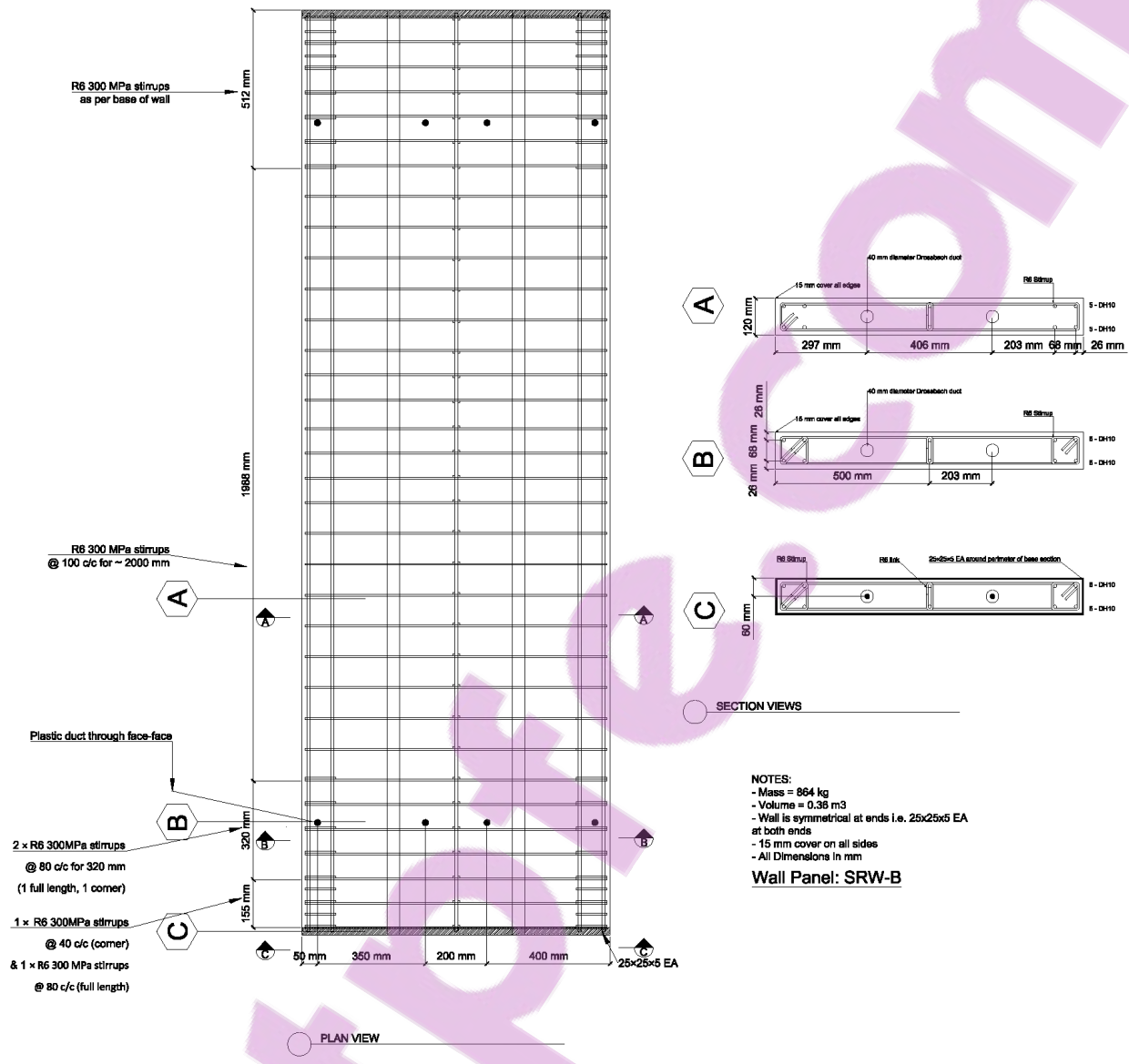


Figure A.4 –SRW-B Construction Details

Appendix A Test setup and construction details

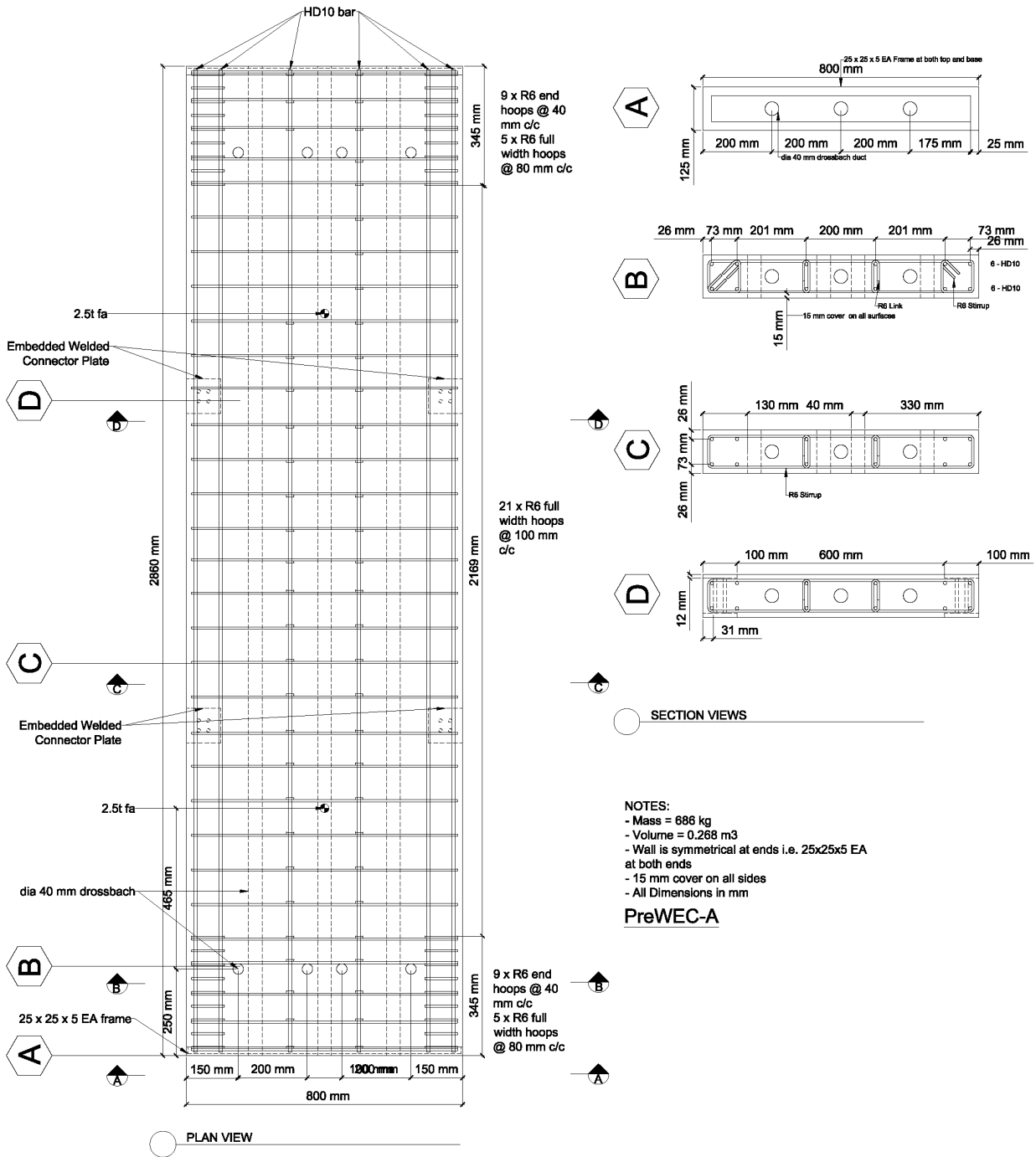


Figure A.5 –PreWEC-A Construction Details

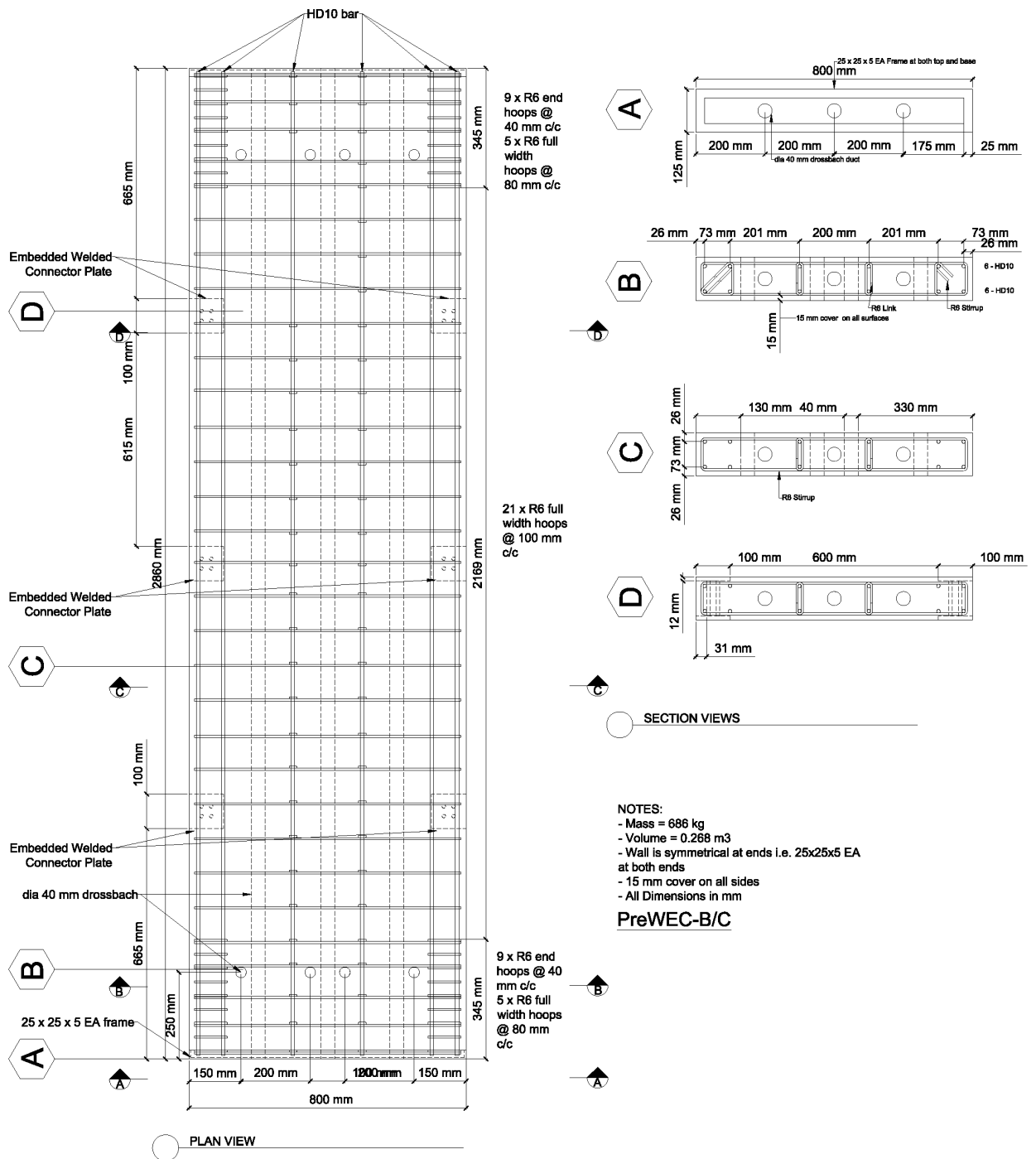


Figure A.6 –PreWEC-B/C Construction Details

A.3 DETAILED CONSTRUCTION DRAWINGS OF TEST SETUP #1 MASS BLOCKS AND FOUNDATION

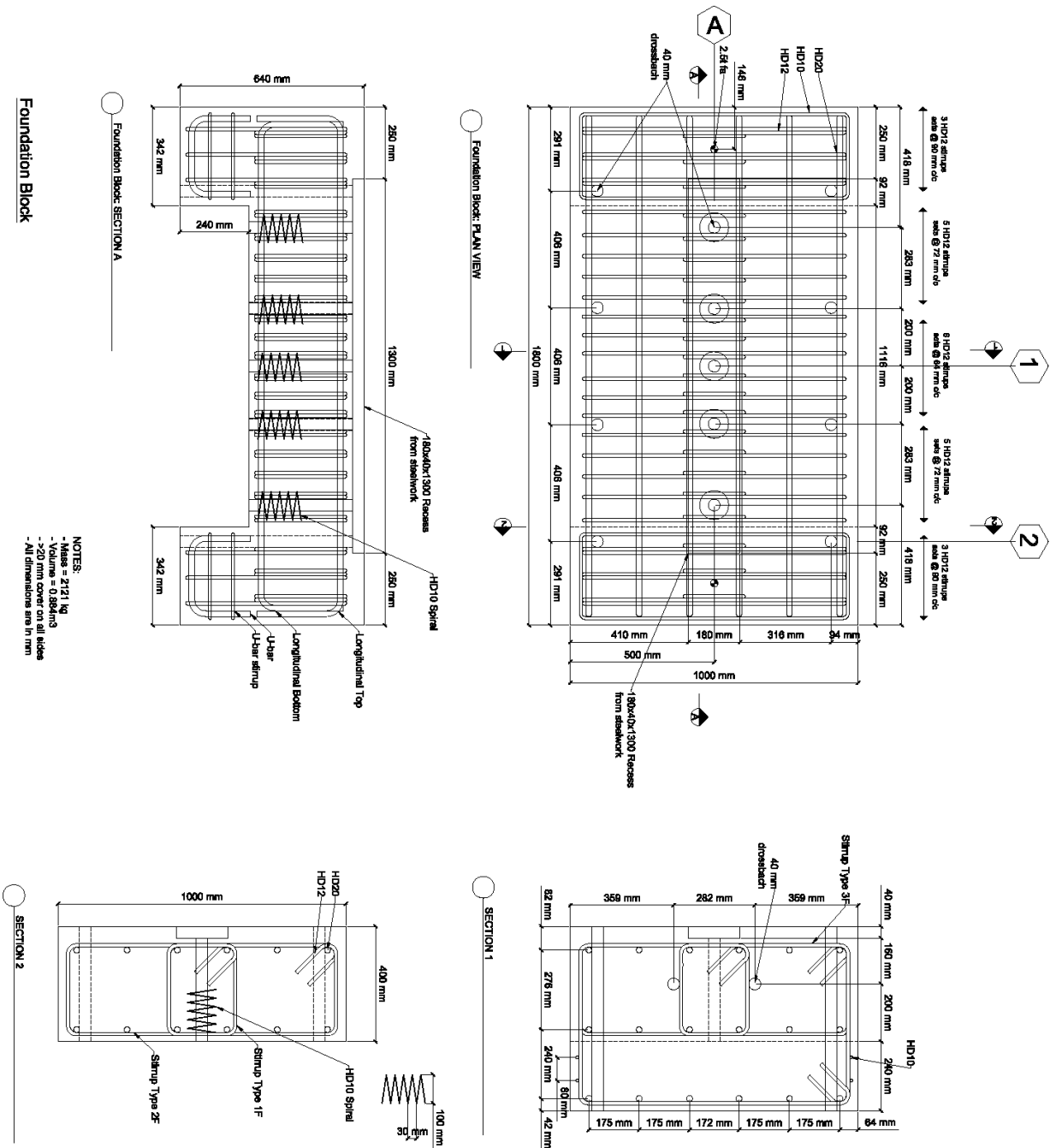


Figure A.7 –Foundation block

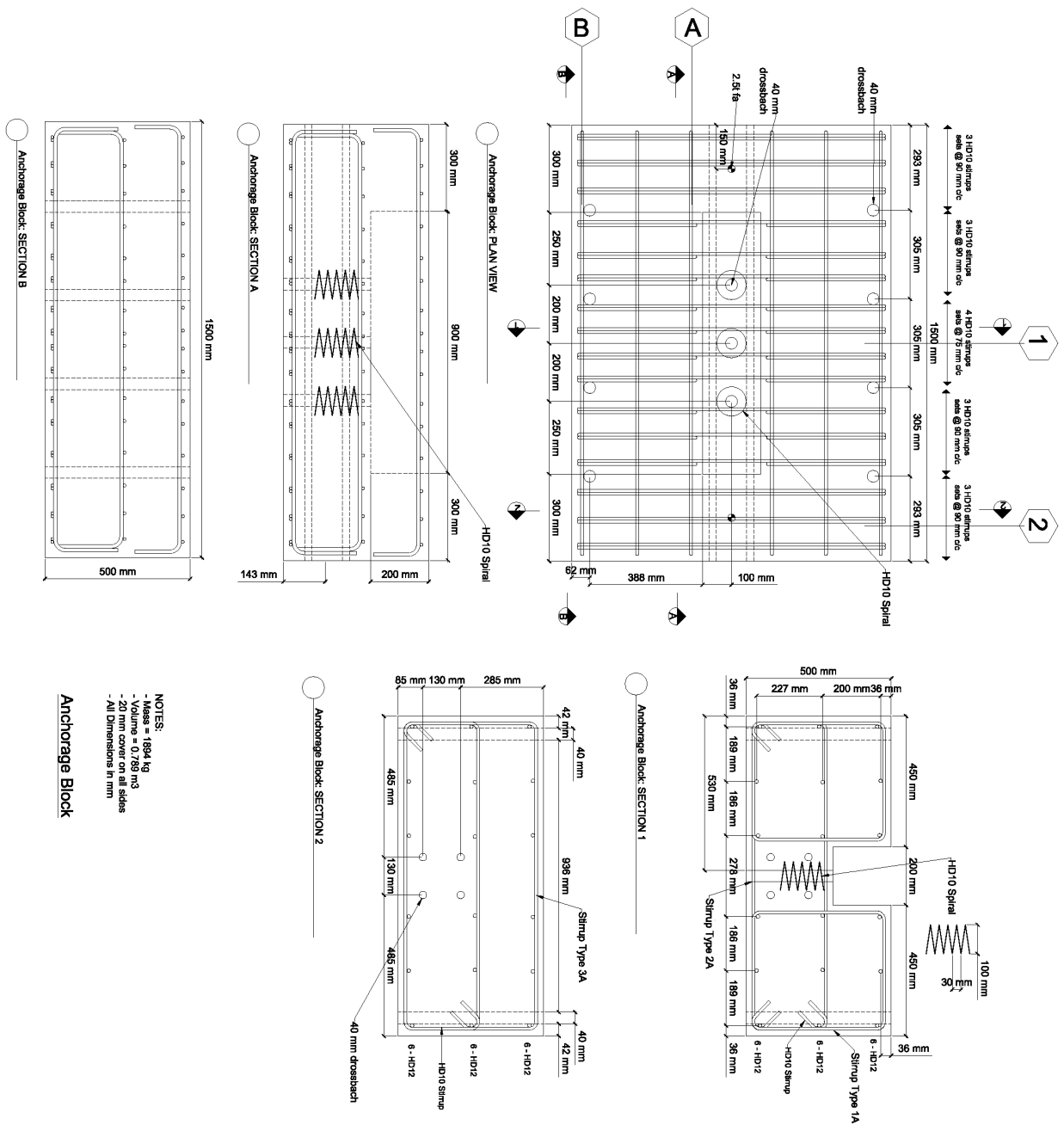


Figure A.8 – Anchorage block

Appendix B.

CONFINED CONCRETE DESIGN

As described in Chapter 4 the confinement reinforcement detail was designed for the wall toe using the confined concrete model described by Mander et al. [1] with the maximum expected compressive strain in the wall toe calculated using the simplified analysis method proposed by Aaleti and Sritharan [2].

The confinement calculations are laid out below for both wall panels:

B.2 SRW-A CONCRETE PANEL

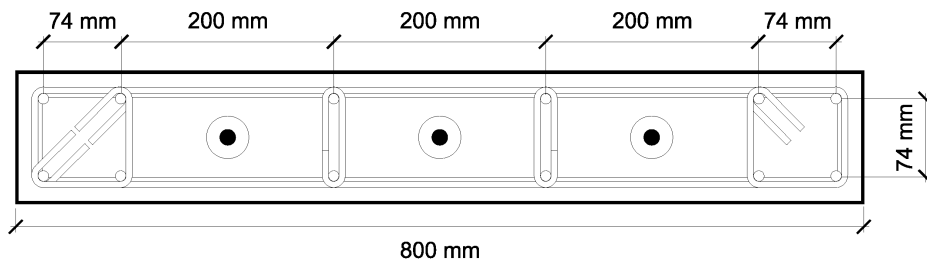


Figure B.1 – SRW-A cross section detail

Reinforcing steel:

- HD10 longitudinal bars (500 MPa)
- R6 stirrups or horizontal bars (300 MPa)

$$S = 40 \text{ mm}$$

$$S' = 40 - 6$$

$$= 34 \text{ mm}$$

$$A_c = 90 \times 90$$

$$= 8100 \text{ mm}^2$$

$$\rho_{cc} = \frac{A_s}{A_c} = \frac{4 \times \frac{10^2 \times \pi}{4}}{8100} = 0.003878$$

$$\sum_{i=1}^n \frac{(w_i')^2}{6b_c d_c} = \frac{3 \times 90^2}{6 \times 8100} = 0.5$$

$$k_e = \frac{(1 - 0.5)(1 - \frac{34}{2 \times 90})(1 - \frac{34}{2 \times 90})}{(1 - 0.003878)} = 0.329$$

$$A_{sx} = A_{sy} = 2 \times \frac{6^2 \times \pi}{4} = 56.55 \text{ mm}^2$$

$$\rho_x = \frac{A_{sx}}{s d_c} = \frac{56.55}{40 \times 90} = 0.01571$$

$$f'_{lx} = \rho_x f_{yh} k_e \text{ (if } f_{yh} = 300 \text{ MPa)} = 0.01571 \times 300 \times 0.329 = 1.55 \text{ MPa}$$

$$f'_{cc} = f'_{co}(-1.254 + 2.254 \sqrt{1 + \frac{7.94f'_l}{f'_{co}} - 2 \frac{f'_l}{f'_{co}}})$$

$$= 40(-1.254 + 2.254 \sqrt{1 + \frac{7.94 \times 1.55}{40} - \frac{2 \times 1.55}{40}}) = 49.84 \text{ MPa}$$

$$\varepsilon_{cc} = \varepsilon_{co} \left[1 + 5 \left(\frac{f'_{cc}}{f'_{co}} - 1 \right) \right] = 0.002 \left[1 + 5 \left(\frac{49.84}{40} - 1 \right) \right] = 0.00446$$

$$\rho_s = \rho_x + \rho_y = 0.01571 + 0.01571 = 0.03142$$

$$\varepsilon_{cu} = 0.004 + \frac{1.4\rho_s f_{yh} \varepsilon_{su}}{f'_{cc}} = 0.004 + \frac{1.4 \times 0.03142 \times 300 \times 0.15}{49.84} = 0.0437$$

From A&S:

$$\varepsilon_{conc} = c_\theta \left(\frac{M_{wall}}{E_c I_{gross}} + \frac{\theta}{0.06H_w} \right) = 0.0108$$

Max strain at 3% drift = 0.0155 << 0.0437 therefore OK

B.3 SRW-B CONCRETE PANEL

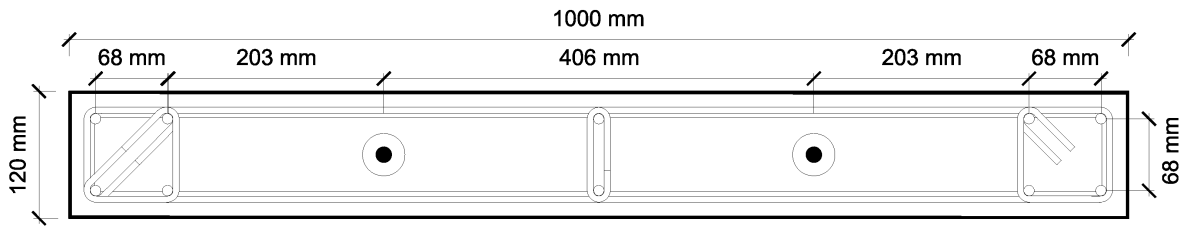


Figure B.2 – SRW-B cross section detail

Reinforcing steel:

- HD10 longitudinal bars (500 MPa)
- R6 stirrups or horizontal bars (300 MPa)

$$S = 40 \text{ mm}$$

$$S' = 40 - 6$$

$$= 34 \text{ mm}$$

$$A_c = 84 \times 84$$

$$= 7056 \text{ mm}^2$$

$$\rho_{cc} = \frac{A_s}{A_c} = \frac{4 \times \frac{10^2 \times \pi}{4}}{7056} = 0.04452$$

$$\sum_{i=1}^n \frac{(w_i')^2}{6b_c d_c} = \frac{3 \times 84^2}{6 \times 7056} = 0.5$$

$$k_e = \frac{(1 - 0.5)(1 - \frac{34}{2 \times 84})(1 - \frac{34}{2 \times 84})}{(1 - 0.04452)} = 0.33292$$

$$A_{sx} = A_{sy} = 2 \times \frac{6^2 \times \pi}{4} = 56.55 \text{ mm}^2$$

$$\rho_x = \frac{A_{sx}}{s d_c} = \frac{56.55}{40 \times 84} = 0.01683$$

$$f'_{lx} = \rho_x f_{yh} k_e \text{ (if } f_{yh} = 300 \text{ MPa)} = 0.01683 \times 300 \times 0.33292 = 1.6809 \text{ MPa}$$

$$f'_{cc} = f_{co}'(-1.254 + 2.254 \sqrt{1 + \frac{7.94f'_l}{f_{co}'} - 2 \frac{f'_l}{f_{co}'}})$$

$$= 40(-1.254 + 2.254 \sqrt{1 + \frac{7.94 \times 1.68}{40} - \frac{2 \times 1.68}{40}}) = 50.59 \text{ MPa}$$

$$\varepsilon_{cc} = \varepsilon_{co} \left[1 + 5 \left(\frac{f'_{cc}}{f_{co}'} - 1 \right) \right] = 0.002 \left[1 + 5 \left(\frac{50.59}{40} - 1 \right) \right] = 0.004648$$

$$\rho_s = \rho_x + \rho_y = 0.01683 + 0.01683 = 0.03366$$

$$\varepsilon_{cu} = 0.004 + \frac{1.4\rho_s f_{yh} \varepsilon_{su}}{f'_{cc}} = 0.004 + \frac{1.4 \times 0.03366 \times 300 \times 0.15}{50.59} = 0.0459$$

From A&S:

$$\varepsilon_{conc} = c_\theta \left(\frac{M_{wall}}{E_c I_{gross}} + \frac{\theta}{0.06H_w} \right) = 0.0108$$

Max strain at 3% drift = 0.0108 << 0.0459 therefore OK

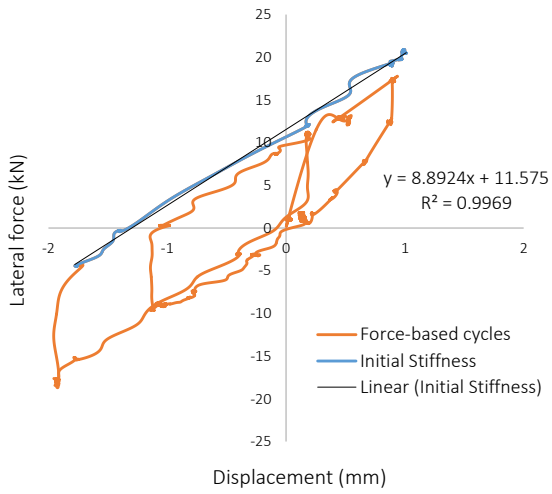
B.4 REFERENCES

1. Mander, J.B., M.J.N. Priestley, and R. Park, *Theoretical stress-strain model for confined concrete*. Journal of structural engineering New York, N.Y., 1988. **114**(8): p. 1804-1826.
2. Aaleti, S. and S. Sritharan, *A simplified analysis method for characterizing unbonded post-tensioned precast wall systems*. Engineering Structures, 2009. **31**(12): p. 2966-2975.

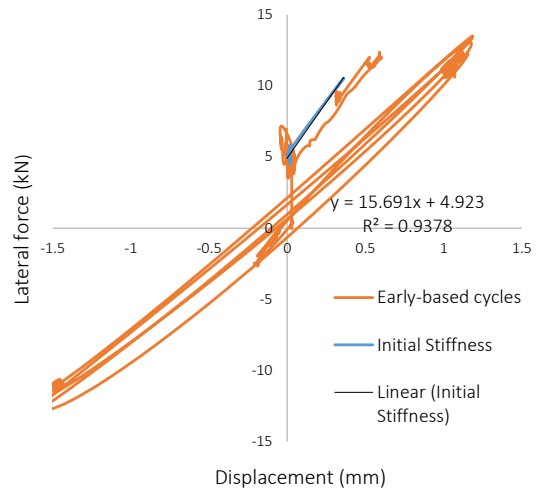
Appendix C.

MEASURED INITIAL STIFFNESS

The measured initial stiffness from the cyclic tests used the initial force based cycles. A best fit linear trend was used to find the slope of the force-displacement loading curve for the largest cycle below decompression of each wall system. The force based cycles and best fit linear equation of the last loading curve before decompression are shown in Figure B.1 for SRW-A and SRW-B. The measured initial stiffness for SRW-A was 8.89 kN/m and 16.36 kN/m for SRW-B. The force based cycles and best fit linear equation of the last loading curve before decompression are shown in Figure C.2 for PreWEC-A1 and A2. The measured initial stiffness for PreWEC-A1 was 12.9 kN/m and 6.34 kN/m for PreWEC-A2. The force based cycles and best fit linear equation of the last loading curve before decompression are shown in Figure C.3 for PreWEC-B, and the measured initial stiffness for PreWEC-B was 12.19 kN/m. For SRW-B the main initial cycles were greater than decompression and represent a soften wall state, however, at the start a small cycle was applied as show in Figure B.1(b) that provides an indication of the initial stiffness.

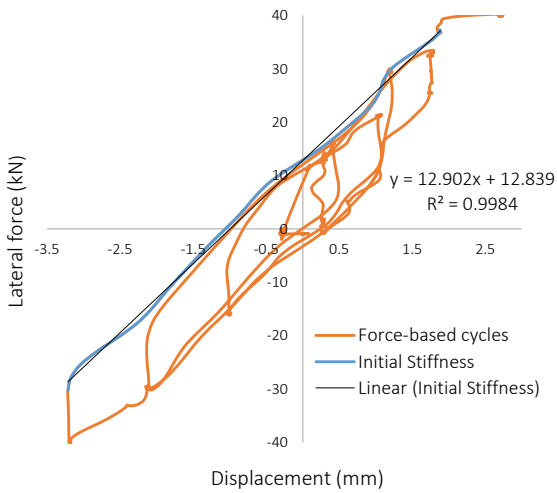


(a) SRW-A

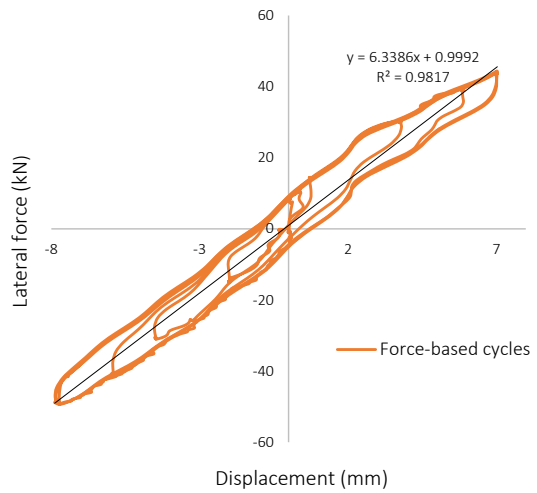


(b) SRW-B

Figure C.1 – SRW-A and B measured initial stiffness



(a) PreWEC-A1



(b) PreWEC-A2

Figure C.2 – PreWEC-A measured initial stiffness

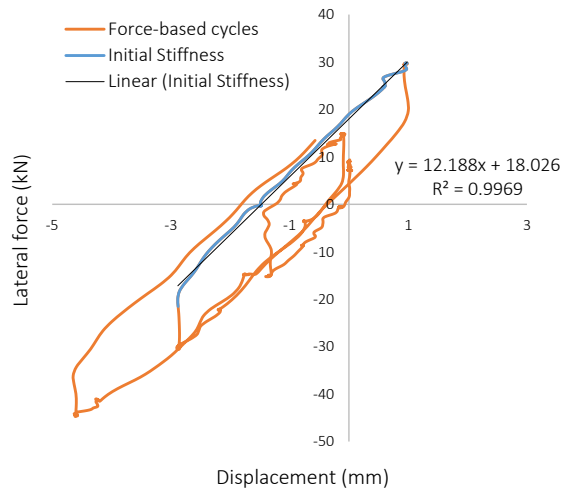


Figure C.3 – PreWEC-B measured initial stiffness

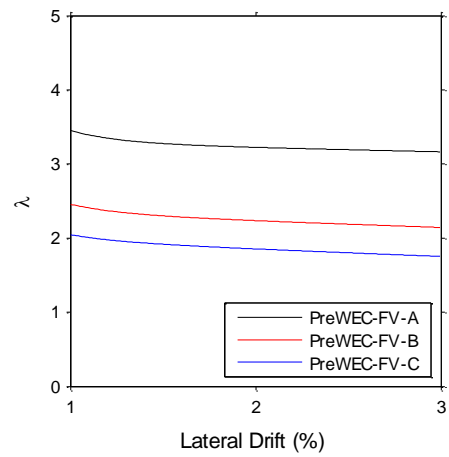
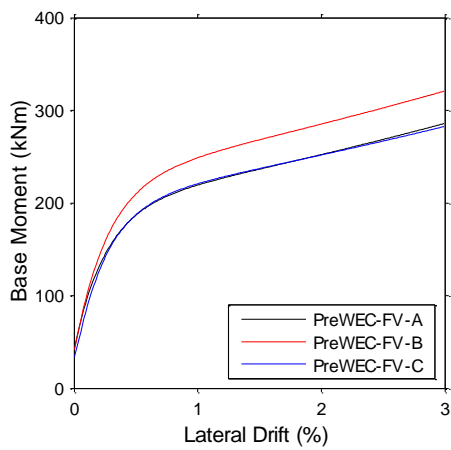
Appendix D.

ADDITIONAL SNAP BACK TEST RESULTS

Complete documentation of the results for each of the four snap back tests is included within this appendix. Observation photos are also included in this appendix for completeness despite no observable damage. The measured and derived results plotted include:

- Moment-lateral drift at the centre of mass.
- Unbonded tendon forces versus drift.
- NA depth and rotation versus centre of mass lateral displacement.
- O-connector vertical displacement versus centre of mass lateral displacement.
- Time histories of uplift, total PT tendon force, vertical connector displacement.

Additionally, presented in Figure D.1(a) is the theoretical moment-drift behaviour of the three PreWEC walls calculated using the analytical method proposed and validated by Aaleti and Sritharan [2]. Also using this analytical method the λ ratios stated in Chapter 6 were derived and the variation of λ with drift is shown in Figure D.1(b).



(c) Moment lateral drift behaviour

(d) λ values for each PreWEC wall

Figure D.1– PreWEC walls theoretical moment versus lateral drift and λ values

D.1 SRW-FV-A

D.1.1 Observation photos

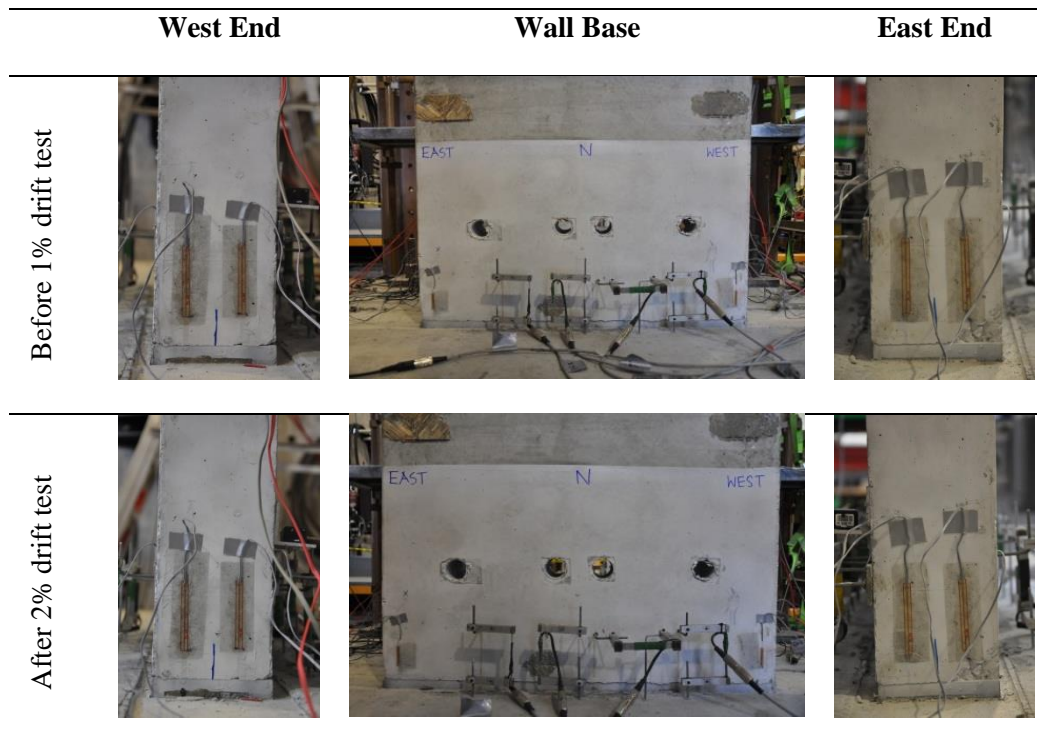
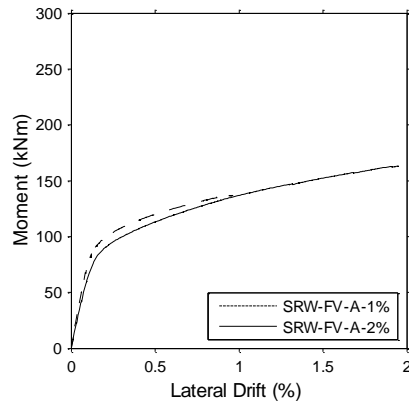
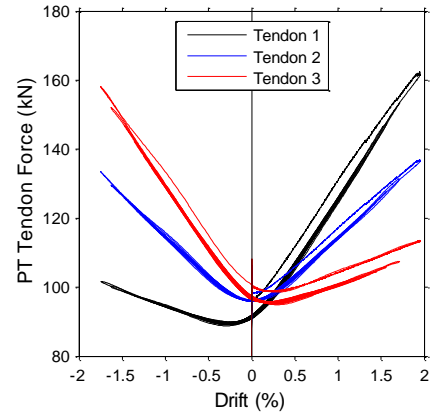


Figure D.2 – SRW-FV-A test before and after photos of wall

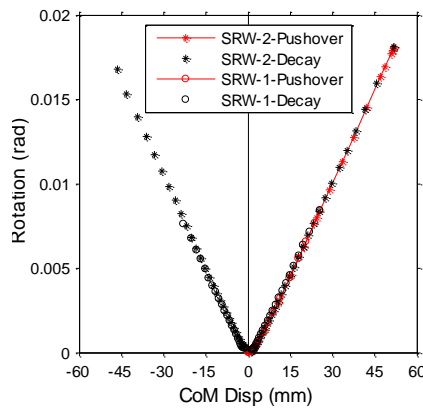
D.1.2 Additional measured and derived results



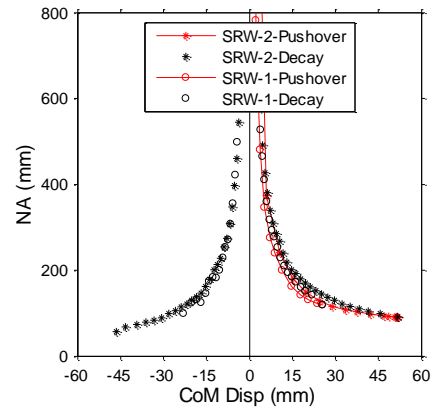
(e) Moment-lateral drift



(f) PT tendon forces



(g) Rotation-drift



(h) NA-lateral drift

Figure D.3 – SRW-FV-A detailed local parameters

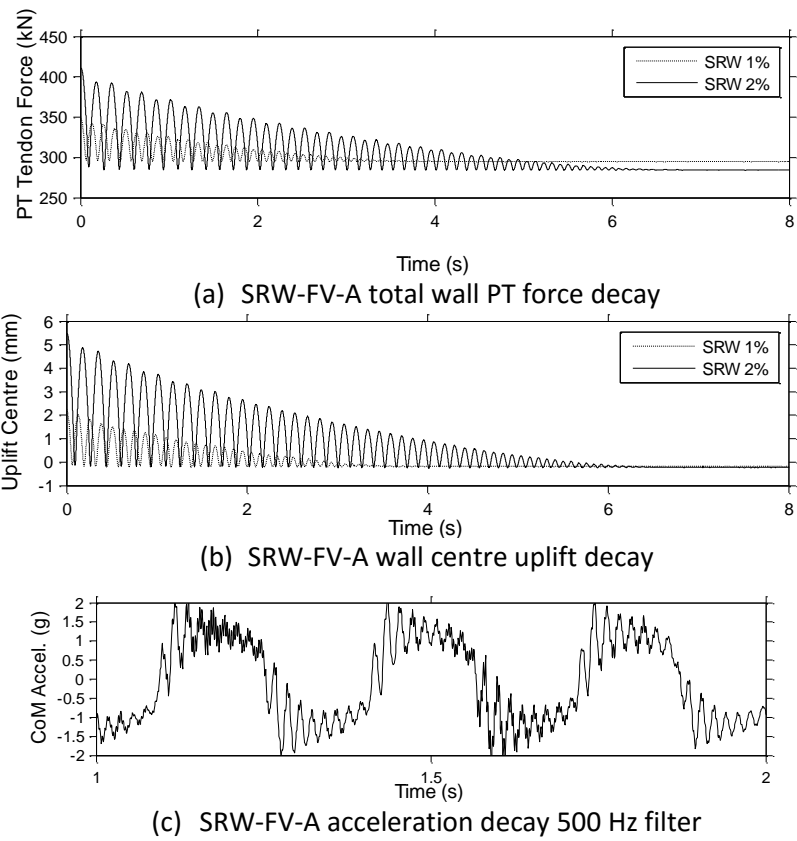


Figure D.4 – Additional time history results for SRW-FV-A

D.2 PREWEC-FV-A

D.2.1 Observation photos

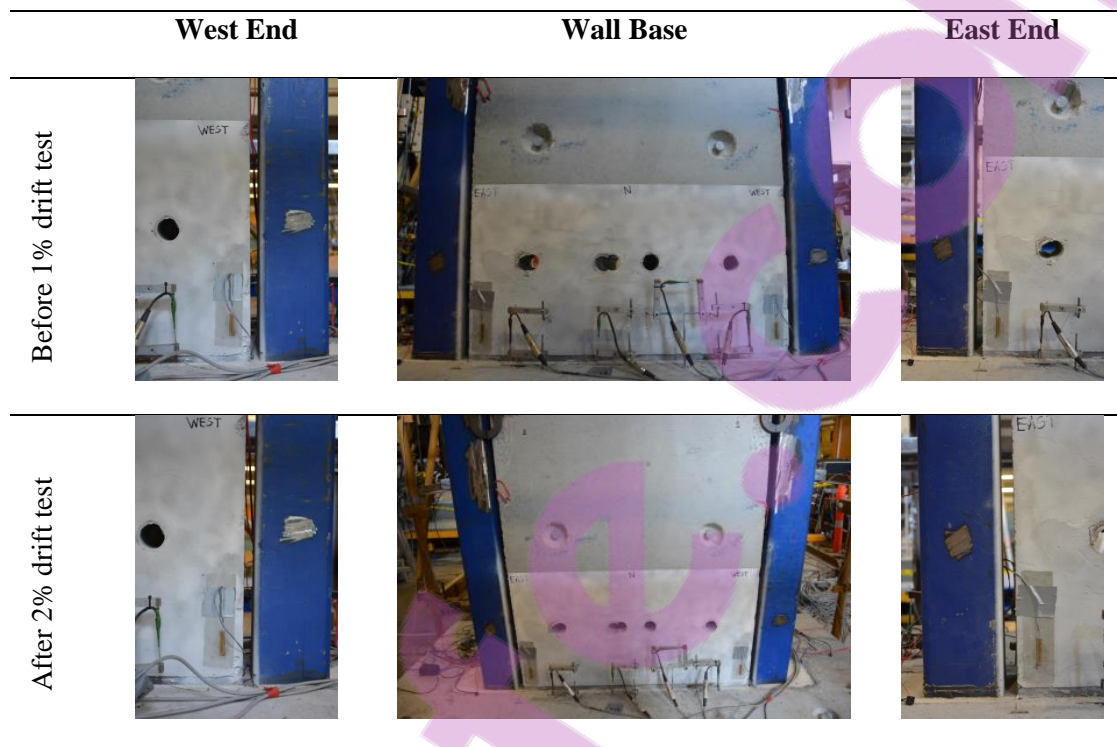
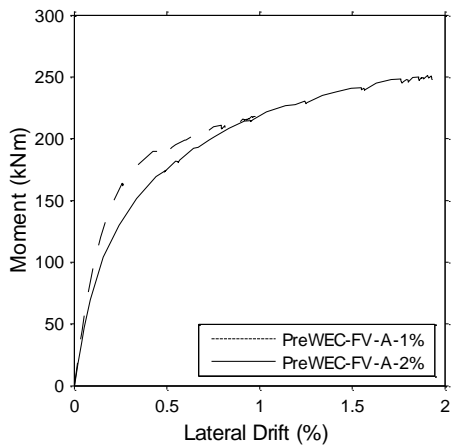


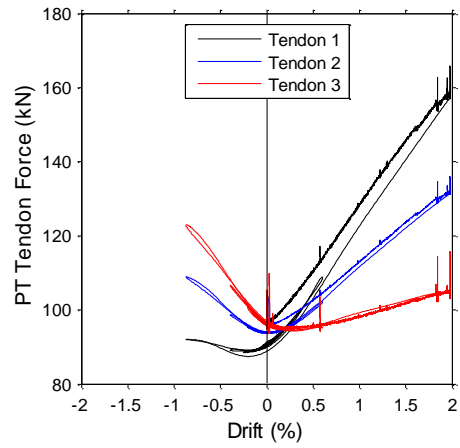
Figure D.5 – PreWEC-FV-A test before and after photos of wall



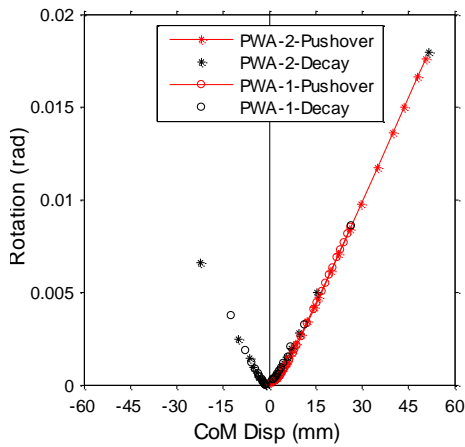
Figure D.6 – PreWEC-FV-A test before and after photos of O-connectors



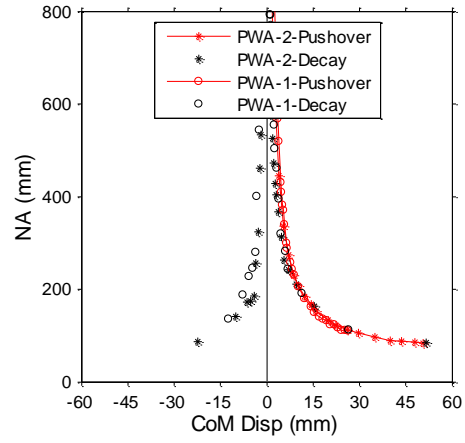
(a) Moment-lateral drift



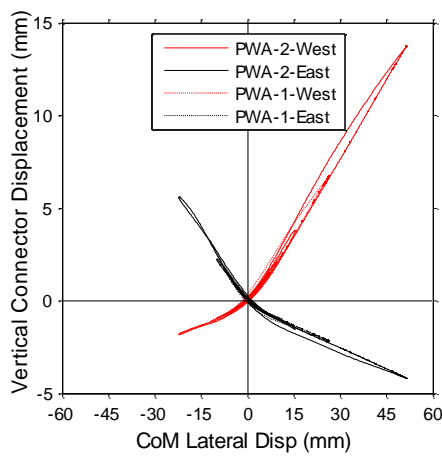
(b) PT tendon forces



(c) Rotation-drift

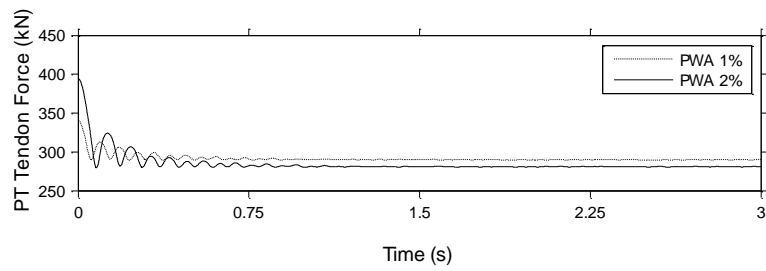


(d) NA-lateral drift

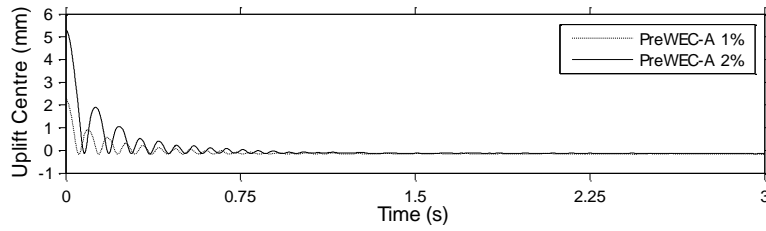


(e) Vertical connector displacement

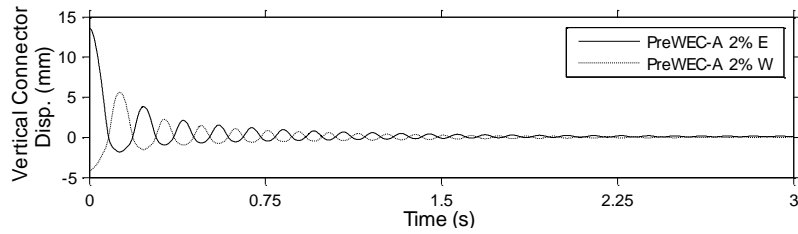
Figure D.7 – PreWEC-FV-A test detailed local parameters



(a) PreWEC-FV-A total wall PT force decay



(b) PreWEC-FV-A wall centre uplift decay



(c) PreWEC-FV-A vertical connector displacement for 2% drift test

Figure D.8 – General snap back test results for PreWEC-FV-A

D.3 PREWEC-FV-B

D.3.1 Observation photos

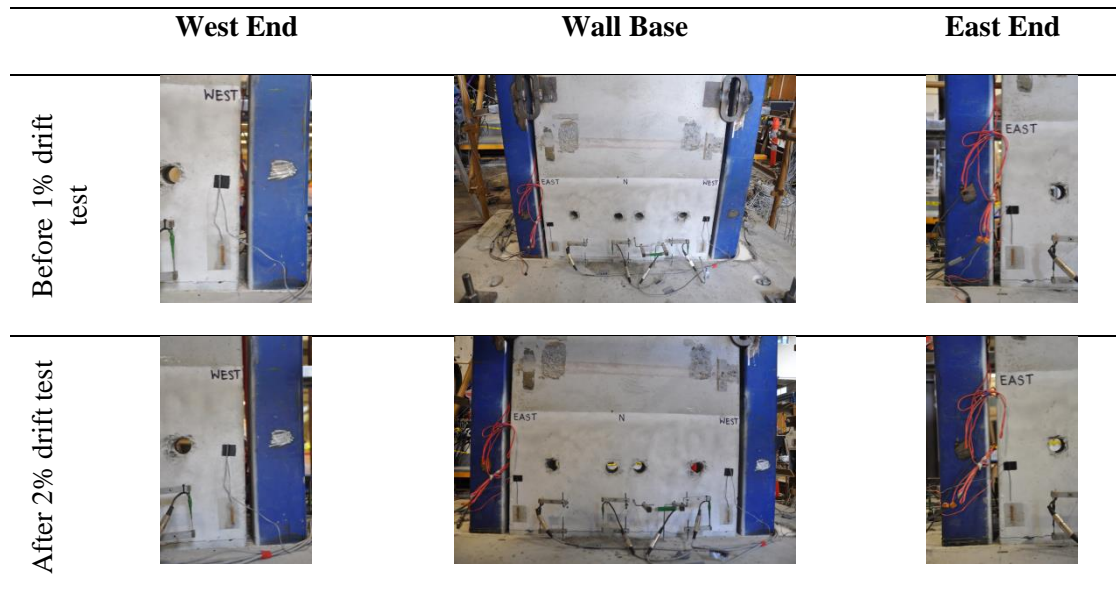


Figure D.9 – PreWEC-FV-B test before and after photos of wall

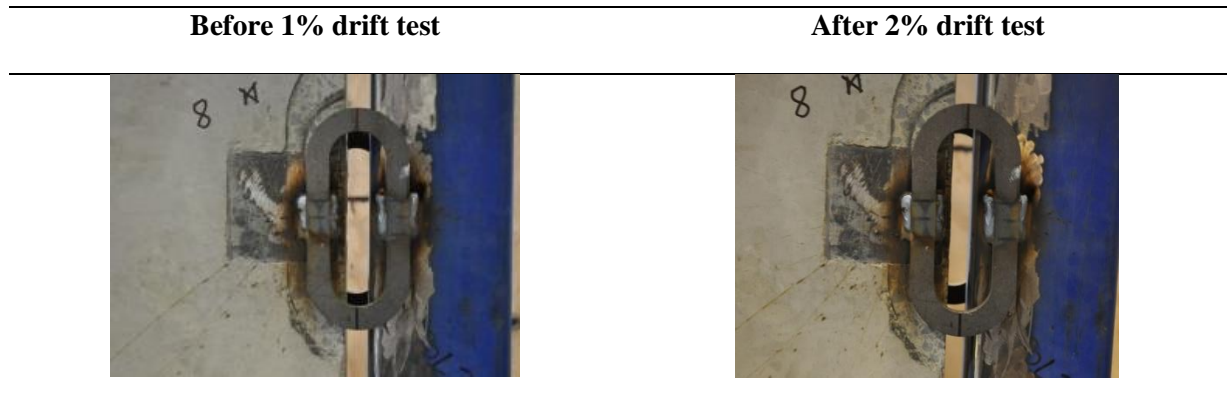
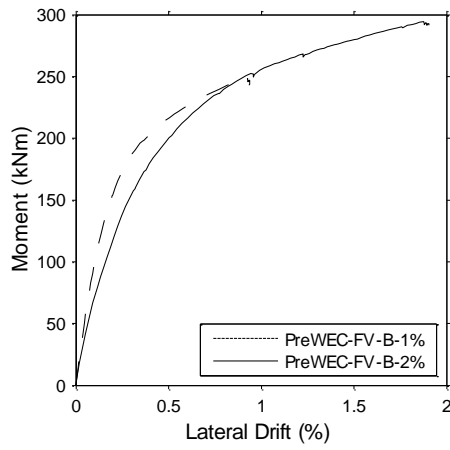
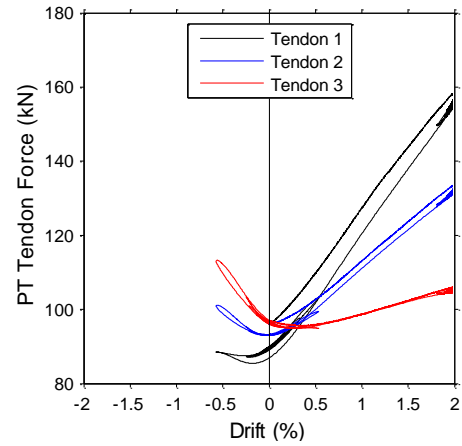


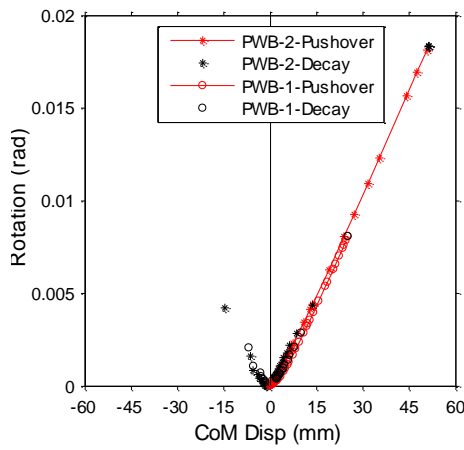
Figure D.10 – PreWEC-FV-B test before and after photos of O-connectors



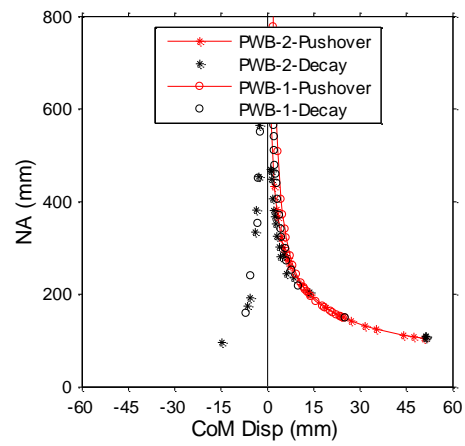
(a) Moment-lateral drift



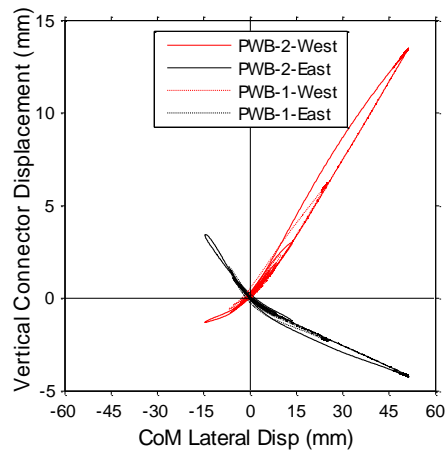
(b) PT tendon forces



(c) Rotation-drift

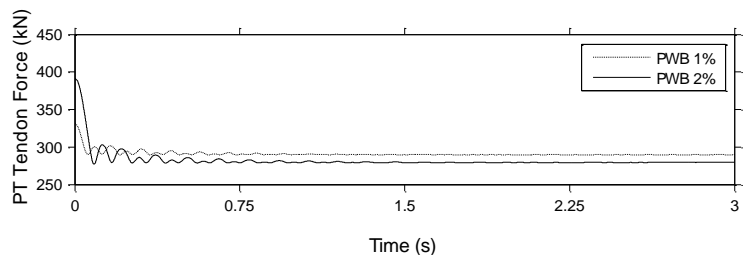


(d) NA-lateral drift

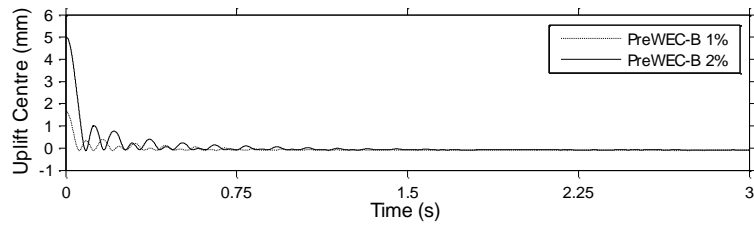


(e) Vertical connector displacement

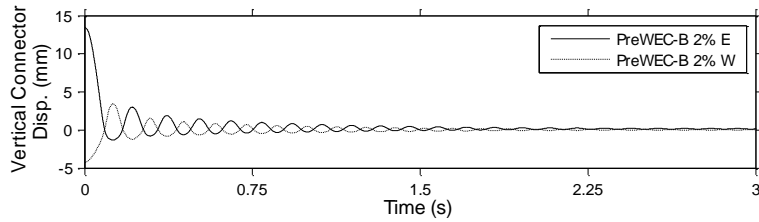
Figure D.11 – PreWEC-FV-B test detailed local parameters



(a) PreWEC-FV-B total wall PT force decay



(b) PreWEC-FV-B wall centre uplift decay



(c) PreWEC-FV-B vertical connector displacement for 2% drift test

Figure D.12 – General snap back test results for PreWEC-FV-B

D.4 PREWEC-FV-C

D.4.1 Observation photos

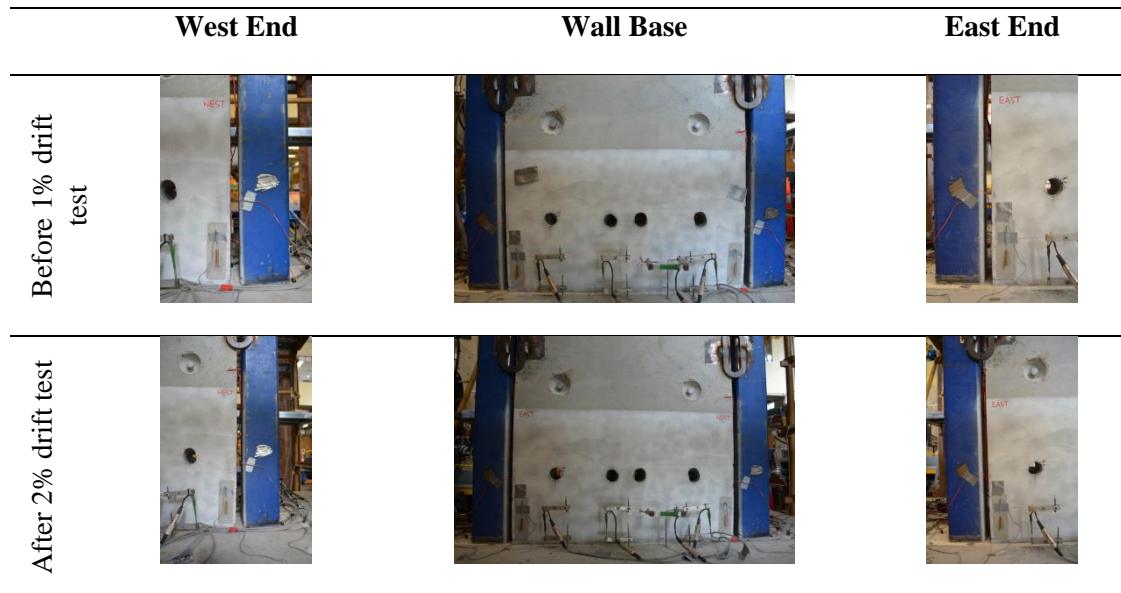


Figure D.13 – PreWEC-FV-C test before and after photos of wall

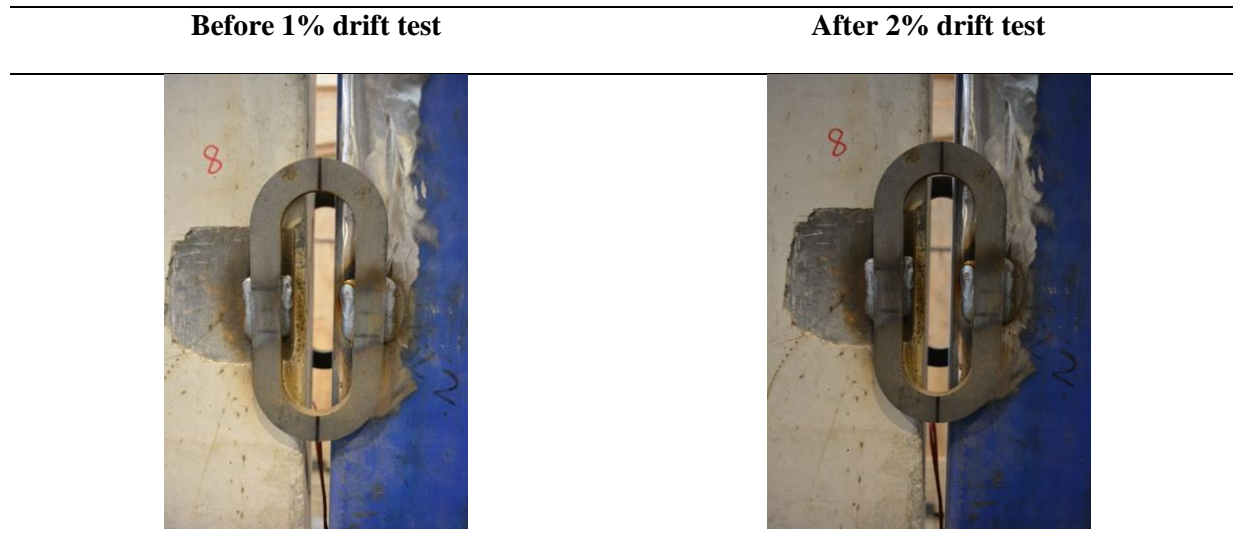
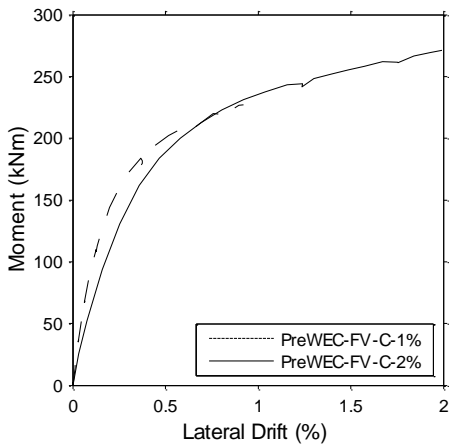
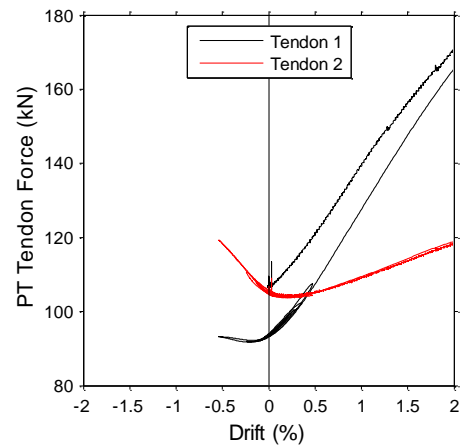


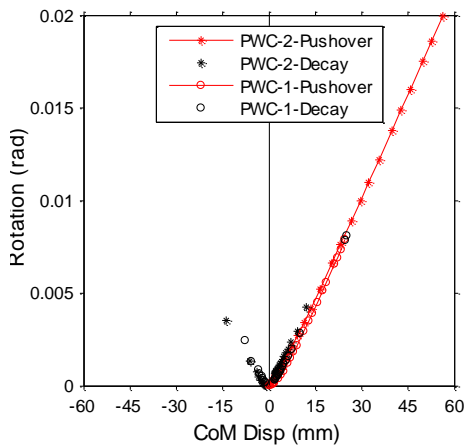
Figure D.14 – PreWEC-FV-C test before and after photos of O-connectors



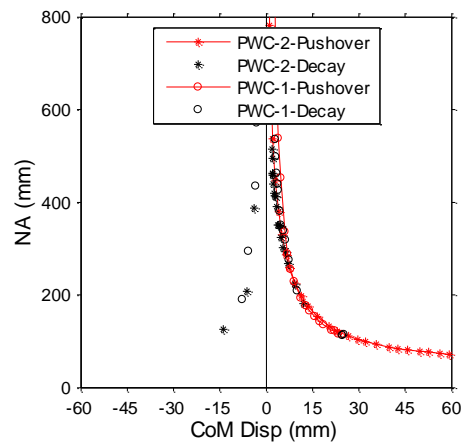
(a) Moment-lateral drift



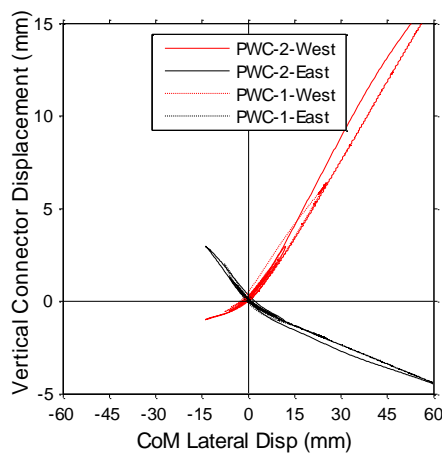
(b) PT tendon forces



(c) Rotation-drift

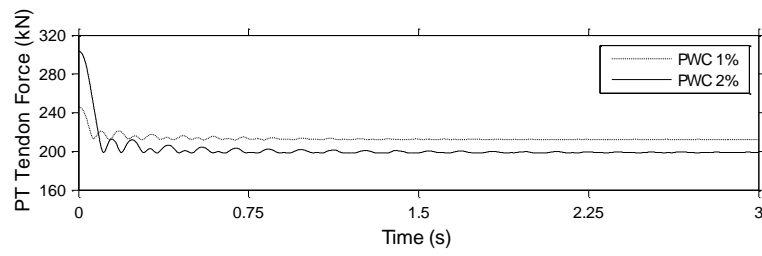


(d) NA-lateral drift

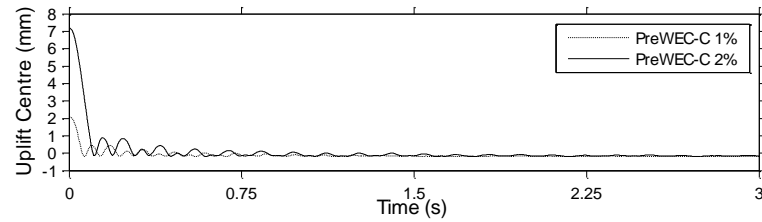


(e) Vertical connector displacement

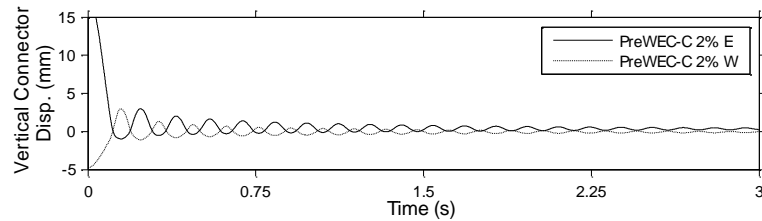
Figure D.15 – PreWEC-FV-C test detailed local parameters



(a) PreWEC-FV-C total wall PT force decay



(b) PreWEC-FV-C wall centre uplift decay



(c) PreWEC-FV-C vertical connector displacement for 2% drift test

Figure D.16 – General snap back test results for PreWEC-FV-C

D.5 REFERENCES

1. Aaleti, S. and S. Sritharan, *A simplified analysis method for characterizing unbonded post-tensioned precast wall systems*. Engineering Structures, 2009. **31**(12): p. 2966-2975.

Appendix E.

COMPLETE SHAKE TABLE TEST RESULTS

E.1 PSEUDO-ACCELERATION SPECTRUM OF RECORDED GROUND MOTIONS

Provided in Figure E.1-Figure E.3 are the pseudo-acceleration spectrum of the recorded ground motion for each intensity level and each wall.

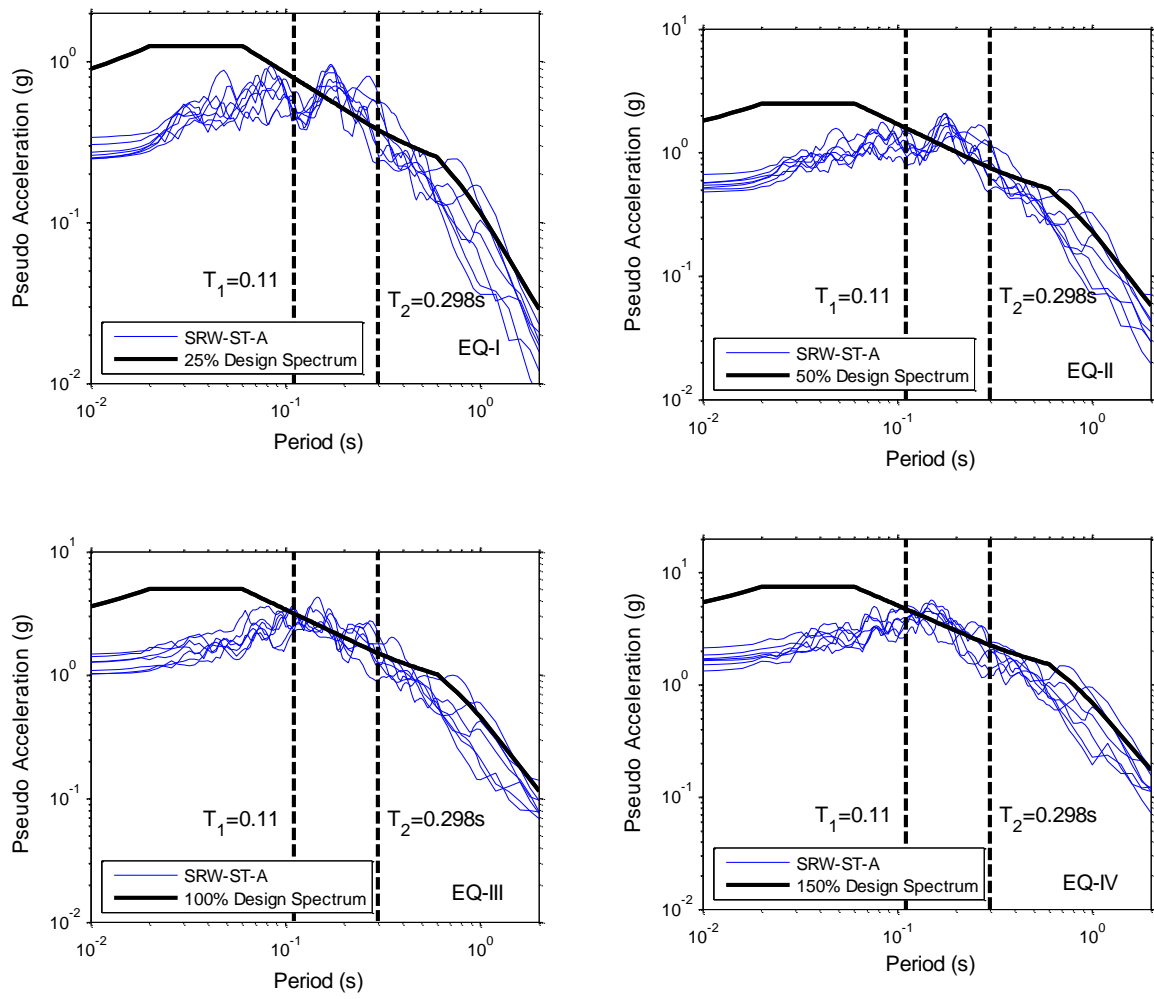


Figure E.1 – SRW-ST-A scaled pseudo acceleration for each intensity level

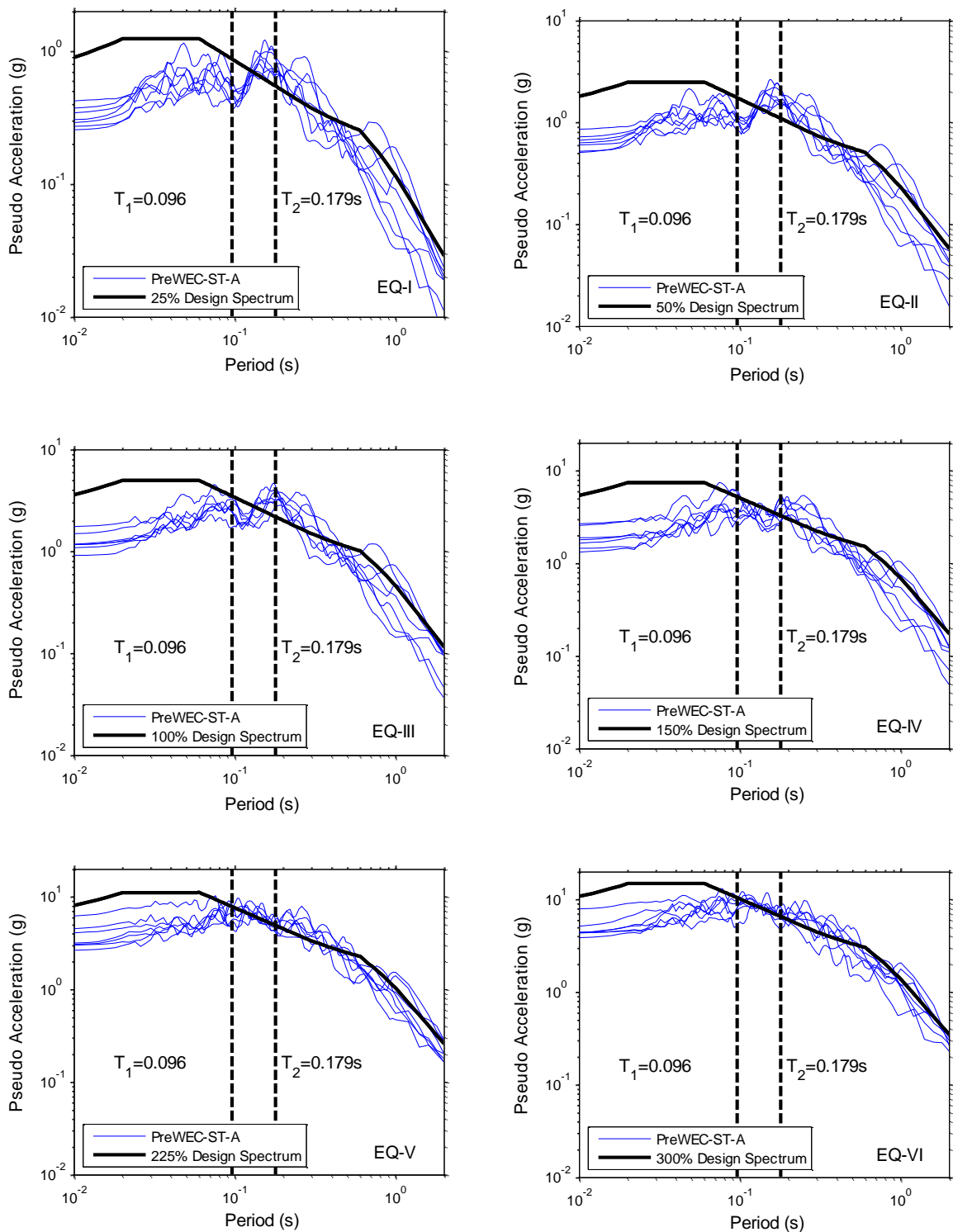


Figure E.2 – PreWEC-ST-A scaled pseudo acceleration for each intensity level

Appendix E Complete shake table test results

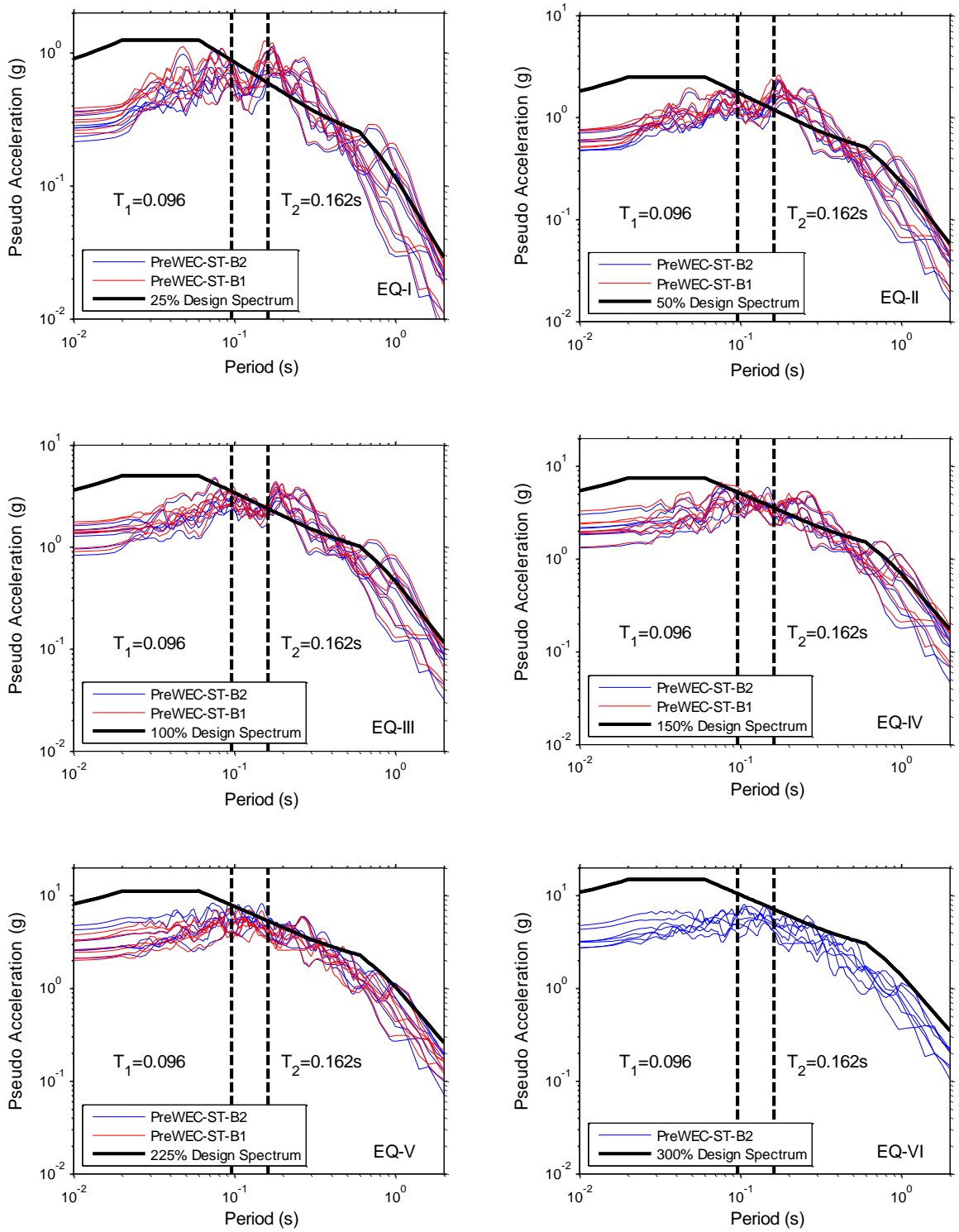


Figure E.3 – PreWEC-ST-B scaled pseudo acceleration for each intensity level

E.2 SHAKE TABLE PGA SUMMARY

Table E.1 - Peak ground acceleration for spectrum compatible GM on all walls

Intensity Level		EQ-I	EQ-II	EQ-III	EQ-IV	EQ-V	EQ-VI
SRW-ST-A	GM1	0.30	0.50	1.29	1.31	-	-
	GM2	0.28	0.56	1.31	1.67	-	-
	GM3	0.23	0.47	1.07	1.82	-	-
	GM4	0.24	0.44	0.93	1.42	-	-
	GM5	0.22	0.46	1.00	1.20	-	-
	GM6	0.24	0.50	1.13	1.63	-	-
	GM7	0.24	0.47	0.99	1.58	-	-
	<i>GM2-R1</i>	-	-	1.02	-	-	-
	<i>GM2-R2</i>	-	-	1.05	-	-	-
	<i>GM2-R3</i>	-	-	1.03	-	-	-
PreWEC-ST-A	GM1	0.32	0.56	1.05	1.29	2.00	2.11
	GM2	0.38	0.79	1.58	2.53	3.44	2.31
	GM3	0.25	0.56	1.22	2.13	2.50	1.62
	GM4	0.29	0.59	1.03	1.49	2.19	2.91
	GM5	0.26	0.52	1.06	1.45	2.19	2.83
	GM6	0.22	0.48	0.98	1.78	1.84	2.50
	GM7	0.27	0.57	1.14	1.13	1.87	2.17
PreWEC-ST-B (sequence B1 in italics)	GM1	0.26	0.52	0.85	1.72	2.20	2.20
		<i>0.31</i>	<i>0.55</i>	<i>1.00</i>	<i>1.69</i>	<i>2.18</i>	-
	GM2	0.31	0.64	1.44	1.88	3.55	3.29
		<i>0.35</i>	<i>0.70</i>	<i>1.58</i>	<i>2.29</i>	<i>2.52</i>	-
	GM3	0.24	0.51	1.22	2.48	3.43	2.20
		<i>0.24</i>	<i>0.56</i>	<i>1.32</i>	<i>2.64</i>	<i>2.81</i>	-
	GM4	0.27	0.56	1.15	1.80	2.54	3.22
		<i>0.28</i>	<i>0.58</i>	<i>1.22</i>	<i>1.89</i>	<i>2.62</i>	-
	GM5	0.28	0.57	1.19	1.66	2.29	2.93
		<i>0.28</i>	<i>0.59</i>	<i>1.20</i>	<i>1.81</i>	<i>2.30</i>	-
	GM6	0.23	0.46	1.30	1.73	2.43	2.58
		<i>0.25</i>	<i>0.52</i>	<i>1.35</i>	<i>1.85</i>	<i>1.98</i>	-
	GM7	0.21	0.41	0.77	1.25	1.98	2.39
	<i>0.25</i>	<i>0.49</i>	<i>0.86</i>	<i>1.25</i>	<i>1.80</i>	-	

E.3 SHAKE TABLE RESIDUAL DRIFT SUMMARY

Table E.2 – Residual displacement (mm) at centre of mass (CoM) for spectrum compatible GM on all walls (CoM=2657 mm)

Intensity Level		EQ-I	EQ-II	EQ-III	EQ-IV	EQ-V	EQ-VI
SRW-ST-A	GM1	0.06	0.11	0.06	0.50	-	-
	GM2	0.03	0.01	0.39	0.23	-	-
	GM3	0.10	0.08	0.03	0.16	-	-
	GM4	0.08	0.08	0.14	0.25	-	-
	GM5	0.01	0.01	0.03	0.10	-	-
	GM6	0.15	0.10	0.15	0.30	-	-
	GM7	0.05	0.01	0.11	0.15	-	-
	<i>GM2-R1</i>	-	-	0.03	-	-	-
	<i>GM2-R2</i>	-	-	0.01	-	-	-
	<i>GM2-R3</i>	-	-	0.05	-	-	-
PreWEC-ST-A	GM1	0.07	0.46	0.07	0.39	0.06	0.53
	GM2	0.28	0.20	0.28	0.51	0.36	0.50
	GM3	0.32	0.59	0.31	0.42	0.02	0.58
	GM4	0.38	0.18	0.81	0.90	0.71	0.44
	GM5	0.21	0.06	0.08	0.17	0.26	0.05
	GM6	0.47	0.55	0.53	0.12	0.16	0.52
	GM7	0.18	0.00	0.17	0.08	0.16	0.35
PreWEC-ST-B (sequence B1 in italics)	GM1	0.01	0.14	0.20	0.02	0.02	0.73
		<i>0.08</i>	<i>0.14</i>	<i>0.53</i>	<i>0.92</i>	<i>0.19</i>	-
	GM2	0.03	0.15	0.06	0.23	0.03	1.20
		<i>0.04</i>	<i>0.04</i>	<i>0.23</i>	<i>0.23</i>	<i>0.05</i>	-
	GM3	0.10	0.07	0.25	0.57	0.08	1.29
		<i>0.05</i>	<i>0.14</i>	<i>0.12</i>	<i>0.55</i>	<i>0.23</i>	-
	GM4	0.07	0.07	0.20	0.50	0.30	0.54
		<i>0.01</i>	<i>0.01</i>	<i>0.01</i>	<i>0.13</i>	<i>0.21</i>	-
	GM5	0.02	0.03	0.08	0.11	0.28	0.32
		<i>0.13</i>	<i>0.13</i>	<i>0.39</i>	<i>0.30</i>	<i>0.67</i>	-
	GM6	0.12	0.15	0.28	0.50	0.10	0.01
		<i>0.06</i>	<i>0.16</i>	<i>0.05</i>	<i>0.10</i>	<i>0.99</i>	-
	GM7	0.01	0.02	0.04	0.15	0.88	0.34
	<i>0.10</i>	<i>0.30</i>	<i>0.56</i>	<i>0.05</i>	<i>0.86</i>	-	

Table E.3 – Residual drift for spectrum compatible GM on all walls

Hazard Level	EQ-I	EQ-II	EQ-III	EQ-IV	EQ-V	EQ-VI	
SRW-ST-A	GM1	0.00	0.00	0.00	0.02	-	-
	GM2	0.00	0.00	0.01	0.01	-	-
	GM3	0.00	0.00	0.00	0.01	-	-
	GM4	0.00	0.00	0.01	0.01	-	-
	GM5	0.00	0.00	0.00	0.00	-	-
	GM6	0.01	0.00	0.01	0.01	-	-
	GM7	0.00	0.00	0.00	0.01	-	-
	<i>GM2-R1</i>	-	-	0.00	-	-	-
	<i>GM2-R2</i>	-	-	0.00	-	-	-
<i>GM2-R3</i>	-	-	0.00	-	-	-	
PreWEC-ST-A	GM1	0.00	0.02	0.00	0.01	0.00	0.02
	GM2	0.01	0.01	0.01	0.02	0.01	0.02
	GM3	0.01	0.02	0.01	0.02	0.00	0.02
	GM4	0.01	0.01	0.03	0.03	0.03	0.02
	GM5	0.01	0.00	0.00	0.01	0.01	0.00
	GM6	0.02	0.02	0.02	0.00	0.01	0.02
	GM7	0.01	0.00	0.01	0.00	0.01	0.01
PreWEC-ST-B (sequence B1 in italics)	GM1	0.00	0.01	0.01	0.00	0.00	0.03
		<i>0.00</i>	<i>0.01</i>	<i>0.02</i>	<i>0.03</i>	<i>0.01</i>	-
	GM2	0.00	0.01	0.00	0.01	0.00	0.05
		<i>0.00</i>	<i>0.00</i>	<i>0.01</i>	<i>0.01</i>	<i>0.00</i>	-
	GM3	0.00	0.00	0.01	0.02	0.00	0.05
		<i>0.00</i>	<i>0.01</i>	<i>0.00</i>	<i>0.02</i>	<i>0.01</i>	-
	GM4	0.00	0.00	0.01	0.02	0.01	0.02
		<i>0.00</i>	<i>0.00</i>	<i>0.00</i>	<i>0.00</i>	<i>0.01</i>	-
	GM5	0.00	0.00	0.00	0.00	0.01	0.01
		<i>0.00</i>	<i>0.01</i>	<i>0.01</i>	<i>0.01</i>	<i>0.03</i>	-
	GM6	0.00	0.01	0.01	0.02	0.00	0.00
		<i>0.00</i>	<i>0.01</i>	<i>0.00</i>	<i>0.00</i>	<i>0.04</i>	-
	GM7	0.00	0.00	0.00	0.01	0.03	0.01
	<i>0.00</i>	<i>0.01</i>	<i>0.02</i>	<i>0.00</i>	<i>0.03</i>	-	

E.4 SHAKE TABLE ADJUSTED RETURN PERIOD FACTOR

Table E.4 – Calculated adjusted return period factors

<i>Hazard Level</i>	<i>Original R</i>	<i>SRW-A</i>	<i>PreWEC-A</i>	<i>PreWEC-B1</i>	<i>PreWEC-B2</i>	
EQ-I	GM1	0.25	0.16	0.17	0.20	0.22
	GM2	0.25	0.19	0.15	0.22	0.22
	GM3	0.25	0.16	0.15	0.24	0.16
	GM4	0.25	0.17	0.16	0.23	0.18
	GM5	0.25	0.15	0.16	0.18	0.21
	GM6	0.25	0.17	0.14	0.20	0.19
	GM7	0.25	0.15	0.13	0.22	0.14
EQ-II	GM1	0.5	0.40	0.41	0.43	0.43
	GM2	0.5	0.47	0.35	0.44	0.51
	GM3	0.5	0.37	0.33	0.45	0.38
	GM4	0.5	0.39	0.40	0.41	0.39
	GM5	0.5	0.37	0.36	0.37	0.44
	GM6	0.5	0.38	0.33	0.46	0.40
	GM7	0.5	0.38	0.31	0.46	0.34
EQ-III	GM1	1	1.07	1.00	0.97	0.79
	GM2	1	1.14	0.83	0.88	0.85
	GM3	1	0.91	0.65	0.96	0.84
	GM4	1	0.88	0.80	0.89	0.84
	GM5	1	1.11	0.79	0.73	0.91
	GM6	1	0.95	0.76	0.78	0.84
	GM7	1	0.97	0.69	0.71	0.69
EQ-IV	GM1	1.5	1.59	1.21	1.20	1.50
	GM2	1.5	1.51	1.34	0.93	1.39
	GM3	1.5	1.24	1.14	1.14	1.37
	GM4	1.5	1.40	1.28	1.19	1.26
	GM5	1.5	1.58	1.38	1.07	1.34
	GM6	1.5	1.71	1.33	1.34	1.35
	GM7	1.5	1.45	1.00	1.09	1.10
EQ-V	GM1	2.25		1.68	1.54	1.98
	GM2	2.25		1.75	1.39	1.85
	GM3	2.25		1.55	1.58	1.91
	GM4	2.25		1.49	1.22	1.63
	GM5	2.25		1.61	1.51	1.79
	GM6	2.25		1.57	1.57	2.03
	GM7	2.25		1.46	1.41	1.70
EQ-VI	GM1	3		1.80		1.60
	GM2	3		1.75		1.68
	GM3	3		1.26		1.61
	GM4	3		1.35		1.40
	GM5	3		1.92		1.92
	GM6	3		1.75		2.06
	GM7	3		1.84		1.99

E.6 SHAKE TABLE COMPLETE RECORDED TIME HISTORY RESULTS

The following figures present the recorded ground acceleration, centre of mass acceleration, and centre of mass drift of each wall during each ground motion.

E.6.1 SRW-ST-A

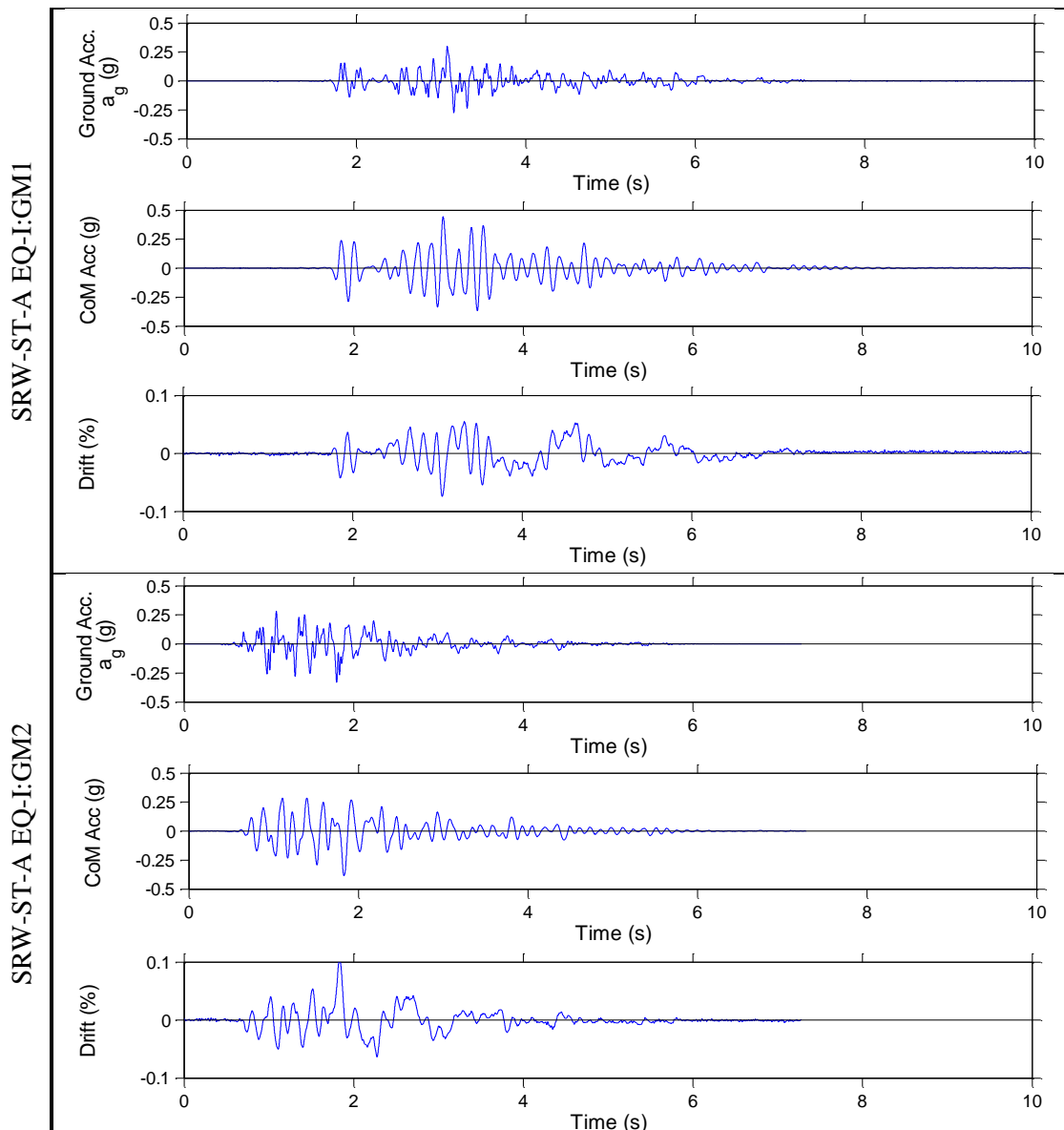


Figure E.4 – Shake table results for SRW-ST-A, EQ-I: GM1-2

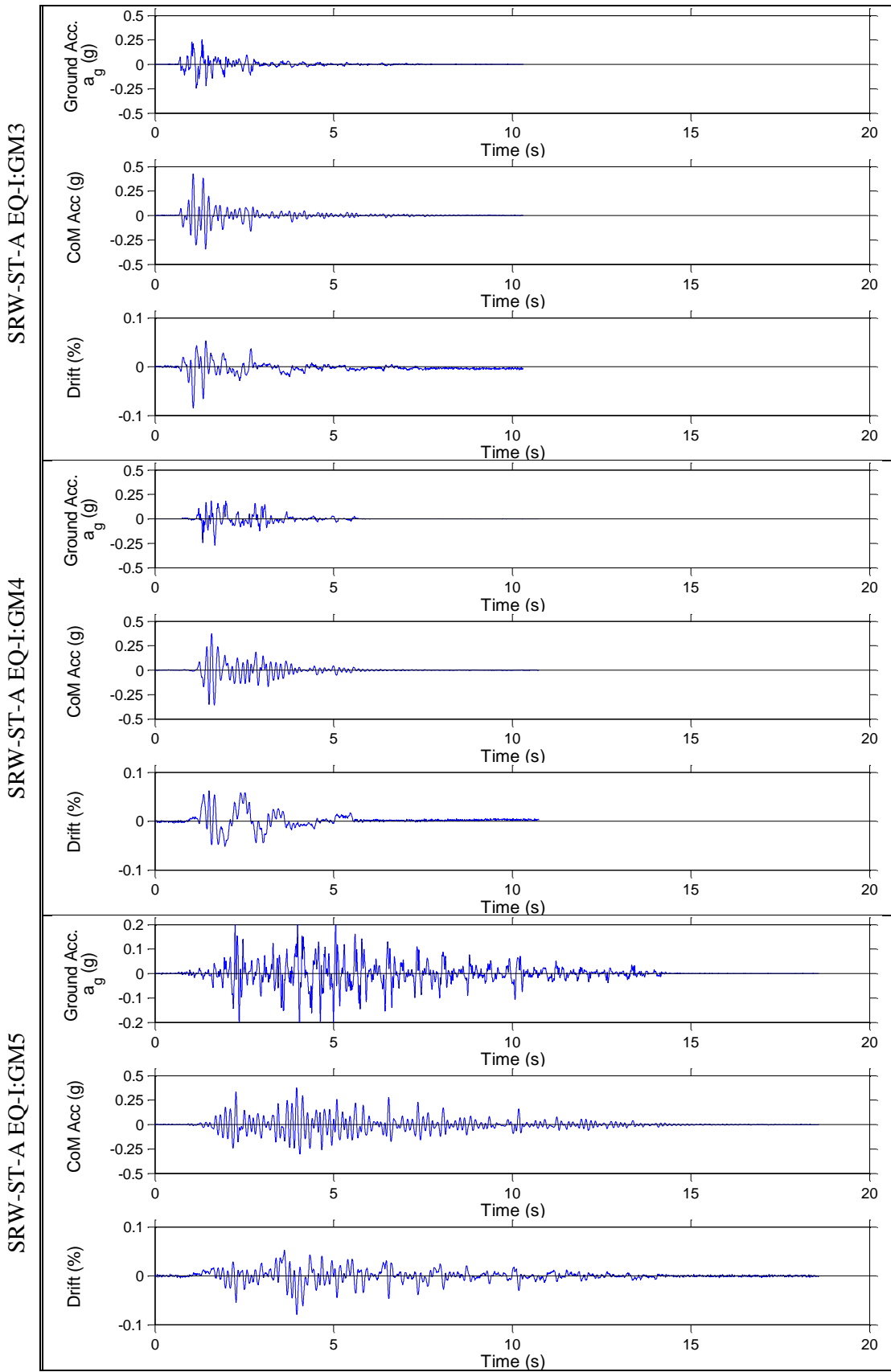


Figure E.5 – Shake table results for SRW-ST-A, EQ-I: GM3-5

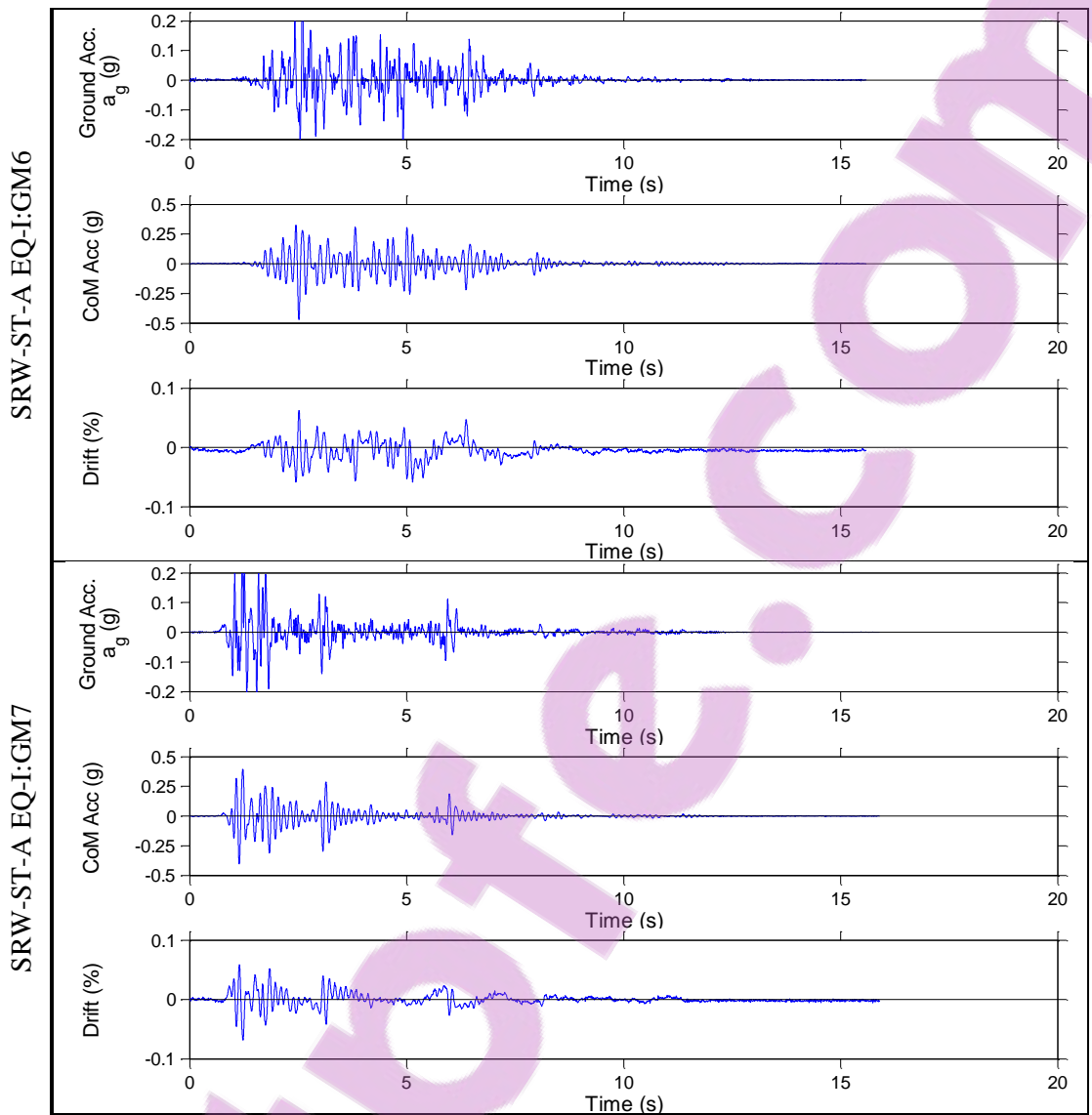


Figure E.6 – Shake table results for SRW-ST-A, EQ-I: GM6-7

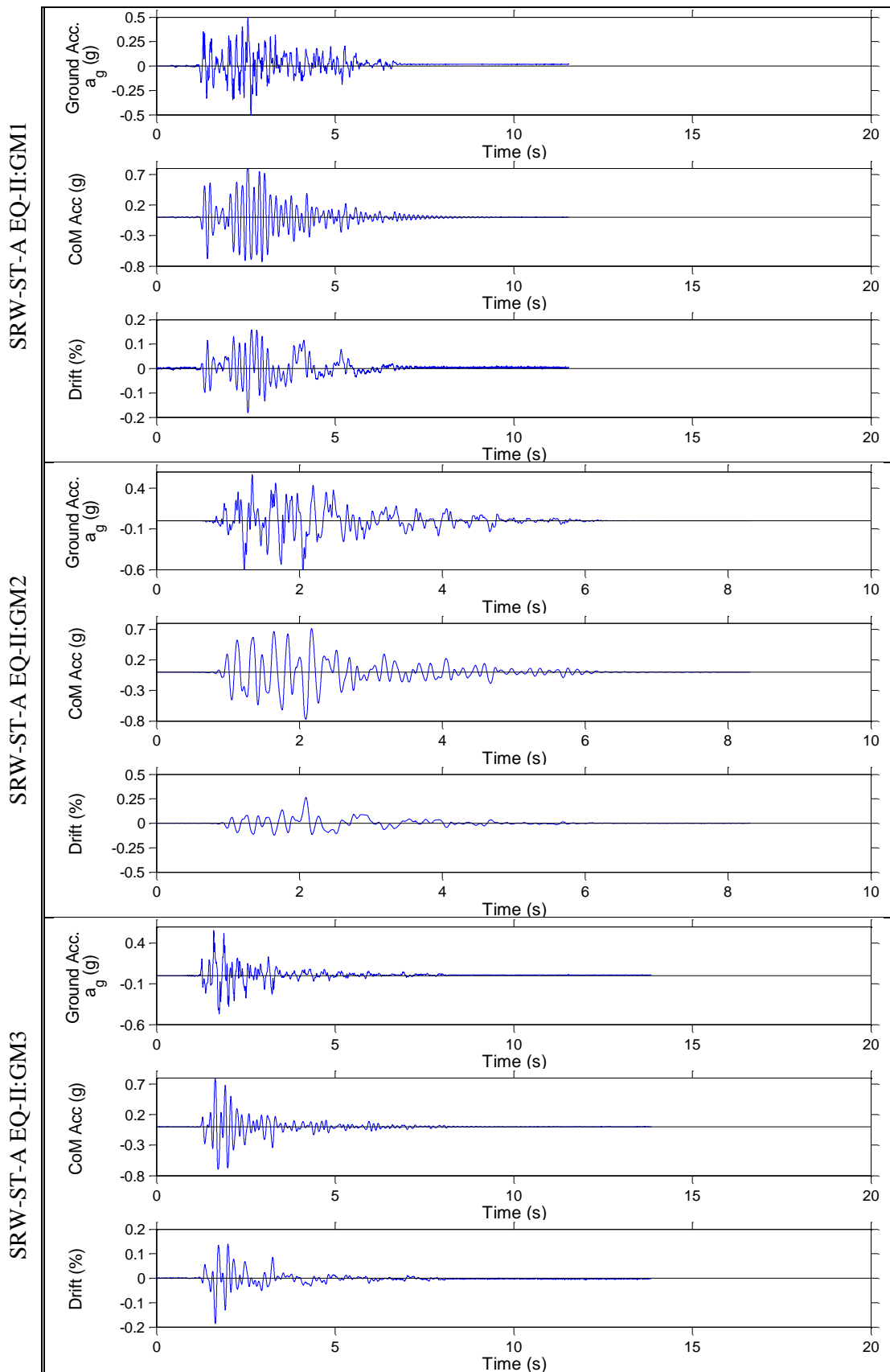


Figure E.7 – Shake table results for SRW-ST-A, EQ-II: GM1-3

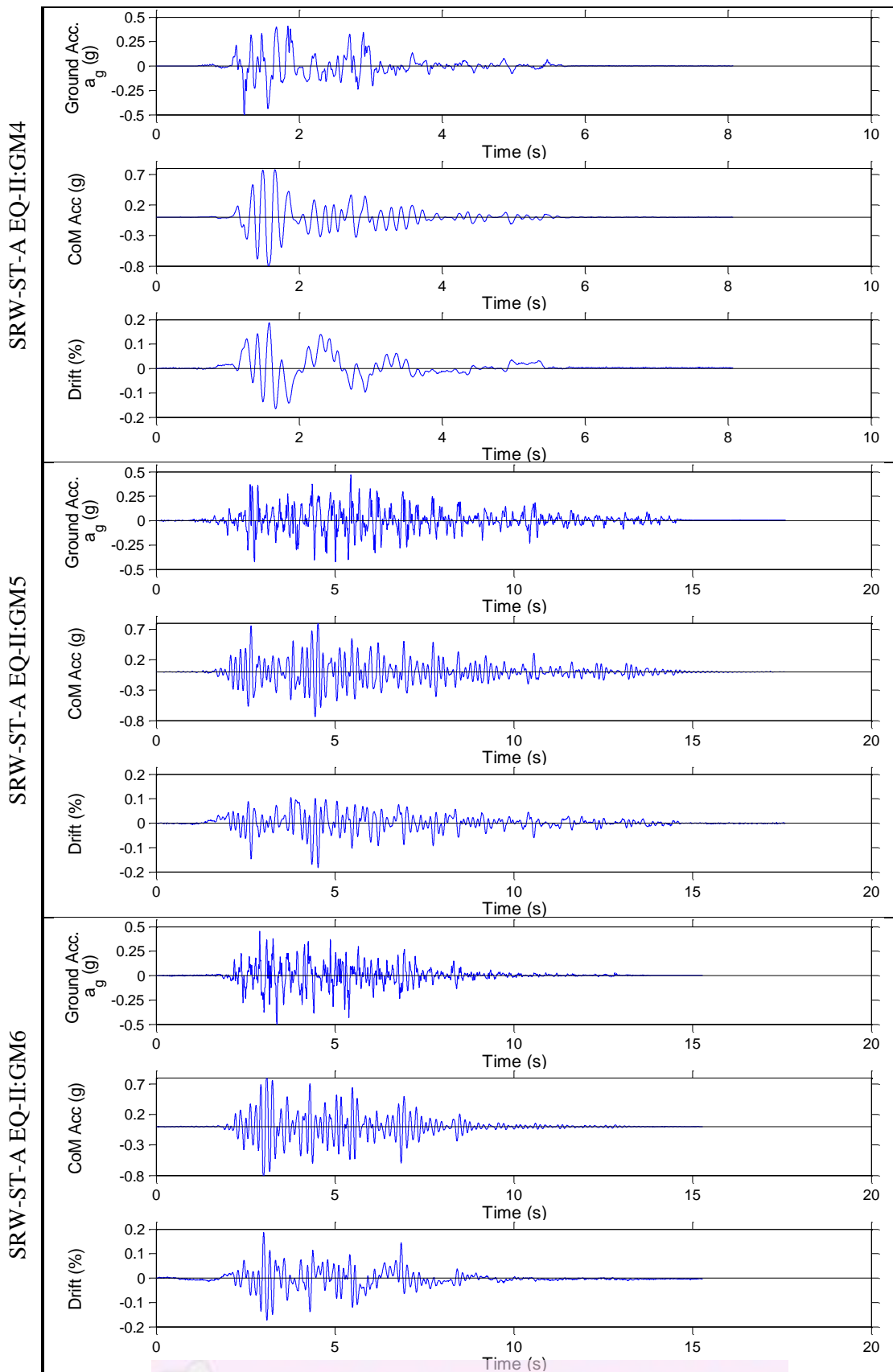


Figure E.8 – Shake table results for SRW-ST-A, EQ-II: GM4-6

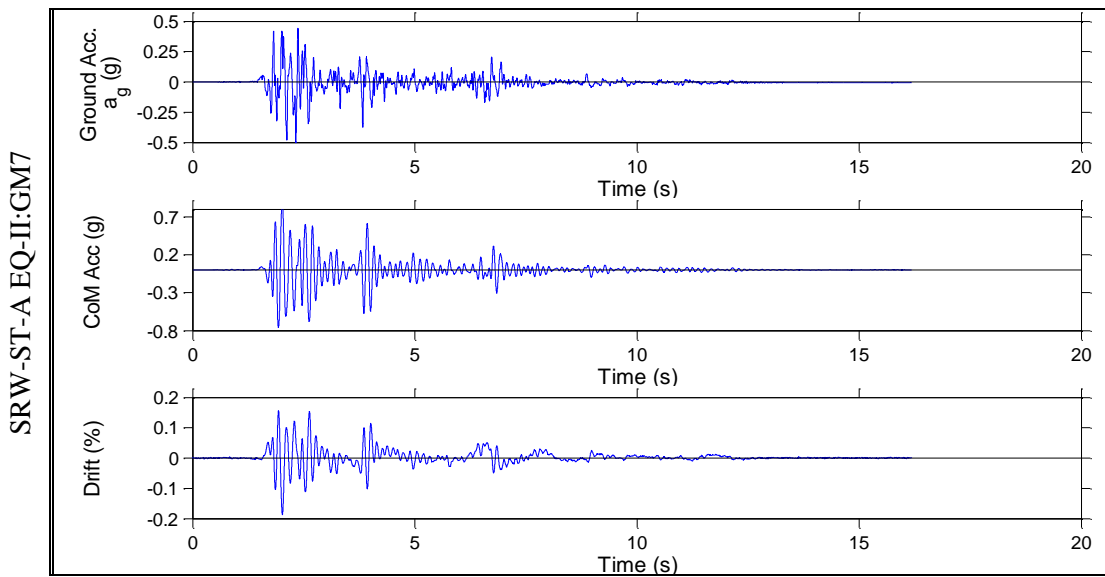


Figure E.9 – Shake table results for SRW-ST-A, EQ-II: GM7

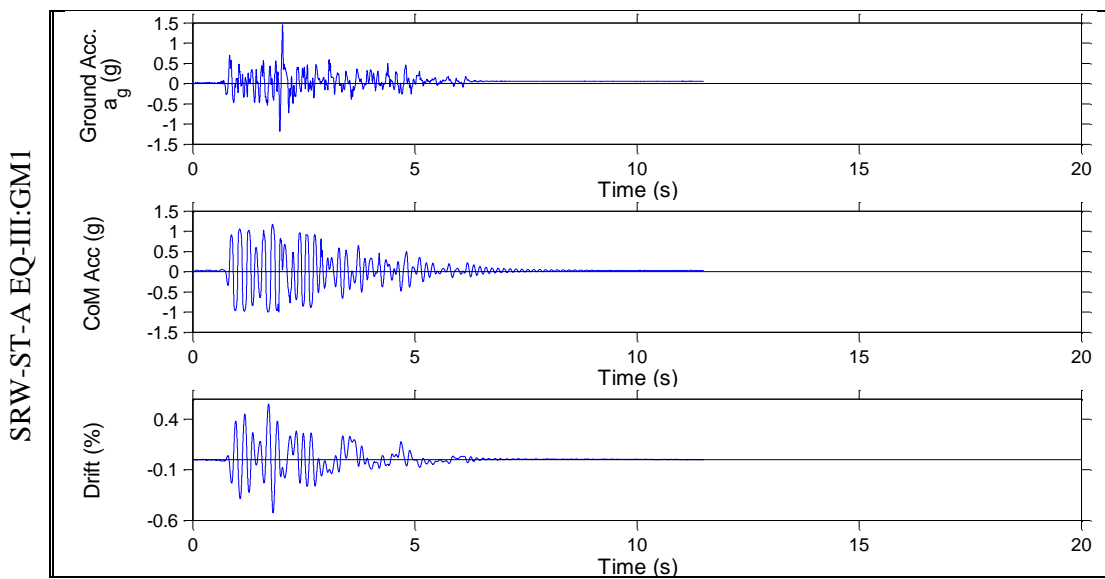


Figure E.10 – Shake table results for SRW-ST-A, EQ-III: GM1

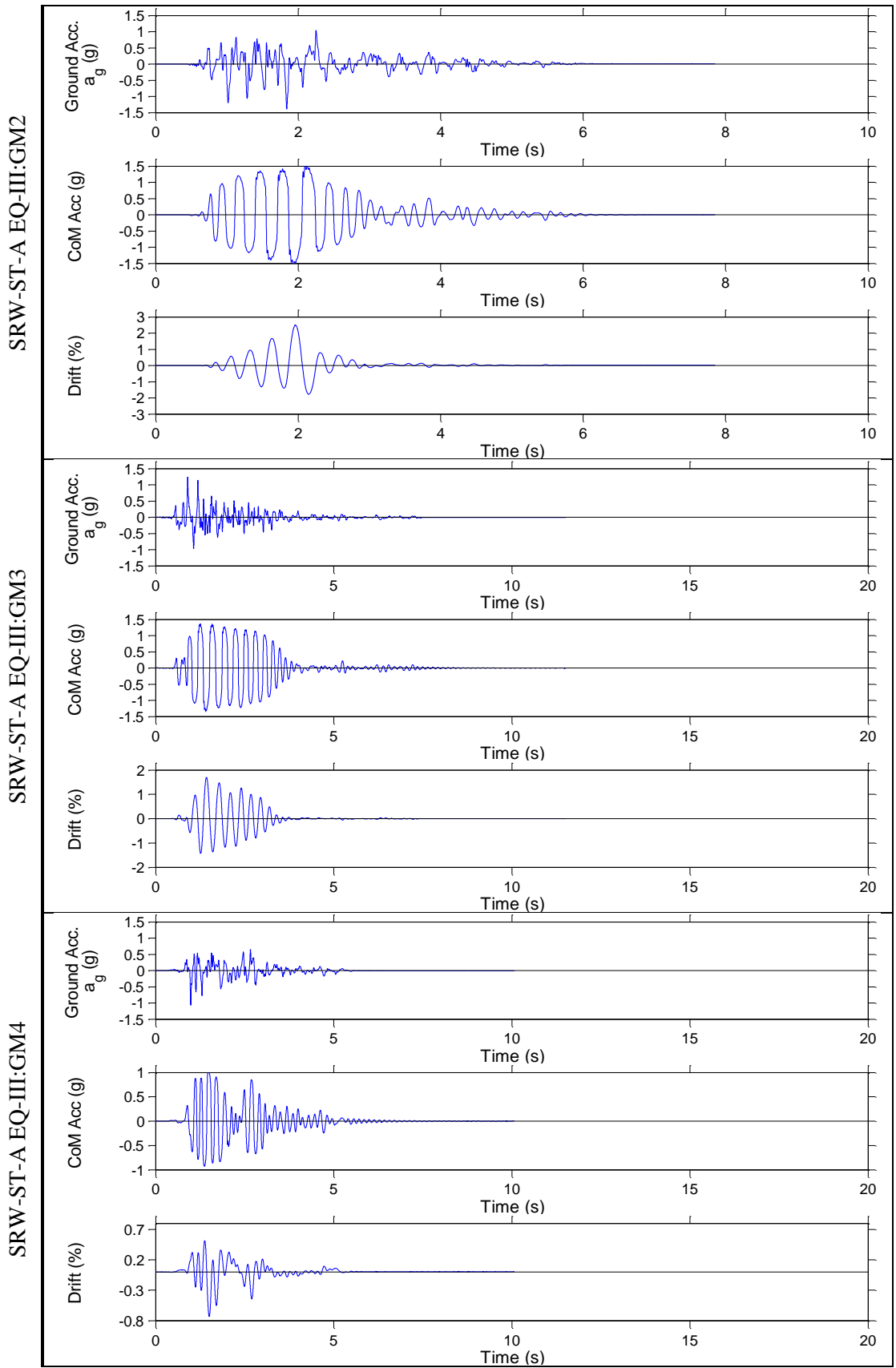


Figure E.11 – Shake table results for SRW-ST-A, EQ-II: GM2-4

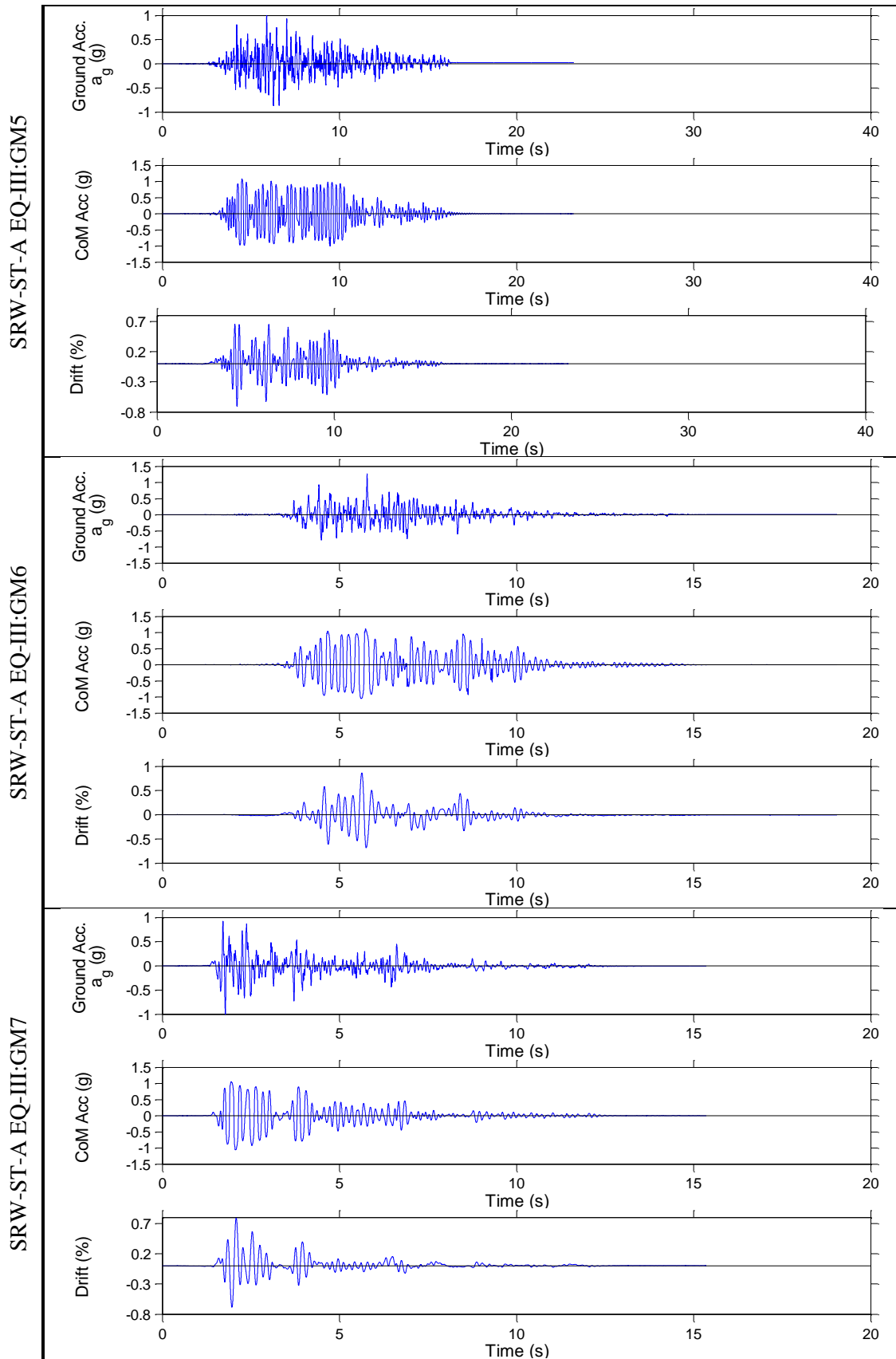


Figure E.12 – Shake table results for SRW-ST-A, EQ-III: GM5-7

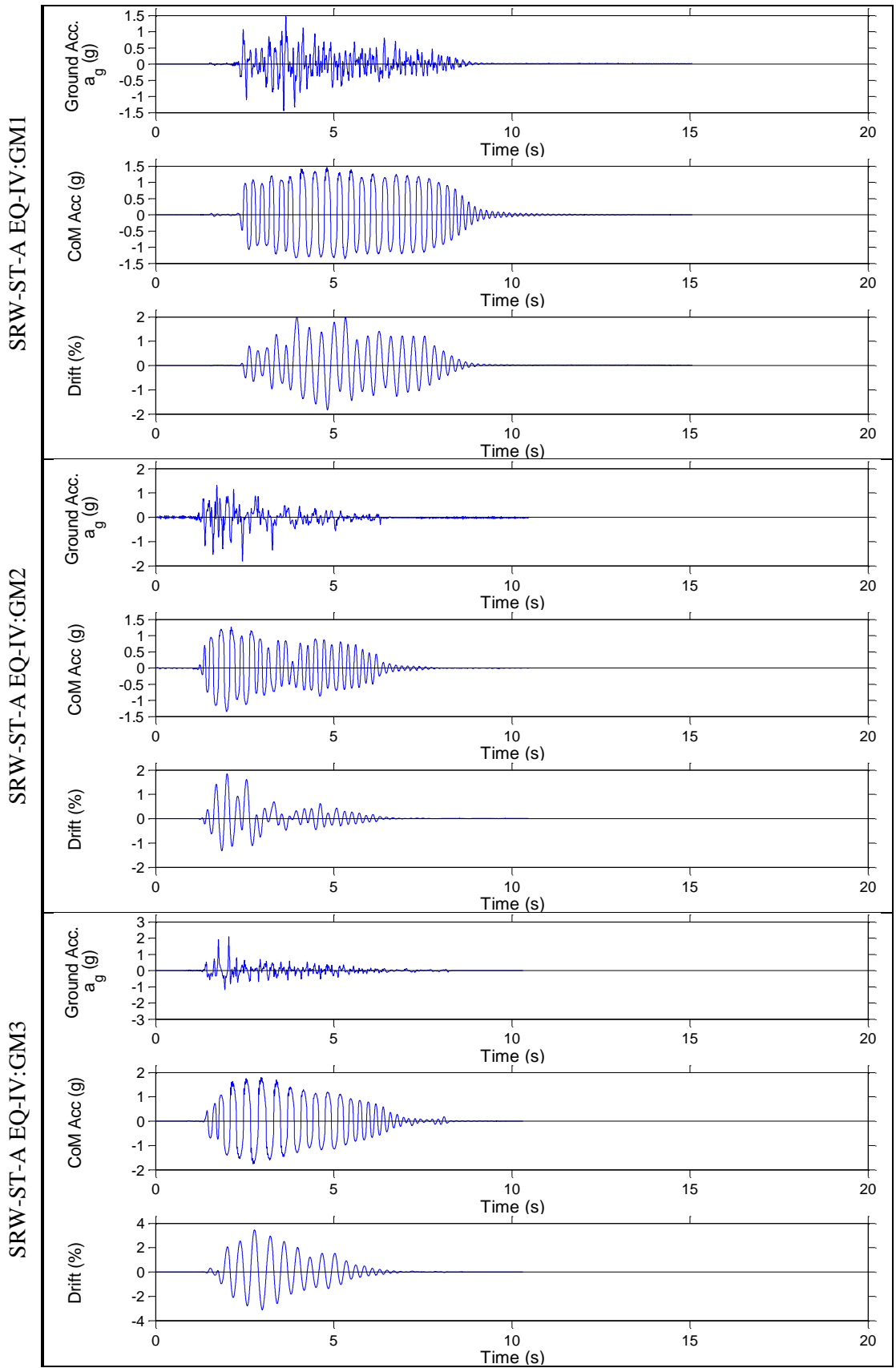


Figure E.13 – Shake table results for SRW-ST-A, EQ-IV: GM1-3

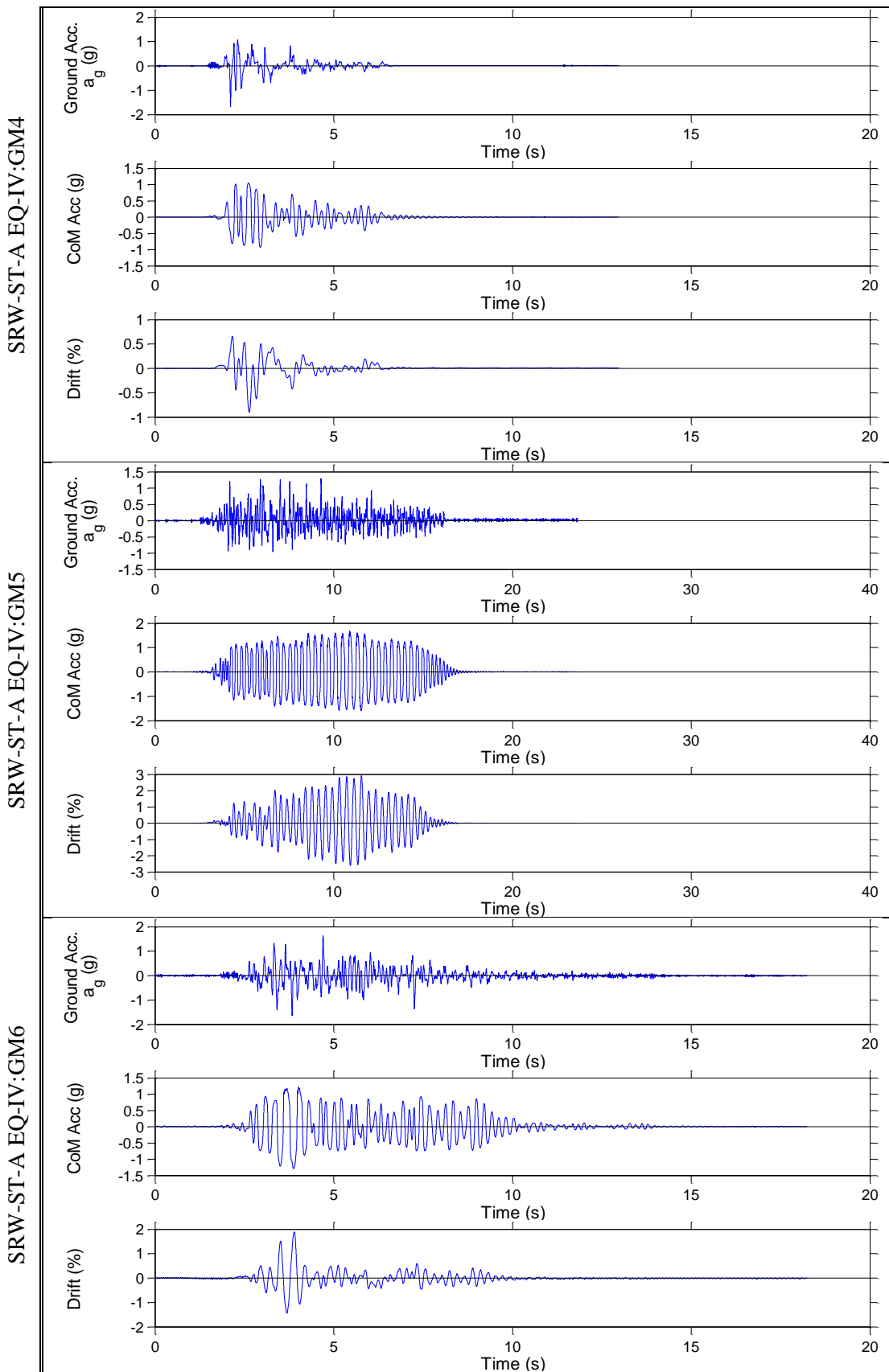


Figure E.14 – Shake table results for SRW-ST-A, EQ-IV: GM4-6

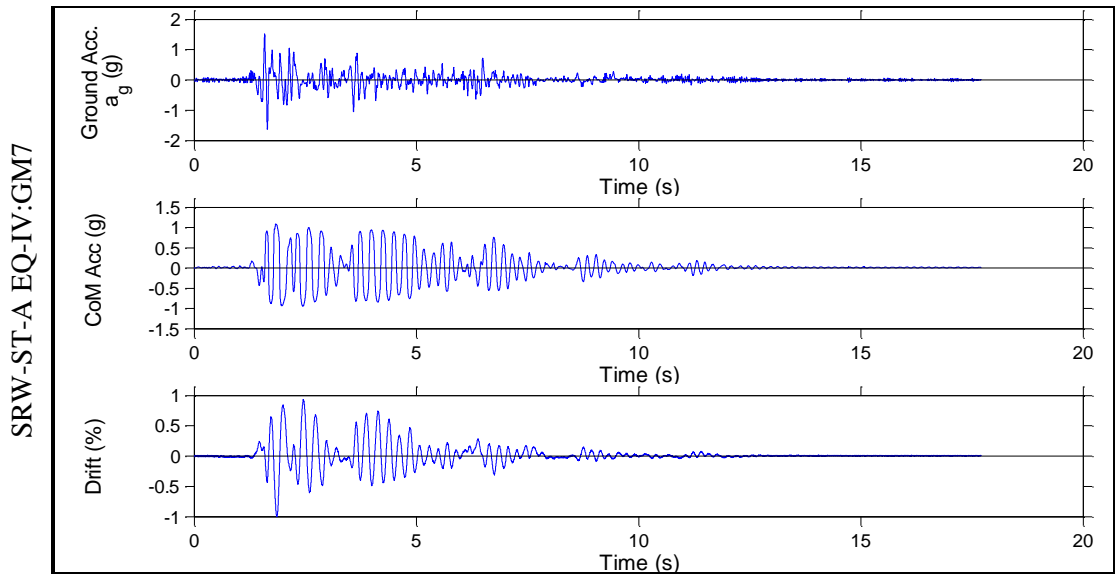


Figure E.15 – Shake table results for SRW-ST-A, EQ-IV: GM7

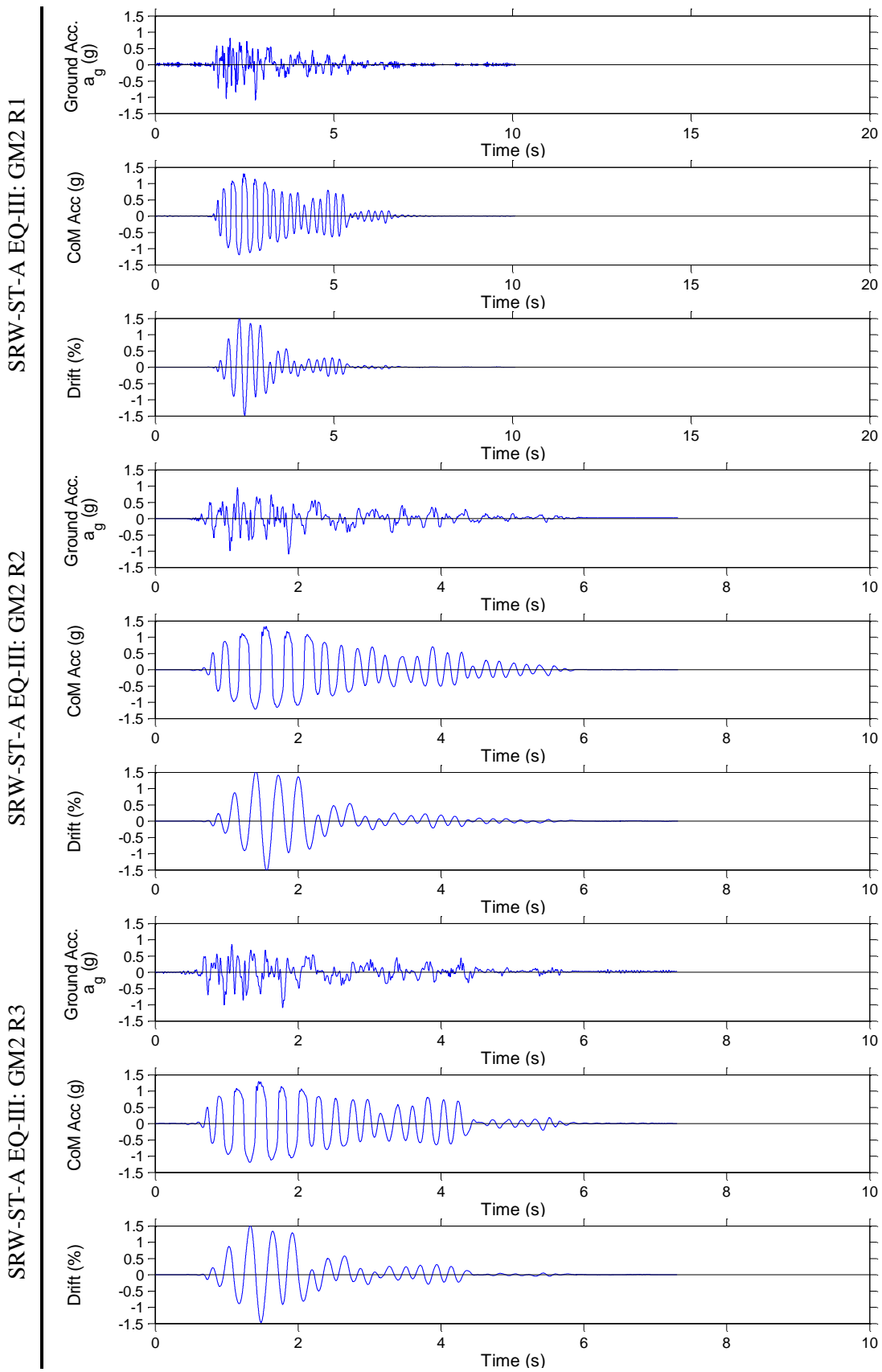
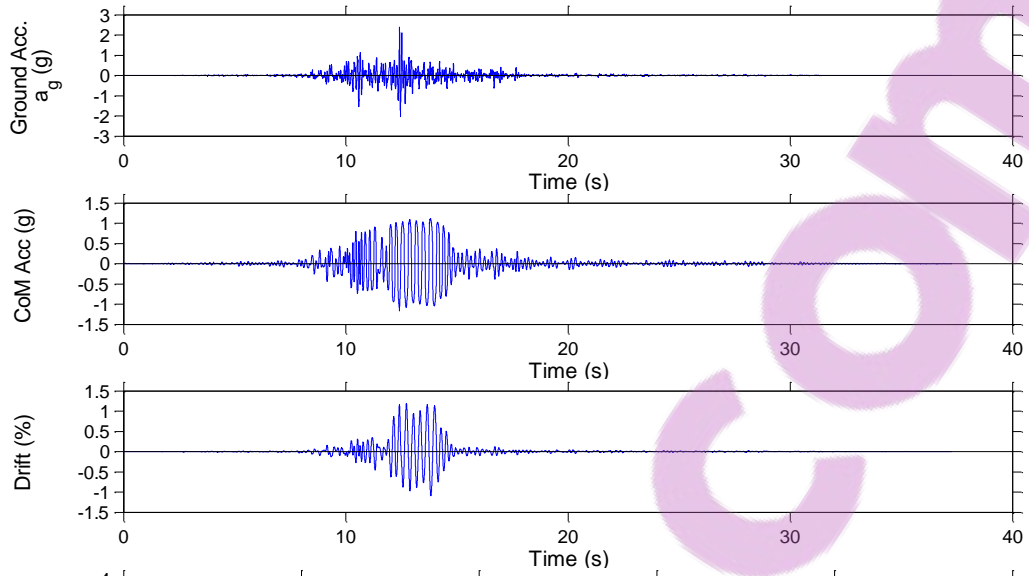
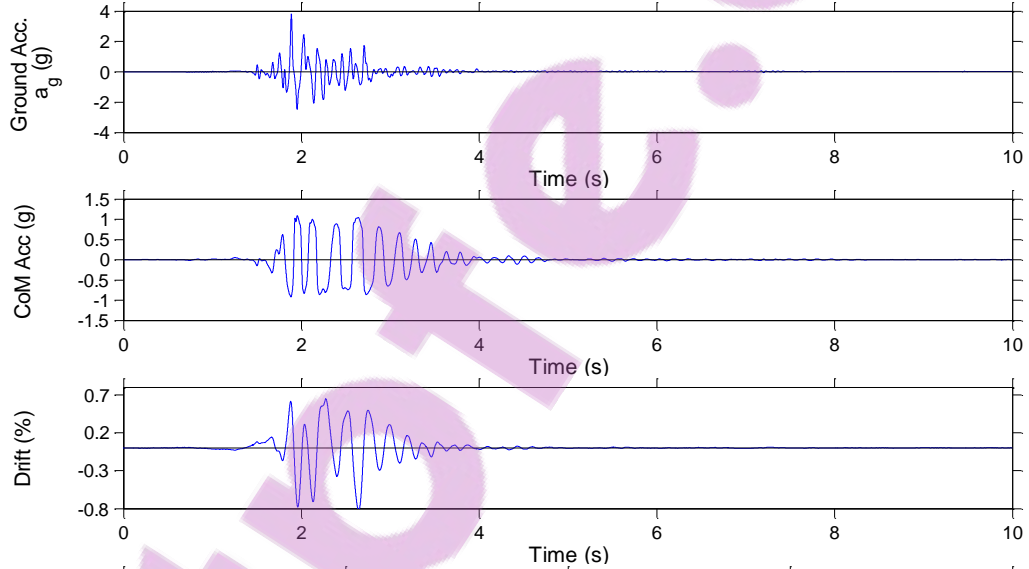


Figure E.16 – Shake table results for SRW-ST-A repeats

SRW-ST-A RGM-I: GM8



SRW-ST-A RGM-I: GM9



SRW-ST-A RGM-I: GM10

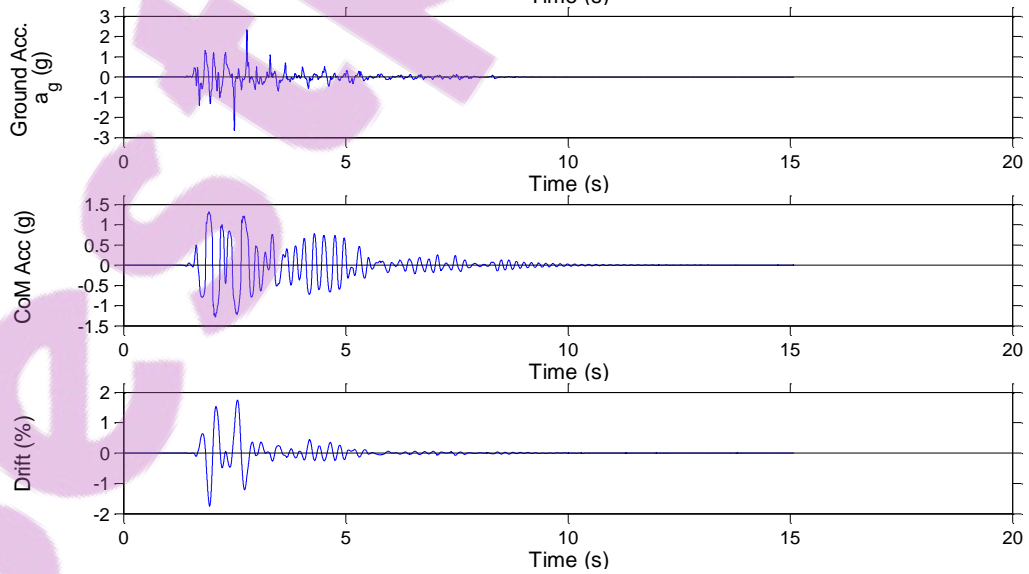


figure E.17 – Shake table results for SRW-ST-A, RGM-I: GM8-10

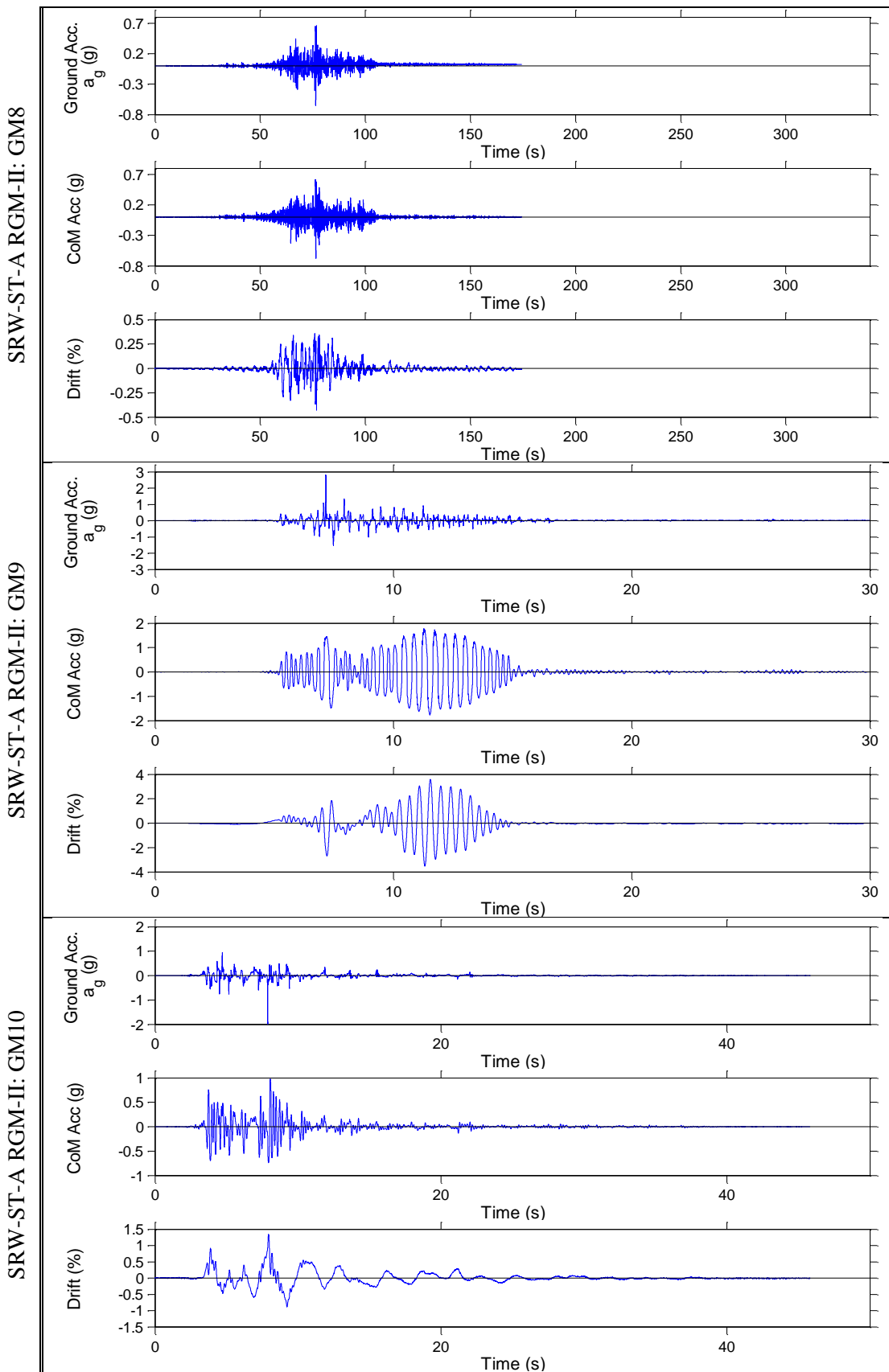


Figure E.18 – Shake table results for SRW-ST-A, RGM-II: GM8-10

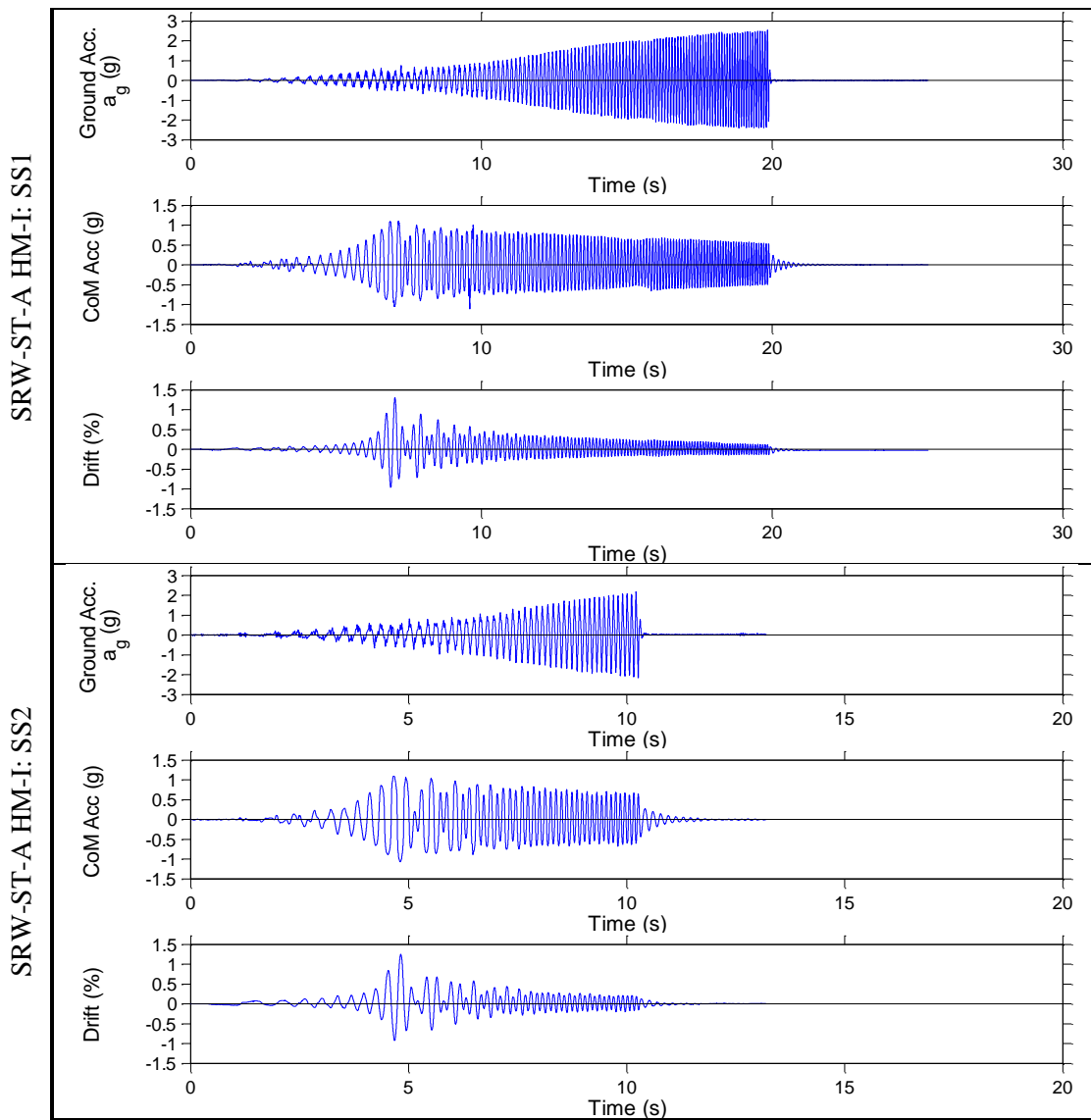


Figure E.19 – Shake table results for SRW-ST-A HM-I

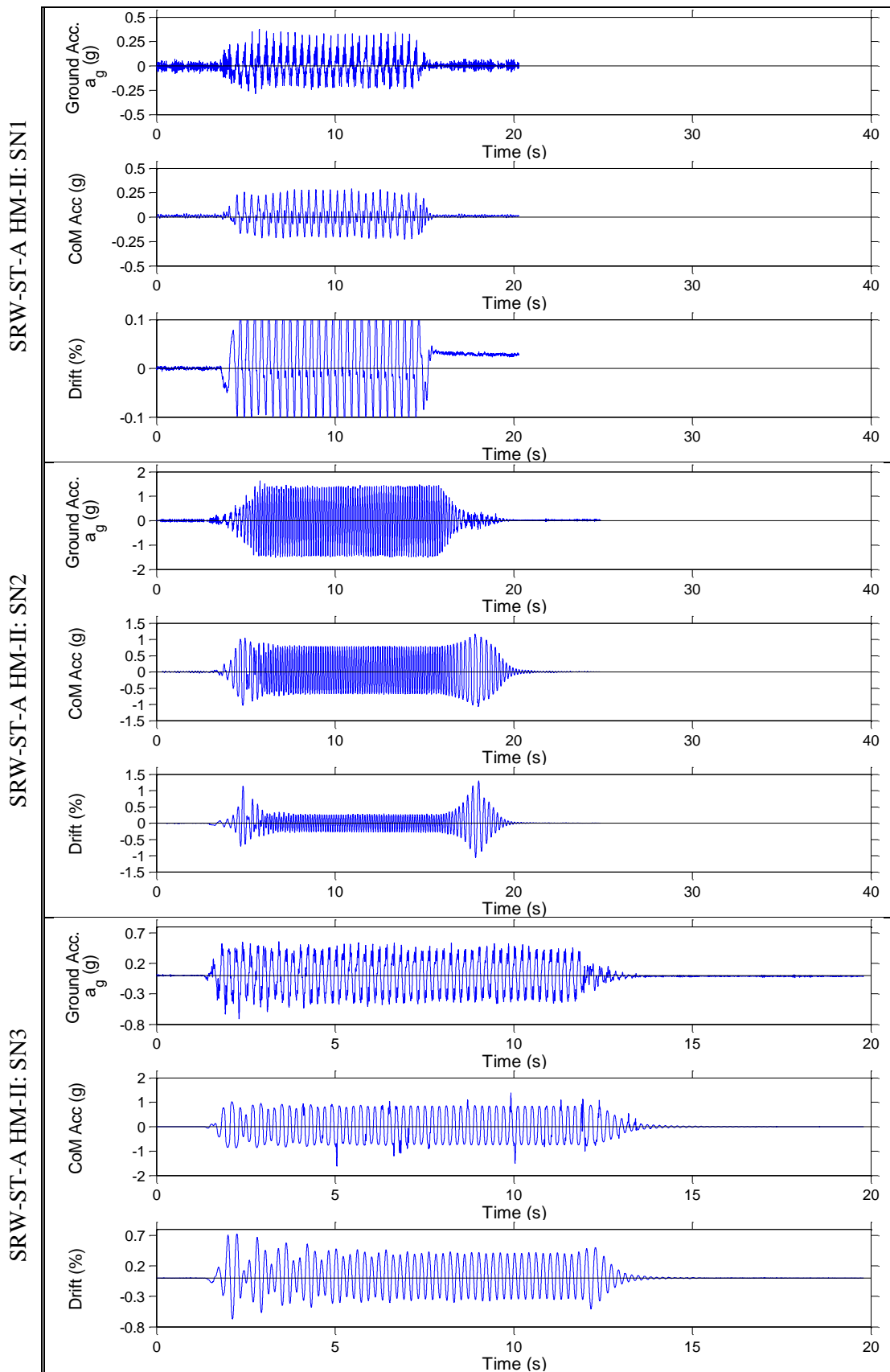


Figure E.20 – Shake table results for SRW-ST-A HM-II SN1-3

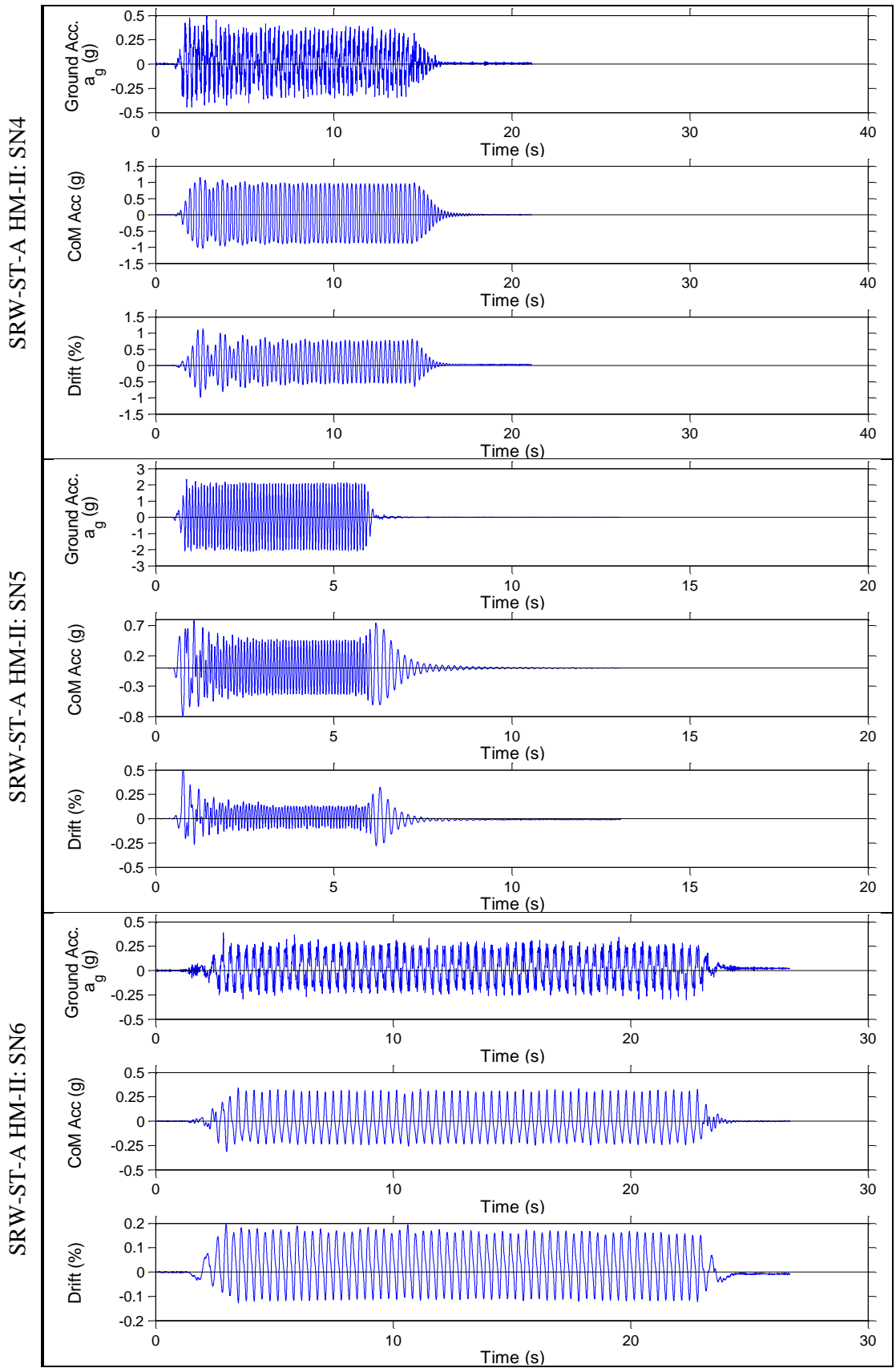


Figure E.21 – Shake table results for SRW-ST-A HM-II SN4-6

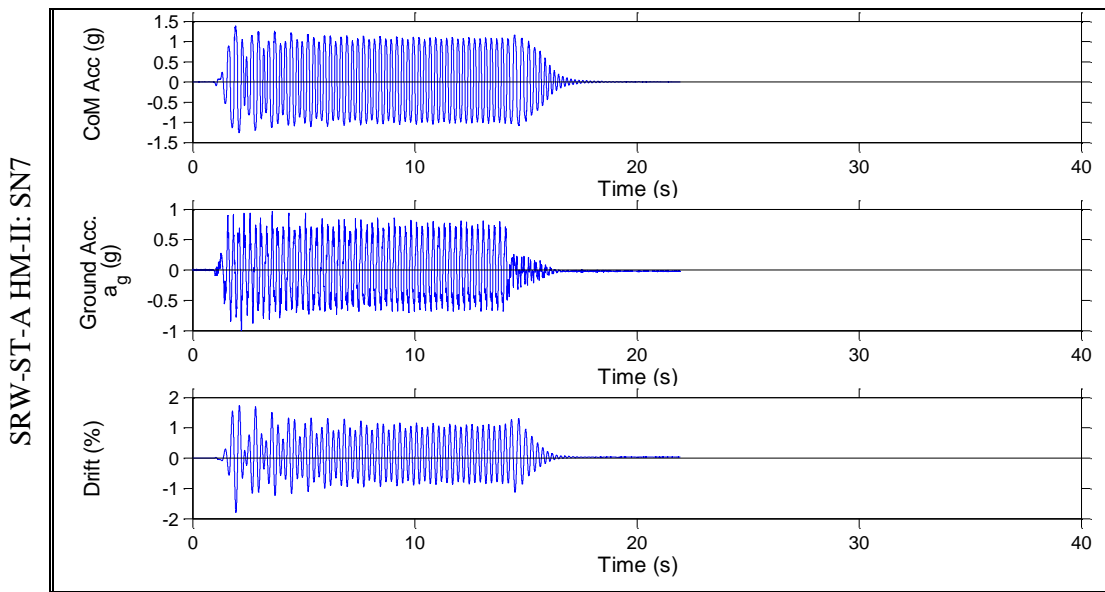


Figure E.22 – Shake table results for SRW-ST-A HM-II SN7

E.6.2 PreWEC-ST-A

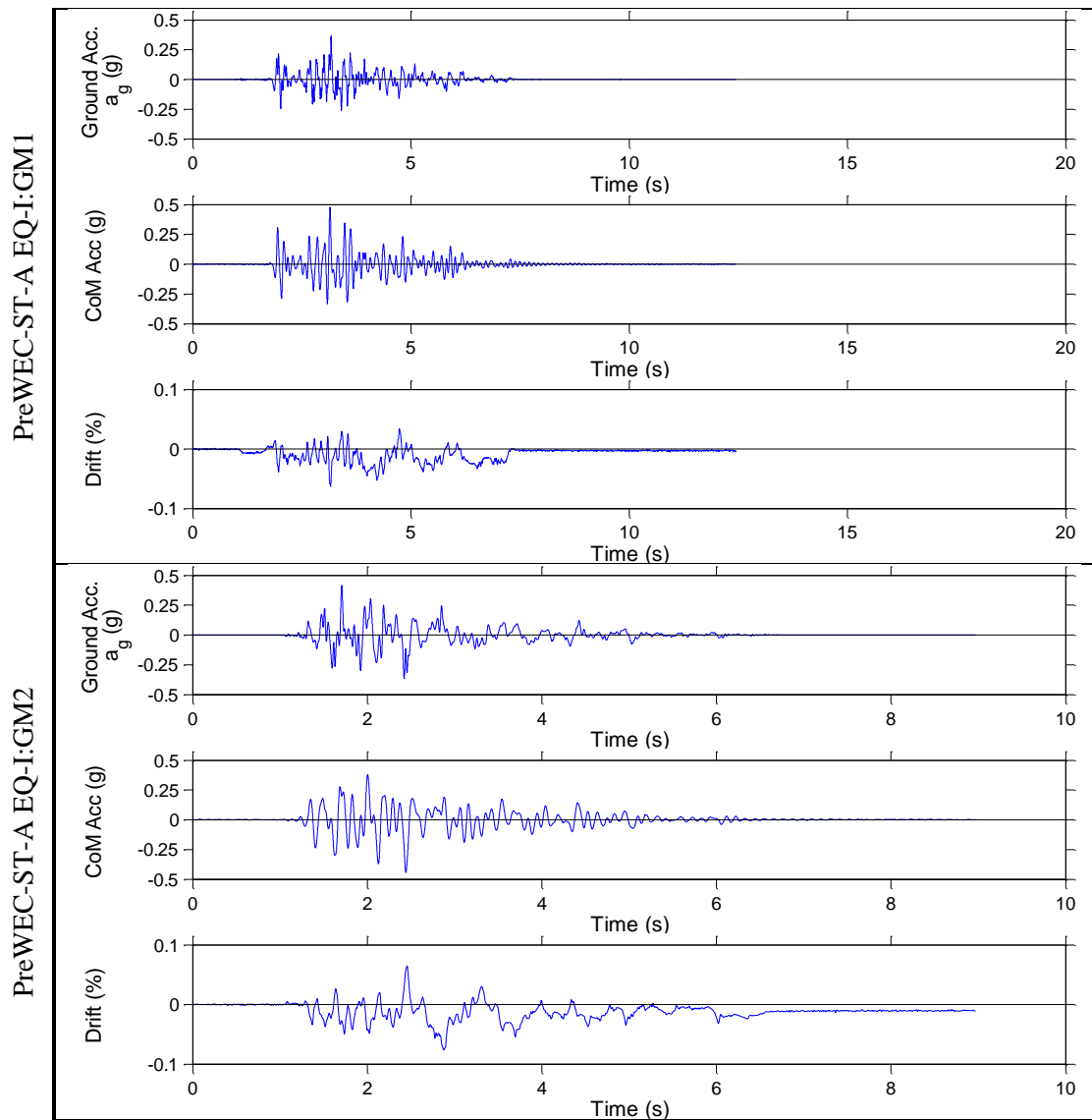


Figure E.23 – Shake table results for PreWEC-ST-A, EQ-I: GM1-2

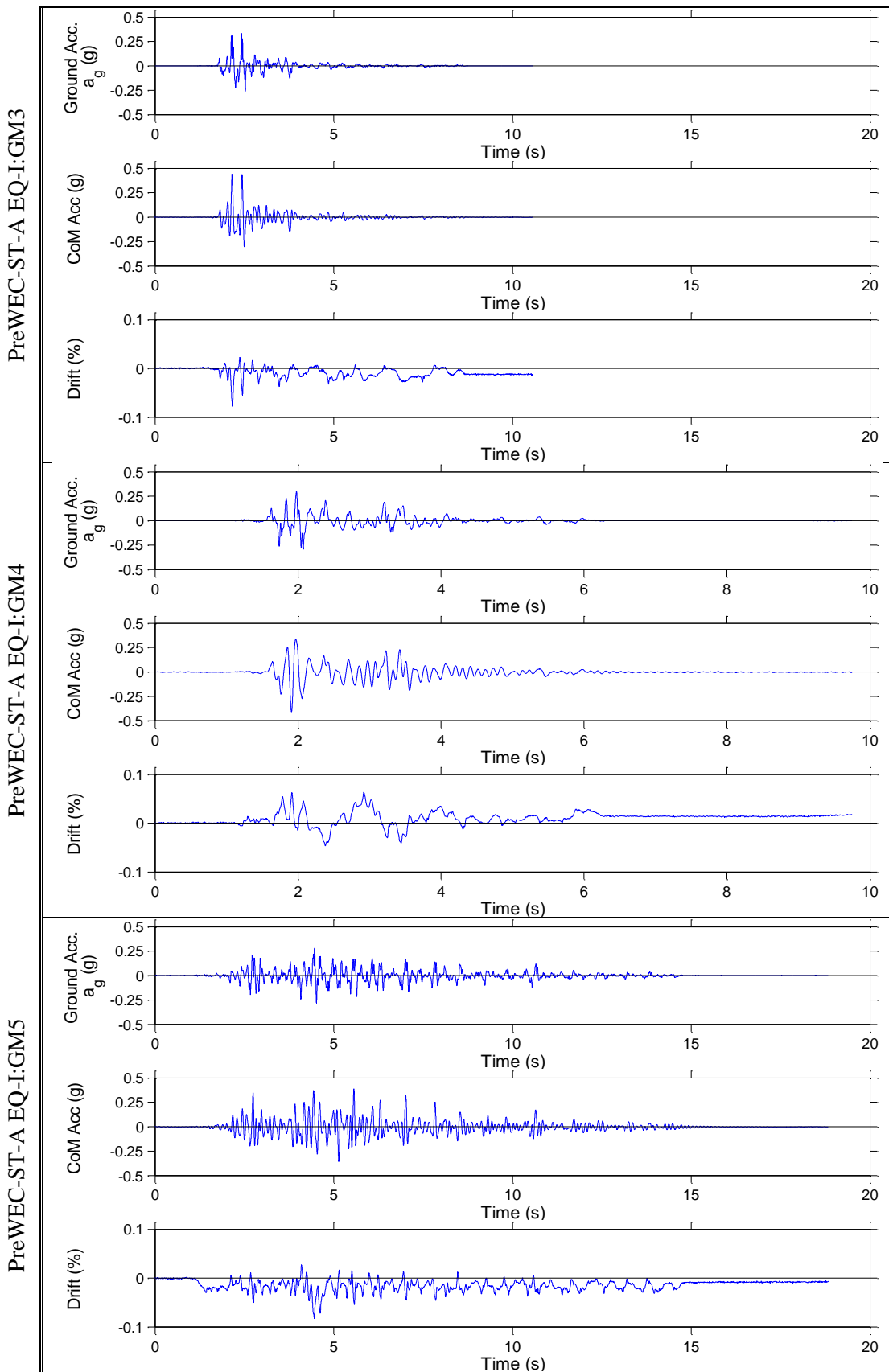


Figure E.24 – Shake table results for PreWEC-ST-A, EQ-I: GM3-5

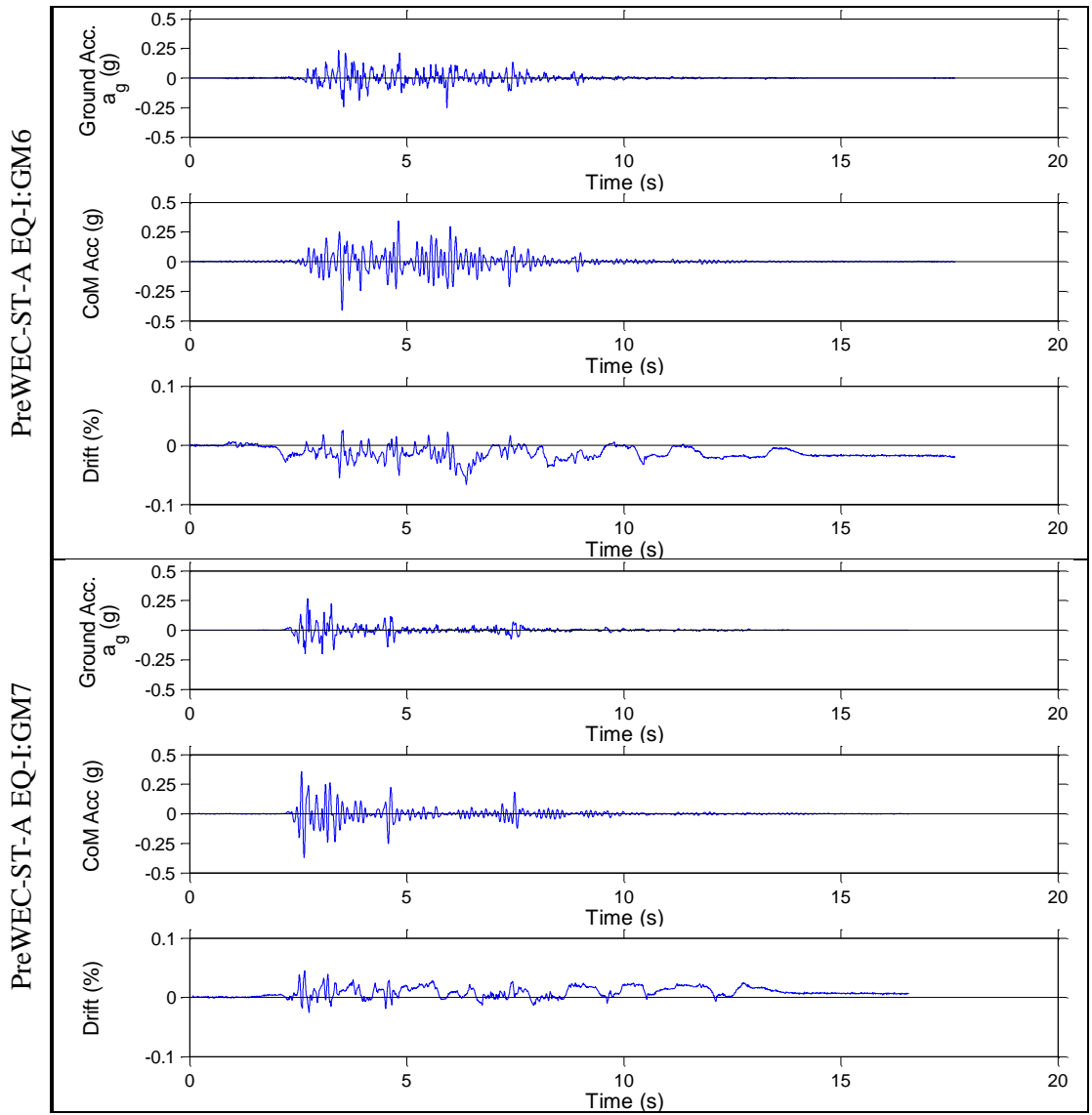


Figure E.25 – Shake table results for PreWEC-ST-A, EQ-I: GM6-7

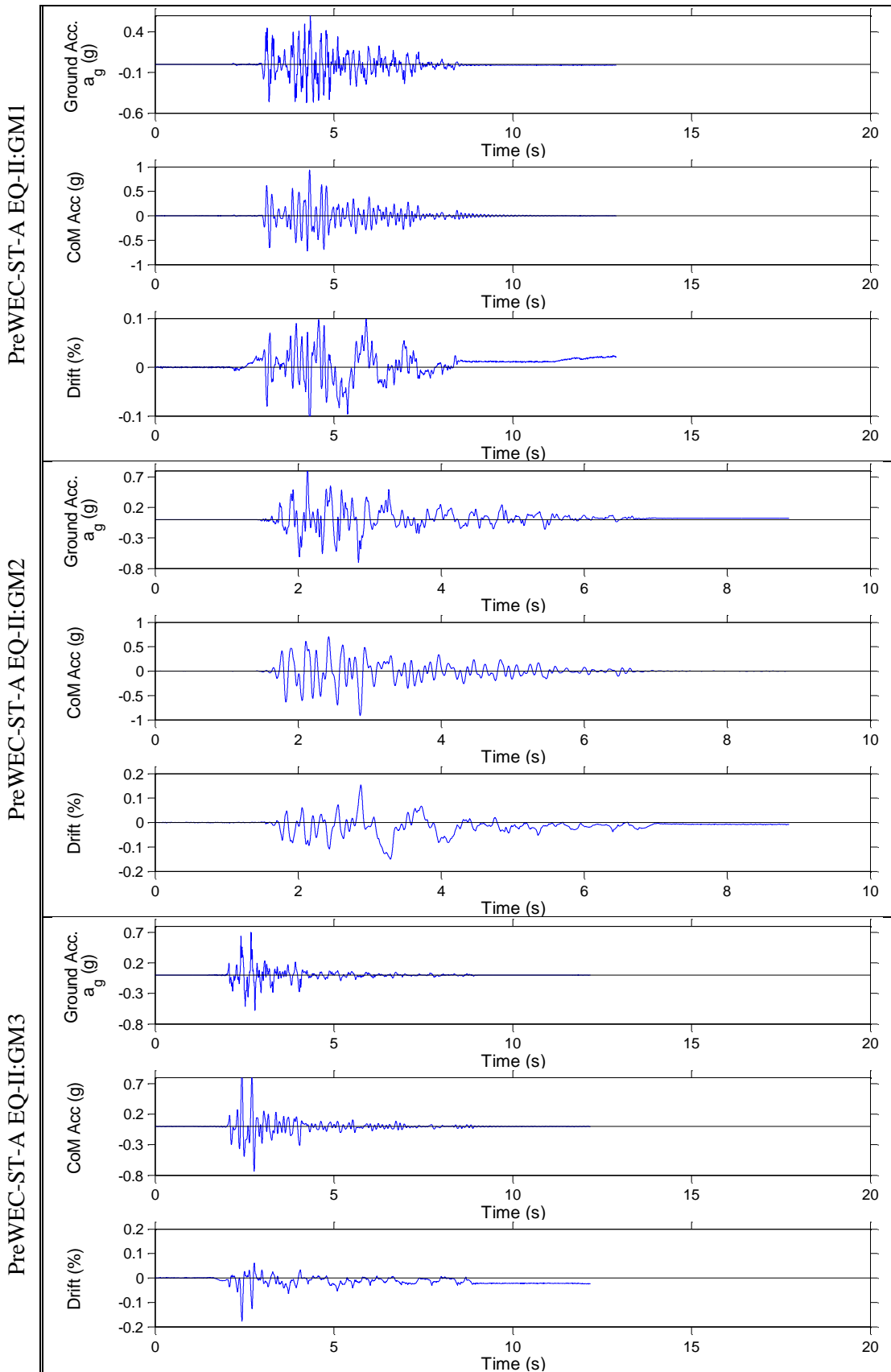


Figure E.26 – Shake table results for PreWEC-ST-A, EQ-II: GM1-3

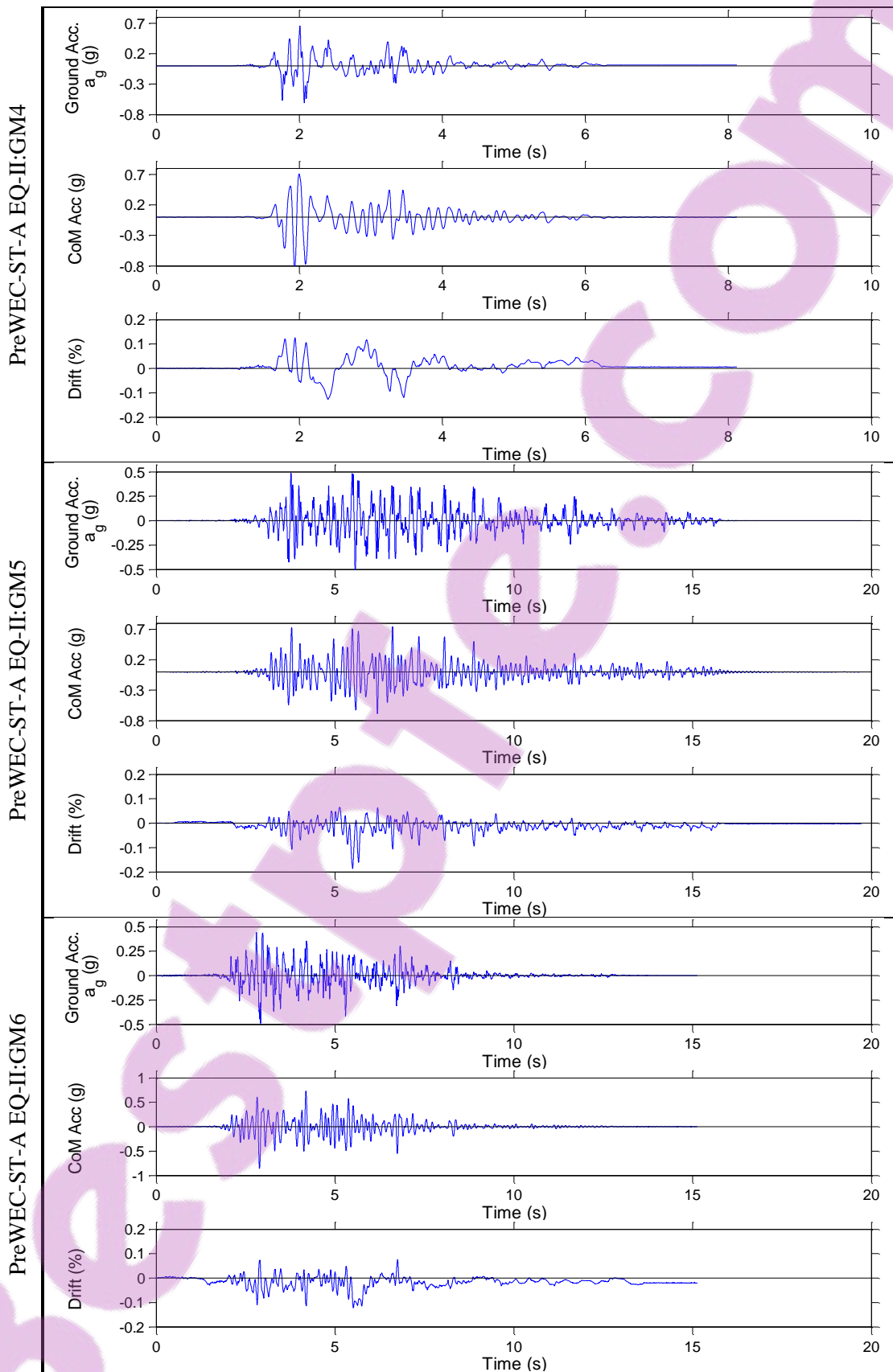


Figure E.27 – Shake table results for PreWEC-ST-A, EQ-II: GM4-6

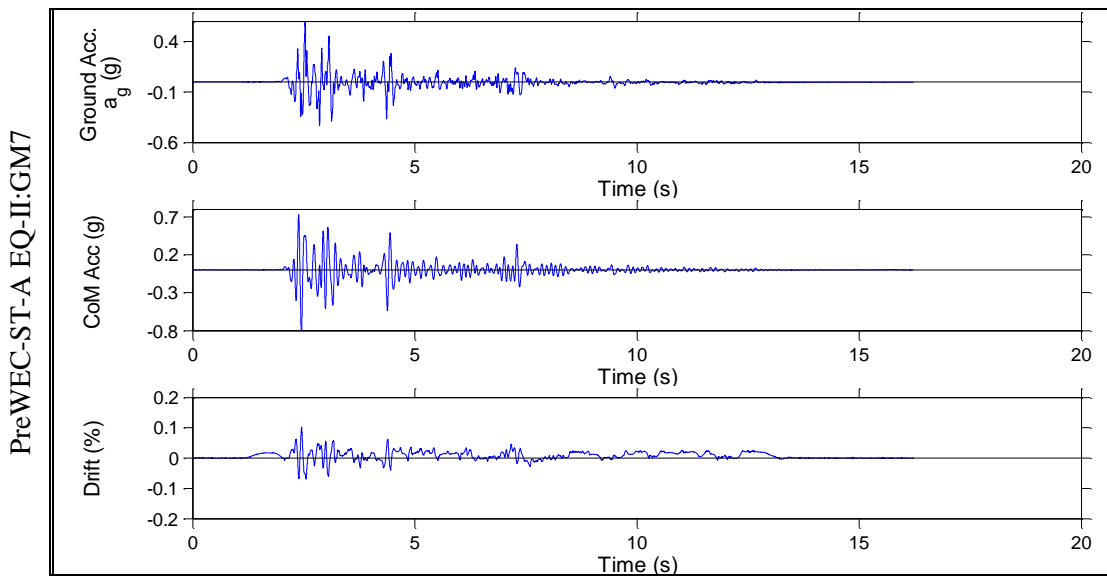


Figure E.28 – Shake table results for PreWEC-ST-A, EQ-II: GM7

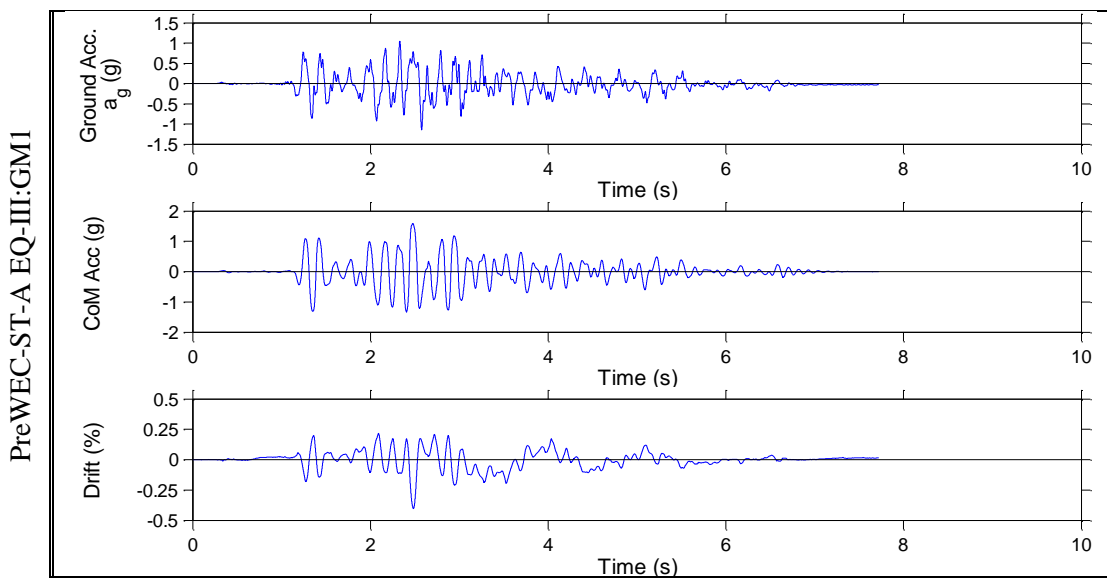


Figure E.29 – Shake table results for PreWEC-ST-A, EQ-III: GM1

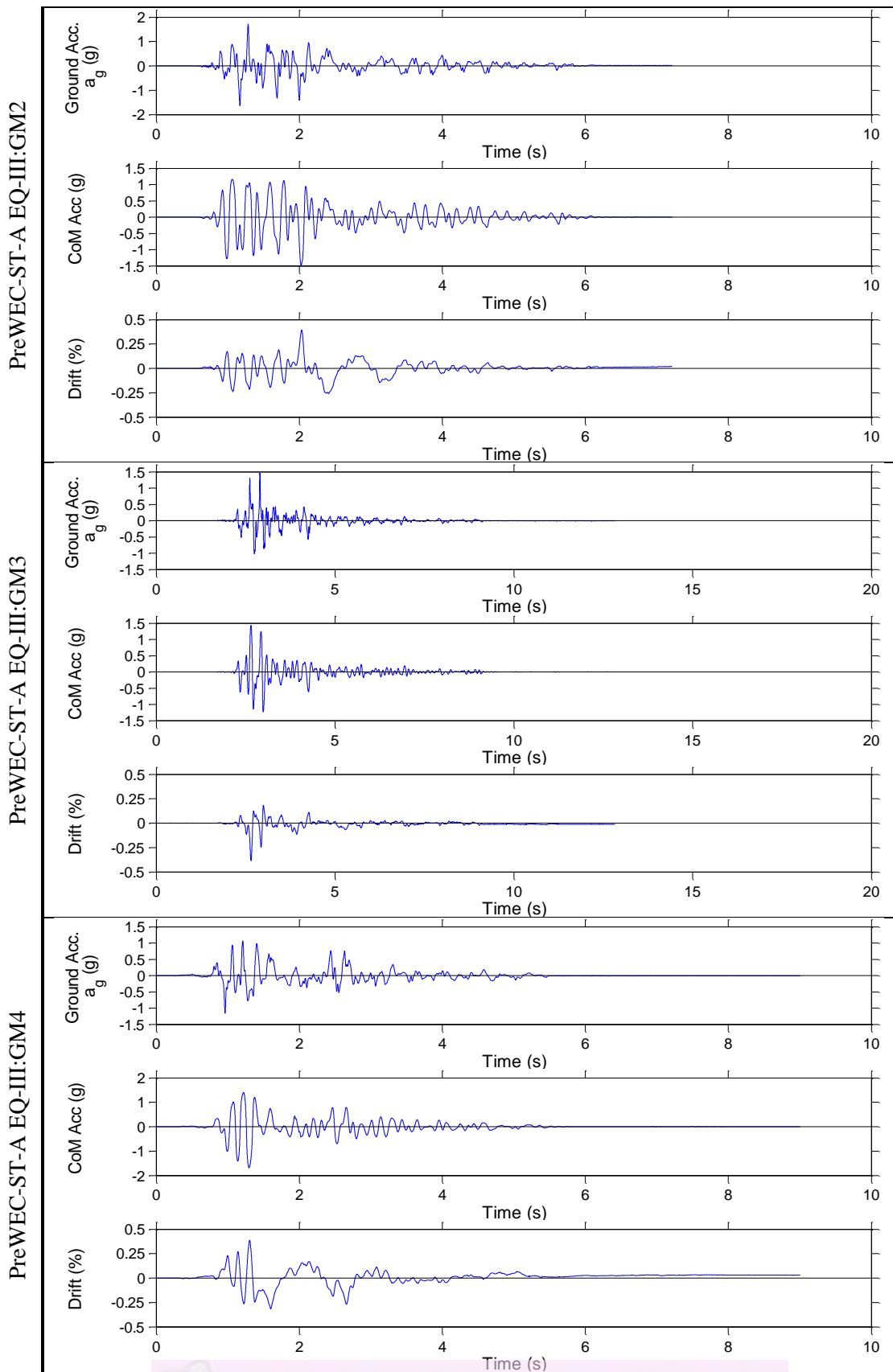


Figure E.30 – Shake table results for PreWEC-ST-A, EQ-II: GM2-4

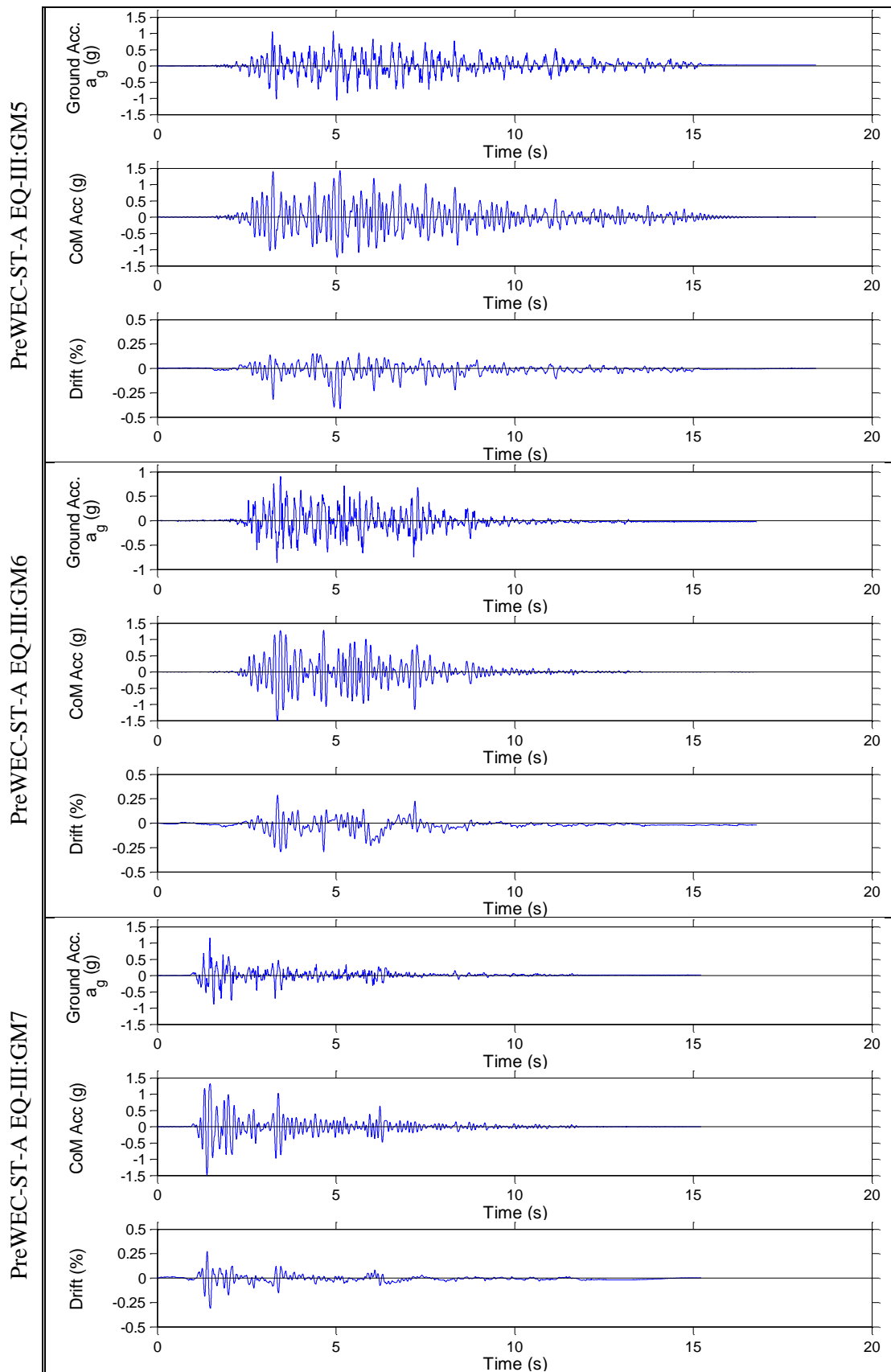


Figure E.31 – Shake table results for PreWEC-ST-A, EQ-III: GM5-7

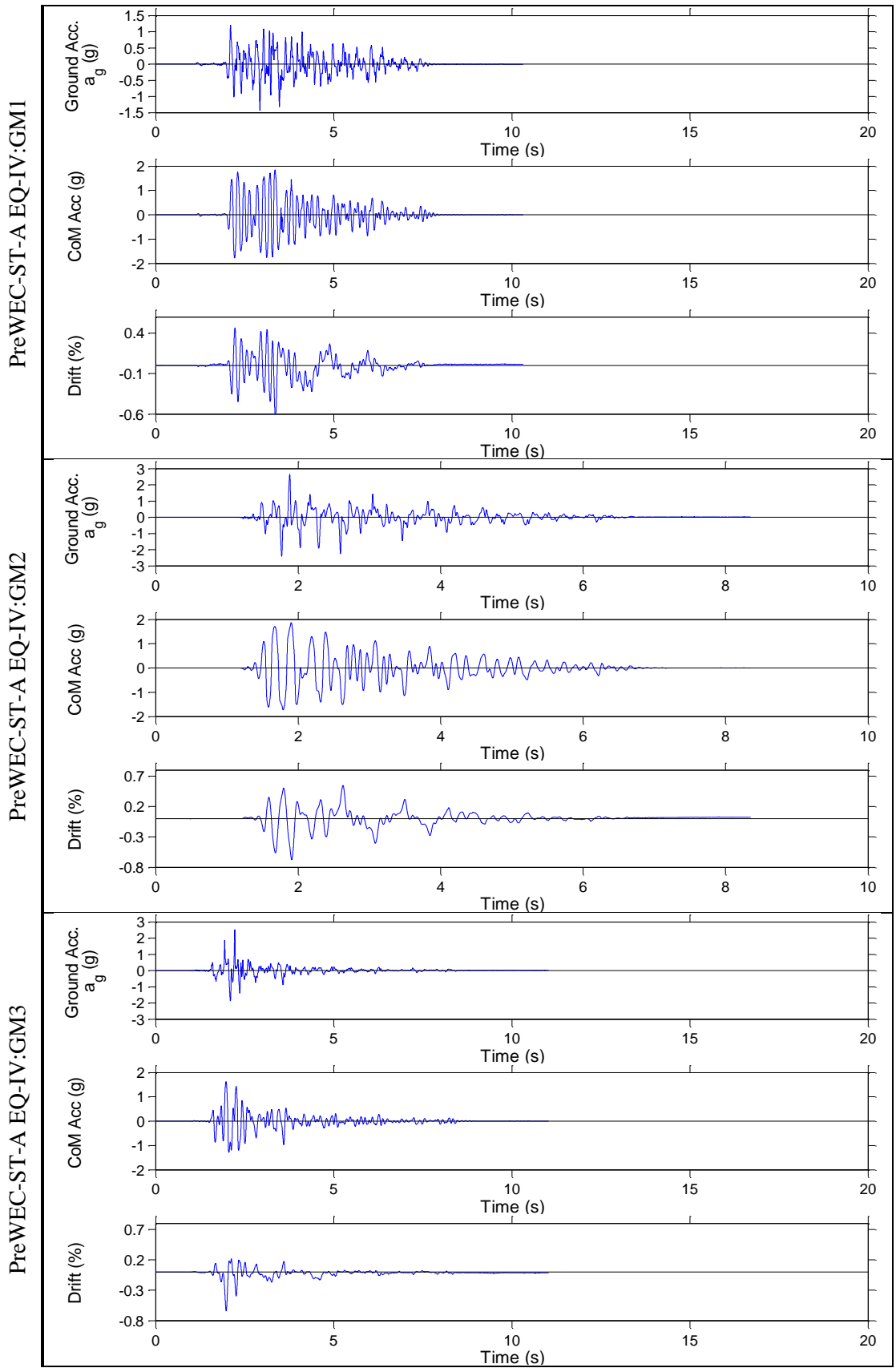


Figure E.32 – Shake table results for PreWEC-ST-A, EQ-IV: GM1-3

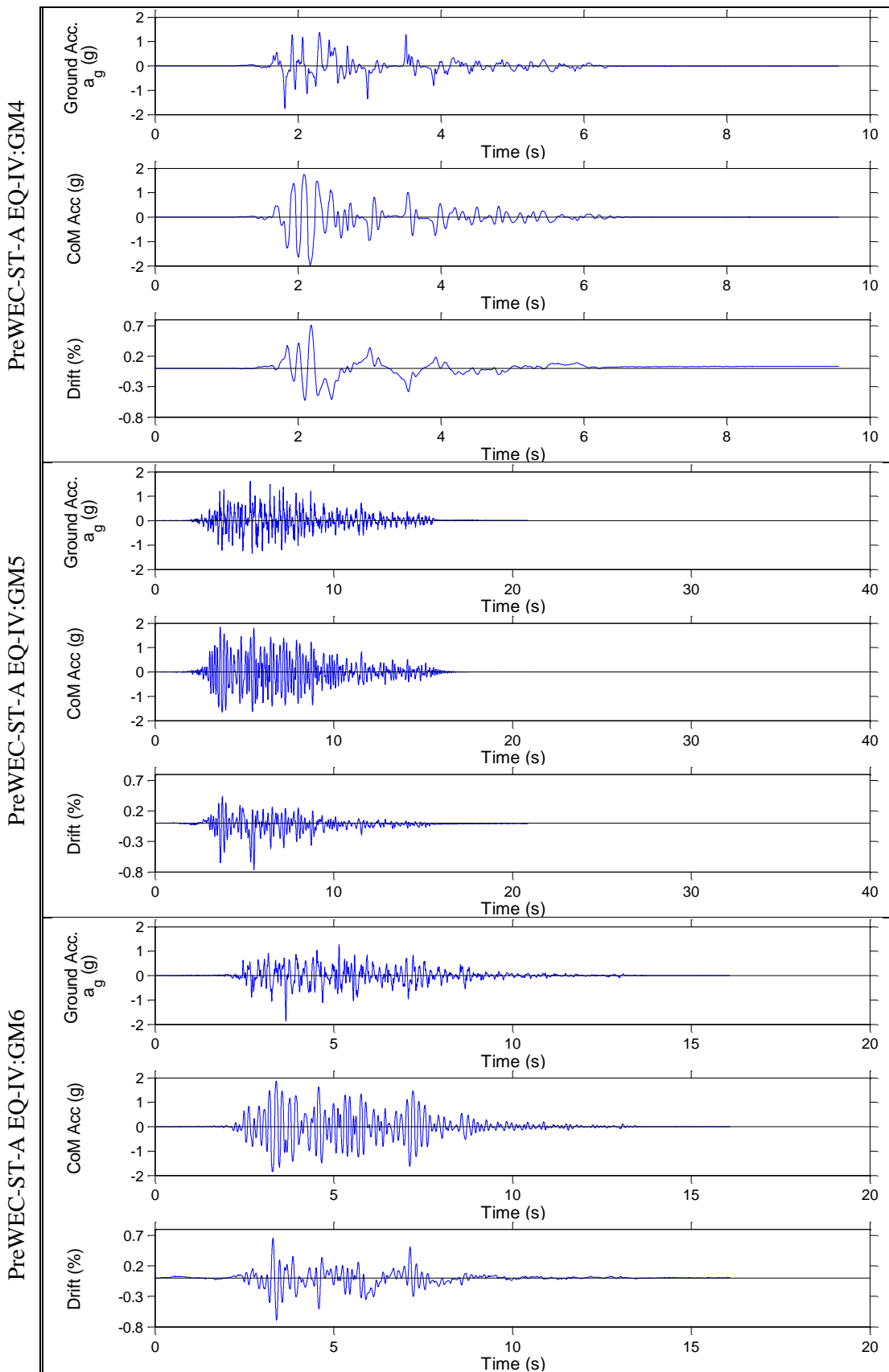


Figure E.33 – Shake table results for PreWEC-ST-A, EQ-IV: GM4-6

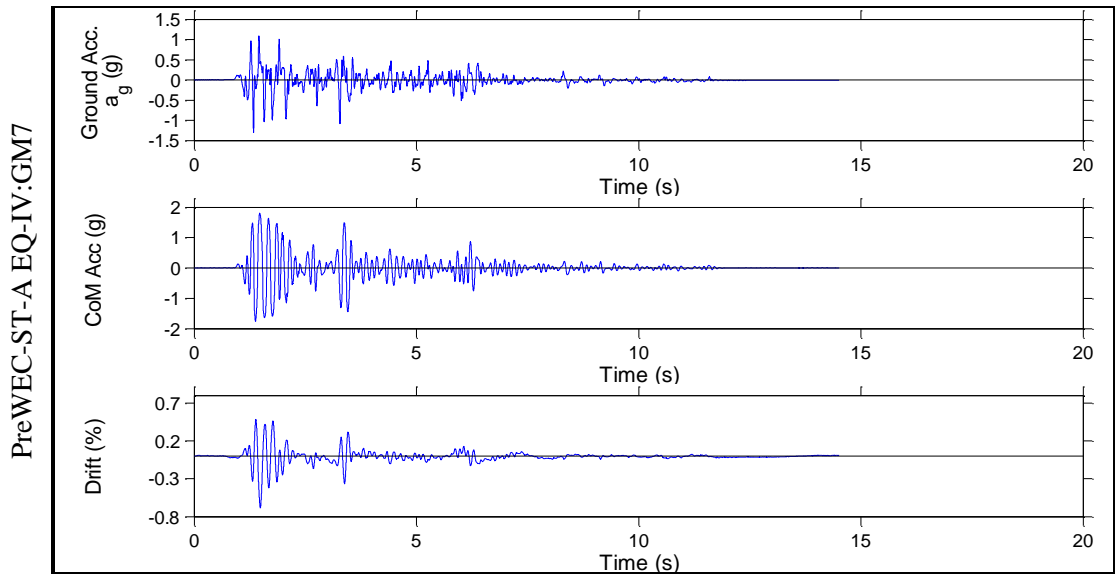


Figure E.34 – Shake table results for PreWEC-ST-A, EQ-IV: GM7

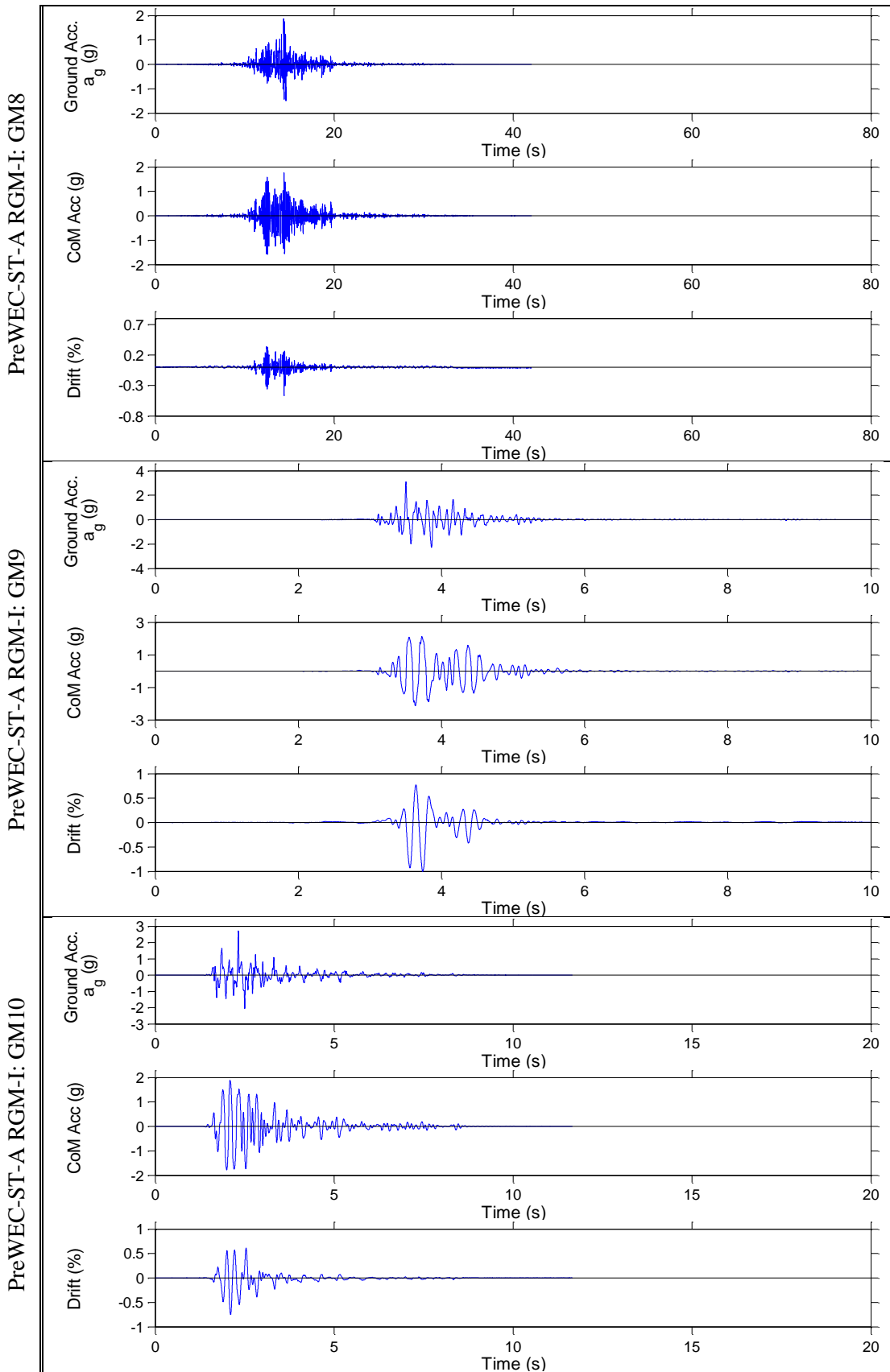


Figure E.35 – Shake table results for PreWEC-ST-A, RGM-I: GM8-10

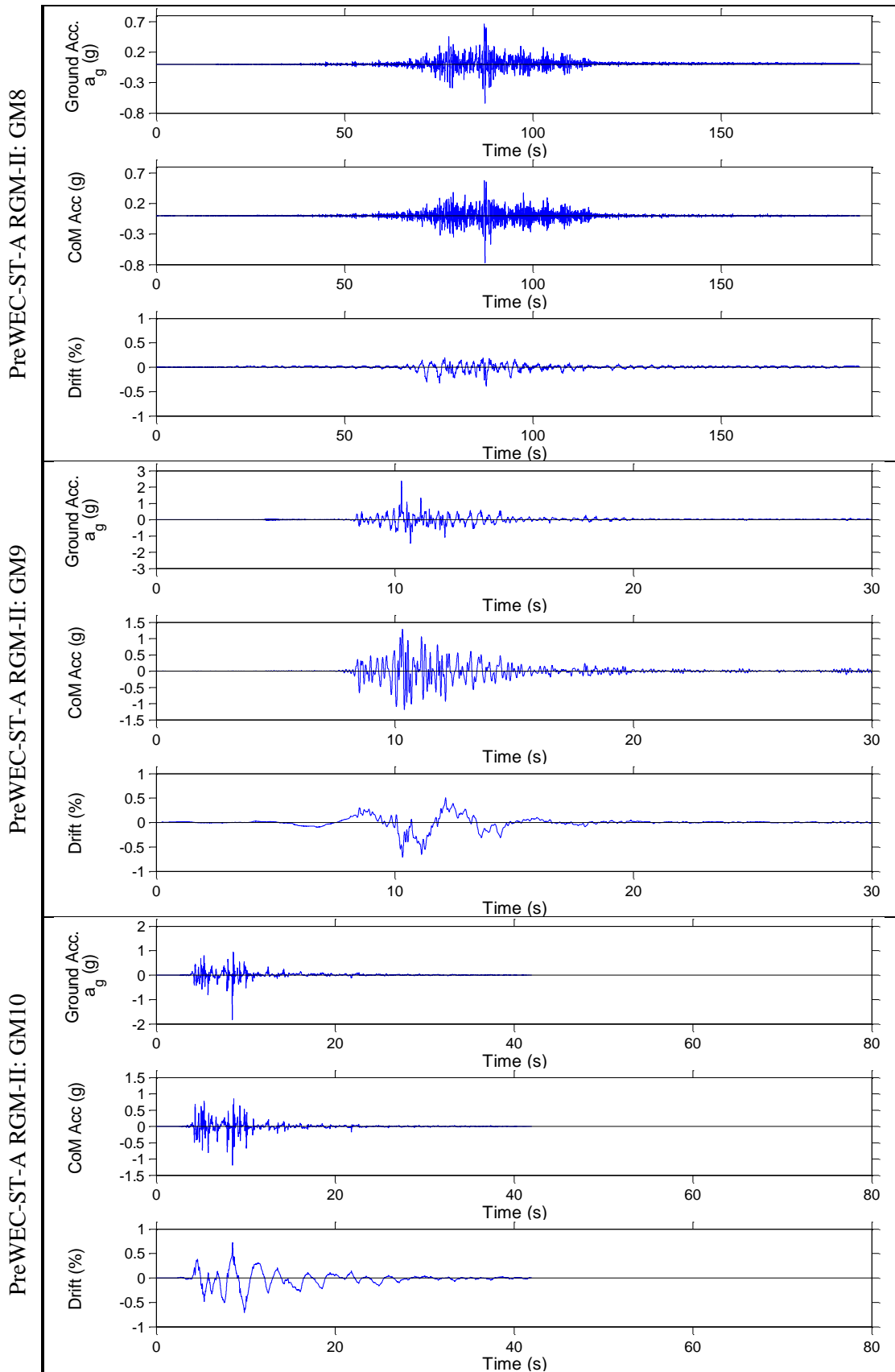


Figure E.36 – Shake table results for PreWEC-ST-A, RGM-II: GM8-10

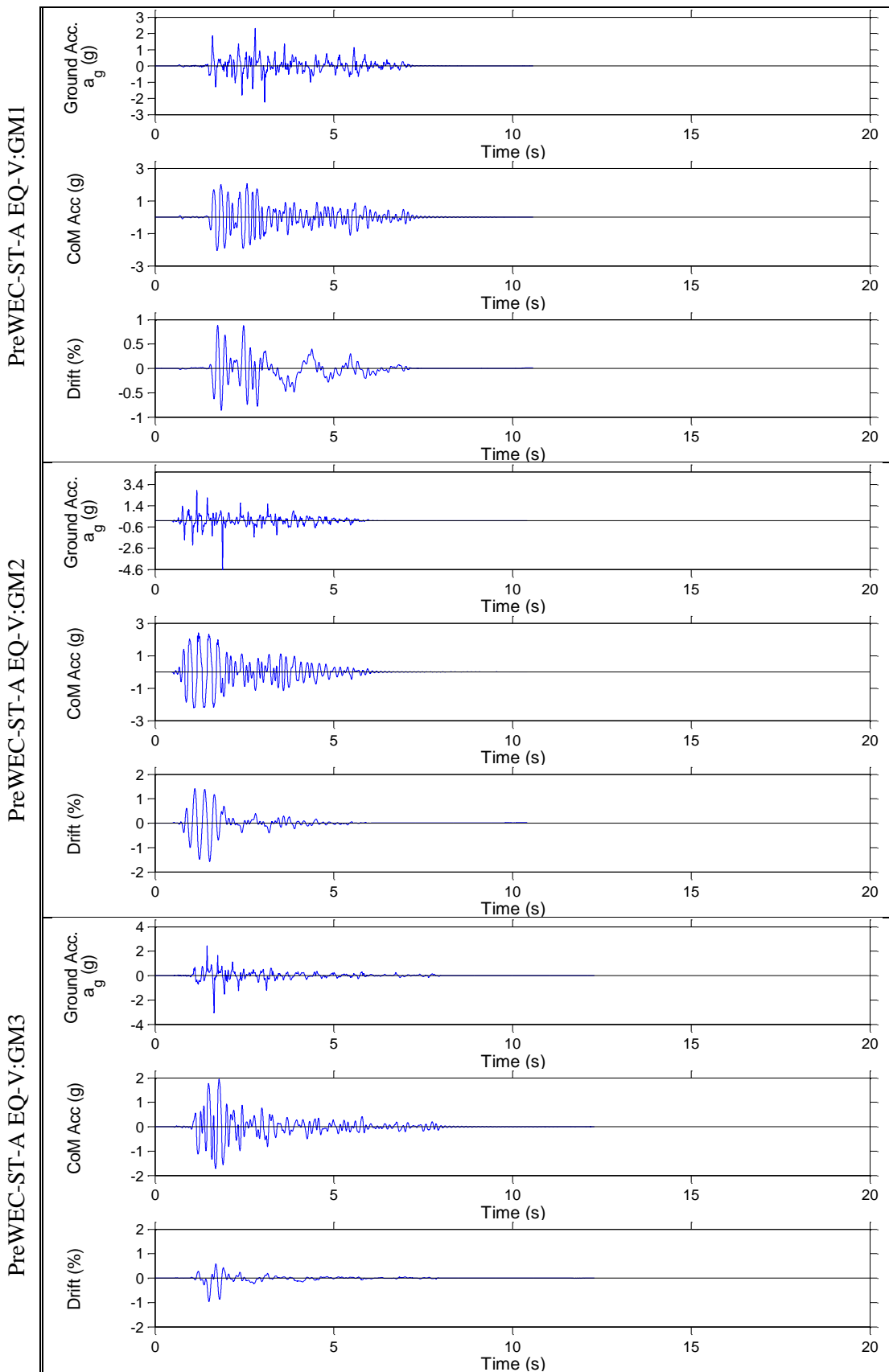


Figure E.37 – Shake table results for PreWEC-ST-A, EQ-V: GM1-3

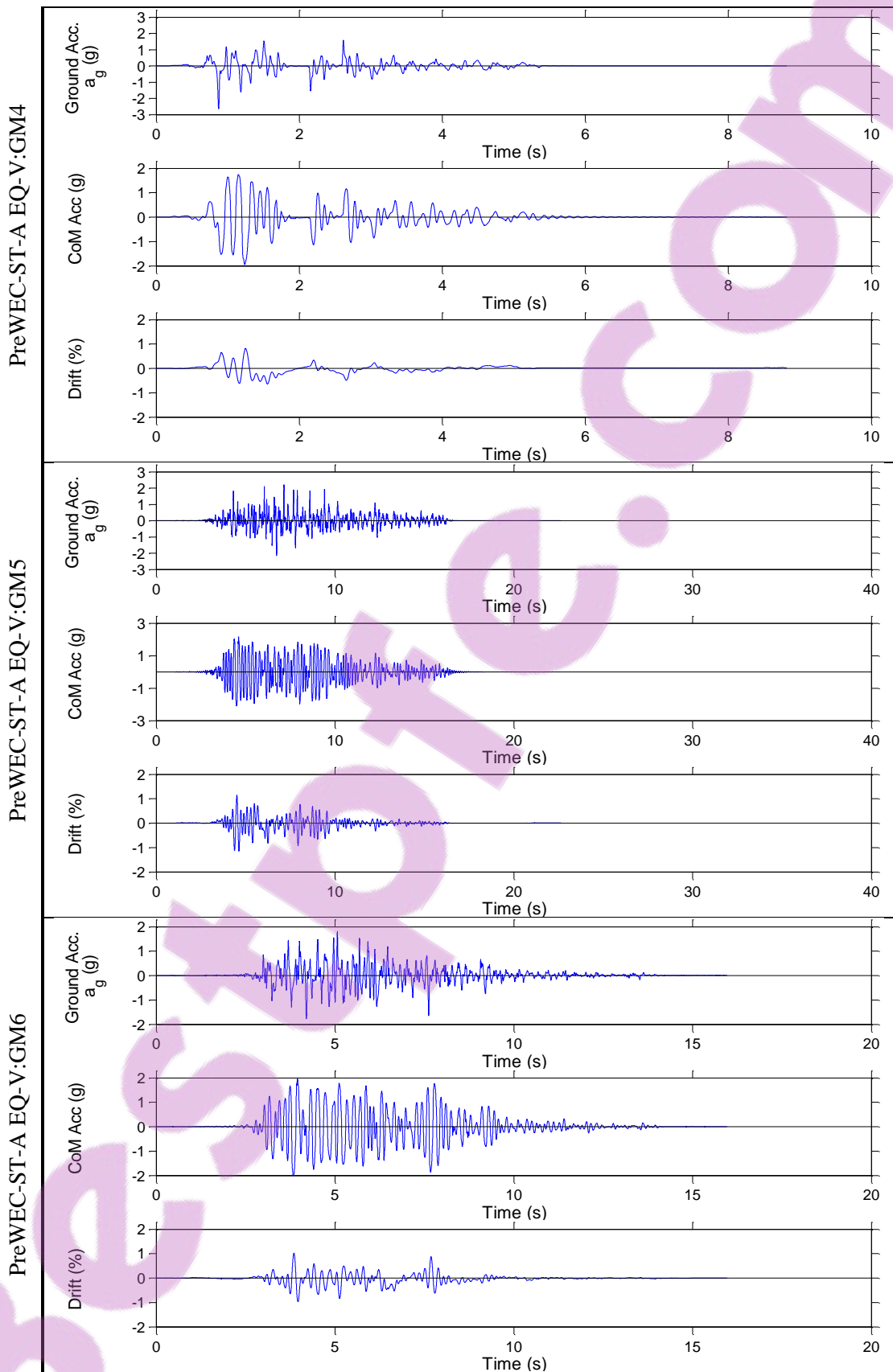


Figure E.38 – Shake table results for PreWEC-ST-A, EQ-V: GM4-6

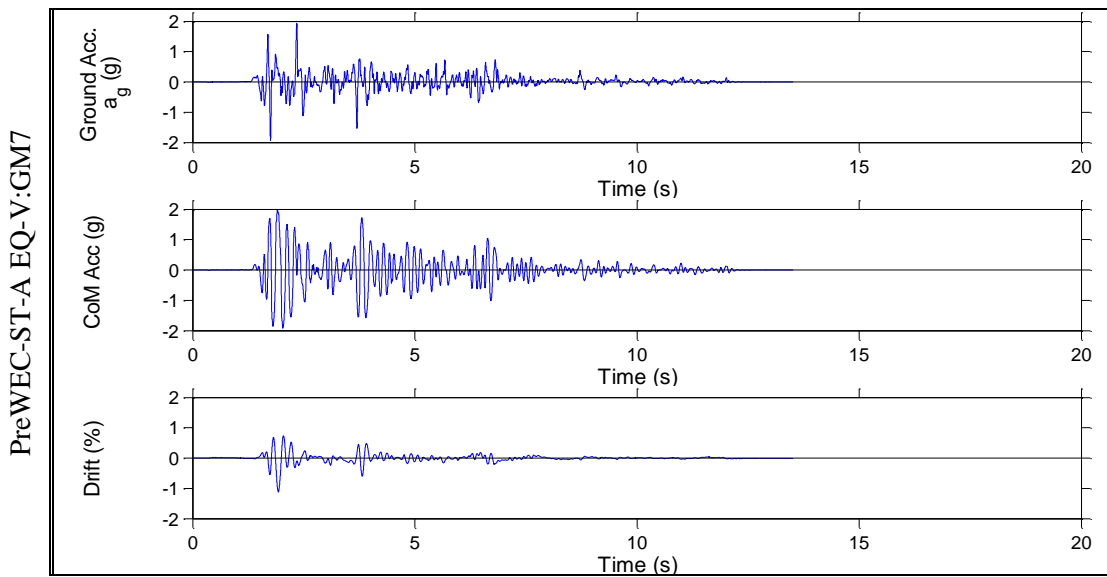


Figure E.39 – Shake table results for PreWEC-ST-A, EQ-V: GM7

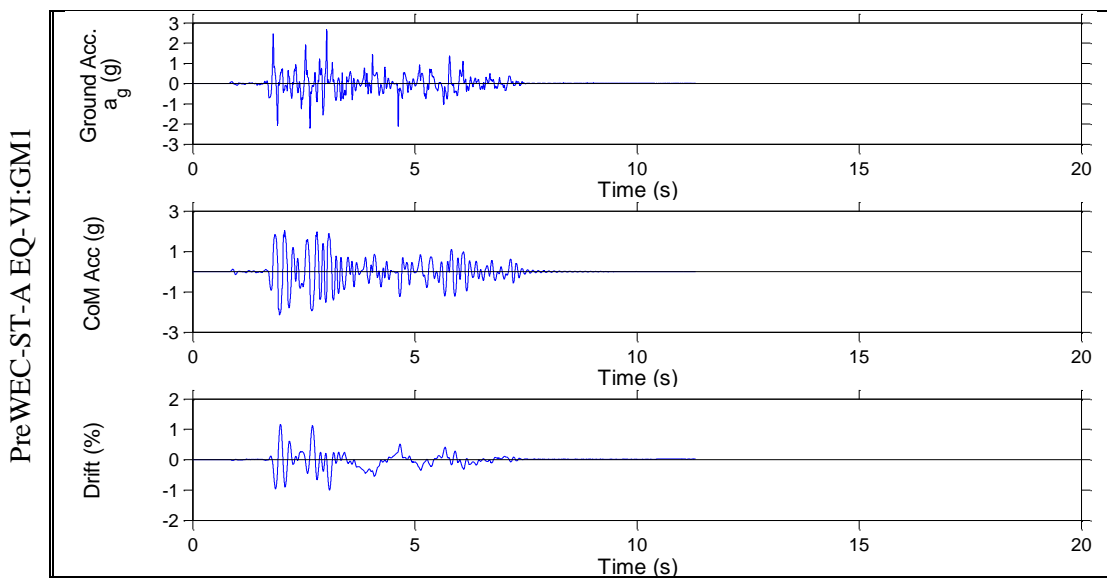


Figure E.40 – Shake table results for PreWEC-ST-A, EQ-VI: GM1

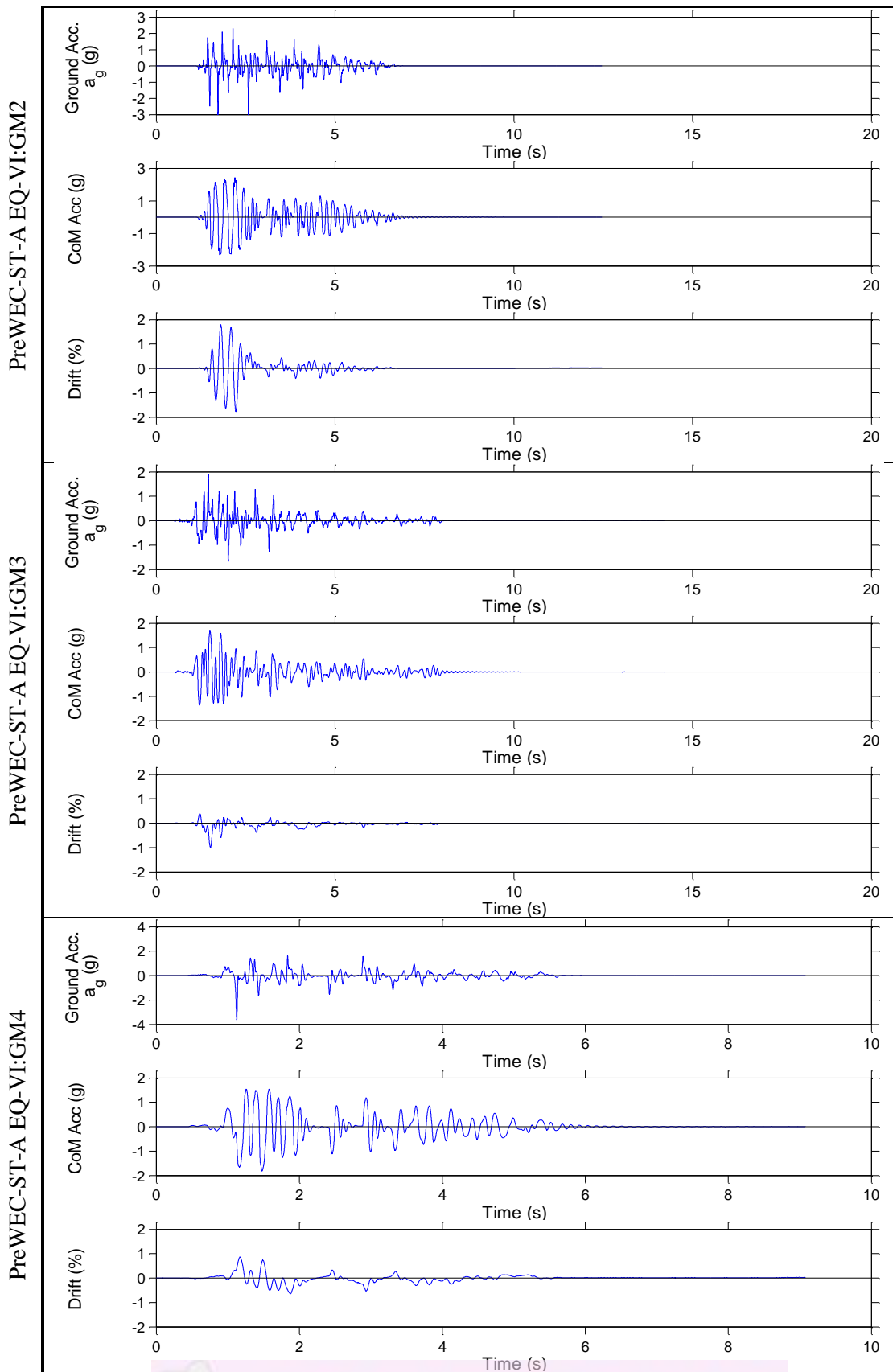


Figure E.41 – Shake table results for PreWEC-ST-A, EQ-VI: GM2-4

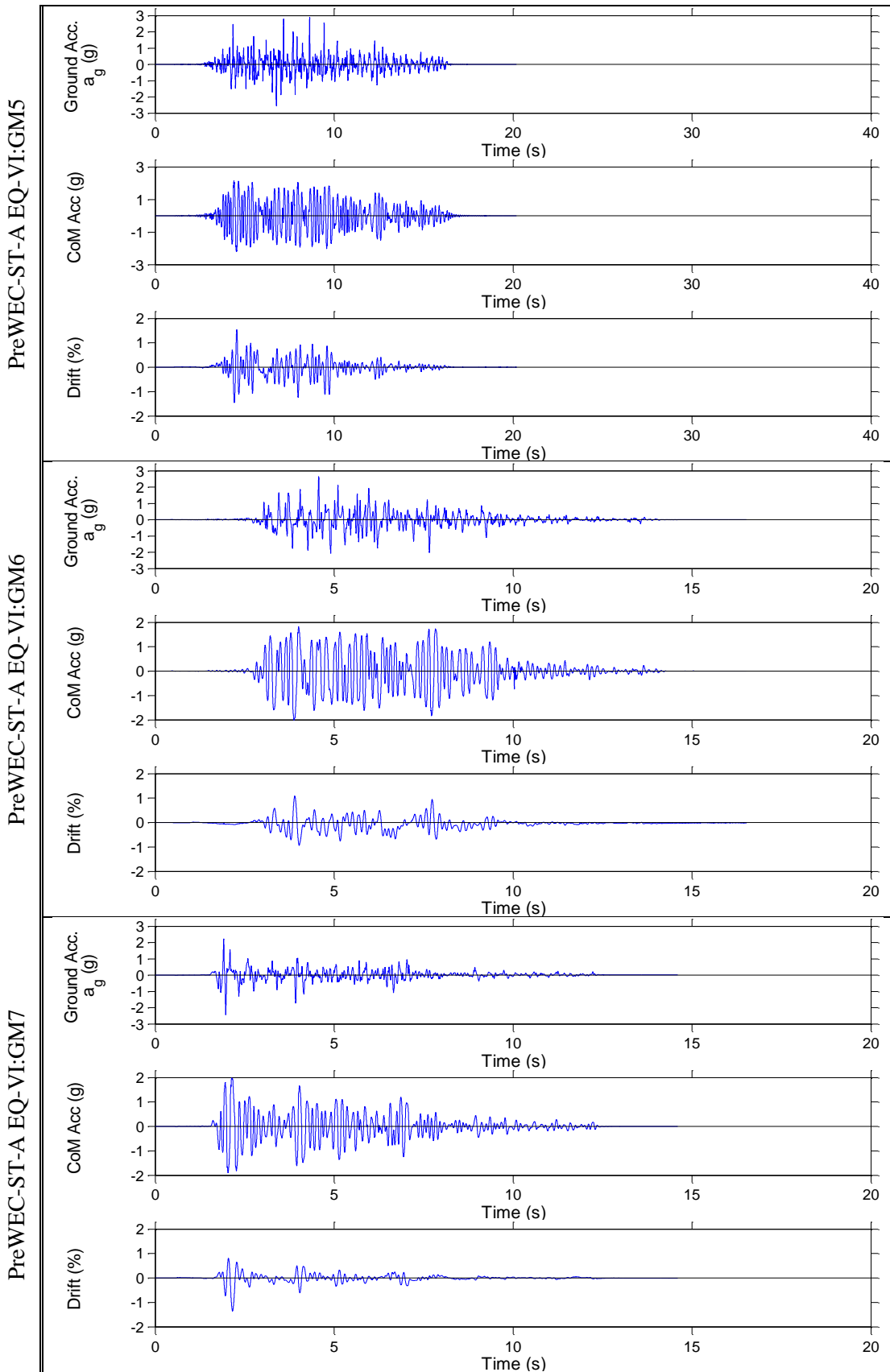


Figure E.42 – Shake table results for PreWEC-ST-A, EQ-VI: GM6-7

E.6.3 PreWEC-ST-B

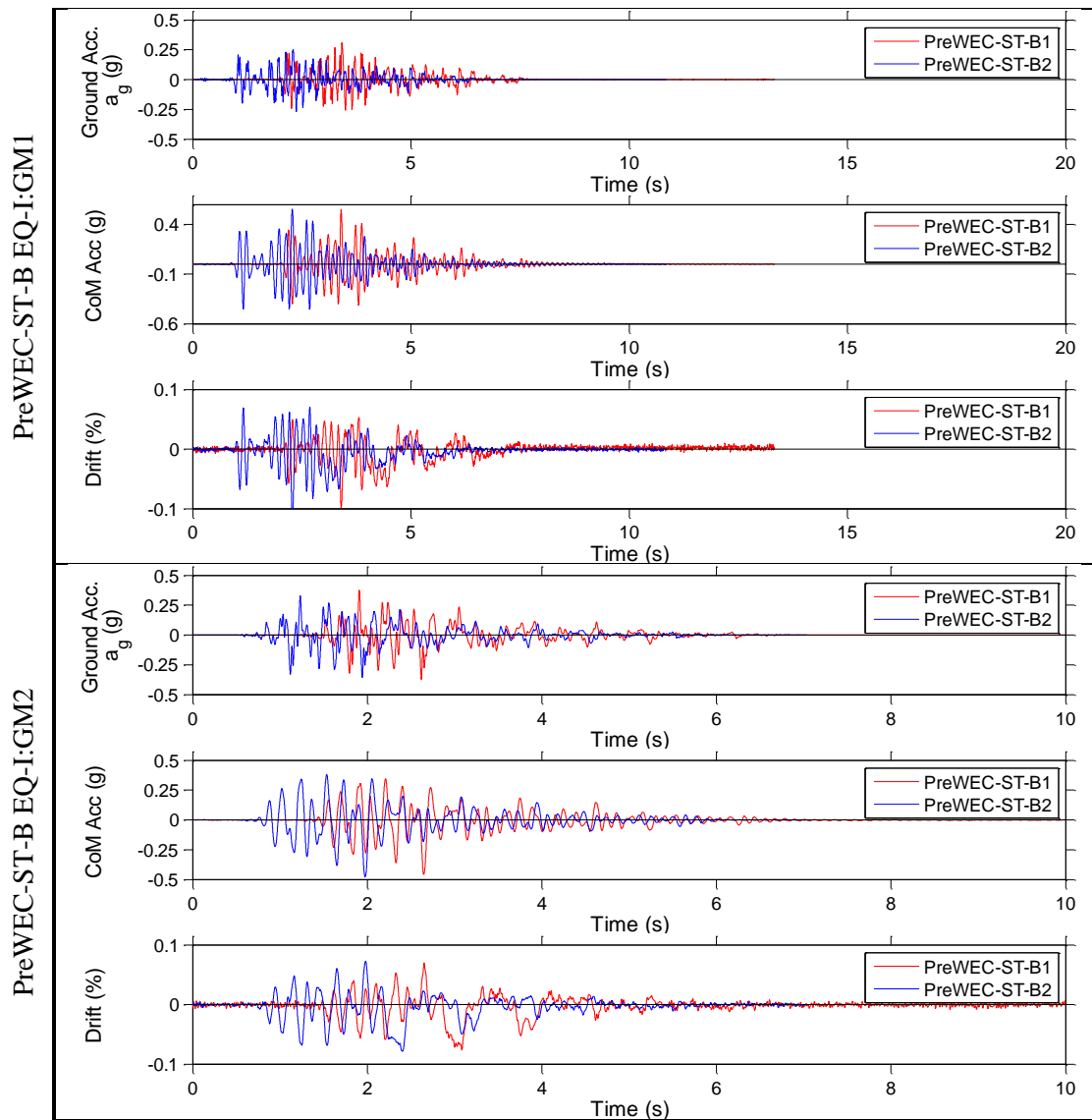


Figure E.43 – Shake table results for PreWEC-ST-B, EQ-I: GM1-2

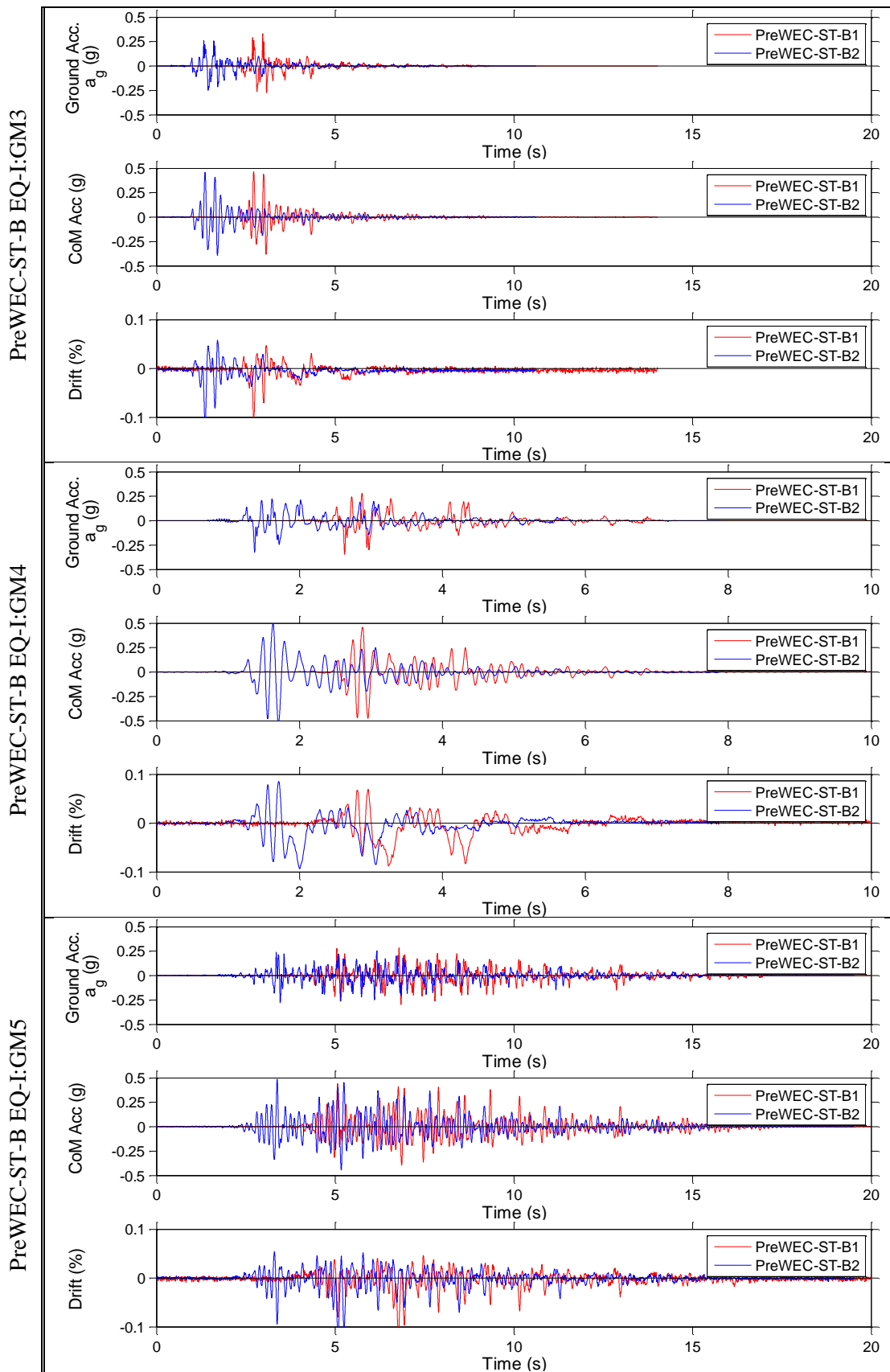


Figure E.44 – Shake table results for PreWEC-ST-B, EQ-I: GM3-5

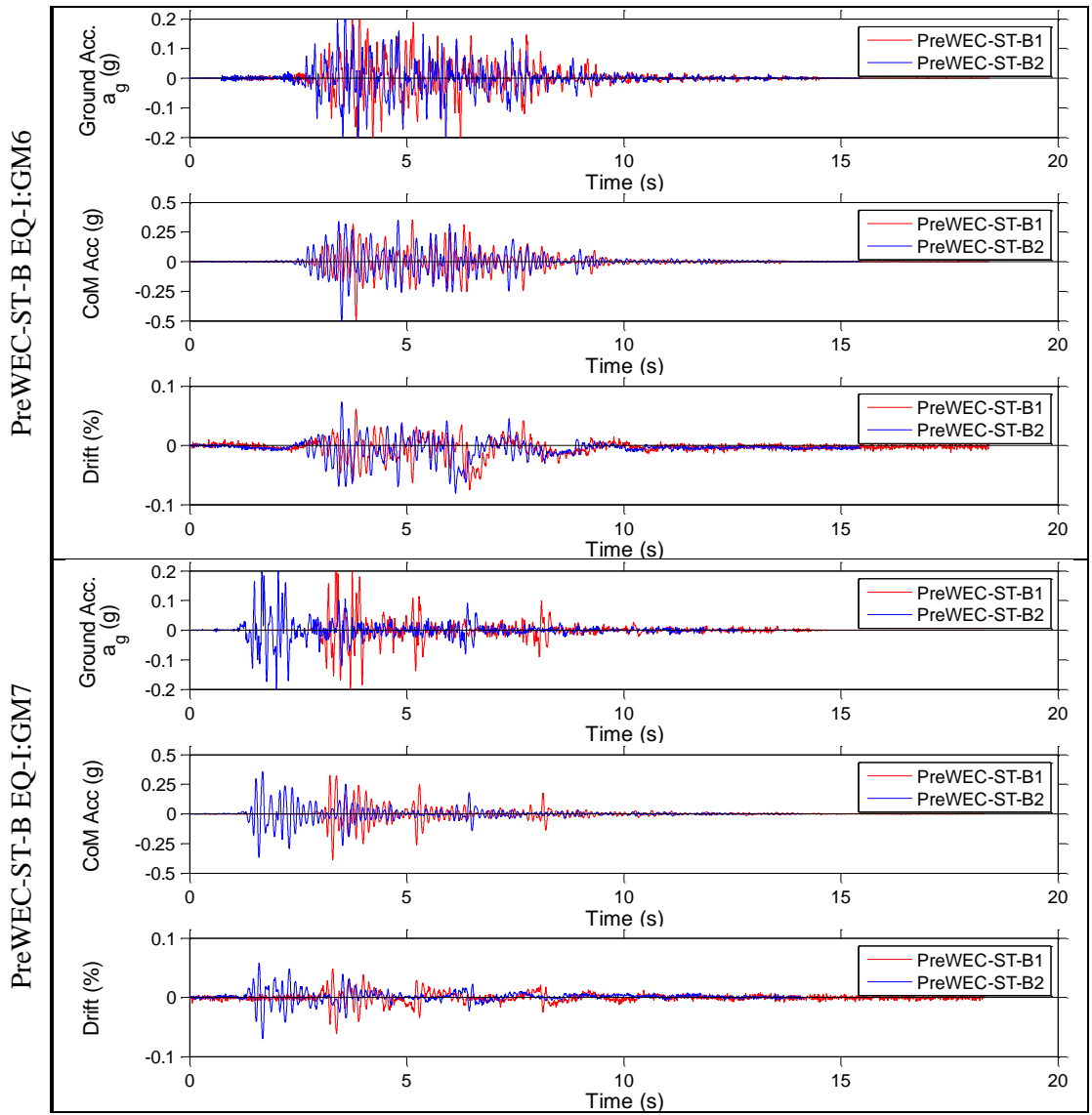


Figure E.45 – Shake table results for PreWEC-ST-B, EQ-I: GM6-7

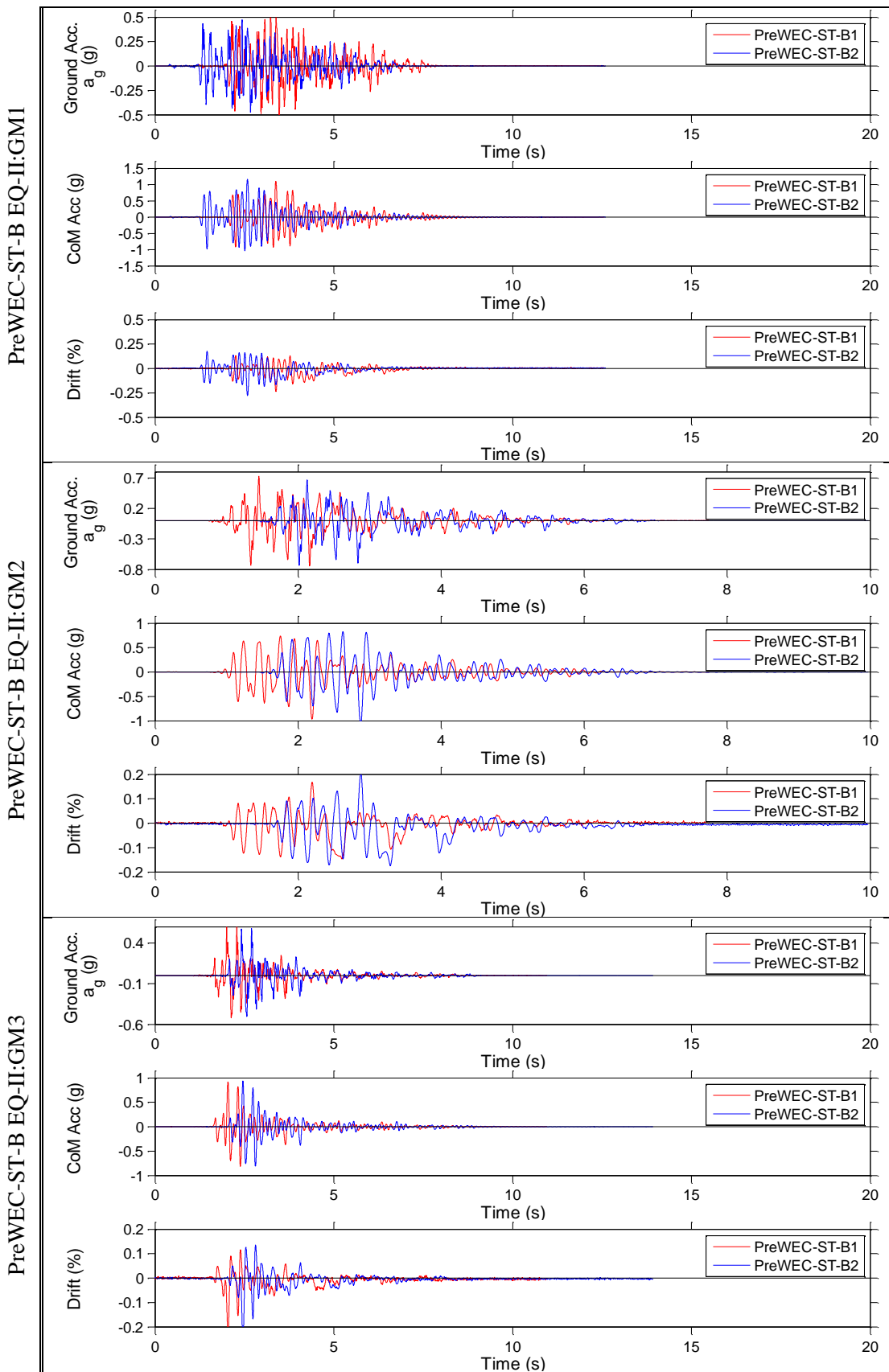


Figure E.46 – Shake table results for PreWEC-ST-B, EQ-II: GM1-3

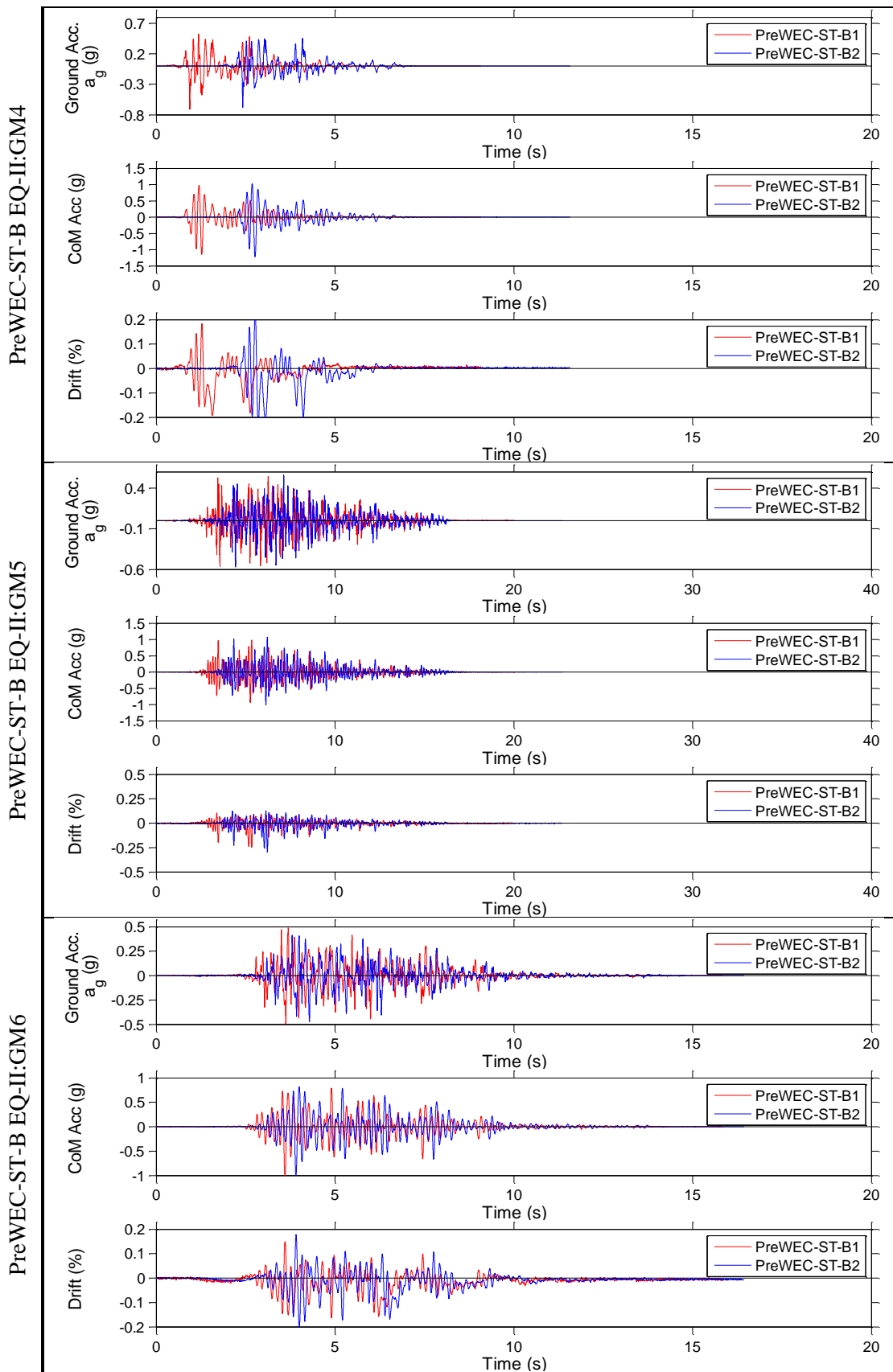


Figure E.47 – Shake table results for PreWEC-ST-B, EQ-II: GM4-6

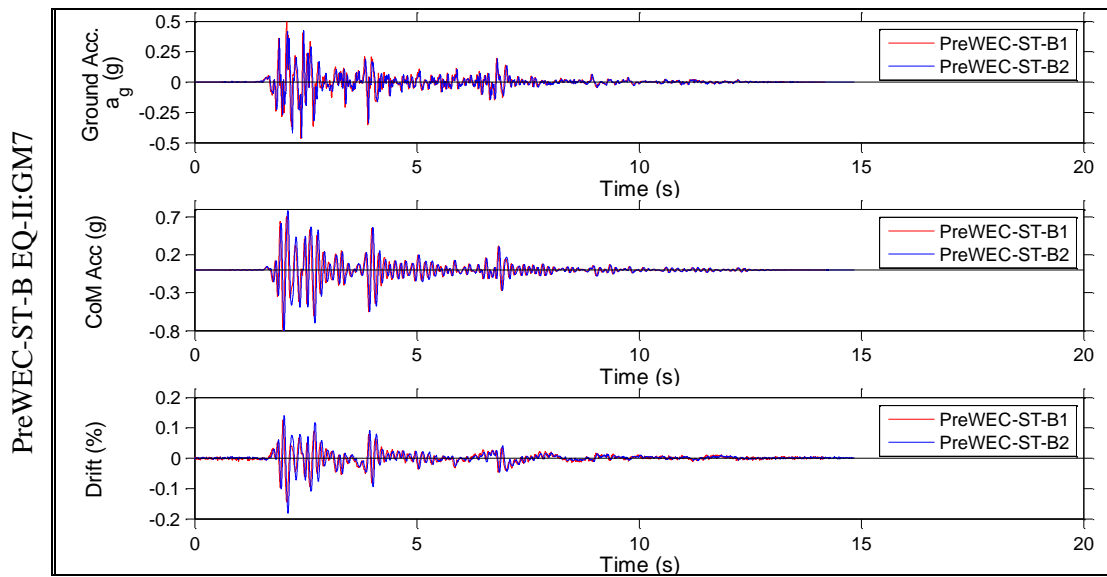


Figure E.48 – Shake table results for PreWEC-ST-B, EQ-II: GM7

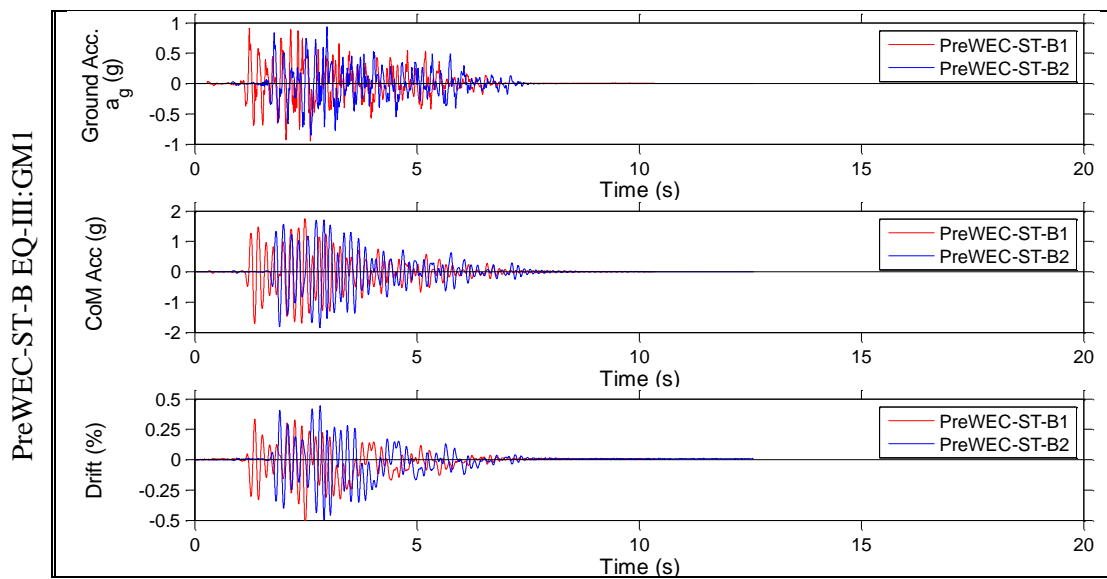


Figure E.49 – Shake table results for PreWEC-ST-B, EQ-III: GM1

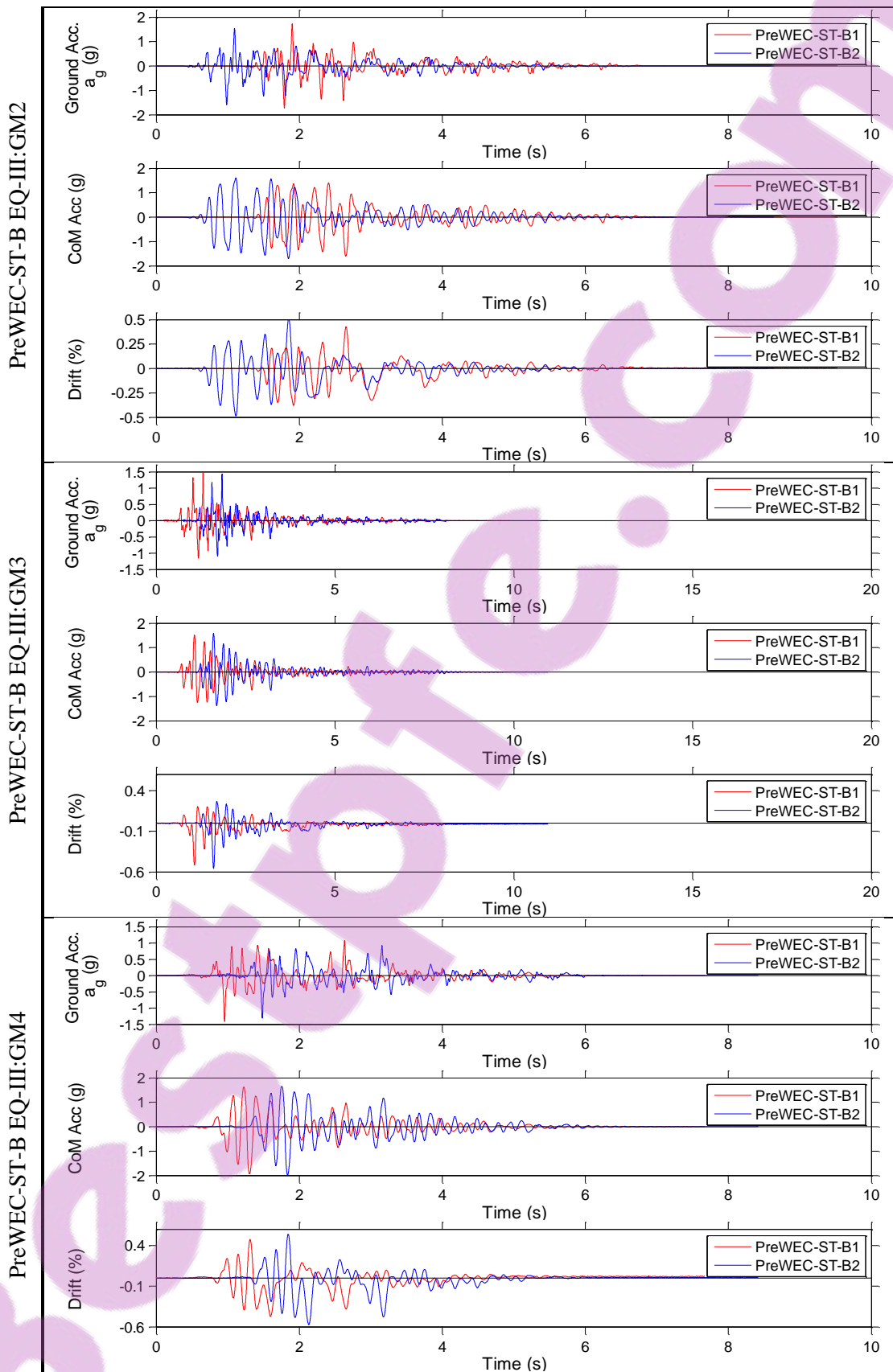


Figure E.50 – Shake table results for PreWEC-ST-B, EQ-II: GM2-4

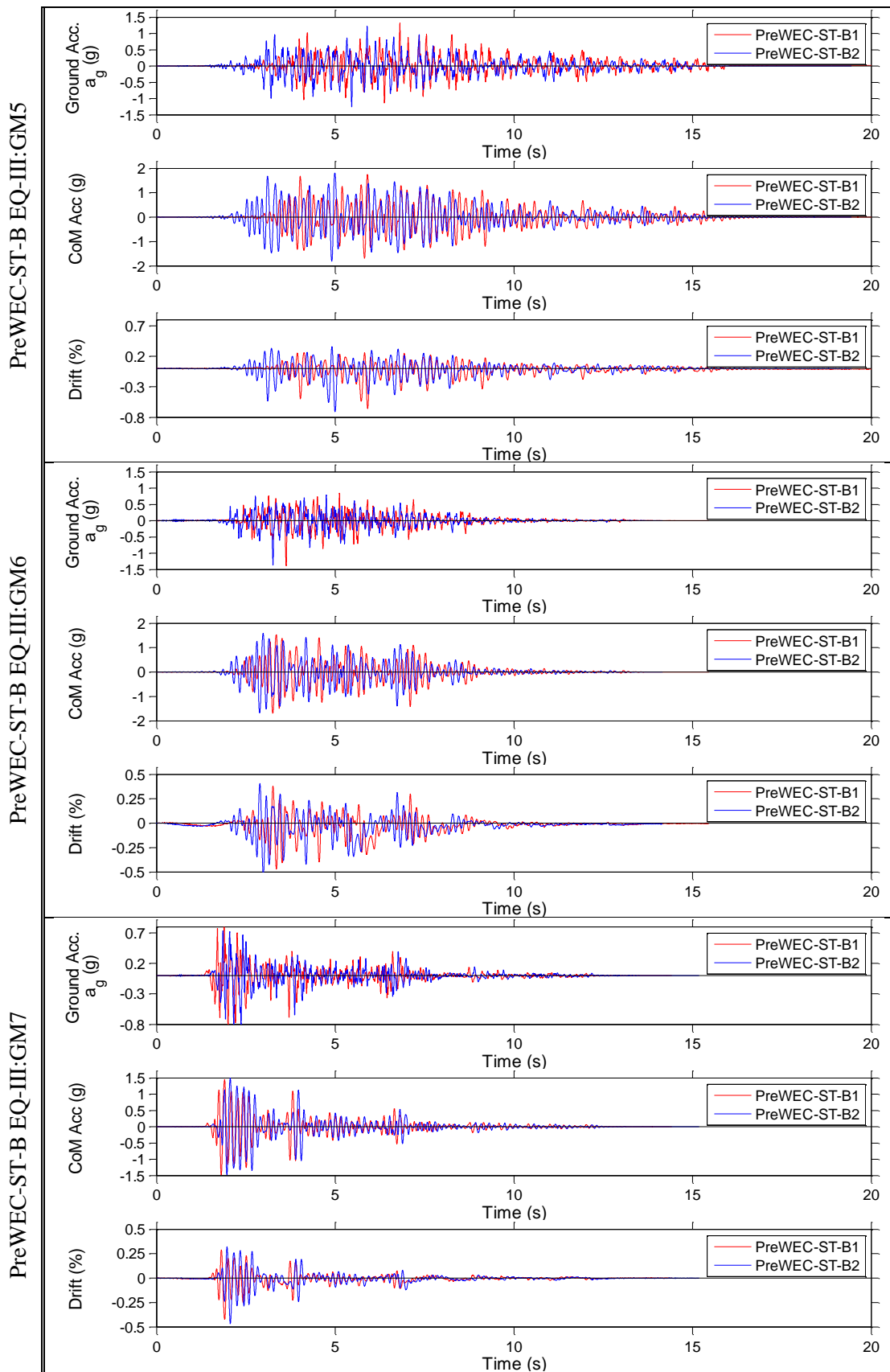


Figure E.51 – Shake table results for PreWEC-ST-B, EQ-III: GM5-7

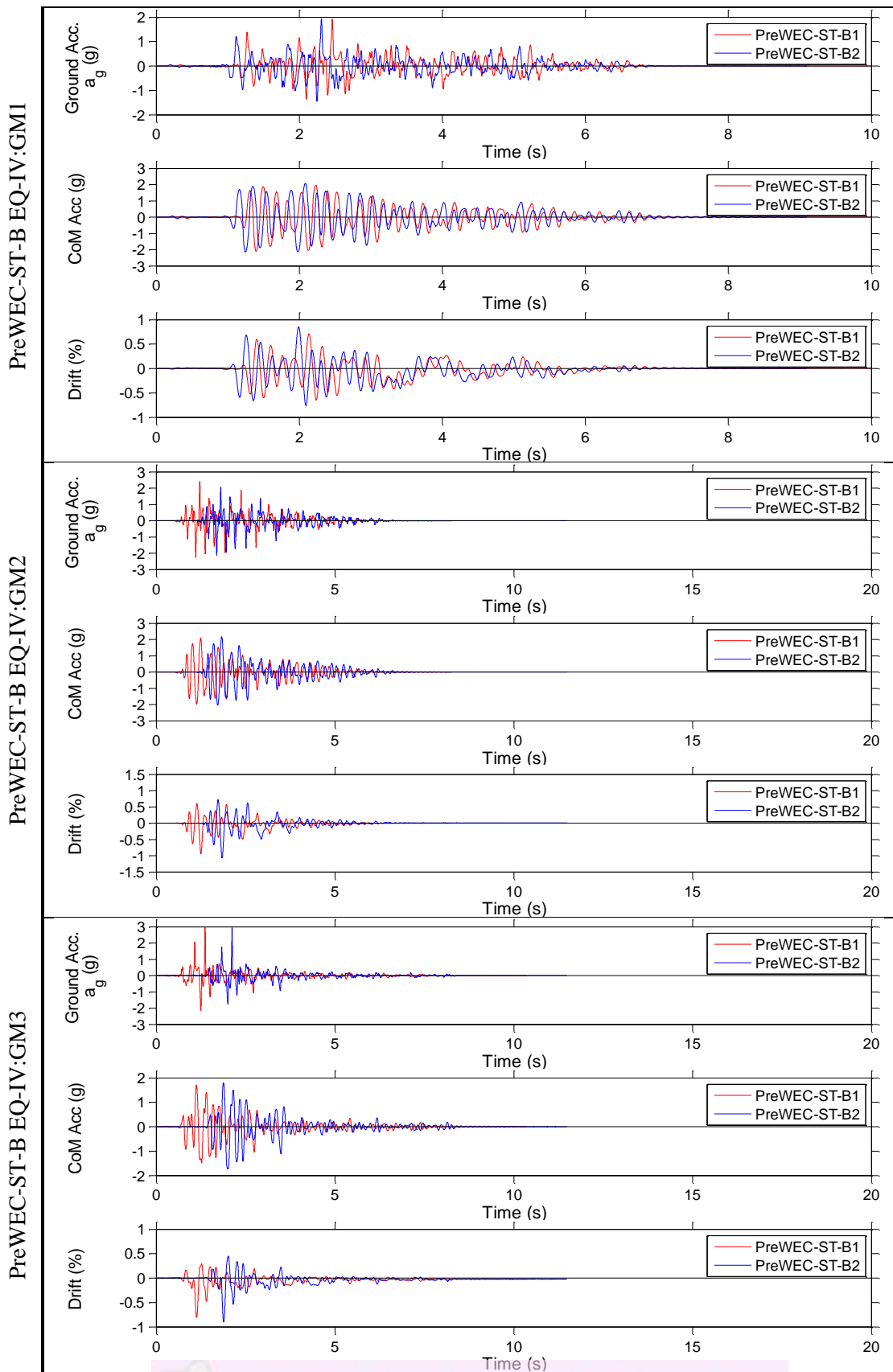


Figure E.52 – Shake table results for PreWEC-ST-B, EQ-IV: GM1-3

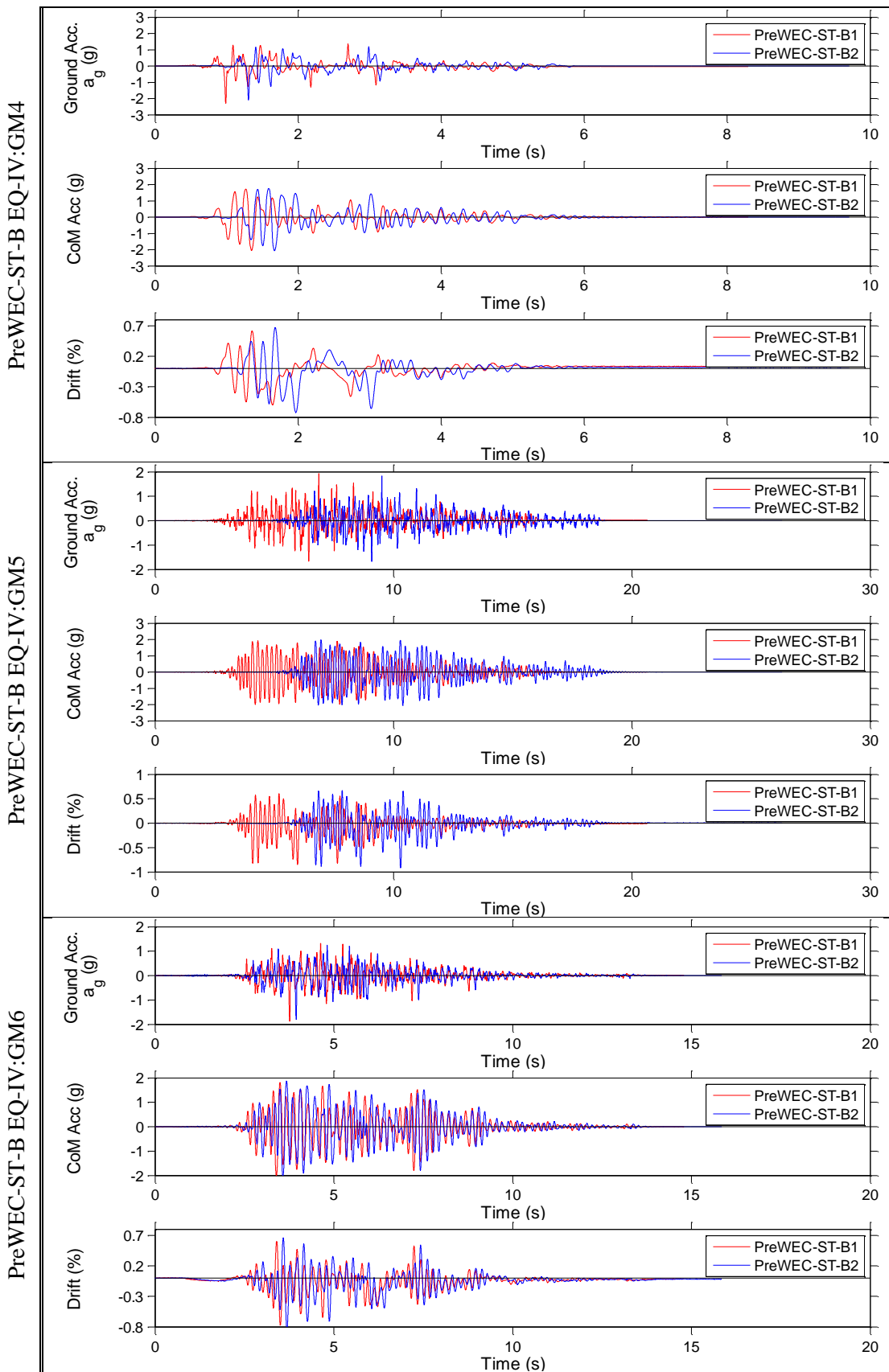


Figure E.53 – Shake table results for PreWEC-ST-B, EQ-IV: GM4-6

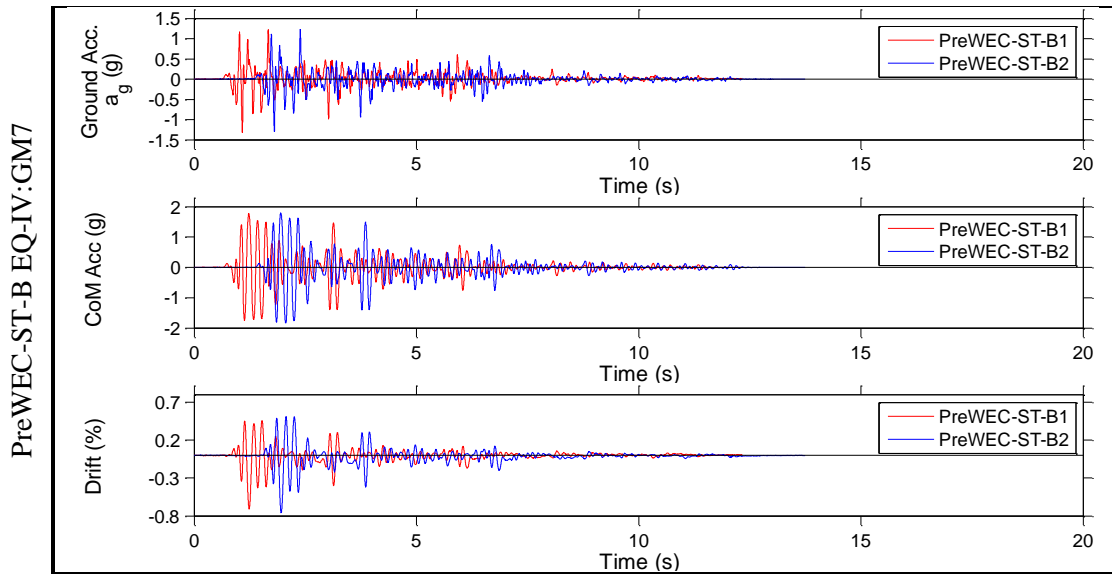


Figure E.54 – Shake table results for PreWEC-ST-B, EQ-IV: GM7

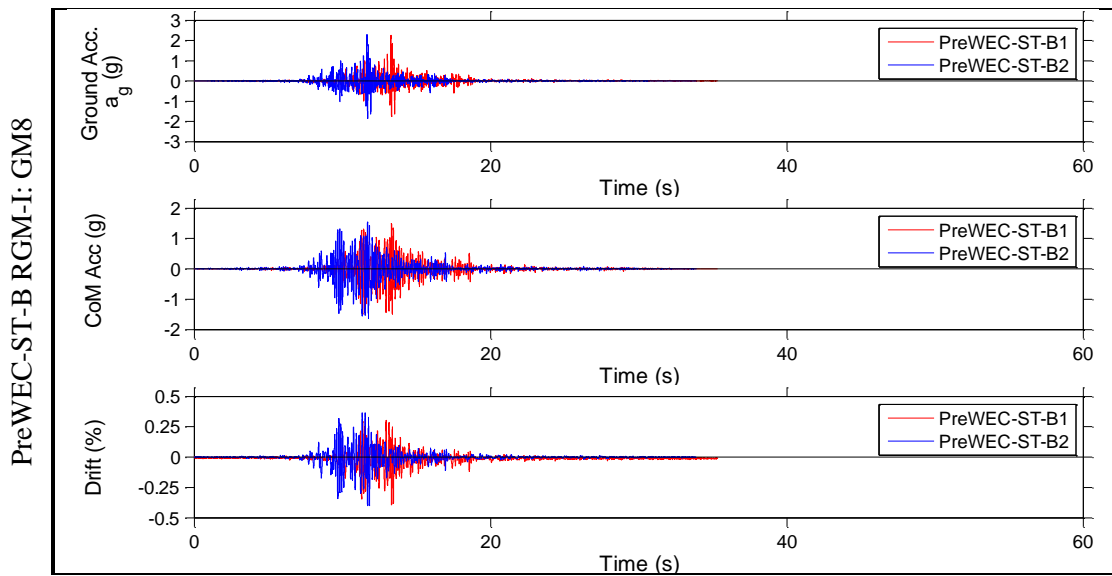


Figure E.55 – Shake table results for PreWEC-ST-B, RGM-I: GM8

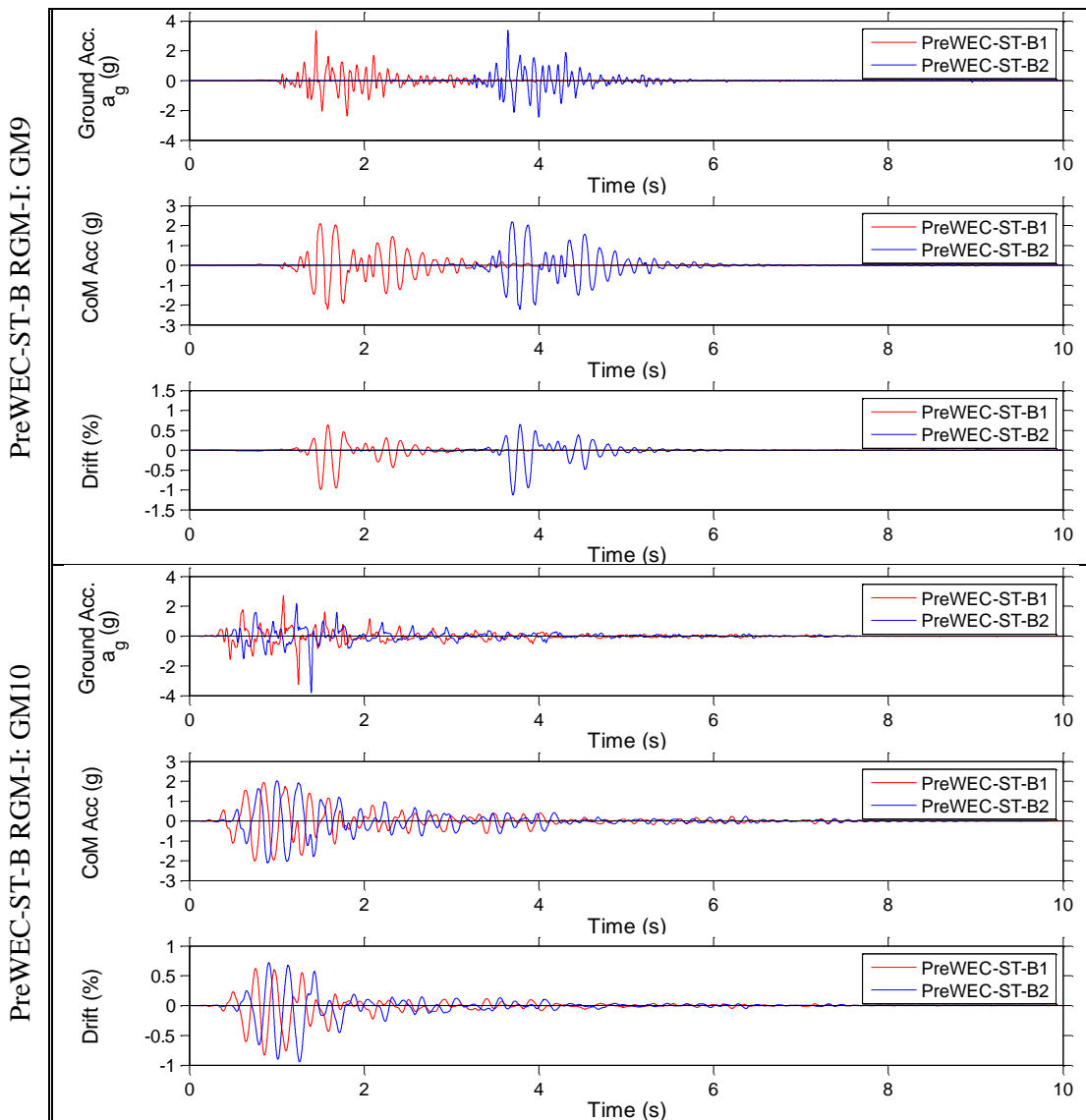


Figure E.56 – Shake table results for PreWEC-ST-B, RGM-I: GM9-10

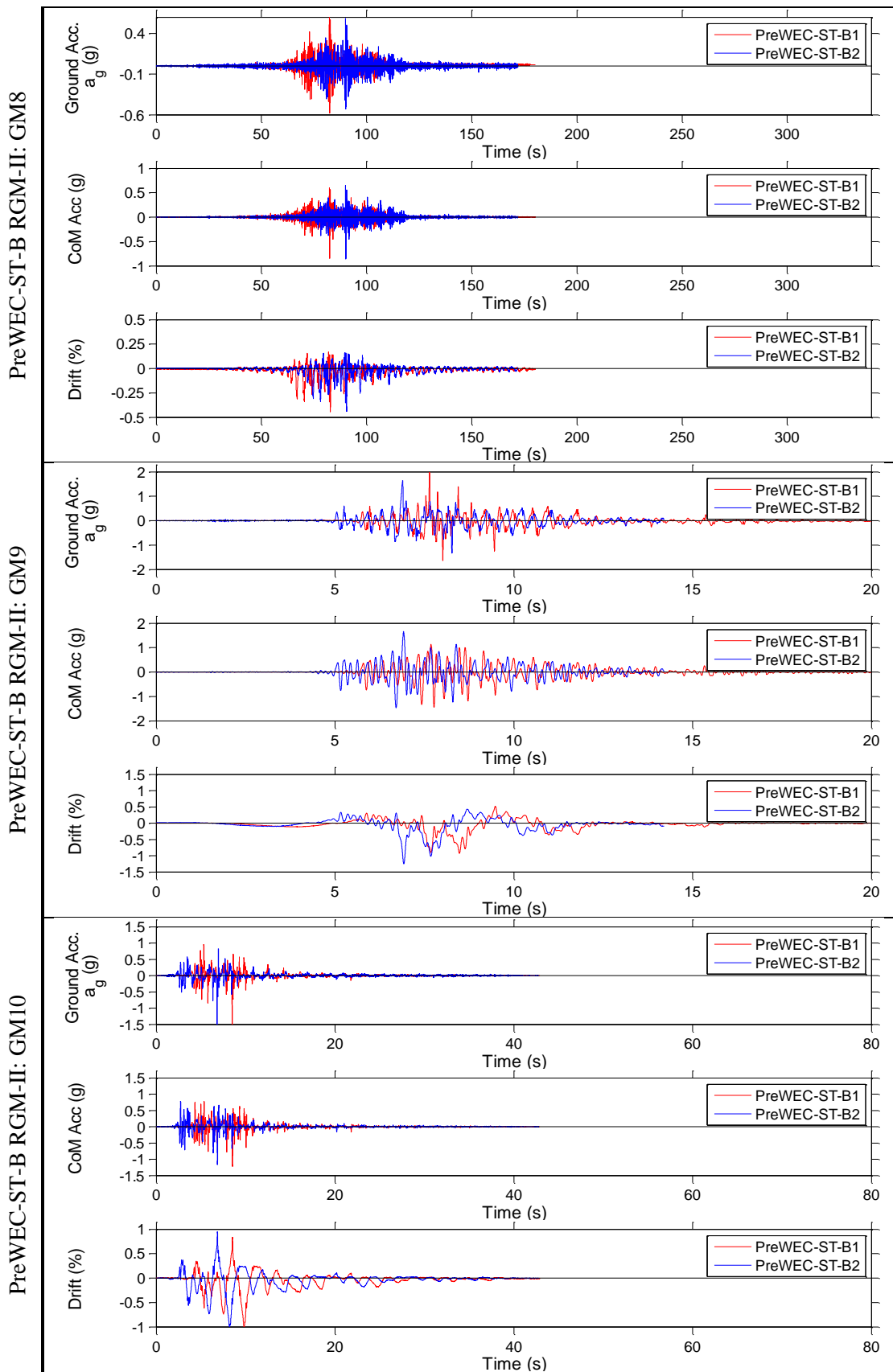


Figure E.57 – Shake table results for PreWEC-ST-B, RGM-II: GM8-10

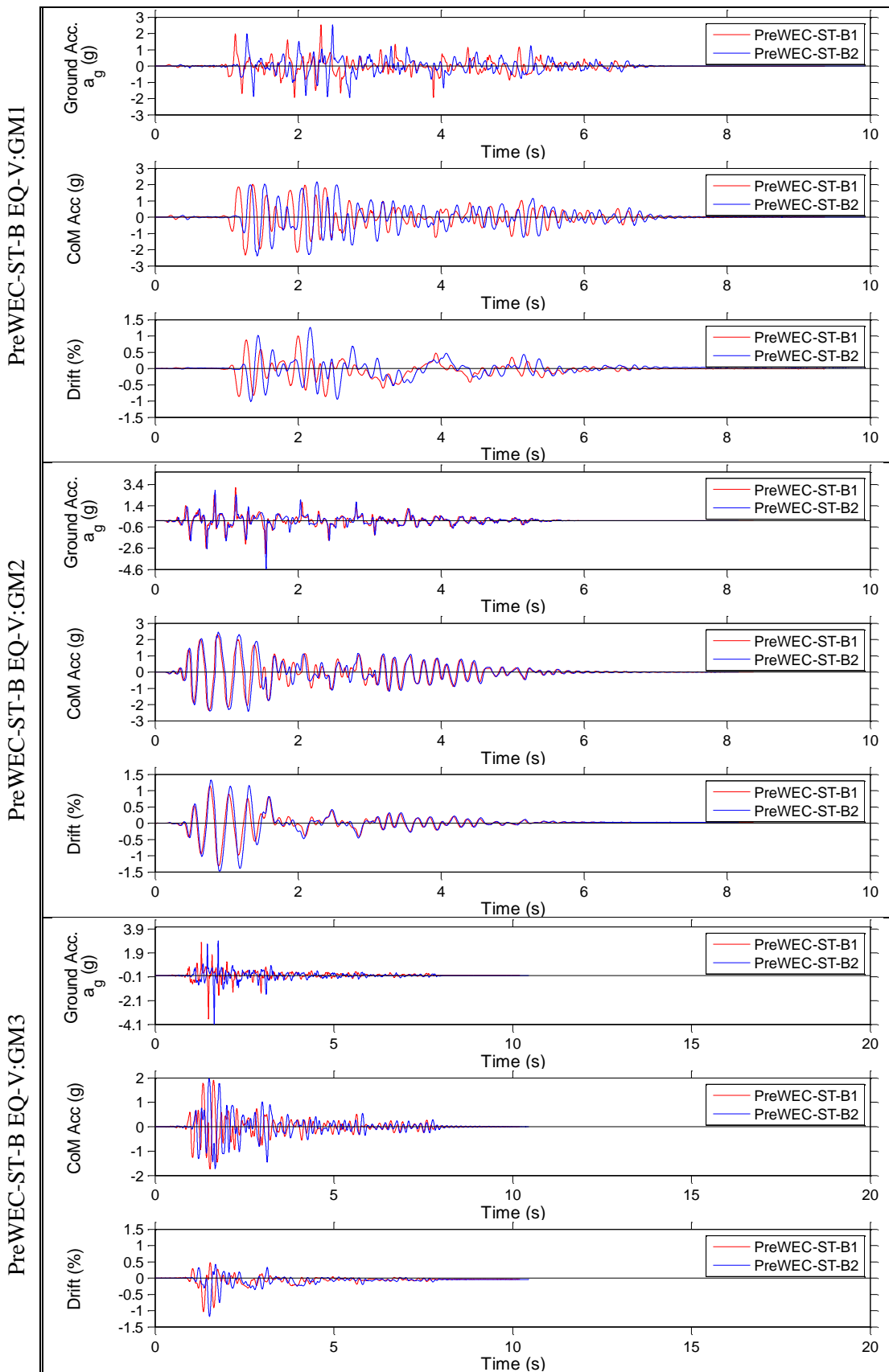


Figure E.58 – Shake table results for PreWEC-ST-B, EQ-V: GM1-3

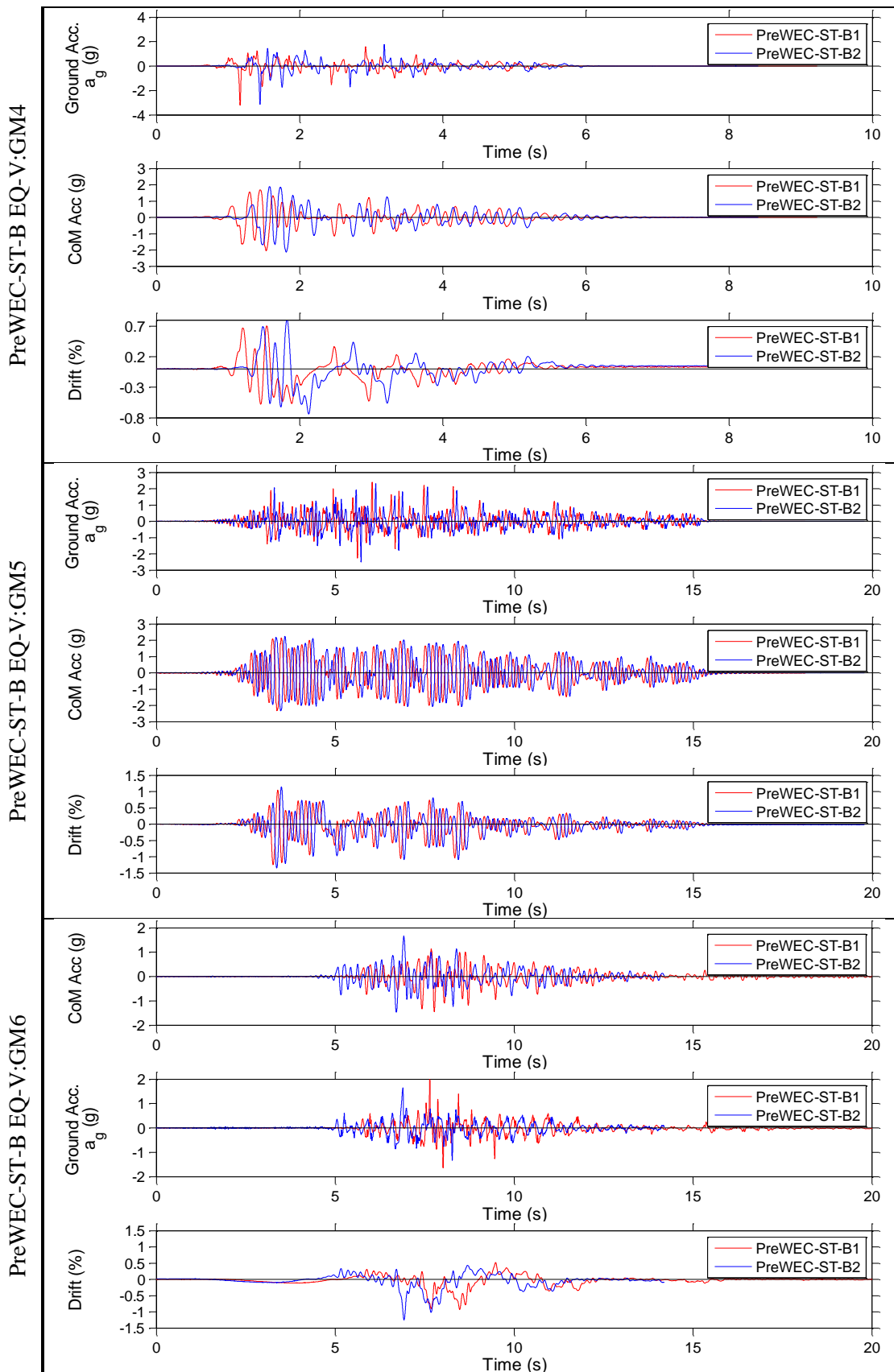


Figure E.59 – Shake table results for PreWEC-ST-B, EQ-V: GM4-6

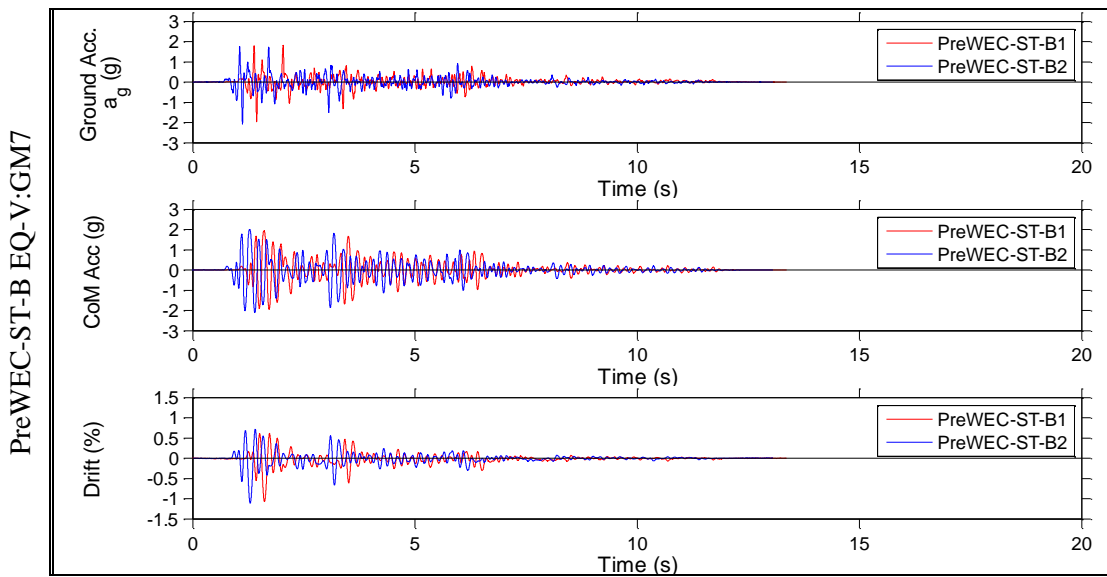


Figure E.60 – Shake table results for PreWEC-ST-B, EQ-V: GM7

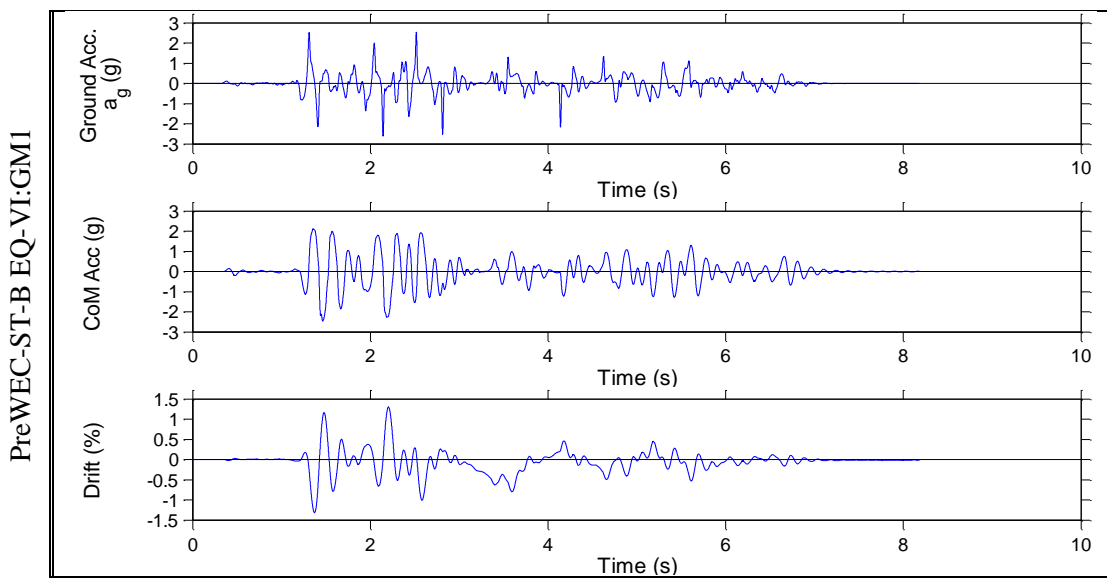


Figure E.61 – Shake table results for PreWEC-ST-B, EQ-VI: GM1

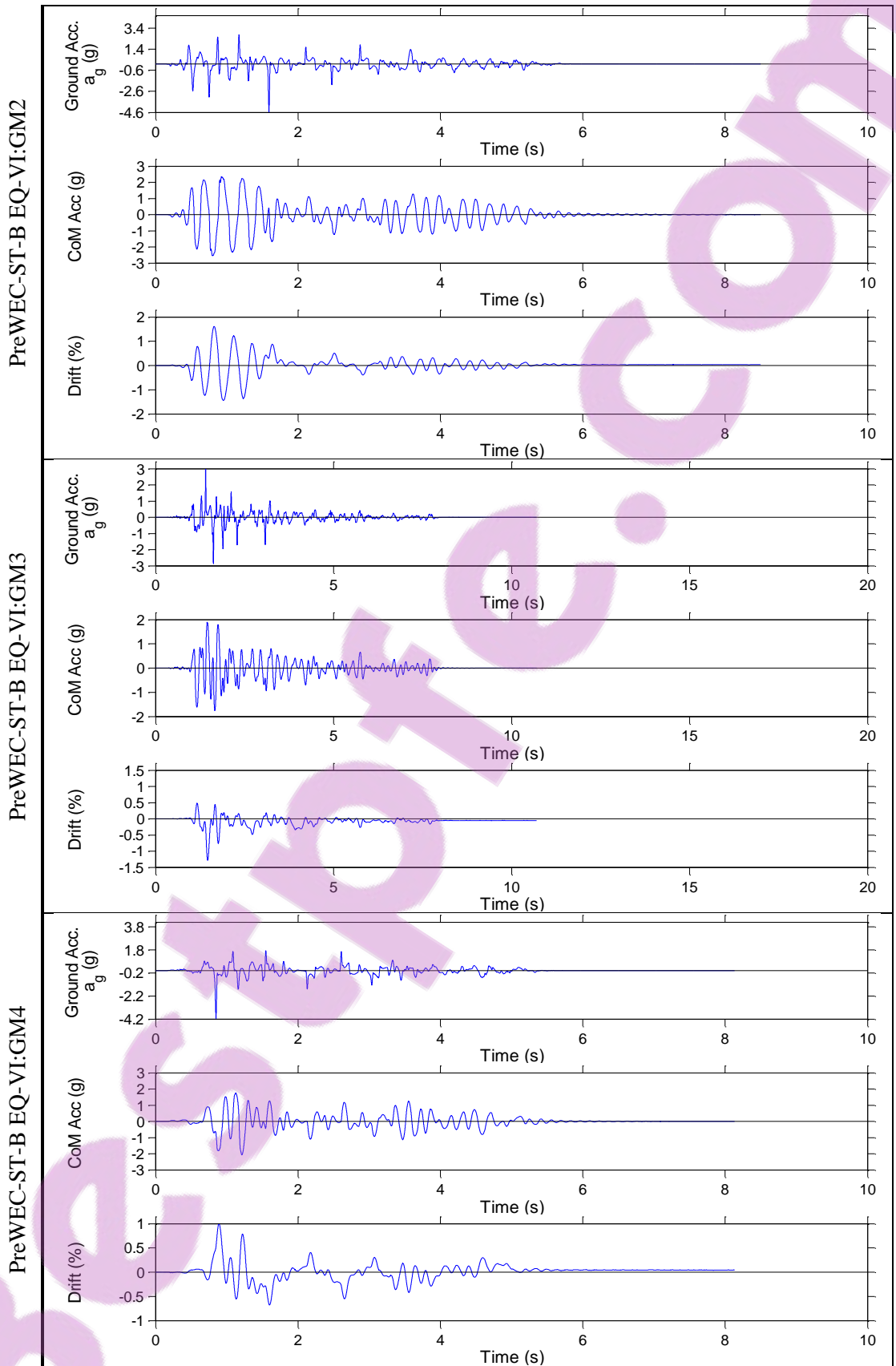


Figure E.62 – Shake table results for PreWEC-ST-B, EQ-VI: GM2-4

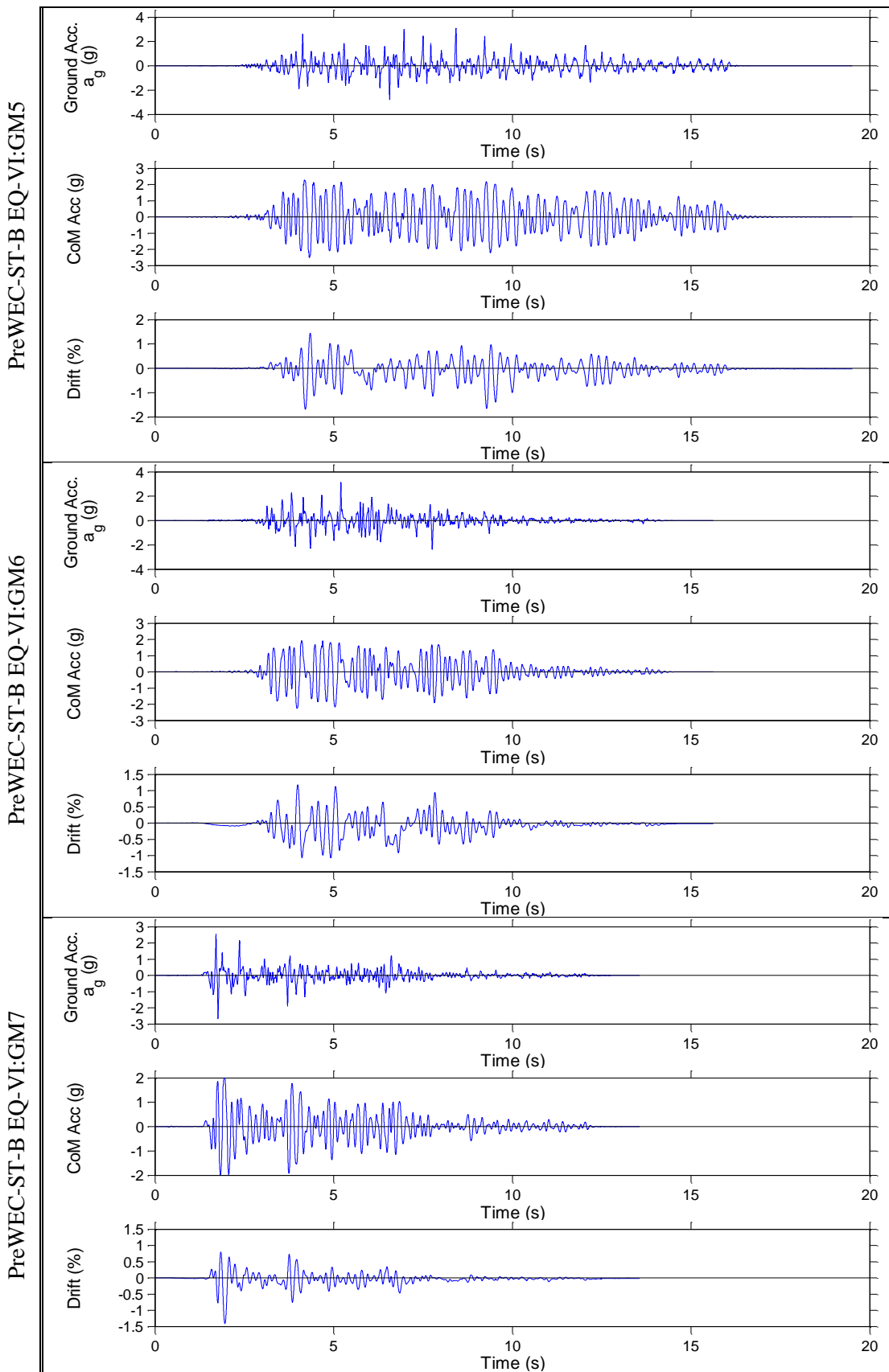


Figure E.63 – Shake table results for PreWEC-ST-B, EQ-VI: GM5-7

REFERENCES

1. Kam, W.Y., S. Pampanin, and K. Elwood, *Seismic performance of reinforced concrete buildings in the 22 February Christchurch (Lyttelton) earthquake*. Bulletin of the New Zealand Society for Earthquake Engineering, 2011. **44**(4): p. 239-278.
2. Sritharan, S., K. Beyer, R.S. Henry, Y.H. Chai, M. Kowalsky, and D. Bull, *Understanding Poor Seismic Performance of Concrete Walls and Design Implications*. Earthquake Spectra, 2014. **30**(1): p. 307-334.
3. Priestley, M.J.N., S.S. Sritharan, J.R. Conley, and S. Pampanin, *Preliminary results and conclusions from the PRESSS five-story precast concrete test building*. PCI Journal, 1999. **44**(6): p. 42-67.
4. Kurama, Y., R. Sause, S. Pessiki, and L.W. Lu, *Lateral load behavior and seismic design of unbonded post-tensioned precast concrete walls*. ACI Structural Journal, 1999. **96**(4): p. 622-632.
5. Erkmen, B. and A.E. Schultz, *Self-centering behavior of unbonded, post-tensioned precast concrete shear walls*. Journal of Earthquake Engineering, 2009. **13**(7): p. 1047-1064.
6. Stavridis, A., I. Koutromanos, and P.B. Shing, *Shake-table tests of a three-story reinforced concrete frame with masonry infill walls*. Earthquake Engineering and Structural Dynamics, 2012. **41**(6): p. 1089-1108.
7. Henry, R.S., N.J. Brooke, S. Sritharan, and J.M. Ingham, *Defining concrete compressive strain in unbonded post-tensioned walls*. ACI Structural Journal, 2012. **109**(1): p. 101-112.
8. Holden, T., J. Restrepo, and J.B. Mander, *Seismic performance of precast reinforced and prestressed concrete walls*. Journal of Structural Engineering, 2003. **129**(3): p. 286-296.
9. Restrepo, J.I. and A. Rahman, *Seismic performance of self-centering structural walls incorporating energy dissipators*. Journal of Structural Engineering, 2007. **133**(11): p. 1560-1570.
10. Smith, B.J., Y.C. Kurama, and M.J. McGinnis, *Design and measured behavior of a hybrid precast concrete wall specimen for seismic regions*. Journal of Structural Engineering, 2011. **137**(10): p. 1052-1062.

References

11. Smith, B.J. and Y.C. Kurama, *Seismic design guidelines for solid and perforated hybrid precast concrete shear walls*. PCI Journal, 2014. **59**(3): p. 43-59.
12. Smith, B.J. and Y.C. Kurama. *Seismic displacement demands for hybrid precast concrete shear walls*. in *Structures Congress 2013: Bridging Your Passion with Your Profession - Proceedings of the 2013 Structures Congress*. 2013.
13. Marriott, D., *The Development of High-Performance Post-Tensioned Rocking Systems for the Seismic Design of Structures*. 2009, University of Canterbury: Christchurch.
14. Sritharan, S., S. Aaleti, R.S. Henry, K.-Y. Liu, and K.-C. Tsai, *Precast concrete wall with end columns (PreWEC) for earthquake resistant design*. Earthquake Engineering & Structural Dynamics, 2015: p. n/a-n/a.
15. Henry, R.S., S. Aaleti, S. Sritharan, and J.M. Ingham, *Concept and finite-element modeling of new steel shear connectors for self-centering wall Systems*. Journal of Engineering Mechanics, 2010. **136**(2): p. 220-229.
16. ACI Innovation Task Group 5., *Acceptance criteria for special unbonded post-tensioned precast structural walls based on validation testing (ITG 5.1-07)*. 2007, American Concrete Institute: Farmington Hills, Mich.
17. ACI Innovation Task Group 5., *Requirements for design of a special unbonded post-tensioned precast shear wall satisfying ACI ITG-5.1 (ACI ITG-5.2-09) and commentary: an ACI standard*. 2009, Farmington Hills, Mich.: American Concrete Institute. 21 p.
18. New Zealand Standard, *Concrete Structures Standard NZS 3101*. 2006: Wellington, New Zealand.
19. Pampanin, S., D. Marriott, A. Palermo, and New Zealand Concrete Society., *PRESSS design handbook*. 2010, Auckland, N.Z.: NZCS. 1 v. (various pagings).
20. Priestley, M.J.N., G.M. Calvi, and M.J. Kowalsky, *Displacement-based seismic design of structures*. 2007, Pavia: IUSS Press : Fondazione Eucentre. xvii, 721 p.
21. Perez, F.J., S. Pessiki, R. Sause, and L.M. Lu, *Lateral load tests of unbonded post-tensioned precast concrete walls*, in *Large-Scale Structural Testing*, M.A. Issa and Y.L. Mo, Editors. 2003, American Concrete Institute: Farmington Hills. p. 161-182.
22. Perez, F.J., S. Pessiki, and R. Sause, *Experimental lateral load response of unbonded post-tensioned precast concrete walls*. ACI Structural Journal, 2013. **110**(6): p. 1045-1055.
23. Pampanin, S. and M. Nishiyama. *Critical aspects in modelling the seismic behaviour of precast/prestressed concrete building connections and systems*. in *1st fib Congress*. 2002. Osaka, Japan.
24. Shen, Q., Y.C. Kurama, and B.D. Weldon, *Seismic design and analytical modeling of posttensioned hybrid coupled wall subassemblages*. Journal of Structural Engineering, 2006. **132**(7): p. 1030-1040.
25. Kurama, Y.C. and Q. Shen, *Seismic design and response evaluation of unbonded post-tensioned hybrid coupled wall structures*. Earthquake Engineering and Structural Dynamics, 2008. **37**(14): p. 1677-1702.
26. Kurama, Y.C., *Seismic design of unbonded post-tensioned precast concrete walls with supplemental viscous damping*. ACI Structural Journal, 2000. **97**(4): p. 648-658.
27. Kurama, Y., S. Pessiki, R. Sause, L.W. Lu, and M. El-Sheikh, *Analytical modelling and lateral load behavior of unbonded post-tensioned precast concrete walls*. 1996, Department of Civil and Environmental Engineering, Lehigh University: Bethlehem, Pennsylvania.

References

28. Henry, R.S., S. Sritharan, and J.M. Ingham. *Recentering requirements for the seismic design of self-centering systems*. in *Proceedings of the Ninth Pacific Conference on Earthquake Engineering*. 2011. Auckland, New Zealand.
29. Wight, G.D., M.J. Kowalsky, and J.M. Ingham, *Shake table testing of posttensioned concrete masonry walls with openings*. *Journal of Structural Engineering*, 2007. **133**(11): p. 1551-1559.
30. Wight, G.D., J.M. Ingham, and M.J. Kowalsky, *Shaketable testing of rectangular post-tensioned concrete masonry walls*. *ACI Structural Journal*, 2006. **103**(4): p. 587-595.
31. Marriott, D., S. Pampanin, D. Bull, and A. Palermo, *Dynamic testing of precast, post-tensioned rocking wall systems with alternative dissipating solutions*. *Bulletin of the New Zealand Society for Earthquake Engineering*, 2008. **41**(2): p. 90-103.
32. Belleri, A., M.J. Schoettler, J.I. Restrepo, and R.B. Fleischman, *Dynamic behavior of rocking and hybrid cantilever walls in a precast concrete building*. *ACI Structural Journal*, 2014. **111**(3): p. 661-671.
33. Gavridou, S., M. Melek, and J.W. Wallace. *Conventional and unbonded post-tensioned lateral force resisting systems: A comparative assessment of expected performance and losses*. in *NCEE 2014 - 10th U.S. National Conference on Earthquake Engineering: Frontiers of Earthquake Engineering*. 2014.
34. Nagae, T., T. Matsumori, H. Shiohara, T. Kabeyasawa, S. Kono, M. Nishiyama, J. Moehle, J. Wallace, R. Sause, and W. Ghannoum. *The 2010 E-defense shaking table test on four-story reinforced concrete and post-tensioned concrete buildings*. in *NCEE 2014 - 10th U.S. National Conference on Earthquake Engineering: Frontiers of Earthquake Engineering*. 2014.
35. Nazari, M., S. Aaleti, and S. Sritharan. *Shake table testing of unbonded post-tensioned precast concrete walls*. in *NCEE 2014 - 10th U.S. National Conference on Earthquake Engineering: Frontiers of Earthquake Engineering*. 2014.
36. Pampanin, S., *Controversial aspects in seismic assessment and retrofit of structures in modern times: Understanding and implementing lessons from ancient heritage*. *Bulletin of the New Zealand Society for Earthquake Engineering*, 2006. **39**(2): p. 120-134.
37. Housner, G.W., *The behavior of inverted pendulum structures during earthquakes*. *Bulletin of the Seismological Society of America*, 1963. **53**(2): p. 403-417.
38. Skinner, R.I., W.H. Robinson, and G.H. McVerry, *An introduction to seismic isolation*, ed. Wiley. 1993, Chichester, England.
39. Aslam, M., W.G. Godden, and D.T. Scalise, *EARTHQUAKE ROCKING RESPONSE OF RIGID BODIES*. *Journal of the Structural Division-Asce*, 1980. **106**(2): p. 377-392.
40. Park, R., *A perspective on the seismic design of precast concrete structures in New Zealand*. *PCI Journal*, 1995. **40**(3): p. 40-60.
41. Henry, R.S., *Self-centering precast concrete walls for buildings in regions with low to high seismicity*. 2011, University of Auckland. p. 441.
42. Weldon, B.D. and Y.C. Kurama, *Nonlinear behavior of precast concrete coupling beams under lateral loads*. *Journal of Structural Engineering*, 2007. **133**(11): p. 1571-1581.
43. Soudki, K.A., J.S. West, S.H. Rizkalla, and B. Blackett, *Horizontal connections for precast concrete shear wall panels under cyclic shear loading*. *PCI Journal*, 1996. **41**(3): p. 64-80.
44. Fintel, M., *Performance of buildings with shear walls in earthquakes of the last thirty years*. *PCI Journal*, 1995. **40**(3): p. 62-80.

References

45. Kurama, Y., S. Pessiki, R. Sause, and L.W. Lu, *Seismic behavior and design of unbonded post-tensioned precast concrete walls*. PCI Journal, 1999. **44**(3): p. 72-89.
46. Stanton, J., W.C. Stone, and G.S. Cheok, *A hybrid reinforced precast frame for seismic regions*. PCI Journal, 1997. **42**(2): p. 20-32.
47. Priestley, M.J.N., *Overview of PRESSS research program*. PCI Journal, 1991. **36**(4): p. 50-57.
48. Priestley, M.J.N. and J.R. Tao, *Seismic Response of Precast Prestressed Concrete Frames with Partially Debonded Tendons*. PCI Journal, 1993. **38**(1): p. 58-69.
49. Perez, F.J., R. Sause, S. Pessiki, and L.W. Lu, *Lateral load behavior of unbonded post-tensioned precast concrete walls*. Advances in Building Technology, Vols I and II, Proceedings, ed. M. Anson, J.M. Ko, and E.S.S. Lam. 2002, Amsterdam: Elsevier Science Bv. 423-430.
50. Perez, F.J., S. Pessiki, and R. Sause, *Lateral load-behavior of unbonded post-tensioned precast concrete walls with vertical joints*. PCI Journal, 2004. **49**(2): p. 48-+.
51. Perez, F.J., S. Pessiki, and R. Sause, *Seismic design of unbonded post-tensioned precast concrete walls with vertical joint connectors*. PCI Journal, 2004. **49**(1): p. 58-+.
52. Perez, F.J., R. Sause, and S. Pessiki, *Analytical and experimental lateral load Behavior of unbonded posttensioned precast concrete walls*. Journal of Structural Engineering-Asce, 2007. **133**(11): p. 1531-1540.
53. Alexander, N.A., O. Oddbjornsson, C.A. Taylor, H.M. Osinga, and D.E. Kelly, *Exploring the dynamics of a class of post-tensioned, moment resisting frames*. Journal of Sound and Vibration, 2011. **330**(15): p. 3710-3728.
54. Nakaki, S.D., J.F. Stanton, and S. Sritharan, *Overview of the PRESSS five-story precast test building*. PCI Journal, 1999. **44**(2): p. 26-39.
55. Rahman, A.M. and J.I. Restrepo, *Earthquake resistant precast concrete buildings : seismic performance of cantilever walls prestressed using unbonded tendons*. Research report,. 2000, Christchurch, NZ: Dept. of Civil Engineering, University of Canterbury. xvii, 110 p.
56. Kurama, Y.C., *Simplified seismic design approach for friction-damped unbonded post-tensioned precast concrete walls*. ACI Structural Journal, 2001. **98**(5): p. 705-716.
57. Sritharan, S., S. Aaleti, R.S. Henry, K.Y. Liu, and K.C. Tsai, *Introduction to PreWEC and key results of a proof of concept test*. M.J. Nigel Priestley Symposium, North Lake Tahoe, California, August 4-5, 2008, ed. M.J.N. Priestley, M.J. Kowalsky, and S. Sritharan. 2008, Pavia, Italy: IUSS Press. 267.
58. Aaleti, S. and S. Sritharan. *A precast wall with End Columns (PreWEC) for Seismic Applications*. in *8th Pacific Conference on Earthquake Engineering*. 2007. Singapore.
59. Aaleti, S., R.S. Henry, K.Y. Liu, S. Sritharan, and K.C. Tsai. *Experimental investigation of a precast wall with end columns (PreWEC) system*. in *Eleventh East Asia-Pacific Conference on Structural Engineering & Construction (EASEC-11) "Building a Sustainable Environment"*. 2008. Taipei, Taiwan.
60. Pampanin, S., M.J.N. Priestley, and S. Sritharan, *Analytical modelling of the seismic behaviour of precast concrete frames designed with ductile connections*. Journal of Earthquake Engineering, 2001. **5**(3): p. 329-367.
61. Palermo, A., *The use of controlled rocking in the seismic design of bridges*, in *Civil Engineering*. 2004, Technical University of Milan: Milan.
62. Aaleti, S. and S. Sritharan, *A simplified analysis method for characterizing unbonded post-tensioned precast wall systems*. Engineering Structures, 2009. **31**(12): p. 2966-2975.

References

63. Cheng, C.T., *Energy dissipation in rocking bridge piers under free vibration tests*. Earthquake Engineering and Structural Dynamics, 2007. **36**(4): p. 503-518.
64. Mander, J.B., C.-T. Cheng, and National Center for Earthquake Engineering Research (U.S.), *Seismic resistance of bridge piers based on damage avoidance design*. Technical report / National Center for Earthquake Engineering Research. 1997, Buffalo, N.Y.: National Center for Earthquake Engineering Research. 1 v. (various pagings).
65. Makris, N. and D. Konstantinidis, *The rocking spectrum and the limitations of practical design methodologies*. Earthquake Engineering and Structural Dynamics, 2003. **32**(2): p. 265-289.
66. FEMA 356, *Prestandard and commentary for the seismic rehabilitation of buildings*. 2000, Prepared by the American Society of Civil Engineering for the Federal Emergency Management Agency: Washington (DC).
67. Priestley, M.J.N., R.J. Evison, and A.J. Carr, *Seismic response of structures free to rock on their foundations*. Bulletin of the New Zealand National Society for Earthquake Engineering, 1978. **11**(3): p. 141-150.
68. Cheng, C.T., *Shaking table tests of a self-centering designed bridge substructure*. Engineering Structures, 2008. **30**(12): p. 3426-3433.
69. Schoettler, M.J., A. Belleri, Z. Dichuan, J.I. Restrepo, and R.B. Fleischman, *Preliminary results of the shake-table testing for the development of a diaphragm seismic design methodology*. PCI Journal, 2009. **54**(1): p. 100-124.
70. Kurama, Y.C., *Hybrid post-tensioned precast concrete walls for use in seismic regions*. PCI Journal, 2002. **47**(5): p. 36-59.
71. Kurama, Y.C., R. Sause, S. Pessiki, and L.W. Lu, *Seismic response evaluation of unbonded post-tensioned precast walls*. ACI Structural Journal, 2002. **99**(5): p. 641-651.
72. Palermo, A., S. Pampanin, and D. Marriott, *Design, modeling, and experimental response of seismic resistant bridge piers with posttensioned dissipating connections*. Journal of Structural Engineering, 2007. **133**(11): p. 1648-1661.
73. Palermo, A., S. Pampanin, and G.M. Calvi, *Concept and development of hybrid solutions for seismic resistant bridge systems*. Journal of Earthquake Engineering, 2005. **9**(6): p. 899-921.
74. Pennucci, D., G.M. Calvi, and T.J. Sullivan, *Displacement - Based Design of Precast Walls with Additional Dampers*. Journal of Earthquake Engineering, 2009. **13**(sup1): p. 40-65.
75. Ma, Q., G.D. Wight, J. Butterworth, and J.M. Ingham, *Assessment of current procedures for predicting the in-plane behaviour of controlled rocking walls*. Proceedings of the 8th U.S. National Conference on Earthquake Engineering, 2006.
76. Ma, Q.T.M., *The mechanics of rocking structures subjected to ground motion*. 2010, University of Auckland. p. xxxii, 280 p.
77. Prieto, F., P.B. Lourenço, and C.S. Oliveira, *Impulsive Dirac-delta forces in the rocking motion*. Earthquake Engineering and Structural Dynamics, 2004. **33**(7): p. 839-857.
78. Humar, J.L., *Dynamics of structures*. 3rd ed.. ed. 2012, Boca Raton, Fla.: Boca Raton, Fla. : CRC Press - Taylor & Francis Croup c2012.
79. American Society of Civil Engineers. and United States. Federal Emergency Management Agency., *Prestandard and commentary for the seismic rehabilitation of*

References

- buildings*. 2000, Washington, D.C.: Federal Emergency Management Agency. 1 v. (various pagings).
80. Wight, G.D., *Seismic performance of a post-tensioned concrete masonry wall system*. 2006, University of Auckland. p. xx, 200 p.
 81. Rahman, M. and S. Sritharan, *An evaluation of force-based design vs. direct displacement-based design of jointed precast post-tensioned wall systems*. *Earthquake Engineering and Engineering Vibration*, 2006. **5**(2): p. 285-296.
 82. Priestley, M.J.N. and G.A. MacRae, *Seismic tests of precast beam-to-column joint subassemblages with unbonded tendons*. *PCI Journal*, 1996. **41**(1): p. 64-80.
 83. Gulkan, P. and M. Sozen, *Inelastic response of reinforced concrete structures to earthquake motions*. *ACI Journal*, 1974. **71**(12): p. 604-610.
 84. Shibata, A. and M.A. Sozen, *Substitute-structure method for seismic design in R/C*. *Journal of the Structural Division-Asce*, 1976. **102**(1): p. 1-8.
 85. Priestley, M.J.N. and D.N. Grant, *Viscous damping in seismic design and analysis*. *Journal of Earthquake Engineering*, 2005. **9**(SPEC. ISS. 2): p. 229-255.
 86. Jacobsen, L.S. *Damping in composite structures*. in *Proceedings of the 2nd World Conference on Earthquake Engineering*. 1960. Tokyo and Kyoto, Japan.
 87. Rosenblueth, E. and I. Herrera, *On a kind of hysteretic damping*. *Journal of the Engineering Mechanics Division, ASCE*, 1964. **90**(No. EM4): p. 37-48.
 88. Dwairi, H.M., M.J. Kowalsky, and J.M. Nau, *Equivalent damping in support of direct displacement-based design*. *Journal of Earthquake Engineering*, 2007. **11**(4): p. 512-530.
 89. Priestley, M.J.N., *Direct displacement-based design of precast/prestressed concrete buildings*. *PCI Journal*, 2002. **47**(6): p. 66-79.
 90. Christopoulos, C., S. Pampanin, and M.J. Nigel Priestley, *Performance-Based Seismic Response of Frame Structures Including Residual Deformations. Part I: Single-Degree of Freedom Systems*. *Journal of Earthquake Engineering*, 2003. **7**(1): p. 97-118.
 91. Ma, X., E. Borchers, A. Pena, H. Krawinkler, S. Billington, and G. Deierlein, *Report No. 173: Design and behavior of steel shear plates with openings as energy dissipating fuses*. 2011, Department of Civil and Environmental Engineering, Stanford University: Stanford, CA.
 92. Kelly, J.M., R.I. Skinner, and A.J. Heine, *Mechanisms of energy absorption in special devices for use in earthquake resistant structures*. *Bulletin of New Zealand Society for Earthquake Engineering*, 1972. **5**(3).
 93. Shultz, A.E. and R.A. Magana, *Seismic behavior of connections in precast concrete walls*, in *Mete A. Sozen Symposium*. 1996, American Concrete Institute: Farmington Hills, MI.
 94. Baird, A., T. Smith, A. Palermo, and S. Pampanin, *Experimental and numerical study of U-shape flexural plate (UFP) dissipators*, in *New Zealand Society for Earthquake Engineering 2014 Technical Conference and AGM*. 2014, New Zealand Society for Earthquake Engineering: Auckland, New Zealand.
 95. Standards New Zealand, *AS/NZS 3678: Structural steel - Hot-rolled plates, floorplates and slabs*. 2011: Wellington.
 96. Standards New Zealand, *AS/NZS 1594: Hot-rolled steel flat products*. 2002: Wellington.
 97. Bluescope *AS/NZS 3676 - 250 XLERPLATE steel: Revision 1*. 2014.
 98. Bluescope *AS/NZS 1584 - HA250: TRU-SPEC Coil Plate Steel*. 2014.

References

99. Standards Association of Australia, *Metallic materials : tensile testing at ambient temperature*. 4th ed. ed. AS 1391-2007. 2007, Sydney, NSW: Sydney, NSW : Standards Australia 2007.
100. Weman, K., *Welding processes handbook*. 2003, Cambridge, England: CRC Press.
101. Standards New, Z., *Structural design actions : AS/NZS 1170*. 2005, Wellington, N.Z. : Standards New Zealand.
102. Harris, H.G., *Structural modeling and experimental techniques [electronic resource] / Harry G. Harris and Gajanan M. Sabnis*, ed. G.M. Sabnis. 1999: Boca Raton : CRC Press c1999.
103. Mander, J.B., M.J.N. Priestley, and R. Park, *Theoretical stress-strain model for confined concrete*. *Journal of structural engineering New York, N.Y.*, 1988. **114**(8): p. 1804-1826.
104. Sritharan, S., S. Aaleti, and D.J. Thomas, *Seismic analysis and design of precast concrete jointed wall systems*, in *ISU-ERI-Ames Report ERI-07404*. 2007, Department of Civil, Construction and Environmental Engineering, Iowa State University: Ames, IA.
105. Walsh, K.Q. and Y.C. Kurama, *Behavior of unbonded post-tensioning monostrand anchorage systems under monotonic tensile loading*. *PCI Journal*, 2010. **55**(1): p. 97-117.
106. Abramson, D., *Comprehensive Evaluation of Multistrand Post-Tensioning Anchorage Systems for Seismic Resilient Rocking Wall Structures*. 2013, The University of Minnesota.
107. Henry, R.S., S. Aaleti, S. Sritharan, and J.M. Ingham, *Seismic analysis of a low-damage PREcast Wall with End Columns (PreWEC) including interaction with floor diaphragms*. *SESOC Journal*, 2012. **25**(1).
108. New Zealand Standard, *Methods of test for concrete NZS 3112.2:1986 in Tests relating to the determination of strength of concrete*. 1986: Wellington.
109. ACI Innovation Task Group 5., *Acceptance criteria for special unbonded post-tensioned precast structural walls based on validation testing and commentary : an ACI standard*. 2008, Farmington Hills, Mich.: American Concrete Institute. 19 p.
110. Chopra, A.K., *Dynamics of structures : Theory and applications to earthquake engineering*. 3rd ed. 2007, Upper Saddle River, NJ: Prentice Hall. xxxiv, 876 p.
111. Barthes, C., M. Hube, and B. Stojadinovic. *Dynamics of a Post-Tensioned Rocking Block*. in *Proceedings of the 9th US National and 10th Canadian Conference on Earthquake Engineering*. 2010.
112. O'Hagan, J., *Damping*, in *Civil and Environmental Engineering*. Unpublished, The University of Auckland: Auckland.
113. Oyarzo-Vera, C.A., G.H. McVerry, and J.M. Ingham, *Seismic zonation and default suite of ground-motion records for time-history analysis in the North Island of New Zealand*. *Earthquake Spectra*, 2012. **28**(2): p. 667-688.
114. Chase, J.G., N.H. Hudson, J. Lin, R. Elliot, and A. Sim, *Nonlinear shake table identification and control for near-field earthquake testing*. *Journal of Earthquake Engineering*, 2005. **9**(4): p. 461-482.
115. Inman, D.J., *Engineering vibration*. Fourth edition.. ed. 2014: Boston : Pearson. 2014.
116. Thomson, W.T., *Theory of vibration with applications*. 4th ed.. ed. 1993, Englewood Cliffs, N.J.: Englewood Cliffs, N.J. : Prentice Hall ©1993.
117. Macrae, G.A. and K. Kawashima, *Post-earthquake residual displacements of bilinear oscillators*. *Earthquake Engineering and Structural Dynamics*, 1997. **26**(7): p. 701-716.

References

118. Vamvatsikos, D. and C. Allin Cornell, *Incremental dynamic analysis*. Earthquake Engineering and Structural Dynamics, 2002. **31**(3): p. 491-514.
119. Kam, W.Y., S. Pampanin, A. Palermo, and A.J. Carr, *Self-centering structural systems with combination of hysteretic and viscous energy dissipations*. Earthquake Engineering and Structural Dynamics, 2010. **39**(10): p. 1083-1108.
120. The MathWorks Inc, *Matlab R2014a*. 2014: Natick, Massachusetts, United States.
121. Carr, A., *Ruaumoko*, in *Inelastic Dynamic Analysis Program Manual*. 2003, University of Canterbury: Christchurch, New Zealand.
122. Ikhouane, F., J. Rodellar, and J.E. Hurtado, *Analytical Characterization of Hysteresis Loops Described by the Bouc-Wen Model*. Mechanics of Advanced Materials & Structures, 2006. **13**(6): p. 463-472.